UNIVERSITÀ DEGLI STUDI DI MILANO

Facoltà di Scienze e Tecnologie

Dipartimento di Chimica

PhD Course in Industrial Chemistry

CO and CO_2 hydrogenation by Fischer Tropsch synthesis promoted with iron based heterogeneous catalysis: data collection and process design

Tutor: Prof. Carlo Pirola

Co-Tutor: Prof.ssa Claudia Letizia Bianchi

PhD Coordinator: Prof. Laura Prati

PhD student:

Grainca Arian

Matr. R13529

A.I. 2021/2022

XXXVII° Ciclo

1. INTRODUCTION 11

1.1. HISTORIC AND CURRENT ENERGY ISSUES 11
1.1.1. The Transition to Clean Energy 12
1.1.2. Energy Diversification 12
1.2. CLIMATE CHANGE AND CARBON MANAGEMENT 13
1.2.1. Role of CO_2 in Climate Change 13
1.2.2. Lowering CO_2 Emissions on a Small-Scale Basis 15
1.2.3. Carbon Capture and Storage (CCS) 15
1.2.4. Carbon Capture and Utilization (CCU) 15
1.2.5. Toward a Net-Zero Future 15
1.3. CARBON UTILIZATION TECHNOLOGICAL INNOVATIONS 16
1.3.1. Carbon Capture and Utilisation (CCU): From Waste to Resource 16
1.3.2. Thermodynamic and Kinetic Barriers 18
1.3.3. Industrial Processes and Constraints 20
1.3.4. CO_2 Hydrogenation to methanol 24
1.4. FISCHER-TROPSCH PROCESS 25
1.4.1. Discussion of limitations and research future directions 26
1.4.2. Fischer-Tropsch synthesis: Classic Fischer Tropsch process 27
1.4.3. History and Important Dates 29
1.4.4. Industrial Deployments in Practice 30
1.5. TRANSITION TO CO_2 BASED FISCHER-TROPSCH 31
1.5.1. Catalyst Fundamentals 34
1.5.2. Advances in Catalyst Design 35
1.5.2.1. Nanostructured Catalysts 35
1.5.2.2. Bimetallic Catalysts 36
1.5.3. Emerging Approaches in Catalyst Design 37
1.5.4. Reaction Mechanisms and Selectivity 38
1.5.4.1. CO_2 Hydrogenation: Mechanistic Pathways 39
1.5.4.2. Catalyst Influence on Selectivity 41
1.5.5. Reaction from CO_2 to MeOH 41
1.5.6. Effects of Support and Interactive Effects with Metals 41
1.6. LIFE CYCLE ASSESSMENT (LCA) 43
1.6.1. LCA Methodology in Catalyst Development 44
1.6.2. The role of LCA in CO_2 Utilization Technologies 44
1.6.3. Challenges and Outlooks 45
1.7. SAFETY AND OPERABILITY FRAMEWORKS REVIEW 45
1.7.1. HAZOP: Proactive Hazard Identification 46
1.7.2. LOPA: Risks & Safeguards 46
1.8. NEURAL NETWORKS IN CATALYSIS 47
1.9. AIM OF THE WORK AND NOVELTY 48
REFERENCES CHAPTER 1 52

2. EXPERIMENTAL AND RIG SET UP 59

2.1. LAB PLANT 59
2.1.1. Flowmeters and equipment for pressure and temperature regulation 63
2.1.2. Fischer-Tropsch reactor 64
2.1.3. Cold Trap 64
2.1.4. Analytical apparatus 65

2.1.4.1. micro-GC analysis 65
2.1.4.2. GC analysis 66
2.1.4.3. Total Organic Carbon (TOC) 67
2.1.5. Analytical instruments calibration 67
2.1.5.1. Flowmeters calibration 67
2.1.5.2. Micro-GC calibration 69
2.1.5.3. Gas chromatograph calibration 73
2.1.5.4. Total Organic Carbon (TOC) Calibration 75
2.2. FT RIG LABORATORY PROCEDURE ... 76
2.2.1. Catalyst preparation and loading into the FT fixed bed reactor 76
2.2.2. Sample activation and FT catalytic test 77
2.2.3. Procedures to manage the end of the run 77
2.3. LEAKAGE TEST ... 78
2.3.1. Evaluation of the thermodynamic model 80
2.3.2. Fluid dynamic of the rig 83
2.3.3. Reynolds number 83
2.3.4. Evaluation of the type of flow inside the pipe 87
2.4. DATA ELABORATION ... 90
2.4.1. Equations concerning the CO conversion, the mixture composition, the molar flowrates and productivity 90
2.4.2. Equations concerning the heavy phase composition and productivity 91
2.4.3. Equations concerning the selectivity and the C_{2+} yield 92
2.4.4. Equations concerning the calculation of α and ASF algorithms 93
2.5. BENCH PLANT ... 94
3. CATALYSTS SYNTHESIS 99
3.1. METALLOSILICATES ... 99
3.1.1. Synthesis 100
3.1.2. Support synthesis 101
3.1.3. Catalyst synthesis 101
3.2. FE-BASED HYDROTALCITES ... 101
3.2.1. Hydrotalcite synthesis: 103
3.2.1.1. Co-precipitation: 103
3.2.1.2. Impregnation: 104
3.2.2. Ultrasound-assisted synthesis (US): 104
3.2.2.1. Stoichiometric calculation for US synthesized catalysts 107
3.2.3. Ball milling synthesis (BM): 109
3.2.3.1. Stoichiometric calculation for BM synthesized catalysts 111
REFERENCES CHAPTER 3 ... 112
4. CHARACTERIZATION 115
4.1. ANALITICAL TECHNIQUES ... 115
4.1.1. BET 115
4.1.2. TEM 116
4.1.3. SEM-EDS 116
4.1.4. XRD 117
4.1.5. XPS 117
4.1.6. Temperature Programmed Methods 118
4.1.6.1. TPR 118

4.1.6.2. CO_2-TPD 119
4.1.6.3. H_2-TPD 119
4.1.7. ICP 120
4.2. METALLOSILICATES CHARACTERIZATION 120
4.2.1. Unpromoted Metallosilicates 120
4.2.1.1. Surface area 120
4.2.1.2. Morphology SEM-EDS 123
4.2.1.3. XRD 125
4.2.1.4. XPS 127
4.2.2. Promoted Metallosilicates 127
4.2.2.1. SEM EDS 127
4.2.2.2. BET 130
4.2.2.3. XRD 133
4.2.2.4. XPS 136
4.3. HYDROTALCITE CHARACTERIZATION 138
4.3.1. XRD 138
4.3.2. BET 141
4.3.3. TEM-SEM EDS 148
4.3.3.1. TEM/ SEM-EDS Fe30 US and BM 148
4.3.3.2. TEM/ SEM-EDS Fe40 US and BM 150
4.3.3.3. TEM/ SEM-EDS Co33 US and BM 153
4.3.3.4. TEM/ SEM-EDS Co45 US and BM 155
4.3.3.5. TEM/ SEM-EDS of FeZn US and BM 157
4.3.4. SEM EDS Spent catalysts 159
4.3.4.1. Fe-rich hydrotalcites 159
4.3.4.2. Co-containing systems 160
4.3.4.3. FeZn US catalyst 160
4.3.5. Gas-solid interactions 161
4.3.5.1. TPR -H_2 General trends 161
4.3.5.2. Desorption Profiles and CO_2 Uptake 175
4.3.6. ICP 179
REFERENCES CHAPTER 4 181
5. RESULTS 185
5.1. CO REACTION 185
5.1.1. Metallosilicates 185
5.1.1.1. Unpromoted Fe-Based Metallosilicate Catalysts 185
5.1.1.2. Alumina supported and Promoted Fe-based Metallosilicates 188
5.1.2. Hydrotalcite: Fe30 US vs BM 194
5.1.2.1. Performance in Syngas Hydrogenation 194
5.1.2.2. Methane Selectivity and Chain Growth Probability 196
5.1.2.3. Light vs. Heavy Hydrocarbon Selectivity and C_{2+} Yields 197
5.1.2.4. Comparison with Metallosilicate-Supported Catalysts 198
5.2. CO_2 REACTION 200
5.2.1. Promoted Fe-based Metallosilicates 200
5.2.1.1. C_{2+} Hydrocarbon Yields and Product Selectivity 201
5.2.1.2. Light vs. Heavy Hydrocarbon Distribution 203
5.2.1.3. Selectivity to CH_4 and CO 204
5.2.1.4. Effects of Contact Time and Reaction Environment 206

5.2.1.5. Catalyst Stability under CO_2 Hydrogenation 208
5.2.2. Hydrotalcite catalysts 209
5.2.2.1. Test #1 - Standard Conditions (H_2/CO_2 = 3, GHSV 3200 h^{-1}) 210
5.2.2.2. Test #2 - Doubled Contact Time (H_2/CO_2 = 3, GHSV 1600 h^{-1}) 212
5.2.2.3. Test #3 – Increased H_2 content (H_2/CO_2 = 4:1, GHSV 3200 h^{-1}) 214
5.2.2.4. Synthesis of Results and Catalyst Trends 215
5.2.3. Macrokinetic Trends in CO_2 Hydrogenation over Fe-Based Catalysts 217
5.2.3.1. Activation Energies and Dual Arrhenius Behavior 217
5.2.4. CO_2 Hydrogenation on Bench-Scale 222
5.2.4.1. Fe30US Catalyst: Effect of Temperature and Pressure 222
5.2.4.2. FeZnUS Catalyst: Effect of Temperature and Pressure 225
5.2.5. Performance of Fe30 in Lab-Scale vs. Bench-Scale Reactors 228
5.2.5.1. Reactor and Catalyst Overview 228
5.2.5.2. CO_2 Conversion Trends 229
5.2.5.3. Selectivity: CH_4 vs. CO (RWGS vs. FT Pathways) 229
5.2.5.4. Light (C_2-C_6) vs. Heavy (C_{7+}) Hydrocarbon Distribution 230
5.3. CONCLUSION ... 231
REFERENCE CHAPTER 5 ... 233
6. SAFETY AND OPERABILITY FRAMEWORKS 241
6.1. HAZARD EVALUATION PROCEDURES ... 241
6.2. INTERACTION MATRIX ... 242
6.3. HAZARD AND OPERABILITY ANALYSIS (HAZOP) ... 243
6.3.1. Roles during the HAZOP 243
6.3.2. Performing the HAZOP analysis 244
6.3.3. HAZOP drawbacks 246
6.4. FUNCTIONAL SAFETY AND LAYER OF PROTECTION ANALYSIS (LOPA) ... 246
6.4.1. Definitions 246
6.4.2. The procedure of LOPA 247
6.4.3. Limitations of LOPA 249
6.4.4. Human factor 250
6.4.5. Equipment for pressure relief 251
6.4.6. Control loop, BPCS and safety interlock 252
6.4.7. MooN structure 252
6.4.8. Ventilation system: Hood 253
6.4.9. Useful IPLs: AutoStart of standby equipment and Backup utility supplies 253
6.5. CASE STUDY: THE FISCHER-TROPSCH SYNTHESIS ... 254
6.5.1. Description of the FT pilot plant 254
6.5.2. Interaction matrix 255
6.5.2.1. Compatibility between Chemicals and Materials 256
6.5.2.2. Compatibility among Chemicals 256
6.5.3. Hazard and Operability Analysis (HAZOP) 257
6.5.4. Case study: LOPA 260
6.5.4.1. Deviations due to human error 262
6.5.4.2. System failure 265
6.5.4.3. Deviations in Node 1: Feeding section 266
6.5.4.4. Deviations in Node 2: the reaction section 273
6.5.4.5. Deviations in Node 3: the separation section 287
6.5.4.6. Deviations in Node 4: the analysis of the gaseous phase. 290

6.5.5. Final comments on the protection layers 290
6.5.6. Conclusions 292
APPENDIX **294**
REFERENCES CHAPTER 6 **337**
7. LIFE CYCLE ASSESSMENT (LCA) **341**
7.1. LCA METHODOLOGY **342**
7.1.1. System Boundaries 342
7.1.2. Functional Units 343
7.1.3. Inventory Data 343
7.2. RESULTS AND DISCUSSION **344**
7.2.1. Environmental impact for catalysts production 344
7.2.1.1. IPCC 2021 GWP100 Analysis 344
7.2.1.2. Cumulative Energy Demand (CED) Analysis 345
7.2.1.3. CML-IA Baseline Analysis 346
7.2.2. Environmental impact for FT products synthesis 348
7.2.2.1. Catalytic results 348
7.2.2.2. CML-IA Baseline Analysis 350
7.2.2.3. IPCC 2021 GWP100 Analysis 352
7.2.2.4. Cumulative Energy Demand (CED) Analysis 352
7.2.3. Carbon Neutrality evaluations 353
7.3. CONCLUSION **356**
REFERENCE CHAPTER 7 **357**
8. NEURAL NETWORK MODELLING **359**
8.1. NEURAL NETWORK ARCHITECTURE **359**
8.1.1. Input variable definition 360
8.1.2. Dataset Compilation for Artificial Neural Network Training 361
8.1.3. Results and Discussion 361
8.1.4. Conclusions 363
8.2. RANDOM FOREST MODELING **363**
8.2.1. Results and Discussion 364
8.2.2. Comparison with ANN Results 368
8.2.3. Implications for Catalyst Design Workflows 368
8.2.4. Conclusion 369
REFERENCE CHAPTER 8 **373**

Abstract

The reduction of CO_2 emissions into the atmosphere has become a global priority, given the crucial role of this greenhouse gas in climate change. A promising approach to mitigate CO_2 is its conversion into fuels and chemicals through processes such as Fischer–Tropsch (FT) synthesis. Traditionally, FT relies on syngas (CO/H_2) over transition-metal catalysts, but the direct hydrogenation of CO_2 has been less explored, particularly with Fe-based heterogeneous catalysts. Iron is an abundant and inexpensive metal, already known for its high activity in conventional FT from CO. This research aims to develop novel Fe-based catalysts effective in both CO and CO_2 derived FT, while also addressing the interconnected challenges of environmental sustainability, operational safety, and predictive process modeling. The ultimate goal is to provide a holistic solution for upgrading CO_2 into hydrocarbons, bridging existing gaps in the development of materials (e.g., Fe-based metallosilicates and hydrotalcites) that have been scarcely investigated to date. To this end, innovative iron-based catalysts were synthesized, tested under CO and CO_2 FT conditions, and evaluated through Life Cycle Assessment (LCA), HAZOP/LOPA safety analysis, and artificial intelligence tools (artificial neural networks) for performance optimization. This integrated approach provides a comprehensive perspective on CO/CO_2 conversion, representing an important step toward the practical implementation of Carbon Capture and Utilization (CCU) technologies.

Two main classes of Fe-based heterogeneous catalysts were investigated: (1) mixed oxides derived from hydrotalcites (e.g. Mg-Fe-Cu), synthesized via ultrasound-assisted co-precipitation (US) and, in some cases, subjected to ball milling (BM), and (2) iron catalysts supported on mesoporous metallosilicates, synthesized by non-hydrolytic sol-gel routes. All catalysts were promoted with potassium and copper, both known to enhance activity and selectivity toward heavier FT hydrocarbons. Potassium acts as an electronic promoter, suppressing methane formation and favouring carbon-chain growth, while the Mg-Fe based mixed oxide matrix provides basicity, enhancing the Water Gas Shift (WGS) reaction and thereby benefiting CO_2 conversion.

Catalytic testing in a fixed-bed reactor yielded highly promising results. With syngas (CO/H_2), the Fe-based catalysts reached high CO conversion levels (up to ~95–98% at 300 °C) and notable selectivity toward liquid hydrocarbons (C_5^+ fraction, ~40–50 wt%), while maintaining low methane production (<5%). For instance, a hydrotalcite-derived Mg-Fe-Cu/K catalyst (denoted Fe30) achieved ~96% CO conversion at 300 °C, with ~40% selectivity to the heavy fraction and ~5% to methane. These performances are comparable or superior to those reported for reference systems: Fe30 matched the activity of Fe/K/Cu catalysts supported on conventional oxides (alumina), reaching >80% conversion at lower temperatures, and outperformed analogous catalysts on mesoporous silicates in terms of stability and selectivity toward heavy products. This confirms that the hydrotalcite-derived nanostructure provides excellent dispersion of active sites and a favorable chemical environment which promote FT reactivity while minimizing undesired byproducts. In direct CO_2 hydrogenation, the iron catalysts displayed significant activity, although the reaction pathway is strongly coupled with the reverse WGS reaction ($CO_2 \rightarrow CO$), resulting in notable co-production of CO. Accordingly, CO_2 feeds yielded higher selectivity to CO and CH_4 compared with syngas operation. However, introducing cobalt into the catalyst

formulation substantially improved liquid hydrocarbon yields: Mg-Fe-Co-Cu/K catalyst (denoted Co45, containing ~42% Co and ~30% Fe) produced a larger C_{7}^{+} fraction and fewer gaseous byproducts than pure Fe catalysts, particularly at higher temperatures. Thus, Co45 proved more efficient in directly hydrogenating CO_2 into long-chain hydrocarbons, with lower CO selectivity and reduced methane formation. This behavior is attributed to cobalt's intrinsic higher activity in FT from CO_2, which remains effective even at 350 °C, whereas iron tends to favor secondary methanation and Boudouard (carbon deposition) reactions under the same conditions. Overall, catalyst composition optimization (Fe ratio, Co incorporation, K promotion) was crucial: the Fe-Co catalyst provided the best balance, maximizing heavy hydrocarbon production while minimizing undesired gaseous emissions, and highlighted the trade-off between catalytic performance and the environmental cost of materials (given cobalt's higher extraction impact relative to iron). The experimental dataset generated thus constitutes a valuable benchmark for both sustainability evaluation and predictive modeling (see chapter 5).

Given the strongly exothermic and high-pressure nature of FT synthesis, safety considerations for the laboratory-scale pilot unit were systematically addressed using industrially derived methodologies. A Hazard and Operability (HAZOP) study was conducted on the FT unit, followed by a Layer of Protection Analysis (LOPA), with the aim of identifying potential hazard scenarios and verifying the adequacy of existing safeguards. This represents an innovative application of such frameworks in an academic setting, motivated by the frequent manual interventions and transient operations typical of laboratory plants. The HAZOP identified several critical deviations from normal operation, such as risks of H_2/CO gas leaks, line blockages, or overheating, particularly in the FT reactor and feeding system, which emerged as the most vulnerable nodes. In some cases, existing protections were found to be insufficient to mitigate the consequences of potential incidents. The subsequent LOPA quantified the level of additional protection required, identifying and prioritizing further independent protection layers. Key recommendations included: increasing automation (to reduce reliance on manual operations), implementing safety interlocks and automatic control loops (e.g., shutdown valves upon leak detection, pressure/temperature control loops), and adding redundancy to critical components. Passive measures were also emphasized, such as improved ventilation (exhaust hoods, fume extraction) and enhanced operator training for correct handling during operation and emergencies. The adoption of these strategies will minimize accident risks and unplanned downtimes, bringing the laboratory-scale setup closer to industrial safety standards. In conclusion, the combined HAZOP–LOPA approach in an academic environment proved effective in raising safety standards and in creating a replicable framework for managing operational risks in complex experimental projects like FT synthesis.

To evaluate the overall sustainability of the process and developed materials, a Life Cycle Assessment (LCA) was carried out. The LCA covered both the production phase of catalysts (from raw material extraction through Fe-based catalyst synthesis) and the operational phase of CO_2 FT conversion into hydrocarbons. Three representative catalysts were compared: Fe30, Fe40, and Co45 (all Cu/K-promoted, with varying Fe/Co ratios) the same tested experimentally, assessing their environmental footprint under optimal operating conditions (350 °C) for the production of 1 kg of C_{2}^{+} hydrocarbons. The analysis was conducted with SimaPro software (CML-IA method, using IPCC GWP100 and CED indicators), evaluating impact categories such

as Global Warming Potential (GWP), Cumulative Energy Demand (CED), and toxicity/ecotoxicity metrics. Results clearly indicated that catalytic efficiency strongly dictates environmental performance: the less efficient Fe40 catalyst generated the highest impacts across nearly all categories. For instance, Fe40 exhibited the largest carbon footprint (~2.39 kg CO_2-eq per kg of product), compared with ~1.31 kg for Fe30 and ~0.98 kg for Co45. In other words, for the same quantity of synthetic fuel, Fe40 contributed roughly double the greenhouse gas emissions of the cobalt-containing catalyst. Similarly, Fe40 showed higher impacts in other categories, e.g., ~67% greater abiotic depletion relative to Co45 and ~41% greater than Fe30. This disparity is due to Fe40's lower catalytic efficiency, which demands higher energy inputs and produces more byproducts per unit of fuel synthesized. Conversely, Co45, despite incorporating cobalt, a critical and environmentally costly metal, compensated through its high activity in operation, leading to lower per-product impacts. In summary, the LCA highlighted a performance vs. environmental impact trade-off: improving catalytic activity (e.g., through Co promotion) can significantly reduce lifecycle impacts per product, even when catalyst production has higher initial burdens. These findings underscore the importance of integrating environmental assessment early in catalyst and process design. The Fe/Co combination emerged as the most promising pathway, suggesting directions for future development of FT catalysts that are both efficient and sustainable.

In parallel with experiments, machine learning (ML) techniques were applied to model and predict FT process performance. Specifically, an Artificial Neural Network (ANN) was trained on the experimental dataset to correlate input variables (operating parameters such as temperature, pressure, GHSV, H_2/CO_2 ratio, and catalyst composition) with performance outputs (CO_2 conversion, CH_4 selectivity, C_2–C_4 fraction, C_5^+ fraction, CO selectivity). The ANN architecture was optimized to minimize prediction error and capture nonlinear relationships, thus providing an alternative predictive tool to conventional kinetic models that require detailed mechanistic knowledge. ANN results showed good accuracy in predicting certain key aspects (e.g., CO_2 conversion and C_2-C_4 selectivity), consistent with trends reported in the literature. Sensitivity analysis confirmed the positive influence of higher Fe content and K promotion in increasing liquid hydrocarbon yields and conversion efficiency. However, limitations emerged: the ANN struggled to accurately predict heavy hydrocarbon (C_5^+) formation and CO selectivity, likely due to the limited size and diversity of experimental data. This suggests that future models should incorporate larger datasets and potentially more advanced architectures (e.g., hybrid AI or deep learning). To complement the ANN, a Random Forest (RF) model was also applied on the same dataset. RF proved particularly robust with limited data, mitigating overfitting risks through ensemble averaging. While RF predictions were comparable in accuracy to ANN, it offered a distinct advantage in interpretability: feature-importance analysis identified which operating conditions and catalyst properties most strongly affected outcomes, aligning well with chemical intuition (e.g., temperature and catalyst composition as dominant factors). Thus, ML models demonstrated their potential as decision-support tools, enabling rapid virtual screening of catalyst/process combinations and accelerating the optimization cycle.

In conclusion, this thesis develops a comprehensive framework for the sustainable conversion of CO_2 into fuels, combining innovation in catalyst design, process optimization, and integrated assessments of safety and environmental impacts. Results demonstrate that Fe-based catalysts, suitably promoted, can achieve high CO_2 FT performance, while Co incorporation further enhances liquid fuel yields and reduces per-product impacts. In parallel, rigorous HAZOP/LOPA studies ensure that such processes can be conducted safely even at laboratory scale, and LCA provides quantitative guidance to steer technological choices toward genuinely sustainable solutions. Finally, the application of AI-based predictive tools offers new perspectives for accelerating catalyst and process development, uncovering hidden correlations, and directing future experimental efforts more effectively. The synergy of these disciplines: industrial chemistry, safety engineering, environmental analysis, and data science, constitutes a holistic and highly innovative approach. This integrated vision facilitates the transition of CO_2-to-fuel FT technology from laboratory to industry, contributing to circular economy goals and decarbonization. Ultimately, the work lays the foundation for CO_2-to-fuels systems that are more efficient, safe, and sustainable, outlining strategies with tangible impact in the context of the ongoing energy and ecological transition.

1. INTRODUCTION

1.1. Historic and Current Energy Issues

The global energy sector has changed more this century alone than perhaps any other economic trade since the dawn of civilization due to advancements in technology, growth and expansion. Since the beginning of the 20th century, coal, oil and natural gas have been the biggest sources of energy worldwide following their deployment in global industrialization and urbanization efforts. Their high energy density and ease of accessibility meant that they were the preferred fuel for use in modern economies, despite their ultimate depletion. Fossil fuels supplied over 80% of global energy consumption by the mid-20th century, a proportion that remains today despite growing evidence of their adverse climate impacts [1].

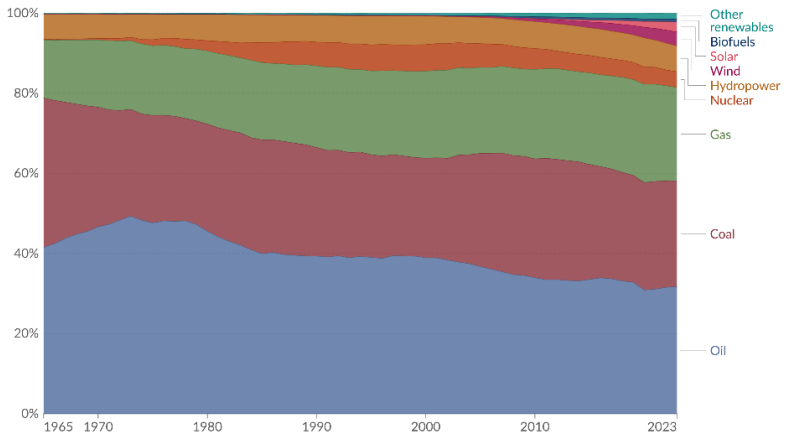

Figure 1.1. Historical trends in global energy consumption by source, Energy Institute - Statistical Review of World Energy (2024) - with major processing by Our World in Data.

Recently, there has been a concern over rising environmental costs. This has not been without a price, however. Their harvesting, processing and use results in significant emissions of greenhouse gases (GHGs) - most notably carbon dioxide (CO_2), the principal driver of climate change. Fossil fuel use is estimated to be responsible for almost 75% of global anthropogenic CO_2 emissions [2].

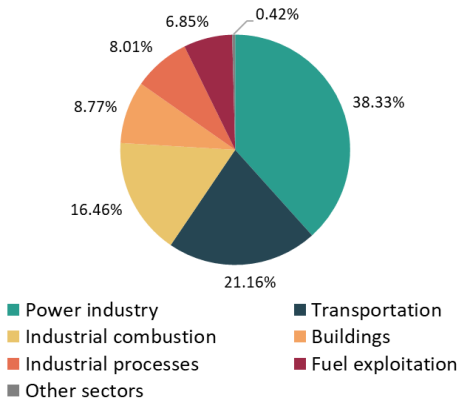

Figure 1.2. Comparative chart of global CO_2 emissions by sector.

That warmth goes direct than is mirrored on the part of Earth, fuelling global warming plus temperature rise, oceans to understand that climb, as well as sending an increasing number of hands in regard impact. The Intergovernmental Panel on Climate Change (IPCC) has estimated

that the global mean surface temperature has risen by 1.1°C above pre-industrial levels, where the central projections are for increase in this wndtar to continue unless rapid and decisive action is taken [3]. As much as these problems, the geopolitical and economic hazards posed by our fossil fuel addiction have grown more obvious. The oil price shocks, resource constraints and political instability in the fossil fuel-rich regions expose how vulnerable fuels from the earth still make our energy systems. Some of the challenges have actually promoted a global move to energy solutions that will be much more resilient and sustainable.

1.1.1. The Transition to Clean Energy

Consequently, the late 20th and early 21st centuries have seen a trend moving toward renewable energy sources to address some of these problems. Technological progress has been exponential in fields like wind, solar, and hydroelectric power driven by falling costs, advances in technology and enabling policy. This includes a price decrease of over 80% for utility-scale solar photovoltaic (PV) systems since 2010, making solar energy one of the most cost-competitive sources of new electricity generation in many countries [4]. And wind power installations have increased to more than 800 GW worldwide by 2021 [5].

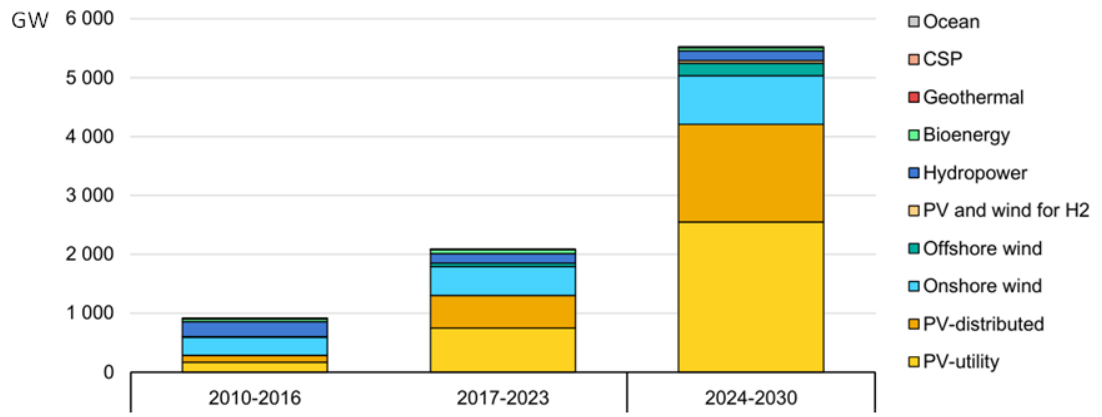

Figure 1.3. IEA (2024), Renewables 2024, Paris https://www.iea.org/reports/renewables-2024, Licence: CC BY 4.0.

In addition, unlike other renewable energy sources, renewables can decouple the production of energy with GHG emissions. The incorporation of distributed energy (DE) into energy systems is a prerequisite to meet objectives defined in international agreements such as the Paris Agreement, which obliges all signatory States to maintain global temperature increase at well below 2°C above pre-industrial levels [6]. The transition to renewables is anything but simple, though. This means innovations will be needed in both storage technologies that can efficiently smooth the variable output of solar and wind energy, as well as flexible grid systems to manage reliability and stability.

1.1.2. Energy Diversification

While renewables are forecasted to be the major component of our energy mix moving forward, we must have a blend of energy sources in order to ensure that we maintain energy security and sustainability. Carbon capture and utilization (CCU) combined with energy carriers such as hydrogen are emerging as a complementary alternative. CCU technologies can be a part of the solution for decreasing emissions from fossil-based processes by converting CO_2 to utilize valuable products and playing important rule in circular carbon economy.

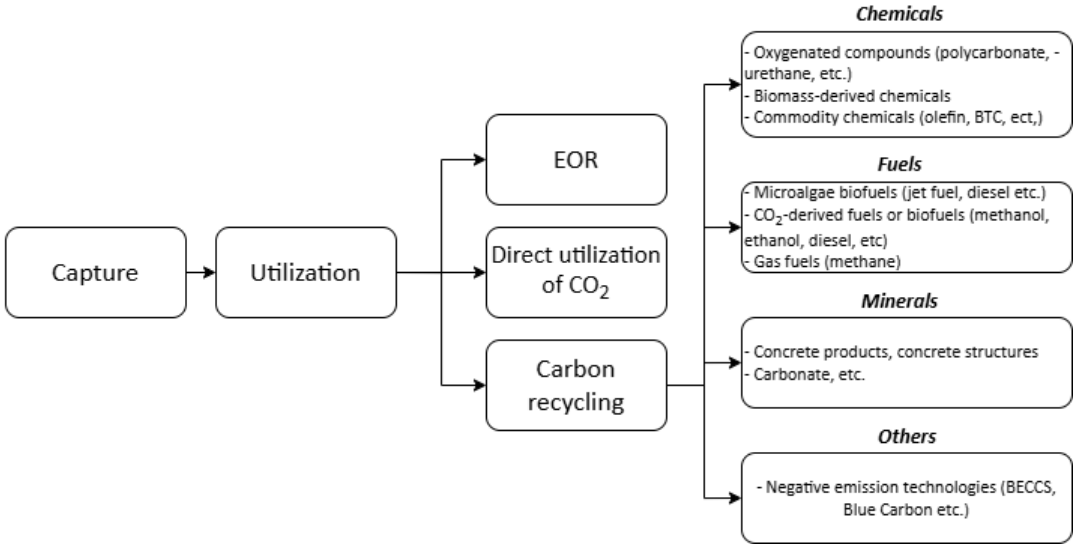

Figure 1.4. Summary of CO_2 utilization pathways and products.

Hydrogen, whether green (generated from renewables) or blue (produced by fossil fuels accompanied by carbon capture), provides an opportunity to decarbonize hard-to-abate sectors as heavy industry and aviation [7].

Bioenergy as renewable carbon source Moreover, energy diversification must of course also account for bioenergy. Bioenergy with carbon capture and storage (BECCS) via modern bioenergy systems that incorporate biomaterials conversion provides a pathway to achieve negative emissions, which is essential for achieving mid-century net-zero targets. That shift is part of a larger trend moving, however tentatively, toward energy systems that respect the environment without hampering economic growth.

1.2. Climate Change and Carbon Management

1.2.1. Role of CO_2 in Climate Change

By far the most important greenhouse gas (GHG) resulting from human activity in terms of its 100-year global warming potential (GWP) is carbon dioxide (CO_2). Although other gases, such as methane (CH_4) and nitrous oxide (N_2O), have higher global warming potentials than CO_2 does, the vast amount of CO_2 emissions result more from being the workhorse that drives global warming. Since the Industrial Revolution, concentration levels of atmospheric CO_2 have increased by over 44 percent from about 280 ppm to well over 400 ppm [8]. The Earth has now accumulated over a century of scientific research showing that the CO_2 concentration in the atmosphere is much higher now than it was two million years ago, and its increase correlates very strongly with the combustion of fossil fuels, deforestation and industrial activities. Higher CO_2 levels provide for the enhanced greenhouse effect, which keeps heat within earth's atmosphere, thus heating up the planet. The IPCC predicts that keeping the global temperature rise below 1.5 °C from pre-industrial levels requires reducing global human-induced net CO_2 emissions by about 45% as of 2030 compared to 2010 through achieving net zero around mid-century [3]. Failure to meet these targets would risk serious consequences that are very likely irreversible, such as sea-level rise, the loss of biodiversity and disruption to global food systems.

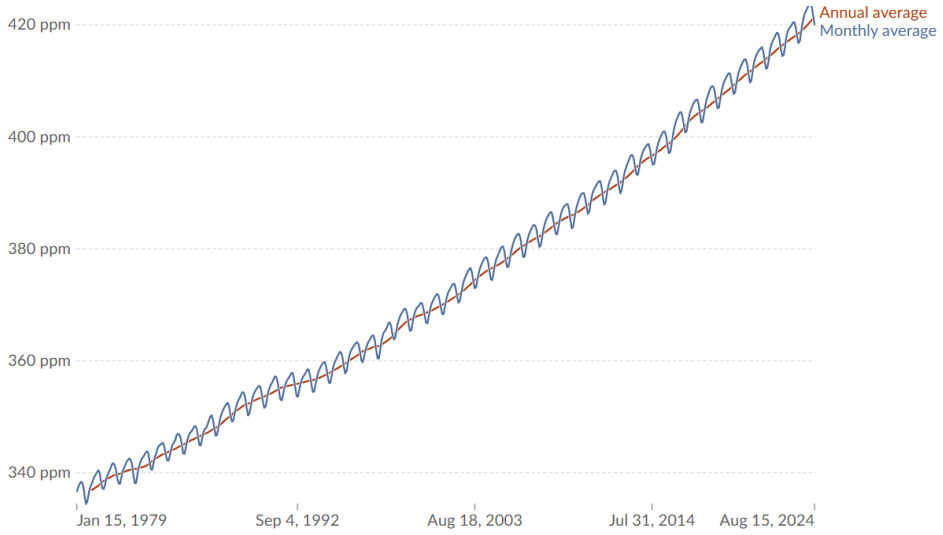

Figure 1.5. Historical trends in atmospheric CO_2 concentration and global temperature; NOAA Global Monitoring Laboratory - Trends in Atmospheric Carbon Dioxide (2024) - with major processing by Our World in Data

Category	Impacts	Examples
Global CO_2 Concentrations	Reached 420 ppm in 2023, with an 11.4% increase over 20 years	Comparable CO_2 levels were last seen 3-5 million years ago when temperatures were 2-3°C higher, and sea levels were 10-20 m higher.
Rate of Increase	2023 CO_2 growth: 2.3 ppm annual increase	Marks the 12th consecutive year with an increase exceeding 2 ppm.
Fossil Fuel Emissions	high emissions dominant driver of rising CO_2 levels	Fossil fuel combustion remains the primary source of CO_2.
Natural Feedback Loops	El Niño effects and wildfires amplified CO_2 levels in 2023	Fires contributed 16% more emissions than average; Canada's wildfire season was its worst on record.
Carbon Sinks	Ocean and land absorbed ~50% of emissions with reduced efficiency	Land uptake reduced due to droughts and fires; warmer oceans absorbed less CO_2.
Methane and N_2O Levels	Methane reached 1,934 ppb, nitrous oxide 336.9 ppb, 265% and 125% of pre-industrial levels	Methane contributes heavily to near-term warming; agriculture is a key source of N_2O emissions.
Radiative Forcing	Increased by 51.5% since 1990	CO_2 accounted for 81% of this increase, driving significant warming.
Natural Disruptions	Transition from La Niña to El Niño reduced CO_2 absorption in 2023	Vegetation fires and droughts further disrupted natural carbon sinks.
Wildfire Emissions	2023 fire carbon emissions were 16% above average, seventh highest since 2003	Australia’s driest period and Canada’s worst wildfire season exacerbated the problem.
Impact on Temperature	Long CO_2 atmospheric lifetime commits the planet to decades of warming, even with net-zero emissions	Temperature levels observed today will persist for decades due to CO_2's slow removal from the atmosphere.

Table 1.1. Key impacts of rising CO_2 levels.

Various climate strategies have been formulated in order to alleviate CO_2 emissions, categorized into mitigation (reduction), capture and storage, and utilization.

1.2.2. Lowering CO_2 Emissions on a Small-Scale Basis

At the same time, however, the best way to confront emissions of CO_2 is by reducing dependence on fossil fuels, which involves improving energy efficiency, increasing the deployment of renewable energy sources as well as electrifying transport and industry. In addition, in many areas policies such as carbon pricing and renewable energy subsidies have already helped to move the needle, with noted declines in CO_2 emissions intensity [9]. These alone wills do not cover sectors that are difficult to address, such as cement production and aviation.

1.2.3. Carbon Capture and Storage (CCS)

CCS technologies work by capturing CO_2 at the point of emission and storing it securely in geological formations, thus keeping CO_2 out of the atmosphere. Examples of CCS methods for reducing traditional CO_2 emissions are post-combustion capture, pre-combustion capture, and oxy-fuel combustion. Post-combustion capture works by chemically capturing CO_2 from flue gases-suitable for the retrofit of existing power plants and industrial facilities (e.g. using chemical solvents). The CO_2 is captured, compressed and then injected into underground reservoirs, (E.g. depleted oil and gas fields or saline aquifers). Despite its promise, CCS is plagued by issues of cost, energy penalty, and consumer rejection of geologic sequestration. However, large-scale demonstration projects such as the Sleipner CO_2 storage site in Norway demonstrate that it is a viable approach [10].

1.2.4. Carbon Capture and Utilization (CCU)

CCU, on the other hand, aims at converting and make use of CO_2 into value-added products connected to industrial processes in order to realize a circular carbon economy but not store it necessarily. Examples of CCU applications include:

- Fuel production: CO_2 is converted to synthetic fuels or methane to be stored and used for energy transportation.
- Chemical synthesis: Manufactured production of methanol, urea and other industrial chemicals from CO_2.
- Materials: Carbonates for construction materials (concrete)

In addition to reducing emissions, CCU can offer economic incentives that are especially appealing when applied within sectors looking for sustainable feedstocks. Still, the scalability of CCU is limited by a lack of renewable hydrogen and cost-intensive CO_2 conversion processes.

1.2.5. Toward a Net-Zero Future

A mix of these pathways, aided by technological progress, policy frameworks, and collaboration on the global scale is essential to move towards net-zero emissions. UVI or Universal Uninterruptible Integration of renewable electricity with CCU and CCS may promise to address both energy decarbonization and carbon removal. Examples include Bioenergy with Carbon Capture and Storage (BECCS) which can provide negative emissions to compensate for residual sectoral emissions, such as those from difficult-to-abate sectors.

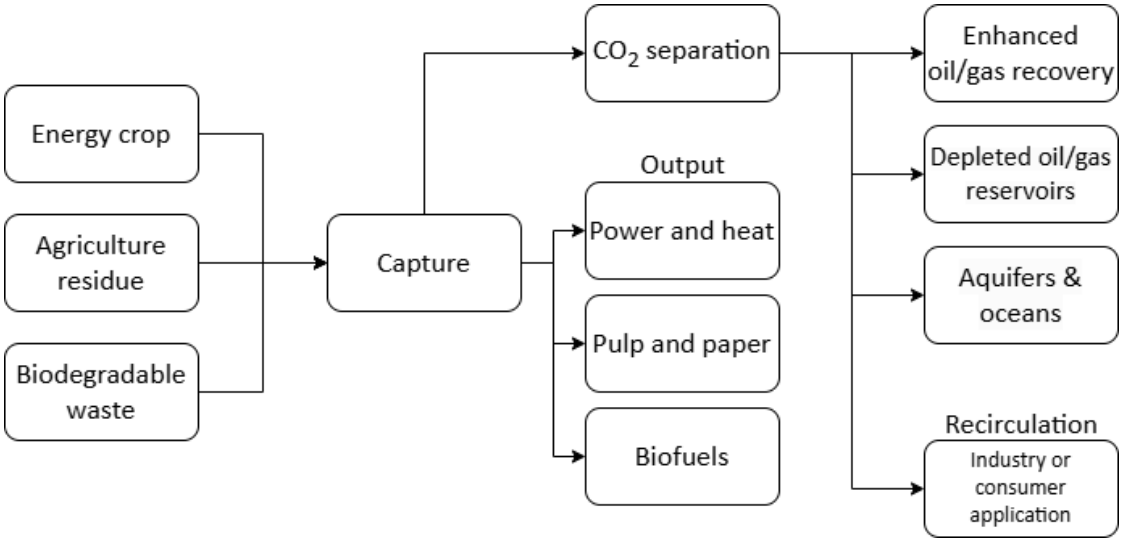

Figure 1.6. Integration of BECCS in net-zero strategies.

The CO_2 management technologies have drastically improved in only a few years; the advent of direct air capture (DAC) systems reflects the fast-moving nature of this domain. DAC systems can operate in a distributed fashion and capture CO_2 directly from the atmosphere, providing an attractive means of scaling to sectors that lack point-source emissions. Yet, the energy-intensive and cost challenge of utilizing these technologies have prevented their adoption for most applications [11]. But given the increasing global emissions, it is inevitable that CO_2 management technologies will play an expanding role. These are innovation and economy strategies as much as they are mitigation.

1.3. Carbon Utilization Technological Innovations

The increasing need to address climate change has led to significant developments of technologies for CO_2 capture, conversion and utilization. These innovations work to create a link between large industrial processes and the environment, in an effort to remove greenhouse gas (GHG) emissions from the atmosphere and convert them into value outlets for emitted CO_2. Among them, Carbon Capture and Utilization (CCU), complementing renewable electricity integration, has emerged as a game-changing alternative route, augmented by its potential for scalability and widespread application.

1.3.1. Carbon Capture and Utilisation (CCU): From Waste to Resource

The Pulawy or Drax projects are examples of CCU and can be considered as a change of direction in the way carbon may possibly be managed rather than storing it indefinitely. This approach follows the tenets of circular economy, turning a pollutant into a product. These processes have been greatly enhanced in terms of efficiency, scalability and economics with the recent developments in CCU. An area within CCU that shows a great promise is electrochemical CO_2 reduction, where renewable electricity is used to convert CO_2 into fuels and chemicals such as formic acid, carbon monoxide (CO) and ethylene. Over the years, catalysts have been improved with the advances in catalytic materials such as metal-organic frameworks (MOFs), and nanostructured catalysts leading to improvements in the efficiency and selectivity of these reactions [12]. Copper-based catalysts, for example, are very active in the production of multi-carbon products and therefore have strong potential for industrial application. Photocatalytic CO_2

reduction is another emerging technology, which emulates the nature photosynthesis to generate hydrocarbons by using the sunlight as a driver for conversion of CO_2 and water. Perfect examples occurred with the emergence of novel semiconductor materials such as plasmonic nanoparticles doped titanium dioxide (TiO_2) which enhanced light absorption and rates of reaction. Although the further development of these systems is still in their early stages, but they have a great potential for economically operated and large scaled CO_2 utilisation may be to regions with abundance solar resources [13].

CCU technologies will work best if partnered with the rising power of renewable energy sources: solar, wind, & hydro. Not only does renewable energy supply the electricity needed for CO_2 conversion, but it ensures these processes support overall net reductions in emissions.

An example of one of the most important applications is the production of green hydrogen obtained by water electrolysis with electricity coming from renewable sources. Green hydrogen provides an essential resource for the use of CO_2 in hydrogenation reactions, which can be used to synthesize methanol, methane or other hydrocarbons. This holistic approach coupling green hydrogen production with CCU technologies comes closest to a no-waste solution in which all carbon is re-used, either in reduced form or bound.

On top of that, power-to-X (PtX) technologies are also increasingly applied to convert excessive available renewable electricity into chemical energy. These are a category of processes in which electricity is used to produce hydrogen or syngas, which may then be combined with CO_2 to create liquid fuels like gasoline, ammonia and synthetic natural gas. These technologies help in decarbonizing energy system, enabling renewable energy to be stored and transported using chemicals which will also contribute to stabilizing the grid and increasing security of supply [14].

In industry sectors with high CO_2 emissions, technological developments in CCU are increasingly being incorporated into industrial processes to enable decarbonization. Such endeavours are being pursued within the cement and steel production industries, which together emit around 10% of global CO_2 emissions and have been investigating new processes where CO_2 serving as feedstock for entirely novel materials - carbonated concrete, synthetic aggregates [15]. Similarly, chemical manufacturers are adopting catalytic and electrochemical processes to produce methanol and urea from captured CO_2, reducing their reliance on fossil-derived feedstocks.

But cutting emissions isn't the only potential benefit of these new technologies. When renewable energy is combined with CCU, industries can go a long way toward meeting commitments made under the Paris Agreement and other global climate agreements. These break-throughs also contribute to innovation and economic growth, developing new markets for sustainable fuels and materials which in turn provide a solution to the dual challenge of energy transition and carbon mitigation. Nevertheless, large scale climate intervention using CCU technologies faces a number of challenges, high capital costs, energy efficiency limitations and policy uncertainties. Further R&D, coupled with supporting legislation, will be vital to enabling these technologies to reach their full development potential and have a positive impact on sustainability.

1.3.2. Thermodynamic and Kinetic Barriers

Heavy-metal catalysts have been used for the conversion of carbon dioxide (CO_2) to chemicals and fuels, but these processes decrease the attractiveness in terms of cost-effectiveness and environmental sustainability. CO_2 is the most oxidized form of carbon and has a high bond dissociation energy of 805 kJ/mol, rendering its reduction to reduced compounds thermodynamically unfavourable and kinetically challenging. To break through these limits, more inventive strategies in catalyst design, energy input and process operation will be the next developing direction.

The thermodynamic restrictions on CO_2 utilization are related to the Gibbs free energy of reduction reactions. In the case of CO_2 hydrogenation, to produce methane (CH_4) or alternatively methanol (CH_3OH), requires substantial energy inputs to drive the reaction toward the desired products. Methane formation is a slightly exergonic reaction, as the standard Gibbs free energy difference ($\Delta G°$) for it is −130.8 kJ/mol. Yet, at low temperature, the equilibrium is located very far to the reactants side. Thus, very high operation temperature as well as pressure required them to carry out the conversions in a significant extent [16].

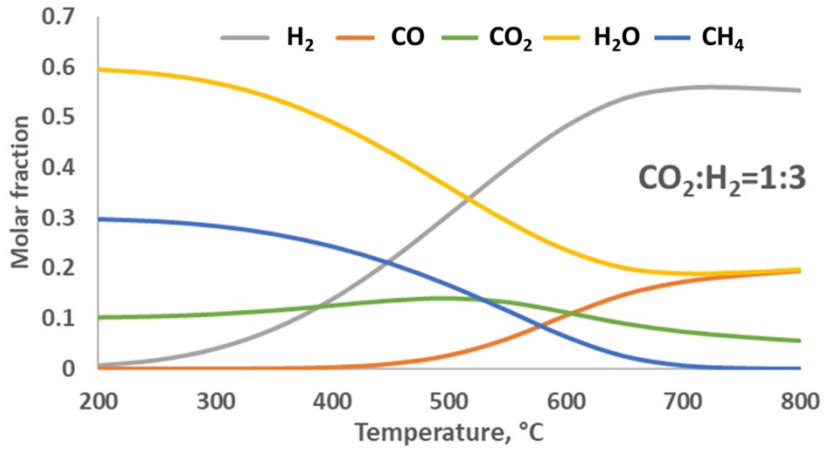

Figure 1.7. Thermodynamic profile of CO_2 hydrogenation reactions.

Likewise, the formation of CO (CO_2 reduction to CO) by reverse water-gas shift (RWGS), it is also an endothermic process with $\Delta H° = +41.2$ kJ/mol [17]. Additionally, it is technically difficult and energy consuming to shift the equilibrium towards CO production, which requires temperatures above 700°C [18]. Moreover, multi-carbon compound production like ethanol or ethylene is associated with complex reaction networks that have higher energy requirements and less thermodynamic favourability than single carbon products. Coupling CO_2 conversion processes with renewable energy sources is essential to achieve these goals. For example, renewable hydrogen production through electrolysis may be integrated to supply the necessary reducing agent minimizing total carbon emissions [19].

Beyond thermodynamics, the kinetic barriers to CO_2 activation also pose another challenge. A catalyst used for CO_2 reduction should have a large number of active sites where CO adsorption, activation, and transformation occurs easily under mild conditions because the molecule has low reactivity due to its linear structure and strong C=O bonds. While advanced catalysts make this easier than before, there are still some significant kinetic challenges.

- Low Turnover Frequencies: CO_2 adsorption on most catalyst surfaces is poor which limits the rate of activation. However, stronger adsorption frequently results in catalyst deactivation via over binding or creation of carbonates.
- Competing reactions: Side reactions, like CH_4 overproduction in methanol synthesis or excessive hydrogen consumption in RWGS, lead to lower process efficiency.
- High Selectivity Challenges: High selectivity to target products, including hydrocarbons or oxygenated compounds, and product purity require the control of reaction intermediates and pathways.

A common example is the rate governing step of CO_2 dissociation to CO in the hydrogenation reaction over cobalt-based catalysts. To carry out this process it is necessary to surpass an activation energy barrier of ~2.6 eV, which can be reduced by promoters as potassium or cerium doping [20]. Iron catalysts on the other hand, tend to exhibit high activity toward inducing RWGS reaction; however, they generally present low selectivity to long-chain hydrocarbons, hence they need structural and compositional tune-up.

To combat these thermodynamic and kinetic challenges, improvements in catalyst design addressed the following:

- Nanostructured Catalysts: Higher surface area and active site density of the catalyst to improve CO_2 adsorption and activation. For example, nano-iron catalysts have been shown to exhibit enhanced activity and selectivity in Fischer-Tropsch synthesis under CO_2 rich streams [21].
- Bimetallic Systems: combining two metals, for example Fe-Co or Cu-Zn can lead to synergistic effects in lowering activation energy improving yield and product selectivity.
- Support Materials: materials such as ceria (CeO_2), that can develop supports with oxygen vacancies to help in CO_2 activation through strong metal-support interactions.
- Electrocatalysts: Renewable electricity used with electrochemical reduction of CO_2 is demonstrated to be a promising method, with advanced materials (e.g., doped graphene and transition metal carbides) as capable catalysts for reducing energy demands

Catalyst Type	Innovation	Examples
Metal-based catalysts	Interface engineering to improve selectivity and reduce overpotential.	Cu-O-Mo interfaces enhance acetic acid production; $NiSe_2$ produces ethanol with high selectivity [80].
Metal-carbon catalysts	Use of nitrogen-doped carbon to stabilize metal sites for CO_2 conversion to ethanol and hydrocarbons.	Cu/N-doped carbon improves C_2+ product selectivity. [81].
MOF-based catalysts	High surface area and tunable pore structures for selective CO_2 adsorption and activation.	CuO/MOF composites achieve high ethylene (C_2H_4) yields [82].
Single-atom catalysts	Precise design for isolated metal sites improving efficiency and reducing noble metal usage.	Single-atom Cu and Ni catalysts enhance ethanol production at high Faradaic efficiency (FE) [83].
Tandem catalysts	Multi-step reaction sites for sequential product transformation pathways.	PTF(Ni)/Cu systems enhance CO_2 conversion to ethylene by promoting CO intermediate coupling [84].
Nanostructured catalysts	Use of unique shapes and sizes to expose more active sites for specific product formation.	Cu nanoparticles tailored for hydrocarbons like methane and ethylene [85].

Table 1.2. Innovations in catalyst design for CO_2 conversion.

The integration of this approach with renewable energy sources has the potential to provide both a sustainable solution to the thermodynamic and kinetic barriers of CO_2 conversion. This presents opportunities to further reduce the total energy footprint of these processes either by integrating CO_2 reduction with renewable hydrogen production or direct use of electricity in electrocatalytic systems. This strategy makes the economic concept feasible and is congruent with global climate aspirations by reduction of net CO_2 emission.

1.3.3. Industrial Processes and Constraints

The use of CO_2 in industrial processes is increasingly being considered as a route to reduce greenhouse gas emissions and move towards the establishment of a circular carbon economy. The conversion of CO_2 into numerous value-added products such as fuels, chemicals and materials would be highly beneficial since apart from providing environmental benefits, this could also provide economic benefit. Yet these are processes that have limited scalability and efficiency, due primarily to thermodynamic, kinetic, and economic considerations. In fact, there exist some industrial processes which make CO_2 a feedstock and this shows the feasibility of using CO_2 as an input to large scale applications.

1. Urea Synthesis: The most mature and used process for the CO_2 utilization, located in over 130 million tons of CO_2 are produced annually [22], is urea production. Urea is an important fertilizer intermediate, and its synthesis from CO_2 is a simple means for making use of CO_2. But the environmental benefits are small, because only so much CO_2 can be sequestered in urea, and eventually that CO_2 is released back to the atmosphere as urea is broken down in soil

2. Methanation: The Sabatier reaction, or methanation process, converts CO_2 and hydrogen (H_2) to methane (CH_4), using metal-based catalysts such as nickel:

$$CO_2 + 4H_2 \leftrightarrow CH_4 + 2H_2O \quad (1)$$

Methanation is particularly important in power-to-gas (PtG) systems where surplus renewable electricity is used to produce green hydrogen that can be then combined with captured CO_2 to produce synthetic natural gas (SNG). This system is used to aggregate renewable resources into the grid adding energy storage capabilities for a better integration of intermittent power like solar and wind power [23]. As useful as methanation is, it is an energy-intensive process and acts only as a temporally short-term carbon management strategy because combustion of CH_4 liberates CO_2 back to the atmosphere.

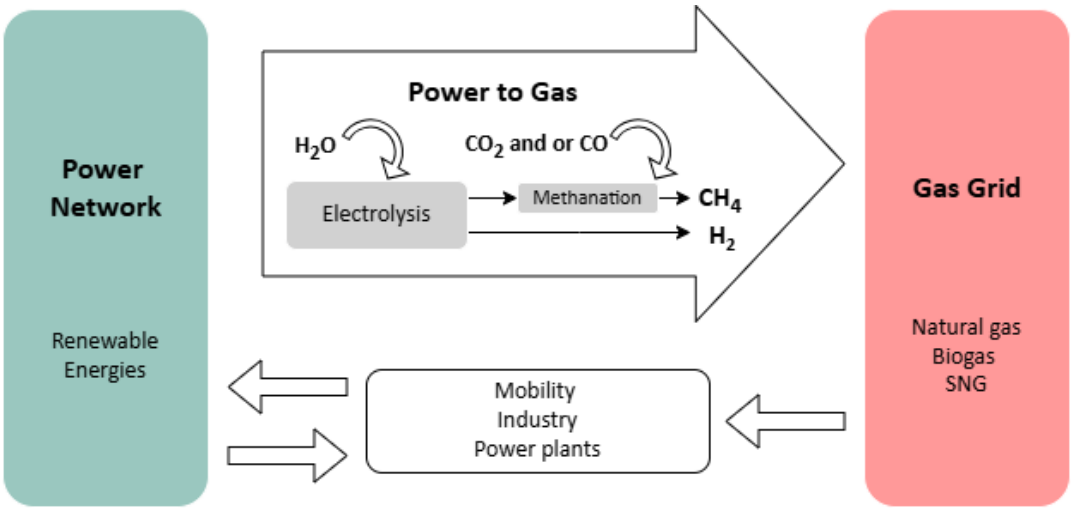

Figure 1.8. Schematic of the methanation in PtG systems.

3. Methanol and Formic Acid Production: The chemical industry is able to produce formic acid and methanol as key intermediates directly from CO_2.

- Formic Acid: Electrochemical CO_2 reduction is an attractive option for production of formic acid, particularly if driven with renewable electricity. More recently, the efficiency of this process has been greatly enhanced by advanced eletrocatalysts such as bismuth-based materials [24].
- Methanol: Referred to as the "methanol economy," the syngas (CO_2 + H_2) can be catalytically converted into methanol, an excellent fuel and plastic precursor. Nevertheless, methanol synthesis faces challenges related to catalyst stability and the high pressures required to achieve reasonable yields.

A number of advanced technologies are also under development to supplement the established industrial processes for CO_2 utilization. These breakthroughs are meant to address the dwindling resources and rising costs needed for a more sustainable future, in particular in energy production, chemical processing, and material production. While most of these pathways are still being researched or tested in pilot plants, the ability to convert CO_2 from a waste material into a valuable feedstock positions them as key players in the future of carbon management. In the next paragraph four of these techniques will be briefly presented. This work will then focus on the fourth route described in paragraph 1.4: the Fischer-Tropsch process.

Increased electrification and the increase of carbon-free, intermittent electricity have attracted global interest towards flexible CCU systems driven by electrical power**. Electrochemical** systems could be used to reduce CO_2 into many different products, according to the wide variety of electrochemical systems under development. For example, proton exchange membrane (PEM) electrolysers work under (near) ambient conditions, while solid-oxide systems can operate at temperatures above 700°C. The electrochemical conversion of CO_2 can result in more efficient (ideally) single-step conversion processes that can lead to purer products and simplify purification steps. Unfortunately, existing CO_2 conversion processes are very energy demanding and expensive. For each CCU technique, the origin of the CO_2 feedstock has important implications for, for instance, the costs, energy demand, accessibility, scale, societal acceptance, and sustainability of the route. [25] reviewed some electrochemical routes to convert CO_2 in useful raw materials such as CO, syngas, formic acid and ethylene and reported their Technology Readiness Levels (TRL). The low temperature (LT) electrochemical reduction of CO_2 into formic acid (FA) requires an electrolysis unit and a series of auxiliary purification units for the production of an aqueous FA stream. CO_2 and H_2O are converted in the process into FA and O_2. The current development stage for the LT CO_2 conversion to FA is claimed to be at a TRL 3-5. The LT electrochemical reduction of CO_2 into ethylene (C_2H_4) consists of an electrolysis unit and a series of auxiliary units for the final production of a purified gaseous C_2H_4 stream. In the chemical reaction CO_2 and H_2O are converted into C_2H_4 and O_2. LT CO_2 conversion to C_2H_4 technology is being validated in the laboratory, which implies a TRL of 3-4. High-temperature (HT) electrolysis in a solid oxide electrolyser (SOE) is the only CO_2 electrolysis technology that is approaching commercialization (TRL 8). The technology is based on solid oxide cell (SOC) technology composed of ceramic-based components able to produce CO via the electrolysis of CO_2 at elevated temperatures (600-800°C). CO_2 is fed to the cathode side of the cell via gas channels, which helps to distribute the gas across the cell. In the porous cathode CO_2 is reduced to CO. Syngas (H_2/CO) of tuneable ratios can be produced in one single process step at high temperature with a similar operating principle in solid oxide cells to that used for CO production. The operating concept of the SOE for syngas production consists of a co-electrolysis (co-SOE) of water and CO_2, able to produce variable H_2 and CO compositions, for further process applications, as for instance, production of green fuels and chemicals such as methane and methanol. Steam and CO_2 are reduced in the SOEC with the H_2/CO ratio in the syngas modified by variations of the steam and CO_2 flows. The production of syngas (H_2/CO) using co-SOE is in the development phase with an achieved TRL of 5 to 6. The outlet gas mixture produced from SOE systems (H_2, CO, CO_2 and steam) requires additional separation processes to feed clean syngas (H_2/CO) for the above-mentioned fuels and chemical production processes. Steam is commonly removed by a condensation process and recycled into the steam system. CO_2 can be removed from the gas stream by absorption, adsorption, or membrane-based separation methods or with absorption-based separation with amine solutions. Separated CO_2 is recycled to the inlet of the SOE system. The heat from SOE outlet gases is recovered using heat exchangers to increase the overall system energy efficiency. Solid oxide technology seems most advanced in technology readiness and applied in larger scale CO_2 electro conversion demonstrative units. These HT systems operate at a relatively high-power density, which is comparable to HT water electrolysis. The investment costs per unit output of HT systems are significantly lower than those of their LT counterparts.

Between the techniques evaluated, the authors found that the most promising to reach break-even costs are LT formic acid production and HT CO production. For ethylene production, saving GHG emissions by the electrochemical routes becomes difficult if the efficiency and power density cannot be substantially improved without raising the investment costs.

Inspired by nature **photosynthesis,** the so-called "solar-to-chemical" energy conversion process will not only reduce energy consumption in the CO_2 utilization process, but also effectively alleviate the problem of the greenhouse effect. At present, the photo-promoted CO_2 hydrogenation to produce fuels can be carried out under sole light irradiation or photo-thermal conditions. However, photocatalysis suffers from limited light utilization and conversion efficiency. Currently, the photothermal effect is widely investigated: to obtain a higher production yield, external heat is introduced besides light irradiation. A much higher CO_2 conversion rate could be achieved with less energy consumption in this photothermal catalytic process compared to conventional thermal catalytic systems.

The fundamental mechanisms of the photocatalytic hydrogenation of CO_2 lie in the transfer of photo-generated electron-hole pairs to the adsorbed reactant molecules. To enhance the efficiency for photocatalytic CO_2 hydrogenation, various strategies have been proposed. For example, through heteroatom doping, defect engineering and hybridization with sensitizers, the light absorption region of catalysts can be effectively expanded. A plethora of metal oxide catalysts have been reported for photocatalytic hydrogenation of CO_2 on account of their appealing band structure, excellent light absorption capacity and robust chemical stability. To further improve the catalytic efficiency of photocatalysts, metal nanoparticles have been deposited on the surface of oxide supports. A catalyst with high activity, optimal selectivity, robust stability and low cost should be further explored. Despite the catalysts reported in literature exhibit promising efficiency and selectivity for CO_2 hydrogenation, the production rate still remains very far from the industrial application requirements. As a result, more effective catalysts are needed. Moreover, most of the currently investigated catalysts are still based on noble metals, so the high cost would be another concern that hinders their wide application. Thus, more tries on non-precious transition metal-based catalysts would be practical in future research. Due to the diverse pathways, obtaining a specific product with high selectivity is still a difficult result to achieve. Under sole light irradiation, the elevated local temperature arising from the photothermal effect could not be quantified so far, which introduced an uncertainty for the thermal contribution from this process. In a photothermal catalytic process, the synergy between external heat and light illumination is also not clear. Similarly, with more and more bimetallic catalysts coming into our field of vision, the synergistic effect of bimetallic catalysts is worth further investigation [26].

A third up-and-coming technology is **CO_2 mineralization**, whereby the CO_2 reacts with alkaline earth metals like calcium or magnesium to produce stable carbonates. This process is thermodynamically driven, offering a lasting carbon sequestration solution that eliminates the potential for CO_2 re-release. Mineralization, besides the fact that it can sequester CO_2, could also be used to manufacture a new type of building material as carbonated concrete that when compared to cement production have some cool benefits and in part offset its carbon footprint. Yet, the sluggish reaction kinetics and high material demand for mineralization processes limit their broad application. For this technology to be economically competitive, additional

advancements in reactor design and process intensification will be necessary as mentioned by [27].

1.3.4. CO_2 Hydrogenation to methanol

Nowadays, the large-scale commercial production of methanol comes mainly from syngas, which is generated by fossil resources (mainly coal and natural gas) via processes including the gasification of coal as well as the steam reforming of natural gas. Small amounts of CO_2 (about 2-8%) are typically added to the CO/H_2 stream to balance the H/C ratio to the desired stoichiometry and to accelerate the reaction rate. The catalysts employed in the syngas conversion to methanol are usually copper based. Compared to the commercial production of methanol via syngas, methanol formation from CO_2 hydrogenation requires an extra amount of hydrogen to remove the additional oxygen. Moreover, the thermodynamics for methanol production from CO_2 are not as favourable as that from CO: the single-pass methanol yield obtained starting from CO_2 (<40% at 200°C) is lower than that of the syngas-based process (>80% at 200°C). In addition, several side reactions can occur in the CO_2 hydrogenation. The equation of the CO/CO_2 hydrogenation to methanol are:

$$CO + 2H_2 \rightarrow CH_3OH \qquad \Delta H = -91\ kJ/mol \tag{2}$$

$$CO_2 + 3H_2 \rightarrow CH_3OH + H_2O \qquad \Delta H = -50\ kJ/mol \tag{3}$$

Similar to methanol synthesis from syngas, also that from CO_2 and H_2 is an exothermal reaction that led to a decrease in molecule number (4 molecules of reactants give 2 molecules of products). So, according to Le Chatelier's principle, the optimization of the reaction conditions such as high pressure and low temperature thermodynamically favours CO_2 conversion to methanol. However, considering the reaction rate and the chemically inert nature of CO_2, a reaction temperature higher than 240°C is usually selected to favour the CO_2 activation, increase the reaction rate and favour methanol formation.

By considering the catalytic kinetics, the development of highly effective Cu-based catalysts in terms of activity, selectivity and stability are necessary for the hydrogenation of CO_2 to methanol. Differently from the reaction using CO, that using CO_2 also produces water, so water resistant catalysts are needed in the second case. The catalysts usually employed contains Cu as main active component and ZnO as support, together with different modifiers. In general, methanol synthesis is operated between 220-300°C and 5-10 bar and different degrees of conversion, selectivity and space-time yield are observed depending on the catalysts. The commercial Cu/ZnO/Al2O3 catalysts are typically composed of 60 wt% Cu, 30 wt% ZnO, and 10 wt% Al2O3. The refractory oxide Al2O3 acts as a structural promoter to increase the distribution of Cu, the total surface area and the mechanical stability of catalysts. ZrO_2 is another widely used support for Cu-based catalysts in CO_2 hydrogenation to methanol. Due to the excellent thermal and mechanical stability, as well as high specific surface area and semiconductor properties, Cu-ZrO_2 based catalysts demonstrate high performance in methanol synthesis from CO_2. Furthermore, the Cu/ZrO_2 based catalysts exhibit higher catalytic performance than Al2O3 supported catalysts. ZnO enhances the Cu dispersion, and both ZrO_2 and ZnO improve the adsorption of CO_2. Recently, metal-organic frameworks (MOFs) have been studied as supports in methanol synthesis, resulting to be very

promising materials. The encapsulation of metal nanoparticles into MOFs not only effectively stabilizes the metal NPs but also displays unique functionalities.

The incorporation of additives (e.g. metal oxides and noble metals) increases the Cu dispersion, modifies the acid-base properties and redox properties, and enhances the catalytic performance and stability [28].

1.4. Fischer-Tropsch process

Syngas conversion to hydrocarbons (Fischer-Tropsch synthesis) or alcohol is a well-known catalytic process that has been widely employed in the past to produce liquid fuel from the gasification of coal. The importance of this process has decreased in the past decades, but nowadays it can become more interesting due to the possible applications for the abatement of CO_2 emissions and reduction of fossil fuels dependence. Moreover, FT-derived fuels present better characteristics respect to the classical oil-derived ones. In fact, they are sulphur-free and contain very little amounts of aromatics. They usually have also better flash points and higher cetane number. The increased interest towards the FT possible applications is evident from the increase of researches and paper published on this topic as reported in Fig. 1.9.

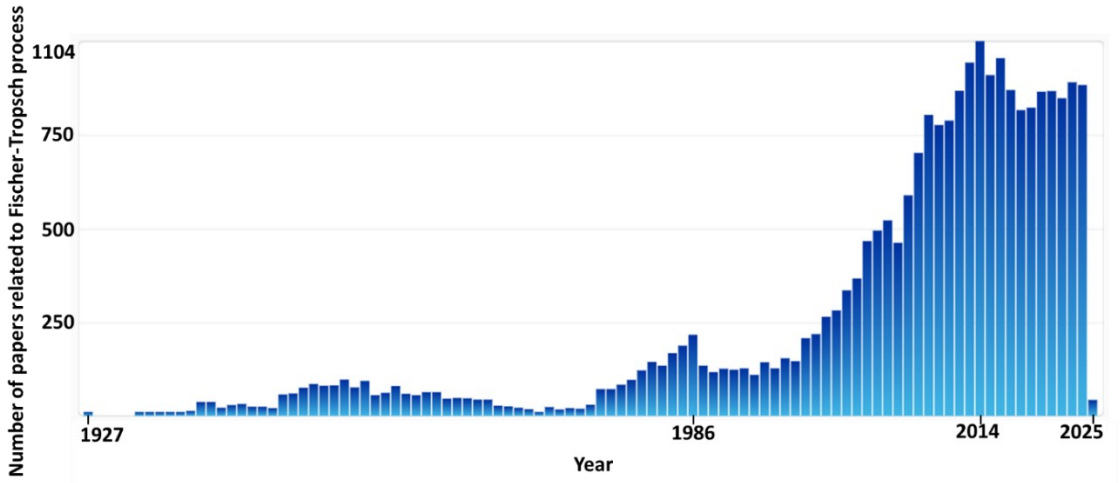

Figure 1.9. Academic papers regarding the FT reaction published in the period 1927- 2025 [29].

Since carbon in CO_2 is in its highest oxidation state, its reduction and transformation need a large energy input. As a high-energy material, hydrogen is generally used for the large-scale catalytic transformation of CO_2 to value-added products. At present, the hydrogen source mainly comes from fossil raw materials (mainly methane). Renewable energies sources can be used along with CO_2 and water to produce low emissions liquid fuels. The concept of "Power to Liquid" (PTL) relies on liquid fuel production by CO_2 hydrogenation with hydrogen obtained by water electrolysis using surplus of renewable energy. Liquid hydrocarbon (C5+) fuels play a fundamental role in the global energy supply chain and are worldwide wildly used for many applications, like in transportations and power generation. Besides, alcohols such as methanol, ethanol and other higher alcohols, mainly produced from biomasses, have been employed since many years as clean and multipurpose fuels. In both academic research and industrial practices, great progresses have been made in the synthesis of methanol from CO_2 hydrogenation. However, direct reduction of CO_2 to C2+ products is still a big challenge due to the lack of efficient catalysts with high stability. In fact, the activity of C−C coupling is low and the formation of water as

byproduct can easily deactivate the various catalysts for CO_2 reduction. Syngas (CO/H_2) and CH3OH are the most important C1 building blocks, and their conversions to value-added products respectively via the Fischer−Tropsch synthesis (FTS) and methanol to hydrocarbons (MTH) processes were extensively applied in industry. Therefore, combining the reverse water−gas shift (RWGS) with FTS and combining high-temperature CO_2 hydrogenation to methanol with MTH over bifunctional/multifunctional catalysts are two efficient strategies for direct CO_2 hydrogenation to C2+ hydrocarbons including liquid hydrocarbons. Moreover, the synthesis of C2+ alcohols is even more challenging than C2+ hydrocarbons either in CO_2 or CO hydrogenation, which requires more precise control of the C−C coupling [29]. Respect to the classical Fischer-Tropsch with syngas, using CO_2 as reactant the synthesis goes through two distinct reactions: the Reverse Water Gas Shift Reaction (RWGS) and the subsequent Fisher-Tropsch synthesis. The first one is endothermic and produces syngas that is converted in the second one that is exothermic. The set of reactions involved in the overall process are described in detail the chapter 1.5.

The classical FT process is usually performed using highly selective cobalt-based catalysts to produce heavy hydrocarbons. However, in the direct CO_2-FTS, Fe-based catalysts are preferred over cobalt ones due to their higher activity towards the RWGS reaction that is the critical step of the process. Fe-based catalysts allow also higher selectivity towards olefins [29]. Additionally, they permit obtaining shorter paraffins and olefins which can be separated into the different fraction (gasoline, diesel and kerosene) without the need of further treatment (i.e., hydrocracking). The addition of potassium to iron-based catalysts promotes the reduction of CO_2 in hydrocarbon chains improving the conversion. K acts as an electronic promoter for Fe-based catalysts and this reduces the formation of short-chain hydrocarbon compounds [30]. [31] found that hydrotalcite-supported cobalt-based catalyst were remarkably active to the FT reaction with syngas. During previous studies we evaluated the performances in the classical FT with syngas of hydrotalcite-supported iron-based catalysts [32]. Since these materials showed great results, it was decided to test them also in the CO_2 FT reaction.

The broader application of these technologies will also require further progress in catalyst development as well as in process integration and renewable energy coupling, but ongoing advancements indicate that these challenges may be amenable to mitigation. The cost-effective application of these technologies to meet ambitious GHG mitigation targets and the opening up of new CO_2 utilisation markets in the decades ahead will rely on their deployment.

1.4.1. Discussion of limitations and research future directions

Despite the promising signs shown by these technologies, a few key hurdles remain before full commercialisation can be achieved. The most prominent and challenging of these is the question of energy intensity. Numerous CO_2 conversion pathways including methanol synthesis, electrochemical reduction, etc., have large energy inputs to overcome thermodynamic as well as kinetic challenges of CO_2 activation. Recognizing that this energy must be renewable is fundamental in order to achieve net carbon reductions; otherwise, we run the risk of simply pushing our emissions around and not dealing with them [33]. They are still far from being economically feasible. These costs generally make the resulting products which are derived from renewable hydrogen like fuels and chemicals more expensive in the market than other options.

As an example, producing methanol/methane by combining CO_2 and green hydrogen may be advantageous solely in areas fortunate enough to own large amounts of low-cost renewable energy [34]. Policy incentives such as carbon pricing or subsidization of low-carbon technologies are likely to be needed to close this gap.

However, scalability remains a challenge for the case of most emerging pathways for CO_2 utilization. Photocatalysis and electrochemical CO_2 reduction are examples of highly promising yet pre-commercialized technologies due to efficiency, durability, and system-level integration issues. Such innovations would benefit from the realization of efficient catalysts, reactor designs, and integrated systems; bringing them to scale requires decades of progress [35].

In the long term, the combination of CO_2 utilization technologies with renewable energy systems could provide an avenue for addressing these bottlenecks. The overall carbon footprint of these technologies can be reduced by combining with processes like methanation/electrochemical reduction with renewable hydrogen production or solar energy. Further increases of process efficiency and product selectivity are anticipated by development of novel catalyst design including nanoparticle-based formulations and bimetallic systems. In addition, hybrid technologies which integrate CCU with carbon capture and storage (CCUS), can offer a compromise between economic and environmental ambitions where emissions are reduced whilst by-products of value are created simultaneously [36].

Such an effort will be necessary to unlock the true potential of CO_2 utilization; but even with that, we may have to look beyond just research. Collaboration on an international scale, fuelled by investments in clean energy and carbon management technologies, is key to the rapid passage from pilot projects through implementation at a large scale.

1.4.2. Fischer-Tropsch synthesis: Classic Fischer Tropsch process

Fischer-Tropsch (FT) synthesis is a classical pathway in chemical engineering, by which the syngas, a mixture of carbon monoxide (CO) and hydrogen (H_2), can be converted to hydrocarbons and oxygenates. This mechanism was first described in the 1920s with studies leading to this discovery conducted by Franz Fischer and Hans Tropsch at the Kaiser Wilhelm Institute in Germany, it has become an essential technology for manufacturing synthetic fuels and chemicals from carbon-rich starting materials. The flexibility of the FT synthesis and its ability to process not only different hydrocarbon sources, but also a variety of raw materials has made the FT process an integral part of gas-to-liquid (GTL), coal-to-liquid (CTL) and renewable biomass-to-liquid fuel technologies (BTL).

As discussed priorly, the FT process catalytically hydrogenates CO to generate a broad spectrum of hydrocarbons, including alkanes, olefins and paraffins [37]. In general, the reaction mechanism is based on a polymerization process where CO and H_2 molecules are adsorbed on a surface of a metallic catalyst, dissociated to form hydrocarbon chains due to successive insertion of CH_2 units. This is the generalized reaction:

$$(2n+1)H_2 + nCO \rightarrow CnH_{2n+2} + nH_2O \qquad \Delta H° < 0 \qquad (4)$$

The product distribution is in accordance with Anderson-Schulz-Flory (ASF) theory which predicts that the chain growth probability (α) determines the ratio of products with varying chain

lengths [38]. Because product selectivity can be fine-tuned by adjusting reaction parameters (temperature, pressure, H_2/CO ratio), the FT process is very versatile.

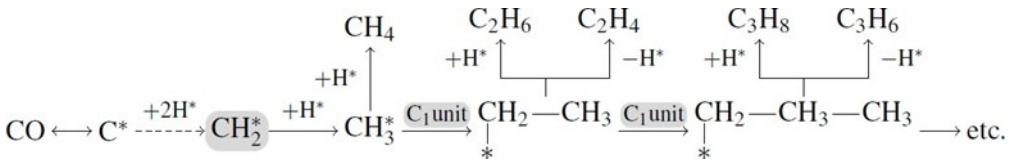

Figure 1.10. Schematic of the FT reaction mechanism.

The product distribution by the ASF model, referred to the mass fraction of products is then defined as [39]:

$$\frac{W_n}{n} = (1-\alpha)^2\,\alpha^{n-1} \tag{5}$$

Where n is the number of carbon atoms in the product, Wn is the weight fraction of product containing n carbon atoms. The α can be estimated by a least-squares linear regression of the logarithmic form of Eq. 5. a is then given by the slope and intercept values.

$$ln\frac{W_n}{n} = ln(1-\alpha)^2 + (n-1)ln\alpha \tag{6}$$

The probability of chain growth determines the spectrum of hydrocarbon products, the longer the hydrocarbon chain, the greater the probability (Fig. 1.11). This probability (denoted as α) is influenced by various factors, including the type of catalyst and process conditions such as H_2/CO ratio, temperature, and pressure. For instance, cobalt catalysts promoted with ruthenium exhibit higher α values compared to large iron-based catalysts.

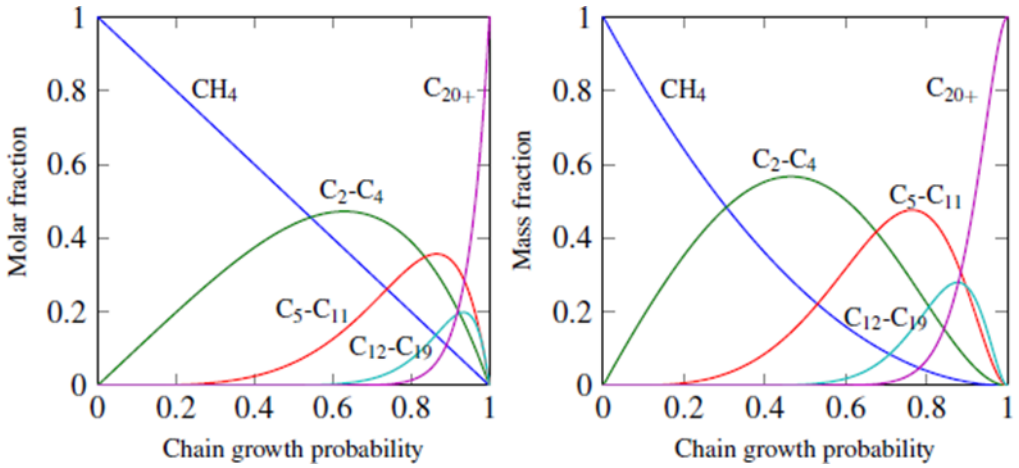

Figure 1.11. Anderson–Schulz–Flory (ASF) distribution curves showing the predicted product distribution in Fischer–Tropsch synthesis as a function of the chain growth probability (α)

The standard Anderson-Schulz-Flory (ASF) model, however, cannot differentiate the specific types of products formed. Instead, it only predicts the molar or mass composition of defined fractions such as C_2, C_3, C_4, and so on. It is well established that the Fischer-Tropsch (FT) reaction produces a range of products, including paraffins, α-olefins, β-olefins, and oxygenated compounds. Although the ASF model provides a foundational understanding, additional studies have been conducted to refine the model and predict a more detailed product distribution. Notably, it has been observed that alcohol productivity corresponds to the hydrocarbon fraction with the same carbon number (n+1). For example, if C_4 hydrocarbons dominate, then C_3H_7OH (propyl

alcohol) is the primary oxygenated product. Anderson improved the model by incorporating chain branching into the product distribution framework, allowing for the addition of a C_1 unit to the β-carbon of a growing chain. Further advancements include the work of Schultz and collaborators, who developed a non-trivial surface polymerization model, emphasizing the role of chain branching in hydrocarbon formation. Although the Anderson-Schulz-Flory (ASF) equation provides a general approximation of product distributions, it is not sufficiently precise for detailed predictions. This limitation arises from deviations in the algorithm. Three primary deviations of the ASF model have been identified:

- Methane Selectivity: The methane (CH_4) selectivity predicted by the ASF model is generally lower than the values observed experimentally. Various mechanisms have been proposed to explain this discrepancy. Sarup et al. [40] estimated that the termination probability for methane formation is 5 to 20 times higher than that for paraffin termination. Other studies [41,42] suggest the existence of specific methanation catalytic sites on the catalyst surface. Additionally, secondary reaction pathways, such as hydrogenolysis by demethylation and spillover effects between catalyst and support, may enhance methane production. Heat and mass transfer phenomena or local hotspots on the catalyst surface, where the partial pressure of H_2 is elevated, could also contribute to increased methane selectivity.
- Anomalies of Ethane and Ethylene: The ASF model predicts the selectivity for the C_2 fraction (ethane and ethylene) to be approximately 30 wt%, yet experimental values often reach only 18 wt%. This discrepancy is commonly attributed to the incorporation or hydrogenolysis of ethylene, which shifts the product distribution and lowers the observed C_2 fraction [43].
- *Not constant α*: in the ASF algorithm the chain growth probability is considered as a constant value. From an experimental point of view, it has been demonstrated that the slope of the hydrocarbons semi logarithmic mole fractions versus the number of carbon atoms increase when the hydrocarbon chain contains 10 or more carbon atoms due to the presence of different catalytic sites or different chain termination reactions on the catalyst surface [44, 45].

1.4.3. History and Important Dates

The FT synthesis process was developed out of necessity in the early 20 th century for synthetic fuels. Germany began producing oil using the FT process on an industrial scale in the 1935, at a time when crude oil was proving to be elusive or unreliable. The plant was some of the early plants that used coal as a feedstock, benefiting from the vast coal reserves found in Europe. The use of the FT process became more famous in World War II, when it fuelled Nazi Germany to produce synth fuels from coal fumes. Over the span of the war, 600,000 tons per year of synthetic fuel was produced with FT technology [46]. Though it was popular at first the end of the post-war era saw it gradually fall to crude oil in terms of cost and accessibility. The 1970s oil crises reignited interest in FT synthesis, particularly among nations with abundant coal or natural gas reserves but limited access to oil. For example, South Africa heavily invested in FT technology for the purpose of avoiding international sanctions and constructed large-scale CTL plants (Sasol

plant). These facilities are among the largest FT installations in the world and contribute a sizeable fraction of South Africa's liquid fuels [47].

1.4.4. Industrial Deployments in Practice

Until today three most wide recognize industrial ways are GTL, CTL and BTL only made from FT synthesis. Every pathway is designed to harness the versatility of FT tech to turn a unique group of feedstocks into high-end products spanning synthetic fuels and an array of specialty chemicals.

- Gas-to-Liquid (GTL):

The GTL processes use natural gas as the primary feedstock, reforming it into syngas before synthesizing hydrocarbons via FT. Global refining hubs, where natural gas resources are abundant, like the Middle East and North America offer most promise for this route. Large-scale GTL plants have been established by companies such as Shell and Qatar Petroleum, with the Pearl GTL facility in Qatar being one example that produces diesel, naphtha, and paraffin waxes. The low sulphur content, high energy density GTL fuels find a lot of use in flying and heavy transport too [48].

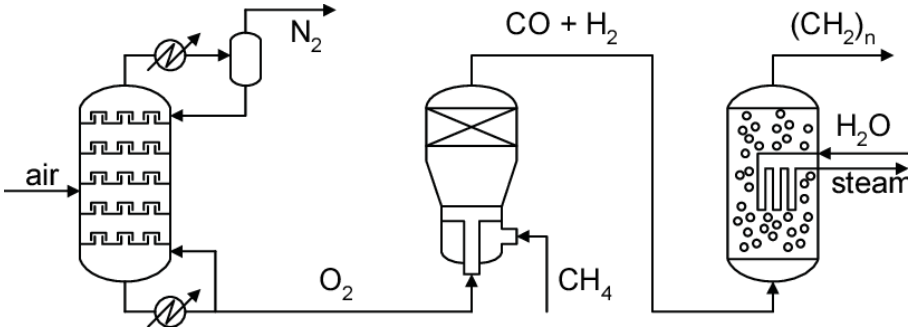

Figure 1.12. Overview of the GTL process.

- Coal-to-Liquid (CTL):

CTL technology is based on Coal gasification for production of syngas and later converted to synfuels, various chemicals by FT. The pathway has been taken by countries with large coal reserves, like China and South Africa. A prime example I: Sasol's Secunda CTL plant, with a 150 barrel/day liquid fuels capacity [49]. CTL provides energy security in coal- abundant regions, but its environmental implications are a consideration both because of CO_2 emissions and water use.

- Biomass-to-Liquid (BTL):

BTL processes use renewable biomass (for example agricultural residues or forestry waste) for FT synthesis. Whereas GTL and CTL are unable to ever be carbon neutral or negative, when coupled with carbon capture technologies, BTL has the capability of moving beyond zero emissions. Nonetheless the commercialization of BTL is still rather modest because of feedstock collection, pre-treatment issues and economy competitiveness. Other projects, such as the BioTfueL initiative in France, are demonstration efforts to determine whether BTL process technology can be scaled up for industrial production [50].

The Fischer-Tropsch Synthesis, a classic example of chemical engineering, as established the groundwork for modern synthetic fuel production. Its versatility in terms of feedstocks and capability to deliver high quality hydrocarbons has made it remain relevant in the energy and chemical sectors. Despite these operational and economic flaws, progress in reactor design,

catalyst development and process integration are shaping the future of FT synthesis towards more sustainable and efficient applications.

1.5. Transition to CO_2 Based Fischer-Tropsch

Fischer-Tropsch (FT) synthesis is a century-old technology that served as the cornerstone of synthetic fuel and chemical production and has been considerably modified to cope with contemporary challenges in sustainability and decarbonization. Part of this evolution is shifting toward CO_2-based FT synthesis, where carbon dioxide itself takes over from coal, natural gas or biomass as the feedstock for carbon. This change is born from the necessity to reduce greenhouse gas emissions and create a circular carbon economy. This advanced FT process will uniquely reduce the concentration of atmospheric CO_2 while providing a means to utilize as a feedstock for valuable hydrocarbons production [51].

In CO_2-based FT synthesis, also referred to as CO_2 hydrogenation, the conventional FT process is modified slightly when reduction of CO_2 is included in the reaction mechanism. While syngas-derived FT directly uses CO and H_2, the hydrogenation of CO_2 involves an additional step for $CO_2 \rightarrow CO$ conversion. For example, CO_2 can be commended free H_2 in a high-temperature endothermic reaction to produce CO and water reverse water-gas shift (RWGS) reaction.

$$CO_2 + H_2 \leftrightarrow H_2O + CO \qquad \Delta H° = +41\ kJ/mol \qquad (7)$$

$$2CO \leftrightarrow CO_2 + C \qquad \Delta H° = -172\ kJ/mol \qquad (8)$$

$$CO + 3H_2 \leftrightarrow CH_4 + H_2O \qquad \Delta H° = -206\ kJ/mol \qquad (9)$$

$$(2n+1)H_2 + nCO \rightarrow C_nH_{2n+2} + nH_2O \qquad \Delta H° < 0 \qquad (10)$$

$$2nH_2 + nCO \rightarrow C_nH_{2n} + nH_2O \qquad \Delta H° < 0 \qquad (11)$$

$$2nH_2 + nCO \rightarrow C_nH_{2n+2}OH + (n-1)H_2O \qquad \Delta H° < 0 \qquad (12)$$

$$(3n+1)H_2 + nCO_2 \rightarrow C_nH_{2n+2} + 2n\,H_2O \qquad \Delta H° < 0 \qquad (13)$$

This dual-step process introduces more thermodynamic and kinetic complexities which require further catalyst designs and reaction optimizations (Eq. 14).

$$CO_2 + 3H_2 \leftrightarrow -(CH_2)_n - + H_2O \qquad (14)$$

Among the different stakeholders interested in FT synthesis, this environmentally minded approach has established carbon-neutral CO_2-based FT synthesis as a key advantage. The process serves as a means to recycle carbon and prevent it from landfilling, incineration or the atmosphere using CO_2 emissions, preferably sourced from industrial point sources, power plants or even direct air capture systems. The entire system can become carbon net zero or even carbon negative if it is powered with renewable hydrogen, which is produced by the electrolysis of water through wind, solar or hydropower. By linking renewable energy with carbon recycling, this method of coupling is perfectly aligned with the overall decarbonisation goals for society, hence CO_2-FT has the potential to be a building block of future sustainable energy systems. Furthermore, CO_2-FT products, such as synthetic fuels and waxes, are very high-quality materials with low sulphur and aromatic content. All of this makes them well-suited to applications where green fuels are mandatory such as aviation, maritime transport and heavy-duty vehicles [52].

Although very attractive for its potential, the shift to CO_2-based FT synthesis is not without drawbacks. One of the most challenging aspects to overcome is due to the high thermodynamic stability of CO_2, necessitating a large amount energy for its activation and subsequent reduction. Although the RWGS reaction is efficient in converting CO_2 to CO it is endothermic and requires temperatures up to 700 °C and higher for appreciable conversion rates. At peak conditions, the energy required is much greater (which, again, costs a lot of money and at source leads to non-renewable production methods). Also, because it adds a CO_2 activation step on top of the Fischer-Tropsch synthesis, it has reduced overall process kinetics. This requires catalysts that are able to concomitantly achieve full RWGS and hydrocarbon chain growth, frequently favouring iron-based systems given their bifunctionality and low cost. Despite this, iron-based catalysts perform less than ideal in terms of selectivity to long-chain hydrocarbons and are prone to deactivation via sintering or carbon deposition [53] (See Fig. 1.13).

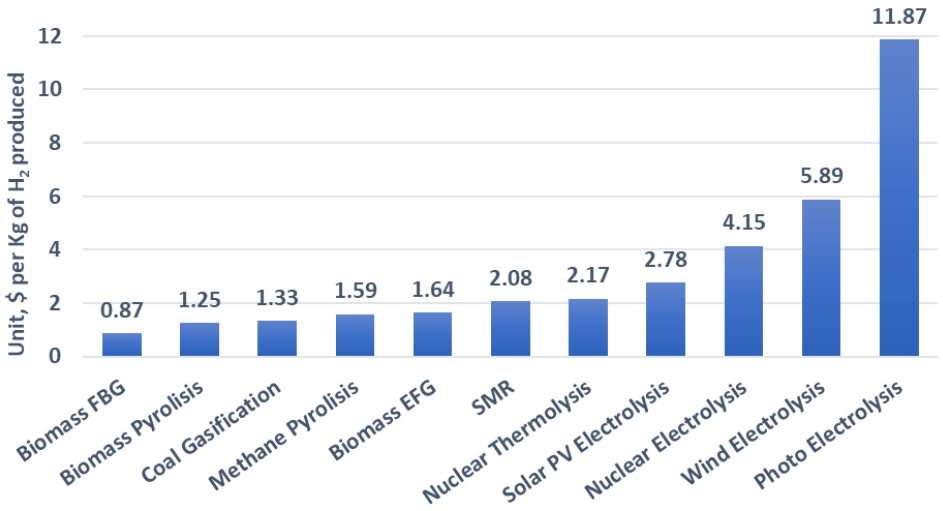

Figure 1.13. Cost comparison of hydrogen sources for CO_2-FT processes.

Hydrogen availability and cost represent another critical challenge in the CO_2-FT process. Hydrogen is a fundamental reactant in the hydrogenation of CO_2, and its source significantly impacts the economic and environmental viability of the system. While renewable hydrogen produced via electrolysis offers the ideal solution for sustainability, its high production costs and the limited capacity of renewable energy infrastructure constrain its widespread use. Alternative hydrogen sources, such as blue hydrogen derived from natural gas with carbon capture, may provide a transitional solution, but they compromise the full carbon-neutral potential of the process. Overcoming this bottleneck requires significant investment in renewable energy capacity, advancements in electrolyzer technology, and supportive policy frameworks to reduce costs and incentivize green hydrogen production [54].

In parallel, the integration of CO_2 capture, hydrogen production and FT synthesis into a single system poses significant engineering and logistical challenges as well. Whereas traditional FT plants are typically designed for a single feedstock (such as syngas), design of a CO_2-FT is complex due to the interdependency between various process units, namely, CO_2 capture, hydrogen generation by catalytic steam reforming or hydrocarbon gasification with autothermal RWGS and FT synthesis. Another characteristic of this complexity includes which requires novel reactor designs able to effectively respond to changes in feedstock compositions and, heat and

mass transfer. Finally, scale up from pilot to industrial scales of these systems will require operational stability and process intensification in order for these technologies to be competitive economically.

Continued catalyst development research is the key to overcoming such challenges. Accessibility to new nanostructured catalysts, such as potassium or cerium-promoted iron-based systems have been reported to enable improved efficiency for the RWGS reaction and favour high hydrocarbons formation. In addition, similarly to most any other bimetallic catalysts that combine iron with cobalt or nickel there are synergistic effects possible (namely both activity and durability). Support materials (as ceria, alumina etc.) are very important too as they give stability and help to create active CO_2 activation sites. At the same time, new strategies such as electrocatalytic and photocatalytic CO_2 hydrogenation are being developed that offer opportunities for more direct incorporation of renewable energy into the chemical transformation in support of CO_2-FT [54].

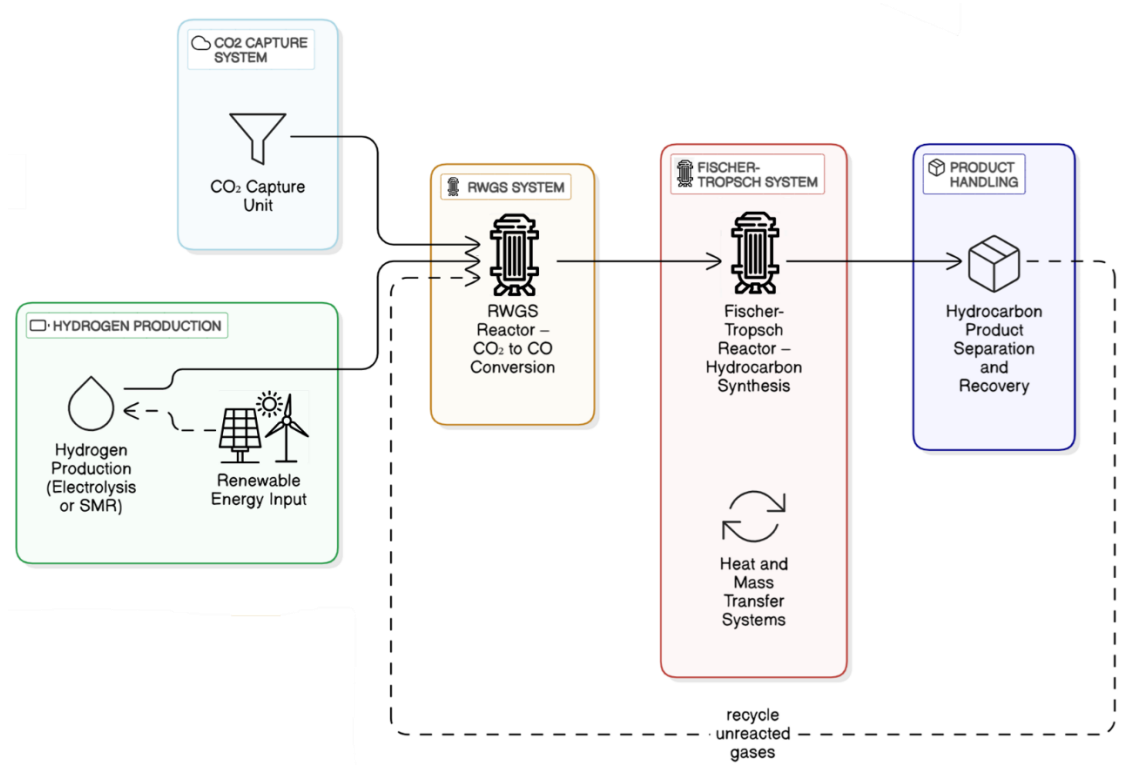

Figure 1.14. Schematic of an integrated CO_2-FT system.

The commercialization of CO_2-based FT synthesis could bring about a paradigm shift in the energy and chemical industries. It also provides a commercially accepted route to converting captured carbon into high-value hydrocarbons, combined with long-term CO_2 storage through the product life cycle - all while delivering an energy security solution and economic benefits at scale. This potential, however, will only be achieved through the collaborative work of many fields including chemistry and engineering to develop renewable energy technologies that are supported by policy and market incentives. Carbon dioxide to fuel technology CO_2-FT is a significant breakthrough in the transformation of the world as it moves forward into a carbon-free future race and seeking sustainable energy systems that would define circular carbon economy.

1.5.1. Catalyst Fundamentals

Catalysts constitute the core of CO_2 hydrogenation technologies, which have the potential to convert this thermodynamically stable molecule into high-value hydrocarbons and oxygenates at industrially relevant conditions. Catalysts assist in the dissociation and reorientation of molecular bonds, by decreasing the activation energies of reactions without being permanently consumed themselves. It is generally agreed that for the CO_2 hydrogenation, a good catalyst must meet a suitable combination of high activity, selectivity and stability to make the reaction as efficient as possible and economically viable.

The performance of a catalyst in the hydrogenation of CO_2 is governed by a large number of intrinsic and extrinsic properties that, together, determine the activity and selectivity thereof.

- Active Sites and Reactivity: These are the active sites of a catalyst- where CO_2 molecules adsorb and become activated. CO_2 hydrogenation involves the cleavage of the intrinsically stable C=O bond, a bottleneck-like step in this reaction pathway which is known to be efficiently catalysed by transition metals especially iron (Fe), cobalt (Co), nickel (Ni) and ruthenium (Ru). For example, Fe-based catalysts are active in catalysing the reverse water-gas shift (RWGS) reaction, resulting in CO as an intermediate for further hydrocarbon synthesis [55]. On the other hand, that results in high activity and selectivity towards long-chain hydrocarbons during hydrogenation of CO_2 thereby Co-based catalysts are a good candidate for Fischer-Tropsch applications. Adsorption strength of CO_2 and reaction intermediates is controlled by the electronic structure of the active sites. A gentle balance is needed: too weak adsorption causes a low activation efficiency, whereas too strong adsorption may be detrimental for catalyst poisoning or deactivation via carbon deposits formation
- Support soft, and metal-support interactions: A large number of active sites is beneficial because many will quickly poison (deactivate) on catalysts. The most common support materials contain alumina (Al_2O_3), silica (SiO_2), titania (TiO_2) or ceria (CeO_2). These supports can also give additional properties. Ceria, for instance, offers oxygen deficiencies to enable CO_2 adsorption and activation, whereas titania associates with metal particles to amplify the catalytic capacity at elevated temperature [56]. The performance of the catalyst is critical, and much may depend on the nature of the interaction between the metal and support. The active metal can have its electronic properties modified by strong interactions leading to synergistic affects and enhancing the rate or selectivity of a reaction. But very strong interactions can also block the activity sites and effectiveness overall. Balancing this balance is a crucial component of catalyst design.
- Selectivity and Product Control: The selectivity, further defined as the propensity of a catalyst to channel reaction pathways for specific products, is key in assessing the economic and environmental viability of hydrogenation reactions involving CO_2. For example, methanol synthesis catalysts are required to inhibit side reactions like methane production in order to achieve the highest yields. By contrast, in Fischer-Tropsch synthesis there is a desire for selectivity towards longer chain hydrocarbons which necessitates the formation of specific products and chain growth probabilities. In an increasingly sophisticated example of promoter design, it has been demonstrated that using alkalis (K for instance) can affect electronically the active sites hence resulting a more selective catalyst [57].

- Thermal and Mechanical Resilience: Catalysts in CO_2 hydrogenation processes are exposed to severe operating conditions, including high temperature, pressure and an extremely reactive environment. Thermal stability ensures the property that catalysts retain their structure and activity during prolonged use; Meanwhile, mechanical strength is necessary to avoid wear or sintering, especially in industrial-scale reactors where catalysts are exposed as fluidized or fixed-bed systems.

In overcoming the thermodynamic and kinetic barriers of CO_2 activation and reduction, catalysts play a vital role. The CO_2 molecule is very stable with a bond dissociation energy of 805 kJ/mol; as such, its direct transformation to reduced products requires a large amount of energy. Catalysts are a class of materials that can provide lower activation energy reaction pathways enabling hydrogenation of CO_2 to proceed at practical temperatures and pressures [58]. Furthermore, catalysts play the key role in the overall transformation of CO_2 into valuable products. Increased activity allows for faster rates of reaction with lower energy usage thus saving in operational costs. High selectivity leads to fewer unwanted by-products, making the process more cost effective and environmentally benign. Stability expands the lifespan of catalysts, which lowers maintenance needs along with their associated replacement burden and accompanying downtime in industrial operations. Recent advancements in catalyst design have focused on developing multi-functional systems capable of addressing the dual challenges of CO_2 activation and hydrocarbon chain growth. For example, bimetallic catalysts, such as Fe-Co or Cu-Zn systems, combine the strengths of individual metals to enhance activity and selectivity. In this way, nanostructured catalysts can be utilized for more CO_2 hydrogenation technologies having well-defined choice of intermediate as reaction intermediates, making them more effective and sustainable [59].

Catalysts will remain at the heart for successful application of CO_2 hydrogenation technologies, from laboratory-scale research to industrial implementation. For these processes to be scaled, it will be critical for innovations in catalyst synthesis, characterization and performance optimization.

1.5.2. Advances in Catalyst Design

The design of efficient catalysts is indispensable for addressing the difficulties encountered during CO_2 hydrogenation. The field of material design has been revolutionized by the discovery of novel synthetic strategies that enable us to design catalytic systems with significantly enhanced activity, selectivity and stability under industrially relevant conditions. Significant work is being pursued around the world in the area of nanostructured and bimetallic systems that offer individual properties to overcome the thermodynamic and kinetic barriers associated with CO_2 activation and its conversion.

1.5.2.1. Nanostructured Catalysts

Nanostructuring has thus transformed catalysis by allowing unprecedented tayloring of both the size, shape and distribution of the active sites. The reduction of catalyst particles to the nanoscale provides a higher surface area, and more active sites for CO_2 adsorption and reaction. Moreover, the electronic and mechanical properties of nanostructured materials may play a critical role in determining the catalytic behaviors. A particularly prominent achievement in the field of nanostructured catalysts has been the development of core-shell structures (where a catalytically

active shell material surrounds a core made from a different material). These designs provide the ability to fine-tune surface properties, while exploiting the core for additional and different functionality like thermal stability or conductive improvement. A typical example is Ru@TiO_2 core-shell nanoparticles which were found to have a superior performance in CO_2 hydrogenation, benefitting from the high reactivity of ruthenium integrated with oxygen storage properties of titania [60]. One more innovation consists of the application of hollow nanospheres and mesoporous materials offering interconnected pores, which significantly enhances the transport of masses and prevents deactivation of catalysts. These structures have enhanced the exposure of active metal sites with multifunctions in a single material for CO_2 adsorption and activation. e.g., hollow silica-supported Ni catalysts have shown enhanced catalytic stability and selectivity for methanation reactions [61].

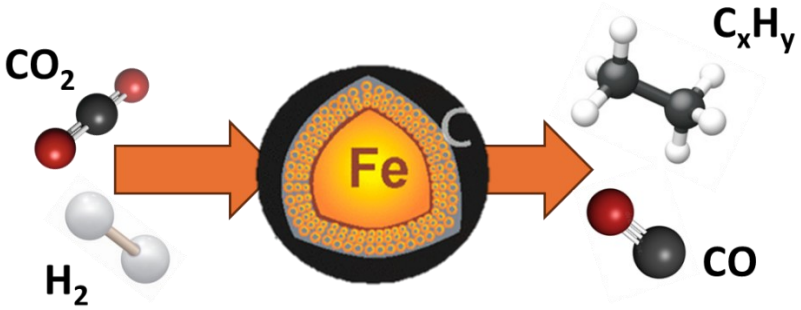

Figure 1.15. Schematic representation of the CNS-Fe core-shell catalyst synthesized for CO_2 hydrogenation.

1.5.2.2. Bimetallic Catalysts

The current approaches to their structural evaluation often create only a limited understanding of how the properties and structure of catalytic systems, especially bimetallic ones, can contribute to underlying synergies for promoting catalysis. By controlling the interplay between different metals, these systems can enhance reaction pathways while decreasing activation energy and rendering them less susceptible to deactivation. Fe-Co aside, Fe is the most widely examined metal because iron has a high RWGS activity and Co is more selective to long-chain products. This mixture has apparently led to considerable benefits in Fischer-Tropsch synthesis processes with the ability to produce long hydrocarbons under CO_2 rich streams Moreover potassium promoters, for example show improved electronic properties of catalyst which leads to an enhancement in CO_2 adsorption and hydrogen activation [62]. Cu-Zn is similarly attractive for methanol synthesis. Copper serves active site for CO_2 activation and hydrogenation, whereas zinc oxide (ZnO) acts as a support to stabilize the catalyst and to facilitate formation of Cu-Zn interfaces. Cu-Zn Catalyst has one of the highest CO_2 hydrogenation activity but by co-precipitation and atomic layer deposition have been improved in the uniformity and dispersion, yielding methanol while suppressing byproduct (Table 1.3).

Bimetallic System	Active Metal	Support	Primary Function	Advantages	Main Products	Promoters/ Modifiers
Fe-Co [86]	Fe	Co	RWGS and Fischer-Tropsch Synthesis	High selectivity to long-chain hydrocarbon, CO_2 utilization	Long-chain hydrocarbons (C_5+)	K (Potassium) Enhances CO_2 adsorption and activation.
Cu-Zn [87]	Cu	ZnO	Methanol Synthesis	High CO_2 hydrogenation activity, stable Cu-Zn interface	Methanol	Zr or Ga Improves methanol selectivity and stability.
Ni-Fe [88]	Ni	Fe	Methanation (Sabatiers Reaction)	Strong methanation activity, cost-effective	CH_4 (Methane)	Ce (Ceria) prevents sintering and deactivation [88]
Ru-TiO_2 [89]	Ru	TiO_2	CO_2 Hydrogenation	Enhanced selectivity to methane and higher hydrocarbons	CH_4, higher hydrocarbons	-
Pd-Ga [90]	Pd	Ga	Methanol Synthesis	Improved methanol yield, reduced byproducts	Methanol	-
Co-Mn [91]	Co	Mn	Fischer-Tropsch Synthesis	Enhances chain growth, suppresses methane formation	C_5+ Hydrocarbons	-

Table 1.3. Comparison of bimetallic systems for CO_2 hydrogenation.

1.5.3. Emerging Approaches in Catalyst Design

In addition to conventional nanostructured and bimetallic catalysts, new methods are expanding traditional strategies of material innovation. These include: Single-Atom Catalysts (SACs), Metal-organic frameworks (MOFs) and covalent organic frameworks (COFs).

SACs disaggregate individual metal layers on a support that allows for optimal use of active metal sites. These catalysts have unique electronic properties which make them selective for particular products. One of the examples is the case of single atom Ni catalysts on graphene, have low overpotentials for CO production from CO_2 [63].

Combining heterogeneous and homogeneous catalytic mechanisms, hybrid systems encapsulate the advantages of solid-state catalysts with molecular-level precision. Metal-organic frameworks

(MOFs) and covalent organic frameworks (COFs) are emerging as highly versatile platforms for designing hybrid catalysts. These materials have tunable pore structures and functionalized surfaces to allow us to control the reaction environments accurately (Fig. 1.16).

Electrocatalysts and Photocatalysts: Combining CO_2 Hydrogenation with renewable energy resources allow the electrical or light inputs to trigger reactions. Here, we investigate this protocol and discuss potential improvements in terms of scalability and efficiency by exploiting materials such as doped semiconductors and plasmonic nanoparticles. This has been demonstrated by the successful photo-reduction of CO_2 under visible illumination using plasmon-enhanced Au/TiO_2 photocatalysts [64].

Though they have come a long way, there are still plenty of hurdles to be cleared before innovative catalysts can be mainstreamed in industries. Nanostructured catalysts always deactivation with time of usage, including sintering or leaching. However, the reproducibility of bimetallic system is very dependent on control of metal ratios and distribution. In addition, because some systems require the use of noble metals are very expensive, they may not be economically viable. More sophisticated synthesis techniques, computer modelling, by a screening catalyst over the traditional way of synthesizing it for many substrates, additionally high cost and inferior catalytic performance has to be optimized. During the path from lab scale to commercial CO_2 hydrogenation, catalyst design innovations are crucial in creating effective, durable materials.

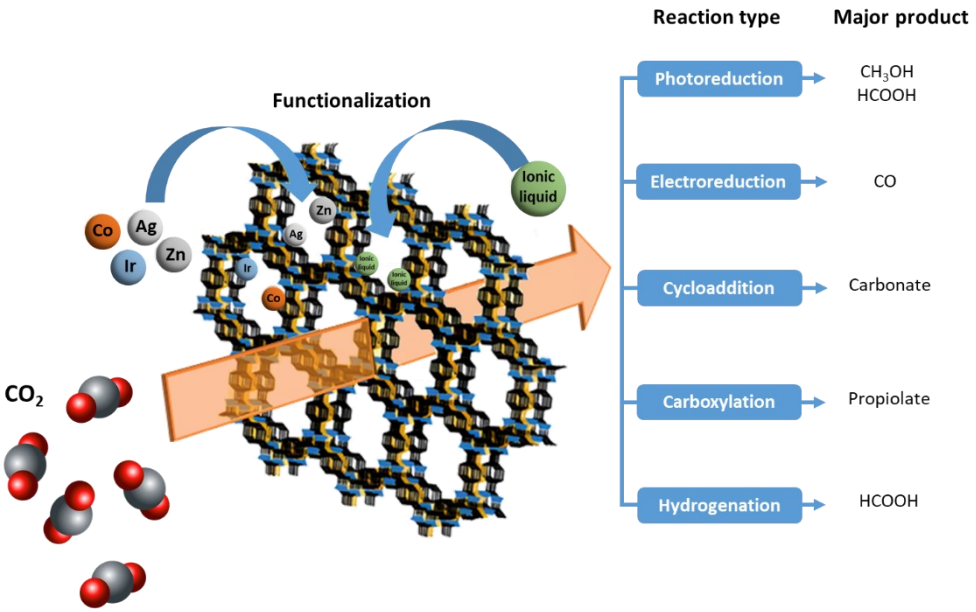

Figure 1.16. Hybrid catalytic systems for CO_2 hydrogenation.

In conclusion, the combination of advanced materials with renewable energy systems could present a promising approach to support technically feasible and economically viable carbon utilization applications which are fundamental towards a decarbonized future.

1.5.4. Reaction Mechanisms and Selectivity

As the hydrogenation of carbon dioxide is governed by an interplay of thermodynamics, kinetics, and catalyst properties it comprises a complex multi-step reaction pathway. Catalysts are key players in steering these pathways that contribute significantly to the conversion efficiency, product selectivity and ultimately process feasibility. It is crucial to learn strategies of catalysts in

promoting CO_2 hydrogenation so as to exploit systems that have high specificity in producing the targeted products and lower selectivity towards side-products.

1.5.4.1. CO_2 Hydrogenation: Mechanistic Pathways

Depending on the catalyst and reaction conditions, two different pathways are typically involved in the hydrogenation of CO_2: direct hydrogenation (Fig. 1.17) or reduction via reverse water-gas shift (Fig. 1.18) with subsequent secondary reactions.

In the case of direct hydrogenation route, CO_2 is absorbed and activated by bond dissociation on to the surface of a catalyst. This gives rise to formation of surface adsorbed intermediates such as formates or carboxylates. These then perform steps of hydrogenation into products, such as methane (CH_4) or methanol (CH_3OH). In the formation process, catalysts act to stabilize formate intermediates, with heterogeneous copper (Cu) being most effective to promote methanol synthesis.

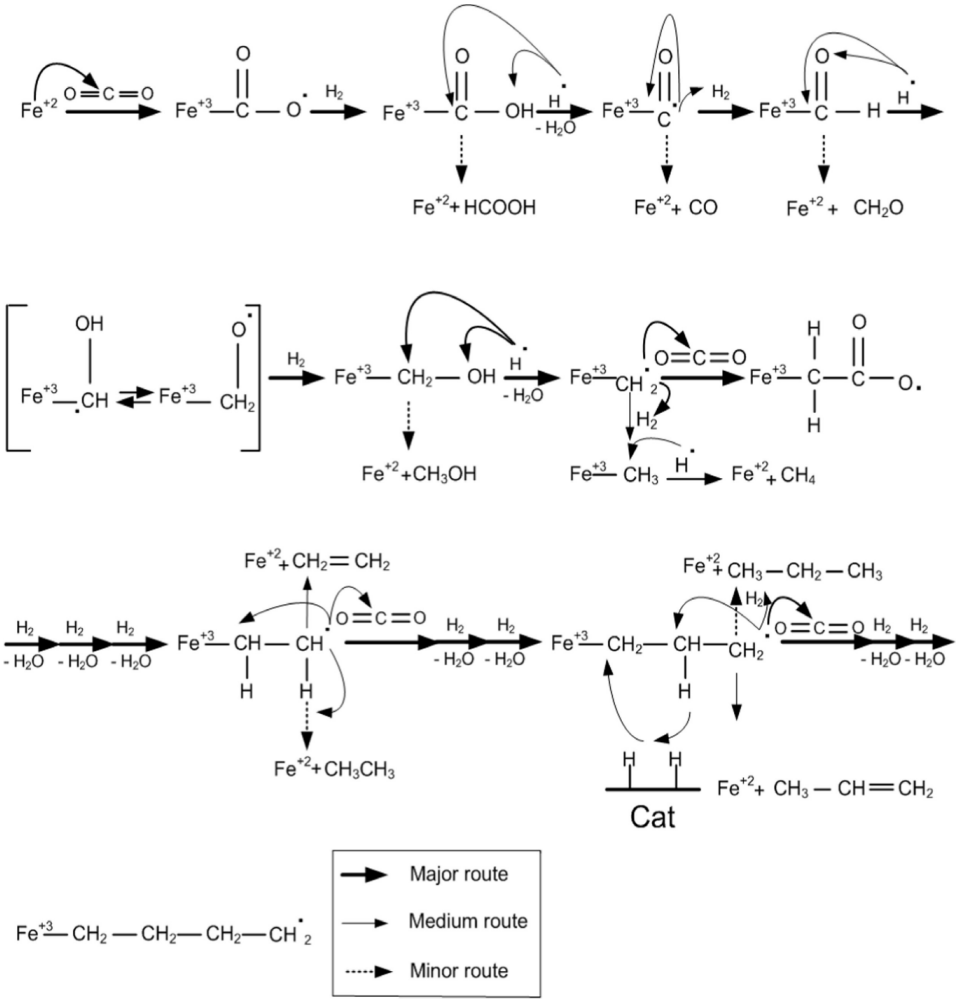

Figure 1.17. reaction mechanism for CO_2 hydrogenation over Fe-based catalysts, showing major, medium, and minor routes for intermediate formation and hydrocarbon chain propagation.

Alternatively, the RWGS pathway involves the reduction of CO_2 to carbon monoxide (CO) via RWGS reaction where CO_2 is hydrogenated to formate species and converted into CO and H_2O:

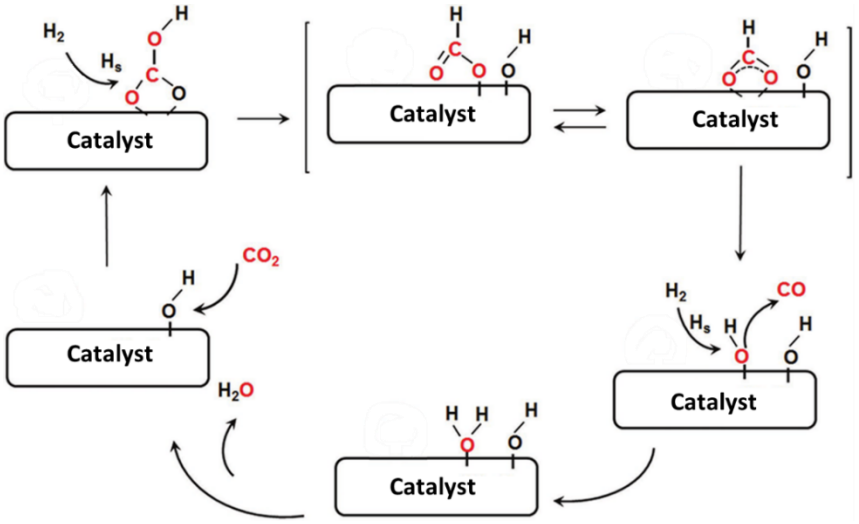

Figure 1.18 Simplified schematic of the CO_2 hydrogenation mechanism via the formate pathway. CO_2 adsorbs onto the catalyst surface and is successively hydrogenated to formate (HCOO), then formic acid and formaldehyde-like intermediates, before eventually forming CO and CH_4 or further undergoing Fischer–Tropsch-type reactions.*

The generated CO is undergoing further hydrogenation through Fischer-Tropsch mechanism where hydrocarbons are produced**.** Iron based are the most interesting catalysts for this pathway due to their dual capacity to drive both RWGS and chain growth process. For example, they are involved in CHx surface species formation and hydrocarbon (methyl/ethylene) synthesis [65].

The complementary roles of Fe and Co catalysts in CO_2 hydrogenation, particularly in RWGS and Fischer-Tropsch processes, can be summarized in Table 1.4.

Parameter	Iron (Fe)	Cobalt (Co)
Cost	Low	High
Primary Function	RWGS + Hydrocarbon Chain Growth	Hydrocarbon Chain Growth
Selectivity	Balanced for olefins and long Chains	Favorable for long-chain hydrocarbons
Activity in Low H_2/CO_2 Ratios	High (supports RWGS)	Moderate
Lifetime	Moderate (carbide stability issues)	High (more resistant to sintering)

Table 1.4. Comparative summary of key performance characteristics between iron- and cobalt-based catalysts for CO_2 hydrogenation.

The ratio between H_2 and CO, the operating conditions of temperature, and the composition of the catalyst determine which pathway dominates over another. For example, direct hydrogenation producing long-chain hydrocarbons are preferred under the higher H_2/CO_2 ratios with cobalt (Co) based catalysts. Fe-based systems on the other hand are capable of compensating for RWGS-dominated conditions where H_2 availability is lower which are usually seen in biomass-derived syngas streams.

1.5.4.2. Catalyst Influence on Selectivity

Among Fe- and Co-based catalysts, the crystalline phases play a pivotal role in determining catalytic behavior. Cobalt exists in two primary phases: hcp (hexagonal close-packed) and fcc (face-centered cubic) with hcp favoring higher hydrocarbon selectivity, while fcc exhibits higher activity for shorter chains. For Fe, the formation of Fe_5C_2 (iron carbide) during FT synthesis is critical for chain growth, but excessive carbide formation can lead to catalyst deactivation through coking. These phase transitions, governed by temperature and pressure, require precise tuning for optimal catalytic performance [66]. Catalysts are instrumental in determining the selectivity of CO_2 hydrogenation processes, directly influencing the distribution of hydrocarbons, alcohols, and byproducts. Selectivity is governed by many factors: the nature of the active sites, the properties of support materials, and the operating conditions. By modulating these, catalysts can steer the reaction pathways toward desired products, improving the overall efficiency and economic viability of the process.

The active sites for the catalyst are where CO_2 molecules bind to initiate hydrogenation. The adsorption of CO_2 at these sites and its properties will affect the pathway of the reaction as well as product selectivity. The poor adsorption usually favors methanol formation because it is easier to form the critical formate ($HCOO^-$) intermediates. These intermediates are stable enough to make the hydrogenation into methanol possible at low temperatures.

1.5.5. Reaction from CO_2 to MeOH

In particular, Cu-based catalysts are well known to be efficient for methanol synthesis because of the stabilization of these intermediates at the surface of Cu elements with a low promotion factor toward CO formation or hydrocarbon formation. Whereas higher CO_2 adsorption corresponding to Fe-based catalysts lead CO_2 dissociation into carbon monoxide (CO) which serves as precursor for hydrocarbon chain growth. This property is particularly useful for Fischer-Tropsch synthesis where low CHx is the key step in long-chain hydrocarbons production. But, if it is too strong, the adsorption becomes so high that carbon deposition or poisoning cause deactivation of the catalyst and, therefore, a careful balance has to be tuned between the electronic properties of the active site. Promoters such as alkali metals (for example K or Cs) are central in controlling the electronic behaviour of the catalyst. The activation of CO_2 with its weakened C=O bond plays a significant role in the catalytic cycle, and some ingredients, such as potassium, contribute to it by increasing the electron density at active sites [67]. In addition, a promoter can stabilize intermediates that Favor one pathway over another (e.g., stabilization of CH_x species for hydrocarbon synthesis or $HCOO^-$ for methanol production), thereby enhancing selectivity and minimizing byproducts [68].

1.5.6. Effects of Support and Interactive Effects with Metals

Catalyst supports stabilize the catalyst structure and affect the dispersion, accessibility, and electron state of active metal particles. This is because the way in which the active metal interacts with the support material contributes to a change in both binding energies and activation energy of active reaction steps, thus significantly changing product distribution. For instance, ceria (CeO_2), a material known for its oxygen storage ability and excess oxygen can be an interesting feature. The vacancies assist in CO_2 adsorption and activation, making it possible for pathways

that lead to CO and hydrocarbon formation. Ceria-supported Fe catalysts have displayed enhanced RWGS activity and hydrocarbon selectivities relative to unsupported systems [69]. On the other side, alumina (Al2O3) is often used for its high-temperature robustness and suppression of the sintering of active metal particles. Its use is very beneficial especially to keep Ni-based catalysts for methanation durable. The metal-support interaction can also change the electronic structures of the corresponding active metals, thus leading to the modification of catalytic activity. Such strong interactions between the particles can result in increased dissociation of CO_2 into CO, which can enhance chain growth and hydrocarbon synthesis. For example, the cobalt (Co) on titania (TiO_2) displays higher selectivity towards longer chain hydrocarbons as the e- is transferred from metal to support. On the other hand, weaker interactions with supports such as silica (SiO_2) enhance methanol production by lowering the activation energy for formate intermediates, which in turn allows them to efficiently reduce to methoxy and dehydrogenate into methane and water. The reaction pathways and product distribution of CO_2 hydrogenation reactions are strongly dependent on the operating conditions, such as temperature, pressure and H_2/CO_2 ratio. An example of this is selective hydrogenation where the conditions needed to achieve high selectivity are different from those that give rise to maximum turnover.

- Temperature Effects: higher temperatures help the RWGS reaction which provides CO as a precursor for Fischer-Tropsch synthesis, typically 600-800°C. Second, for CO-dependent hydrocarbon formation pathways such as Fe-based catalysts. At temperatures too high may cause side reactions resulting in extra methane or coke production, and that translates as a loss of efficiency. In contrast, methanol synthesis is favored at lower temperatures, from 200 to 300°C, and especially with Cu-Zn catalysts that stabilize formate intermediates.
- Pressure Effects: Higher pressure generally improves the conversion of CO_2 to liquid hydrocarbons or methanol. Under higher pressures, the hydrogenation reactions shifts equilibrium in favour of condensed phase products, which goes to Le Chatelier´s principle. The possibility of catalyst deactivation by over-hydrogenation or sintering can increase due to high pressure, especially in unsupported or poorly dispersed catalysts. Table 1.5 summarizes the key parameters in relation to the kinetics.

Catalyst	Temp (°C)	Pressure (bar)	H_2/CO_2 Ratio	Main Product
Cu-Zn	200-300	50-100	3 to 1	Methanol
Fe	300-500	20-40	1 to 1	Hydrocarbons, CO
Co	200-400	20-40	2 to 1	Long-chain hydrocarbons

Table 1.5. Typical operating conditions and product distributions for major catalyst systems used in CO_2 hydrogenation.

- H_2/CO_2 Ratio: The availability of reducing agents, which in turn define the pathway and product distribution, is determined by the H_2/CO_2 ratio. The increased ratio can mitigate side reactions such as coke formation, and drive hydrogenation of intermediates to the desired products. A 3:1 ratio is ideal for the production of methanol, with ratios somewhat closer to 1:1 favouring hydrocarbons production in Fischer-Tropsch synthesis. Catalysts designed for specific ratios, such as Cu-based systems for methanol or Fe-based systems for hydrocarbons, exhibit significantly improved performance under their respective conditions [70].

Recent progress in the development of operando spectroscopic techniques (e.g. X-ray photoelectron spectroscopy (XPS), Fourier-transform infrared spectroscopy (FTIR) have made it possible for mechanism studies at molecular level. Together, the studies illuminate active sites and intermediates that fluctuate during CO_2 hydrogenation which could be explored for improved catalyst optimization strategies. As an example, time-resolved spectroscopy has revealed that transient CHx species on Fe-Co catalysts are important intermediates in chain-growth reactions leading to the rational design of catalysts with better selectivity for longer chained hydrocarbons [71].

Despite these advancements, achieving control over product distribution remains a challenge. Due to competing reactions, such as methane overproduction in methanol synthesis or olefin hydrogenation in Fischer-Tropsch processes, the products yields might become economically less attractive. Ongoing research should be directed toward the development of multi-functional catalysts that can adjust reaction pathways according to demand, enabling less energy input and a minimum of byproducts.

1.6. Life Cycle Assessment (LCA)

Life Cycle Assessment (LCA) is an important tool for quantifying and assessing the environmental effects of processes, products or systems across their life cycle. Sustainable technologies become more and more famous all over the world, leading to LCA as pivotal methodology in estimating trade-offs and long-term sustainability in different methods especially as an example in catalysis or CO_2 utilization. Through the identification of pollutants and resource use hotspots, LCA underlies decision-making for pollution prevention techniques and circular economies.

It is a technique for evaluating the potential environmental burdens associated with all life cycle stages of a product or process: from raw material acquisition, through production and use phases, to end-of-life management. Such a comprehensive approach prevents so-called burden shifting where reductions in one stage inadvertently increase impacts elsewhere.

The ISO 14040 and 14044 standards define the structure of an LCA, comprising four interconnected phases:

- Goal and scope: Describing what is to be investigated, objectives of research, system boundaries, functional unit. For example, when evaluating CO_2 hydrogenation catalysts, the functional unit may be expressed as "kgCO_2/kg catalyst over its lifetime".
- Life Cycle Inventory (LCI): gathering data on the inputs (e.g., raw materials, energy) and outputs (e.g., emissions, waste) within the system boundary.
- Life Cycle Impact Assessment (LCIA): In LCIA, LCI data are transformed into potential impacts on the environment measured by categories such as global warming potential (GWP), eutrophication and resource depletion.
- Interpretation: Summarizing and reporting results to facilitate decision making, generalized conclusions.

The components are used iteratively in order to change system boundaries, data quality or assumptions resulting in more accurate objectives output and decision making.

1.6.1. LCA Methodology in Catalyst Development

The development of catalysts is crucial to CO_2 utilization technologies, but the production of catalysts usually involves energy- and material-intensive processes. Life cycle assessment offers a quantitative approach to this environmental evaluation, above and beyond the limited insights derived from lab-scale efficiencies. An example of this lies in the synthesis of materials known as hydrotalcite-derived catalysts, which have been used for CO_2 hydrogenation whereby such preparation methods require energy-intensive steps including calcination or drying, contributing to associated carbon emissions. A life-cycle analysis (LCA) study could show that the calcination step is the biggest contributor to a catalyst's carbon footprint. Based on such findings, researchers can then investigate other lower energy synthetic routes, e.g., microwave-assisted calcination [72].

In addition, LCA is important for comparing environmental profile between different catalyst systems. Fe-based catalysts, for example, are very efficient CO_2 hydrogenation, but tend to operate at higher temperatures, which in turn increases the energy intensity. In contrast, the low-temperature Cu-Zn catalysts for methanol synthesis can be produced with much lower resource consumption or involve increased production cost. LCA makes it possible quantify and evaluate these trade-offs that occur within specific industrial context.

1.6.2. The role of LCA in CO_2 Utilization Technologies

Life cycle assessments (LCAs) are required to estimate the overall environmental performance of CO_2 utilization processes such as methanation, methanol synthesis and Fischer-Tropsch (FT) synthesis [73-75]. Although these processes consume CO_2, their total effect is very much upstream-dependent by the nature of those factors (e.g., energy sources and hydrogen).

CO_2 hydrogenation requires a considerable amount of hydrogen and its source of production can significantly impact the environmental assessment. While green hydrogen, produced by water electrolysis powered by renewable electricity, is clean, its production cost is high. The process of producing blue hydrogen, which is derived from natural gas and requires carbon capture, offers a similar option but involves added emissions. These scenarios are analysed comparatively by an LCA to demonstrate the balances between cost, emissions, and scalability [76]. LCA takes into account the systems-level performance of adsorptive processes integrated with CO_2 capture, utilization, and storage (CCUS). In the former case, renewable electricity makes hydrogen that is reacted with captured CO_2 to form methane (power-to-gas) in a closed loop system. This approach allows the identification of under which conditions such systems are able to achieve net negative emissions, while taking into consideration further aspects like energy inputs, conversion efficiencies and emissions from auxiliary processes. The environmental impact of CO_2-based products goes beyond the first production steps, also including their use and end-of-life. For example, synthetic fuels from CO_2 hydrogenation are commonly burned, essentially recycling the captured CO_2 back into the atmosphere. LCA accounts for this by comparing the emissions of CO_2 of produced fuels against traditional fossil fuels, and hence how powerful they are to help close the carbon loop if working alongside effective CO_2 capturing efforts. Today, LCA is more

commonly applied to assess new CO_2 utilization pathways like electrocatalytic and photocatalytic reduction. Many of these technologies are promising but carry a high material cost or have limited scalability. LCA studies bring out these areas of challenge as well light the way toward new avenues for improvement, such as recyclable or less energy-intensive catalyst systems. In addition, LCA can make substantial contributions to policy, as it is the only approach that uses evidence-based principles to evaluate such things as subsidies, carbon pricing and regulatory approaches. Policymakers use results from LCAs to inform their decisions on where and how they should invest in low-carbon technologies, like renewable hydrogen infrastructure or advanced catalysts.

1.6.3. Challenges and Outlooks

Being a powerful tool, LCA, bears some limitations as well. Among them:

- Data integrity and Accessibility:
  New technologies come with non-standardized data which to some extent brings an ambiguity for making decisions and even assumptions in the process. Finally, a more comprehensive characterization of database items (e.g. new materials or processes) will contribute to the quality and reliability of LCA data by providing more detailed information for the assessment.
- Variance by Type and Region:
  LCA methodology commonly assume static conditions resulting in ignoring regional differences in many fields such as energy grids, resource availability or production scales. The integration of dynamic and spatially resolved data will allow for more accurate assessments.
- Integration with other metric:
  In the context of sustainability, LCA combined with techno-economic analysis (TEA) and environmental risk assessments could provide a more complete evaluation. As a prime example, eliminating the carbon footprint of a catalyst does not necessarily make it economically feasible or environmentally preferable if toxicity and resource scarcity undermine sustainability.

Resolution of these issues will allow LCA to progress as a key platform technique for sustainable innovation in catalysis and CO_2 utilization technologies. Further details regarding this study are addressed in detail in the corresponding Chapter 7.

1.7. Safety and Operability Frameworks Review

Safety and operability are by far some of the most important aspects in the development as well as implementation of any chemical processes to protect both personnel and equipment, but also maintaining long term sustainability and efficient operations. Given the risks associated with chemical reactions, high pressure systems, and energy-intensive processes, requiring a very deliberate approach to risk assessment and management. Hazard and Operability Studies (HAZOP) and Layers of Protection Analysis (LOPA) are two most commonly used methodologies, especially in industrial context. These methodologies give a systematic format to

recognize the predictors of hazards, gradate their consequences, and lead to counteractions which cannot overlooked in both laboratory and industrial environments.

1.7.1. HAZOP: Proactive Hazard Identification

The HAZard and OPerability (HAZOP) study is a qualitative hazard identification method that targets systematically with potential operating deviations from the process intended conditions as well as thier consequences. Used in the chemical process industries, it is a group review of process diagrams looking at every node (reactor, pump, valve), checking for deviations such as high temperature, low pressure wrong flowrates and so on. The process starts with a structured brainstorming session, in which guidewords (such as more, less, none etc.) are used on the process parameters to discover deviations. For example, a deviation such as “increased pressure” in a reactor could cause situations like equipment malfunction or rapid reactions. For each group, any identified deviation is analyzed for root causes, consequences and safeguards and recommendations are provided to prevent or minimize risks. In laboratories, the HAZOP method is very useful when scaling up experimental processes. In the case of a high-pressure and high-temperature H_2 fed CO_2/CO hydrogenation setup, this may mean being at risk of hydrogen leaking, thermal runaway or catalyst poisoning. A HAZOP study would identify these risks and may suggest measures such as the installation of pressure relief valves, continuous monitoring systems or automatic shutdown devices to mitigate them.

1.7.2. LOPA: Risks & Safeguards

While HAZOP provides a qualitative overview of risks, other methods such as LOPA analysis give a semi quantitative evaluation of safeguards by investigating layers of protection. Each of these layers (e.g., alarms, safety interlocks, relief systems) is judged in terms of its probability off failure and ability to prevent or mitigate the hazard. In this method, LOPA the first step is to identify hazard scenario during HAZOP and moderate it on likelihood and consequence leads a particular risk level. It next assesses whether existing protections are adequate to lower the hazard down to an appropriate level. If they are not, additional layers of protection are advisable. In a Fischer-Tropsch synthesis reactor, for instance, where high-temperature exothermic reactions can cause the reactor to overheat, LOPA may test the efficacy of a cooling system, temperature alarms and an emergency shutdown system to see if additional safeguards such as backup cooling loops are required. LOPA is of good practical utility in an industrial setting in which the availability of quantitative data from process monitoring can increase the accuracy level of risk assessments. It ensures that the cost of implementing such safety measures is congruent with the course risk, matching operational safety without going overboard.

Because smaller-scale operations are often considered simple, safety and operability analyses can be ignored in laboratory settings. Yet, it is the case that even relatively small experimental setups for CO_2 hydrogenation or catalyst testing are risks when working with pressurised systems, flammable gasses and high temperatures. For example, on a front-end engineering design (FEED) study, HAZOP can identify that a hydrogen leak initiated by blocked flow lines could occur in the heat pipe; LOPA then follows up by quantifying whether gas detectors and fail-safe mechanisms are needed to protect against such an event. However, in industrial settings where the processes run continuously and at larger scale, the stakes are much higher. The synthesis of

CO_2-based hydrocarbons often involves the manipulation of high pressures in the presence of compressed gases, and exothermic reaction steps that need careful control. When combined with both HAZOP and LOPA, the goal is to minimize downtime due to unplanned incidents by integrating a system of preventative measures for reducing catastrophic failures during both design and at operational turnovers. This practice of incorporating HAZOP & LOPA methodologies at a very early stage in the process development is remark of a proactive risk management culture, prepared not just to face but to avoid these hazards from aggravating. This demand is on the rise due to the further complexity in chemical processes which are increasingly integrated and have multiple functions like CO_2 utilization, renewable energy incorporation etc. which required novel safety analysis tools. Many opportunities for improvements exist with innovative technologies like digital twins and real-time monitoring systems, which can make HAZOP and LOPA applications more effective. By practically introducing potential process deviations and dynamically risk-assessing them, a more accurate view into what is happening right now can be provided making the solution safer and more operable.

Further details regarding this study are addressed in detail in the corresponding Chapter 6.

1.8. Neural Networks in Catalysis

The rise of machine learning (ML) and artificial intelligence (AI) has greatly impacted scientific research, catalysis being no exception. One of such machine learning techniques that is now very much popular for speeding up the discovery, development and optimisation of catalytic systems are neural networks. Neural networks are used to model complex chemical processes and predict catalyst behavior, making it possible to discover materials with astonishing efficiency. The development of a catalyst is at best laborious, and essentially it has copied the procedure for catalyst design (development) by empirical investigation. These limitations are mitigated by neural networks that learn the patterns from the data available through prior studies and can predict from composition, structure, and operation conditions of new catalysts.

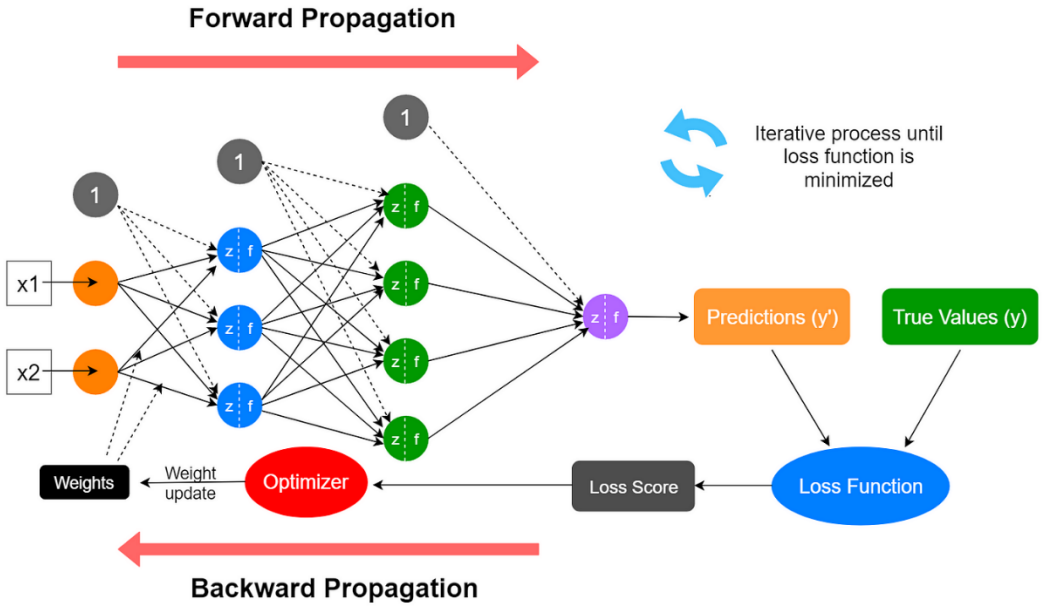

Figure 1.19. Schematic representation of an artificial neural network (ANN) training cycle. The forward propagation phase calculates predictions from input variables (x_1, x_2), followed by loss evaluation against true values.

In another application, deep learning frameworks have been used to screen bimetallic catalysts for CO_2 hydrogenation to identify compositions that deliver optimal activity and selectivity without exhaustive experimental testing [77]. Density functional theory (DFT) and other high-throughput computational methods can be used to compute catalyst properties, e.g., adsorption energies or reaction pathways. This data is then compiled together with experimental results by the neural networks to yield much power predictive models. These models can then be used to help researchers identify candidate materials for further study, significantly reducing the time needed to find optimal catalysts (Fig. 1.19)

Neural networks are important, not only to discover new catalysts but also to enhance existing systematics. The catalytic performance is strongly affected by the process parameters, temperature, pressure, and reactant ratios. By analysing experimental and process data, neural networks can be used to determine the best operating conditions leading to maximum conversion efficiency and product selectivity. One example can be seen with neural networks being implemented as a method for modelling the relationship between reaction conditions and product distribution in CO_2 hydrogenation processes, which traditional empirical approaches can overlook [78]. Models with higher level, such as Recurrent Neural Networks (RNNs) and Convolutional Neural Networks (CNNs), which can capture temporal or spatial variations in the catalytic system have shown better performance for dynamic optimization of reactor operation [79]. Although promising, the application of neural networks also faces practical challenges related to accurate dataset acquisition and model interpretability when applied to catalysis. To mitigate these shortcomings, the field of explainable AI (XAI) helps addressing these limitations by providing insights into how neural networks make predictions, thereby increasing understandability in their outputs. Neural network integration with experimental workflow enables state-of-the-art identification and rationalization of activity descriptors, with advanced characterization techniques offering unprecedented detail (and challenges) for catalyst screening as data-driven methods mature. This symbiosis of AI and proven research tools opens pathways for groundbreaking creations in sustainable chemical processes and materials.

Further details regarding this study are addressed in detail in the corresponding Chapter 8.

1.9. Aim of the Work and Novelty

The urgent need to stop climate change and minimise greenhouse gas emissions world-wide, has increased research on sustainable methods for carbon utilisation. Carbon dioxide (CO_2) is by far the most important among the greenhouse gases causally responsible for global warming, but it has been calculated as contributing to around three-quarters of all anthropogenically sourced carbon dioxide emissions. With a traditional technique such as Carbon Capture and Storage (CCS), which has been able to store just enough but not employ it into other commercially viable products. This deficiency emphasizes the necessity of other approaches, such as carbon capture and utilization (CCU), in which CO_2 is captured but also converted to fuels and chemicals and cycled into a closed loop carbon economy.

Catalysis is essential for the efficient and selective transformation of CO_2 into value added products like hydrocarbons or methanol. Therefore, the traditional catalytic systems frequently suffer from high-energy consumption, poor selectivity and stability under reaction conditions. To

address these challenges, new catalysts have to be developed that can work in an environmental and sustainable way. In addition, the incorporation of CO_2 hydrogenation processes within existing industrial contexts presents a set of new challenges related to quantifying process hazards, environmental impacts and system optimization. In this context, the synthesis and application of novel catalysts for CO_2 and CO hydrogenation offer a promising pathway toward addressing these challenges. By employing sustainable synthesis methods, advanced risk assessment frameworks, and interdisciplinary approaches such as Life Cycle Assessment (LCA) and Artificial Neural Networks (ANNs), the boundaries of catalytic science and process engineering can be expanded.

The primary objective of this research are the design and synthesis of novel Iron based catalysts: hydrotalcite-like materials and Metallo-silicates systems suitable for selective CO and CO_2 hydrogenation.
The first set of catalysts consisted of iron-based catalysts supported on metallosilicates, synthesized using a nonhydrolytic surfactant-assisted sol-gel method. Support synthesis as well as catalysts synthesis were performed in Polytechnique of Montreal by PhD Eran Tugce under the supervision of Prof. Gregory Patience. These supports included commercial aluminium oxides by the name of Catalox and Dispal and Ce, Zr, V, and Ti metallosilicates, which were selected for their tunable molecular sieve properties and ability to influence catalytic performance. They are devided into three classes named (i) Iron metallosilicates, (ii) Promoted Iron Metallosilicates and (iii) Iron supported aluminium oxides. The investigated catalysts are the following:

(i) **$Fe/Ce/SiO_2$**; **$Fe/Zr/SiO_2$**; **$Fe/V/SiO_2$**; **$Fe/Ti/SiO_2$**
(ii) **$Fe/Ce/SiO_2$-K,Cu**; **$Fe/Zr/SiO_2$-K,Cu**
(iii) **Fe/Catalox-K,Cu**; **Fe/Dispal-K,Cu**
the loading of Fe for all the systems is 10% by weight.

Regarding the second class of catalysts, Hydrotalcite-like Iron based materials, they were synthesized by the application of two eco-friendly and cost-effective methodologies namely ultrasonic-assisted precipitation and ball milling. Both techniques offer significant advantages in terms of environmental impact and energy efficiency, compared to traditional synthesis methods. Ultrasonic Assisted Precipitation use high-frequency sound waves to promote mixing, as well improve reaction rates during catalyst formation. The approach could help decrease the energy intensity while saving time and avoid certain hazardous chemicals required to make catalysts under very high temperature which would produce more greenhouse gases. In the same manner, ball milling provides a mechanochemical method for catalyst synthesis by replacing solvents and therefore further reducing its environmental impact. Because these approaches are in line with green chemistry principles, they provide a route to sustainable catalyst design.

The synthesized catalysts throughout both Ultrasonic assisted precipitation and ball-milling synthesis are the following:

$Mg_{0.60}Fe_{0.34}Cu$ (Fe30)
$Mg_{0.55}Fe_{0.40}Cu$ (Fe40)
$Mg_{0.32}Co_{0.33}Fe_{0.30}Cu$ (Co33)
$Mg_{0.24}Co_{0.42}Fe_{0.29}Cu$ (Co45)
$Zn_{0.60}Fe_{0.35}Cu$ (FeZn)

The synthesized hydrotalcite-like compounds serve as highly effective catalysts for CO and CO_2 hydrogenation, addressing key challenges in catalysis, including poor selectivity, low efficiency, and limited stability under reaction conditions. By optimizing their composition and structure, these catalysts demonstrate exceptional performance, with higher catalytic efficiencies and product selectivities compared to conventional iron-based systems. Additionally, their remarkable stability under operating conditions ensures consistent performance, making them suitable for both laboratory-scale testing and potential industrial applications.

Not only is this important from the standpoint of catalyst development, but it also serves the larger objectives that have recently caught considerable public attention carbon utilization and greenhouse gas mitigation. The catalysts synthesized for this study underwent extensive characterization at various stages to establish a clear correlation between their physicochemical properties and catalytic performance. These analyses were conducted immediately after synthesis, following the activation pretreatment, and, in certain cases, after the completion of the catalytic runs. This approach ensured a comprehensive understanding of how the structural and surface properties of the catalysts influenced their behavior under reaction conditions. To confirm the exact composition and rule out the presence of impurities, Inductively Coupled Plasma (ICP) were performed on the synthesized samples. These techniques provided precise weight percentages of the elemental components. Temperature-Programmed Reduction (TPR) experiments were conducted to identify the optimal activation conditions, ensuring that the active sites were prepared under appropriate pretreatment protocols. Additionally, Transmission Electron Microscopy (TEM) and Scanning Electron Microscopy coupled with Energy-Dispersive X-ray Spectroscopy (SEM/EDS) were utilized to investigate the dispersion of active metals and the nanoparticle sizes distributed across the support. These methods allowed for detailed visualization and mapping of the metal particles, shedding light on the uniformity and quality of the catalysts. To further characterize the catalysts, Brunauer-Emmett-Teller (BET) surface area measurements were carried out to quantify their porosity and surface area, critical parameters for assessing their suitability for Fischer-Tropsch synthesis. Moreover, X-ray Powder Diffraction (XRPD) was employed to determine the crystallographic phases of the catalysts and to identify the presence of specific metal oxides or other crystalline structures. The catalytic performance of these materials was then rigorously evaluated under various conditions, including different reaction temperatures, time-on-stream (TOS), H_2/CO_2 ratios and in some cases different pressures using two different dedicated plants. Moreover, the experimental approach integrated data collection from two different reactor scales, a manual lab-scale system and a fully automated bench-scale system, providing a rich dataset that combine laboratory conditions and scaled-up process behavior. The design, setup, and operation of these experimental rigs, including details of its functionality and configuration, will be described thoroughly in Chapter 2 of this thesis.

This research also has several other objectives including performance evaluation of new materials, assessing sustainability, minimizing operational risks and use in tandem with cutting-edge data analytics. These provide a holistic perspective on the issues in CO and CO_2 hydrogenation and lead to significant steps toward realizing the practical use of carbon utilization technologies. This research integrates a comprehensive Life Cycle Assessment (LCA) to evaluate the sustainability of both catalyst production and the Fischer-Tropsch CO_2 hydrogenation process. The study

focused on iron-based nano hydrotalcite catalysts synthesized via ultrasonic-assisted co-precipitation, including **Fe30** ($Mg_{0.65}Fe_{0.3}Cu_{0.05}$), **Fe40** ($Mg_{0.55}Fe_{0.4}Cu_{0.05}$), and **Co45** ($Mg_{0.23}Co_{0.42}Fe_{0.3}Cu_{0.05}$). These catalysts were selected for their diverse catalytic properties and environmental impacts, offering insights into the trade-offs between performance and sustainability.

Using SimaPro 9.4, the environmental impacts were assessed from raw material extraction through catalyst production and process operation. Functional units of 1 g of catalyst and 1 g of hydrocarbon product allowed for a dual evaluation of production and operational phases. The study employed Global Warming Potential, Cumulative Energy Demand, and Human Toxicity Potential as metrics to quantify environmental performance.

As mentioned before, safety is a fundamental aspect in Fischer-Tropsch synthesis, especially when dealing with high-pressure and exothermic reactions. This study implemented Hazard and Operability Analysis (HAZOP) and Layers of Protection Analysis (LOPA) to systematically evaluate and mitigate risks associated with laboratory-scale FT synthesis experiments. The integration of these industrial frameworks in an academic setting provided a novel approach to addressing the unique safety challenges present in manual operations and transient processes. Key risk areas, including the Fischer-Tropsch reactor and feed system, were identified, with specific deviations linked to manual interventions and insufficient safety infrastructure. HAZOP analysis highlighted critical deviations, while LOPA quantified the required safety layers to prevent accidents. Recommendations included enhanced automation, safety interlocks, and control loops to minimize human error. Ventilation, redundancy in safety measures, and improved operator training were emphasized as essential strategies. This approach not only elevated safety standards but also provided a framework for adapting industrial safety methodologies to academic environments. By addressing operational vulnerabilities, the study offers a model for safer and more efficient laboratory-scale FT synthesis processes.

Furthermore, to address challenges in predicting Fischer-Tropsch synthesis outcomes, this research employed Artificial Neural Networks (ANN) and Random Forest (RF) as a data-driven tool for modelling catalytic performance. Unlike traditional kinetic models that require detailed reaction mechanisms, ANN and RF were used to predict outputs such as CH_4, C_{2-4} hydrocarbons, C_{5+}, CO_2 conversion, and CO selectivity based on inputs like temperature, pressure, gas hourly space velocity (GHSV), H_2/CO_2 ratio, and catalyst composition. The ANN architecture was designed for minimal error, validated against a comprehensive experimental database, and optimized to uncover non-linear relationships between input variables and product distributions. For example, the study demonstrated the influence of Fe content and K promotion on hydrocarbon yields and CO_2 conversion efficiency. By bridging the gap between experimental data and computational models, the ANN approach provides actionable insights into catalyst optimization and process design. This methodology offers a powerful alternative to conventional modeling, enabling rapid evaluation of operating conditions and catalyst formulations. Its application in this research highlights the potential of machine learning in accelerating advancements in catalyst development and carbon utilization technologies.

The detailed research work done with each aspect is explained in the upcoming paragraphs.

References Chapter 1

[1] Loáiciga HA. Challenges to Phasing out Fossil Fuels as the Major Source of the World's Energy. Energy & Environment 2011;22:659–79. https://doi.org/10.1260/0958-305X.22.6.659.

[2] Trends in global CO_2 and total greenhouse gas emissions: 2020 Report n.d.

[3] Intergovernmental Panel on Climate Change (IPCC): Climate Change 2021 – The Physical Science Basis 2023.

[4] Reichelstein S, Yorston M. The prospects for cost competitive solar PV power. Energy Policy 2013;55:117–27. https://doi.org/10.1016/j.enpol.2012.11.003.

[5] Henrique AID, Zhao F, Backwell B, Clarke E, Ladwa R, Jayasurya F, et al. Global Wind Energy Council n.d.

[6] Boretti A, Pollet BG. Hydrogen economy: Paving the path to a sustainable, low-carbon future. International Journal of Hydrogen Energy 2024;93:307–19. https://doi.org/10.1016/j.ijhydene.2024.10.350.

[7] Beck E-G. 180 Years of Atmospheric CO_2 Gas Analysis by Chemical Methods n.d.

[8] THE PARIS AGREEMENT, 2016.

[9] Raihan A, Farhana S, Muhtasim DA, Hasan MAU, Paul A, Faruk O. The nexus between carbon emission, energy use, and health expenditure: empirical evidence from Bangladesh. Carbon Res 2022;1:30. https://doi.org/10.1007/s44246-022-00030-4.

[10] Hudson M, Carbon Capture and Storage in the United Kingdom. History, Policies and Politics. Taylor & Francis, 27 mar 2024 - 132 pagine

[11] Bisotti F, Hoff KA, Mathisen A, Hovland J. Direct Air capture (DAC) deployment: A review of the industrial deployment. Chemical Engineering Science 2024;283:119416. https://doi.org/10.1016/j.ces.2023.119416.

[12] Bavykina A, Kolobov N, Khan IS, Bau JA, Ramirez A, Gascon J. Metal–Organic Frameworks in Heterogeneous Catalysis: Recent Progress, New Trends, and Future Perspectives.ChemRev 2020;120:8468–535. https://doi.org/10.1021/acs.chemrev.9b00685.

[13] Shih CF, Zhang T, Li J, Bai C. Powering the Future with Liquid Sunshine. Joule 2018;2:1925–49. https://doi.org/10.1016/j.joule.2018.08.016.

[14] Rego De Vasconcelos B, Lavoie J-M. Recent Advances in Power-to-X Technology for the Production of Fuels and Chemicals. Front Chem 2019;7:392. https://doi.org/10.3389/fchem.2019.00392.

[15] Müller LJ, Kätelhön A, Bringezu S, McCoy S, Suh S, Edwards R, et al. The carbon footprint of the carbon feedstock CO_2. Energy Environ Sci 2020;13:2979–92. https://doi.org/10.1039/D0EE01530J.

[16] Jia C, Gao J, Dai Y, Zhang J, Yang Y. The thermodynamics analysis and experimental validation for complicated systems in CO 2 hydrogenation process. Journal of Energy Chemistry 2016;25:1027–37. https://doi.org/10.1016/j.jechem.2016.10.003.

[17] Triviño MLT, Arriola NC, Kang YS, Seo JG. Transforming CO_2 to valuable feedstocks: Emerging catalytic and technological advances for the reverse water gas shift reaction. Chemical Engineering Journal 2024;487:150369. https://doi.org/10.1016/j.cej.2024.150369.

[18] Ghoniem AF. Needs, resources and climate change: Clean and efficient conversion technologies. Progress in Energy and Combustion Science 2011;37:15–51. https://doi.org/10.1016/j.pecs.2010.02.006.

[19] Wang Z, Song H, Liu H, Ye J. Coupling of Solar Energy and Thermal Energy for Carbon Dioxide Reduction: Status and Prospects. Angew Chem Int Ed 2020;59:8016–35. https://doi.org/10.1002/anie.201907443.

[20] Wang B, Zhu X, Huang F, Quan Y, Liu G, Zhang X, et al. Porous edge confinement: High carrier potential and low activation energy barrier synergistically boosting the efficiency of selective photocatalytic CO_2 conversion. Applied Catalysis B: Environmental 2023;325:122304. https://doi.org/10.1016/j.apcatb.2022.122304.

[21] Zhou C, Zhang J, Fu Y, Dai H. Recent Advances in the Reverse Water–Gas Conversion Reaction. Molecules 2023;28:7657. https://doi.org/10.3390/molecules28227657.

[22] Li N, Mo L, Unluer C. Emerging CO_2 utilization technologies for construction materials: A review. Journal of CO_2 Utilization 2022;65:102237. https://doi.org/10.1016/j.jcou.2022.102237.

[23] Eveloy V, Gebreegziabher T. A Review of Projected Power-to-Gas Deployment Scenarios. Energies 2018;11:1824. https://doi.org/10.3390/en11071824.

[24] Orlić M, Hochenauer C, Nagpal R, Subotić V. Electrochemical reduction of CO_2: A roadmap to formic and acetic acid synthesis for efficient hydrogen storage. Energy Conversion and Management 2024;314:118601. https://doi.org/10.1016/j.enconman.2024.118601.

[25] Detz RJ, Ferchaud CJ, Kalkman AJ, Kemper J, Sánchez-Martínez C, Saric M, et al. Electrochemical CO_2 conversion technologies: state-of-the-art and future perspectives. Sustainable Energy Fuels 2023;7:5445–72. https://doi.org/10.1039/D3SE00775H.

[26] Fan J, Du H, Zhao Y, Wang Q, Liu Y, Li D, et al. Recent Progress on Rational Design of Bimetallic Pd Based Catalysts and Their Advanced Catalysis. ACS Catal 2020;10:13560–83. https://doi.org/10.1021/acscatal.0c03280.

[27] Li H, Bian Y, Liu M, Lin J, Dai M, Xie H, et al. CO_2 mineralization and utilization by tailings sand in China for potential carbon sinks and spatial project layout. Resources, Conservation and Recycling 2024;206:107598. https://doi.org/10.1016/j.resconrec.2024.107598.

[28] Luo P, Shi P, Yan Z, Han J, Wang J, Li Y, et al. Ternary synergistic interaction of Cu-ZnO-ZrO2 promoting CO_2 hydrogenation to methanol. Applied Catalysis A: General 2025;689:120006. https://doi.org/10.1016/j.apcata.2024.120006.

[29] Mandal SC, Das A, Roy D, Das S, Nair AS, Pathak B. Developments of the heterogeneous and homogeneous CO_2 hydrogenation to value-added C2+-based hydrocarbons and oxygenated products. Coordination Chemistry Reviews 2022;471:214737. https://doi.org/10.1016/j.ccr.2022.214737.

[30] Han Y, Fang C, Ji X, Wei J, Ge Q, Sun J. Interfacing with Carbonaceous Potassium Promoters Boosts Catalytic CO_2 Hydrogenation of Iron. ACS Catal 2020;10:12098–108. https://doi.org/10.1021/acscatal.0c03215.

[31] Wang S, Rohani V, Ye T, Dupont P, Pagnon S, Sennour M, et al. Effect of K-promoter use in iron-based plasma-catalytic conversion of CO_2 and CH4 into higher value products.

Applied Catalysis A: General 2023;663:119315. https://doi.org/10.1016/j.apcata.2023.119315.

[32] Grainca A, Michele AD, Sugliani C, Boccalon E, Nocchetti M, Bianchi C, et al. Iron Based Nano-hydrotalcites Promoted with Cu as Catalysts for Fischer-Tropsch Synthesis in iomass to Liquid Process n.d.

[33] Kamkeng ADN, Wang M, Hu J, Du W, Qian F. Transformation technologies for CO_2 utilisation: Current status, challenges and future prospects. Chemical Engineering Journal 2021;409:128138. https://doi.org/10.1016/j.cej.2020.128138.

[34] Nuuttila N. M.Sc. Business Administration and Economics. Master's Thesis n.d.

[35] Grim RG, Huang Z, Guarnieri MT, Ferrell JR, Tao L, Schaidle JA. Transforming the carbon economy: challenges and opportunities in the convergence of low-cost electricity and reductive CO_2 utilization. Energy Environ Sci 2020;13:472–94. https://doi.org/10.1039/C9EE02410G.

[36] Yan Y, Borhani TN, Subraveti SG, Pai KN, Prasad V, Rajendran A, et al. Harnessing the power of machine learning for carbon capture, utilisation, and storage (CCUS) – a state-of-the-art review. Energy Environ Sci 2021;14:6122–57. https://doi.org/10.1039/D1EE02395K.

[37] Chae HJ, Kim J-H, Lee SC, Kim H-S, Jo SB, Ryu J-H, et al. Catalytic Technologies for CO Hydrogenation for the Production of Light Hydrocarbons and Middle Distillates. Catalysts 2020;10:99. https://doi.org/10.3390/catal10010099.

[38] Förtsch D, Pabst K, Groß-Hardt E. The product distribution in Fischer–Tropsch synthesis: An extension of the ASF model to describe common deviations. Chemical Engineering Science 2015;138:333–46. https://doi.org/10.1016/j.ces.2015.07.005.

[39] Tavakoli A, Sohrabi M, Kargari A. Application of Anderson–Schulz–Flory (ASF) equation in the product distribution of slurry phase FT synthesis with nanosized iron catalysts. Chemical Engineering Journal 2008;136:358–63. https://doi.org/10.1016/j.cej.2007.04.017.

[40] Bhatelia T, Li C, Sun Y, Hazewinkel P, Burke N, Sage V. Chain length dependent olefin re-adsorption model for Fischer–Tropsch synthesis over Co-Al2O3 catalyst. Fuel Processing Technology 2014;125:277–89. https://doi.org/10.1016/j.fuproc.2014.03.028.

[41] Gao X, Wang Z, Huang Q, Jiang M, Askari S, Dewangan N, et al. State-of-art modifications of heterogeneous catalysts for CO_2 methanation – Active sites, surface basicity and oxygen defects. Catalysis Today 2022;402:88–103. https://doi.org/10.1016/j.cattod.2022.03.017.

[42] Tada S, Nagase H, Fujiwara N, Kikuchi R. What Are the Best Active Sites for CO_2 Methanation over Ni/CeO_2 ? Energy Fuels 2021;35:5241–51. https://doi.org/10.1021/acs.energyfuels.0c04238.

[43] Kruit KD, Vervloet D, Kapteijn F, Van Ommen JR. Selectivity of the Fischer–Tropsch process: deviations from single alpha product distribution explained by gradients in process conditions. Catal Sci Technol 2013;3:2210. https://doi.org/10.1039/c3cy00080j.

[44] Janssens P, Poissonnier J, Chakkingal A, Bos R, Thybaut JW. Recent advances in the use of Steady-State Isotopic Transient Kinetic Analysis data in (micro)kinetic modeling for

catalyst and process design. Catalysis Communications 2023;179:106688. https://doi.org/10.1016/j.catcom.2023.106688.

[45] Bhatelia T, Li C, Sun Y, Hazewinkel P, Burke N, Sage V. Chain length dependent olefin re-adsorption model for Fischer–Tropsch synthesis over Co-Al2O3 catalyst. Fuel Processing Technology 2014;125:277–89. https://doi.org/10.1016/j.fuproc.2014.03.028.

[46] Stranges AN. A History of the Fischer-Tropsch Synthesis in Germany 1926–45. Studies in Surface Science and Catalysis, vol. 163, Elsevier; 2007, p. 1–27.

[47] Ail SS, Dasappa S. Biomass to liquid transportation fuel via Fischer Tropsch synthesis – Technology review and current scenario. Renewable and Sustainable Energy Reviews 2016;58:267–86. https://doi.org/10.1016/j.rser.2015.12.143.

[48] Wood DA, Nwaoha C, Towler BF. Gas-to-liquids (GTL): A review of an industry offering several routes for monetizing natural gas. Journal of Natural Gas Science and Engineering 2012;9:196–208. https://doi.org/10.1016/j.jngse.2012.07.001.

[49] S. Mabengu, N. Mthembu, A. H. Mohammadi: An overview of Secunda Coal To Liquid process. 2017

[50] Viguié J-C, Ullrich N, Porot P, Bournay L, Hecquet M, Rousseau J. BioTfueL project: targeting the development of second-generation biodiesel and biojet fuels. n.d.

[51] Wang P, Robinson AJ, Papadokonstantakis S. Prospective techno-economic and life cycle assessment: a review across established and emerging carbon capture, storage and utilization (CCS/CCU) technologies. Front Energy Res 2024;12:1412770. https://doi.org/10.3389/fenrg.2024.1412770.

[52] Al-Mohannadi AA, Ertogral K, Erkoc M. Alternative Fuels in Sustainable Logistics Applications, Challenges, and Solutions. Sustainability 2024;16:8484. https://doi.org/10.3390/su16198484.

[53] Moodley DJ, Van De Loosdrecht J, Saib AM, Overett MJ, Datye AK, Niemantsverdriet JW. Carbon deposition as a deactivation mechanism of cobalt-based Fischer–Tropsch synthesis catalysts under realistic conditions. Applied Catalysis A: General 2009;354:102–10. https://doi.org/10.1016/j.apcata.2008.11.015.

[54] Abdin Z. Empowering the hydrogen economy: The transformative potential of blockchain technology. Renewable and Sustainable Energy Reviews 2024;200:114572. https://doi.org/10.1016/j.rser.2024.114572.

[55] Zhou L, Liu Y, Liu S, Zhang H, Wu X, Shen R, et al. For more and purer hydrogen-the progress and challenges in water gas shift reaction. Journal of Energy Chemistry 2023;83:363–96. https://doi.org/10.1016/j.jechem.2023.03.055.

[56] Beniwal A, Bagaria A, Chen T-Y, Bhalothia D. Advancements in CO_2 conversion technologies: a comprehensive review on catalyst design strategies for high-performance CO_2 methanation. Sustainable Energy Fuels 2025;9:2261–86. https://doi.org/10.1039/D5SE00167F.

[57] Hao Z, Shen Z, Li Y, Wang H, Zheng L, Wang R, et al. The Role of Alkali Metal in α-MnO_2 Catalyzed Ammonia-Selective Catalysis. Angewandte Chemie 2019;131:6417–22. https://doi.org/10.1002/ange.201901771.

[58] Xu L, Xiu Y, Liu F, Liang Y, Wang S. Research Progress in Conversion of CO_2 to Valuable Fuels. Molecules 2020;25:3653. https://doi.org/10.3390/molecules25163653.

[59] Wang W, Toshcheva E, Ramirez A, Shterk G, Ahmad R, Caglayan M, et al. Bimetallic Fe–Co catalysts for the one step selective hydrogenation of CO_2 to liquid hydrocarbons. Catal Sci Technol 2023;13:1527–40. https://doi.org/10.1039/D2CY01880B.

[60] Wang L-X, Wang L, Xiao F-S. Tuning product selectivity in CO_2 hydrogenation over metal-based catalysts. Chem Sci 2021;12:14660–73. https://doi.org/10.1039/D1SC03109K.

[61] Weber D, Rui N, Zhang F, Zhang H, Vovchok D, Wildy M, et al. Carbon Nanosphere-Encapsulated Fe Core–Shell Structures for Catalytic CO_2 Hydrogenation. ACS Appl Nano Mater 2022;5:11605–16. https://doi.org/10.1021/acsanm.2c02602.

[62] Loiland JA, Wulfers MJ, Marinkovic NS, Lobo RF. Fe/γ-Al_2O_3 and Fe–K/γ-Al_2O_3 as reverse water-gas shift catalysts. Catal Sci Technol 2016;6:5267–79. https://doi.org/10.1039/C5CY02111A.

[63] Melchionna M, Fornasiero P. On the Tracks to "Smart" Single-Atom Catalysts. J Am Chem Soc 2025;147:2275–90. https://doi.org/10.1021/jacs.4c15803.

[64] Wang K, Yoshiiri K, Rosa L, Wei Z, Juodkazis S, Ohtani B, et al. TiO2/Au/TiO2 plasmonic photocatalyst with enhanced photocatalytic activity and stability under visible-light irradiation. Catalysis Today 2022;397–399:257–64. https://doi.org/10.1016/j.cattod.2021.09.023.

[65] Ojeda M, Nabar R, Nilekar AU, Ishikawa A, Mavrikakis M, Iglesia E. CO activation pathways and the mechanism of Fischer–Tropsch synthesis. Journal of Catalysis 2010;272:287–97. https://doi.org/10.1016/j.jcat.2010.04.012.

[66] Ochoa A, Bilbao J, Gayubo AG, Castaño P. Coke formation and deactivation during catalytic reforming of biomass and waste pyrolysis products: A review. Renewable and Sustainable Energy Reviews 2020;119:109600. https://doi.org/10.1016/j.rser.2019.109600.

[67] Al Harthi A, Abri MA, Younus HA, Hajri RA. Criteria and cutting-edge catalysts for CO_2 electrochemical reduction at the industrial scale. Journal of CO_2 Utilization 2024;83:102819. https://doi.org/10.1016/j.jcou.2024.102819.

[68] Li Y, Wu C, Wang W, Xin J, Mi X, Yang G, et al. Research progress on CO_2 catalytic conversion to value-added oxygenates. Journal of Fuel Chemistry and Technology 2024;52:496–511. https://doi.org/10.1016/S1872-5813(23)60404-9.

[69] Garcia X, Soler L, Divins NJ, Vendrell X, Serrano I, Lucentini I, et al. Ceria-Based Catalysts Studied by Near Ambient Pressure X-ray Photoelectron Spectroscopy: A Review. Catalysts 2020;10:286. https://doi.org/10.3390/catal10030286.

[70] Yang Q, Kondratenko EV. From Understanding of Catalyst Functioning toward Controlling Selectivity in CO_2 Hydrogenation to Higher Hydrocarbons over Fe-Based Catalysts. Acc Mater Res 2024;5:1314–28. https://doi.org/10.1021/accountsmr.4c00160.

[71] Chen W, Filot IAW, Pestman R, Hensen EJM. Mechanism of Cobalt-Catalyzed CO Hydrogenation: 2. Fischer–Tropsch Synthesis. ACS Catal 2017;7:8061–71. https://doi.org/10.1021/acscatal.7b02758.

[72] Benavides PT, Cronauer DC, Adom F, Wang Z, Dunn JB. The influence of catalysts on biofuel life cycle analysis (LCA). Sustainable Materials and Technologies 2017;11:53–9. https://doi.org/10.1016/j.susmat.2017.01.002.

[73] Liu CM, Sandhu NK, McCoy ST, Bergerson JA. A life cycle assessment of greenhouse gas emissions from direct air capture and Fischer–Tropsch fuel production. Sustainable Energy Fuels 2020;4:3129–42. https://doi.org/10.1039/C9SE00479C.

[74] Sadhukhan J, Fisher OJ, Cummings B, Xuan J. Novel comprehensive life cycle assessment (LCA) of sustainable flue gas carbon capture and utilization (CCU) for surfactant and fuel via Fischer-Tropsch synthesis. Journal of CO_2 Utilization 2025;92:103013. https://doi.org/10.1016/j.jcou.2024.103013.

[75] Cuéllar-Franca R, García-Gutiérrez P, Dimitriou I, Elder RH, Allen RWK, Azapagic A. Utilising carbon dioxide for transport fuels: The economic and environmental sustainability of different Fischer-Tropsch process designs. Applied Energy 2019;253:113560. https://doi.org/10.1016/j.apenergy.2019.113560.

[76] Erakca M, Baumann M, Helbig C, Weil M. Systematic review of scale-up methods for prospective life cycle assessment of emerging technologies. Journal of Cleaner Production 2024;451:142161. https://doi.org/10.1016/j.jclepro.2024.142161.

[77] Liu Z, Tian W, Cui Z, Liu B. A universal microkinetic-machine learning bimetallic catalyst screening method for steam methane reforming. Separation and Purification Technology 2023;311:123270. https://doi.org/10.1016/j.seppur.2023.123270.

[78] Sun Y, Yang G, Wen C, Zhang L, Sun Z. Artificial neural networks with response surface methodology for optimization of selective CO_2 hydrogenation using K-promoted iron catalyst in a microchannel reactor. Journal of CO_2 Utilization 2018;24:10–21. https://doi.org/10.1016/j.jcou.2017.11.013.

[79] Kimaev G, Ricardez-Sandoval LA. Artificial Neural Networks for dynamic optimization of stochastic multiscale systems subject to uncertainty. Chemical Engineering Research and Design 2020;161:11–25. https://doi.org/10.1016/j.cherd.2020.06.017.

[80] Apurv Saxena, Wipula Liyanage, Shubhender Kapila, Manashi Nath. Nickel Selenide as Efficient Electrocatalyst for Selective Reduction of Carbon Dioxide to Carbon-rich Products. Catalysis Science & Technology, 2022.

[81] Rhimi, B., Zhou, M., Yan, Z. *et al.* Cu-Based Materials for Enhanced C_{2+} Product Selectivity in Photo-/Electro-Catalytic CO_2 Reduction: Challenges and Prospects. *Nano-Micro Lett.* **16**, 64 (2024). https://doi.org/10.1007/s40820-023-01276-2.

[82] Qin C, Li X, Wang T, Xu Z, Chen KJ, Pan F. Metal-Organic Frameworks-Based Copper Catalysts for CO_2 Electroreduction Toward Multicarbon Products. Exploration (Beijing). 2025 Feb 12;5(3):270011. doi: 10.1002/EXP.70011. PMID: 40585756; PMCID: PMC12199389.

[83] Soressa Abera Chala, Keseven Lakshmanan, Wei-Hsiang Huang, Amaha Woldu Kahsay, Chia-Yu Chang, Fikiru Temesgen Angerasa, Yen-Fa Liao, Jyh-Fu Lee, Hongjie Dai, Meng-Che Tsai, Wei-Nien Su, Bing Joe Hwang, Cooperative dual single atom Ni/Cu catalyst for highly selective CO2-to-ethanol reduction, Applied Catalysis B: Environment and Energy, 2024, https://doi.org/10.1016/j.apcatb.2024.124420.

[84] Meng DL, Zhang MD, Si DH, Mao MJ, Hou Y, Huang YB, Cao R. Highly Selective Tandem Electroreduction of CO_2 to Ethylene over Atomically Isolated Nickel-Nitrogen Site/Copper Nanoparticle Catalysts. Angew Chem Int Ed Engl. 2021 Nov

22;60(48):25485-25492. doi: 10.1002/anie.202111136. Epub 2021 Oct 28. PMID: 34533874.

[85] David Ríos-Ruiz, Pablo Arévalo-Cid, Jesús Cebollada, Verónica Celorrio, María Victoria Martínez-Huerta, Tailoring of single copper atoms anchored on N, P co-doped carbon for electrochemical CO2 reduction, Catalysis Today, 2025, https://doi.org/10.1016/j.cattod.2025.115284.

[86] Sonal, Kishore Kondamudi, Kamal K. Pant, Sreedevi Upadhyayula, Sonal, Synergistic Effect of Fe-Co Bimetallic Catalyst on FTS and WGS Activity in the Fischer-Tropsch Process: A Kinetic Study. Industrial & Engineering Chemistry Research, 2017. https://doi.org/10.1021/acs.iecr.6b04517.

[87] Cássia S. Santana, Letícia F. Rasteiro, Francielle C.F. Marcos, Elisabete M. Assaf, Janaina F. Gomes, José M. Assaf, Influence of Al, Cr, Ga, or Zr as promoters on the performance of Cu/ZnO catalyst for CO2 hydrogenation to methanol, Molecular Catalysis, 2022, https://doi.org/10.1016/j.mcat.2022.112512.

[88] Tsiotsias AI, Charisiou ND, Yentekakis IV, Goula MA. Bimetallic Ni-Based Catalysts for CO_2 Methanation: A Review. Nanomaterials (Basel). 2020 Dec 24;11(1):28. doi: 10.3390/nano11010028. PMID: 33374436; PMCID: PMC7824481.

[89] Zhou, J., Gao, Z., Xiang, G. *et al.* Interfacial compatibility critically controls Ru/TiO_2 metal-support interaction modes in CO_2 hydrogenation. *Nat Commun* **13**, 327 (2022). https://doi.org/10.1038/s41467-021-27910-4.

[90] Naomi Lawes , Isla E. Gow , Louise R. Smith , Kieran J. Aggett , James S. Hayward , Lara Kabalan , Andrew J. Logsdail , Thomas J. A. Slater , Malcolm Dearg , David J. Morgan , Nicholas F. Dummer , Stuart H. Taylor , Michael Bowker , C. Richard A. Catlow and Graham J. Hutchings *. Methanol synthesis from CO2 and H2 using supported Pd alloy catalysts, Faraday Discussions. https://doi.org/10.1039/D2FD00119E

[91] Chen H, Lian Z, Zhao X, Wan J, Pieters PF, Oliver-Meseguer J, Yang J, Pach E, Carenco S, Treps L, Liakakos N, Shan Y, Altoe V, Wong E, Zhuo Z, Yang F, Su J, Guo J, Blum M, H Lapidus S, Hunt A, Waluyo I, Ogasawara H, Zheng H, Yang P, Bell AT, López N, Salmeron M. The role of manganese in $CoMnO_x$ catalysts for selective long-chain hydrocarbon production via Fischer-Tropsch synthesis. Nat Commun. 2024 Nov 27;15(1):10294. doi: 10.1038/s41467-024-54578-3. Erratum in: Nat Commun. 2025 Jan 20;16(1):863. doi: 10.1038/s41467-025-56202-4. PMID: 39604416; PMCID: PMC11603050.

2. EXPERIMENTAL AND RIG SET UP

The experimental catalytic tests were conducted using two distinct continuous-flow systems: a laboratory-scale plant and a bench-scale plant. The primary differences between these setups reside in their overall volumes, reactor dimensions, and operational features. The laboratory plant has a total volume of 250 mL and features a reactor with an internal diameter of 6 mm, whereas the bench-scale plant has a larger total volume of approximately 600 mL and a reactor with an internal diameter of 10 mm. Additionally, the laboratory plant is operated manually, while the bench-scale plant is fully automated, offering remote control capabilities. The laboratory-scale plant was primarily utilized to assess the performance of various catalysts under different operating conditions, with an upper pressure limit of 20 bar. To extend the range of operational pressures beyond this limit, the bench-scale plant was employed, allowing for pressures up to 35 bar. This larger plant was used to test two selected catalysts under diverse operating conditions.

A detailed description of each plant and the specific operating conditions utilized during the experiments will be provided in the following sections.

2.1. Lab plant

The FT lab plant scheme is very simple. The reagents are fed through four mass flowmeters, each one calibrated for a specific gas. The gas available are CO, CO_2, H_2 and N_2. The selected mixture is fed to the reactor that is a 6mm diameter stainless steel pipe packed with the catalyst. Reactor heating is performed by a furnace and two thermocouples allow to continuously monitor the temperature of the reactor and of the furnace itself. The outlet stream is sent to a condenser (trap) which is held at 5°C by a cooling jacket. Here, the heaviest products are condensed and are recovered at the end of the process. The uncondensed gases pass then trough a back pressure regulator pneumatic valve that keeps the pressure inside the plant to the selected value. Then the stream is split and sent to an Agilent 3000A micro gas chromatograph and to a bubble flowmeter. These two last devices allow to calculate the outlet flowrate and its composition and so the conversion and the selectivity to the different products. A three-way valve placed just before the reactor allows to deviate the inlet stream directly to the outlet of the plant through a bypass line. Downstream the reactor, a rupture disc is placed to avoid excessive pressure rising.

The catalyst is charged in the reactor from the top and is sustained and kept in place by some quartz wool as represented in Fig. 2.1. Since the catalytic bed is sustained only by the quartz wool and is absent any fixed structure, is necessary to avoid any sudden change of the pressure to prevent packing motion. For each test, 1g of powdered catalyst was employed. In some cases, when the catalysts showed a strong tendence to sintering, silica can be used as diluent.

Before starting the catalytic test, each catalyst was activated in situ with a stream of 30 ml/min of hydrogen and 15 ml/min of carbon monoxide, at 4 bar and 350°C. CO was necessary to form, on the catalyst surface, a layer of metal carbide which is known to be active to the FT reaction [1].

The activation step lasted four hours and, once finished, the pressure was increased to 20 bar and the temperature was decreased to the operating one. The composition of the gas mixture fed to the plant was switched according to the catalytic test setting.

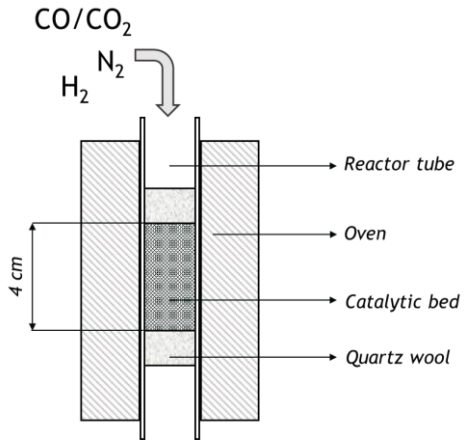

Figure 2.1. Representation of reactor set up during testing.

Nitrogen is not a reactant but is used as an internal standard for the microGC. At the end of the test, the plant was carefully depressurized and the liquid products condensed in the trap were collected to be analysed. For each catalyst two tests were performed. In the first the reaction was carried out for around one week by increasing the reactor temperature every day (from 250 to 350°C). This test was mainly devoted to the evaluation of the selectivity towards lighter products at different temperatures. The selectivity to heavier hydrocarbons was better evaluated by performing tests in isothermal conditions by keeping the reactor at 300°C for the whole time. Some catalysts were also tested by modifying the reactant ratio or the feed flowrate to see how it affected the conversion and selectivity. Tables 2.1 and 2.2 report a summary of the operating conditions.

Test conditions summary: CO_2 hydrogenation					
Test	Inlet mixture (ml/min)			Temperature (°C)	Pressure (bar)
	H_2	CO_2	N_2		
Ramp	36	12	5	250	20
				270	
				300	
				320	
				350	
Isotherm	36	12	5	300	20
Reactant ratio 4:1	38.5	9.5	5	250	20
				270	
				300	
				320	
				350	
Double residence time	18	6	2.5	250	20
				270	
				300	
				320	
				350	

Table 2.1. Lab plant tests conditions during carbon dioxide hydrogenation.

Test conditions summary: Fischer-Tropsch					
Test	Inlet mixture (ml/min)			Temperature (°C)	Pressure (bar)
	H_2	CO	N_2		
Ramp	32	16	5	200	20
				220	
				250	
				270	
				300	
Isotherm	32	16	5	300	20

Table 2.2. Lab plant tests conditions during Fischer Tropsch testing.

The general flowsheet of the FT plant is reported in Fig. 2.2. The key explanation of every plant part is reported hereinafter:

- 1, 2, 3, 4: H_2, N_2, CO and CO_2 gas cylinders;
- 5, 6, 7, 8: Volumetric flowmeters;
- 9: Gas mixer;
- 10: FT fixed-bed reactor;
- 11, 12: Reactor temperature controller and regulator;
- 13: Cold Trap;
- 14: Back pressure regulating valve;
- 15*/15: 3-way valve and by-pass line;
- 16: Bubble Flow-meter;
- 17: Vent under the hood;
- 18: micro-GC;

A picture of the FT plant is reported in Fig. 2.3.

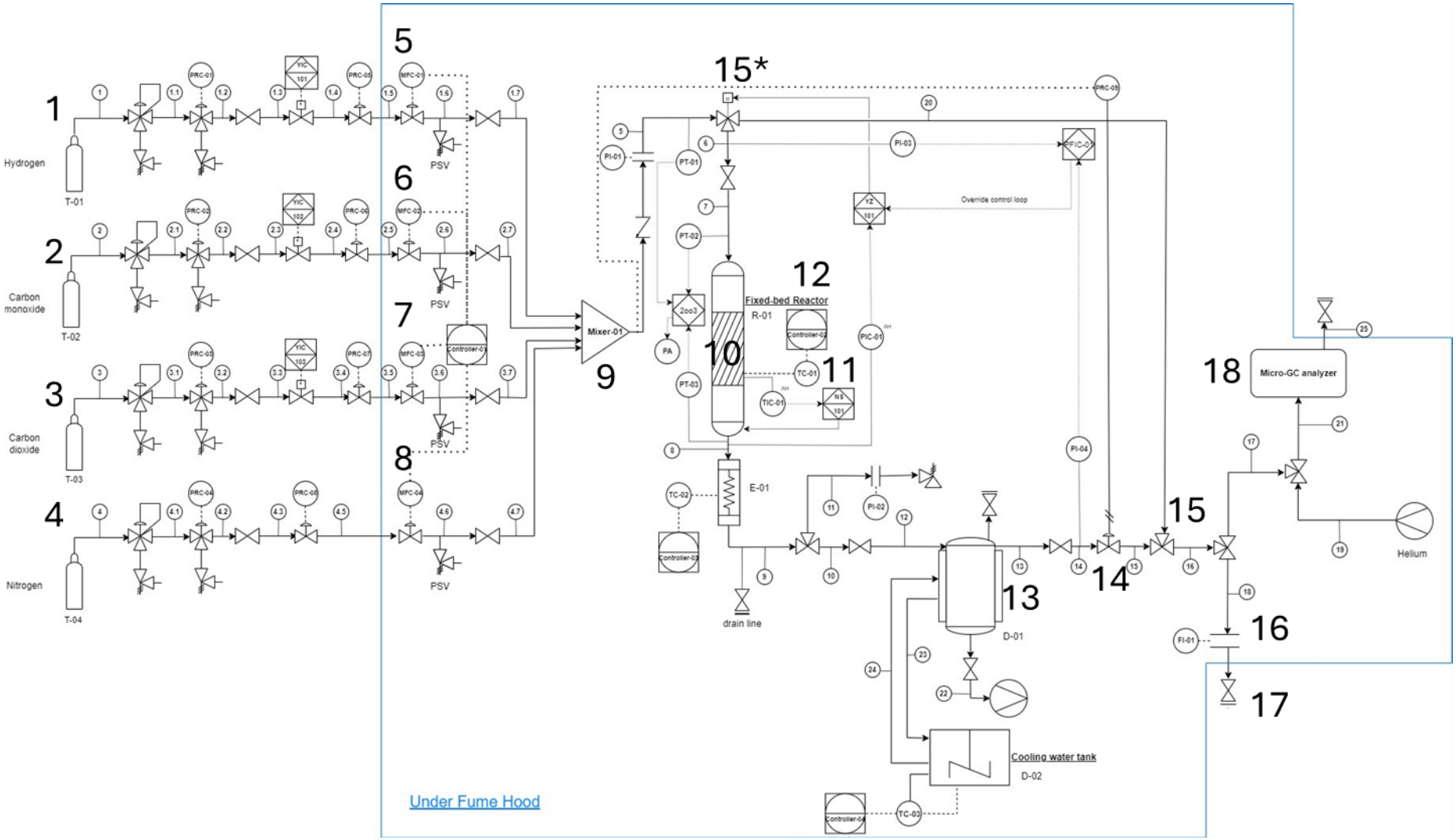

Figure 2.2. Detailed P&ID of the FT Lab plant set up.

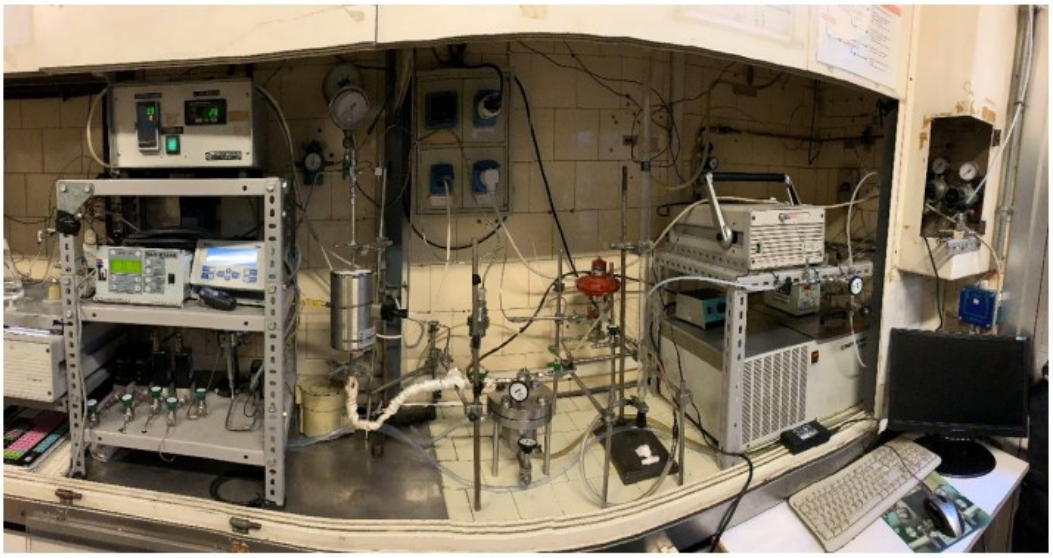

Figure 2.3. Picture of the FT rig.

2.1.1. Flowmeters and equipment for pressure and temperature regulation

FT laboratory plant pressure is controlled by an electronic controller (Brooks®); this controller directly acts on an automatic valve placed after the cold trap. This valve works thanks to a pneumatic actuator and is able to work with a pressure up to 25bar with a sensibility of 0.1 bar. In order to avoid possible damage to the valve due to the condensation of some heavy hydrocarbons which have not been condensed in the cold trap, also the valve is heated and kept at T=110°C using heating tape in glass fiber with heating power of 780 W.

Figure 2.4. Picture on the left Brooks mass flow meters while on the right the back pressure regulating valve.

To calculate the selectivity of the product and the total carbon molar balance it is needed to know the total gas volume and to monitor the exact volumetric flow rate which flows out from the plant. The inlet flow of the reactant mixture and nitrogen is totalized by the same flowmeters that regulate the volumetric flow (Brooks® Instruments SLA5800 series) before the gas mixer, while the outlet flow which contains the unreacted gasses, nitrogen, the light products and the by-products is calculated with a glass bubble flowmeter.

2.1.2. Fischer-Tropsch reactor

The FT fixed bed reactor has been produced by Renato Brignole ® Company. The tubular reactor, which has an internal diameter of 6 mm and an external one of 9 mm, allows to put the catalyst, the inert and eventually other types of support vertically. The reactor is made of AISI 316 stainless steel. A picture is reported below in Figure 4.3.

Figure 2.5. Fischer-Tropsch reactor.

The direction of the gases is from the top to the bottom of the catalytic bed, so it is a downflow reactor and the catalytic bed has a volume of, around, 2.8 cm^3. The temperature of the circular furnace was measured with a k-type thermocouple. A second k-type thermocouple monitored the reactor's internal temperature.

The main characteristics of the FT reactor are summarized in Table 2.3.

Volume (cm^3)	Max. operating pressure (bar)	Max operating temperature (°C)	Internal diameter (mm)	Height (mm)
5	100	400	6	180

Table 2.3. Main characteristics of FT reactor.

2.1.3. Cold Trap

The condensation of the heavy hydrocarbons (>C7) and the aqueous phase is obtained in the cold trap. The trap is placed after the reactor and before the pressure control valve; this allows to the trap to work at the same pressure of the reactor (P=20 bar) and T=5 °C. The Volume, height and width of the cold trap are, respectively, 150 ml, 100 mm and 40 mm. The temperature of the cold trap is maintained constant by an external system in which circulates cold water from a thermocriostat (Crioterm® 190 isco).

Figure 2.6. Cold trap.

The cold trap can be opened only at the end of the catalytic test in order not to compromise the process equilibria and stability. Since it is not possible to withdraw liquid samples during the test, the one that will be found at the end of the run represents an average value of the whole TOS. The cold trap is opened by an upper flange fixed with four screws. Once the trap is opened, the liquid phase is extracted and weighted. The final stage requires thorough washing with acetone to clean the internal chamber and the junctions in which products might reside hindering the outcome of successive tests.

2.1.4. Analytical apparatus

2.1.4.1. micro-GC analysis

To quantify the amount of produced and unreacted gases, the mixture is on-line analyzed every 120 minutes during the whole test with a micro-GC Agilent® 3000A. In this instrument the analyzed sample is divided in two different modules and analyzed at the same time. The first one has a chromatographic column filled with molecular sieves (molsieve) which is able to separate the molecule as a function of their size, in particular it can separate He (used as carrier), He, H_2, Ne, Ar, O_2, N_2, CH_4 and CO; the second one is a OV-1 module filled with polydimethylsiloxane by which it is possible to separate CO_2 and all the hydrocarbons in the range C_2-C_6. Each module is equipped with a thermo-conductibility detector (TCD) which guarantees a sensibility limit of the analyses of about 50 ppm for each compound. In Fig. 2.7 is possible to observe the micro-GC set-up and some of the parameters related to the analysis.

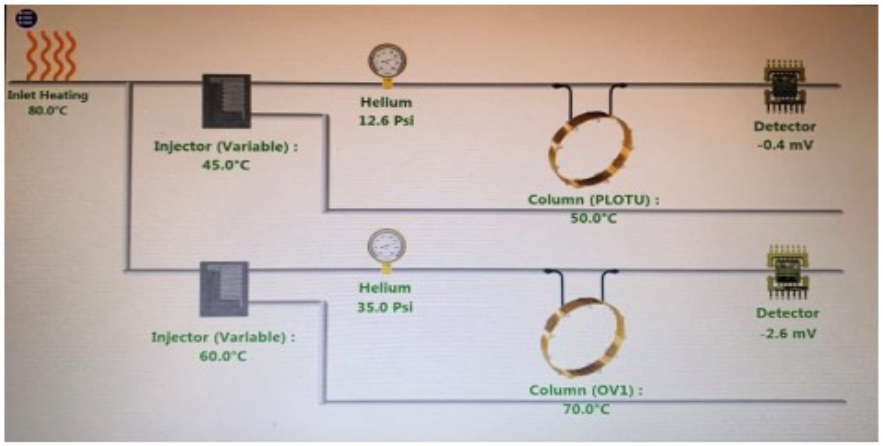

Figure 2.7. Micro-GC status.

An example of an analysis is here reported:

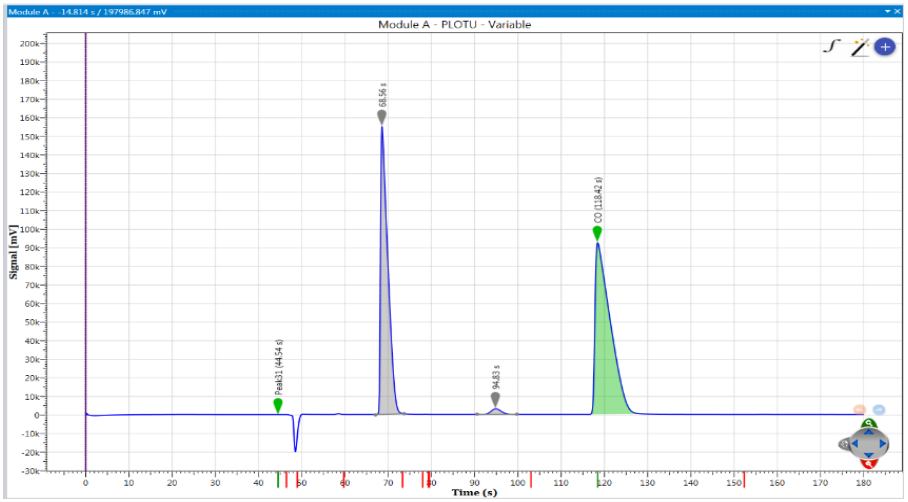

Figure 2.8. Module A analysis.

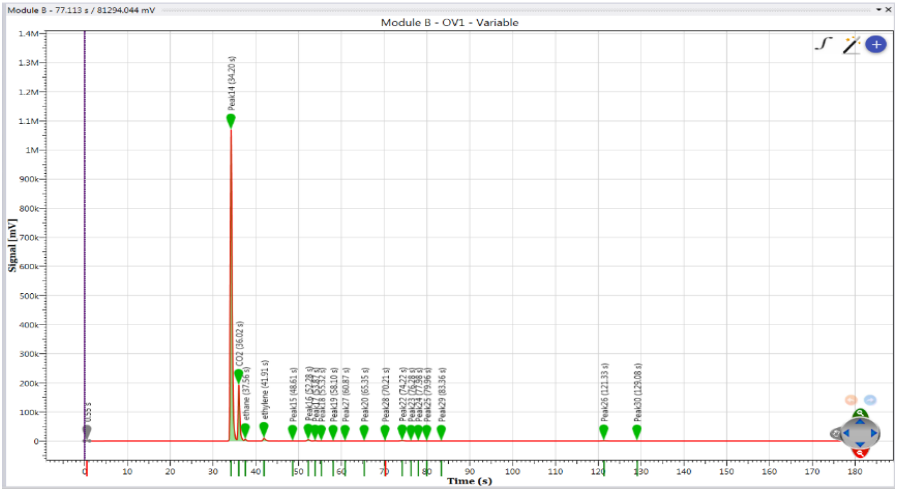

Figure 2.9. Module B analysis.

2.1.4.2. GC analysis

To determine the composition of the heavy organic fraction phase a HP 5890 series II GC was employed equipped with a Supelco SP^{tm} 2380 fused silica capillary column with a length of 60m and film thickness of 0.2 mm and an FID detector. This set up is capable of separating the

compounds containing 7 up to 30 carbon atoms with a limit of detection of 100 ppm for each molecule. The analysis starts with an isotherm at 70 °C for 4 minutes followed by a ramp in temperature up to 250 °C with a rate of 10 °C min^{-1}. After the analysis ends a regeneration process is required to restore the initial condition of the column. This step involves heating the column to 265 °C for 60 mins. An example chromatograph of the analysis is depicted in Fig. 2.10.

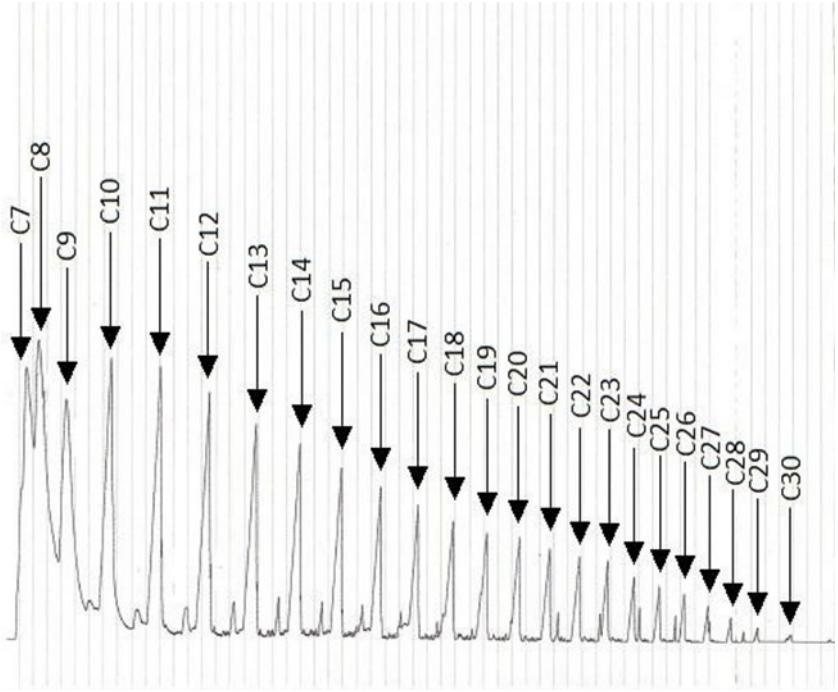

Figure 2.10. Example chromatograph of the analysis.

2.1.4.3. Total Organic Carbon (TOC)

The analysis of the organic compounds dissolved in the aqueous phase separated from the heavy hydrocarbon fraction, contained in the cold trap at the end of the run, is carried out with a Shimadzu TOC 5000A. Once the sample is inserted in the dedicated chamber, a portion of it is vaporized and undergoes an oxidation process imparted by a reactor filled with a Pt-based catalysts at temperature of 700°C. At this stage all the organic carbon present in the sample is totally oxidized to CO_2 and quantified through a IR detector.

2.1.5. Analytical instruments calibration

2.1.5.1. Flowmeters calibration

The flowmeters calibration was carried out directly by the production company Brooks®. The obtained calibration results for all the three flowmeters are reported hereinafter in Table 2.4- 2.7.

The calibration of the bubble flowmeter was carried out after the calibration of the electronic flowmeters, setting up a known value of the gas mixture and then checking the results measured through the bubble flowmeter.

- H_2 flowmeter:

Set flow (Nml/min)	Measured flow (Nml/min)	Error %
5	5.085	1.7
10	10.09	0.9
25	25.11	0.44
50	50.18	0.36

Table 2.4. Calibration of H_2 flowmeter.

- N_2 flowmeter:

Set flow (Nml/min)	Measured flow (Nml/min)	Error %
1	1.18	18
2	2.21	10.5
5	5.19	3.8
10	10.17	1.7

Table 2.5. Calibration of N_2 flowmeter.

- CO flowmeter:

Set flow (Nml/min)	Measured flow (Nml/min)	Error %
2.5	2.47	-1.2
5	4.96	-0.8
12.5	12.42	-0.64
25	24.86	-0.56

Table 2.6. Calibration of CO flowmeter.

- CO_2 flowmeter:

Set flow (Nml/min)	Measured flow (Nml/min)	Error %
2.5	2.53	1.2
5	5.05	1.01
12.5	12.7	1.6
25	25.2	0.8

Table 2.7. Calibration of CO_2 flowmeter.

Set flow CO (Nml/min)	Set flow N_2 (Nml/min)	Measured flow (Nml/min)	Error %
20	10	28.46	-5.12
30	10	38.56	-3.61
30	20	47.44	-5.12
40	20	57.83	-3.61
50	20	68.56	-2.06

Table 2.8. Calibration of bubble flowmeter.

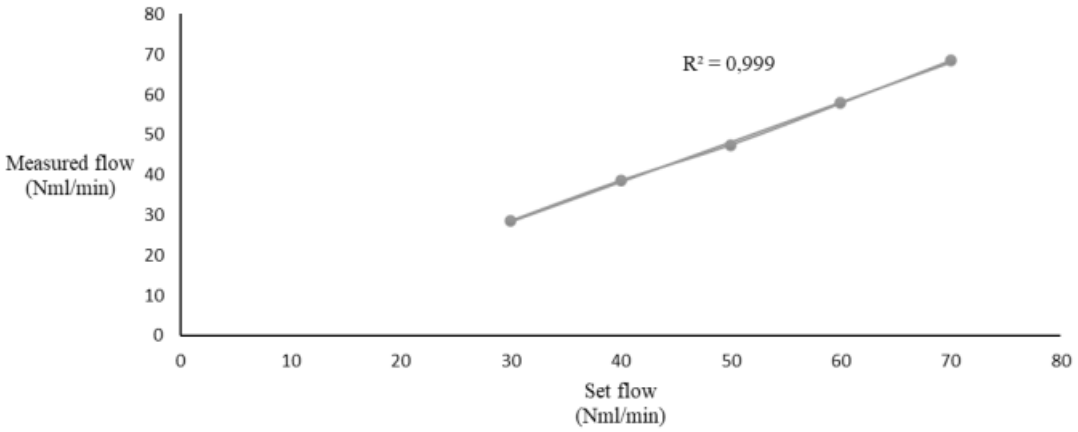

Figure 2.11. Bubble flowmeter calibration curve.

2.1.5.2. Micro-GC calibration

In order to perform the calibration, parameters related to the analysis were optimized and are reported in the Table 2.9.

Parameter	Module 1(molsieve)	Module 2 (OV-1)
Injector Heating (°C)	45	60
Column Heating (°C)	50	70
Injection time (ms)	50	50
Column pressure (psi)	12.6	35
Analysis time (s)	180	180
Sampling time(s)	120	120
Post analysis time (s)	0	0
Detector sensibility	Standard	Standard

Table 2.9. Micro-GC parameters.

Two different gas mixtures in form of cylinders manufactured by Sapio® company, were used for the calibration of the two modules, their respective compositions are reported in *Table 2.10* and *2.11.*

The micro-GC is equipped with an automatic loop system of injection therefore the volume injected in the modules is always the same, so it is possible to calibrate directly CO_2 and light hydrocarbon with a direct calibration without the use of an internal standard. The chromatographic area is directly correlated with the concentration of the compound in the mixture, so the calibration factors have been determined with Eq. 1.

$$calibration\ factor = \frac{chromatographic\ area}{compound\ concentration} \quad (1)$$

Once all the calibration factors are calculated using the standard mixtures, it is easy to figure out how to calculate the concentration of a "i" compound during a typical FT run. The equations used are here reported (Eq. 2- 4).

$$\%v_{"i"} = \frac{area_{"i"}}{calibration\ factor_{"i"}} \quad (2)$$

It's important to remember that in the FT plant flows N_2, used as internal standard. Since N_2 is not a FT gas (reactant or product) Eq. 16 has to be rearranged into Eq. 3:

$$\%v_{"i"} = \frac{Area_{"i"}}{calibration\ factor_{"i"}} \cdot \frac{Flow_{total}}{Flow_{FT}} \quad (3)$$

Where:

$$Flow_{FT} = Flow_{total} - Flow_{N_2} \quad (4)$$

In order to better understand this issue, an example is here reported; if during a run a FT flow equal to 20 Nml·min^{-1} is measured, and a concentration of 4% of CO_2 is detected, it means that a flow of 0.8 Nml·min^{-1} of CO_2 is passing thought the plant. However, if N_2 flow is set to 10 Nml·min^{-1} it means that the total flow will be 30 Nml·min^{-1} (20 Nml·min^{-1} + 10 Nml·min^{-1}). If the % of CO_2 is calculated just by using the total flow, the result would be:

$$\%v_{"CO_2"} = \frac{Flow_{"CO_2"}}{Flow_{"Total"}} \cdot 100 = \frac{0.8\ Nml \cdot min^{-1}}{30\ Nml \cdot min^{-1}} \cdot 100 = 2.66\%$$

Which is obviously an incorrect value. If Equation 17 is used the result will be:

$$\%v_{"CO_2"} = \frac{Flow_{"CO_2"}}{Flow_{"total"}} \cdot 100 \cdot \frac{Flow_{"Total"}}{Flow_{"FT"}} = \frac{0.8\ Nml \cdot min^{-1}}{30\ Nml \cdot min^{-1}} \cdot 100 \cdot \frac{30\ Nml \cdot min^{-1}}{20\ Nml \cdot min^{-1}} = 4\%$$

The calibration factor for each compound present in the standard mixtures is reported below, Table 2.10, together with retention time and molar fraction given by the manufacturer.

Compound	Molar fraction (%)	Retention time (min)	Calibration factor
CH_4	1.99	1.47	24966
CO_2	2.11	0.60	37538
Ethane	0.509	0.63	9318
Propane	0.527	0.71	11400
I-butane	0.51	0.82	13147
N-butane	0.503	0.90	13702
I-pentane	0.098	1.17	2838
N-pentane	0.098	1.30	2830
N-hexane	0.101	2.14	3015

Table 2.10. Composition of the #1 gas tank used for calibration.

Compound	Molar fraction (%)	Retention time (min)	Calibration factor
CH_4	5	1.47	24966
CO_2	5	0.60	37538
CO	5	2.00	9318
H_2	5	0.81	11400

Table 2.11 Composition of the #2 gas tank used for calibration.

The limitations of the current modules hinder the quantification of unsaturated compounds, as the OV-1 module, filled with polydimethylsiloxane, is unable to separate hydrocarbons from their corresponding olefins. As a result, separation between ethane and ethylene or propene and propylene cannot be achieved. Additionally, for hydrocarbons with more than three carbon atoms, it is impossible to distinguish isomers from olefins. This limitation is the reason why the scientific approach in this work approximates the hydrocarbon products as fully saturated.

Regarding the CO and CO_2 calibrations it was made exploiting the use of an internal standard, N_2, the choice of the nitrogen was made because it is a gas that is not involved in the FT reaction, so it passes through the FT rig acting as inert and moreover in the μ-GC the nitrogen can be seen in the same module of the carbon monoxide, the module A. It is preferable to use an internal analytical standard to measure with an higher degree of precision the outlet CO flow since it determines the CO conversion value and all the products selectivity.

In this method, the ratio between the areas of CO and N_2 is linearly correlated with the ratio between their flowrates.

The experimental results obtained during the calibration are reported in the Tab. 2.12.

Flow CO (Nml min-1)	**Flow N_2 (Nml min-1)**	**Flow CO/ Flow N_2**	**Area CO**	**Area N_2**	**Area CO/ Area N_2**
15.91	4.99	3.19	1192066	311434	3.83
9.89	4.99	1.98	1066549	441477	2.42
4.88	4.99	0.98	826805	680935	1.21
9.89	9.99	0.99	828036	685616	1.21
4.89	14.99	0.33	412130	1096684	0.38

Table 2.12. CO calibration of the micro-GC.

The calibration factor of the carbon monoxide is calculated by calculating the slope of the straight line obtained by plotting the ratio of the chromatograph areas against the ratio of the flowrates presented in Fig. 2.12.

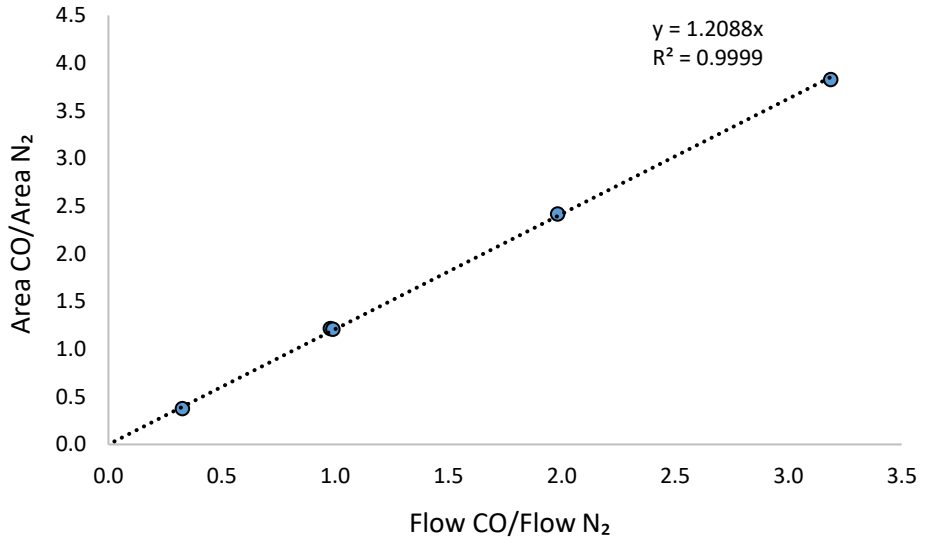

Figure 2.12. Regression line obtained during the calibration of the gas chromatograph with CO.

The correlation between the reported ratios is reported in Eq. 5.

$$\frac{Area_{CO}}{Area_{N2}} = 1.2088 \cdot \frac{Flow_{CO}}{Flow_{N2}} \tag{5}$$

During an experimental run, where the areas of CO and N_2 are given by the μ-GC and the N_2 flow is known, the Flow of CO can be calculated as reported in Eq. 6.

$$Flow_{CO} = \frac{Area_{CO} \cdot Flow_{N2}}{Area_{N2} \cdot 1.2088} \tag{6}$$

Finally, the percentage of CO converted can be calculated.

$$CO_{conversion} = \frac{Flow\ CO_{in} - Flow\ CO_{out}}{Flow\ CO_{in}} \cdot 100 \tag{7}$$

For the same reasons before mentioned, a calibration of CO_2 with N_2 as internal standard was performed. In Table 2.13 are visible the data used for the calibration.

Flow CO_2 (Nml/min)	**Flow N_2 (Nml/min)**	**Flow CO_2/ Flow N_2**	**Area CO_2**	**Area N_2**	**Area CO_2/ Area N_2**
15.91	4.99	3.19	1265736	331017.5	3.82
9.92	9.99	0.99	875262.7	712326.7	1.23
9.92	4.99	1.99	1130775	464859	2.43
4.9	14.99	0.33	459633.7	1100765	0.42
14.91	14.99	0.99	848870.3	731883	1.16

Table 2.13. Data collection and parameters used during calibration..

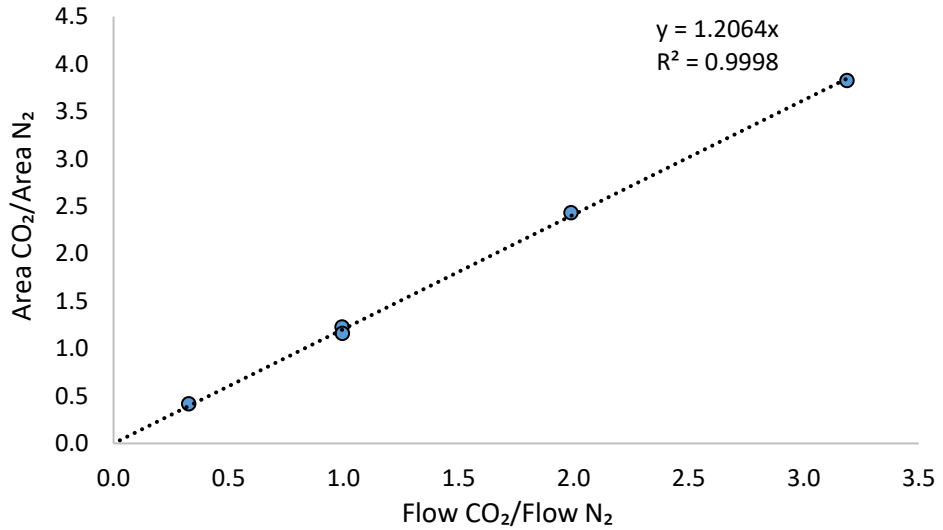

Figure 2.13. Regression line obtained during the calibration of the gas chromatograph with CO_2.

and with analogue procedure the percentage of CO_2 converted can be calculated.

$$CO_{2conversion} = \frac{Flow\ CO_{2in} - Flow\ CO_{2out}}{Flow\ CO_{2in}} \cdot 100 \tag{8}$$

2.1.5.3. Gas chromatograph calibration

As discussed in the preceding sections, this instrument is associated with the heavy organic phase. In this context, it enables the calculation of calibration factors for each fraction. The calibration equation, presented in Eq. 9, is as follows:

$$\frac{Area_{"i"}}{\%\, mol_{"i"}} \cdot f_{"i"} = \frac{Area_{"j"}}{\%\, mol_{"j"}} \cdot f_{"j"} \tag{9}$$

In this equation, “i” and “j” represent the components of the mixture, Area “i” and Area “j” refer to the GC areas obtained during analysis, and % mol “i” and % mol “j” indicate the molar fractions of the two components in the mixture. This approach, known as the “internal standard method,” involves setting the calibration factor of the selected internal standard to 1. This internal standard typically has a well-defined composition in the heavy organic phase and is entirely condensed in the trap. Eq. 9 can be reformulated into Eq. 10 as shown below:

$$f_{"i"} = f_{n-heptane} \cdot \frac{Area_{n-heptane}}{\%\, mol_{n-heptane}} \cdot \frac{\%\, mol_{"i"}}{Area_{"i"}} \tag{10}$$

In this scenario, the calibration factor for n-heptane is assigned a value of 1 thus allowing for the determination of all the calibration factors. If hydrocarbons within the C7-C30 range are unavailable, it is possible to use a subset of them in the standard mixture and then extrapolate the remaining calibration factors. The composition of the standard mixture used for calibration is outlined in Table 2.14.

N° carbon	Compound	M(g)	PM (g mol-1)	Molar fractio	A (mV)
7	n-heptane	0.15	100.2013	0.243157	8672.1
8	n-octane	0.1255	114.2278	0.17846	6990.7
10	n-decane	0.125	142.2808	0.142703	6279.4
12	Dodecane	0.202	170.3338	0.192628	9276.5
15	Pentadecane	0.146	212.4133	0.111645	6771.6
16	Hexadecane	0.146	226.4286	0.104735	3605.3
22	Docosane	0.051	310.5834	0.026672	4278.2

Table 2.14. Data collection as result of heavy hydrocarbon calibration through GC analysis.

The standard mixture in Table 2.14 serves as a typical example. Multiple reproducibility tests have been conducted using different standard mixtures, and the average calibration factors calculated from these mixtures are displayed in Figure 2.14.

The trend line used for data interpolation is expressed in Eq. 11:

$$f_{"i"} = 8.716 \cdot n^{-1.109} \tag{11}$$

In this equation, fi represents the calibration factor for component i, and n corresponds to the number of carbon atoms in molecule i. Eq. 11 facilitates the determination of calibration factors for each component. The results of this interpolation are provided in Table 2.15.

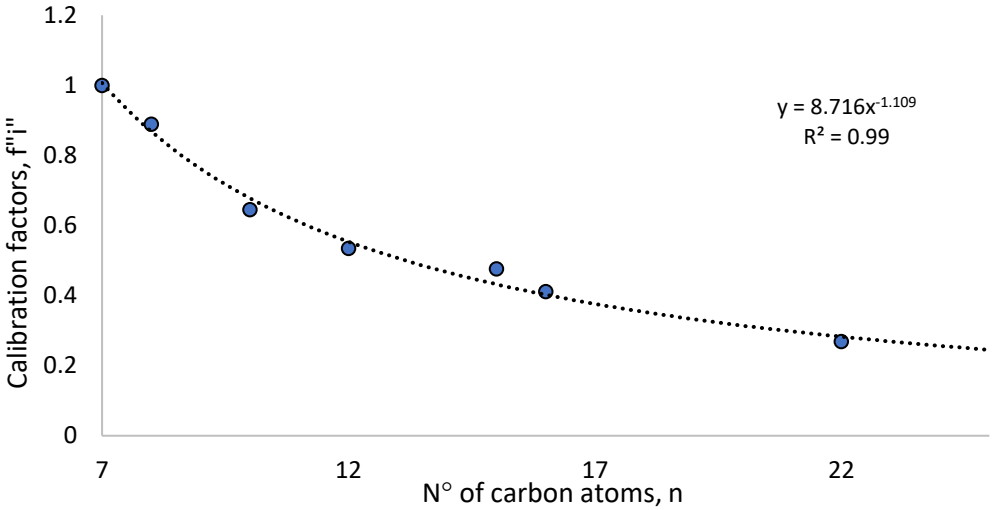

Figure 2.14. Calibration curve with calibration factors and number of carbon atoms.

N° of Carbon atoms	Calibration factor
7	0.9928
8	0.9119
9	0.8376
10	0.7693
11	0.7067
12	0.6491
13	0.5962
14	0.5476
15	0.5030
16	0.4620
17	0.4243
18	0.3898
19	0.3580
20	0.3288
21	0.3020
22	0.2774
23	0.2548
24	0.2341
25	0.2150
26	0.1975
27	0.1814
28	0.1666
29	0.1530
30	0.1405

Table 2.15. List of simulated calibration factors using calibration equation in Figure 2.14.

Additionally, the GC enables a qualitative assessment of the components in the heavy organic phase by utilizing their retention times. Specifically, the retention times for all fractions, as a function of the number of carbon atoms, is calculated through the same procedure as for the calibration factors.

Retention times of each compound the standard mixture was measured and plotted against the number of carbon atoms to gather the dependency between those two. Having found a quadratic relationship between the two, the equation was then employed in determining the retention time of all the compounds till C30, which is shown in Fig. 2.15.

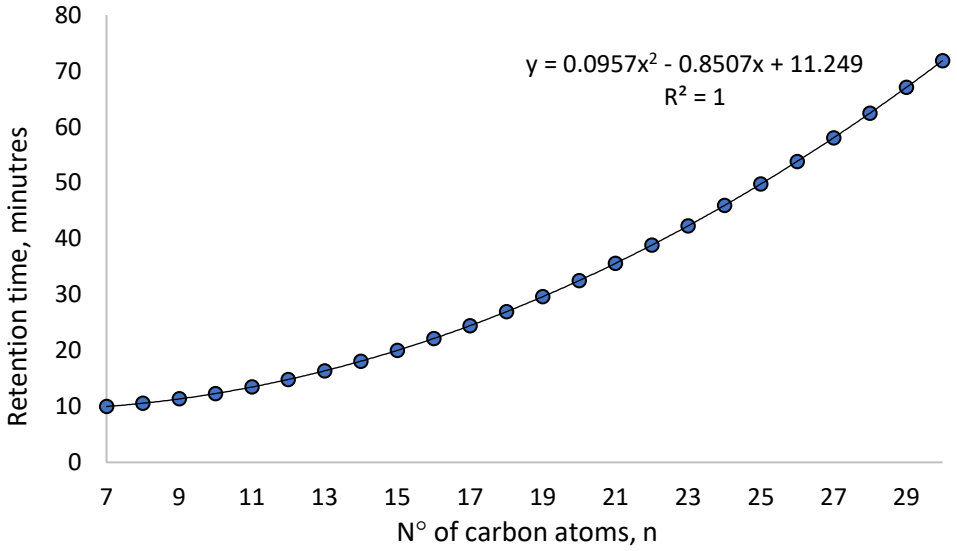

Figure 2.15. Simulated retention time of hydrocarbons.

2.1.5.4. Total Organic Carbon (TOC) Calibration

The Shimadzu® TOC 5000A enables the execution of calibration procedures using a solution with a standardized carbon content. This method is feasible due to the stability, high water solubility, and non-volatility of the compounds used for TOC calibration. The calibration relies on the linear relationship between the concentration of dissolved carbon and the areas detected by the instrument. The resulting TOC calibration curve is presented in Fig. 2.16.

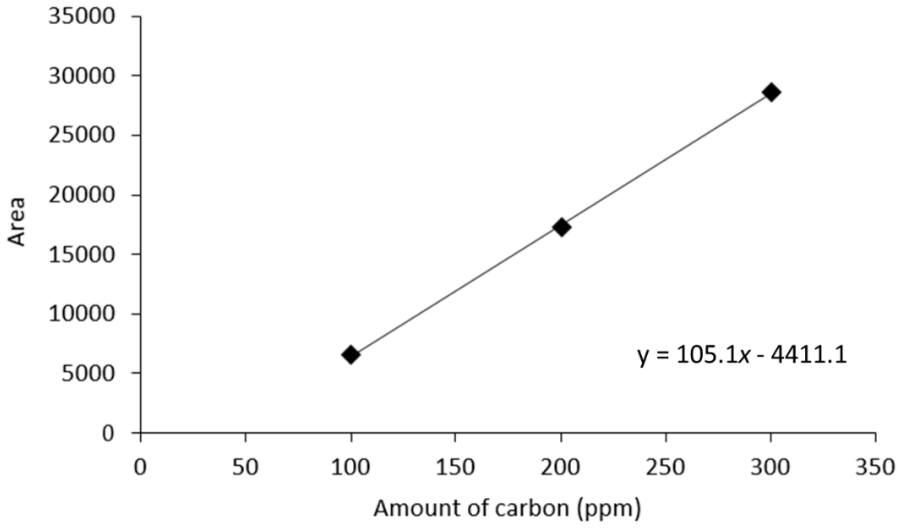

Figure 2.16. TOC linear regression calibration.

2.2. FT rig laboratory procedure

All catalytic runs have been conducted following a precise and well-structured procedure to ensure data comparability, as variations in experimental conditions could compromise the reproducibility of results. This procedure is organized into sequential steps, outlined as follows:

- Preparation of the catalyst and its loading into the FT fixed-bed reactor.
- Activation of the sample and execution of the FT catalytic test.
- Completion of the run, including opening the cold trap and recovering the aqueous and organic phases.
- Cleaning of the reactor and analytical apparatus.

2.2.1. Catalyst preparation and loading into the FT fixed bed reactor

The procedure described applies consistently to all the samples tested in the described set up. The catalyst is pressed in order to form pellets that are crushed and selected size-wise through the use of two sieves, between 105 and 150 mesh (micron). Once prepared, the catalyst is placed in an oven at 120 °C for at least 12 hours to remove any residual moisture present in the powder. In all experimental runs, 1 g of catalyst has been used. Once the catalyst is prepared, it can be loaded into the reactor. It is crucial to position the catalyst in the middle of the reactor pipe, as this is where the temperature remains constant.

The temperature profile of the reactor was examined to address the non-uniform heating and heat distribution within the system. Measurements were taken along the reactor length using an external thermocouple at three set temperatures: 250 °C, 300 °C, and 350 °C. The portion of the reactor in direct contact with the furnace spans approximately 10 cm, while the catalytic bed, excluding any additional layers, is around 1.5 cm in length. This investigation is crucial because the catalytic activity is highly dependent on the catalyst's temperature.

Based on the results, it was determined that the middle section of the reactor maintains a temperature closest to the set point. Therefore, positioning the catalytic bed in the middle of the reactor is optimal.

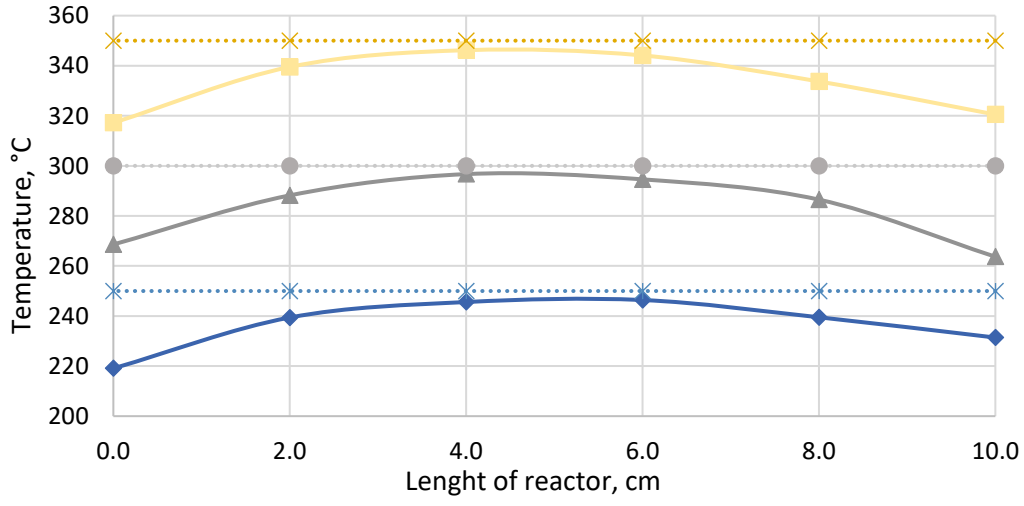

Figure 2.17. Continuous blue line refers to the experimental temperature measured inside the reactor when the outside heating source, represented by the dotted blu line, measures 250°C. Grey refers to 300 °C whereas yellow to 350°C.

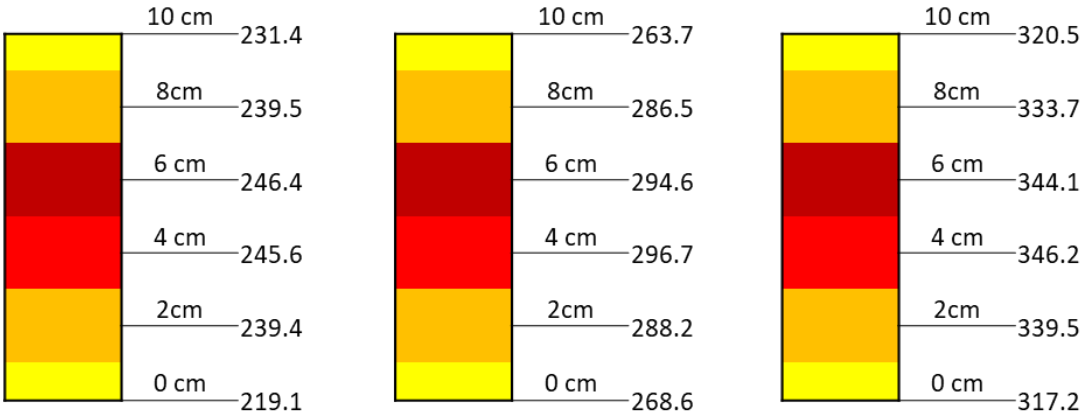

Figure 2.18. Visual representation of the temperature zones inside the reactor, left image's set point is 250°C, central representation's set point is 300°C and right one is 350°C.

The catalyst bed is immobilized with quartz wool placed above and below the catalytic layer to ensure stability. During loading, it is important to handle the material carefully and distribute it evenly to achieve a uniform catalytic bed. Once the catalyst is loaded, the upper and lower reactor junctions can be securely closed, allowing the experimental test to begin.

2.2.2. Sample activation and FT catalytic test

Before each catalytic run, the catalyst undergoes an activation procedure involving a reduction reaction. The activation parameters have been detailed in section *2.1 Lab Plant*. During this process, it is essential to pressurize the system using the appropriate reducing gas or gas mixture to the specified value. Once the system reaches the target pressure, it is recommended to close the valve before the reactor and monitor the pressure to ensure there are no leaks. If the pressure remains stable, the temperature can then be increased to the optimized value required for the activation step.

After completing the activation step, the pressure should be raised to 20 bars, and the temperature adjusted to the desired value for the FT test. Once both pressure and temperature have been stabilized at the required levels, the on-line μ-GC must be set to perform an analysis every 120 minutes. Additionally, the flowrate should be measured using a bubble flowmeter. It is also crucial to activate the cold trap cryostat and the heating tape along the reactor outlet pipe to prevent condensation of products, as well as the heating system around the back-pressure regulator.

Under standard conditions, a test typically lasts for 90 hours, running continuously from Monday afternoon until Friday morning.

2.2.3. Procedures to manage the end of the run

At the end of the catalytic run, the pressure must be reduced to atmospheric level and all heating systems should be switched off. Additionally, the automatic analysis system of the μ-GC can also be deactivated. Once the pressure within the system stabilizes at atmospheric levels, the cold trap can be disconnected from the rest of the setup and opened to collect the liquid products. The recovered liquids are then separated into two distinct phases: aqueous and organic.

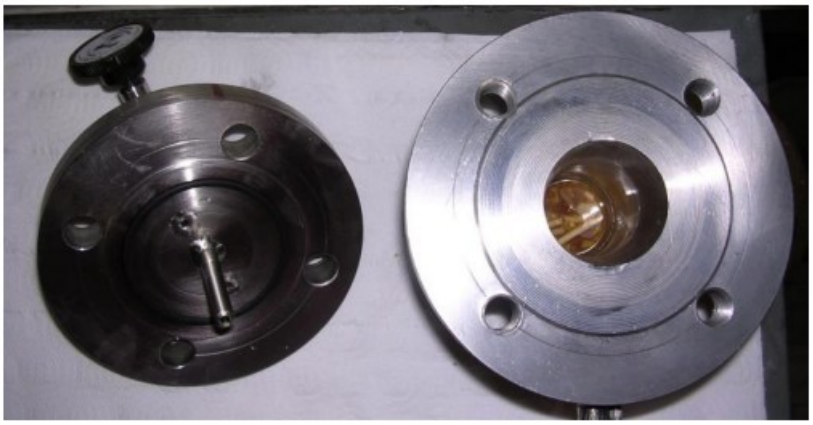

Figure 2.19. view of the inside of the cold trap at the end of a run.

After turning off the μ-GC system, the two modules can be regenerated. The regeneration procedure, which is included in the available methods list, can be easily selected and adjusted via the instrument's software. The purpose of this procedure is to clean the columns by removing any residual compounds that may still be adsorbed on the stationary phase. This is achieved by increasing both pressure and temperature during the regeneration process. Once the process is complete, the detector (TCD filament) can be switched off, and the instrument can be powered down.

The FT reactor must then be disconnected from the pipelines to allow it to be opened. The catalyst is removed from the bottom of the reactor with the aid of a thin pipe that is inserted from the top of the reactor and breaks the catalyst bed. Finally, the used catalyst can be collected in a vial for post-test characterization if necessary.

Following this, the FT reactor is thoroughly cleaned by rinsing multiple times with water and acetone. After completing the cleaning process, the reactor is left drying and ready for a new test.

2.3. Leakage test

This kind of test was made before starting the kinetic runs, in order to be sure about the tightness of the plant. In order to gather reliable and reproducible data is important to avoid any type of leakage both, before and after the reactor section of the plant. In fact, a leakage would bring to errors in the conversion and selectivity values.

The “leak test” is a procedure necessary to verify the pneumatic tightness of the plant. Since every week the plants is disassemble for the ordinary maintenance, this test is essential to verify the correct assembly for the next tests. The test was carried out with a gas mixture that is representative of the reaction mixture:

- 5 $Nml \cdot min^{-1}$ of N_2
- 10 $Nml \cdot min^{-1}$ of CO_2
- 30 $Nml \cdot min^{-1}$ of H_2

The plant is pressurized until 20 bar and the increase of P vs t is recorded. With no leakage in the plant, should be obtained a straight line, otherwise, if a joint has a leakage we should see an increase in the time needed to increase the pressure of a certain value. As can be seen from figure

4.12 if a loss is present there is a deviation from the ideal path. Normally the deviation is seen at high pressure, but less tightened is a joint more the loss can be noticed at lower pressure.

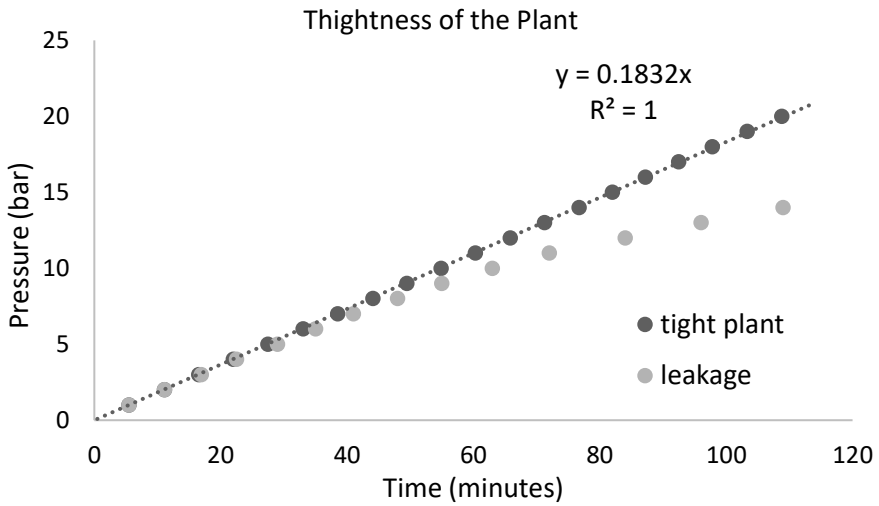

Figure 2.20. Comparison of expected pressure in the tight plant versus the same plant under occurring leakage.

The data obtained by this test can be also used to extrapolate a value for the geometric volume of the plant. The concept is to measure how much time is needed to increase the pressure inside the plant of 1 atmosphere, knowing that this time can be also used to calculate the volume of gas delivered by the flowmeter, and so the volume of the plant itself. It has to be remembered that the electronic flowmeter uses as UOM the bar while for the purpose of this equation we have to use the atm so the time measure (the one necessary to increase the pressure of 1 bar) has to be corrected for a correction factor (1.013). Also, the obtained data has the volume expressed in Nml and a correction considering the temperature has to be done. The formula used to calculate the volume is here displayed.

$$Flow\left(\frac{Nml}{min}\right)\cdot\Delta t\left(\frac{\min}{bar}\right)\cdot 1.013\left(\frac{\text{bar}}{atm}\right)\cdot\frac{T(°\text{C})}{T°(°\text{C})}\cdot 1\,(atm)=Vg(ml) \tag{12}$$

Plotting the pressure inside the plant during the test (on the X-axis) against the geometric volume calculated for each pressure that was used we should obtain a series of dot on a straight line parallel to the X-axis. In the case in which it is present a loss should be seen, at higher pressures, an, apparent, increase of the geometric volume, due to the fact that is need more time to increase the pressure inside the plant of a certain value. In this latter case the dot should be crossed by a straight line with a positive slope. The result obtained by this test are displayed in Fig. 2.21.

From the Fig. 2.21 and its regression line can be seen a negative slope. The presence of a negative slope could be seen as an experimental error or, maybe, an error of the operator but this data can be explained considering the fact that at high pressures (P>10 bar) the gasses don't act as perfect gas, following the model of the ideal gas, but they behave as real gas, so we have to take in account the fugacity of the gas. Thus, the obtained data have to be corrected.

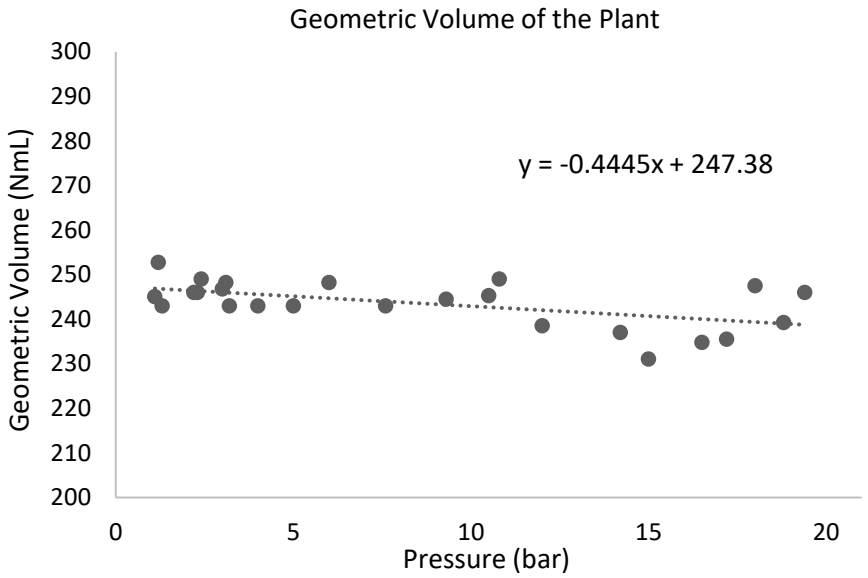

Figure 2.21. Experimental evaluation of geometric volume of the lab plant.

2.3.1. Evaluation of the thermodynamic model

In order to evaluate the difference between the behavior of a perfect gas and a real one was used the software PROII. This software is dedicated to the simulation process in steady state.

The aim of this part is the simulation on the software of a process able to represent the flows presents in the FT plant. To simulate the conditions in which the previous experiment was carried out the flows on the software have been set up, not considering the volumetric flowrates, in fact it is the variable that we want to investigate, but considering the flowrates expressed on molar basis.

Within the software it is possible to select various thermodynamic models, with various characteristics, able to better represent certain compounds. For this experiment it was chosen to use the ideal model (to represent the perfect gas) and the Soave-Redlich-Kwong (SRK) model. The choice of the first model is obvious, in fact all the calculations carried out up to now on the gases have been carried out considering the perfect behavior of the gases and then applying the EoS of the ideal gases. For the second model, the choice was made in accordance with the manual contained within the software, according to which the SRK method is accurate in giving predictions for the behavior of non-polar mixtures. In fact, the mixture with which the test was carried out can be considered apolar, H_2 and N_2 are apolar, while CO despite the electronegative difference between C and O ($\Delta E = 0.4$) can be considered apolar since the charges present on the molecule balance the polarity of bonds ($\mu = 0.11D$).

Once the models to be used for the comparison have been chosen, the set-up of the experiment must be chosen. To do this, the problem must be abstracted to understand which data are needed to verify the theory. The problem that arises in the experiment is possibly attributable to the fact that real gases have a $\Delta V_{mix} \neq 0$. So $V_f \neq V_1 + V_2$.

Streams have been prepared within the software, one with the ideal thermodynamic model, the other with the SRK model, within which a representative gas mixture flows. The amount of gas inside the stream was set not on the basis of the volumetric flowrates (default choice) since it is

the variable that hast to be studied, but on a molar basis. The streams are connected to a flash, which has the sole purpose of making the software implement the EOS. Finally, 2 pipes come out of each flash, one for liquid products (empty pipe) while gaseous products come out in the other one. This last stream is the one of interest, in fact the volumetric flowrate coming out of them will be studied.

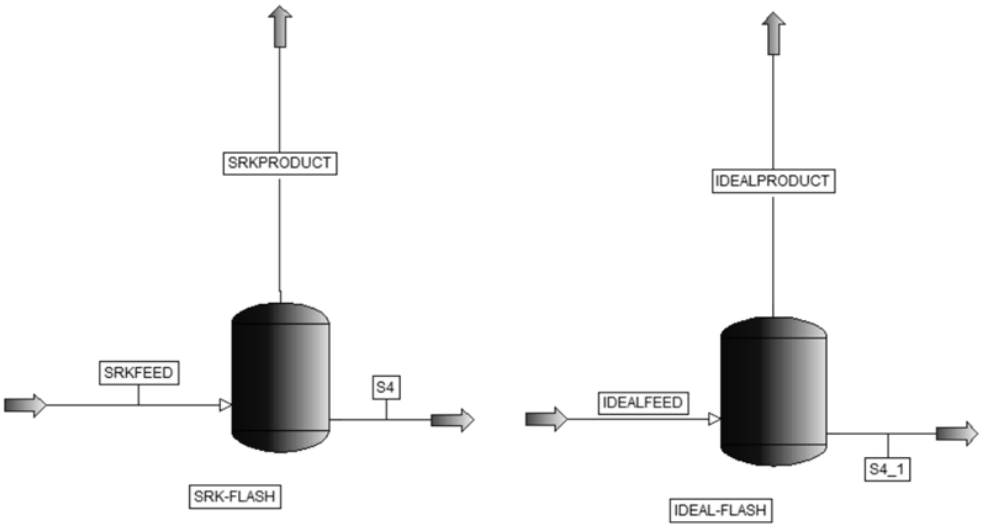

Figure 2.22. Simplistic representation of the plant through simulation software Aveva PRO/II.

Once the system and the flowrates have been set-up, it's needed to choose the T and P to use. The T chosen is the one recorded inside the room containing FT plant (25°C) while for the P which is a variable of interest it was decided to use a case of study, with this function the software will perform multiple simulations, in each of which will use a different pressure (between 1 and 20 bar, the pressures of our interest), recording any data that can then be compared. For the comparison will be taken the flowrates present inside the streams called "srkproduct" and "idealproduct" making a comparison between the volumetric flowrates. The table below shows some of the data obtained.

Pressure (bar)	Ideal V. flowrate (ml/min)	SRK V. flowrate (ml/min)	Ratio [ideal/SRK]
1	49.40	49.39	1.0002
2	24.70	24.69	1.0004
4	12.35	12.34	1.0008
6	8.23	8.22	1.0011
8	6.17	6.17	1.0015
10	4.94	4.93	1.0018
12	4.12	4.11	1.0021
14	3.53	3.52	1.0025
16	3.09	3.08	1.0028
17	2.91	2.90	1.0029
18	2.74	2.74	1.0030
19	2.60	2.59	1.0032
20	2.47	2.46	1.0033

Table 2.16. Some of the results obtained by PROII.

From the ratio between the 2 flowrates can be seen that at high pressure, so, in the field of the real gas we should have a $\Delta V_{mix}<0$. In fact, the ratio is higher than 1.

With the complete data-set can be obtained a graph that plots the pressure against the ratio between the V flowrates ideal and SRK. The equation extrapolated from the regression line can be used to obtain a correction factor for each pression.

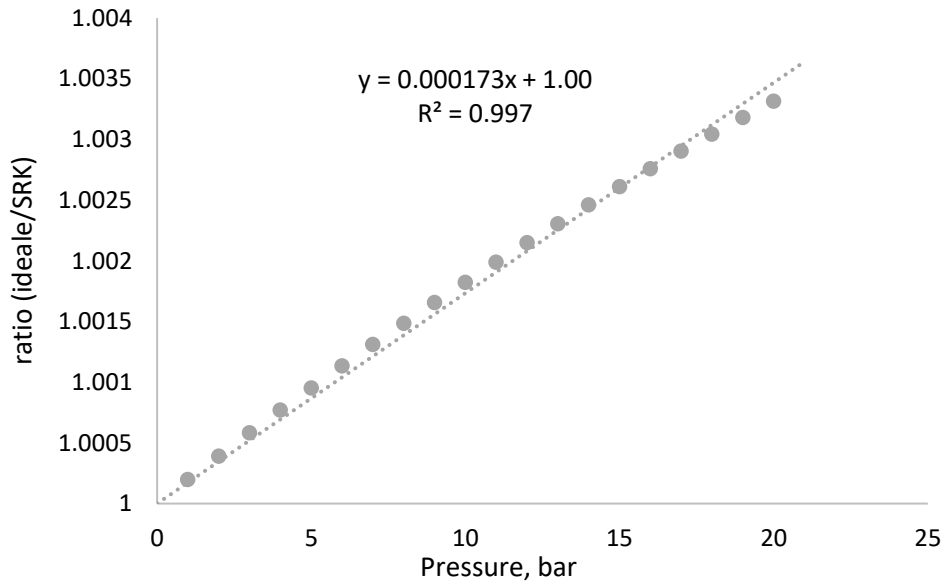

Figure 2.23. Correlation between deviation from ideality and pressure.

Once it's obtained the correction factor for each pressure used to calculate the geometric volume in Fig. 2.21 the found value can be corrected, and the dots should give a straight line parallel to the x-axis.

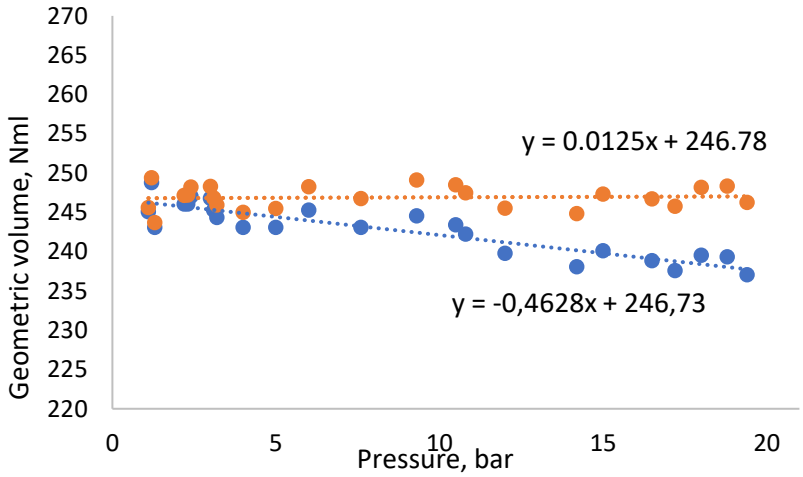

Figure 2.24. Comparison between the data considering in one case the gas ideal in blu, and in the other case real in orange.

From the graph can be seen that, substantially, if the value found considering the gas as perfect is corrected by the non-ideality it's obtained a constant volume. That is the geometric volume of the plant. That is, consider the Eq. 12:

$$Vg = 273\ ml$$

The volume of the plant was also calculated excluding the cold trap. In order to assess the importance of a volume, that, due to the small-scale of the plant, can deeply affect the fluid dynamic of the system. The equation applied is still Eq. 12:

$$Vg(without\ cold\ trap) = 115\ ml$$

By difference can be also found the volume of the cold trap (158 ml) that is a value aligned with specification given: (150 ml).

2.3.2. Fluid dynamic of the rig

In order to have a deeper understanding of the rig and the system a brief evaluation of the fluid dynamic of the plant was carried out. The collected data will be useful in the near future for the simulation of FT plant on a software capable of reproducing a dynamic simulation.

For this part of the thesis two main studies have been done. The first one is the calculation of the Reynolds number, that is an adimensional number, that can be obtained knowing certain properties of the fluid and the environment. It describes the type of movement of a fluid inside an empty pipe, laminar flow (Re<2000) or turbulent flow (Re>2000). Also, the Reynolds number can be used to estimate the type of flow through a porous mass, in this case the porous mass is represented by the catalytic bed, the movement of the fluid is laminar if Re_p<10 otherwise if is higher than 10 can be considered as turbulent. The second study is the calculation of how much time is needed by the plant to reach a steady state after a change in the conditions of the flow. This study as two main purposes, the first one is the evaluation of the phenomena of diffusion and mixing inside the pipes at different pressures: if there aren't mixing phenomena a plug-flow should be present, this means that the μ-GC should detect a rapid change in the composition of the flow, in the other case the phenomena of diffusion play a non-secondary role and so the composition will change gradually. The second purpose is the evaluation of the effect of a large volume, such as the cold trap.

2.3.3. Reynolds number

The Reynolds number helps to predict flow patterns in different fluid flow situations. At low Reynolds numbers (Re<2000), flows tend to be dominated by laminar (sheet-like) flow, while at high Reynolds numbers flows tend to be turbulent. The turbulence results from differences in the fluid's speed and direction, which may sometimes intersect or even move counter to the overall direction of the flow (eddy currents).

In the laminar flow the fluids can be seen as a series of thin sheets that flow one above the other without interfering between themselves. This behavior leads to a formation of gradients (velocity, viscosity, temperature) inside the pipes, because there aren't mixing phenomena.

On the other hand, the turbulent flow (Re>2000) is characterized by mixing phenomena. The fluids inside the pipes tend to have no gradient and the profile of the various measures looks like a plug-flow.

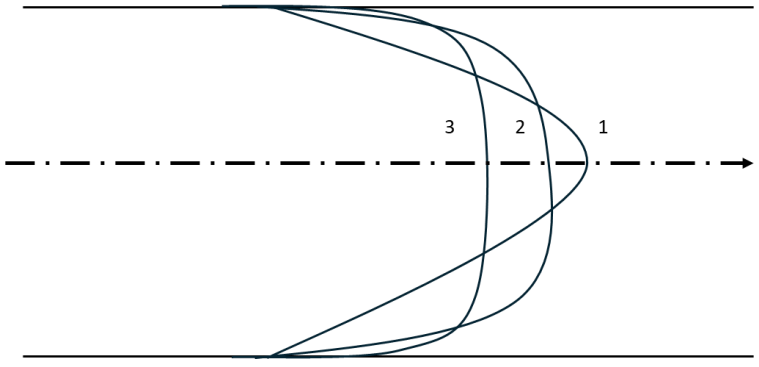

Figure 2.25. Profiles of velocity for different Re: 1 laminar, 2 and 3 turbulent.

The equation to calculate the Reynold number is:

$$Re = \frac{\rho \cdot L \cdot u}{\mu} \tag{13}$$

Where:

- ρ is the density of the fluid (kg/m^3);
- L is a characteristic linear dimension (m) for fluid; in the case of a fluid in a pipe is the diameter of the pipe itself;
- u is the flow speed (m/s);
- μ is the dynamic viscosity of the fluid (kg/(m·s)).

For the calculation of the Reynolds number inside the plant have been considered 2 gas-mixture, one for the CO test and the other one for the CO_2 test. The calculations have been made considering the plant at operative pressure of 20 bar and the temperature at 300K.

	CO test	**CO_2 test**
H_2 (Nml/min)	32	36
N_2 (Nml/min)	5	5
CO/CO_2 (Nml/min)	16	12

Table 2.17. Flows used to calculate Re

To calculate the density of the mixtures the following equation was employed, considering a weighted average pf all the molecular weight that is a derivation from the law of the ideal gas:

$$\rho = \frac{m}{V} = \frac{P \cdot MW}{R \cdot T} \tag{14}$$

With this formula it was obtained that the densities of the two gas mixtures were:

- 9.91 (kg/m^3) for the CO test;
- 11.22 (kg/m^3) for the CO_2 test.

The diameter of pipe is taken as a data given by the producer of the pipe itself and is 0.006m.

The velocity of the flow is calculated as the length of the pipes divided by the time necessary for the electronics flowmeters to deliver a volume of gas equal to the one present inside the plant, so theoretically the time needed for a molecule gas to travel from the beginning of the plant to the end of the plant itself.

$$u = \frac{L}{\frac{Vg \cdot P}{F}} \tag{15}$$

Where:

- L is the length of the pipe (m);
- Vg is the geometric volume of the plant without cold trap (m^3/atm);
- P is the pressure inside the plant (atm);
- F is the flowrate (m^3/s).

The final value of the velocity is the same for both the gas-mixture and is:

- 0.00115 (m/s)

Viscosity is the last value that has to be estimated. Also, this case, the viscosity was considered as a weighted average of the viscosity of the single compounds present inside the mixture. For the calculation of the viscosity was made a comparison between the value obtained using a nomograph (analogical method) and the value given by the software PROII (digital method) were compared. For an higher degree of precision the data given by PROII were taken. The final values of the viscosity are:

- 0.0124 (cP) for the CO test.
- 0.0111 (cP) for the CO_2 test.

Having all the values, the Reynolds number for two different tests can be finally calculated:

	CO test	**CO_2 test**
Re	0.0551	0.0697

Table 2.18. Reynolds number for the two different tests.

It results that the Re<<2000 and so the movement of the fluid inside the empty pipes is, strictly, laminar.

The velocity profile of the fluid inside the pipes can be obtained. Using the following equation:

$$u = 2u_m \cdot \left[1 - \left(\frac{r}{r_w}\right)^2\right] \tag{16}$$

Where:

- u_m is the average velocity, already found with Eq. 15;
- r is the radial distance between the point that has to be studied and the axis of the pipe;
- r_w is the radius of the pipe.

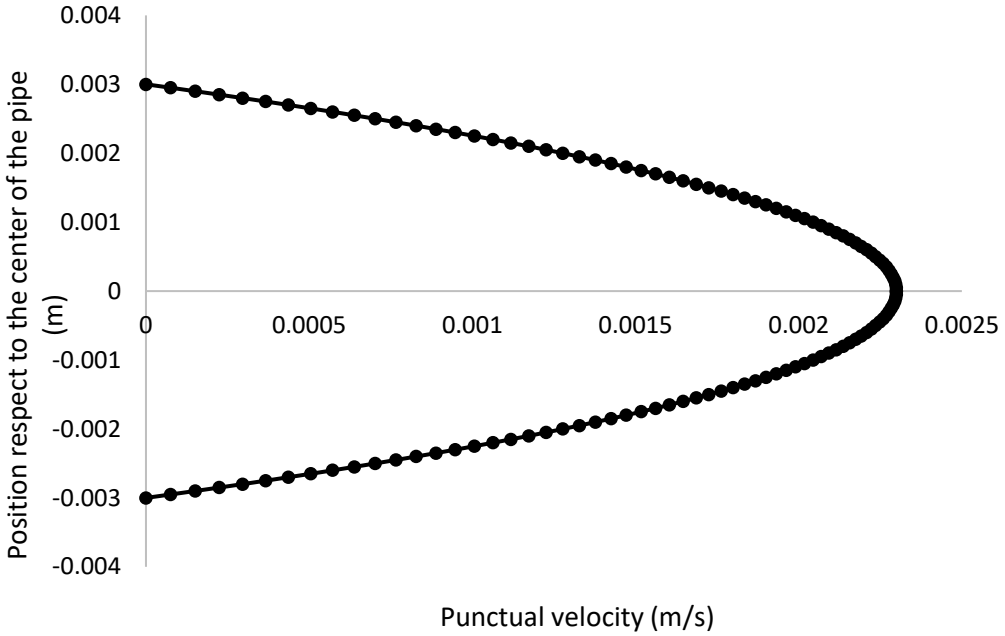

Figure 2.26. Velocity profile inside the pipes.

The graph obtained (Fig. 2.26) is further evidence that the flow is laminar, in fact it is possible to observe the classical "V", which means that there is a rapid decrease of the velocity moving away from the center of the pipe.

Can be also of interest the evaluation of the Reynolds numbers for the fluid in motion through a porous mass, that in our case, is represented by the catalytic bed. In this case the equation that has to be used is the following one:

$$Re_p = \frac{u_s \, \rho \, D_p}{\mu \, (1 - \varepsilon)} \tag{17}$$

Where:

- u_s is the superficial velocity, findable as the ratio between the velocity and the porosity of the catalytic bed;
- ρ is the density of the gas;
- D_p is the diameter of the particle;
- μ is the viscosity of the gas;
- ε is the porosity of the catalytic bed.

The porosity was found using tabulated values for smooth spherical particles. The density and viscosity were already found. D_p was considered as the average value of the selected particles. Thus, the values obtained are:

- ε = 0.335
- us = 0.00343 (m/s)
- Dp = 0.000125 (m)

With this data it is possible to calculate the Reynolds number for fluid through porous masses and the value obtained are:

	CO test	CO_2 test
Re	0.0051	0.0065

Table 2.19 Reynolds numbers calculated for the specific tests.

The obtained values confirm that not only the movement inside the empty pipes is laminar, but also the one between the catalytic bed.

2.3.4. Evaluation of the type of flow inside the pipe

To understand how the presence of the cold trap affects the mixing phenomena an experiment was set-up. The main aim of the experiment is to evaluate how much time is needed for the plant to reach a steady state (S.S.) after that a variation of the conditions of the flows happens (i.e., an increase in the conversion).

The set-up of the experiment was the following one: the FT plant was assembled as usual; no material was loaded into the reactor and the plant was operated at room temperature. The flow used inside the plant is representative of a reaction mixture (16 Nml of CO, 32 Nml of H_2 and 5 Nml of N_2). The variation was simulated by reducing the CO flow by 5 Nml and continuously analyzing by μ-GC, the time needed to reach a steady state again. Then the CO flow was again brought back to 16 Nml and the time necessary to return to the initial condition was calculated.

This experiment was simulated under different conditions: varying the pressures (20 bar, 10 bar, 5 bar) keeping constant the temperature at room temperature, to evaluate the effect of the pressure, and keeping constant the pressure at 20 bar comparing the behavior of the system at room temperature and in hot condition reactor (275 °C). Furthermore, the experiment was carried out removing the cold trap to evaluate the mixing phenomena, without considering any possible mixing given by the cold trap.

The main variables of interest for this experiment are:

- the time necessary to see an initial change in flow after this has changed
- the time necessary to reach the S.S.

These variables can then be used to calculate the amount of gas delivered with respect to the amount of total gas present in the system. The more the flow of gas inside the system is plug-like and without mixing phenomena, the more these two events (the initial variation and the achievement of the S.S.) are temporally close to each other and the fraction of gas delivered compared to that contained in the plant is close to 1.

Hereinafter some of the results obtained by the test are shown:

After 52 minutes the flow is reduced.

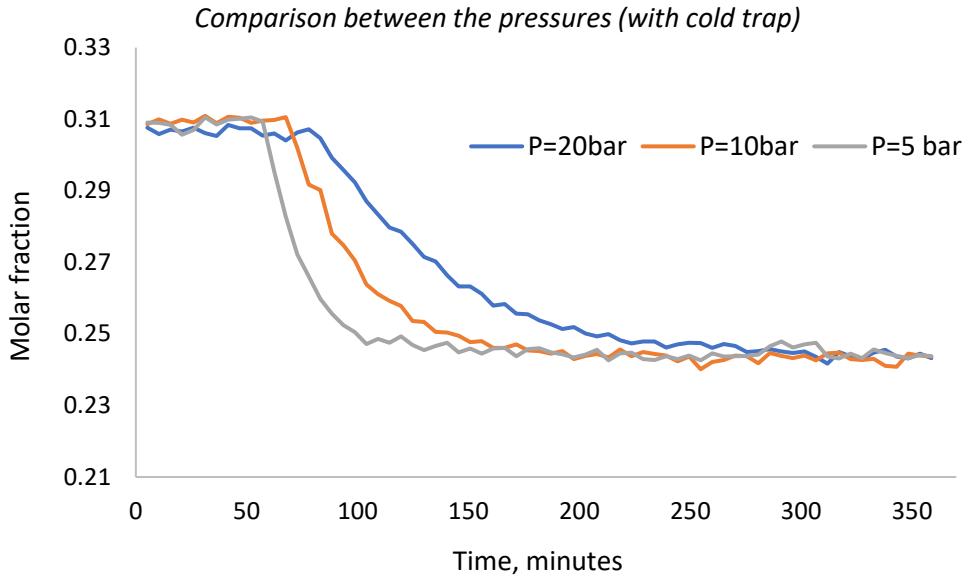

Figure 2.27. Comparison of the flows at different pressures.

Pressure (bar)	Time needed to notice a variation (minutes)	Fraction of the gas needed to notice a variation	Time needed to reach S.S. (minutes)	Fraction of the gas needed to reach S.S
20	31.2	0.280	202.8	1.817
10	20.8	0.373	150.4	2.695
5	10.4	0.466	78	2.800

Table 2.20. Some of the variables of interest.

From the graph and the table, it can be seen that the presence of mixing phenomena is quite high. At higher Pressure the change in composition is slower, and this was a foreseeable behavior. At 20 bar the gas fraction delivered before to note a variation is the smallest one, and it is significantly lower than 1, also the gas fraction needed to reach the S.S. is significantly higher than 1. This means that the mixing phenomena are present inside the plant. In particular increasing the pressure the mixing phenomena increase. Indeed, lowering the pressure, the fraction of gas needed to notice a variation grows closer to 1. On the other hand, the gas-fraction needed to reach a S.S. seems to follow reverse order, with higher mixing phenomena for lower pressures. This phenomenon can be explained by referring to the laminar motion present inside the pipes, in fact the layers of gas closest to the walls have the same composition as the innermost layers during the S.S. even if they have a lower speed. Changing the composition, the outer layers, that are slower, take longer to leave the system "retaining" the characteristics of the composition. In the case of the plant working at low pressure, the lower residence time reduce the possibility of diffusion phenomena between neighboring layers while in the case of high pressure the increased residence time of the gasses favors a condition of uniformity respect to the radius of the pipes, reducing the fraction of gas necessary to reach the S.S.

Hereinafter it can be seen a graph where the flow is increased, the behavior very similar to the one seen before but mirrored.

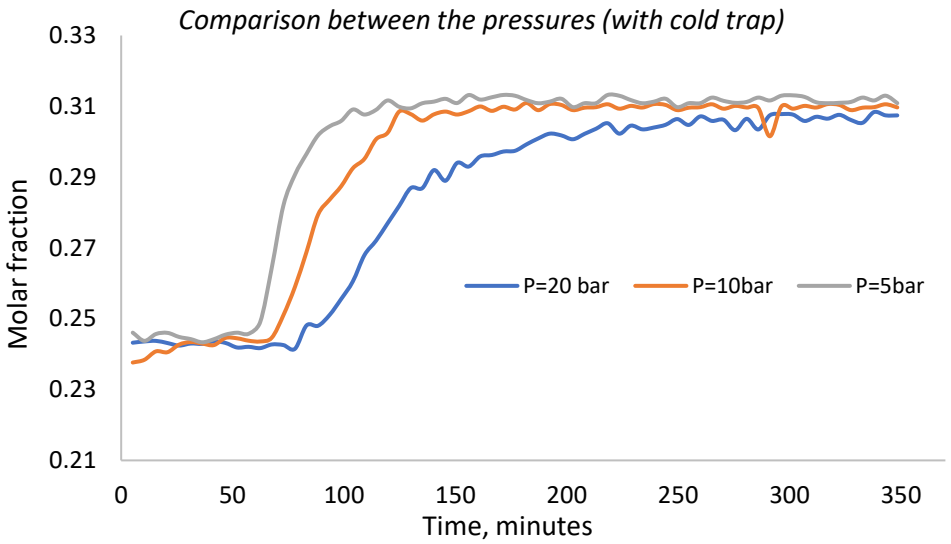

Figure 2.28. Comparison of the flows at different pressures.

After having conduct the test with the plant in standard configuration the cold trap was removed and the experiment was conducted again.

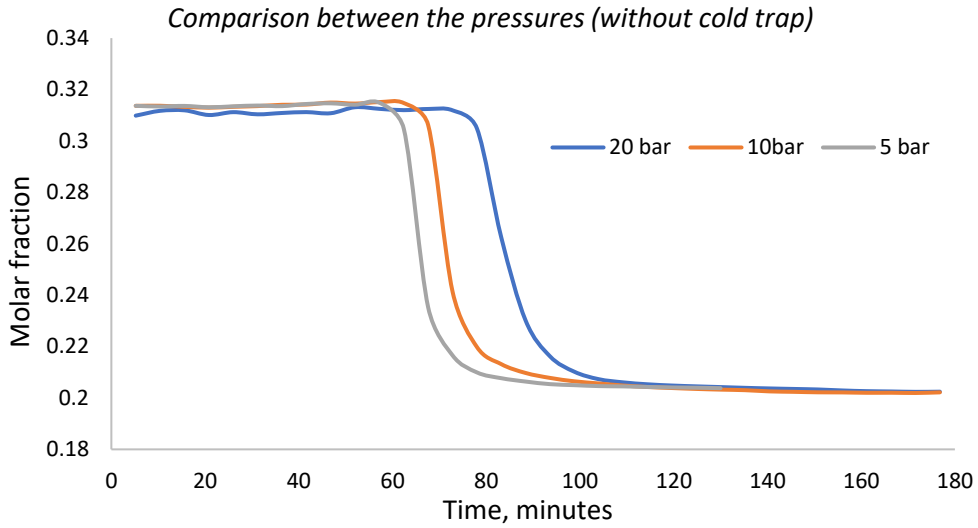

Figure 2.29. Comparison of the flows at different pressures.

Pressure (bar)	Time needed to notice a variation (minutes)	Fraction of the gas needed to notice a variation	Time needed to reach S.S. (minutes)	Fraction of the gas needed to reach S.S
20	26	0.512	98.8	1.944
10	15.6	0.614	62.4	2.456
5	10.4	0.819	67.6	5.322

Table 2.21. Some variables of interest.

The pattern is very similar to the one seen for the plant with the cold trap, but the fraction of gas needed to notice a variation is much closer to one, this means that the phenomena of mixing are reduced. This is due to the absence of the cold trap that act as mixing tank. Moreover, at lower pressure the fraction of gas is closer to one meaning that the flow moves as a plug, this phenomenon is probably also due to the fact that at lower pressure there is a lower time of residence inside the plant and this reduce the possibility of mixing phenomena. For what concern

the fraction of gas needed to reach the S.S. the values are very similar to the one found for the plant with the cold trap this could be due to the highly laminar flow of gas inside the plant that doesn't allow the change of the gas in the pipe with the same pace for every position inside the pipe itself, Fig 2.26. This can lead to an higher time needed to reach S.S.

Finally, the test at two different temperatures was carried out. From the graph hereinafter it seems that the temperature doesn't have any kind of effect on the mixing phenomena.

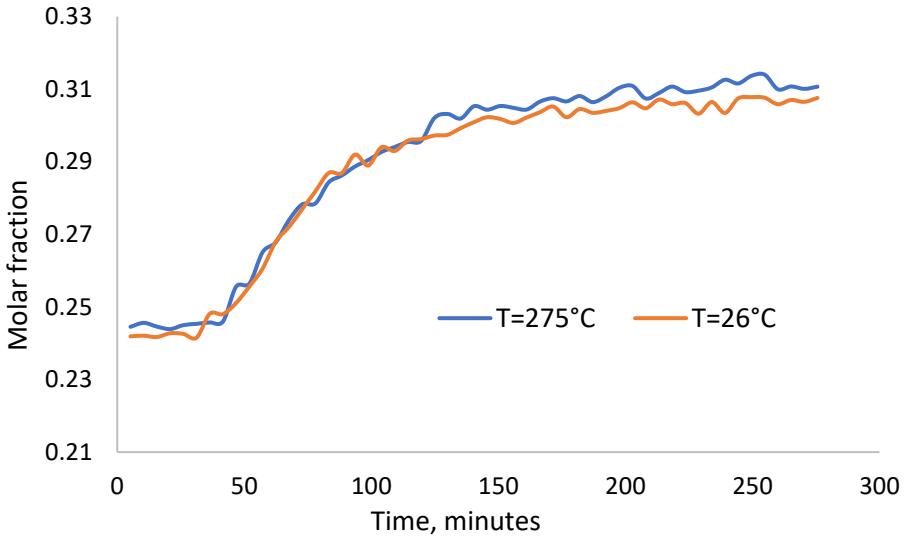

Figure 2.30. Comparison of the data obtained at 20 bars and two different temperatures

2.4. Data elaboration

With the analytical apparatus integrated into the FT plant, it is possible to measure:

- The temperature and pressure;
- The inlet flowrates of each gas and the total outlet flowrate;
- The composition of the light hydrocarbons fraction (made by μ-GC);
- The weight of the organic and aqueous phase collected in the cold trap.

After the experimental elaboration it is possible to calculate:

- The conversion of CO;
- The molar flowrates of all the light hydrocarbons;
- The selectivity of CH_4, CO_2, the light fraction and the heavy fraction.

2.4.1. *Equations concerning the CO conversion, the mixture composition, the molar flowrates and productivity*

$$Flow_{FT} = Flow_{Total} - Flow_{N2} \tag{18}$$

$$CO_{conversion} = \frac{Flow\ CO_{in} - Flow\ CO_{out}}{Flow\ CO_{in}} \cdot 100 \tag{19}$$

$$\%\ CO\ = \frac{Flow\ CO_{out}}{Flow_{FT}} \cdot 100 \tag{20}$$

$$\%"i,n" = \frac{area_{"i"}}{calibration\ factor_{"i"}} \cdot \frac{Flow_{Total}}{Flow_{FT}} \quad (21)$$

Where:

- "i" is a generic light product with n carbon atoms;
- %CO: is the molar fraction of the i,n molecule;
- $Flow_{FT}$: is the out coming volumetric flowrate (Nml·min^{-1});
- $Area_{"i,n"}$: is the chromatographic area given by the μ-GC;
- Calibration factor: is the factor (one for each component) determined by the μ-GC calibration which correlates the area and the composition.

$$"i,n"\ molar\ flowrate = \frac{Flow_{FT} \cdot 0.001 \cdot \%"i,n"}{22.414} \quad (22)$$

$$C_{molar\ flowrate\ of\ "i,n"} = "i,n"_{molar\ flowrate} \cdot nc \quad (23)$$

$$CO_{in\ molar\ flowrate} = \frac{Flow\ CO_{in}}{22.414} \cdot 0.001 \quad (24)$$

$$CO_{out\ molare\ flowrate} = \frac{Flow\ CO_{out}}{22.414} \cdot 0.001 \quad (25)$$

$$Total\ C_{out\ mol.flowrate} = CO_{out\ mol.flowrate} + \sum_{n=1}^{n=6} C_{mol.flowrate\ of\ "i"} \quad (26)$$

Where:

- $i,n_{molar\ flowrate}$: is the outlet molar flowrate of i,n component;
- $C_{molar\ flowrate\ of\ "i,n"}$: is the outlet molar flowrate referred to the moles of C in the i,n compound;
- $CO_{IN\ molar\ flowrate}$: is the inlet molar flowrate of CO;
- $CO_{OUT\ molar\ flowrate}$: is the outlet molar flowrate of CO;
- Total $C_{OUT\ molar\ flowrate}$: are all the moles of carbon that left the plant in gas phase;
- 0.001: is the conversion factor from Nml·min^{-1} to NL·min^{-1} ;
- 22.414: is the volume expressed in L which has a mole of gas in standard conditions;
- nc: is the number of carbon atom in the "i,n" molecule.

2.4.2. Equations concerning the heavy phase composition and productivity

The heavy fraction is assumed to be a series of -CH_2-, thus the total number of moles of the organic phase are calculated as reported in Eq. 27:

$$moles\ of\ (-CH_2-) = \frac{Weight > C7}{14} \quad (27)$$

Where:

- moles of (-CH_2-): is the total number of methylene units in the heavy phase;
- Weight>C7: is the mass of the heavy organic phase collected in the cold trap;
- 14: is the molecular weight of the -CH_2- unit.

$$\%\ "j,n" = \frac{Area_{"j,n"} \cdot fc}{Area_{Total}} \cdot 100 \quad (28)$$

$$moles\ of\ "j,n" = \%\ "j,n" \cdot moles\ of\ (-CH_2-) \tag{29}$$

$$"j,n"_{molar\ flowrate} = \frac{moles\ of\ "j,n"}{TOS} \tag{30}$$

$$C_{\ molar\ flowrate\ of\ "j,n"} = "j,n"_{molar\ flowrate} \cdot n_c \tag{31}$$

Where:

- "j,n": a generic heavy product containing n carbon atoms;
- "j,n" molar flowrate: the molar flowrate corresponding to the j, n compound;
- C molar flowrate of "j,n" : The outlet molar flowrate calculated based on the moles of carbon in the j,n compound;
- n_c: the number of carbon atoms in the j molecule
- Area "j,n": the chromatographic area recorded by the GC for the j,n compound;
- Area total: the total chromatographic area recorded by the GC within the C_7-C_{30};
- f_c: the calibration factor obtained from the GC calibration process.
- TOS: time on stream, expressed in hours, measured at the end of the experiment

2.4.3. Equations concerning the selectivity and the C_{2+} yield

$$S_{"CO2"}\frac{CO_{2\ molar\ flowrate}}{CO_{in\ molar\ flowrate} - CO_{out\ molar\ flowrate}} \tag{32}$$

$$S_{"CH4"}\frac{CH_{4\ molar\ flowrate}}{CO_{in\ molar\ flowrate} - CO_{out\ molar\ flowrate}} \tag{33}$$

$$S_{"i,n"}\frac{C_{\ molar\ flowrate}}{CO_{in\ molar\ flowrate} - CO_{out\ molar\ flowrate}} \tag{34}$$

Where:

- S_{CO_2}: is the selectivity to CO_2;
- S_{CH_4}: is the selectivity to CH_4;
- $S_{"i,n"}$: is the selectivity to the generic light "i,n" product;
- $S_{<c7}$: is the selectivity to the light products phase.

The selectivity toward the heavy phase can be calculated as reported in Eq. 49:

$$S_{>C7} = 100 - S_{CO2} - S_{CH4} - S_{<C7} \tag{35}$$

The C_{2+} yield is given by Eq. 50:

$$C_{2+}yield = CO\ conversion\frac{(>C7_{selectivity} + <C7_{selectivity})}{100} \tag{36}$$

Carbon balance can be determined with Eq. 51:

$$\%C = (\frac{mol, C_{in} - mol, C_{out(CO,CO2,CH4)} - mol, C_{out(<C7)} - mol, C_{out(>C7)} - mol, C_{out(H2O)}}{mol, C_{in}}) \cdot 100 \tag{37}$$

Where:

- mol, $\mathbf{C_{IN}}$: total number of C moles IN;

- mol, $\mathbf{C_{OUT\ (CO,\ CO_2,\ CH_4)}}$**:** total number of C moles OUT from unreacted CO, produced CO_2 and CH_4;
- mol, $\mathbf{C_{OUT(C7)}}$: total number of C moles OUT from heavy products (>C7);
- mol, $\mathbf{C_{OUT\ (H_2O)}}$: total number of C moles OUT from carbonaceous species dissolved in H_2O;

2.4.4. Equations concerning the calculation of α and ASF algorithms

The probability of chain growth, α, is a key parameter in understanding the product distribution in Fischer Tropsch synthesis. This probability can be estimated from experimental data using the Anderson Schulz Flory (ASF) model, which describes the molar (or weight) distribution of hydrocarbons as a function of chain length.

A linearized form of the ASF equation is given as:

$$\ln(W_{n,j}) = \ln(1-\alpha)^2 + (n_c - 1)\cdot \ln(\alpha) \tag{38}$$

Where:

- $W_{n,j}$ is the weight fraction of hydrocarbon product *j* containing *n* carbon atoms,
- α is the chain growth probability,
- n_c is the number of carbon atoms in the *j* molecule.

By plotting $\ln(W_{n,j})$ versus n_c , the value of α can be determined from the slope of the linear regression.

The value $W_{n,j}/n$, required for ASF linearization, can be computed using the following steps:

Moles of carbon in compound j,n:

$$\text{moles of } C_{j,n} = C_{\text{molar flowrate of } j,n}\cdot \text{TOS} \tag{39}$$

Weight of carbon in j,n:

$$\text{weight of } C_{j,n} = \text{moles of } C_{j,n}\cdot 14\ \text{g/mol} \tag{40}$$

(*CH_2 unit = 14 g/mol*)

Total weight of carbon in the heavy phase:

$$\text{total weight of } C = \sum_{n=1}^{30} \text{weight of } C_{j,n} \tag{41}$$

Weight fraction of compound j,n:

$$W_{n,j} = \frac{\text{weight of } C_{j,n}}{\text{total weight of } C} \tag{42}$$

ASF input parameter:

$$\frac{W_{n,j}}{n} = \frac{W_{n,j}}{n_c} \tag{43}$$

- $C_{j,n}$ is the total number of moles of CH_2 units in compound *j* with *n* carbon atoms,
- The weight of carbon in j,n is calculated using the standard molar mass of the methylene group,

- $W_{n,j}$ is the weight fraction of product *j* referred to the heavy phase,
- $W_{n,j}/n$ is used for the ASF plot to linearize the distribution and extract α.

To determine α, a graph is constructed by plotting log ($W_{n,j}/n$) vs. n. The slope of the linear portion of this plot corresponds to log(α), from which α can be derived by inverse logarithm.

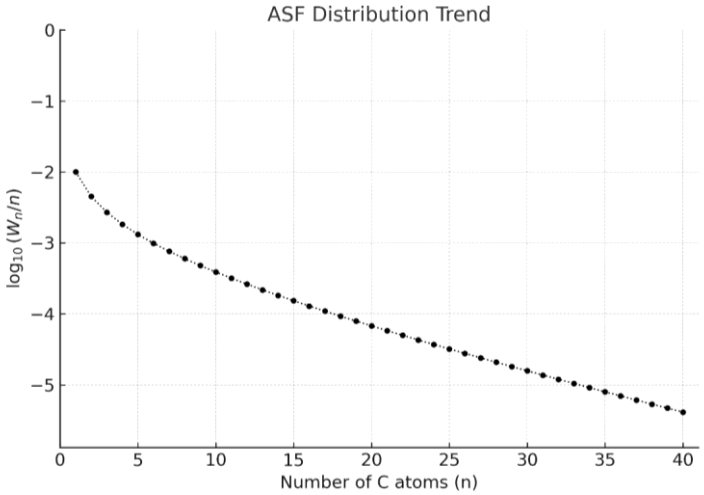

Figure 2.31. ASF distribution plot showing log(Wn,j/n) versus carbon number n. The trend reflects the theoretical Anderson Schulz Flory model, and the slope of the linear region is used to calculate the chain growth probability α.

The plot presented below is based on the theoretical Anderson-Schulz-Flory (ASF) distribution, assuming a constant chain growth probability (α=0.90). It serves as a reference to illustrate the expected logarithmic decay of Wn,j/n with increasing carbon number. In real experimental data, deviations from this trend can occur due to kinetic effects, diffusion limitations, or secondary reactions.

2.5. Bench plant

The bench scale plant was employed since it allows to reach higher operating pressures. The general scheme is quite similar to the lab-scale one. One of the biggest differences is that the bench plant is controlled by software and is fully automatized. The software guarantees also remote control of the operations. The gases are fed to the plant through six flowmeters that allow to select the composition of the reactant mixture. The gases available are H_2, CO, CO_2, CH_4, air, N_2, high- and low-pressure Ar and He. The gases are mixed and fed to the reactor after being preheated. The preheating is carried on in an oven that contains the reactor, the bypass line and the first part of the outlet pipes. If needed, the reactor can be bypassed by an automatic three-way valve. The stream exiting the reactor passes through a series of three condensers which can be operated at different temperatures to obtain a rough separation of the products. Each condenser can be discharged through an on/off valve controlled by the software. To control the outlet flowrate, downstream to the on/off valve is placed a needle one that can be regulated manually. The height of the liquid in the condenser is measured by a sensor that allows the automatic discharge once a certain, selected level is reached. The first two condensers are equipped with cooling fans and electrical heaters that allow them to work between room temperature and 150°C if high boiling point products are obtained. The third condenser is cooled by a Peltier device that allows it to work between room temperature and -10°C. The uncondensed products are sent to an on-line Agilent 990 micro-GC for the analysis of the composition and then pass through a TG0.5/5

Ritter flowmeter. A back pressure regulator controls the pressure of the plant by a diaphragm valve operated by a N_2 pressure.

The valve allows the gases to exit from the plant once their pressure overcomes the one exerted by the N_2 on the diaphragm. The plant can treat also liquid reactants that are injected before the reactor by an HPLC pump. In case of need, the plant is equipped with a line specific to the use of ammonia.

For safety reasons, automatic shutdown of the plant with interruption of heating and closing of all the mass flow controllers occurs if a certain value of temperature or pressure is exceeded. These values can be selected by the operator before starting the operations. The plant is also equipped with three rupture discs to avoid uncontrolled pressure rising. Some check valved distributes in the plant make the flow unidirectional and prevent reactant contamination in case of the plant pressure overcomes cylinders ones.

The process flow diagram is reported in Fig. 2.32.

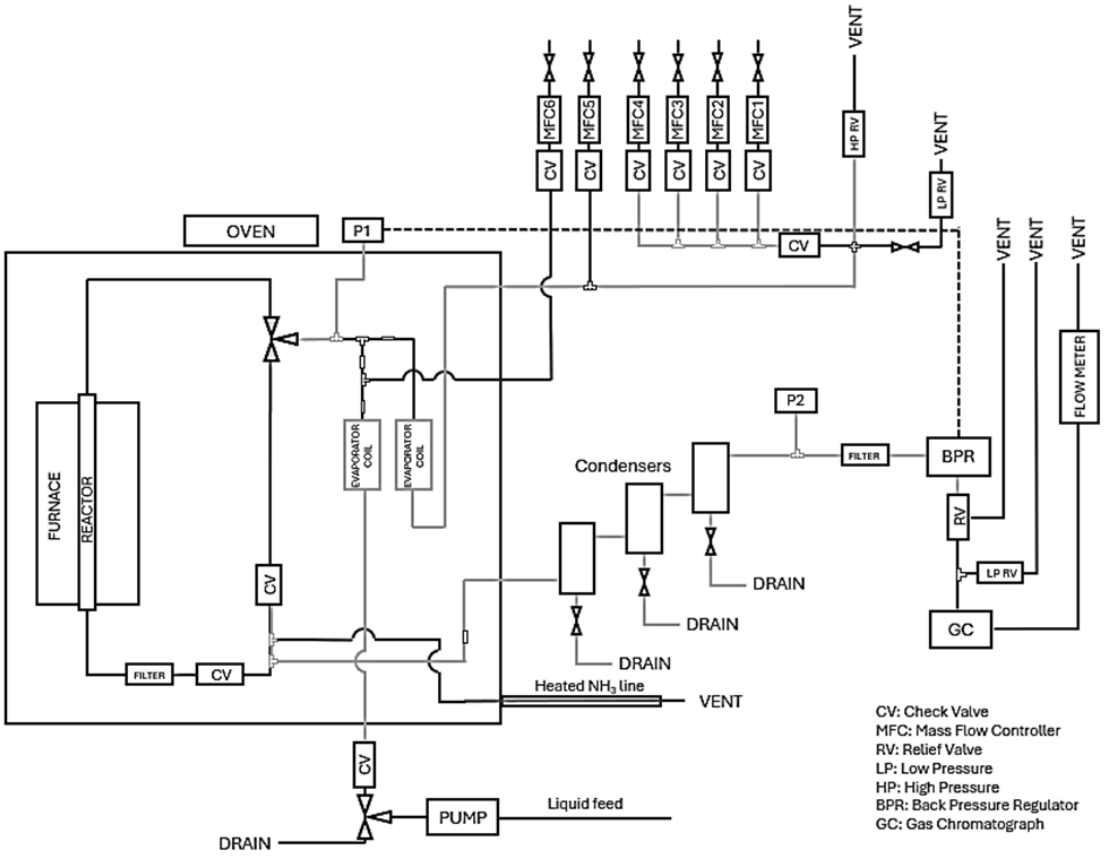

Figure 2.32. Block flow representation of the Bench scale plant (Named "CNR")

Figure 2.33. Picture of the Bench scale plant

The reactor is a stainless-steel-flanged pipe with an internal diameter of 10mm. A rod placed coaxial to the reactor allows the insertion of a thermocouple to monitor the exact temperature of the catalytic bed. Quartz reactors are available if very high temperatures are required. The catalytic bed is charged from the top of the reactor and is sustained by a perforated plate fixed to the rod; to avoid any movement of the packing, some quartz wool is placed on the top and on the bottom. The catalyst cannot be used in powder but must be in pellet between 35 to 45 mesh. The reactor is heated by a furnace divided into three independent sections that allow to select a constant operating temperature or to set a gradient. The furnace can be opened, and the reactor can be removed for cleaning and maintenance operations. A filter downstream to the reactor prevents solid particles from reaching other parts of the plant in case they escape from the packing bed. A representation of the catalytic bed is reported in Fig. 2.34.

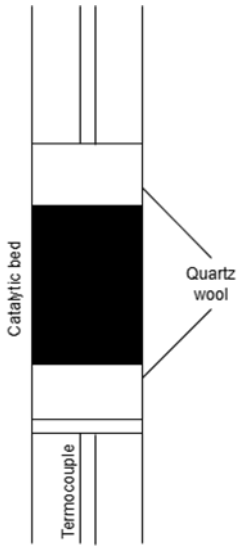

Figure 2.34. Schematic representation of inner reactor pipe set up.

The conditions of the process were kept as similar as possible to those in the laboratory plant. 1 gram of catalyst was loaded in the reactor for each test. The first step was the reduction and activation of the catalyst that was performed by feeding 30mL/min of hydrogen and 15mL/min of carbon monoxide at 4 bar (relative pressure) and 350°C. The temperature of the oven was set at 150°C, the condensers were held respectively at 120, 30 and -10°C. The activation lasted 4 hours. After this time the conditions were switched to the reaction ones. The composition of the inlet mixture was modified in 36mL/min of hydrogen, 12mL/min of CO_2 and 5mL/min of argon. The temperature decreased to 250°C and the pressure increased to the operating one (20, 25 and 30 bar).

In Table 2.22 below the detailed set of conditions is addressed. During the test the temperature increased and kept to the selected value for around one day. The unreacted reagents and the products were quantified by the on-line micro-GC. Water and heavier hydrocarbons were condensed and recovered at the end of the analysis.

Test conditions summary: CO_2 hydrogenation					
Test	**Inlet mixture (ml/min)**			**Temperature (°C)**	**Pressure (bar)**
	H_2	**CO_2**	**N_2**		
Ramp	36	12	5	250	20
				300	
				320	
				350	
Ramp	36	12	5	250	25
				300	
				320	
				350	
Ramp	36	12	5	250	30
				300	
				320	
				350	
Isotherm	36	12	5	300	15 20 25 30

Table 2.22. Operating parameters during CO_2 hydrogenation in Bench scale plant.

3. CATALYSTS SYNTHESIS

Two types of catalysts have been tested:

- Fe-based metallosilicates (wt.%=10%). Supports used are based on Ce, Ti, Zr and V, silicates and commercially available ones namely “Dispal” and “Catolox”;
- Fe-based nano-hydrotalcites promoted with Cu and K.

The first type of catalyst was synthesized with the sol-gel method at Polytechnique of Montreal, Canada.

3.1. Metallosilicates

Metallosilicates are crystalline silicate materials composed of corner-sharing TO_4 tetrahedra. In their conventional form, T represents Si and Al, and the materials are known as aluminosilicates. In such materials, neighboring SiO_4 and AlO_4- tetrahedra are bridged by oxygen atoms and are regularly arranged into a three-dimensional system of cages and pores.

Mesoporous silicates, such as the most common MCM-41 and SBA-15 are porous silicates with ordered arrays of cylindrical mesopores. Since they offer high surface areas (800 $m^2 \cdot g^{-1}$ to 1400 $m^2 \cdot g^{-1}$) and large pore volume, mesoporous silica noticeably facilitates the adsorption of gases during the reaction.

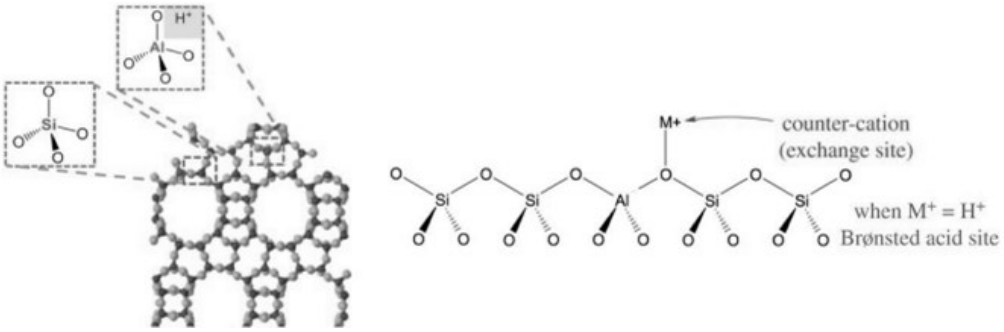

Figure 3.1. Metallosilicates structure.

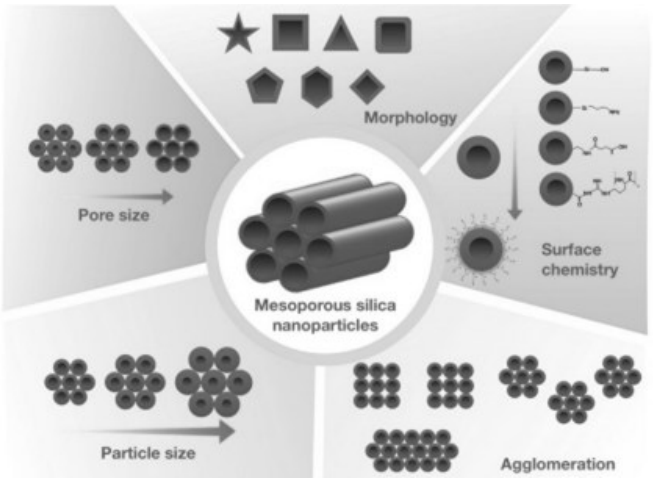

Figure 3.2. Mesoporous silica.

Large pores of mesoporous silica promote mass transfer and diffusion while the high surface area increases the concentration of active sites on the surface. The mesoporous structure yields high molecular weight products and prevents deactivation by coke or pore blocking.

Zeolites mostly have micro-porous pore structures (ZSM-5, modernite etc.) and are common supports for Fischer-Tropsch catalysts. Micropores limit carbon monoxide diffusion and thus adsorption rates at active sites in narrow pores. This leads to lighter hydrocarbons since the chain growth is limited. The crystalline nature of zeolites provides better control of characteristics of the active sites and thermal stability. This improves the catalyst performance stability compared to the amorphous character of mesoporous silica [1].

The few studies with metallosilicates to catalyze the Fischer-Tropsch reaction have concentrated on cobalt as the active phase [2] highlighting the fact that mesoporous silica supports are more active and selective to C_{5+} fractions compared to SiO_2, Al_2O_3 and TiO_2. Very few reports have been addressed so far on iron FT catalysts supported by silica mesoporous materials. Therefore, the synthesis was focused on mesoporous metallosilicates and modification of the zeolite nature by using different metals such as Zr and Ce as support for the iron active phase, eventually promoted with K and Cu.

3.1.1. Synthesis

It's well known that the method used during the synthesis deeply affects the catalyst structure and its performance, and if correctly performed, it can favor the formation of a homogeneous structure with specific physic-chemical properties as pore size distribution, morphology and particle size. Moreover, the preparation methods facilitate various interactions between the active metal and supporter or promoters.

Some of the advantages of sol-gel method are high homogeneity and dispersion, excellent control of the catalyst structure such as particle size or porosity and a large range of the compositions. In addition, reproducibility, high surface-to-volume ratio and low temperature chemistry are other advantages. It is important to note that the metallosilicate catalysts were synthesized externally at Polytechnique Montréal using a previously established sol-gel methodology.

Since these materials were not prepared directly within the scope of this doctoral project, only the essential synthesis parameters are reported here to ensure completeness and enable comparison with the catalysts developed in this work. The 5-steps synthesis includes: (i) solution preparation with precursors, (ii) hydrolysis and partial condensation for "sol" formation, (iii) gel formation due to polycondensation of hydrolyzed precursors, (iv) drying, and (v) calcination. The promotion of the catalyst cannot be disclosed due to a patent pending. An aging process step can be included since it modifies the structure or composition of the material depending on the hydrolysis or condensation rate. Electronegativity of the metal concerning oxygen causes the M-O-C bonds to be highly polarized and increase the hydrolysis rate. It is known that the lower electro-negativity of the transition metals and the possibility of enlarging the coordination sphere account for the high reactivity. The electro-negativities of Zr and Ce are 1.33 and 1.12. They are chosen for their lower electronegativity reason.

3.1.2. Support synthesis

For the metallosilicates support synthesis, it was modified and applied the method described by Kamath et al. (2018) [2]. Triethanolamine (TEA) was used as a mesopore directing agent and a complexing ligand that stabilizes metal cations (bifunctional template). Also, TEA creates porosity while minimizing adverse physical phenomena (capillary pressure) and chemical effects (condensation) while drying. Tetraethyl orthosilicate (TEOS, 99 %, liquid, 25 mL) was the silica source for support synthesis. TEOS and metal precursor (ammonium cerium (IV) nitrate, zirconium (IV) ethoxide, ammonium metavanadate and titanium (IV) butoxide) were added and stirred for 30 min to homogenize the solution. Triethanolamine (TEA) was added, and the solution was stirred for another 30 min. Then water was added dropwise to the obtained mixture, and the stirring continued further for 60 min. To induce hydrolysis, Tetraethyl ammonium hydroxide (TEAOH) was added, and the mixture was aged for 24 h at ambient conditions. The molar ratio of the resulting gel was 1 SiO_2:0.1 MxOy:0.3 TEA:0.1 TEAOH:11 H_2O. The gel dried at 100 °C for 24 h and the dried powder was calcined at 700°C for 10 h with a heating rate of 1°C·min^{-1} in air.

3.1.3. Catalyst synthesis

The sol-gel synthesis of the support was combined with an induced evaporation by a self-assembly method using ethanol (20 ml) and the block copolymer Pluronic P123 (1.3g) as a template. The mixture was stirred at room temperature for 30 min. Then, metallosilicate supports (3g) and iron nitrate nonahydrate (2.17g), (to obtain 10g loading) were added to this solution. We chose a metal coverage of 10% to be in the same range as suggested by the literature [3]. It was stirred another 30 min and the final sol solution was transferred to a petri dish and gelled in an oven at 40℃ with a relative humidity of 50%. After aging for 5 days, we recovered a solid that was still humid. The same procedure for drying and calcining was followed for all catalysts. The gel dried at 100°C for 24 h and the dried powder calcined at 700℃ for 10 h with a heating rate of 1°C min.

3.2. Fe-based Hydrotalcites

Hydrotalcites, also known as layered double hydroxides, are broad classes of materials that exhibit catalytic activity due to their unique structural and chemical properties [4, 5]. They consist of a lamellar structure containing positively charged brucite-like layers separated by an interlayer region filled with negatively charged anions and water molecules. Their general formula can be expressed as:

$$[M^{2+}{}_{1-x}\, M^{3+}{}_{x}(OH)_2]^{x+} \cdot (A^{n-})_{x}/_{n} \cdot yH_2O \quad (1)$$

where M^{2+} and M^{3+} are divalent and trivalent cations, respectively, while A^{n-} is the intercalated anion.

The structural flexibility allows for precise tuning of the hydrotalcites' composition, which can be adjusted by selecting suitable metal cations and interlayer anions.

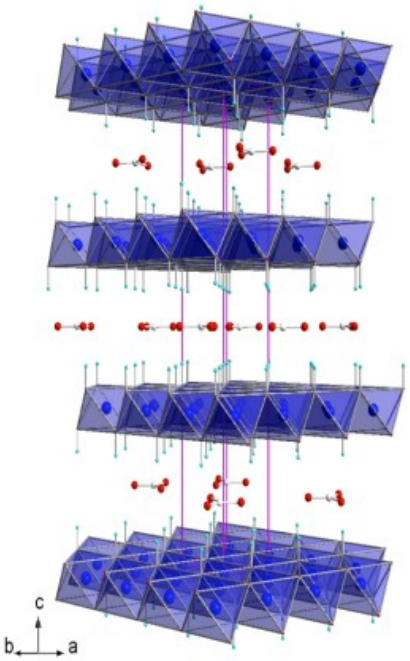

Figure 3.3. Hydrotalcite structure.

Due to this, hydrotalcites can incorporate a wide range of metal cations, such as Mg, Al, Fe, Ni, Cu, Co, and Zn, among others, affecting the catalytic properties of the materials. For example, Mg-based hydrotalcites are thermally stable, while Fe and Co promote redox behavior, making them suitable for reactions such as CO_2 hydrogenation and Fischer-Tropsch synthesis [6]. Different crystal morphology (flat, sand-rose), crystal size (from nanometric to micrometric crystals) and amount of solvents interlayer can be possible. This gives hydrotalcite a wide range of applications based on the different properties of the species used during the synthesis.

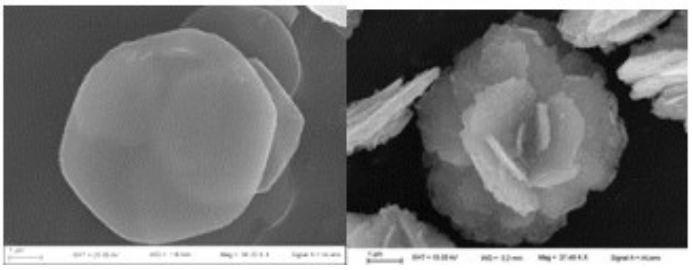

Figure 3.4. Crystal morphology.

The thermal decomposition of hydrotalcites at moderate temperatures results in the formation of mixed metal oxides with high surface area and basicity, which allows for diverse catalytic applications. The application of hydrotalcites in CO_2 hydrogenation offers several benefits over traditional catalysts. Their ability to incorporate multiple metals at an atomic level favors a high density of active sites. The high surface area and mesoporous structure of hydrotalcites enhance mass transfer, allowing efficient adsorption and activation of CO_2 and hydrogen. Furthermore, their basicity can be fine-tuned by adjusting the M(II) M(III) ratio, which directly impacts the catalytic activity and selectivity. In CO and CO_2 hydrogenation processes, hydrotalcites have demonstrated promising performance, particularly in producing long-chain hydrocarbons through the Fischer-Tropsch mechanism [7]. For example, MgAl-based hydrotalcites, when promoted with potassium (K), exhibit enhanced CO_2 adsorption and desorption activity as described in the

work of [8]. The presence of potassium (K) enhances the CO_2 sorption process by promoting the formation of surface-active sites, such as potassium carbonate (K_2CO_3), which react with CO_2 to form stable bicarbonate or carbonate species. Potassium also increases the basicity of the material, improving its affinity for acidic CO_2 molecules and facilitating efficient adsorption and desorption cycles. This contributes to higher cyclic sorption capacities and faster kinetics. In another study, Mg-Al hydrotalcites were used as precursors for mixed oxides supporting Ba/Co catalysts in ammonia synthesis, demonstrating excellent suitability as supports. The catalysts exhibited consistent properties and activity across Mg/Al ratios (2-5), highlighting their reliability and uniform performance [9]. In addition to Fe and Co, other metals such as ruthenium (Ru) have been explored in hydrotalcite-derived catalysts for CO_2 hydrogenation. Ru-containing Mg-Al hydrotalcite-derived catalysts have shown promise for CO_2 hydrogenation due to their strong interaction with the basic MgAlOx matrix and highly dispersed Ru nanoparticles. However, their performance favored CO production over CH_4, highlighting the need for further optimization of Ru particle size and catalytic properties to enhance CH_4 selectivity in CO_2 hydrogenation processes [10].

In conclusion, the versatility and tunability of hydrotalcites make them a valid candidate in the development of advanced catalysts for CO_2 hydrogenation. Their ability to integrate multiple functionalities within a single material highlights their potential to address the dual challenges of environmental sustainability and energy efficiency in catalysis.

3.2.1. Hydrotalcite synthesis:

The catalysts treated in this section are: $Mg_{0.60}Fe_{0.34}Cu_{0.06}$ (Fe30), $Mg_{0.55}Fe_{0.40}Cu_{0.05}$ (Fe40), $Mg_{0.32}Co_{0.33}Fe_{0.30}Cu_{0.05}$ (Co33), $Mg_{0.24}Co_{0.42}Fe_{0.29}Cu_{0.05}$ (Co45), $Zn_{0.60}Fe_{0.35}Cu_{0.05}$ (FeZn).

The synthesis of this class of materials is typically carried out using traditional methods such as co-precipitation and impregnation. These methods are favored for their simplicity and cost-effectiveness, making them suitable for large-scale production. However, they often result in catalysts with uneven metal dispersion, limited control over particle size and porosity, and lower reproducibility, which can affect catalytic performance.

3.2.1.1. Co-precipitation:

This method involves the simultaneous precipitation of metal hydroxides from an aqueous solution containing the desired metal salts. An alkaline precipitating agent, such as sodium hydroxide (NaOH) or ammonium hydroxide (NH_4OH), is added to adjust the pH, typically between 9 and 11, facilitating the formation of the hydrotalcite structure. The resulting precipitate is then aged, filtered, washed, dried, and calcined to obtain the final product. While co-precipitation offers decent structural homogeneity, it provides limited control over particle size and porosity. Factors such as the rate of addition of the precipitating agent, solution pH, temperature, and aging time significantly affect the final properties of the hydrotalcites. For instance, rapid precipitation can lead to agglomeration and uneven particle dispersion, whereas prolonged aging improves crystallinity but may reduce surface area [11].

3.2.1.2. Impregnation:

In this method, metal precursors are deposited onto pre-formed supports. For hydrotalcites, impregnation is often used to introduce additional active phases or promoters onto pre-synthesized hydrotalcite structures or their calcined mixed oxides. The process involves soaking the support in a solution of the metal precursor, followed by drying and calcination to integrate the metal into the hydrotalcite matrix. Impregnation is straightforward and cost-effective but often results in uneven metal dispersion, as the precursor can agglomerate on the support surface, leading to reduced catalytic efficiency. [12]

While these traditional methods are widely used, their limitations in controlling the structural properties of hydrotalcites and sustainability concerns have led researchers to explore alternative synthesis techniques to achieve both better control over structural properties (particle size, porosity, and metal dispersion) and eco-friendly synthetic pathways. Therefore, the following discussion is related to the use of two sustainable synthetic pathways performed in this thesis project.

3.2.2. Ultrasound-assisted synthesis (US):

Ultrasonic-assisted synthesis has emerged as a transformative technique in the preparation of nanostructured materials [13]. This method utilizes high-intensity ultrasound to create localized extreme conditions within a liquid medium, a phenomenon known as acoustic cavitation. These conditions characterized by temperatures reaching up to 5000 K, pressures around 150 MPa, and rapid cooling rates of approximately 109 K/s facilitate accelerated chemical reactions, improve precursor dispersion, and lead to the formation of materials with exceptional uniformity and activity.

Figure 3.5. Set-up used for the US synthesis.

The central mechanism driving ultrasonic synthesis is acoustic cavitation, which involves the formation, growth, and subsequent implosive collapse of microscopic bubbles within the liquid (Fig.3.6). This collapse generates transient hot spots and high-energy microjets, creating an environment conducive to the nucleation of nanoparticles. Rapid energy release enhances material properties in several ways, including the production of smaller, uniformly distributed particles, improved crystallinity, and a high degree of dispersion for active metals on support materials.

These features are critical for catalytic applications, where maximizing surface area and ensuring accessibility to active sites are paramount. [14].

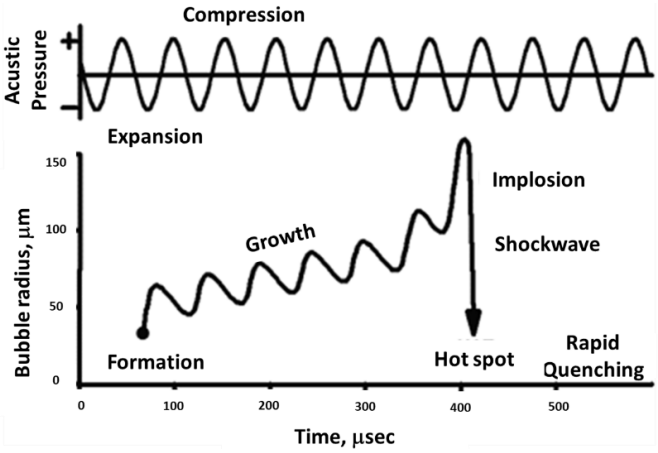

Figure 3.6. Illustration of the acoustic cavitation process induced by ultrasound, showing the cyclical expansion and compression of a cavitation bubble over time

One of the most significant benefits of ultrasonic-assisted synthesis is its ability to produce catalysts with superior textural and compositional properties. Studies have demonstrated that hydrotalcites synthesized using ultrasound typically exhibit smaller particle sizes, enhanced surface areas, and larger pore volumes compared to those prepared by conventional methods. These structural improvements directly impact the catalysts' performance by facilitating the adsorption and activation of CO_2 molecules. The enhanced dispersion of active sites further contributes to higher conversion rates and improved selectivity toward desired products, such as long-chain hydrocarbons or alcohols. Additionally, the structural robustness provided by ultrasonic synthesis minimizes the risks of deactivation due to sintering or carbon deposition, particularly during high-temperature reactions.[15]

The synthesis of hydrotalcites using ultrasonic-assisted methods typically involves a sequence of carefully controlled steps, in the following paragraph the synthesis of sample Fe30 (Mg0.60Fe0.34Cu) is described in detail. The same procedure is employed for the synthesis of the other samples mentioned in chapter *1.9 Aim of the Work and Novelty*, the summary and the main characteristics of the precursors used both for ultrasonic assisted co-precipitation and ball-milled preparation are reported in the Table 3.1.

Precursors	Features
$Mg(NO_3)_2 \cdot 6H_2O$	Company: Sigma Aldrich Purity: ≥ 99% Molecular weight: 256,41 g/mol
$Cu(NO_3)_2 \cdot 2.5H_2O$	Company: Sigma Aldrich Purity: ≥ 98% Molecular weight: 232,59 g/mol
$Fe(NO_3)_3 \cdot 9H_2O$	Company: Sigma Aldrich Purity: ≥ 98% Molecular weight: 403,95 g/mol
$Co(NO_3)_2 \cdot 6H_2O$	Company: Sigma Aldrich Purity: ≥ 99% Molecular weight: 291,03 g/mol
$Zn(NO_3)_2 \cdot 6H_2O$	Company: Sigma Aldrich Purity: ≥ 98% Molecular weight: 297,49 g/mol
NaOH	Company: Sigma Aldrich Purity: ≥ 99 % Molecular weight: 40,08 g/mol
Na_2CO_3	Company: Sigma Aldrich Purity: ≥ 99% Molecular weight: 105,99 g/mol
KNO_3	Company: Sigma Aldrich Purity: ≥ 99% Molecular weight: 101,10 g/mol
Deionized water was used as the solvent for the preparation of all precursor solutions	

Table 3.1. General table with all the precursors needed for the sysnthesis of the above mentioned catalaysts.

The synthesis of the sonochemical samples is a quick process which has a total duration that is usually shorter than one day. All the preparation steps are reported hereinafter:

1M solution of nitrate salts, such as magnesium, iron, and copper, is prepared in stoichiometric proportions with distilled water (molar ratio Mg/Fe/Cu=13.2/6/1). To this solution, a 50 ml mixture of sodium hydroxide (1M) and sodium bicarbonate (2M) is added dropwise under continuous ultrasonic irradiation, which is maintained at a frequency of 20 kHz for 3.5 min. The process is performed at a controlled temperature of approximately 5°C to prevent unwanted side reactions. The cavitation induced by ultrasonic waves promotes rapid nucleation and uniform precipitation of metal hydroxides evidenced by the precipitation of a yellowish-brown precipitate. The resulting solid is diluted with 100 ml of distilled water, recovered by centrifugation and washed repeatedly with deionized water. The precipitate is then dried at 60°C in oven under atmospheric ambient. The final composition, determined by ICP-MS, of MgCuFe-US is: $[Mg_{0.59}Cu_{0.007}Fe_{0.34}(OH)_2](CO_3)_{0.17}0.5H_2O$.

As a final step, the dried catalyst samples were subjected to potassium promotion. The samples were soaked in a KNO3 solution (K = 0.5wt%) at 80°C for 2 hours. This step was designed to enhance the catalyst's electronic properties and promote its activity and selectivity during catalytic reactions.

Ultrasonic-assisted synthesis has many advantages, but there are challenges as well. The need for specialized ultrasonic equipment is a drawback for its widespread implementation, especially for large-scale industrial end users. Moreover, the localized high-temperature high-pressure conditions created at cavitation sites are needed for particle formation but are precisely time-sensitive and have to be controlled to prevent undesired side reactions or degradation of the precursors.

3.2.2.1. Stoichiometric calculation for US synthesized catalysts

For the preparation of Mg0.60Fe0.34Cu and the other samples the calculation is the following: the quantity of each precursor was calculated based on the stoichiometric coefficients of the metals in the target LDH composition, using the molar mass of the LDH formula unit (93.72 g/mol) as a reference. The general formula applied for the mentioned example is the following [16]:

$$\left[\mathrm{Mg_xCu_zFe_y(OH)_2}\right]^{y+}(\mathrm{CO_3})_{y/2} \cdot 0.5\,\mathrm{H_2}O \qquad (2)$$

In the specific case the target composition is:

$$[\mathrm{Mg_{0.65}Cu_{0.05}Fe_{0.30}(OH)_2}]^{0.30+}(\mathrm{CO_3})_{0.15} \cdot 0.5\,\mathrm{H_2}O$$

Since a 1M solution of nitrate salts is needed, starting from the desired composition of:

$$[Mg^{2+}] = 0.65 \text{ mol}$$

$$[Cu^{2+}] = 0.05 \text{ mol}$$

$$[Fe^{3+}] = 0.30 \text{ mol}$$

In order to produce 4g of catalysts, the required mass of each nitrate salt was calculated using the following expression:

$$g_{\text{precursor}} = \left(\frac{\text{mass} \times \text{stoichiometric coefficient}}{\text{molar mass of LDH unit}}\right) \times \text{molar mass of precursor} \qquad (3)$$

where:

- The mass is the total mass of LDH to synthesize (e.g., 4 g);
- The metal stoichiometry is taken from the desired composition.
- The molar mass of the LDH formula unit is calculated from the general stoichiometric expression (Eq. 2);
- The molar mass of the precursor corresponds to the hydrated nitrate salt used during synthesis.

Therefore:

$$g_{\mathrm{Mg(NO_3)_2 \cdot 6H_2O}} = \left(\frac{4\,\mathrm{g} \times 0.65}{93.72\,\mathrm{g/mol}}\right) x\ MM\ (\mathrm{Mg(NO_3)_2 \cdot 6H_2O}) = 0.02774\,\mathrm{mol} \times 256.41\,\mathrm{g/mol} = 7.11\,\mathrm{g}$$

$$g_{\mathrm{Fe(NO_3)_3 \cdot 9H_2O}} = \left(\frac{4\,\mathrm{g} \times 0.30}{93.72\,\mathrm{g/mol}}\right) x\ MM\ (\mathrm{Fe(NO_3)_3 \cdot 9H_2O}) = 0.01280\,\mathrm{mol} \times 403.95\,\mathrm{g/mol} = 5.17\,\mathrm{g}$$

$$g_{Cu(NO_3)_2\cdot 2.5H_2O} = \left(\frac{4\,\text{g} \times 0.05}{93.72\,\text{g/mol}}\right) x\ MM\ (Cu(NO_3)_2 \cdot 2.5H_2O) = 0.00213\,\text{mol} \times 232.59\,\text{g/mol}$$
$$= 0.50\,\text{g}$$

The sum of moles divided by the total molarity, which is 1, yields the volume of water needed for the solution preparation:

$$V_{\text{solution}}\,[\text{mL}] = \left(n_{Mg^{2+}} + n_{Fe^{3+}} + n_{Cu^{2+}}\right) \times 1000 \quad (4)$$

Therefore:

$$V_{\text{solution}}\,[\text{mL}] = (0.02774 + 0.01280 + 0.00213)\text{mol} \times 1000\ mmol/mol \cong 50\,\text{mmol} = 50\,\text{ml}$$

A crucial step during ultrasonic co-precipitation is the controlled addition of hydroxide ions and carbonate anions to trigger both metal precipitation and interlayer anion incorporation.

In this synthesis, NaOH provides a direct and immediate source of OH^- to initiate the precipitation of metal hydroxides, while Na_2CO_3 contributes both carbonate ions (CO_3^{2-}) for intercalation and additional OH^- through its weak base character.

The total hydroxide requirement is determined by the stoichiometry of the metal cations, according to the following reaction scheme:

$$Mg^{2+} + 2OH^- \rightarrow Mg(OH)_2\downarrow \quad (5)$$

$$Fe^{3+} + 3OH^- \rightarrow Fe(OH)_3\downarrow \quad (6)$$

$$Cu^{2+} + 2OH^- \rightarrow Cu(OH)_2\downarrow \quad (7)$$

Accordingly, the total OH^- requirement can be determined using the following expression:

$$n_{NaOH} = 2 \cdot \left(n_{Mg^{2+}} + n_{Cu^{2+}}\right) + 3 \cdot n_{Fe^{3+}} \quad (8)$$

In this example:

$$n_{NaOH} = 2 \cdot (0.02774 + 0.00213) + 3 \cdot 0.01280 = 0.09734\,\text{mol}$$

The remaining OH^- requirement not covered by NaOH is met by the basic character of Na_2CO_3, while simultaneously ensuring a sufficient supply of CO_3^{2-} for intercalation into the LDH structure.

As last step potassium was added as a promoter in the form of potassium nitrate (KNO_3) at 0.5 wt% with respect to the total catalyst mass.

$$m_K = 4\,\text{g} \times 0.005 = 0.02\,\text{g}$$

$$n_K = \frac{m_K}{M_K} = \frac{0.02\,\text{g}}{39.098\,\text{g/mol}} = 5.11 \times 10^{-4}\,\text{mol}$$

$$m_{KNO_3} = n_K \times M_{KNO_3} = 5.11 \times 10^{-4}\,\text{mol} \times 101.103\,\text{g/mol} = 0.052\,\text{g}$$

These calculations define the exact reagent quantities necessary to achieve the target LDH structure and composition under ultrasonic co-precipitation conditions.

3.2.3. Ball milling synthesis (BM):

Ball milling has become a widely adopted method for the synthesis of nanostructured materials, offering unique advantages in terms of simplicity, scalability, and material property control. The technique involves mechanical grinding and blending of materials inside a rotating cylindrical shell, using balls as the grinding medium. The mechanical energy generated during milling facilitates the fracture, deformation, and welding of particles, producing highly homogeneous materials with tailored compositions and structures [17]. This method is particularly suited for catalyst preparation, where maximizing surface area and ensuring the dispersion of active sites are critical. Ball milling allows for a high degree of control over particle size and morphology, which are essential for catalytic applications. The impact and attrition mechanisms inherent to ball milling make it effective for breaking down bulk materials into nanoscale particles, significantly enhancing their reactive properties [18].

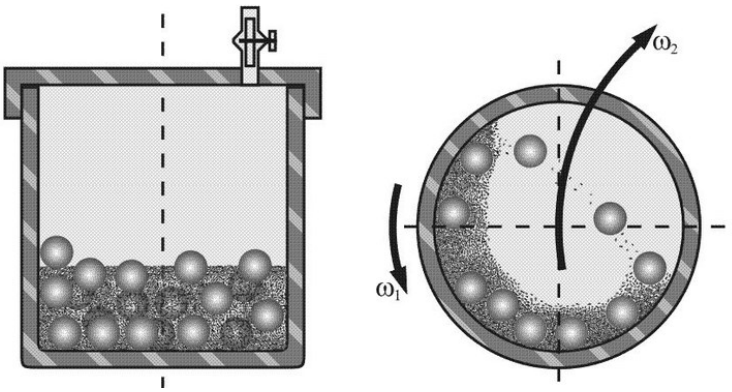

Table 3.2. Schematic representation of a ball mill, including labeled components such as the grinding balls, cylinder, and rotation mechanism.

A typical ball mill comprises a hollow cylindrical shell that rotates about its axis. The shell is partially filled with grinding balls made of materials such as stainless steel, zirconia, or tungsten carbide, depending on the hardness and chemical compatibility with the material being processed. As the mill rotates, the balls are lifted along the inner wall and then cascade downward, generating localized high-energy impacts and shearing forces [19,20].

The mechanical processes involved in ball milling include:

- Impact and Fracture: High-energy collisions between the balls and the material reduce particle size and create fresh surfaces.
- Attrition: Shearing forces refine particle morphology, ensuring uniformity in size and shape.
- Cold Welding: Repeated deformation and adhesion lead to the formation of nanostructures with enhanced surface properties [21].

The milling process parameters, such as rotation speed, ball-to-powder ratio, and milling time, play a critical role in determining the properties of the resulting material. Higher rotation speeds and smaller ball sizes typically yield finer particles and increased surface areas, though excessive milling can lead to material contamination or loss of crystalline structure.

Ball milling offers numerous benefits for preparing nanostructured catalysts, particularly for hydrotalcite-based systems. One significant advantage is its ability to produce materials with

homogeneous composition and high dispersion of active sites. This uniformity enhances the catalytic activity and selectivity, as each active site is fully accessible to reactants [22]. Additionally, the process improves textural properties such as surface area and porosity. The mechanical forces exerted during milling create a porous structure, which facilitates gas diffusion and increases the availability of active sites for CO_2 adsorption and hydrogenation. The technique also offers a high degree of versatility, accommodating a wide range of materials, including oxides, carbides, and nitrides, for various catalytic applications [23]. Furthermore, the cost of installation and grinding medium is low; the capacity and fineness can be adjusted by adjusting the diameter of the ball; it is suitable for both batch and continuous operation. This makes the ball milling system a suitable candidate for the preparation of catalyst on an industrial scale. Despite these advantages, it does have limitations. The mechanical energy imparted during milling can introduce impurities from the grinding media or lead to local overheating, which may hinder material properties. Prolonged milling times can also cause particle agglomeration or amorphization, necessitating careful optimization of process parameters [24].

In the context of the work, as mentioned before in the section related to the ultrasonic assisted precipitation synthesis, the preparation of one catalyst, namely Fe30 (Mg0.60Fe0.34Cu) is addressed in detail in the following paragraph and from now on the label given to the synthetized catalyst will have a suffix indicating the type of synthesis performed either US that stands for Ultrasound or BM for Ball-Milling.

The synthesis of Fe30-BM involved mixing the metal salts with sodium hydroxide (NaOH) pellets in stoichiometric proportions. Specifically, for the preparation of 1 g of catalyst, 1.96 g of magnesium nitrate hexahydrate ($Mg(NO_3)_2 \cdot 6H_2O$), 0.14 g of copper nitrate trihydrate ($Cu(NO_3)_2 \cdot 3H_2O$), 1.34 g of iron nitrate nonahydrate ($Fe(NO_3)_3 \cdot 9H_2O$), and 0.888 g of NaOH (corresponding to a molar ratio of Mg/NaOH = 3:1 and Mg/Fe/Cu = 13.2:6:1) were used. The reagents were milled in a planetary ball mill (Retsch MM200 swing mill) with a capacity of 10 mL. The milling process was conducted at a frequency of 30 Hz for 30 minutes using zirconia balls with a diameter of 10 mm. The mechanical energy imparted during milling promoted the thorough mixing and interaction of the precursor materials, resulting in the formation of the hydrotalcite structure. The solid product obtained after milling was transferred to a Teflon bottle containing 50 mL of distilled water. This suspension was subjected to an aging process in an oven at 80°C for 3 days to enhance the crystallinity and stability of the resulting material. The aged solid was then recovered by centrifugation and washed three times with deionized water to remove residual impurities. The purified product was subsequently dried in an oven at 60°C to yield the final catalyst.

Characterization of the Fe30-BM catalyst by inductively coupled plasma optical emission spectrometry (ICP-MS) revealed the composition to be $[Mg_{0.62}Cu_{0.006}Fe_{0.32}(OH)_2](CO_3)_{0.16}$.

This composition aligns well with the intended stoichiometry, demonstrating the reliability of the synthesis method. The final promotion with K through wet impregnation is the same as reported in the ultrasound assisted synthesis.

3.2.3.1. Stoichiometric calculation for BM synthesized catalysts

The general expression used for the synthesis of ultrasound (US) catalysts also applies to those prepared via ball milling (BM), with some important exceptions.

Unlike the ultrasound-assisted synthesis, the ball milling route does not involve an aqueous medium during the initial mixing phase. As a consequence, carbonate anions (CO_3^{2-}) are not added directly and Na_2CO_3 is omitted from the precursor formulation. Instead, NaOH is introduced as a solid base, and its amount is not determined based on the full theoretical OH^- demand but rather follows an empirical molar ratio relative to Mg^{2+}.

Specifically:

$$\text{mmol NaOH} : \text{mmol } Mg^{2+} = 1:3 \quad (9)$$

Although the methodologies differ in terms of base and anion incorporation, the strategy for potassium promotion remained unchanged.

In both ultrasound and ball milling syntheses, K was included at 0.5 wt% of the final catalyst mass to promote catalytic performance under comparable conditions.

References Chapter 3

[1] Abelló S, Montané D. Exploring Iron-based Multifunctional Catalysts for Fischer–Tropsch Synthesis: A Review. ChemSusChem 2011;4:1538–56. https://doi.org/10.1002/cssc.201100189.

[2] Kamath G, Badoga S, Dalai AK. Synthesis and Application of Metallosilicate Supports for Cobalt-Based Fischer–Tropsch Synthesis Catalysts. Energy Fuels 2019;33:551–60. https://doi.org/10.1021/acs.energyfuels.8b03209.

[3] Cheng K, Virginie M, Ordomsky VV, Cordier C, Chernavskii PA, Ivantsov MI, et al. Pore size effects in high-temperature Fischer–Tropsch synthesis over supported iron catalysts. Journal of Catalysis 2015;328:139–50. https://doi.org/10.1016/j.jcat.2014.12.007.

[4] Di Fronzo A, Pirola C, Comazzi A, Galli F, Bianchi CL, Di Michele A, et al. Co-based hydrotalcites as new catalysts for the Fischer–Tropsch synthesis process. Fuel 2014;119:62–9. https://doi.org/10.1016/j.fuel.2013.11.014.

[5] Gholami Z, Tišler Z, Velvarská R, Kocík J. CoMn Catalysts Derived from Hydrotalcite-Like Precursors for Direct Conversion of Syngas to Fuel Range Hydrocarbons. Catalysts 2020;10:813. https://doi.org/10.3390/catal10080813.

[6] Benito P, Fornasari G, Basile F, Tabanelli T, Lucarelli C, Fasolini A, et al. The several hydrotalcites investigated as precursors of catalysts by Angelo Vaccari. Catalysis Today 2024;439:114791. https://doi.org/10.1016/j.cattod.2024.114791.

[7] Ren H, Yang H, Xin J, Wu C, Wang H, Zhang J, et al. Direct carbon dioxide hydrogenation to long-chain α-olefins over FeMnK catalysts. Applied Catalysis B: Environment and Energy 2024;358:124440. https://doi.org/10.1016/j.apcatb.2024.124440.

[8] Xin K, Boon J, Van Dijk HAJ, Van Sint Annaland M. Stability of potassium-promoted hydrotalcites for CO_2 capture over numerous repetitive adsorption and desorption cycles. Front Chem Eng 2024;6:1272152. https://doi.org/10.3389/fceng.2024.1272152.

[9] Zybert M, Ronduda H, Dziewulska A, Sobczak K, Ostrowski A, Patkowski W, et al. Influence of the Support Composition on the Activity of Cobalt Catalysts Supported on Hydrotalcite-Derived Mg-Al Mixed Oxides in Ammonia Synthesis. Chemistry 2022;4:480–93. https://doi.org/10.3390/chemistry4020035.

[10] Misol A, Giarnieri I, Ospitali F, Ballarini A, Jiménez-Jiménez J, Rodríguez-Castellón E, et al. CO_2 hydrogenation over Ru hydrotalcite-derived catalysts. Catalysis Today 2024;425:114362. https://doi.org/10.1016/j.cattod.2023.114362.

[11] Sepuluh Nopember Institute of Technology, Kurnia Julianti N, Kusuma Wardani T, Sepuluh Nopember Institute of Technology, Gunardi I, Sepuluh Nopember Institute of Technology, et al. Effect of Calcination at Synthesis of Mg-Al Hydrotalcite Using co-Precipitation Method. J Pure App Chem Res 2017;6:7–13. https://doi.org/10.21776/ub.jpacr.2017.006.01.280.

[12] Ghashghaee M, Shirvani S, Farzaneh V, Sadjadi S. Hydrotalcite-impregnated copper and chromium-doped copper as novel and efficient catalysts for vapor-phase hydrogenation of furfural: effect of clay pretreatment. Braz J Chem Eng 2018;35:669–78. https://doi.org/10.1590/0104-6632.20180352s20160703.

[13] Comazzi A, Pirola C, Longhi M, Bianchi CLM, Suslick KS. Fe-based heterogeneous catalysts for the Fischer-Tropsch reaction: Sonochemical synthesis and bench-scale experimental tests. Ultrasonics Sonochemistry 2017;34:774–80. https://doi.org/10.1016/j.ultsonch.2016.07.012.

[14] Suslick KS, Didenko Y, Fang MM, Hyeon T, Kolbeck KJ, McNamara WB, et al. Acoustic cavitation and its chemical consequences. Philosophical Transactions of the Royal Society of London Series A: Mathematical, Physical and Engineering Sciences 1999;357:335–53. https://doi.org/10.1098/rsta.1999.0330.

[15] Obeid M, Poupin C, Labaki M, Gupta S, Aouad S, Delattre F, et al. Influence of the ultrasound power density in the ultrasound-assisted synthesis of Ni-based LDH catalysts for CO_2 methanation. Journal of Environmental Chemical Engineering 2024;12:114059. https://doi.org/10.1016/j.jece.2024.114059.

[16] Johnson CA, Glasser FP. Hydrotalcite-Like Minerals in the Environment: Synthesis, Characterization and Thermodynamic Stability. Clays and Clay Miner 2003;51:1–8. https://doi.org/10.1346/CCMN.2003.510101.

[17] Suryanarayana C. Mechanical alloying and milling n.d.

[18] Benjamin JS, Volin TE. The mechanism of mechanical alloying. Metall Trans 1974; 5:1929–34. https://doi.org/10.1007/BF02644161.

[19] Sorrentino A, Gorrasi G, Tortora M, Vittoria V, Costantino U, Marmottini F, et al. Incorporation of Mg–Al hydrotalcite into a biodegradable Poly(ε-caprolactone) by high energy ball milling. Polymer 2005;46:1601–8. https://doi.org/10.1016/j.polymer.2004.12.018.

[20] H. K. D. H. Bhadeshia: Recrystallisation of Practical Mechanically Alloyed Iron–Base and and Nickel–Base Superalloys. Materials Science and Engineering 1997.

[21] Kumar M, Xiong X, Wan Z, Sun Y, Tsang DCW, Gupta J, et al. Ball milling as a mechanochemical technology for fabrication of novel biochar nanomaterials. Bioresource Technology 2020; 312:123613. https://doi.org/10.1016/j.biortech.2020.123613.

[22] Behling R, Valange S, Chatel G. Heterogeneous catalytic oxidation for lignin valorization into valuable chemicals: what results? What limitations? What trends? Green Chem 2016; 18:1839–54. https://doi.org/10.1039/C5GC03061G.

[23] Joy J, Krishnamoorthy A, Tanna A, Kamathe V, Nagar R, Srinivasan S. Recent Developments on the Synthesis of Nanocomposite Materials via Ball Milling Approach for Energy Storage Applications. Applied Sciences 2022; 12:9312. https://doi.org/10.3390/app12189312.

[24] Jamkhande PG, Ghule NW, Bamer AH, Kalaskar MG. Metal nanoparticles synthesis: An overview on methods of preparation, advantages and disadvantages, and applications. Journal of Drug Delivery Science and Technology 2019; 53:101174. https://doi.org/10.1016/j.jddst.2019.101174.

4. CHARACTERIZATION

4.1. Analitical Techniques

4.1.1. BET

The specific surface area of each catalyst was assessed by nitrogen physisorption, a method that measures the amount of N_2 required to form an adsorbed monolayer on the sample. Knowing the cross-sectional area occupied by a single N_2 molecule, the total surface area (expressed in $m^2\ g^{-1}$) can be calculated. A small, non-reactive probe gas such as nitrogen is preferred so that it can access even the finest surface features without steric hindrance.

The calculation follows the Brunauer-Emmett-Teller (BET) model, which extends the Langmuir monolayer theory by assuming:

(i) physical adsorption in successive, infinite layers,

(ii) no lateral interactions between molecules in different layers, and

(iii) Langmuir behaviour within each individual layer.

Under these assumptions the multilayer adsorption isotherm is described by Eq. 1.

$$\frac{V}{Vm} = \frac{C \cdot \frac{P}{P^{\circ}}}{[1 - \frac{P}{P^{\circ}}] \cdot [1 + (C - 1) \cdot \frac{P}{P^{\circ}}]} \tag{1}$$

where V is the volume adsorbed at pressure P, P^0 the saturation pressure, and C the BET constant.

The constant C is related to the difference between the heat of adsorption of the first layer (q_1) and that of the higher layers (q^L) via Eq. 2.

$$C = e^{\frac{(q1 - qL)}{RT}} \tag{2}$$

For practical use, the BET expression is linearised over the relative-pressure window $0.05 \leq P/P^0 \leq 0.30$, yielding Eq. 3.

$$\frac{\frac{P}{P^{\circ}}}{V \cdot [1 - \frac{P}{P^{\circ}}]} = \frac{1}{C \cdot Vm} + \frac{(C - 1) \cdot \frac{P}{P^{\circ}}}{C \cdot Vm} \tag{3}$$

A plot of the left-hand term in Eq. 3 versus P/P^0 yields a straight line whose slope and intercept give the monolayer capacity V_m.

The specific surface area is finally obtained from Eq. 4.

$$S.A. = \frac{Vm \cdot Nav \cdot Amol}{Vmol} \tag{4}$$

where Nav is Avogadro's number, Amol the molecular cross-section of nitrogen (16.2 Å²), and V_{mol} the molar volume of an ideal gas at standard conditions (22.414 L mol^{-1}).

All measurements were conducted on a Micromeritics TriStar II 3020 analyser. Samples were outgassed under flowing N_2 at 200 °C for 1 h, then cooled to -196 °C for the adsorption run. Isotherms were processed with the instrument software (v 1.03); the linear BET fit was taken in the 0.05-0.30 relative-pressure range.

4.1.2. TEM

Transmission Electron Microscopy is employed to visualise nanometre-scale features by transmitting a high-energy electron beam through an electron-transparent specimen. Because the de Broglie wavelength of accelerated electrons (typically 0.002-0.004 nm at 100-200 kV) is orders of magnitude shorter than that of visible light, TEM routinely attains lattice-level resolution that is inaccessible to optical techniques. After emission from a thermionic (W filament) or field-emission gun, the electron beam is accelerated, condensed and focused by a sequence of electromagnetic lenses and apertures. The transmitted (and, where required, diffracted) electrons are then magnified to form an image on a fluorescent screen or a CCD/CMOS camera.

For supported metal/oxide catalysts TEM is indispensable: particles as small as 2-3 nm can be measured directly, allowing statistical analysis of size, morphology and spatial distribution across the support. In this work all TEM data were collected in collaboration with the University of Perugia. Fresh and spent powders were ultrasonically dispersed in ethanol; a single drop of the suspension was deposited on a copper grid coated with a Formvar film and dried in air at ambient temperature. Imaging was performed on a Philips 208 Transmission Electron Microscope.

4.1.3. SEM-EDS

Scanning Electron Microscopy generates surface images by rastering a focused electron probe across the specimen and collecting the resulting interaction signals. Because the beam is reflected, rather than transmitted, bulk specimens (pellets, powders, fracture surfaces) can be examined with minimal preparation. Three principal signals are exploited in this study:

- Secondary electrons (SE): low-energy electrons ejected from the top few nanometres of the surface, giving high-resolution topography with pronounced three-dimensional relief.
- Back-scattered electrons (BSE): elastically reflected primary electrons whose intensity scales roughly with atomic number, thus highlighting compositional contrast (heavier regions appear brighter).
- Characteristic X-rays (EDS): element-specific photons emitted as inner-shell vacancies are filled; mapping these photons yields quantitative surface-element distributions and local atomic ratios.

The spatial resolution attainable depends on accelerating voltage, spot size and beam-sample interactions; modern field-emission instruments routinely resolve features down to 2-3 nm, while conventional thermionic guns give 20-30 nm. Although this is coarser than the lattice-resolution achievable by TEM, SEM offers a much larger depth of field and intuitive, three-dimensional images that are invaluable for assessing agglomerate morphology, particle packing and macroporosity.

All SEM-EDS characterisation was performed in collaboration with the University of Perugia. Overview and high-magnification images were acquired on a LEO 1525 ZEISS, while high-resolution while Elemental composition and chemical mapping were determined using a Bruker Quantax EDS.

4.1.4. XRD

Powder X-ray diffraction is the primary, non-destructive method for identifying crystalline phases in solids. A monochromatic X-ray beam impinges on the specimen and is elastically scattered by the periodic array of lattice planes. Constructive interference occurs only at specific incident angles, generating a set of diffraction peaks whose positions are governed by Bragg's law:

$$2 \cdot d \cdot sin\theta = n \cdot \lambda \quad (5)$$

Where:

- d is the inter-planar spacing,
- θ is the Bragg angle,
- λ is the wavelength of the incident radiation,
- n is an integer order of reflection.

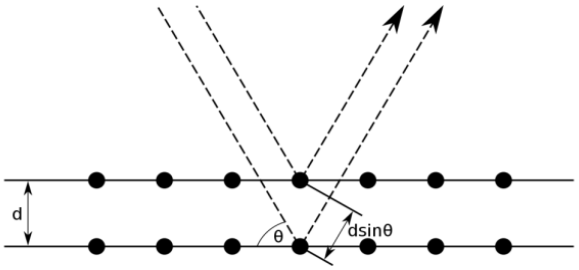

Figure 4.1. Graphical explanation of the Bragg law.

Each crystalline phase possesses a unique collection of *d*-spacings (and thus 2θ values) that acts as a fingerprint. By matching the measured pattern against reference databases (ICDD PDF-4+, Crystallography Open Database, etc.) the phases present can be identified and, where peak overlap permits, quantified by Rietveld refinement. Amorphous or nanocrystalline components appear as broad humps or contribute little to the diffracted intensity and are therefore reported as "XRD-amorphous".

Diffractograms were recorded on a Philips PW-1710 diffractometer equipped with a CuKα sealed tube (λ = 1.5406 Å), operating at 40 kV and 20 mA. Data were collected at room temperature over 2θ = 2-40° with a step size of 0.02° and a counting time of 1 s per step (equivalent to 1° min^{-1} scan rate). Silicon powder (NIST SRM 640d) was used to verify peak positions and instrument broadening. Peak assignments and refinements were performed with *HighScore Plus* v4.9.

4.1.5. XPS

XPS is a surface-analytical technique that exploits the photoelectric effect to probe the first ~5 nm of a material. When monochromatic X-rays irradiate the sample, photoelectrons are emitted only from atoms located within the escape depth of the surface. By measuring the kinetic energy (E_k) of those electrons, their binding energy (E_β) can be obtained through the energy conservation expression.

$$E_{binding} = E_{photon} - (E_{kinetic} + \emptyset) \quad (6)$$

where hv is the photon energy and φ the spectrometer work-function correction.

Each element exhibits characteristic binding energies for its core levels (e.g. Fe 2p, Co 2p, Zn 2p), while chemical-state shifts allow oxidation state and ligand environment to be inferred. In general, a higher oxidation state produces a positive shift of several eV relative to the metallic element.

Spectra were acquired on a Surface Science Instruments M-Probe using monochromated Al Kα radiation (hν=1486.6 eV). The spot size was adjusted between 200 μm and 750 μm; a pass energy of 25 eV provided an overall energy resolution of 0.74 eV. Binding-energy values are accurate to ±0.2 eV after calibration against the C 1s adventitious carbon peak at 284.8 eV. Survey scans (0-1100 eV) and high-resolution windows for Fe 2p, Co 2p, Zn 2p, Cu 2p, O 1s and C 1s were collected for all samples. Quantification employed sensitivity factors supplied with the instrument software (*CasaXPS* v2.3).

4.1.6. Temperature Programmed Methods

4.1.6.1. TPR

The Temperature Programmed Reductions were performed by a Microtrac BELCAT II catalyst analyser. The instrument allows to employ a wide variety of carriers and analytic gases to perform different characterizations. The sample is placed in a cylindric quartz reactor, coaxial to a quartz pipe and a thermocouple as reported in Fig. 4.2.

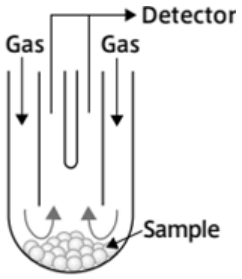

Figure 4.2. Schematic representation of a Temperature Programmed Reduction (TPR) setup

The gas flows on the surface of the sample and then is sent to the detector. A furnace allows a sharp control of the temperature. The analytical signal is given by a TCD. In addition to continuous gas feeding, the instrument is also equipped with a loop ($1cm^3$) that allows to send to the sample definite volumes of gas (pulse injection).

Table TPR conditions:

TPR	T	Ramp rate	Hold	Gas flow	
	°C	°C/min	min	Type	(ml/min)
Pretreatment	130	13	60	Ar	40
	40	-	5	Ar	40
Stabilization	40	-	30	Ar	40
Analysis	800	8	10	H_2	3.2
				Ar	36.8

Table 4.1. TPR conditions.

For the TPR analysis, argon was chosen as carrier gas instead of helium, since the thermal conductivity of the second is too similar to that of the hydrogen (analyte). The samples were

pretreated at 130°C with 40ml/min of Ar to remove any impurities that could be present. These conditions were kept for 60 min, then the temperature was decreased to 40°C and held for 30 min to let the TCD stabilize. The analysis was carried on by heating the sample at 800°C with a temperature ramp of 8°C/min by feeding 3,2 ml/min of hydrogen and 36,8ml/min of argon. The TCD measures the variation of the gas composition due to the hydrogen consumption by the reduction of the catalyst.

4.1.6.2. CO_2-TPD

The CO_2 Temperature Programmed Desorptions were performed with the same instrument described for TPR in the previous chapter. In this case helium was selected as carrier gas instead of argon. The sample was cleaned from any adsorbed impurities by feeding 30ml/min of He, at 110°C for 30 minutes. Then it was cooled to 40°C and pulses of CO_2 were sent until saturation. The sample was considered saturated when the TCD signal showed three consequential peaks of the same height. The last step of the pretreatment was the cleaning of the surface again with 30ml/min He at 40°C for 30 minutes. Finally, the proper TPD analysis was performed by heating the sample to 1000°C with a temperature ramp of 10°C/min by keeping the same He flux.

Table CO_2-TPD conditions:

CO_2-TPD	**T**	**Ramp rate**	**Hold**	**Gas flow**	
	°C	**°C/min**	**min**	**Type**	**(ml/min)**
Pre-treatment	110	10	30	He	30
	40	-	-	He	30
Saturation	40	-	Till saturation	CO_2	Pulse
Cleaning	40	-	30	He	30
Analyses	1000	10	1	He	30

Table 4.2. CO_2-TPD conditions.

4.1.6.3. H_2-TPD

The H_2-TPD was performed by employing Ar as carrier gas instead of helium. The sample was cleaned from any adsorbed impurities by feeding 30ml/min of Ar, at 150°C for 45 minutes. Then it was cooled to 40°C and pulses of H_2 were sent until saturation. As before, the sample was considered saturated when the TCD signal showed three consequential peaks of the same height. The last step of the pretreatment was the cleaning of the surface again with 30ml/min Ar at 40°C for 45 minutes. Finally, the proper TPD analysis was performed by heating the sample to 1000°C with a temperature ramp of 10°C/min by keeping the same Ar flux.

Table H_2-TPD conditions:

H_2-TPD	T	Ramp rate	Hold	Gas flow	
	°C	°C/min	min	Type	(ml/min)
Pre-treatment	150	10	45	Ar	30
	40	-	-	Ar	30
Saturation	40	-	Till saturation	H_2	Pulse
Cleaning	40	-	45	Ar	30
Analyses	1000	10	1	Ar	30

Table 4.3. H_2-TPD conditions.

4.1.7. ICP

ICP-MS provides bulk elemental quantification at sub-ppm levels and is the method of choice for verifying metal loadings after synthesis. The procedure involves three sequential stages:

1. Sample dissolution. Each catalyst (~20 mg) was digested in aqua regia (HNO_3 :HCl = 1 : 3 v/v) under reflux until a clear solution was obtained, then diluted to 50 mL with ultrapure water. Complete dissolution is essential so that every metal ion enters the plasma in molecularly dispersed form.

2. Aerosol generation and ionisation. The acidic solution is nebulised into an argon carrier stream, passed through a spray chamber to remove large droplets, and delivered to a radio-frequency plasma (≈ 6000-8000 K). At this temperature the aerosol is desolvated, atoms are excited and then ionised, typically to M^+.

3. Mass separation and detection. The ions are extracted through a series of cones into a quadrupole mass analyser, where they are filtered according to their mass-to-charge ratio (m/z). Ion counts are converted to concentration via external calibration; isotopic interferences are corrected using collision/reaction cell (DRC) chemistry when needed.

With a detection limit in the low-ppt range, the technique readily confirms target metal loadings and uncovers trace contaminants. In this study analyses were performed on a PerkinElmer SCIEX ELAN DRCe (collision gas: 7% H_2 in Ar, flow 0.7 mL min^{-1}) operated in standard mode for transition metals and in DRC mode for Fe/Zn to suppress ArO^+ overlaps. Reported concentrations are accurate to ±2 % relative, based on replicate digests and NIST SRM 2711a (Montana Soil) as control.

4.2. Metallosilicates Characterization

4.2.1. Unpromoted Metallosilicates

4.2.1.1. Surface area

The BET analysis provides critical insights into the textural properties of the synthesized iron-based metallosilicate catalysts, including surface area, pore size distribution, and cumulative pore volume. The results for both fresh and spent catalysts reveal differences between the various

supports (Ti, Ce, Zr, and V), underscoring the impact of support material on the physical and catalytic properties.

The BET surface areas of the fresh catalysts are summarized in Table 4.4, with clear differences in textural properties among the different supports. Fe/Zr-SiO_2 exhibited the highest surface area (335 m^2/g), followed by Fe/Ti-SiO_2 (228 m^2/g). In contrast, Fe/Ce-SiO_2 and Fe/V-SiO_2 showed significantly lower surface areas, at 54 m^2/g and 5.7 m^2/g, respectively. The low surface area of Fe/V-SiO_2 can be attributed to the large pore diameter (212 Å) and potential formation of bulk vanadium oxide in form of poly and mono-vanadate crystals, which limit pore availability.

Catalyst	BET Surface Area (m^2/g)	BJH adsorption average pore diameter (Å)	BJH Adsorption cumulative volume of pores (cm^3/g)
Fe_{10}/Ti-SiO_2	228	61	0,38
Fe_{10}/Ce-SiO_2	54	75	0,10
Fe_{10}/Zr-SiO_2	335	36	0,27
Fe_{10}/V-SiO_2	5,7	212	0,029

Table 4.4. BET surface area, pore diameter, and pore volume of fresh catalysts.

The sol-gel synthesis method used for these catalysts has a great influence in determining their structural properties. The formation of a cross-linked framework between support, active phase, transition metals and oxides determine the morphology, surface area, and porosity. When the framework of the metal oxide and silica is formed, crystals might precipitate as bulk metal oxide particles rather than uniform two-dimensional domains, particularly for Fe/V-SiO_2 and Fe/Ce-SiO_2. This explains the reduced surface area and pore volume observed for these samples.

Catalyst	BET Surface Area (m^2/g)	BJH adsorption average pore diameter (Å)	BJH Adsorption cumulative volume of pores (cm^3/g)
Fe_{10}/Ti-SiO_2	172,5	63	0,30
Fe_{10}/Ce-SiO_2	32,8	110	0,11
Fe_{10}/Zr-SiO_2	286,8	38	0,29
Fe_{10}/V-SiO_2	9,3	156	0,03

Table 4.5. Changes in Surface Area After Fischer-Tropsch Testing.

BET analysis conducted after Fischer-Tropsch (FT) testing (Table 4.5) revealed substantial changes in surface area and porosity. Ce, Ti, and Zr-based catalysts experienced reductions in surface area, with Fe/Ti-SiO_2 decreasing to 172.5 m^2/g and Fe/Ce-SiO_2 to 32.8 m^2/g. On the other hand, Fe/V-SiO_2 showed a slight increase in surface area, from 5.7 m^2/g to 9.3 m^2/g, despite remaining relatively low. The increase in surface area for Fe/V-SiO_2 can be attributed to the unclogging of pores and the elimination of bulk agglomerated vanadium oxide crystals during FT testing. In contrast, the reduction in surface area for other samples may result from sintering or coke deposition, as indicated by changes in pore diameter and volume. For instance, the average

pore diameter of Fe/Ce-SiO_2 increased from 75 Å to 110 Å, suggesting potential pore enlargement due to structural changes under high-temperature reaction conditions. The pore size distribution, shown in Table 4.6, highlights the mesoporous nature of Ce, Ti, and Zr-based catalysts, with significant contributions from pores in the 2-10 nm range. Fe/Zr-SiO_2 displayed the highest proportion of mesopores [1], with 90.7% of its pore volume in the 2-5 nm range. Conversely, Fe/V-SiO_2 exhibited a predominantly macroporous structure, with larger pores contributing to its low surface area. The adsorption isotherms (Figures 4.3 and 4.4) further validate the mesoporous structure of these catalysts, characterized by type IV isotherms with H1 hysteresis loops for Ce, Ti, and Zr-based samples. In contrast, Fe/V-SiO_2 displayed type II isotherms, indicative of macroporosity and low pore connectivity.

Pore diameter range (nm)	Fe/Ce-SiO_2	Fe/V-SiO_2	Fe/Zr-SiO_2	Fe/Ti-SiO_2
d<2	0	0	0	0
2<d<5	51,3	58,5	90,7	67,9
5<d<10	28,0	12,2	8,3	22,6
10<d<20	11,1	10,1	0,7	6,3
20<d<50	5,6	11,3	0,2	2,3
d>50	4,0	7,9	0,1	0,9

Table 4.6. Pore size distribution of spent catalysts.

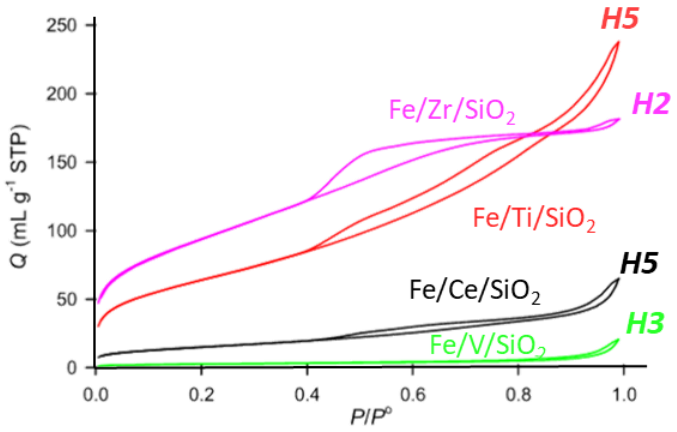

Figure 4.3. BET adsorption isotherms before catalytic test.

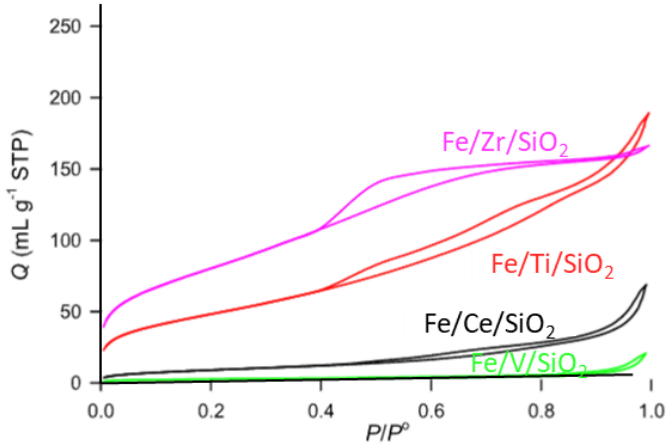

Figure 4.4. BET adsorption isotherms after catalytic test.

The structural differences observed in BET analysis are expected to have significant implications for catalytic performance. The high surface area and mesoporosity of Fe/Zr-SiO_2 and Fe/Ti-SiO_2 make them suitable for high CO conversion and selectivity toward long-chain hydrocarbons. On the other hand, the macroporous structure of Fe/V-SiO_2 limits its activity, highlighting the importance of optimizing support materials for effective catalyst design.

4.2.1.2. Morphology SEM-EDS

SEM-EDS analysis provide insights into the morphological and compositional characteristics of the synthesized catalysts such as structural integrity, dispersion of the metallic phases, and potential modifications in elemental composition occurring before and after catalytic testing.

The SEM micrographs of the fresh catalysts revealed distinct morphological differences among the Fe-based metallosilicates. Fe/Zr-SiO_2 exhibited a well-dispersed and homogeneously distributed morphology, suggesting an effective integration of zirconium into the silica framework. This structure is in agreement with the previously observed high BET surface area, indicating that the sol-gel synthesis method successfully generated a mesoporous support. In contrast, Fe/Ti-SiO_2 displayed slightly more irregular aggregates, which could be attributed to the partial crystallization of TiO_2 species, possibly forming anatase or rutile domains. Fe/Ce-SiO_2, characterized by a lower surface area, showed large particle clusters in the SEM images, which could be associated with the formation of dense cerium oxide domains. This tendency of aggregation during synthesis can contribute to the lower accessibility of active sites. Lastly, Fe/V-SiO_2 displayed highly irregular shapes with a macroporous structure, likely due to the formation of bulk vanadium oxide. The presence of such large agglomerates is confirming the significantly lower BET surface area and pore volume observed in this sample. Upon examining the spent catalysts after Fischer-Tropsch testing there aren't any major structural or morphological transformations, indicating that the metallosilicate framework provided good thermal and mechanical stability.

However, some minor modifications were evident in some samples. Fe/Zr-SiO_2 and Fe/Ti-SiO_2 exhibited minor agglomeration of iron species, possibly due to metal migration under reaction conditions. In Fe/V-SiO_2, an increased degree of surface roughness was noted, which may be linked to the removal of loosely bound vanadium oxides during reaction. On the other hand, Fe/Ce-SiO_2 retained a structure similar to its fresh counterpart, suggesting good resistance to sintering and physical degradation.

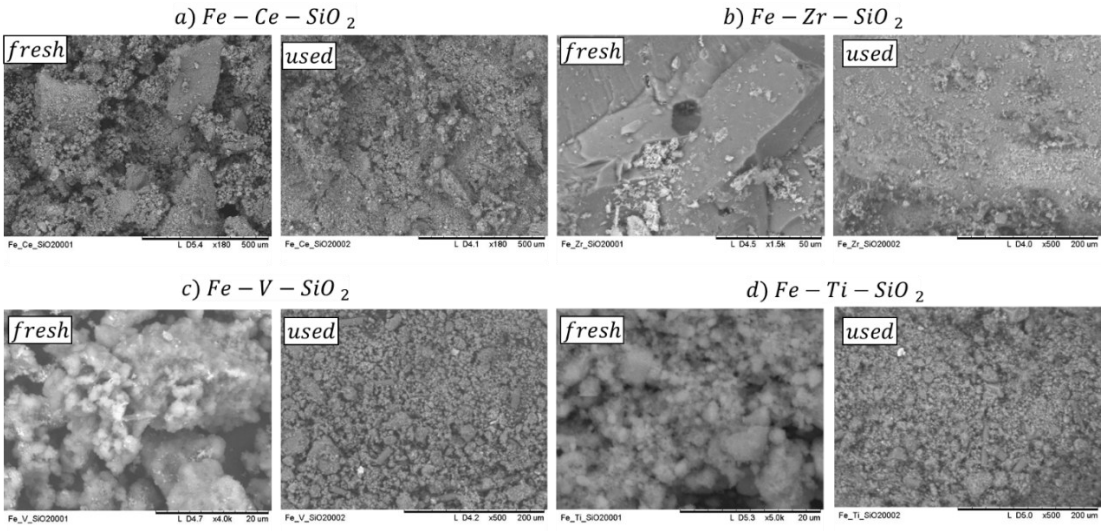

Figure 4.5. SEM micrographs of fresh and spent Fe-based metallosilicate catalysts.

The EDS results confirmed the expected elemental composition for all catalysts, verifying the successful incorporation of Fe, Si, and the respective metal oxide promoters (Ce, Ti, Zr, and V). The analysis showed that Fe/Zr-SiO_2 had the highest silica content, likely contributing to its well-dispersed morphology and higher surface area. Fe/Ti-SiO_2 exhibited a relatively uniform distribution of Ti in the sample, although localized regions with a higher Ti concentration were observed, indicating possible metal segregation. Fe/Ce-SiO_2 presented a high cerium content, reinforcing the hypothesis that CeO_2-rich domains formed within the silica support, leading to the observed clustering in SEM images. Similarly, Fe/V-SiO_2 displayed the highest vanadium content among the samples, supporting the hypothesis that bulk V_2O_5 structures may have formed. The EDS analysis of the spent catalysts revealed minor changes in the elemental distribution. Fe/Ti-SiO_2 exhibited a noticeable increase in Ti content, suggesting that the high-temperature reaction environment may have induced the redistribution of TiO_2 phases within the material. Fe/Zr-SiO_2 displayed a slight enrichment in Fe, which may indicate metal migration or clustering of iron species on the surface. Conversely, Fe/Ce-SiO_2 and Fe/V-SiO_2 maintained relatively stable compositions, suggesting minimal redistribution under reaction conditions.

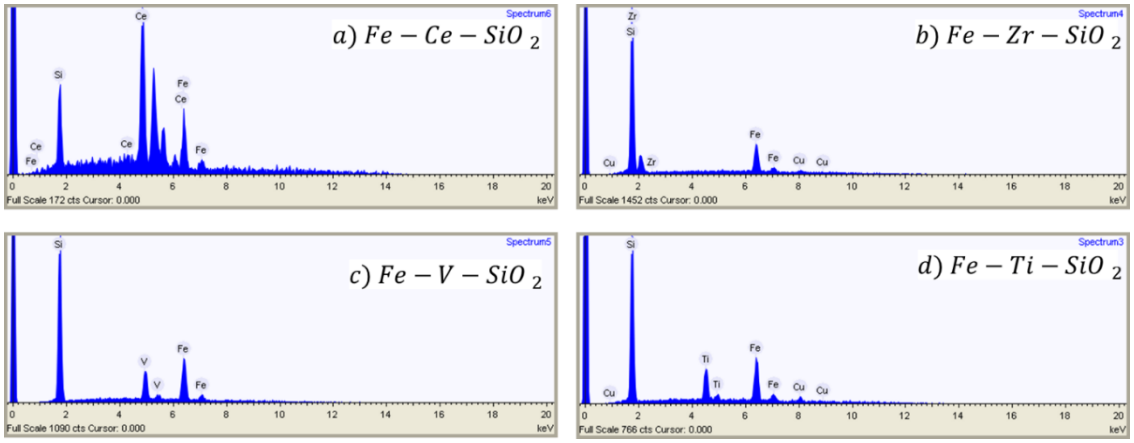

Figure 4.6. EDS spectra comparing fresh and spent Fe-based unpromoted metallosilicates.

Fresh catalyst	Element weight %					
	Fe	Si	Ti	Ce	Zr	V
$Fe_{10}/Ti\text{-}SiO_2$	52,77	34,93	12,13			
$Fe_{10}/Ce\text{-}SiO_2$	13,43	8,57		78,00		
$Fe_{10}/Zr\text{-}SiO_2$	39,80	44,60			15,60	
$Fe_{10}/V\text{-}SiO_2$	44,73	34,67				20,43
Spent catalyst	**Element weight %**					
	Fe	**Si**	**Ti**	**Ce**	**Zr**	**V**
$Fe_{10}/Ti\text{-}SiO_2$	55,63	21,20	22,50			
$Fe_{10}/Ce\text{-}SiO_2$	17,27	7,03		75,70		
$Fe_{10}/Zr\text{-}SiO_2$	56,77	31,13			12,10	
$Fe_{10}/V\text{-}SiO_2$	46,27	35,30				17,67

Table 4.7.EDS elemental composition of fresh and spent catalysts.

The SEM-EDS characterization of Fe-based metallosilicates demonstrated that the synthesis method successfully generated catalysts with diverse morphological and compositional properties. Fe/Zr-SiO_2 and Fe/Ti-SiO_2 exhibited well-distributed phases but showed minor iron migration after reaction. Fe/Ce-SiO_2 and Fe/V-SiO_2 displayed relatively stable compositions, though their tendency to form bulk oxide domains may impact catalytic performance. These findings highlight the importance of support material selection and post-synthesis modifications to optimize catalyst structure and long-term stability.

4.2.1.3. XRD

X-ray diffraction (XRD) analysis was conducted to identify the crystalline phases present in the synthesized Fe-based metallosilicate catalysts and to assess the structural stability of these materials. The XRD patterns (Figure 4.7) and the corresponding phase analysis (Table 4.8) indicate that Fe_2O_3 was the dominant iron-containing phase in all catalysts. This suggests that iron was primarily present in the form of hematite, a stable oxide phase commonly observed in iron-based catalysts. Additionally, CeO_2, Ti_2O_3, and V_6O_{13} were detected in samples containing cerium, titanium, and vanadium, respectively, confirming the presence of these metal oxides as distinct crystalline phases. The diffraction patterns of Fe/Zr-SiO_2, Fe/Ti-SiO_2, and Fe/V-SiO_2 exhibited broad peaks in the $2\theta = 15°\text{-}30°$ range, indicative of an amorphous silica structure. The predominance of these amorphous features suggests that Ti, Zr, and V species were initially incorporated into the silica matrix but may have segregated as extra-framework species during calcination. Interestingly, the diffractogram of the Fe/V-SiO_2 exhibited a lack of sharp peaks, implying that vanadium may have been fully incorporated into the silica network rather than existing as a distinct crystalline phase. This structural incorporation could influence both textural properties and catalytic behavior, as previously observed in the BET analysis.

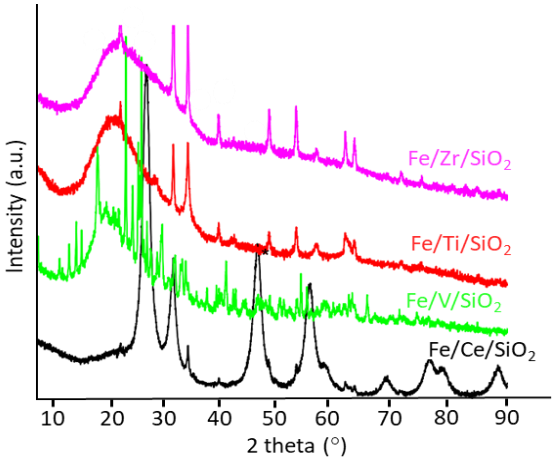

Figure 4.7. XRD patterns of fresh Fe-based metallosilicate catalysts.

XRD	Phases		Crystallinity%
$Fe_{10}/Ce\text{-}SiO_2$	Fe_2O_3	CeO_2	61,8
$Fe_{10}/Zr\text{-}SiO_2$	Fe_2O_3		34,3
$Fe_{10}/Ti\text{-}SiO_2$	Fe_2O_3	Ti_2O_3	37,3
$Fe_{10}/V\text{-}SiO_2$	Fe_2SiV	V_6O_{13}	48,3

Table 4.8. Crystalline phases and degree of crystallinity for each catalyst.

The crystallinity percentage was obtained from the XRD diffractograms using the software's peak area integration, which separates the crystalline reflections from the amorphous background. The ratio of crystalline to total integrated area was used as a measure of relative crystallinity. The value varied significantly among the samples. Fe/Ce-SiO_2 exhibited the highest crystallinity (61.8%), primarily due to the presence of well-defined CeO_2 and Fe_2O_3 phases. In contrast, Fe/Zr-SiO_2 had the lowest crystallinity (34.3%), suggesting that zirconium was more effectively dispersed in the amorphous silica phase. The crystallinity of Fe/Ti-SiO_2 (37.3%) and Fe/V-SiO_2 (48.3%) fell within an intermediate range, reflecting the influence of Ti_2O_3 and V_6O_{13} on phase formation. The presence of bulk metal oxides in Fe/Ti-SiO_2 and Fe/Ce-SiO_2 correlates with their relatively low BET surface areas, as larger oxide crystals tend to reduce overall porosity. This suggests that controlling calcination conditions and metal dispersion strategies could further optimize these materials for catalytic applications.

4.2.1.4. XPS

Performing the XPS analysis resulted in a confirmation of the theoretical sample compositions, furthermore a detection of metal oxides was clear by the analysis due to the last step of the synthesis being a high temperature oxidation treatment. Reported as follows are the details of the analysis.

	Atom %							
XPS Line	**Fe 2p3**	**O 1s**	**C 1s**	**Si 2p**	**Ce 3d3**	**Zr 3d5**	**Ti 2p3**	**V 2p3**
$Fe_{10}/Ti\text{-}SiO_2$	8,02	54,57	11,14	24,53			1,75	
$Fe_{10}/Ce\text{-}SiO_2$	0,48	17,49	79,80	2,05	0,19			
$Fe_{10}/Zr\text{-}SiO_2$	13,96	50,66	17,24	15,15		3		
$Fe_{10}/V\text{-}SiO_2$	8,05	51,58	18,99	19,81				1,58

Table 4.9. XPS % of fresh samples.

	Atom %								
XPS Line	**Fe 2p**	**O 1s**	**C 1s**	**Si 2p**	**Si 2s**	**Ce 3d**	**Zr 3d**	**Ti 2p**	**V 2p**
$Fe_{10}/Ti\text{-}SiO_2$	3,11	55,75	17,01	23,30				0,84	
$Fe_{10}/Ce\text{-}SiO_2$	2,14	21,10	71,78	1,98	4,75	1,62			
$Fe_{10}/Zr\text{-}SiO_2$	6,04	47,78	28,10	16,45			1,63		
$Fe_{10}/V\text{-}SiO_2$	2,81	45,35	33,75	17,31					0,78

Table 4.10. XPS % of spent samples.

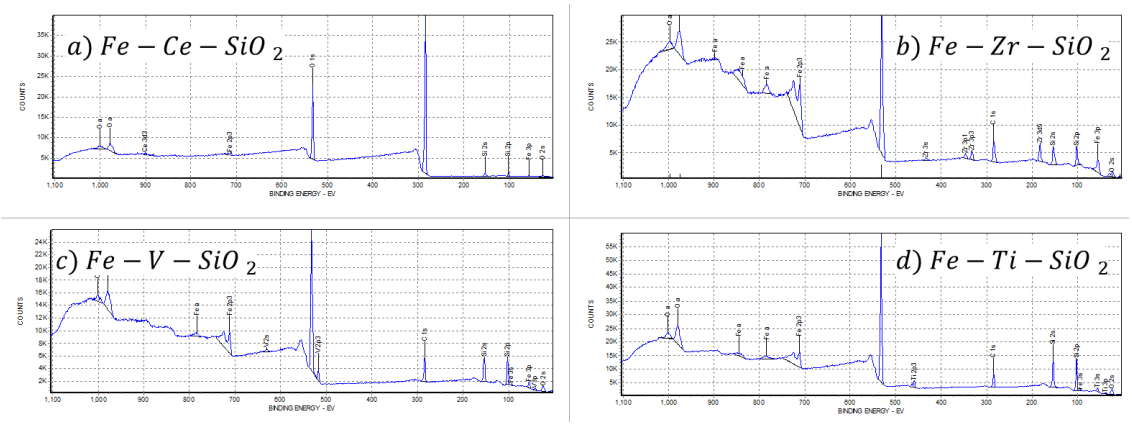

Figure 4.8. Survey XPS spectra of the fresh sample.

4.2.2. Promoted Metallosilicates

4.2.2.1. SEM EDS

SEM-EDS analyses were conducted to examine the morphological and compositional characteristics of the second class of Iron catalysts studied, which is divided into: the promoted Fe-based metallosilicate and metalloaluminate catalysts. These analyses aimed to evaluate the distribution of the active metal phases, the effect of potassium and copper promoters, and any structural modifications introduced by different support materials.

Starting from the promoted metallosilicates, imaging of $Fe/Ce/SiO_2$-K,Cu revealed a relatively well-distributed morphology, where cerium appeared to be the most homogeneously dispersed

element on the surface. Iron and silica were also evenly distributed, but some iron species were embedded within the silica matrix, forming islands of iron clusters. This is likely due to weak interactions between Fe and Si, which may cause Fe species to aggregate around silica sites rather than dispersing uniformly [2,3].

In Fe/Zr/SiO_2-K,Cu, iron was more homogeneously distributed on the catalyst surface compared to the cerium-supported counterpart. The zirconium species also appeared more uniformly dispersed, which may indicate a stronger interaction between Fe and Zr compared to Fe-Si. The potassium and copper promoters, despite their low mass loading, were still detectable in the SEM-EDS analysis, though their images appeared darker due to their lower concentration.

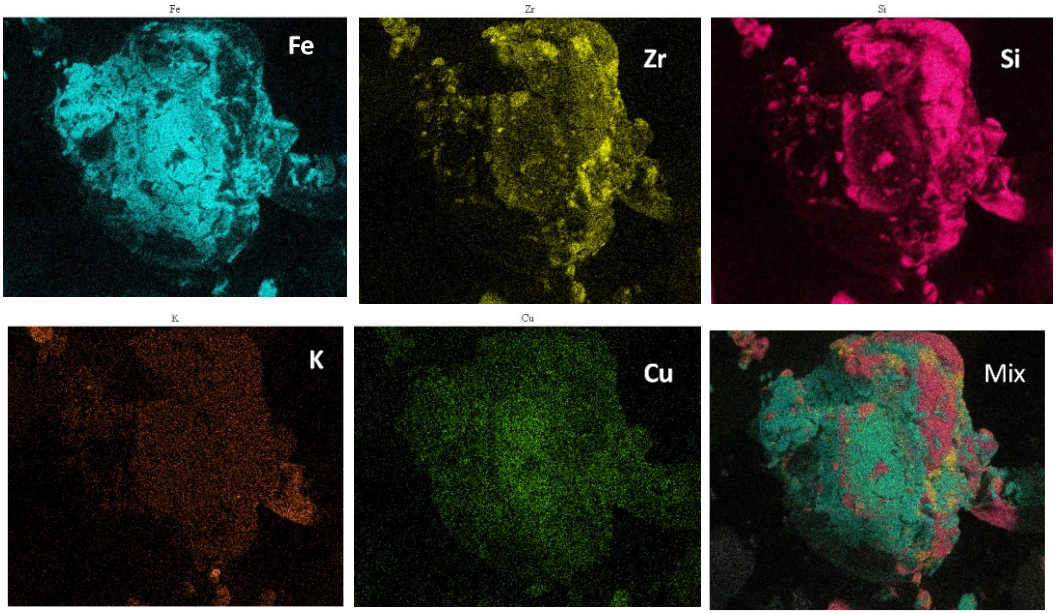

Figure 4.9. SEM-EDS elemental mapping of Fe/Ce/SiO_2-K,Cu.

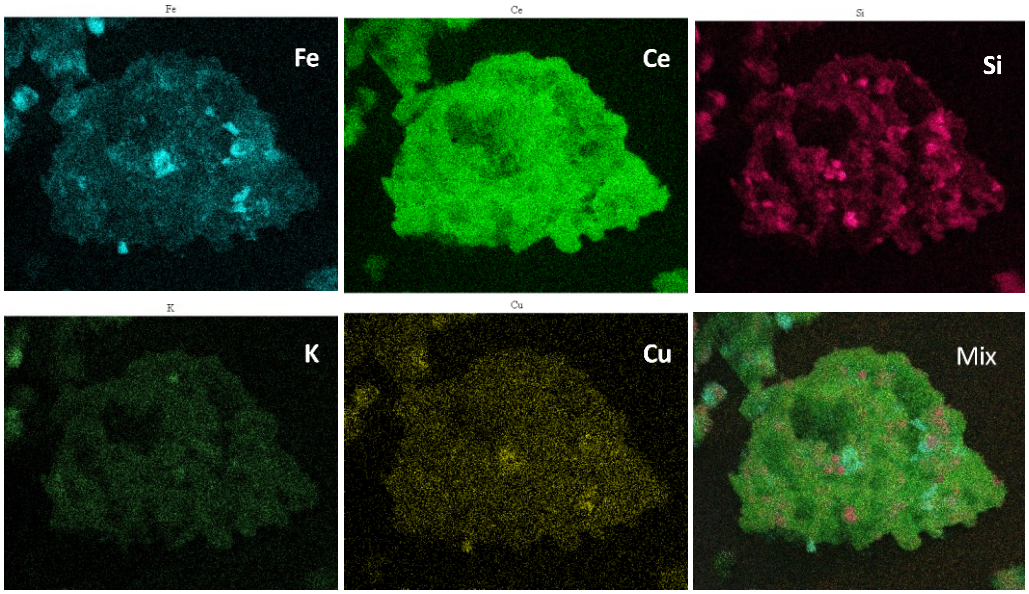

Figure 4.10. SEM-EDS elemental mapping of Fe/Zr/SiO_2-K,Cu.

The addition of K and Cu promoters visibly altered the porosity and rigidity of both catalysts. Compared to their non-promoted counterparts, the promoted metallosilicates exhibited denser and less porous structures, suggesting that promoter deposition partially blocked some of the available

porosity. This effect was particularly evident in Fe/Ce/SiO_2-K,Cu, where previously open pores appeared partially converted into small cavities due to the accumulation of cerium and iron species on the surface (Fig. 4.11 b-1, b-2) [4].

The Fe/Zr/SiO_2-K,Cu catalyst, on the other hand, displayed small surface cracks, likely resulting from capillary forces or high-temperature exposure during the calcination process. Additionally, particle size differences were noted between the two samples, with Fe/Ce/SiO_2-K,Cu exhibiting an average particle size of ~100 μm, while Fe/Zr/SiO_2-K,Cu displayed slightly larger 150 μm particles.

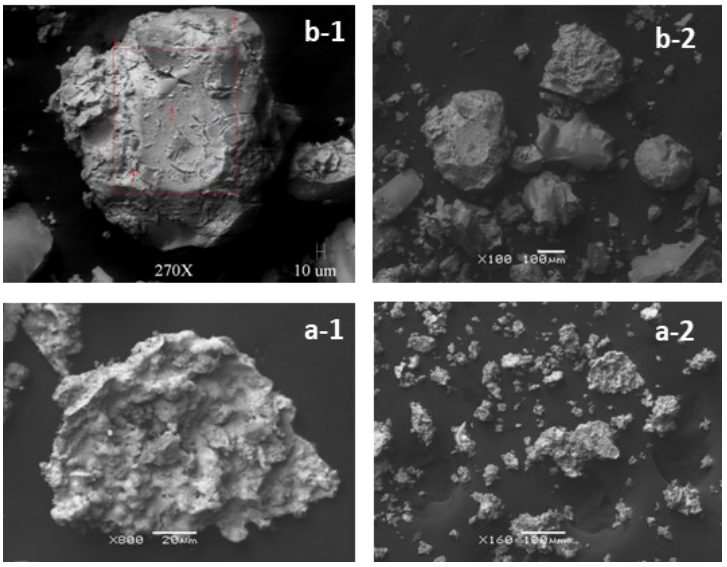

Figure 4.11. (The Scanning Electron Microscope Images of both Fe/Ce/SiO_2-K,Cu (a-1: x800 and a-2: x160 magnification) and Fe/Zr/SiO_2-K,Cu (b-1: x270 and b-2: x100 magnification)

The catalysts prepared with Sasol's alumina-based supports (Catalox and Dispal) exhibited distinctly spherical morphologies, as shown in Figures 4.12 c-1 and c-2. The spherical shape observed in Fe/Catalox-K,Cu closely matched the morphology of the original Catalox support, as indicated in the Sasol technical sheet. This suggests that the NHSG (Non-Hydrolytic Sol-Gel) synthesis method successfully retained the shape and structure of the precursor material while facilitating the incorporation of additional metal oxides on the surface.

Despite this, some iron species still formed isolated islands, clustering in localized regions rather than achieving complete uniformity. The distribution of Al, Cu, and K appeared relatively even, with a few iron and potassium particles detected within voids in the structure.

In contrast, Fe/Dispal-K,Cu exhibited a slightly different elemental distribution, with EDS spot analysis indicating that Fe, K, and Cu weight percentages were approximately 5% lower than those observed in the Catalox-supported catalyst. This suggests that the choice of alumina support influences the final dispersion of active metals, potentially affecting catalytic performance.

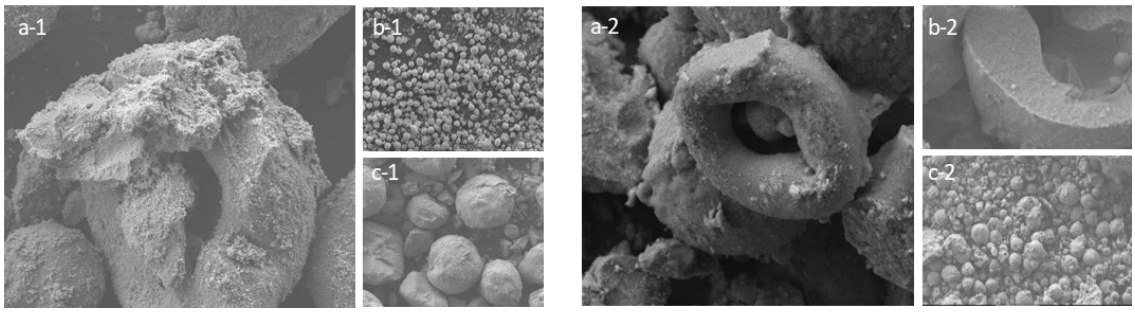

Figure 4.12. SEM results of Fe/Catalox-K,Cu (a-1) x1400, (b-1) x65 and (c-1) x1000 magnification and of Fe/Dispal-K,Cu (a-2) x3500 (b-2) x5000 (c-2) x250 magnification.

The EDS mapping confirmed the successful incorporation of Fe, Ce, Zr, Si, K, Cu, and Al in the promoted catalysts. The analysis revealed that Ce and Zr were predominantly surface-dispersed, whereas Fe species were more present within the silica and alumina matrices. The distribution of K and Cu was relatively homogeneous, though the low promoter content made their detection more challenging. In Fe/Zr/SiO_2-K,Cu, zirconium and iron were more evenly distributed, reinforcing the observation that Zr provided a more homogeneous structural framework compared to cerium. Conversely, Fe/Ce/SiO_2-K,Cu showed a slightly more heterogeneous elemental distribution, with Fe species appearing partially covered by cerium domains. For the alumina-supported catalysts, Fe/Catalox-K,Cu demonstrated a more even elemental distribution compared to Fe/Dispal-K,Cu, where Fe, K, and Cu were detected in lower weight percentages. This could be attributed to differences in porosity and surface area between the two supports, affecting metal deposition and accessibility. The addition of potassium and copper promoters clearly altered the morphology and porosity of both metallosilicate and metalloaluminate catalysts. SEM analysis suggests that these modifications led to:

- A decrease in surface porosity, particularly in Fe/Ce/SiO_2-K,Cu, where some pores appeared to transform into small cavities due to promoter accumulation.
- Improved metal dispersion, particularly in Fe/Zr/SiO_2-K,Cu, where Fe and Zr exhibited a more homogeneous distribution.
- Structural stabilization of the alumina-supported catalysts, with Fe/Catalox-K,Cu retaining its precursor morphology, while Fe/Dispal-K,Cu showed a slight reduction in promoter content compared to its Catalox-based counterpart.

4.2.2.2. BET

BET analysis was conducted to evaluate differences in the textural properties of the promoted Fe-based metallosilicate and metalloaluminate catalysts. Measurements were performed on the fresh catalysts and repeated after 100 hours of reaction under Fischer-Tropsch conditions to assess potential structural modifications due to coke deposition and pore blockage.

Table 4.11 summarizes the BET surface area, average pore diameter, and pore volume for the fresh promoted catalysts.

Catalyst	Surface Area (m^2/g)	Adsorption Average Pore Diameter (Å)	Pore Volume (cm^3/g)
Fe/Ce/SiO_2-K,Cu	24.0	156.4	0.11
Fe/Zr/SiO_2-K,Cu	204.8	41.0	0.18
Fe/Catalox-K,Cu	84.0	50.0	0.21
Fe/Dispal-K,Cu	150.0	50.0	0.19

Table 4.11. BET results for fresh promoted catalysts.

The BET surface area of the promoted catalysts was lower than that of their unpromoted counterparts, a trend consistent with the addition of potassium and copper promoters, which reduce the available surface area by partially blocking mesopores. Among the silica-supported catalysts, Fe/Zr/SiO_2-K,Cu exhibited the highest surface area (204.8 m^2/g), significantly higher than Fe/Ce/SiO_2-K,Cu (24.0 m^2/g). This difference is largely due to the precursor effect during the sol-gel synthesis process, which influences hydrolysis and condensation rates, ultimately affecting porosity and crystallinity. In contrast, the alumina-supported catalysts (Fe/Catalox-K,Cu and Fe/Dispal-K,Cu) displayed intermediate surface areas (84.0 and 150.0 m^2/g, respectively), with relatively similar pore sizes (~50 Å). This confirms that alumina-based supports maintain a stable mesoporous structure, even after metal loading and promoter incorporation.

To evaluate structural stability and potential pore modifications, BET analysis was repeated after 100 hours of reaction with syngas ($H_2/CO = 2$) at 20 bar, with the temperature increasing from 275°C to 325°C. The results are summarized in Table 4.12.

Catalyst	Surface Area (m^2/g)	Adsorption Average Pore Diameter (Å)	Pore Volume (cm^3/g)
Fe/Ce/SiO_2-K,Cu	12.2	222.2	0.08
Fe/Zr/SiO_2-K,Cu	207.9	41.8	0.25

Table 4.12. BET results for spent promoted catalysts.

The BET surface area of Fe/Ce/SiO_2-K,Cu decreased from 24.0 to 12.2 m^2/g, indicating significant pore blockage due to coke deposition. However, Fe/Zr/SiO_2-K,Cu retained its surface area, suggesting greater resistance to carbon deposition, potentially due to the structural stability provided by zirconium oxide domains. The increase in average pore diameter for Fe/Ce/SiO_2-K,Cu (from 156.4 Å to 222.2 Å) suggests that smaller pores were selectively blocked, shifting the pore size distribution toward larger values. This behavior is typical of catalysts undergoing progressive deactivation due to carbon buildup, as narrower pores are more susceptible to clogging.

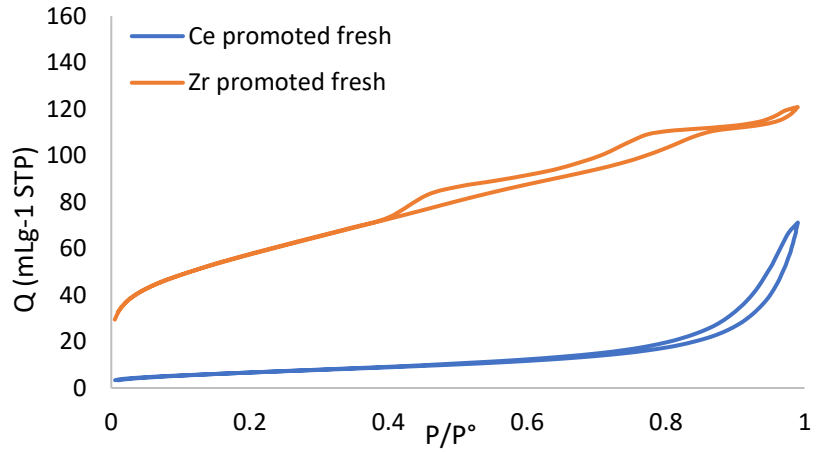

Figure 4.13. BET adsorption-desorption isotherms of fresh Fe/Ce/SiO₂-K,Cu and Fe/Zr/SiO₂-K,Cu .

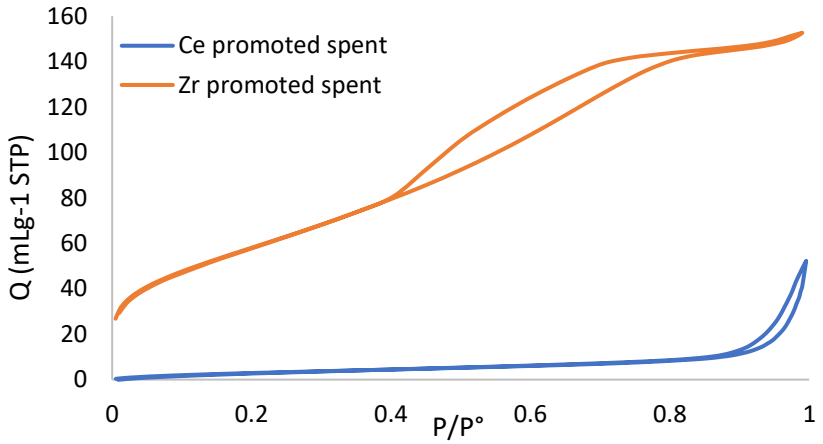

Figure 4.14. BET adsorption-desorption isotherms of spent Fe/Ce/SiO₂-K,Cu and Fe/Zr/SiO₂-K,Cu.

The zirconia-supported catalyst, in contrast, maintained almost identical pore size (41.0 vs. 41.8 Å), reinforcing the hypothesis that carbon deposition had a minimal impact on its porous network. Additionally, the pore volume of Fe/Zr/SiO₂-K,Cu increased slightly, likely due to partial restructuring of mesoporous domains under reaction conditions.

The adsorption-desorption isotherms provide further insight into the textural modifications occurring during Fischer-Tropsch synthesis.

- Fe/Ce/SiO₂-K,Cu followed a Type III isotherm with an H3 hysteresis loop, typically associated with non-rigid aggregates of plate-like particles.
- Fe/Zr/SiO₂-K,Cu exhibited a transition from a Type IV (H5) hysteresis loop in the fresh catalyst indicative of partially open pores to a Type IV (H2) loop after reaction, which suggests bottle-necked pore structures, similar to those found in porous glasses and silica gels [5].

This evolution of pore structure in Fe/Zr/SiO₂-K,Cu is consistent with the formation of interconnected mesoporous networks, which may contribute to enhanced stability and prolonged catalytic lifetime. Table 4.13 summarizes the pore size distribution of the fresh and spent promoted metallosilicate catalysts, highlighting the shifts induced by carbon deposition.

Pore diameter range (nm)	Fe/Ce fresh	Fe/Ce spent	Fe/Zr fresh	Fe/Zr spent
d<2	0	0	0	0
2<d<5	43.9	55.1	84.1	78.1
5<d<10	18.9	9.7	11.7	20.1
10<d<20	16.8	9.4	3.5	1.4
20<d<50	14.2	14.7	0.4	0.3
d>50	6.2	11.2	0.3	0,1

Table 4.13. Pore size distribution of promoted metallosilicates.

For Fe/Ce/SiO_2-K,Cu, a significant increase in the proportion of small pores (2-5 nm) was observed, while pores in the 10-20 nm range decreased. This confirms that carbon deposition selectively blocked medium-sized pores, leading to a shift in the overall pore distribution. For Fe/Zr/SiO_2-K,Cu, the opposite trend was observed, with a reduction in the smallest pore fraction and an increase in 5-10 nm pores. This suggests that while some pores were clogged, others were restructured into slightly larger openings, potentially improving mass transport properties.

4.2.2.3. XRD

The X-ray diffraction (XRD) analysis was conducted to identify the crystalline phases, structural integrity, and phase transformations in Fe-based catalysts supported on silica (Fe/Ce/SiO_2-K,Cu and Fe/Zr/SiO_2-K,Cu) and alumina (Fe/Catalox-K,Cu and Fe/Dispal-K,Cu). These catalysts contain potassium and copper promoters, which can influence crystallinity, metal-support interactions, and phase stabilization. The diffractograms were analyzed using EXP$O_2$014 and Match! software, referencing the Crystallography Open Database (COD) and the International Centre for Diffraction Data (ICDD) for phase identification. The results provide critical insights into the nature of iron oxide phases, metal dispersion, and the role of support materials. The XRD patterns of Fe/Ce/SiO_2-K,Cu (Fig. 4.15) exhibit sharp diffraction peaks corresponding to hematite (Fe_2O_3, black star) as the primary iron oxide phase. Well-defined peaks for CeO_2 (black square) confirm the crystalline nature of cerium oxide, while CuO (black circle) appears in minor amounts, indicating the presence of copper oxide as a separate phase rather than in solid solution with Fe or Ce. The presence of K_2O (red star) suggests that potassium is deposited on the surface without significant structural incorporation.

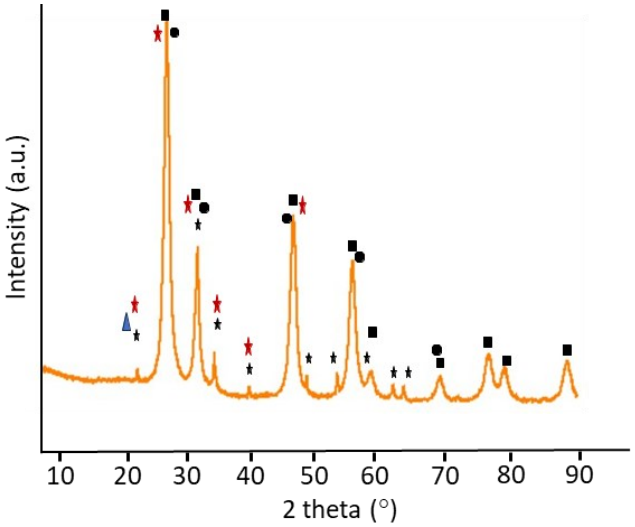

Figure 4.15. XRD patterns of Fe/Ce/SiO_2-K,Cu with phase identification: Fe_2O_3 (black star), CeO_2 (black square), CuO (black circle), K_2O (red star).

For Fe/Zr/SiO_2-K,Cu, the diffractogram (Fig. 4.16) shows a combination of hematite (Fe_2O_3), zirconium oxide (ZrO_2, black square), and Cu_4O_3 (black circle). The presence of Cu_4O_3 instead of CuO indicates that the oxidation conditions during synthesis led to the formation of paramelaconite rather than tenorite. The amorphous nature of silica is evident from the broad background hump in the diffractogram, suggesting that the sol-gel synthesis process suppressed excessive crystallization.

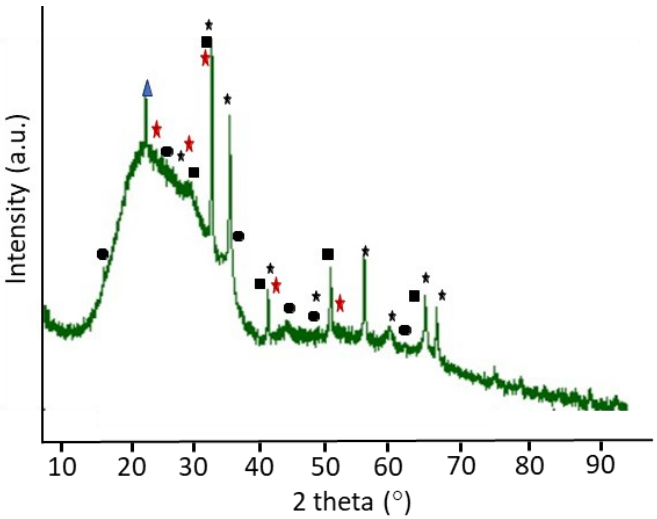

Figure 4.16. XRD patterns of Fe/Zr/SiO_2-K,Cu with phase identification: Fe_2O_3 (black star), ZrO_2 (black square), Cu_3O_4 (black circle), K_2O (red star).

The XRD pattern of Fe/Catalox-K,Cu (Fig. 4.17) reveals a mixture of hematite (Fe_2O_3, black star) and magnetite (Fe_3O_4, black circle). The presence of both Fe^{2+} and Fe^{3+} species suggests that partial reduction occurred during synthesis or calcination. The alumina phase appears as θ-Al_2O_3 (black triangle), indicating that the thermal treatment maintained a stable alumina framework. Weak peaks for K_2O and Cu_4O_3 confirm the presence of promoters but suggest that their loadings are relatively low. The overlapping diffraction angles of the mixed oxide phases of both catalysts in the 30-40° (2θ) range make distinguishing between different phases difficult. More precisely, Fe_2O_3 [7], Fe_3O_4 [8], K_2O [9], CuO [10,11], Al_2O_3 [12], and Cu_4O_3 [13] all exhibit at least two

general diffraction peaks in this range. This results in overlaps of some reflections, making it difficult to definitively identify crystalline type.

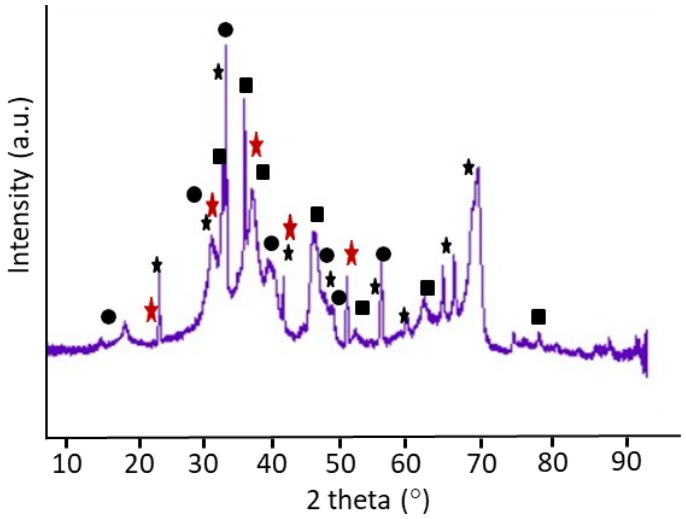

Figure 4.17. XRD patterns of Fe/Catalox-K,Cu : Fe_2O_3 (black star), Al_2O_3 (black square), CuO (black circle), K_2O (red star).

The Fe/Dispal-K,Cu catalyst (Fig. 4.18) displayed a different iron oxide phase composition, with Fe_3O_4 as the dominant iron phase and only minor traces of Fe_2O_3. This indicates that the Dispal support stabilizes magnetite over hematite, potentially due to stronger metal-support interactions. The alumina phase in this catalyst appears largely amorphous, as evidenced by the lack of well-defined Al_2O_3 peaks. The copper species is primarily present as CuO (black circle), rather than Cu_4O_3, indicating different oxidation behavior compared to Fe/Catalox-K,Cu.

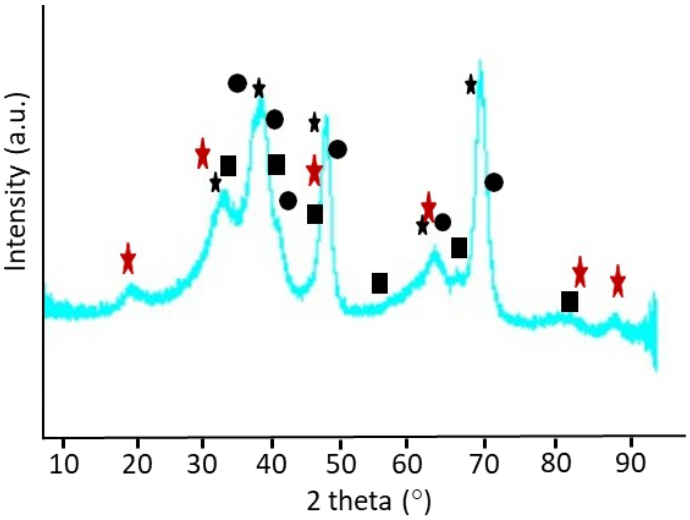

Figure 4.18. XRD patterns of Fe/Dispal-K,Cu : Fe_3O_4 (black star), Al_2O_3 (black square), Cu_3O_4 (black circle), K_2O (red star).

To further analyze the degree of crystallinity and phase dispersion, the crystallite size of Fe_2O_3 and Fe_3O_4 was determined using the Scherrer equation. The values obtained are summarized in Table 4.14.

Catalyst	Crystallite Size (nm)
Fe/Ce/SiO_2-K,Cu	7.0
Fe/Zr/SiO_2-K,Cu	16.1
Fe/Catalox-K,Cu	11.9
Fe/Dispal-K,Cu	3.1

Table 4.14. Crystallite Sizes of Fe Phases in Promoted Catalysts.

The smallest crystallite size was observed for Fe/Dispal-K,Cu (3.1 nm), confirming that iron species in this catalyst are highly dispersed. In contrast, Fe/Zr/SiO_2-K,Cu exhibited the largest crystallites (16.1 nm), suggesting that weaker interactions between zirconia and Fe_2O_3 facilitated larger particle growth. The presence of Fe_3O_4 in Fe/Dispal-K,Cu compared to Fe_2O_3 dominance in Fe/Catalox-K,Cu suggests that the Dispal support promoted the partial reduction of iron oxide, leading to the formation of more active sites for CO_2 activation. Similarly, the Fe/Zr/SiO_2-K,Cu system demonstrated phase separation, with zirconia favoring the stabilization of Fe_2O_3 crystallites rather than forming a strong metal-support interaction. For Fe/Ce/SiO_2-K,Cu, the higher crystallinity observed compared to Fe/Zr/SiO_2-K,Cu suggests that CeO_2 contributes to structural stabilization, limiting the amorphous nature of the silica framework. The identification of $CeSiO_2$ and $ZrSiO_4$ phases via $EXPO_2014$ further supports the notion that Ce and Zr form stable silicate structures rather than existing as free oxides.

4.2.2.4. XPS

The X-ray photoelectron spectroscopy (XPS) analysis was conducted to assess the surface composition, oxidation states, and elemental distribution of the Fe-based catalysts supported on silica supported (Fe/Ce/SiO_2-K,Cu and Fe/Zr/SiO_2-K,Cu) and alumina supported catalysts (Fe/Catalox-K,Cu and Fe/Dispal-K,Cu). The results were compared with the bulk characterization techniques (XRD and SEM-EDS) to evaluate the surface-to-bulk consistency of the catalysts. The findings confirmed the presence of key metal oxides, promoters, and support materials, providing crucial insights into their role in catalytic performance. The C1s peak at 284.8 eV was observed in all catalysts, attributed to carbon contamination introduced during the calcination process. In the silica-supported catalysts, the presence of Si2s at 153.4 eV confirmed the SiO_2 framework. Additionally, for Fe/Zr/SiO_2-K,Cu, a peak was detected at 183.2 eV, which was assigned to $ZrSiO_4$ (zircon phase), corroborating the findings from XRD analysis, which suggested the formation of silicate phases rather than free zirconia species. The iron species in all catalysts appeared primarily in the Fe^{3+} oxidation state (Fe_2O_3), as evidenced by the Fe2p3 peak at ~710 eV, which is characteristic of hematite.

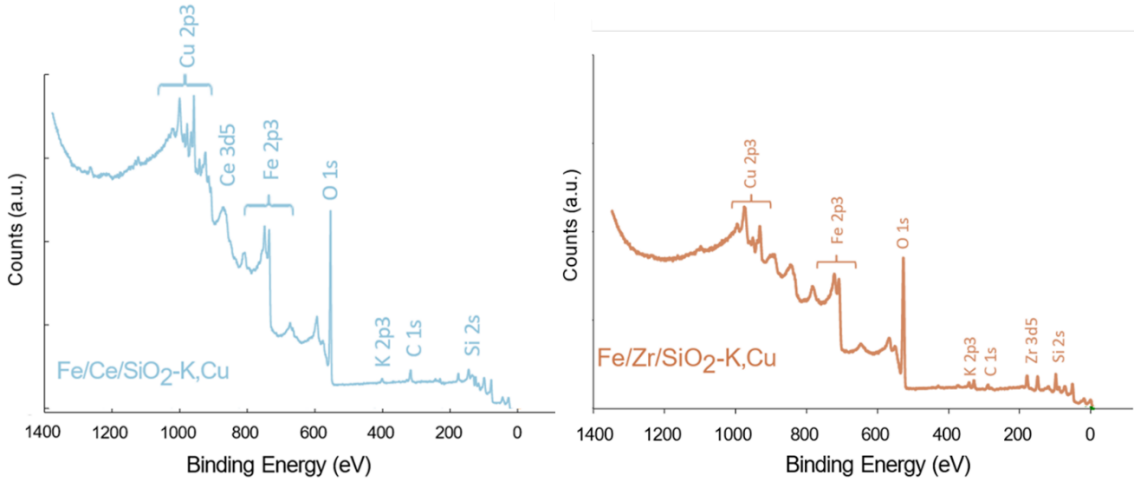

Figure 4.19.XPS survey spectra of promoted metallosilicates.

This was particularly evident in Fe/Ce/SiO_2-K,Cu and Fe/Zr/SiO_2-K,Cu, where the dominant Fe_2O_3 phase aligned with the XRD findings. No significant peaks for Fe^{2+} were detected, suggesting limited magnetite (Fe_3O_4) formation in the silica-supported catalysts. In contrast, for the alumina-supported catalysts (Fe/Catalox-K,Cu and Fe/Dispal-K,Cu), the $Fe2p_3$ binding energy indicated a mixture of Fe^{3+} (Fe_2O_3) and Fe^{2+} (Fe_3O_4) species, confirming the dual-phase nature of iron oxides observed in XRD. This suggests that the alumina support facilitated partial reduction of Fe_3^{+} to Fe^{2+}, likely due to stronger metal-support interactions. The presence of Ce (IV) in Fe/Ce/SiO_2-K,Cu was confirmed by the $Ce3d_5$ peak, corresponding to CeO_2, further supporting XRD results. Similarly, in Fe/Zr/SiO_2-K,Cu, Zr(IV) species at 182 eV confirmed the stabilization of zirconia within the silica framework. The copper oxidation states were identified in all catalysts, with Cu(II) peaks at ~889.6 eV ($Cu2p_3$), characteristic of CuO. Interestingly, Fe/Zr/SiO_2-K,Cu displayed additional Cu(III) contributions, indicating a partial formation of Cu_3O_4, which could influence the electronic properties of the catalyst. The presence of K_2O was confirmed in all catalysts, with $K2p_3$ peaks appearing at ~293.6 eV. The potassium content was uniformly distributed across both silica and alumina-supported catalysts, suggesting that K was surface-enriched rather than diffused into the bulk phase. This is significant as K_2O acts as an electronic promoter, enhancing CO_2 adsorption and facilitating C-C coupling in Fischer-Tropsch reactions.

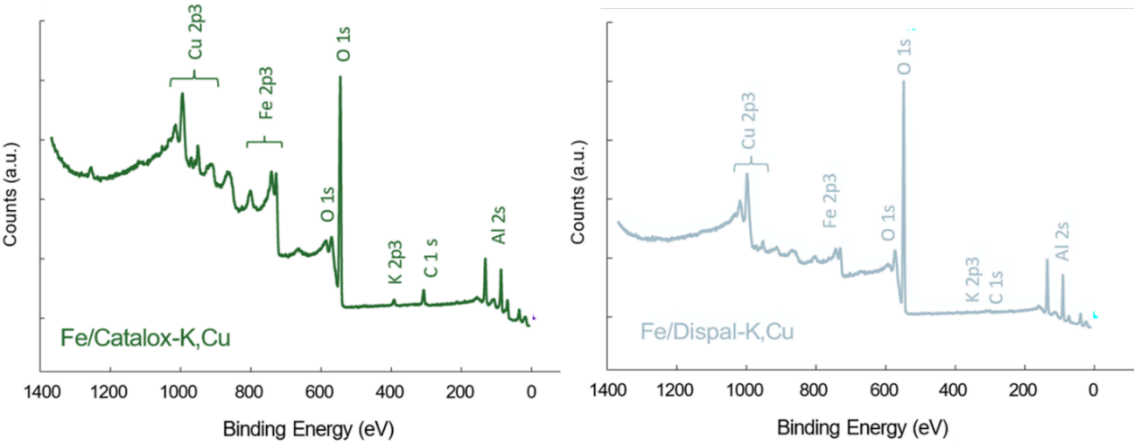

Figure 4.20. XPS survey spectra of alumina supported Iron based catalysts.

The alumina-supported catalysts exhibited a higher potassium intensity, indicating that K_2O is more strongly retained on alumina than on silica. This difference could impact basicity and CO_2 activation mechanisms, influencing product selectivity. In terms of copper promotion, both Cu $2p_3$ and Cu Auger peaks were consistent across Fe/Ce/SiO_2-K,Cu, Fe/Zr/SiO_2-K,Cu, Fe/Catalox-K,Cu, and Fe/Dispal-K,Cu. However, the alumina-supported catalysts displayed slightly lower Cu intensities, suggesting that Cu is more embedded within the support matrix rather than exclusively on the surface. A comparison between XPS and SEM-EDS results highlights differences in surface versus bulk metal distribution. For the silica-supported catalysts, XPS results indicated that SiO_2 is present beneath the catalyst surface, while Fe, Cu, K, and Ce/Zr species remain exposed. This confirms that the active sites are surface-accessible, enhancing catalytic efficiency. In contrast, for the alumina-supported catalysts, the XPS findings suggest that Al_2O_3 forms an external layer covering some of the metal components, particularly Fe and Cu. This observation aligns with SEM-EDS data, which showed a higher atomic percentage of Al on the catalyst surface compared to the bulk composition. The higher amorphous Al_2O_3 content in Dispal (33%) compared to Catalox (24%) further supports this conclusion. The encapsulation effect in Fe/Dispal-K,Cu may affect metal dispersion, influencing catalytic performance.

4.3. Hydrotalcite Characterization

4.3.1. XRD

The X-ray diffraction patterns of all freshly synthesized catalysts exhibit the characteristic reflections of hydrotalcite-like materials at approximately $2\theta = 11.6°$, 23.3°, 34.3°, 59.6°, and 61.0°, corresponding to the (003), (006), (012), (110), and (013) planes, respectively [see e.g., [14,15]. The presence of these peaks confirms the formation of a brucite-type layered structure, in which the interlayer region is occupied by carbonate ions, as evidenced by the first reflection at $2\theta \approx 11.6°$ [16]. A comparison among the different catalysts suggests that partial substitution of Mg with Fe, Co, or Zn modifies the relative intensity and broadening of the peaks, consistent with variations in lattice parameters and crystallinity [17]. For instance, in Fe30 and Fe40, the reflections appear relatively well-defined, and no peaks attributable to secondary phases or spinel structures are detected. This observation indicates that iron is successfully integrated into the hydrotalcite framework without producing significant amounts of extraneous phases [18]. Similarly, Co33 and Co45 display the same main reflections, although the introduction of cobalt may slightly broaden certain peaks, suggesting partial lattice distortion or a reduction in average crystallite size [19]. In the case of FeZn, no clear hydrotalcite-like reflections were observed. The diffractogram of FeZn shows only the characteristic reflections of ZnO, indicating that the layered double hydroxide (LDH) phase was not formed under the adopted synthesis conditions. For the FeZn-US sample, a very broad and low-intensity reflection was detected, which could suggest the presence of only a negligible amount of LDH. Overall, these results point to ZnO as the dominant crystalline phase in both FeZn-BM and FeZn-US samples, with minimal or absent contribution from LDH structures.

A direct comparison of the ultrasound (US) and ball-milling (BM) synthesis methods reveals a few differences. The US-derived samples tend to show sharper and more intense peaks, which are typically associated with a slightly higher degree of crystallinity or greater structural order [20]. In contrast, ball-milled samples often exhibit broader peaks and somewhat reduced intensities,

reflecting partial disorder in the crystal planes introduced by mechanical energy. This difference is particularly notable in Fe30 and Fe40, where the BM-diffraction profiles appear more "blurred," confirming that the milling process can reduce crystallite size and introduce lattice defects [21]. Despite these variations, in all cases the diffraction patterns remain consistent with the hydrotalcite-like structure, demonstrating the robustness of these materials under different synthesis conditions.

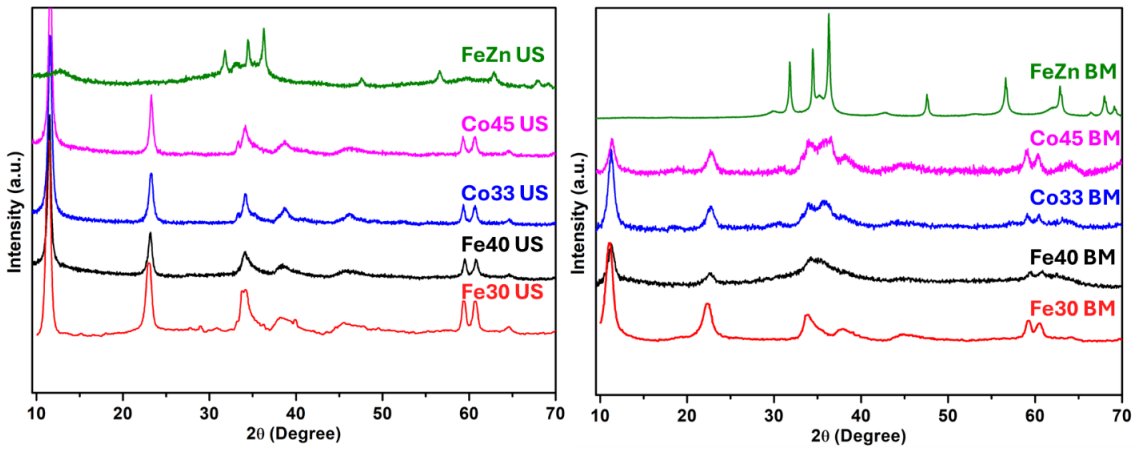

Figure 4.21. X-ray diffractogram of US (on the left) and BM (on the right) hydrotalcite catalysts.

After the activation treatment the XRD patterns of Fe30 and Fe40 show significant structural changes relative to the previously visible hydrotalcite-like structure. Figure 4.22 illustrate the post-activation patterns for the ultrasound (US) and ball-milled (BM) samples, each stacked to highlight phase identification but offset along the Y-axis for clarity. The primary reflections in both Fe30 and Fe40 can be assigned to a combination of magnesium carbonates ($MgCO_3$), spinel-like oxides ($MgFe_2O_4/Fe_3O_4$), and iron carbides (Fe_2C_5). Minor peaks attributed to sodium magnesium carbonate ($Na_2Mg(CO_3)_2$) are also observed, indicating that some carbonate phases remain intact or re-form under activation conditions [14,15]. In both Fe30 and Fe40, the presence of iron carbides demonstrates that partial carbidization takes place during reduction in CO/H_2, an important transformation for catalytic activity in CO_2 hydrogenation or other related processes [16,17]. Fe30 and Fe40 samples prepared via ultrasound exhibit generally sharper reflections than their ball-milled counterparts.

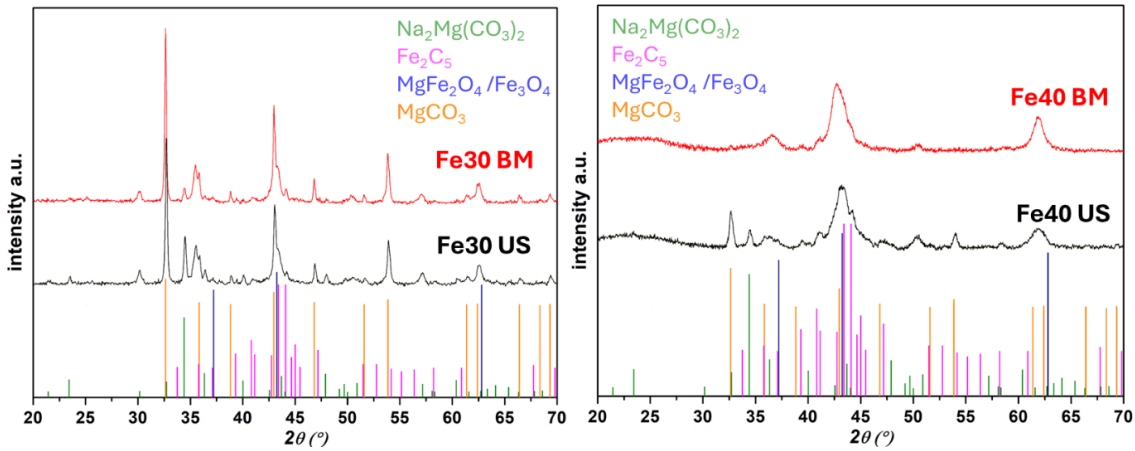

Figure 4.22. Diffractograms of Fe30 and Fe40 hydrotalcite after activation step.

In Fe30 US, for instance, the peaks assigned to spinel and carbide phases are comparatively narrower, suggesting a more uniform crystallite size or reduced lattice strain. This observation aligns with the earlier findings on fresh materials, where US-synthesized samples often showed higher crystallinity or better-defined reflections. Fe30 BM, on the other hand, presents slightly broader peaks, which may indicate smaller or more strained crystallites likely a consequence of the mechanical energy introduced during ball milling. A similar trend is observed in Fe40: while both US and BM samples display characteristic reflections of spinel-like oxides and Fe_2C_5, the US sample exhibits relatively sharper peaks. The higher iron content in Fe40 leads to more prominent carbide-related reflections, reflecting an increased tendency for Fe to form carbide under the reducing/carburizing atmosphere. However, these reflections still appear somewhat broader in the BM sample compared to its US counterpart, suggesting that mechanical milling accentuates crystallite refinement or defect formation. Co33 and Co45 activated samples, in Fig.4.23, both show diffraction patterns that differ notably from the original hydrotalcite-like structure. Certain reflections gain intensity, while others become less pronounced, indicating that partial decomposition and rearrangement has occurred. Some broad signals appear in the typical 2θ range (roughly 35-45°) where cobalt oxides are often detected, yet their identification remains challenging because these peaks can overlap with reflections from magnesium ferrite-type phases or other mixed oxides.

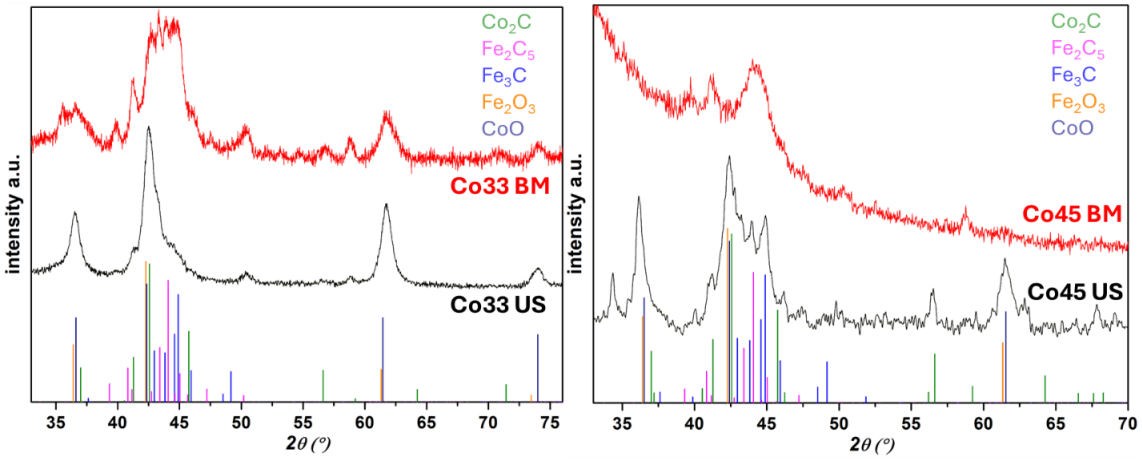

Figure 4.23. Diffractograms of Co33 and Co45 hydrotalcite after activation step.

In Co33, the post-activation pattern still shows a few broad reflections consistent with residual carbonates, suggesting that the activation temperature was not high enough to completely remove or transform all carbonate species. The ultrasound sample tends to display somewhat sharper peaks overall than the ball-milled version. Meanwhile, the BM sample frequently exhibits more peak broadening, possibly reflecting smaller particle sizes or increased lattice strain brought about by the mechanical milling process. A similar scenario emerges in Co45. The higher cobalt content could, encourage the formation of cobalt-rich spinel phases (e.g., $CoFe_2O_4$) [22,23], especially under reducing conditions. However, the XRD patterns do not unequivocally confirm such a phase, because overlapping reflections in the same region complicate phase assignment. What can be stated with more confidence is that various mixed oxides are likely present, given the partial decomposition of the hydrotalcite framework and the presence of cobalt, magnesium, and iron ions. Also, in this instance the US-derived Co45 shows somewhat narrower reflections than its BM counterpart, hinting at differences in crystallite size or defect density. Both Co33 and Co45

present carbide species in a different manner. Particularly, Co45 display a sharper and more abundant set of peaks related to carbide phases identified as Fe_3C, Fe_2C_5, Co_2C. Since the region of 2θ range is overloaded, clear assignment could not be obtained.

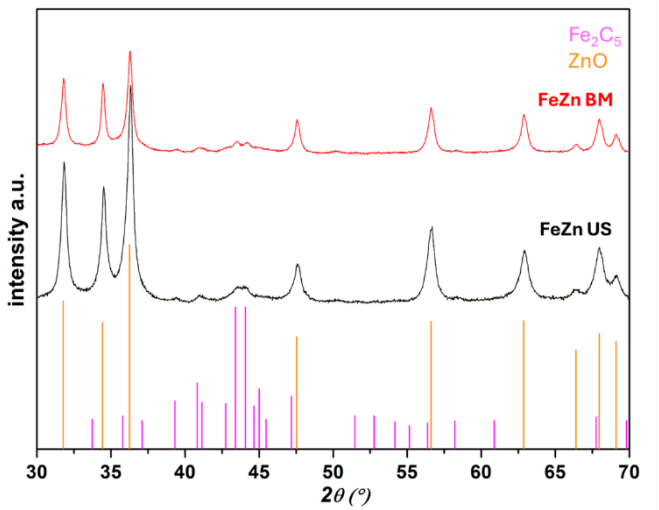

Figure 4.24. Diffractogram of FeZn hydrotalcite after activation step.

Regarding FeZn in Fig.4.24 post activation XRD analysis, the diffraction patterns show two primary sets of reflections: ZnO (already present in the as synthesized sample) and iron carbide (Fe_2C_5). This combination indicates partial carbidization of the iron component while zinc is predominantly present as crystalline ZnO, consistent with the absence (or negligible presence) of Zn-containing LDH phases. The US-derived sample generally shows relatively sharp ZnO peaks, suggesting a well-defined crystalline domain. Meanwhile, the BM-prepared sample exhibits reflections for the same phases but with a slight broadening. In the broader context of the other activated catalysts (Fe30, Fe40, Co33, and Co45), FeZn stands out for its absence of mixed-oxide or carbonate signals at higher 2θ angles. Instead, the primary phases are limited to ZnO and Fe_2C_5, reflecting zinc's tendency to form a stable oxide under these reduction conditions. In contrast, systems containing magnesium and cobalt often retain some carbonate-like structures or spinel-type mixed oxides. The FeZn sample thus undergoes a more straightforward transformation during activation, likely benefiting from the simpler redox chemistry of Zn relative to Mg or Co [24]. Despite the differences in crystallite size or defect density caused by synthesis methods, both FeZn US and FeZn BM show similar diffraction patterns, dominated by ZnO and iron carbides. As result, it seems that the iron zinc interaction favors formation of well-crystallized oxide and carbide phases under the chosen activation procedure offering a less complex phase evolution than the Mg- or Co- analogues.

4.3.2. BET

From the fresh samples, it is clear that ball milling often yields higher surface areas than ultrasound. For instance, Fe30 BM reaches 114 m^2/g versus 84 m^2/g for Fe30 US, and Co33 BM shows 123 m^2/g while its US counterpart stands at 52 m^2/g. The main outlier is FeZn, where US starts at 120 m^2/g, noticeably above the 98 m^2/g of FeZn BM. Upon activation, most catalysts see their surface areas drop, likely due to partial sintering or the collapse of some pore structures as high-temperature treatments drive phase changes. Yet the trend is not uniform: for example, Fe40 BM retains 56 m^2/g (down from 117 m^2/g) but still exceeds Fe40 US at 30 m^2/g (down from

99 m²/g). In contrast, FeZn follows a different path, with US retaining a relatively high 39 m²/g whereas BM falls to 15 m²/g, highlighting that the outcome of activation can vary significantly based on both composition and synthesis method.

Surface Area measurements (m^2/g)						
	Fresh		**Activated**		**Spent**	
	US	**BM**	**US**	**BM**	**US**	**BM**
Fe30	84	114	31	41	34	10
Fe40	99	117	30	56	22	5
Co33	52	123	36	67	10	13
Co45	52	51	30	31	10	3
FeZn	120	98	39	15	53	30

Table 4.15. Surface area measurements of fresh, activated and spent hydrotalcite catalysts, both US and BM.

The spent samples, collected after reaction, often show further decreases in surface area. Fe30 BM decreases from 41 m²/g to just 10 m²/g, possibly due to sintering or pore blockage during operation. On the other hand, FeZn exhibits an atypical increase in the US variant (rising from 39 m²/g to 53 m²/g), suggesting that reaction by-products might have been removed or re-organized, thus exposing more surface. This behaviour reinforces the view that different metals particularly zinc, can alter how the catalyst's textural properties evolve under working conditions.

These surface area profiles make more sense when viewed considering the XRD data. For iron-substituted samples (Fe30, Fe40), the formation of spinel-like oxides often corresponds to a reduction in surface area as the lattice reorganizes, and in some cases sinters. Ball-milled catalysts initially display larger surface areas but can lose that advantage once crystalline domains grow, or pores collapse during activation and reaction. Ultrasound-derived materials, while sometimes starting lower in area, may preserve more stable pore structures, limiting the extent of sintering.

Across the fresh samples, the US-prepared materials typically exhibit pore volumes comparable to, or occasionally exceeding, those of BM analogues, except for Co33 and Co45, where the BM variants begin with lower initial volumes. Upon activation, several catalysts follow the pattern of decreased pore volume (e.g., Fe30 US from 0.35 to 0.23 cm³/g; Fe40 US from 0.38 to 0.19 cm³/g), likely due to pore collapse or partial sintering as phases reorganize. However, others (Co33 US and Co33 BM) unexpectedly gain pore volume (0.39 to 0.41 cm³/g and 0.20 to 0.34 cm³/g, respectively), suggesting that structural changes, possibly linked to carbonate removal or oxide formation, can open new voids. In the spent state, most catalysts see further reductions, but the extent varies. FeZn US holds steady at 0.29 cm³/g from activated to spent, such stability contrasts with the more pronounced losses observed in, for example, Fe40 US (from 0.19 down to 0.02 cm³/g).

Cumulative volume of pores (cm^3/g)						
	Fresh		Activated		Spent	
	US	BM	US	BM	US	BM
Fe30	0.35	0.28	0.23	0.19	0.05	0.17
Fe40	0.38	0.42	0.19	0.38	0.02	0.15
Co33	0.39	0.20	0.41	0.34	0.12	0.09
Co45	0.34	0.12	0.30	0.12	0.06	0.01
FeZn	0.14	0.20	0.29	0.09	0.29	0.15

Table 4.16. Pore volume measurements of fresh, activated and spent hydrotalcite catalysts, both US and BM.

Regarding average pore diameter measurements, for fresh catalysts, US-derived materials often possess larger average pore diameters. Upon activation, diameters typically increase, as partial crystallite reorganization can enlarge existing pores.

Average pore diameter (nm)						
	Fresh		Activated		Spent	
	US	BM	US	BM	US	BM
Fe30	16	9	26	12	16	17
Fe40	9	14	19	22	12	23
Co33	30	6	31	18	50	23
Co45	23	8	14	22	19	18
FeZn	6	7	22	19	17	14

Table 4.17. Pore diameter measurements of fresh, activated and spent hydrotalcite catalysts, both US and BM.

For spent catalysts, the trend becomes more heterogeneous. Certain samples revert to intermediate pore sizes (Fe30 US: 16 nm), whereas others continue to grow, Co33 US jumps from 31 to 50 nm. These shifts likely reflect a balance between sintering (which can shrink or collapse pores) and potential removal of reaction by-products (which may open or enlarge channels). The FeZn system again proves distinctive: FeZn US goes from 22 nm down to 17 nm, suggesting modest pore contraction, while remaining higher than its fresh state (6 nm). Taken together, these data align well with the surface-area and XRD results. Catalysts that undergo major crystalline rearrangements, such as Fe30, Fe40, Co33, often experience substantial changes in pore structure and volume, in part from sintering and in part from the formation or removal of phases like carbonates or spinel-type oxides. Ball milling, which sometimes boosts initial surface area and pore volume, generally exhibits porosity losses depending on how the material evolves under reaction conditions. In contrast, ultrasound US samples may start with somewhat different pore features often larger diameters yet still undergo shifts during activation that expand or shrink those pores. The FeZn catalyst, with its relatively straightforward transition to ZnO and iron carbide, stands out for maintaining or re-exposing pore volume and slightly reducing pore size in the spent state. Ultimately, the interplay between phase changes (as indicated by XRD) and textural evolution (as revealed by BET) underscores the importance of carefully matching synthesis routes with the desired catalytic functionality.

From the pore distributions studies represented in Figure 4.25 a recurring pattern can be seen, activation process often shifts a portion of the pore volume from micropores (<2 nm) and very small mesopores (2-5 nm) into intermediate size ranges (5-20 nm). This trend typically reflects the partial decomposition of hydrotalcite-like layers, removal of interlayer carbonates, and possible formation of new oxide/carbide phases. While some catalysts (e.g., Co33) gain mesopore volume, others (like Fe30 US) display only moderate shifts, indicating that the extent of pore rearrangement is tied to both composition and prior treatment. Ball-milled catalysts often begin with a substantial fraction of smaller pores, presumably due to the mechanical stresses that generate fine particles and fracturing. However, these pores can merge, collapse, or otherwise transform during activation and reaction, leading to either a shift toward mid-range mesopores or, in some cases, a more pronounced loss of microporosity. Ultrasound-derived samples tend to maintain a broader distribution from the start, with less drastic changes overall. Notably, exceptions exist where US catalysts also exhibit significant pore enlargement (such as Fe40 US), reminding us that composition is a major factor as well. In the spent catalysts, some show further movement of the pore distribution (toward either larger mesopores or smaller ones), pointing to continuing sintering under reaction conditions. Others, like FeZn US, regain pore accessibility that was initially lost, an outcome possibly linked to the removal of carbonaceous deposits or reorganization of the Zn/Fe oxide phases. This interplay of sintering, deposit formation, and deposit removal underscores how dynamic the pore structure remains even after the initial thermal activation. In other words, while all compositions may end up showing carbide phases, the path by which they achieve that state, and the impact on their pore structure, remains highly sensitive to the initial synthesis route. The result is that some US samples can preserve or even widen their mesopore network, whereas BM variants might consolidate into fewer, larger pores or lose significant mesopore volume altogether.

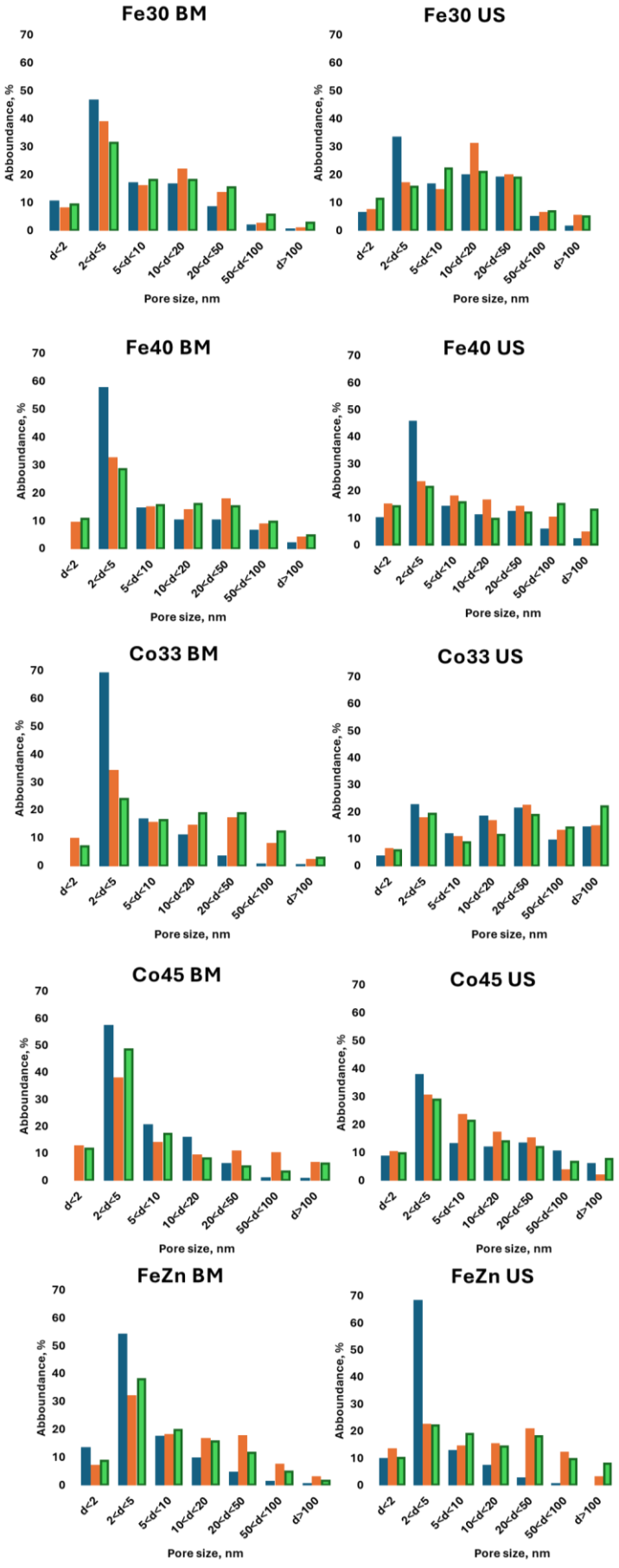

Figure 4.25. Pore size distribution of each set of US and BM catalyst. In blue the distribution regarding the fresh catalyst, in orange the activated one and in green the used catalyst.

All the isotherms shown in Figure 4.26 fall under the category of Type IV behavior typical of mesoporous materials, with hysteresis loops in the H3 class [25] which typically indicates the presence of slit-shaped mesopores, or pores formed by plate-like particles. Looking across fresh, activated, and spent samples, the overall H3-type loop shape persists, although the extent of the hysteresis can change due to pore sintering, partial collapse, or pore enlargement over time. In nearly every case, the fresh catalyst exhibits relatively steep adsorption at higher relative pressures, consistent with the presence of mesopores, while the subsequent desorption branch shifts according to the extent of pore blocking or pore connectivity. Upon activation, the overall uptake frequently decreases, mirroring the drop in BET surface area noted earlier, and the hysteresis loop may become more pronounced, suggesting that new mesopores form or existing pores enlarge as carbonates decompose and mixed oxides or carbides emerge [26]. This can be seen, for example, in the Co33 or Co45 samples, where the shift in adsorption capacity matches the significant rearrangements deduced from both pore size distributions and XRD analysis. In contrast, Fe30 and Fe40 often show a reduction in adsorption volume after activation, accompanied by a reduced loop area, pointing to partial sintering or closure of smaller channels. The spent materials, particularly those containing zinc (FeZn), sometimes exhibit a moderate rebound in adsorption capacity, consistent with the removal of surface deposits or further pore rearrangements during reaction. These trends align with the earlier observations that ball-milled samples, despite starting with higher initial surface areas in some instances, can lose more of their porosity upon thermal and reactive treatments, whereas ultrasound-derived catalysts may show either a gentler decline or a partial redistribution of pore sizes [27]. Overall, the previously gathered pore volume and diameter data reinforce the conclusion that each catalyst's thermal history, along with its composition, dictates the precise evolution of mesoporosity through the fresh, activated, and spent phases.

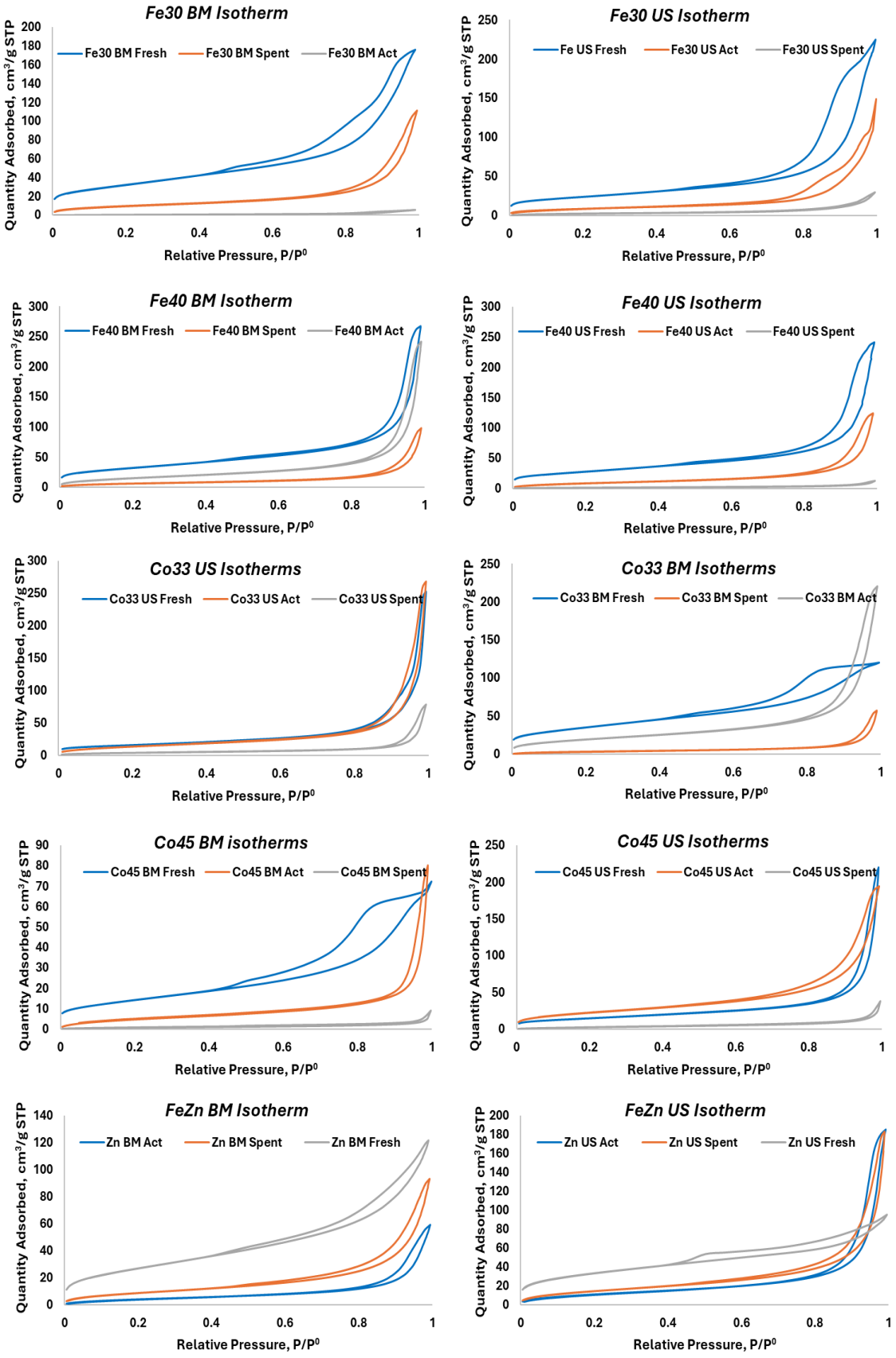

Figure 4.26. Adsorption desorption isotherms of each set of catalysts, as synthetized, activated and spent.

4.3.3. TEM-SEM EDS

4.3.3.1. TEM/ SEM-EDS Fe30 US and BM

Under SEM (Fig. 4.27), the ball-milled (BM) Fe30 sample appears composed of smaller, angular grains, presumably produced by the high mechanical forces of milling. Most particles are irregularly shaped and display sharp edges, quite different from the comparatively smoother agglomerates observed in the ultrasound-prepared sample. At mid-range magnifications, it becomes evident that these particles cluster into larger assemblies, creating a somewhat heterogeneous size distribution. TEM (Fig. 4.27) clearly reveals that the catalysts are composed of nanosized particles with heterogeneous shapes and sizes. The images show that the oxide particles are well-dispersed, forming clusters of crystallites typically below 50 nm. In some regions, sheet-like or platelet morphologies can be distinguished, which are characteristic of partially preserved hydrotalcite-derived structures.

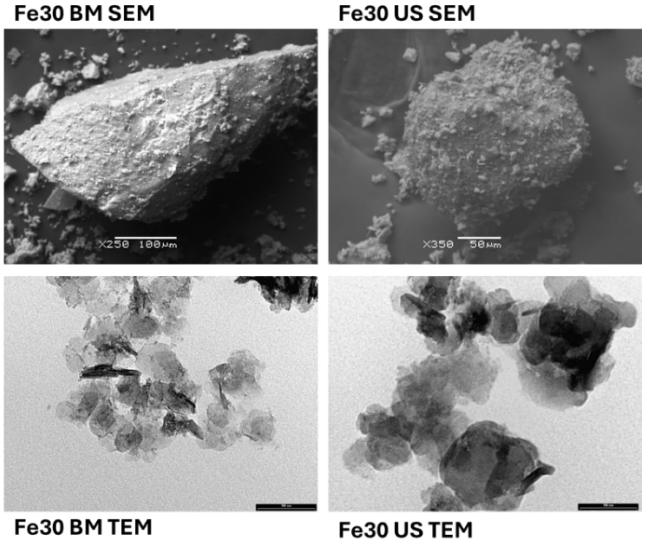

Figure 4.27. SEM and TEM images of Fe30. TEM scale (Black rectangle) is 100 nm.

The accompanying EDS mapping Fig. 4.28 e 29 provides a closer look at how the major elements Fe, Cu, Mg, K, and O are distributed over the particle surfaces.

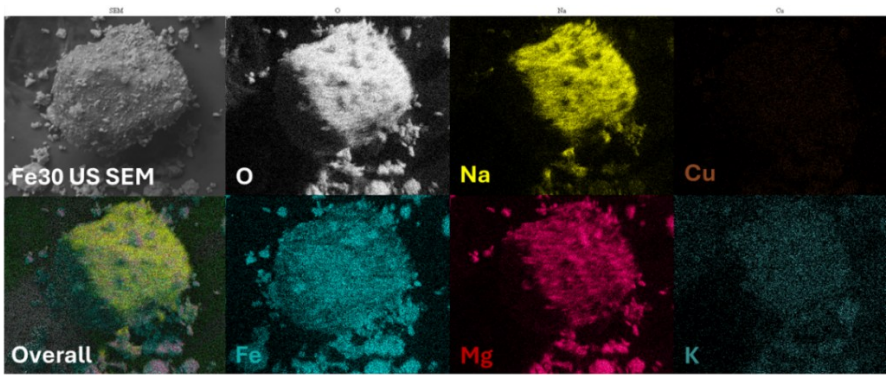

Figure 4.28. SEM-EDS of Fe30 US sample.

Despite the mechanical fragmentation, iron appears relatively well dispersed in the mapped regions, indicating that the milling process does not produce substantial iron-rich "hotspots." Copper exhibits a comparable pattern, although occasional domains show slightly more intense Cu signals, suggesting local variations in how the metals mix or deposit. Magnesium and oxygen

are naturally the most widespread, consistent with the layered, brucite-type framework. Potassium, introduced intentionally as a promoter, shows up in small yet distinct patches, implying that K may not be perfectly homogeneously distributed across all grains but remains present at modest levels (~0.7 wt%).

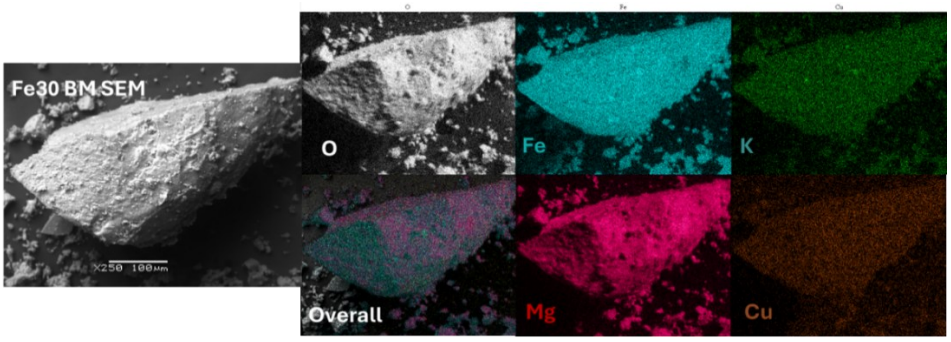

Figure 4.29. SEM-EDS of Fe30 BM sample.

TEM micrographs Fig. 4.27 confirm that these SEM-scale clusters are composed of dense aggregates of nanoscale crystallites. Some of the thinner plate-like particles display partial layering, hinting at the residual lamellar structure characteristic of hydrotalcite-like compounds. However, much of this ordering is disrupted, and edges appear slightly amorphous or rough, indicating that ball milling has generated lattice defects and possibly facilitated local mixing of the metal cations. Variations in electron contrast across the grains, seen in bright-field TEM, likely reflect these microdomains of iron, copper, or magnesium-rich regions, though the overall distribution is still relatively uniform at the nanoscale, consistent with the EDS mapping. Taken together, the SEM-EDS and TEM analyses of fresh Fe30 BM illustrate how mechanical treatment shapes both the morphology and elemental distribution. While the sample remains predominantly a magnesium-iron-copper-based layered material, the ball-milling process disrupts the lamellar structure, creating smaller, more irregular particles in which the key elements remain intermixed at a fine scale. This microstructural state sets the stage for the catalyst's subsequent transformation under thermal activation and can be expected to influence active site accessibility and catalytic behavior during reaction.

- **Fe30 US Activated**

After activation, the ultrasound-derived Fe30 sample Fig. 4.30 presents a mix of rounded particles (~20-50 nm) and smaller, loosely connected domains. High-resolution TEM images reveal lattice fringes with an interplanar spacing of approximately 0.205 nm, which corresponds to an Fe_2C_5 (iron carbide) plane. This identification is consistent with XRD findings suggesting that, under CO/H_2 activation, iron-containing species partially convert into carbides. In the selected-area electron diffraction (SAED) pattern, distinct spots arranged in a roughly concentric fashion confirm that these particles are polycrystalline. SAED is performed by restricting the electron beam to a localized region of the sample, which then generates a diffraction pattern specific to that nano-area. Because each ring or spot in the SAED correlates to atomic planes in the crystal, this method provides local structural information that complements the bulk phase data from XRD. Hence, observing diffraction spots matching the Fe_2C_5 plane spacing at 0.205 nm offers strong evidence of localized carbide formation.

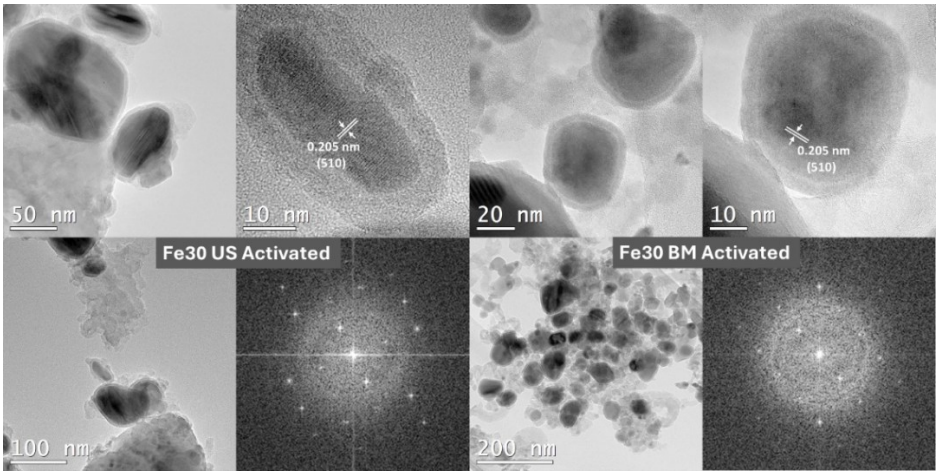

Figure 4.30. Fe30 US and BM HR-TEM.

- **Fe30 BM Activated**

In the ball-milled version of Fe30 Fig. 4.30 activation similarly produces nanometric particles, often appearing as 10-30 nm spheroids or aggregates. Here too, high-resolution images display the characteristic 0.205 nm fringes of Fe_2C_5, confirming that ball milling does not fundamentally change the nature of the carbide phase formed only its distribution and morphology. The SAED pattern reveals multiple ring-like features and discrete spots, indicating the presence of small, randomly oriented crystallites. Again, this local diffraction analysis matches the bulk XRD data in pointing to an iron carbide structure.

Although both activation treatments yield Fe_2C_5 nanocrystals with the same 0.205 nm lattice spacing, the morphology of Fe30 remains strongly route dependent. Ultrasound synthesis preserves rounded stacks of thin lamellae, so the activated solid shows 20-50 nm plate-like grains separated by residual inter-plate voids. Ball-milling, in contrast, compacts the precursor into dense clusters; after activation these appear as near-spherical 10-30 nm crystallites tightly welded together. SAED confirms identical carbide chemistry in the two materials, yet the spatial distribution differs lamellar coatings in the US sample versus numerous, randomly oriented nanocrystals in the BM analogue. This structural divergence mirrors earlier textural data: Fe30-US retains higher mesoporosity and external surface area, whereas Fe30-BM exhibits a more micro-mesoporous, compact framework that may influence active-site accessibility during reaction.

4.3.3.2. TEM/ SEM-EDS Fe40 US and BM

The SEM micrographs of Fe40 US (Fig. 4.31, left image) display densely intergrown plate-like particles that form continuous, cauliflower-like crusts on the micrometre scale. At 100 k× (200 nm bar) the surfaces are covered by stacked lamellae only a few tens of nanometres thick; zooming to 500 k× (20 nm bar) resolves individual, slightly curved platelets 30-80 nm across. Their rounded edges suggest that the ultrasound synthesis favours gentle aggregation rather than the sharp fracture facets seen for ball-milled materials.

Elemental maps collected on the same region (Fig. 4.31, right) confirm that Mg, Fe and O are evenly distributed throughout the plates, indicating a well-mixed hydrotalcite-like matrix. Cu appears as a fine, nearly ubiquitous speckle pattern rather than isolated “hot spots”, implying that

the copper phase is finely dispersed consistent with the absence of Cu-rich reflections in the fresh XRD pattern.

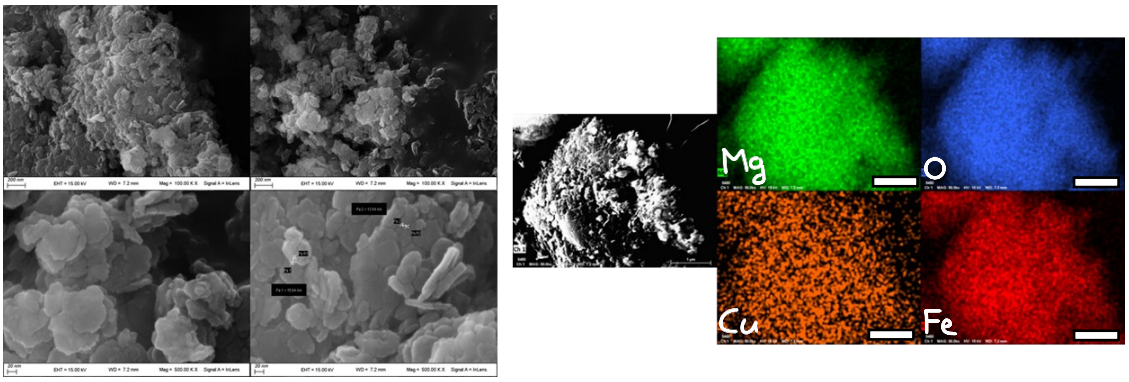

Figure 4.31. Fe40 US SEM analysis on the left at different magnifications and EDS mapping on the right, white bar displays scale of 1 µm.

TEM images (Fig. 4.32) provide a complementary, higher-resolution view. Clusters 80-120 nm wide are built from quasi-hexagonal nanoplates 10-25 nm thick whose outlines are just visible at the particle periphery. The internal contrast varies smoothly, suggesting that the individual lamellae overlap in projection and retain a degree of lattice order typical of hydrotalcite layers. No large crystalline domains or metal clusters are apparent, again pointing to an intimate mixing of Mg, Fe and Cu at the nanoscale.

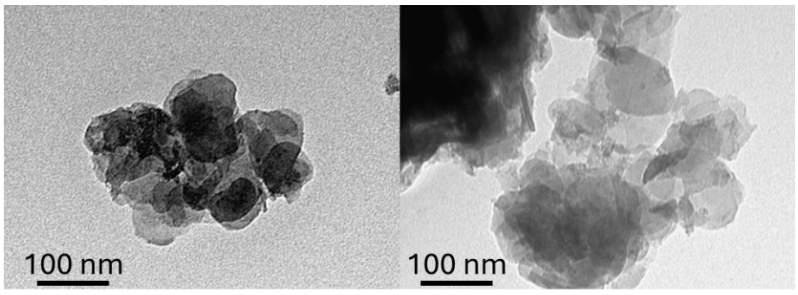

Figure 4.32. TEM images of Fe40 US sample.

Overall, the microscopy of Fe40 US depicts a highly lamellar material with uniform metal distribution and plate thickness in the tens-of-nanometres range. This morphology is expected to give a relatively high external surface but also a significant fraction of slit-shaped mesopores features already hinted at by the H3 hysteresis loop and the mid-range mesopore volume in the BET data. The fine Cu dispersion observed here is a favourable starting point for later activation, when copper is expected to segregate into redox-active sites without causing excessive sintering.

The ball-milled Fe40 sample looks denser and more compact than the ultrasound-derived material discussed earlier. At 50 k× (200 nm bar) the SEM image (Fig. 4.33, left image) shows broad, almost featureless fracture planes separated by occasional shrinkage cracks. Moving to 100 k× and 250 k× (Fig. 4.33, left image) the apparently smooth surface resolves into tightly interlocking nanosheets, their edges curling upward like scales on a fish. A further zoom to 500 k× (20 nm bar, Fig. 4.33, left image) reveals individual lamellae only 10-15 nm thick; a few isolated platelets measure ~35 nm across, consistent with the size markers super-imposed in the micrograph. These sheets lie flush against one another, leaving narrow slit-like voids a morphology that usually translates into H3-type hysteresis in N_2 isotherms, exactly what the BET data show for Fe40.

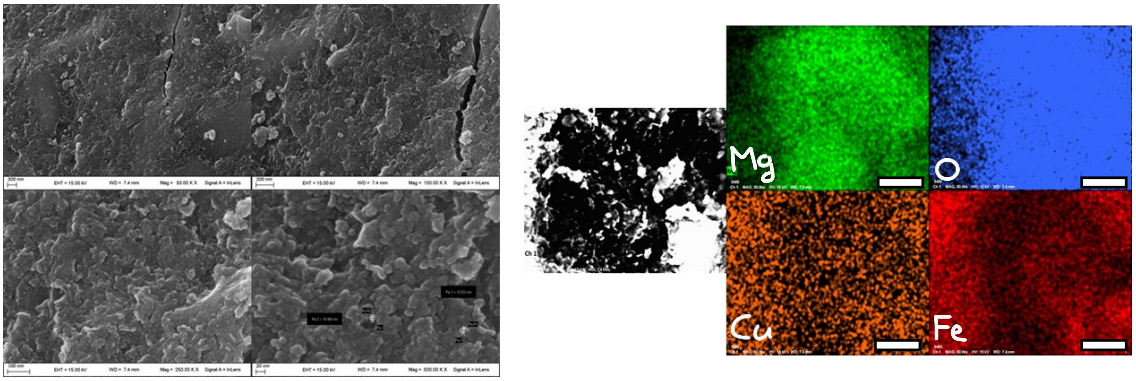

Figure 4.33. Fe40 BM SEM analysis on the left at different magnifications and EDS mapping on the right, white bar displays scale of 1 μm.

Elemental maps acquired on the same region (Fig. 4.33, right image) confirm that Mg, Fe, Cu and O are homogeneously distributed across the lamellar crust. Copper appears as a finely speckled signal, suggesting nanometric dispersion rather than segregated islands, while iron shows a continuous background appearance.

TEM images (Fig. 4.34) provide a complementary view. Aggregates 80-150 nm in diameter are built from overlapping nanoplates only a few nanometres thick; their outlines are discernible at the particle periphery, but the interiors appear almost solid because the plates are closely stacked.

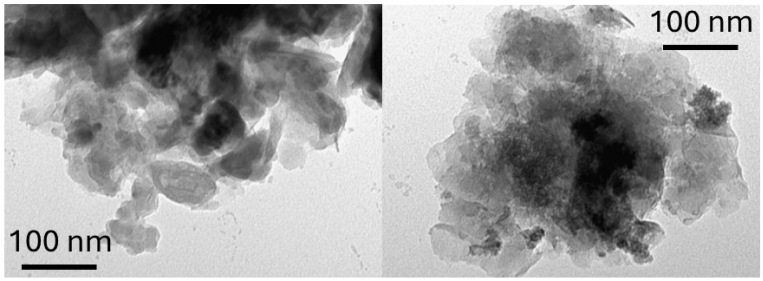

Figure 4.34. TEM images of Fe40 BM sample.

Compared with Fe40 US where individual lamellae remain partially separated Fe40 BM clearly shows tighter packing and fewer inter-plate voids; this is consistent with the lower pore volume measured for the ball-milled sample in the fresh state. No distinct Cu- or Fe-rich nanoparticles are observed, supporting the EDS evidence that both metals are still incorporated in the hydrotalcite framework at this stage.

A direct comparison of the two preparation routes shows that ultrasound and ball-milling drive Fe40 toward different microstructures. The ultrasound-derived solid crystallises as light, open aggregates of thin hydrotalcite plates. In the SEM these plates give the surface a “cauliflower” relief and, under TEM, remain partially separated so that inter-plate voids survive throughout the cluster. Elemental maps reveal a uniform dispersion of Mg, Fe and Cu across these lamellae. Texturally, the loose packing of the plates explains both the higher external surface area and the broad H3 hysteresis loop centred in the mid-mesopore range recorded by nitrogen sorption. Ball-milling, in contrast, forces the same lamellae into dense, continuous crusts. SEM shows extensive flat fracture planes that crack only where the mechanical stress is highest; at higher magnification these planes resolve into tightly interlocking nanosheets. TEM confirms that the plates lie almost flush against each other, giving the aggregates an apparently solid interior and leaving only

narrow slit-like pores. The EDS maps remain chemically uniform Mg, Fe and Cu are still intimately mixed, and the overall particle packing becomes much more compact. This denser architecture translates into a lower external surface area and a larger fraction of micropores and very small mesopores in the BET analysis.

Raising the iron content from 30 mol % to 40 mol % makes Fe40 essentially a denser, iron-richer analogue of Fe30. In the fresh state, SEM and TEM show that both catalysts consist of thin hydrotalcite plates, but those plates are slightly thicker and more tightly stacked in Fe40, which might explain the small drop in BET surface area and the shift toward finer (< 5 nm) pores recorded for that material. Elemental mapping confirms that iron, magnesium and copper remain uniformly mixed in both solids, with the higher Fe loading in Fe40 simply intensifying the Fe signal without introducing new compositional heterogeneity. Under CO/H_2 activation the same Fe_2C_5 and spinel phases appear in both catalysts; XRD in fact suggests these domains develop a little more rapidly and strongly in Fe40, as one would expect from the greater iron supply. Beyond these points, the two materials behave alike, and no additional structural complexity emerges from the modest increase in iron.

4.3.3.3. TEM/ SEM-EDS Co33 US and BM

The ultrasound-synthesised Co33 sample consists of thin, plate-like crystallites tightly stacked into ragged, cauliflower-style aggregates. In the SEM images (100 k× and 250 k×) individual lamellae appear 30-45 nm across and only a few nanometres thick; at 500 k× the edges curl slightly, exposing slit-shaped gaps between plates. Elemental mapping shows Mg, Co, Fe, Cu and O distributed uniformly over the same region, with no cobalt-rich islands or copper hotspots, evidence that the ultrasound route mixes the metals homogeneously at the micron scale.

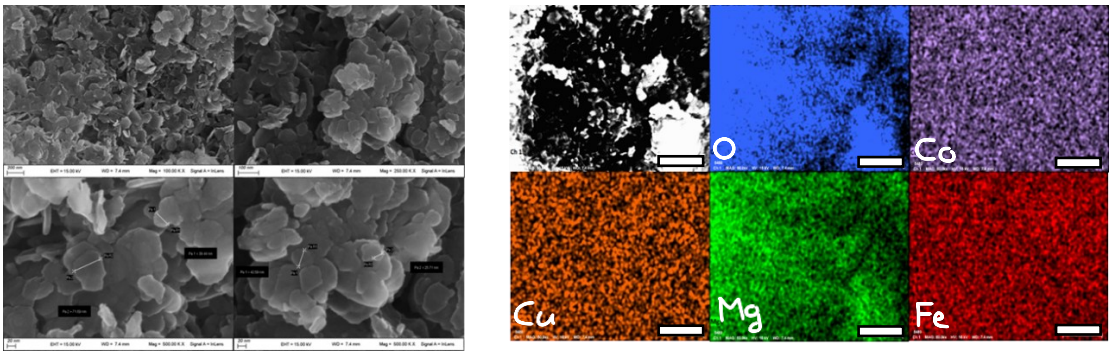

Figure 4.35. Co33 US SEM analysis on the left at different magnifications and EDS mapping on the right, white bar displays scale of 1 μm.

TEM confirms the picture: clusters 80-120 nm wide are built from translucent nanoplates that overlap like roof tiles, leaving narrow inter-plate voids. The overall morphology is therefore an open, platelet network in which all cations are intimately blended an arrangement that underpins the relatively high external surface area and mid-mesopore volume recorded for Co33-US in the BET data.

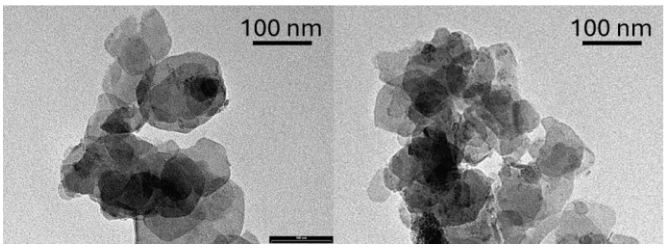

Figure 4.36. TEM images of Co33 US sample.

- **Co33 after activation**

After H_2/CO activation the cobalt catalyst retains the texture seen in the fresh material. SEM (Fig. 4.37, left image) shows that most of the 20 - 30 nm platelets simply sinter, narrowing the inter-granular voids but not collapsing the overall mesoporous network. Element-mapping (Fig. 4.37, right image) confirms that Co, Cu and Fe remain fully co-distributed with Mg layers, while the K promoter is still atomically scattered no cobalt-rich islands or copper segregation can be detected.

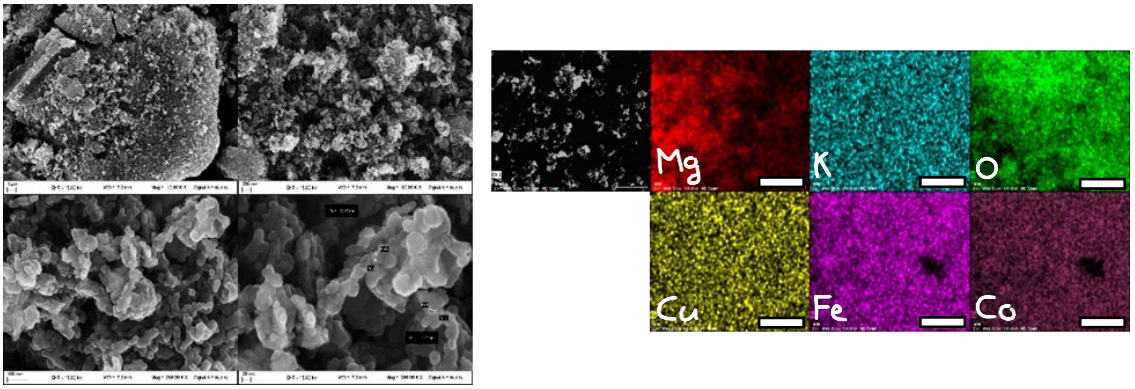

Figure 4.37. Activated Co33 US SEM analysis on the left at different magnifications and EDS mapping on the right, white bar displays scale of 1 µm.

Taken together, the micrograph suggests a topotactic contraction rather than wholesale recrystallisation, explaining why the BET surface area falls only modestly after activation.

The ball-milled fresh Co33 catalyst keeps the same platelet motif seen in the ultrasound sample, but the plates are noticeably thicker and far more densely packed. SEM (Fig. 4.38, left image) reveals broad, almost continuous lamellar carpets; only at 250-500 k× do individual sheets become discernible, measuring roughly 40-80 nm across and 8-15 nm thick. Elemental maps (Fig. 4.38, right image) confirm that Co, Mg, Fe, Cu and O remain evenly mixed throughout the crust milling does not drive cobalt or copper into segregated islands. TEM supports the SEM view: clusters about 100 nm in diameter are built from tightly overlapping nanoplates whose cores look nearly solid because the inter-plate gaps have largely collapsed.

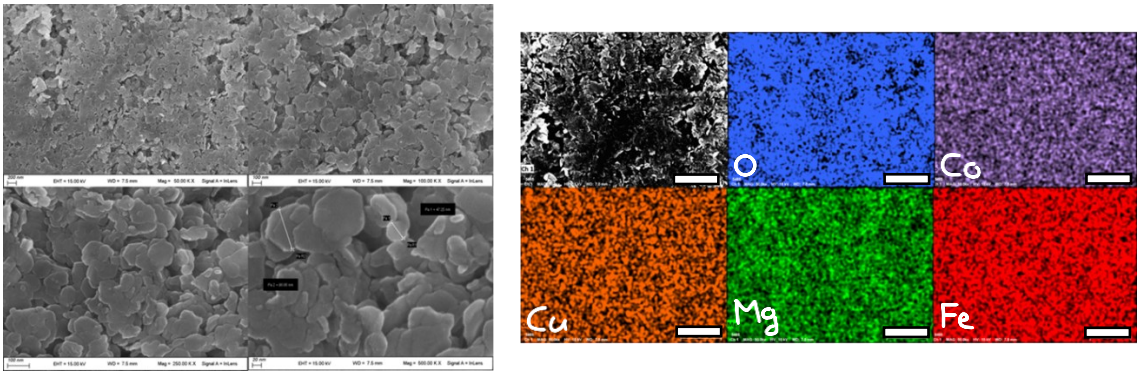

Figure 4.38. Co33 BM SEM analysis on the left at different magnifications and EDS mapping on the right, white bar displays scale of 1 µm.

Ultrasound synthesis leaves an airy stack of thin lamellae with inter-plate voids; ball-milling compresses those lamellae into thicker, closely interlocked sheets. Both routes give homogeneous metal dispersion, but the BM texture is denser, which aligns with its lower fresh surface area and higher fraction of sub-5 nm pores reported by BET.

4.3.3.4. TEM/ SEM-EDS Co45 US and BM

The ultrasound-prepared Co45 catalyst retains the plate-stacked morphology seen in Co33, but the lamellae are noticeably larger and thicker. SEM at 100 k× shows broad piles of overlapping sheets; zooming to 250-500 k× reveals individual plates roughly 60-90 nm across and 8-15 nm thick about twice the lateral dimension measured for Co33-US. TEM confirms that each aggregate is a loose stack of semi-transparent nanoplates whose interiors remain porous.

Elemental maps display a fully homogeneous distribution of Mg, Co, Fe, Cu and O; no cobalt-rich islands or copper segregation is detectable, indicating that the higher Co loading (42 mol %) is still well integrated into the hydrotalcite framework.

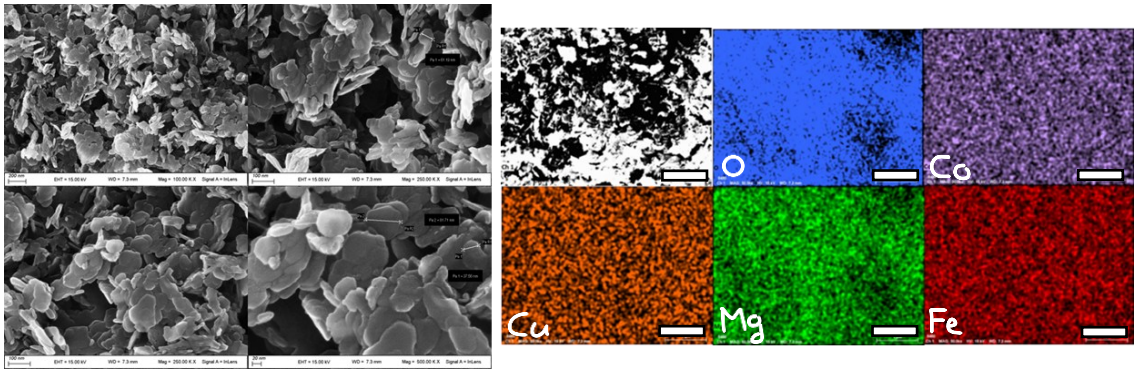

Figure 4.39. Co45 US SEM analysis on the left at different magnifications and EDS mapping on the right, white bar displays scale of 1 µm.

The slightly bulkier plates explain the small drop in BET surface area and the right-shift of the pore-size distribution relative to Co33-US, yet the open stacking means Co45-US still offers ample mesoporosity for gas access.

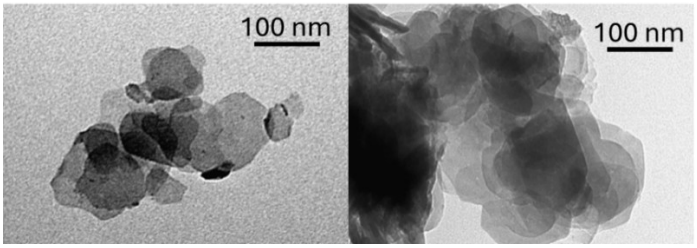

Figure 4.40. TEM images of Co45 US sample.

Ball-milling compresses the Co45 lamellae into a dense crust. Low-magnification SEM (Fig. 4.41, left image) shows broad fracture planes, while at 250-500 k× individual sheets appear 50-90 nm across but lie tightly interlocked, leaving only narrow slit-like voids. EDS mapping (Fig. 4.41, right image) is largely homogeneous for Mg, Co, Fe, Cu and O, though a faint Co/Fe enrichment is visible near the centre of some plates an incipient segregation not seen in the ultrasound analogue.

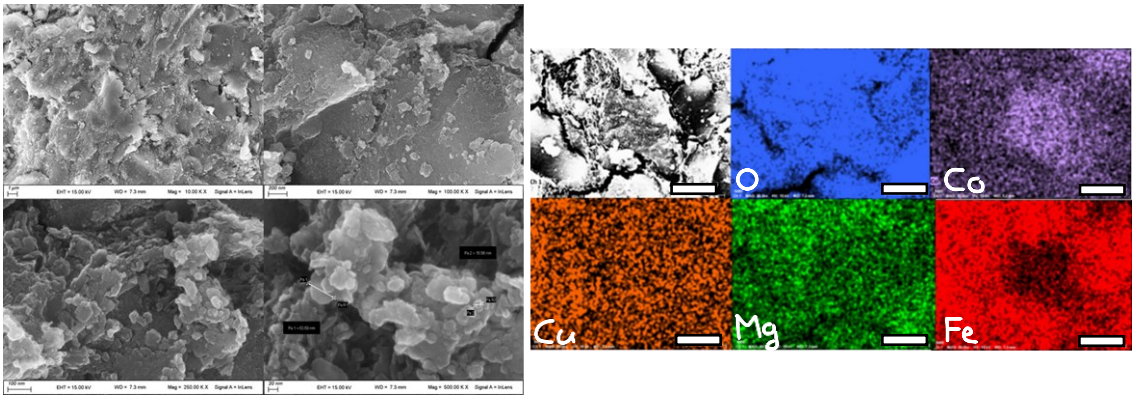

Figure 4.41. Co45 BM SEM analysis on the left at different magnifications and EDS mapping on the right, white bar displays scale of 1μm.

TEM confirms compact 80-120 nm aggregates whose interiors look almost solid because the nanoplates have collapsed onto one another. This morphology explains the lower BET area and the micropore-skewed distribution measured for Co 45 BM.

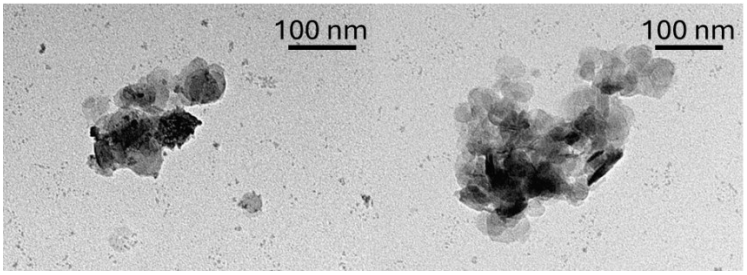

Figure 4.42. TEM images of Co45 BM sample.

Ultrasound keeps Co 45 in open stacks of relatively large plates (60-90 nm) with inter-plate voids; ball-milling forces those plates into a laminated, crack-lined crust. Both materials retain an even Mg/Co/Fe/Cu dispersion overall, but the BM solid shows the first hint of Co-Fe clustering. Texturally, US preserves higher mesoporosity, whereas BM shifts porosity toward the micro-meso boundary and reduces external surface area. Raising the cobalt fraction from 33 to 42 mol % mainly enlarges the lamellae and tightens their packing. Plate thickness and lateral size roughly double, which translates into slightly lower BET area and a modest right-shift in pore sizes for

Co 45, but the basic platelet architecture and homogeneous metal mixing remain unchanged. No additional structural complexity arises beyond these gradual, loading-related adjustments.

4.3.3.5. TEM/ SEM-EDS of FeZn US and BM

Ultrasound synthesis gives FeZn a granular, nearly sponge-like microstructure rather than the plate stacks seen in the Mg/Fe and Mg/Co systems. SEM at 100 k× resolves rounded primary particles 40-70 nm across that join into open, cauliflower-shaped agglomerates. Elemental maps show Zn, Fe, Cu and O uniformly intermixed; the Zn signal is continuous with no large zinc-rich islands indicating that Zn substitutes smoothly into the mixed-metal lattice at this stage. Copper remains finely speckled, while the Fe map mirrors Zn, confirming intimate mixing.

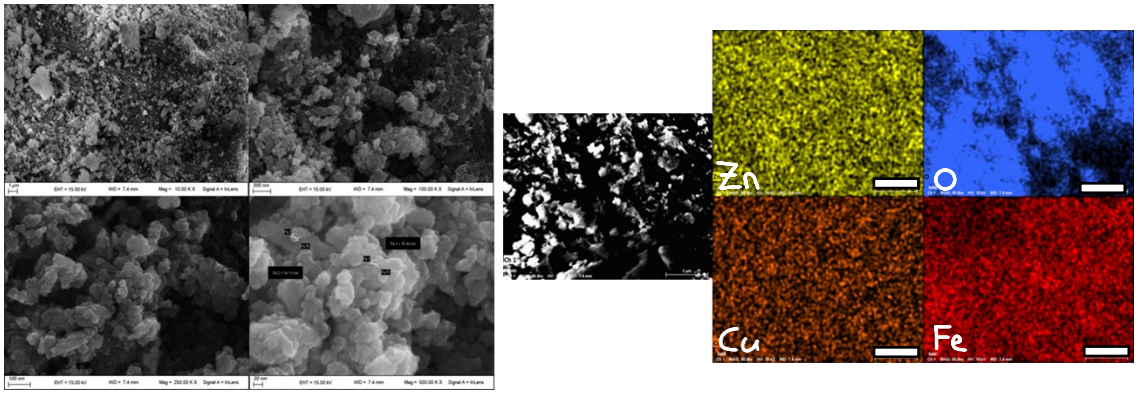

Figure 4.43. FeZn US SEM analysis on the left at different magnifications and EDS mapping on the right, white bar displays scale of 1 μm.

TEM supports the SEM view: each 100-nm cluster is a dense assembly of 5-10 nm sub-grains whose high contrast hints at a less-lamellar, more oxide-like framework. This granular texture explains FeZn-US's distinctive textural data moderate surface area, narrow mesopore range and unusually low microporosity compared with the Mg-based catalysts.

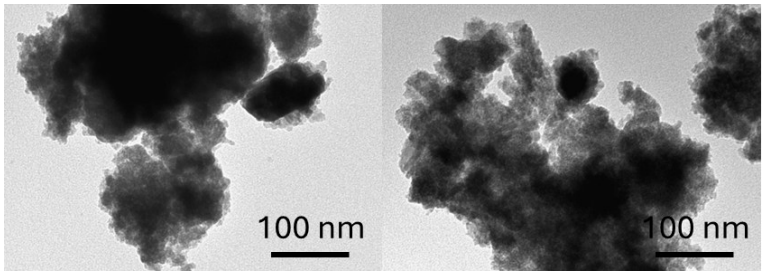

Figure 4.44. TEM images of FeZn US sample.

- **FeZn after activation**

Upon H_2/CO activation the agglomerates seen in the fresh FeZn-US sample tighten only slightly. The 25-35 nm rounded grains fuse at their contact points, but the particle still presents a highly textured, open surface rather than a consolidated block. Element-mapping shows Zn, Fe and Cu remain nearly co-distributed; only a small Zn enrichment appears on a few grain edges [28], in line with the early spinel-type rearrangement suggested by XRD performed after activation.

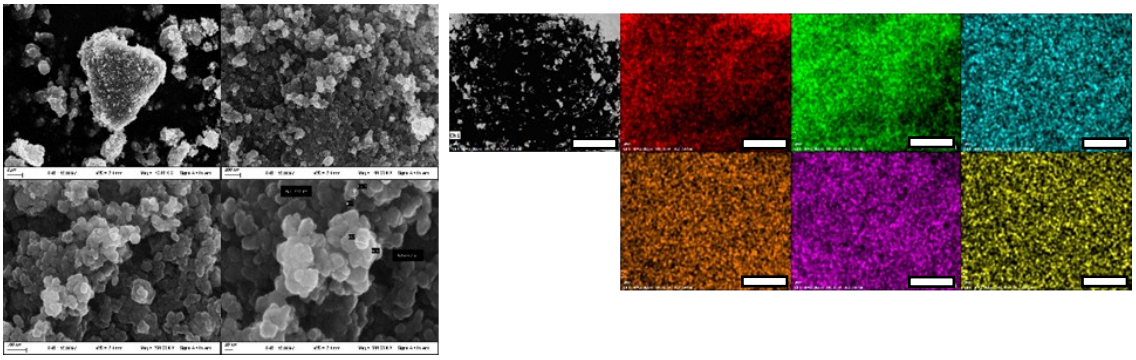

Figure 4.45. Activated FeZn US SEM analysis on the left at different magnifications and EDS mapping on the right, white bar displays scale of 1 μm.

Ball-milling compacts FeZn into dense, cauliflower-shaped agglomerates. SEM (Fig. 4.46, left image) at 50-100 k× shows individual primary particles 30-60 nm across welded into micrometre-sized lumps; higher magnification reveals their surfaces to be built from near-spherical sub-grains rather than plates. TEM corroborates this granular architecture: each 100 nm cluster is a close-packed assembly of 5-10 nm crystallites that leave very little open void space. EDS mapping (Fig. 4.46, right image) remains broadly homogeneous for Zn, Fe and O, yet small Zn-rich cores and Fe-halo domains appear inside a few larger lumps, suggesting that milling has induced slight metal segregation. Copper is still dispersed as fine speckles, similar to the US material.

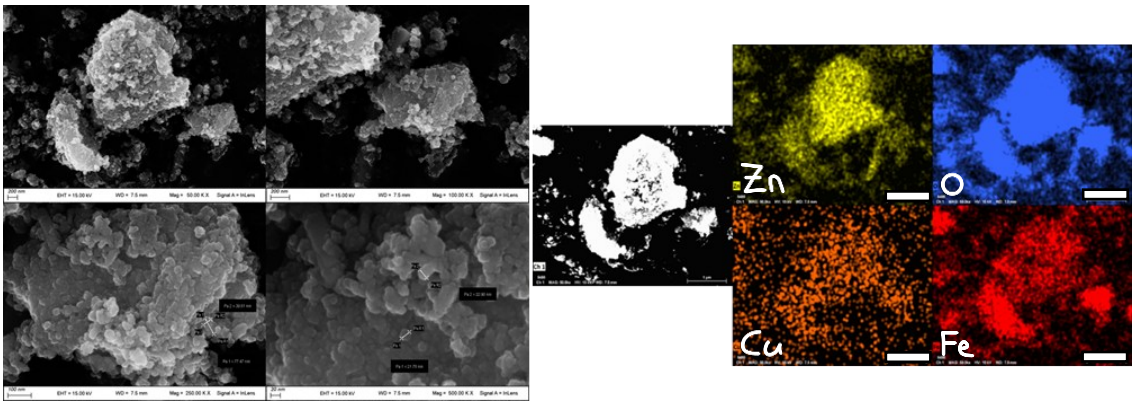

Figure 4.46. FeZn BM SEM analysis on the left at different magnifications and EDS mapping on the right, white bar displays scale of 1 μm.

The collapsed porosity explains the lowest BET area of all fresh catalysts and the dominance of micropores inferred from the sorption data.

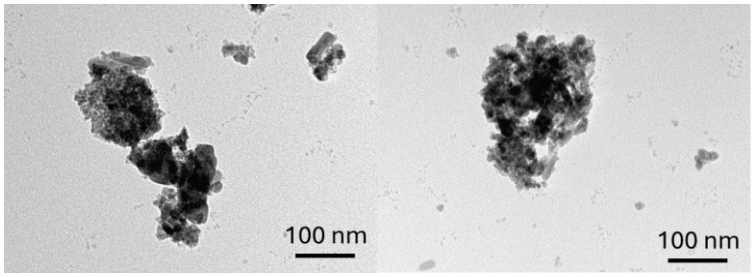

Figure 4.47. TEM images of FeZn BM sample.

In the ultrasound-prepared FeZn, loosely bonded primary grains 40-70 nm in size assemble into a porous, sponge-like network that retains moderate mesoporosity and shows a fully homogeneous mix of Zn, Fe and Cu. Ball-milling compacts these same grains into dense agglomerates; within some of the larger clusters a slight Zn-rich core and Fe-rich halo become

visible, indicating the onset of metal segregation. This compaction lowers the external surface area and shifts the pore profile toward the micro-meso boundary. Thus, as already observed for the Mg-based catalysts, ultrasound preserves an open, highly accessible texture, whereas ball-milling trades surface area for structural compactness.

Across all five compositions a simple pattern emerges:

- Synthesis route dominates texture. Ultrasound keeps lamellae or grains loosely stacked, sustaining higher surface area and broader mesoporosity. Ball-milling collapses the same building blocks into dense crusts or granules, lowering BET area and shifting pores toward ≤5 nm.
- Metal loading subtly tunes plate/grain size. Raising Fe from 30 % to 40 % or Co from 33 % to 42 % thickens lamellae by roughly a factor of two, trimming area but not altering the basic morphology. Substituting Zn abolishes the lamellar habit altogether, producing fine oxide-like grains.
- Elemental distribution stays largely uniform. EDS shows that Mg/Fe/Cu, Mg/Co/Cu, and Zn/Fe/Cu remain intermixed at the micrometre scale in fresh solids; only in ball-milled FeZn do incipient Zn-Fe domains appear.

4.3.4. SEM EDS Spent catalysts

4.3.4.1. Fe-rich hydrotalcites

Fe40-US (ultrasound) retains its fluffy, loosely bonded aggregates even after 40 h on stream. The open, sponge-like network visible in the SEM overview is corroborated by an element map in which Fe, Mg, Cu and promoter K remain finely intermixed; only a faint, sub-micrometric Fe-enriched patch is detectable. The absence of extended Fe-rich crusts suggests that carburised iron nuclei formed in situ did not migrate to the outer surface.

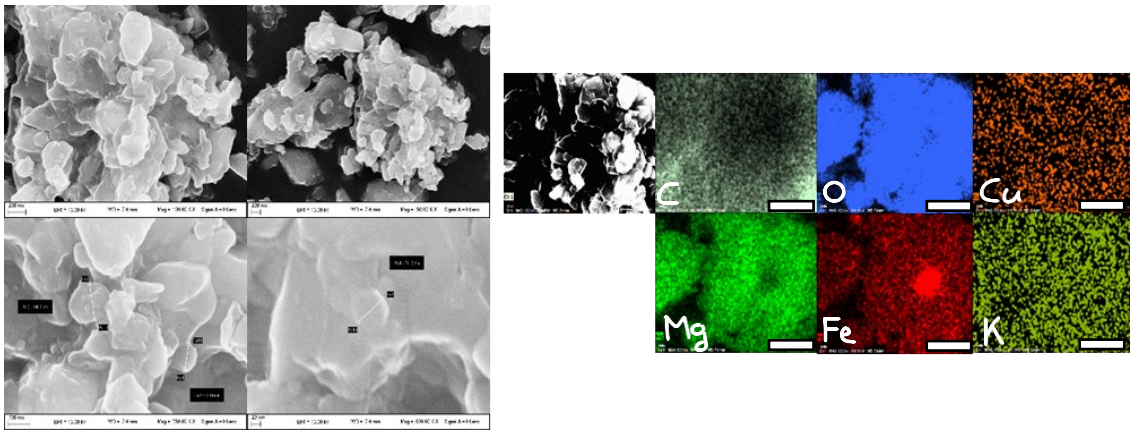

Figure 4.48. Spent Fe40 US SEM analysis on the left at different magnifications and EDS mapping on the right, white bar displays scale of 1 µm.

In sharp contrast, Fe40-BM (ball-milled) evolves into compact, almost sintered agglomerates. Coalesced platelets co-exist with dense spheroids and the EDS map now reveals discrete Fe-rich islands, implying limited outward diffusion of iron under CO-rich conditions. Such local segregation is consistent with the larger BET surface-loss observed for this sample (Table 4.15) and with the sharper iron-carbide reflections seen in the post-run XRD (Section 4.3.1).

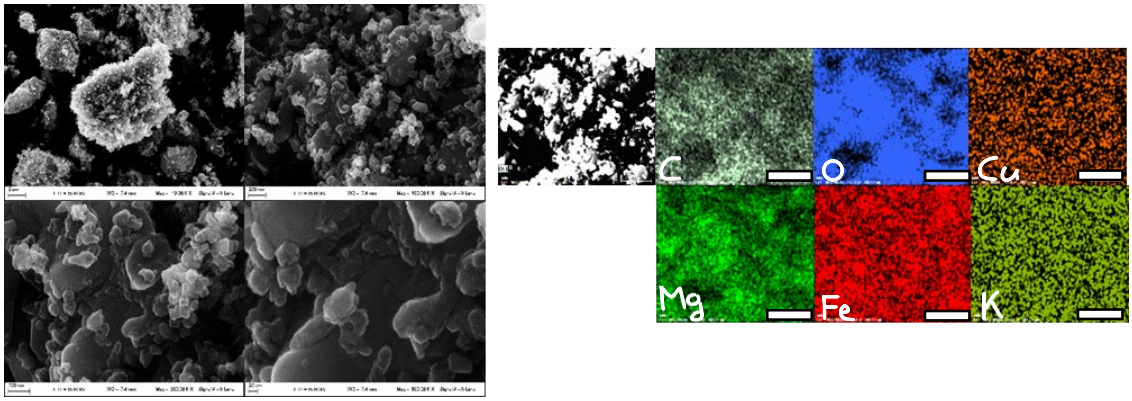

Figure 4.49. Spent Fe40 BM SEM analysis on the left at different magnifications and EDS mapping on the right, white bar displays scale of 1 μm.

4.3.4.2. Co-containing systems

Among the cobalt series, the spent Co33-BM is the most illustrative. Even after reaction the material still shows the small, cauliflower-like grains typical of the fresh sample, indicating that Co^{2+}-Mg^{2+} lamellae are intrinsically more resistant to collapse than their iron-rich analogues. Elemental maps are virtually featureless no Co-rich "hot-spots," no Cu ex-solution demonstrating that bulk cobalt remains well dispersed, in line with the mild surface-area drop registered after use.

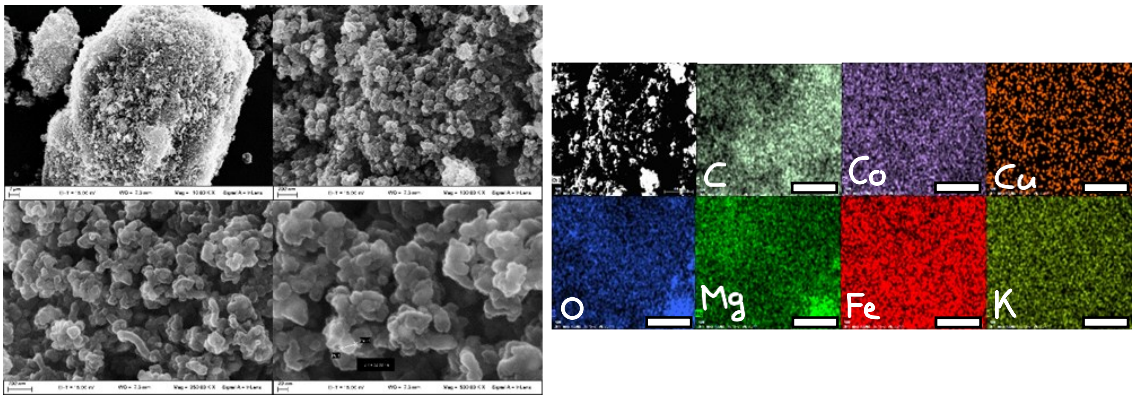

Figure 4.50. Spent Co33 BM SEM analysis on the left at different magnifications and EDS mapping on the right, white bar displays scale of 1 μm.

4.3.4.3. FeZn US catalyst

The spent FeZn-US still displays the loose aggregate of 40-70 nm grains inherited from its fresh precursor. Zinc, iron and copper stay homogeneously co-located, and remarkably no dark carbonaceous crust is visible in back-scatter mode, hinting at the coking-mitigation role of zinc already proposed from TPD-CO_2 data (Section 4.3.5.3).

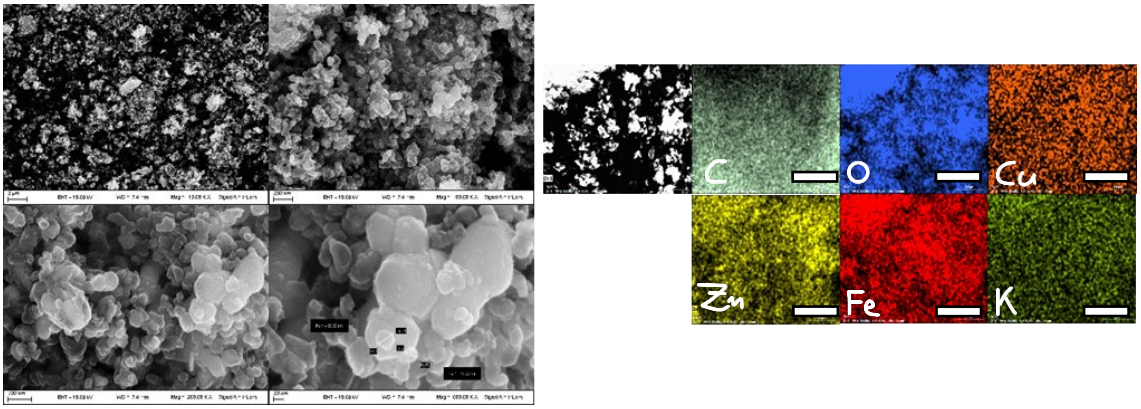

Figure 4.51. Spent FeZn US SEM analysis on the left at different magnifications and EDS mapping on the right, white bar displays scale of 1 μm.

Across every composition examined, the same ageing motif can be recognised. Catalysts prepared by the ultrasound route evolve with minimal structural disruption: the initially open, sponge-like aggregates merely tighten a little and, crucially, the constituent metals remain thoroughly intermixed. Those produced by ball-milling follow a constrictive path instead: individual platelets or nanograins weld into dense clusters, and small pockets of metal segregation mostly for iron begin to appear. Within this framework, cobalt-rich materials prove inherently more resistant to sintering than their iron-rich analogues, while the inclusion of zinc clearly moderates both grain densification and the build-up of surface carbon. The microstructural hierarchy observed here aligns perfectly with the residual BET surface areas measured after reaction (ultrasound > ball-milling) and helps to explain why ultrasound-derived Fe and Zn catalysts sustain higher productivity over time (see Chapter 5)**.** It also sheds light on the sharper X-ray reflections recorded for spent ball-milled samples: larger, locally enriched crystallites scatter the X-ray beam more coherently than the finely mixed domains preserved in the ultrasound series.

4.3.5. Gas-solid interactions

4.3.5.1. TPR -H_2 General trends

It should be noted that the as-synthesized catalysts are hydrotalcite-type hydroxides. During the TPR experiment (*conditions reported in Chapter 4.1.6.1*), these precursors decompose (loss of OH^- and CO_3^{2-}) to form mixed oxides and/or spinel phases in situ, which are then reduced under H_2. Accordingly, the following discussion assigns the observed peaks to the reduction of oxide species formed during this decomposition

Fe-Based Catalysts (Fe30 and Fe40)

Ultrasound-Synthesized Fe30/Fe40: The Fe-based catalysts show the expected two-step reduction of iron oxide. In Fe30 and Fe40 prepared by ultrasound (US), the H_2-TPR profiles exhibit a first peak around 300-350 °C, corresponding to the reduction of Fe_2O_3 (hematite) to Fe_3O_4 (magnetite). A second broad feature or shoulder appears at higher temperature (~450-500 °C), attributable to further reduction of Fe_3O_4 to metallic Fe (or possibly iron carbides, Fe_xC_y, under CO/H_2). The relatively sharp, well-defined peaks in the US samples indicate a more crystalline iron oxide phase with minimal mixing into the support. This aligns with XRD observations that ultrasound synthesis yields highly crystalline structures, as also noted in literature for sonochemically prepared oxides [29]. After an activation pre-reduction (e.g. H_2/CO at 350 °C), the ultrasound Fe

catalysts show greatly diminished TPR signals. The main Fe_3O_4 reduction peak is much smaller or absent in the activated sample, indicating that most Fe_2O_3/Fe_3O_4 was already reduced to Fe^0 (and possibly carburized) during activation. Only a minor low-temperature feature (~200 °C) may remain, suggesting the presence of easy-to-reduce species like iron carbides formed during. In summary, ultrasound-prepared Fe30/Fe40 catalysts are readily reducible: Fe_2O_3 reduces in a clear two-step process at relatively low temperatures, and activation reduces a majority of the iron oxide phase.

Ball-Milled Fe30/Fe40: In Fe30 and Fe40 prepared by ball milling (BM), the overall reduction profile shifts and broadens, evidencing stronger metal-support interactions and possibly mixed-phase formation. The initial $Fe_2O_3 \rightarrow Fe_3O_4$ reduction appears as a broad peak spanning ~280-330 ° slightly lower in onset but much less sharp than in the US sample. This broadening suggests the Fe_2O_3 is highly dispersed or partially incorporated into other phases, rather than existing as well-defined crystallites. A second reduction step for $Fe_3O_4 \rightarrow Fe$ shifts to higher temperatures (~500-600 °C). This high-T shoulder is significantly more pronounced in the BM catalysts, indicating that a fraction of iron oxide is much harder to reduce. Such behavior points to strong Fe-support interactions or formation of mixed oxides that require more energy to reduce. Indeed, incorporating Fe into a magnesium oxide matrix can yield magnesium ferrite ($MgFe_2O_4$) spinel, which is less reducible than pure Fe_2O_3 [30]. The literature shows that $MgFe_2O_4$ and similar mixed spinels resist reduction; for example, α-Fe_2O_3 alone shows a clear two-peak TPR ($Fe_2O_3 \rightarrow Fe_3O_4$ at ~370 °C and $Fe_3O_4 \rightarrow Fe^0$ at higher T) [30], whereas in Fe-Mg mixed oxides the $Fe_2O_3 \rightarrow Fe_3O_4$ peak shifts to lower temperature (due to facilitated initial reduction) but the overall hydrogen consumption decreases because some Fe is tied up in $MgFe_2O_4$ [30]. The $MgFe_2O_4$ itself is quite difficult to reduce fully, essentially acting as a structural stabilizer that does not readily convert to metal under H_2 [30].

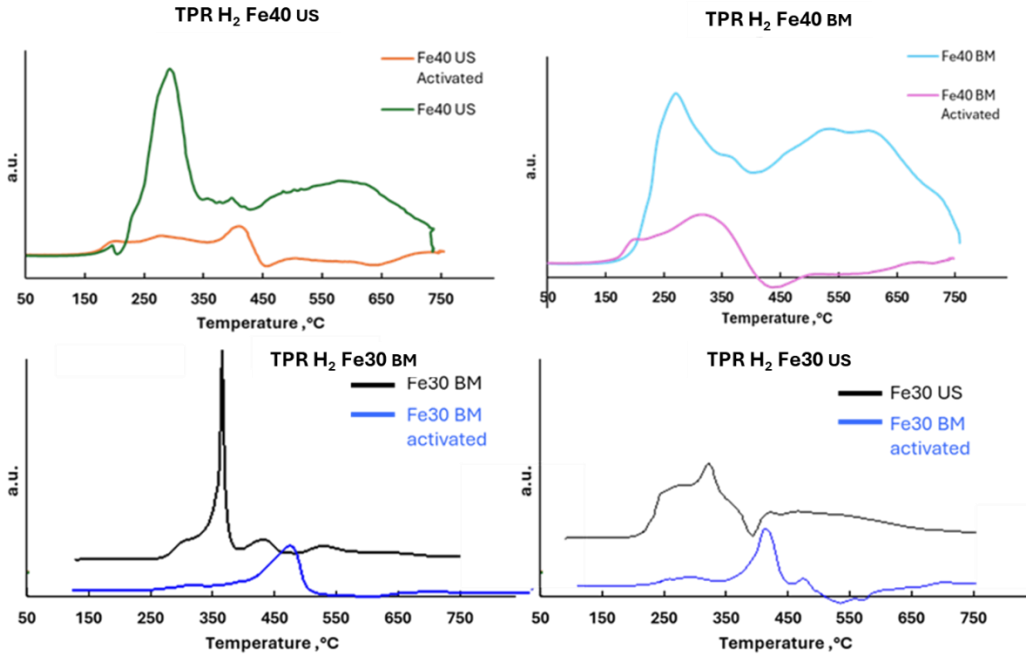

Figure 4.52. Temperature programmed reductions of Fe30 and Fe40 both US and BM samples.

This explains why Fe40 BM shows residual reduction up to 600 °C: mechanical milling likely promoted the formation of $MgFe_2O_4$ or similar robust phases, making the final Fe^0 formation step

more difficult. By contrast, the Fe30/Fe40 US samples likely retained more free Fe_2O_3 (separate from Mg), which undergoes complete reduction at lower temperatures. After activation, the ball-milled Fe samples still exhibit considerable TPR peaks. Notably, a broad feature around 400-500 °C remains in the activated Fe40 BM, indicating that a significant portion of iron oxide was *not* reduced during the 350 °C activation. This contrasts with the US case and confirms that strong Fe-support bonding in BM samples hinders reduction by H_2/CO at moderate temperatures. Only upon the subsequent TPR (to higher T) do this oxide species reduce. Such behavior is analogous to known solid solution formation in mechanochemically treated systems: for example, NiO interacting with MgO can form Ni^{2+} in MgO (solid solution or spinel) that is non-reducible or only reduces at much higher T [31]. In a Ni/MgO study, higher-temperature calcination led to Ni^{2+} incorporation into MgO (NiO-MgO solid solution) which "hindered… reducibility" and eventually became "non-reducible" NiO-MgO by 1000+ K, whereas physically mixed NiO remained easily reducible at lower temperature [31]. Similarly, ball milling increases atomic-scale mixing between Fe and the surrounding matrix (Mg, Cu, or Al), producing tightly bound oxide environments that shift TPR peaks to higher temperatures due to stronger interactions and reduced reducibility. In summary, Fe30 and Fe40 TPR data demonstrate that ultrasound synthesis yields Fe oxides reducible in the typical two-step manner (~350 °C and ~500 °C), while ball milling produces more stabilized oxide domains that require >500 °C for full reduction. The key point is that mechanical processing alters reducibility: US samples are largely reduced by activation (TPR peaks nearly vanish), whereas BM samples retain hard-to-reduce oxides even after activation, confirming less accessible or more stabilized phases.

Co-Based Catalysts (Co33 and Co45)

Ultrasound-Synthesized Co33/Co45: The Co-based catalysts also exhibit distinct reduction behavior depending on preparation. In Co33 and Co45 ultrasound samples, the dominant TPR peak occurs around 320-350 °C. This is the characteristic reduction of $Co_3O_4 \rightarrow CoO \rightarrow Co^0$ in hydrogen. Cobalt (III) oxide (Co_3O_4) typically reduces in two steps: Co^{3+} to Co^{2+} (Co_3O_4 to CoO) followed by Co^{2+} to Co^0 (CoO to metallic Co) [32]. In many cases these steps are close in temperature and can appear as a single composite peak or two overlapping peaks around the mid-300 °C range [32]. The sharp, narrow peak near 330 °C in Co33/Co45 US suggests a well-defined Co_3O_4 phase that reduces readily, again indicating good crystallinity and relatively independent Co oxide domains. A very minor H_2 consumption up to ~500-600 °C is observed in the fresh US samples as a weak shoulder. This faint high-T feature could be due to a small fraction of cobalt interacting with other elements (e.g. a Co-Fe mixed oxide or a cobalt ferrite spinel if Fe is present in the catalyst). However, in the ultrasound case this fraction is low - the overall reduction is "clean and well-defined", and the major Co_3O_4 phase is reduced at the expected low temperature. After activation, the Co_3O_4-related peak essentially disappears in Co33/Co45 US, confirming that most cobalt oxide was already reduced to Co^0 during the H_2/CO pretreatment. The activated US samples show only very weak residual signals around 500-600 °C, which likely correspond to trace amounts of residual oxidic cobalt (or perhaps cobalt carbides) that resisted the mild activation. In essence, the ultrasound Co catalysts are highly reducible: their Co_3O_4 converts to metallic Co at ~350 °C, and a standard activation step largely accomplishes this reduction, leaving little for the subsequent TPR.

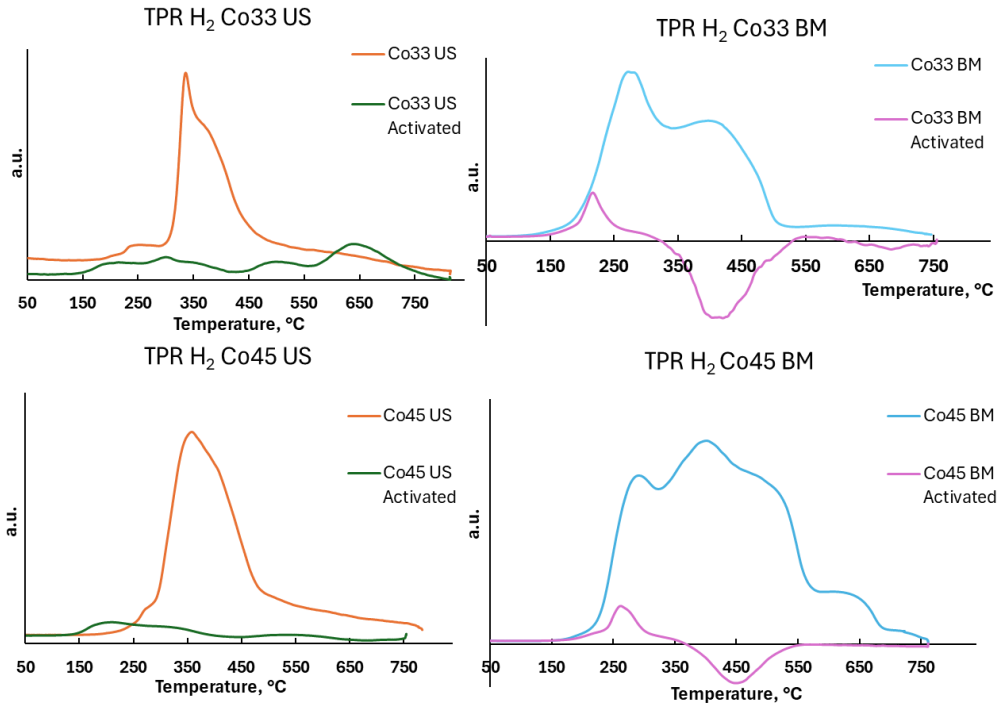

Figure 4.53. Temperature programmed reductions of Co33 and Co45 hydrotalcite catalysts.

Ball-Milled Co33/Co45: The activated Co33 and Co45 BM samples show markedly broader and higher-temperature reduction features. For Co45 BM, the TPR profile lacks a sharp 330 °C peak; instead, there is a broad reduction band spanning ~300-500 °C. This indicates that the two-step Co_3O_4 reduction is no longer well-resolved - $Co^{3+} \rightarrow Co^{2+}$ and $Co^{2+} \rightarrow Co^0$ transitions likely overlap over a wide temperature range due to a distribution of cobalt oxide environments. The broadening and upward shift suggest cobalt oxide is interacting strongly with the support or with Fe/Mg in the catalyst, making it less accessible to H_2. Indeed, a very broad tail extending beyond 600 °C is present for Co45 BM, implying the presence of an especially refractory phase. One likely candidate is cobalt ferrite ($CoFe_2O_4$) or related mixed oxides if Fe is in the formulation. Cobalt ferrite spinel, which could form when Co and Fe oxides are intimately milled together, is known to be much harder to reduce than pure Co_3O_4. For example, $CoFe_2O_4$ prepared from nitrate precursors shows a main H_2-TPR peak at ~530 °C (attributed to Co^0 and Fe_3O_4 formation) [33], and typically $CoFe_2O_4$ exhibits multiple reduction peaks around 350-550 °C (with the complete reduction to $Co^0 + Fe^0$ only achieved at the higher end of this range) [34]. In the Co45 BM catalyst, the TPR tail >600 °C suggests some $CoFe_2O_4$-like phase or strong Co-support compound that isn't fully reduced until very high temperature. The Co33 BM sample (which likely has a Co:Fe ratio near the stoichiometry for $CoFe_2O_4$) also shows evidence of mixed-phase behavior. Its TPR has a distinguishable peak around 300-350 °C, indicating that not all Co is in a strongly interacting form - some Co_3O_4-like phase still reduces at the normal temperature. However, Co33 BM also has significant H_2 consumption continuing beyond 500 °C, pointing to a portion of Co that is in a more resistant state (likely as cobalt ferrite or Co-support complexes). After activation, the differences become even clearer: activated Co-BM samples still require substantial high-temperature reduction, whereas activated Co-US samples do not. For Co45 BM, the post-activation TPR shows remaining peaks in the 400-600 °C range meaning the 350 °C H_2/CO treatment failed to fully reduce some cobalt species. This is consistent with a strong cobalt-support

interaction (e.g. formation of Co-Fe spinel or cobalt silicate/aluminate if the support were SiO_2/Al_2O_3) that prevents reduction at 350 °C. Co33 BM after activation similarly shows a broad 400-600 °C reduction profile, indicating residual mixed oxide phases. Notably, Co33 BM's activated TPR still resembles the fresh profile in the high-T region, suggesting the same hard-to-reduce cobalt-iron oxide persists through activation. These results echo the Fe-catalyst case: ball milling creates integrated Co-Fe oxides that are stable against reduction. Literature on strong metal-support interactions (SMSI) supports this interpretation - when a transition metal oxide forms a compound with another oxide (support), its reduction peak shifts to higher T due to the stronger bonding. For instance, Ni^{2+} ions in a MgO matrix (Ni-MgO solid solution) require much higher temperatures to reduce than NiO crystallites [31]. Likewise, Co in a Fe_2O_3 or oxide matrix (cobalt ferrite spinel) has reduction peaks hundreds of degrees higher than free Co_3O_4 [33, 34]. TPR cannot directly identify the phase causing the >600 °C consumption, but given the catalyst composition, a reasonable inference (supported by the data and references) is cobalt ferrite. We avoid definitively assigning every peak to a phase without corroborating XRD, but we can state: the BM samples clearly exhibit broad, high-T TPR features symptomatic of complex oxide phases (Co-Fe spinel or strongly bound Co oxide), whereas the US samples show mostly Co_3O_4 reduction at low T. In summary, ultrasound Co33/Co45 catalysts reduce readily (sharp 320-350 °C peaks, little residual after activation), whereas ball-milled catalysts show hindered reducibility (broad 300-500 °C reduction and significant >500 °C peaks), reflecting strong interactions and possibly spinel formation. This means mechanical treatment incorporated cobalt into a mixed lattice that H_2 finds harder to reduce, consistent with known SMSI effects where reduction peaks shift to higher temperature with increased metal-support interaction [35].

Zn-Containing Catalysts

The Zn-based catalyst in this series exhibits TPR behavior influenced by the reducibility of multiple metal oxides. Notably, pure ZnO itself is *not* readily reducible by H_2 - in TPR experiments ZnO generally shows no distinct reduction peak up to high temperatures [36]. Any hydrogen consumption in Zn-Fe samples, therefore, is mainly due to the reduction of iron oxides (or other reducible components like Cu, if present), while ZnO remains as ZnO (or converts to Zn metal only at extremely high T, beyond typical TPR ranges).

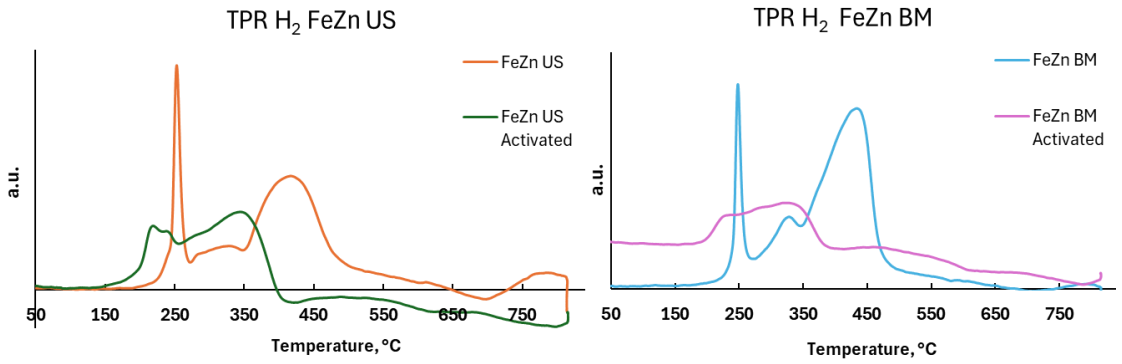

Figure 4.54. Temperature programmed reduction of FeZn catalysts.

Ultrasound-Synthesized ZnFe: The fresh ZnFe catalyst prepared by ultrasound shows multiple peaks corresponding to its multi-component nature. If the catalyst is a Zn-Fe binary (e.g. $ZnFe_2O_4$ spinel plus perhaps excess ZnO or Fe_2O_3), we would expect a two-step Fe-based reduction similar

to Fe_2O_3/Fe_3O_4, albeit modified by Zn. In the provided data for a ZnCuFe ultrasound sample (which we assume is similar, with Cu as an additional reducible component), distinct low-temperature peaks were observed: one around 200-250 °C and another around 300-350 °C. These were initially attributed in the draft to "ZnO and CuO" reductions, but based on known chemistry, it is more likely the peak at ~250 °C is $CuO \rightarrow Cu^0$, and the ~300-350 °C peak is related to $Fe_2O_3 \rightarrow Fe_3O_4$. Copper(II) oxide reduces easily in H_2 (often ~200-250 °C for dispersed CuO), whereas ZnO does not reduce at 300 °C without a facilitator. In a Zn-Fe-Cu system, the presence of Cu can actually promote reduction of Fe_2O_3 via hydrogen spillover [30], potentially lowering the $Fe^{3+} \rightarrow Fe^{2+}$ step temperature. Thus, the US ZnFe(Cu) catalyst likely has: CuO reducing at ~240 °C (giving a sharp peak for Cu^0 formation), followed by Fe_2O_3 reducing around 300-350 °C. Any ZnO present would remain largely unreduced (no clear ZnO peak), consistent with ZnO's inertness in TPR [36]. After those, a broad shoulder from ~400 up to 600 °C appears. This high-temperature region corresponds to the further reduction of iron oxides: notably conversion of Fe_3O_4 to FeO/Fe^0, and possibly the reduction of any $ZnFe_2O_4$ spinel phase present. $ZnFe_2O_4$ typically reduces in a stepwise fashion where Fe^{3+} is reduced to Fe^{2+} (forming Fe_3O_4 and ZnO) at an intermediate temperature, and then Fe^{2+} to Fe^0 at a higher temperature (while ZnO persists) [30]. The distinct separation of peaks in the US sample suggests the phases are relatively well-defined: e.g. CuO, Fe_2O_3 (or a separate $ZnFe_2O_4$ phase) each reducing in turn. This points to a structured, less-intermixed system, consistent with ultrasound yielding a crystallized multi-oxide where each component behaves somewhat independently. After activation (H_2/CO at 350 °C), the ultrasound ZnFe catalyst's TPR profile is greatly diminished. In the ZnCuFe example, post-activation TPR showed that the low-T peaks for CuO (and any easily-reduced ZnO surface species) had vanished indicating Cu^0 and any reducible Zn species were already formed during activation. The only remaining feature was a residual 500-600 °C signal, implying a small amount of iron oxide (or perhaps a Zn-Fe mixed oxide) still needed to be reduced. This again demonstrates that US-prepared catalysts were mostly reduced by the activation step, leaving only the most stubborn oxides for the TPR.

Ball-Milled ZnFe: The fresh ZnFe catalyst prepared by ball milling exhibits a more convoluted reduction profile, reflecting increased complexity and stronger coupling between Zn and Fe. In the ZnCuFe BM case (as a proxy), the first notable reduction peak is around 240 °C, corresponding to $CuO \rightarrow Cu^0$. The fact that this Cu peak is clearly observed in BM indicates copper oxide is still present as a recognizable phase (albeit likely well-dispersed). Following that, instead of a sharp Fe_2O_3 reduction, the BM sample shows a broad peak around 400-450 °C. This broad feature is attributed to the reduction of iron oxides in a much less uniform environment - likely Fe^{3+} within a $ZnFe_2O_4$ spinel or highly dispersed among ZnO. Compared to the US sample, the $Fe^{3+} \rightarrow Fe^{2+}$ reduction in BM is shifted to higher temperature and spread out, suggesting that Fe is largely tied up in a Zn-Fe matrix that resists reduction. Indeed, mechanical milling is known to facilitate solid-state reactions between components; it likely induced the formation of $ZnFe_2O_4$ spinel during subsequent calcination or even in situ. Such spinel (and generally stronger Zn-Fe interactions) would elevate the reduction temperature, since $ZnFe_2O_4$ is more difficult to reduce than separate Fe_2O_3 [30]. The TPR of the BM sample also shows a persistent H_2 consumption tail above 500 °C, which was attributed to "resistant ZnO or interactions between iron and zinc". In practical terms, this tail likely reflects the final reduction of Fe^{2+} to Fe^0 within a $ZnFe_2O_4$

framework and the fact that ZnO remains unreduced (ZnO itself would not give a peak, but any attempt to reduce it or any minor reduction of $ZnFe_2O_4$'s Zn could contribute a very high-T baseline). After activation, the ball-milled ZnFe catalyst still shows notable features in TPR. The CuO peak (~240 °C) is greatly diminished in the activated BM sample, confirming that CuO was largely reduced to Cu^0 during the H_2/CO pretreatment (similar to the US case). However, a residual Fe-related peak around ~400 °C remains even after activation. This indicates that, unlike in the US sample, the Fe species in the BM sample were *not* fully reduced by the 350 °C activation - they required higher temperatures, again highlighting their stabilizing interaction with Zn. The high-temperature tail (>500 °C) also remains in the activated BM sample, signifying that ZnO or Zn-Fe oxide interactions continue to resist reduction. In summary, the ball-milled ZnFe catalyst shows broader and higher-temperature reduction features than its ultrasound counterpart, directly paralleling the trends seen in the Fe and Co families. The mechanical milling introduced Zn-Fe interactions (spinel formation, defect-rich interfaces) that increase the reduction temperature of the Fe component. This is supported by the general understanding that doping Fe_2O_3 with Zn or forming $ZnFe_2O_4$ decreases the amount of reducible Fe^{3+} and shifts reduction to higher temperature ranges [30]**.** TPR confirms what XRD would likely show: the BM ZnFe sample is more homogeneous (single spinel-like phase), whereas the US sample may contain a mix of distinct ZnO, Fe_2O_3 (and CuO) phases. By not over-interpreting the TPR, we refrain from claiming detection of any particular phase that isn't evidenced by other data; however, the disappearance of clear Fe_2O_3 reduction peaks and the emergence of high-T broad peaks in BM strongly *imply* the formation of a $ZnFe_2O_4$ spinel phase (or analogous complex) during milling/calcination. This phase is known to be thermodynamically more stable against H_2 - as one study notes, $ZnFe_2O_4$ acts as a "textural promoter" that, while improving dispersion, remains largely unreduced under typical FT reduction conditions [30]**.** Finally, it's worth noting that ZnO's role in TPR is mostly indirect: it modifies Fe's reducibility rather than getting reduced itself. In both US and BM ZnFe, the ZnO (either free or as part of spinel) will persist after TPR; the difference is that in BM, much more Fe is locked in $ZnFe_2O_4$ (hence the need for >500 °C to extract it as Fe^0), whereas in US, more Fe_2O_3 is free (hence reduced by ~350 °C).

Comparative Analysis of Ultrasound vs. Ball-Milling

Effect of Synthesis Method on Reducibility: Across the Fe, Co, and Zn-Fe catalyst families, a clear pattern emerges in H_2-TPR results: Ultrasound-synthesized (US) catalysts are more readily and cleanly reducible, while ball-milled (BM) catalysts show impeded and more complex reducibility. Ultrasound yields catalysts with sharper and lower-temperature TPR peaks, whereas ball milling produces broader peaks often shifted to higher temperatures. These differences directly reflect the catalysts' structural and chemical differences induced by the preparation methods:

- Phase Purity and Crystallinity: Ultrasound-assisted synthesis often promotes the formation of well-crystallized particles [29]. In our case, US samples like Fe40 and Co45 showed distinct TPR peaks corresponding neatly to known single-phase reductions. The sharper peaks for US samples indicate a more uniform reduction event, characteristic of a homogeneous phase. Ball milling, conversely, introduces significant lattice distortion and intimate mixing of components. BM samples exhibit broadened TPR signals, signifying a heterogeneous distribution of reducible sites.

In BM catalysts, highly dispersed phases reduce more gradually, spreading the signal over a broad temperature interval.

- Metal-Support and Metal-Metal Interactions: The TPR shifts can be understood by considering that both US and BM routes initially yield hydrotalcite-type (HTlc) hydroxides, where the key structural feature is the intimate dispersion of metal cations within the hydroxide layers. Upon activation (calcination), these HTlcs transform into mixed oxides. The different reducibility observed in TPR is therefore not due to direct oxide formation during synthesis, but rather to differences in the crystallinity and the possible presence of amorphous phases in the calcined materials. In BM-derived samples, the stronger broadening and shift of the reduction peaks to higher temperatures suggest that activation produced composite oxides with more defect-rich, entangled, or solid-solution-like structures, in which cations are strongly incorporated and thus more resistant to hydrogen reduction. This is consistent with literature reports on mechanochemical synthesis, where high-energy milling enhances cation intermixing and favors formation of complex oxide matrices that reduce only at elevated temperatures [31]. By contrast, the US method, which imposes milder mixing through localized cavitation, tends to preserve better-defined domains and higher crystallinity. After calcination, this results in oxide phases that are less entangled and more surface-exposed, hence showing sharper and lower-temperature reduction peaks. The exception is the Zn–Fe system, where oxide domains can already form during synthesis, in line with previous observations [35]. Overall, the comparison shows that while both methods proceed through HTlc precursors, BM produces catalysts with stronger metal–support interactions and harder-to-reduce oxide structures, whereas US favors more accessible oxide phases.

- Particle Size and Defects: Both US and BM reduce particle size, but the resulting materials differ significantly in their microstructure. Ultrasound promotes the formation of nanocrystalline HTlc phases with relatively narrow size distribution and good structural order [29]. Upon calcination, these precursors yield well-defined oxide phases, where smaller crystallites and accessible surfaces facilitate hydrogen reduction. This explains the low reduction temperatures observed in our US catalysts, where the benefits of high surface area and phase purity were not counteracted by stabilizing interactions. Ball milling, in contrast, produces very fine HTlc domains but also introduces a high density of defects, disorder, and amorphous fractions. While such defects can enhance reducibility in single oxides by promoting oxygen mobility [37], in our multi-component systems they mainly favored solid-state transformations during calcination. In particular, the BM precursors tended to lose long-range order and form intimately mixed, defect-rich oxide matrices (e.g. Mg–Fe or Co–Fe composites) after activation. These mixed oxides, although nanostructured, are intrinsically harder to reduce than their separate counterparts because of the stronger metal–oxygen–metal linkages within spinel- or solid-solution-type structures. Thus, any potential lowering of the reduction barrier from defects was outweighed by the stabilization effect of multi-metal oxide formation. In summary, BM-induced disorder and defects promote cation intermixing and phase entanglement, which makes reduction more difficult, whereas US yields purer, more crystalline domains that reduce more easily after activation.

- Implications for Catalytic Behavior: The easier reducibility of the US-derived catalysts means that, upon calcination and subsequent prereduction, they more readily generate the metallic active phases (Fe^0, Co^0, etc.) and associated species (such as Fe carbides). By contrast, the BM-derived catalysts, which after activation contain a significant fraction of cations locked in strongly bound mixed oxides, may achieve a lower degree of reduction under the same activation conditions. This could translate into lower initial dispersion of metallic sites or fewer accessible active centers, unless harsher activation conditions are applied. At the same time, the stronger interactions present in the BM-derived materials may provide other advantages, such as improved structural stability, resistance to sintering, or the generation of bifunctional active sites. Importantly, TPR alone does not directly predict catalytic performance, but it indicates that BM catalysts can retain residual unreduced phases after activation. For example, our TPR data suggest that activated BM Fe catalysts still contain Fe_3O_4, whereas US Fe catalysts are largely converted to Fe^0/FexCy. If Fe^0 is indeed the more active phase for the target reaction, US catalysts could show higher initial activity. On the other hand, the presence of stable phases such as $ZnFe_2O_4$ in BM catalysts, although unreducible, may act as a textural promoter, improving the dispersion of Fe^0 once it eventually forms [30]. Thus, each method offers trade-offs: ultrasound favors immediate and extensive reduction, while ball milling enhances cation mixing and may create synergistic adsorption or stability effects, as reflected in the higher H_2/CO_2 uptakes per m^2 observed for some BM samples.

TPD-H_2 Characterization of Activated Hydrotalcite-Based Catalysts

Iron catalysts.

Fe40 catalysts exhibit a main H_2 desorption peak at approximately 430 ± 10 °C, followed by a very faint shoulder around 600 °C. The presence of this minor high-temperature shoulder suggests a small fraction of strongly binding sites, consistent with reports that Fe-containing oxide catalysts often show additional H_2 desorption signals in the 500-800 °C range [38]. The peak shapes differ with preparation method. Ultrasound-prepared samples display narrow, symmetric desorption peaks that return to baseline within about a 70-100 °C span, whereas the ball-milled counterparts show much broader desorption envelopes whose high-temperature tails extend well beyond 650 °C. This contrast indicates that ball-milling produces a wider distribution of adsorption site strengths, i.e. a greater heterogeneity in how tightly hydrogen binds on the surface [39]. Such broad, high-temperature features are plausibly a consequence of defects introduced by mechanical milling [40], which create extra “deep” adsorption sites that retain H_2 more strongly. In other words, the key difference is not how much hydrogen these Fe-based samples can take up, but how tightly that hydrogen is retained: ball-milling shifts a portion of the H_2 into sites of higher binding energy, whereas ultrasound yields more uniform, moderately binding sites.

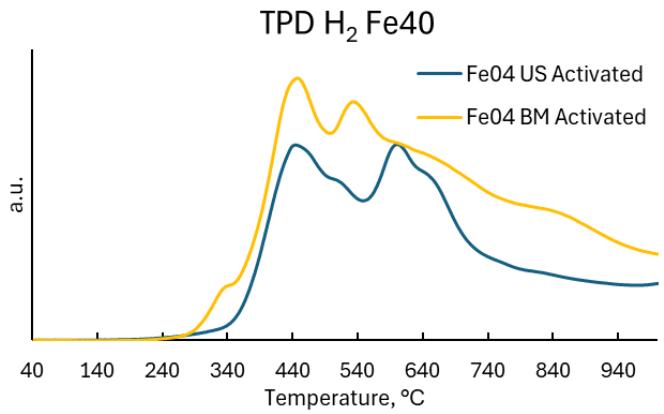

Figure 4.55. Activated Fe40 US and BM Temperature programmed desorption using H_2 as probe.

Cobalt catalysts

The Co33 and Co45 catalysts both display their principal H_2 desorption maxima at roughly 410 °C - about 20 °C lower than the Fe-based samples. This slight shift to lower temperature suggests that, in the cobalt-containing solids, the majority of adsorption sites bind hydrogen a bit less strongly than those in the iron-containing analogues (in line with the general expectation that Co-O sites might be less polar or acidic than Fe-O sites, though the exact nature of sites is not assigned here). As observed in the Fe series, the ultrasound-derived Co catalysts show sharper, more symmetric TPD profiles than the ball-milled ones. Co45-US has a narrow main peak (~410 °C) with a subtle high-temperature shoulder near 770 °C, whereas Co45-BM lacks any distinct feature above ~600 °C. The fact that a small H_2-desorption shoulder is present in the ultrasound sample but vanishes upon ball-milling suggests that the ultrasound route preserves a minor population of strong-yet-reversible H_2-binding sites, which are eliminated or further stabilized in the milled solid (such that H_2 is not released within the experimental temperature window). In Co45-US, these few very strong sites still release hydrogen (albeit at high T, ~770 °C), but in Co45-BM the hydrogen may remain trapped beyond 800 °C or be rendered undetectable as a separate peak. Aside from this difference at the extreme tail, both Co33 and Co45 show the same general trend as the Fe family: the ball-milled samples have broader desorption curves (extended tails toward higher T), indicating a wider range of binding energies, whereas the ultrasound samples desorb H_2 in a tighter temperature interval.

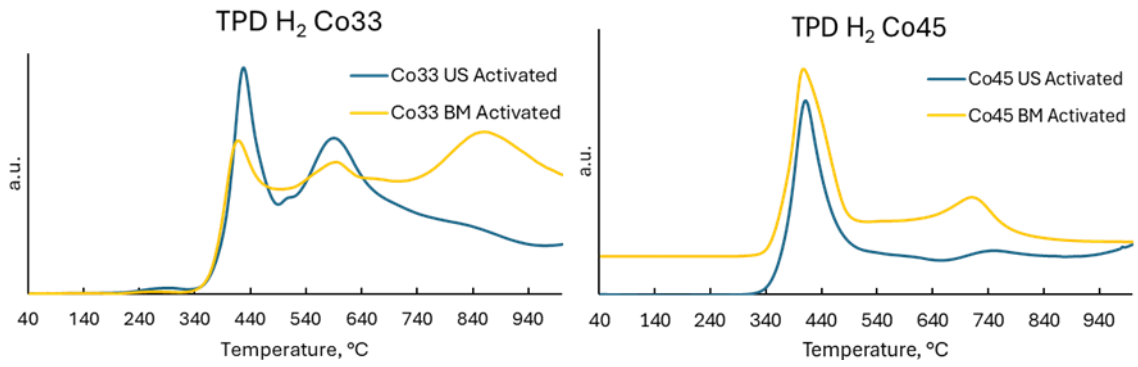

Figure 4.56. Activated Co rich catalysts US and BM Temperature programmed desorption using H_2 as probe.

FeZn catalyst

The FeZn catalyst exhibits distinctly different H_2 desorption behavior from the Fe-only and Co-only families. The ultrasound-prepared FeZn (FeZn-US) releases the bulk of its hydrogen in a single, symmetric desorption event centered at approximately 450 °C, and thereafter the signal returns to baseline abruptly. This clean, one-peak profile with an absence of high-temperature tailing is reminiscent of well-defined Cu-ZnO surfaces reported in the literature, which predominantly adsorb hydrogen on a uniform set of sites and show minimal desorption above the main peak [41]. In contrast, the ball-milled FeZn sample (FeZn-BM) stores nearly twice as much H_2 per gram but desorbs it over a much broader temperature span (roughly a 300 °C range). The FeZn-BM TPD trace covers both the 450 °C main region and a long tail extending to higher temperatures, indicating that mechanical treatment created a substantial fraction of "deep" or defect sites in this material. These strong-binding sites allow FeZn-BM to uptake more hydrogen overall than FeZn-US, but they release H_2 only at elevated temperatures (well above typical reaction conditions, as discussed later). This behavioral shift caused by ball-milling from a sharp, well-defined H_2 release in FeZn-US (typical of uniform moderate-strength Cu/ZnO-type sites) to a broad, high-temperature release in FeZn-BM underlines how the synthesis route can drastically alter the distribution of hydrogen adsorption sites in the catalyst.

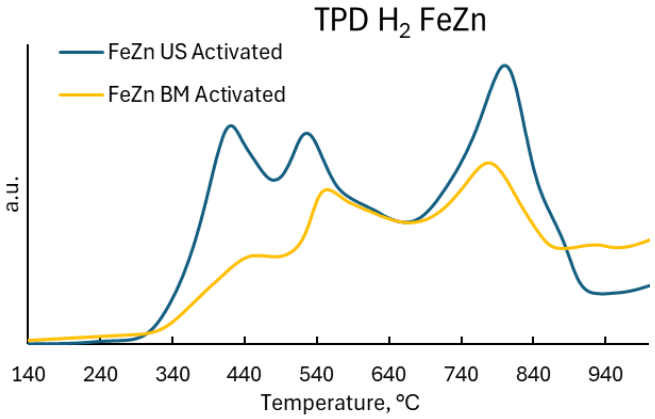

Figure 4.57. Activated FeZn Temperature programmed desorption using H_2 as probe.

To quantify these observations, Table 4.18 compiles BET surface area and H_2-TPD uptake data for each catalyst, including normalized capacities per surface area.

Catalyst	BET ($m^2\ g^{-1}$)	H_2 released ($\mu mol\ g^{-1}$)	H_2 released ($\mu mol\ m^{-2}$)
Fe30 US	30.9	1.75	0.056
Fe30 BM	41.2	2.13	0.052
Fe40 US	30.4	1.58	0.052
Fe40 BM	56.4	3.36	0.060
Co33 US	35.6	2.33	0.065
Co33 BM	67.5	3.10	0.046
Co45 US	29.6	2.81	0.095
Co45 BM	31.3	2.01	0.064
FeZn US	39.2	4.90	0.125
FeZn BM	15.0	2.67	0.178

Table 4.18 BET surface area, total hydrogen desorbed (in $\mu mol \cdot g^{-1}$), and normalized hydrogen uptake (in $\mu mol \cdot m^{-2}$) for each catalyst, as determined by H_2-TPD analysis. Normalized values reflect the density of accessible hydrogen adsorption sites per unit surface and highlight the influence of synthesis method on hydrogen storage and release properties.

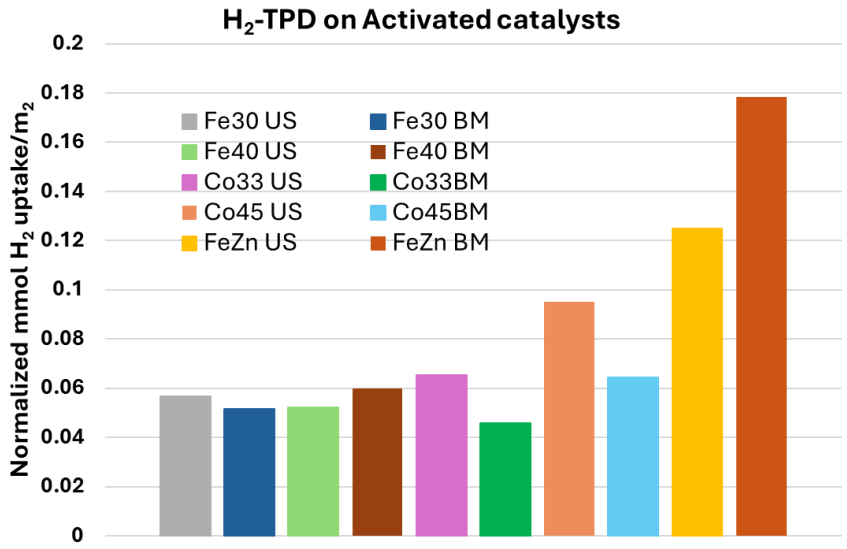

Figure 4.58. Normalized H_2 release ($\mu mol\ H_2$ per m^2) for all samples, using data from Table 4.18.

Two clear trends emerge from this comparison:

- Total vs. surface-normalized capacity**:** On a weight ($\mu mol\ H_2$ per g) basis, the hydrogen capacity roughly follows the expected order of metal loading or reducible metal content (with the Zn-Cu-Fe sample ≈ Co samples > Fe samples, reflecting the presence of more H_2-adsorbing components in ZnCuFe and Co formulations). However, once the H_2 uptake is normalized to surface area ($\mu mol\ H_2$ per m^2), the decisive variable is the preparation route rather than the metal identity. The ultrasound-assisted (US) catalysts cluster tightly around approximately 0.05-0.065 $\mu mol\ H_2$ per m^2, whereas most ball-milled (BM) catalysts show either similar or lower normalized uptakes with two notable outliers discussed next. The consistent areal uptake for all US samples suggests that sonication produces a comparable population density of accessible adsorption sites of moderate strength in each case [42]. In practical terms, ultrasound-derived catalysts seem to

have a uniform adsorption site density and strength, leading to nearly the same H_2 capacity per unit surface area across different compositions. Ball-milling, on the other hand, does not simply increase capacity proportionally to new surface area - instead it tends to create some sites that are not readily accessible at moderate temperature (lowering the effective μmol/m² in some cases, as seen for Co33-BM vs Co33-US).

- **"**Deep" vs. readily releasing hydrogen: The two catalysts that lie above the 0.05-0.065 μmol/m² band are FeZn-BM (0.178 μmol/m²) and Co45-US (0.095 μmol/m²). These higher normalized uptakes are explained by the presence of a second population of high-temperature adsorption sites which inflate the total H_2 capacity. FeZn-BM shows an exceptionally high H_2 uptake per m² owing to its large fraction of strong-binding defect sites introduced by milling. Co45-US also has a moderately elevated areal capacity, attributable to the small high-T shoulder (770 °C) unique to that sample. Importantly, however, hydrogen stored in these very strong sites is released only at temperatures exceeding ~600 °C, meaning it would not be readily available under typical reaction conditions. In the literature, such high-temperature H_2 desorption is often attributed to hydrogen spillover into oxide supports or trapping at defect sites, which desorbs only upon heating to elevated T [41]. In our catalysts, the "deep" sites in ball-milled FeZn (and the few present in Co45-US) undoubtedly boost the total H_2 uptake measured by TPD, but this hydrogen would be largely unavailable for catalysis at normal operation temperatures (e.g., 200-400 °C). Thus, not all stored hydrogen is equally useful: the mild-binding sites (desorbing H_2 below ~500 °C) are likely to contribute to reaction kinetics, whereas the ultra-strong sites serve more as a hydrogen reservoir that only empties at prolonged high temperature.

These distinctions highlight that synthesis route strongly influences not just how much hydrogen a catalyst can take up, but how that hydrogen is distributed among sites of different strength. Ultrasound yields consistently moderate-strength, readily desorbed H_2, while ball-milling can create extra capacity in the form of strongly bound H_2 that may or may not be practically accessible.

Implications

From the above analysis, we can draw several cautious conclusions about how H_2 adsorption characteristics relate to catalyst design and potential performance:

- Ultrasound-derived samples provide accessible hydrogen in a narrow temperature window. The sonicated catalysts consistently adsorb and release hydrogen within a tight ~70-100 °C range (around 350-450 °C in absolute terms for these materials). Such a narrow site-energy distribution means that once the catalyst sees temperatures above the desorption threshold, most of the stored hydrogen can rapidly recombine and become available. This behavior is likely advantageous for fast catalytic turnover in reactions where hydrogen supply (via spillover or surface recombination) is rate-limiting. In essence, the ultrasound method favors moderate-strength H_2 sites that strike a balance: strong enough to hold hydrogen at reaction temperature, yet weak enough to release it when needed. Indeed, studies have noted that catalysts which adsorb H_2 only weakly or at lower temperatures often exhibit superior activity in hydrogenation reactions [38]. This is consistent with the Sabatier principle, which posits that an ideal catalyst binds reactants neither too strongly

nor too weakly [43]. Here, the ultrasound catalysts exemplify that principle by avoiding overly strong H_2 binding. We expect this trait to be beneficial in contexts such as hydrogen spillover-driven reactions or any mechanism where accessible (mobile) surface hydrogen is crucial for the reaction to proceed.

- Ball-milling increases the population of "deep" hydrogen sites: beneficial for storage, but less so for active turnover**.** The mechanically treated (BM) catalysts tend to have a broader distribution of H_2 binding energies, including a significant fraction of very strong-binding sites (as evidenced by the high-temperature TPD tails). These sites can store larger amounts of hydrogen (which might be of interest for hydrogen storage applications per se), but they release H_2 only slowly or at extreme conditions. In the Fe and Co systems, this manifests as broad desorption profiles extending to high temperatures; in the Zn-containing system (FeZn-BM), it yields a record high H_2 capacity (per m^2) but also a protracted desorption spanning several hundred degrees. For catalytic reactions operated at typical temperatures, such strongly bound hydrogen is essentially immobilized - it does not participate in the catalytic cycle in a timely manner. Thus, ball-milling trades some immediacy of hydrogen access for a higher total capacity. This could be detrimental or beneficial depending on the application: for continuous catalytic processes, rapid H_2 availability is generally more important than maximum storage, whereas for hydrogen-storage materials the opposite may hold true.

- Structure-performance link (qualitative): Within each catalyst family, the sample that combines a high *effective* hydrogen capacity with a narrow desorption peak tends to correspond to the best steady-state performance in reactions (as detailed in Chapter 5). For instance, Co45-US and FeZn-US - both of which showed the highest surface-normalized H_2 uptakes among their peers *and* released that hydrogen in a concentrated temperature range - also achieved the highest productivity in the tested reaction. This correlation must be viewed as qualitative and not as proof of causation; nevertheless, it supports the kinetic argument that readily accessible hydrogen (at operative temperatures), rather than just total hydrogen uptake, is what governs catalytic performance. In other words, a catalyst that can quickly supply hydrogen to active sites under reaction conditions may outperform one that holds a larger amount of hydrogen too tightly to use. This concept echoes the findings of other researchers - for example, a Co-based catalyst that showed only low-temperature H_2 desorption was found to be the most active for CO_2-to-CH_4 conversion, implying that weaker hydrogen binding was favorable for that reaction [38]. It is also in agreement with the Sabatier principle's classic insight that if adsorbed species do not desorb readily, the surface can become blocked and turnover is limited [43]. Thus, while our TPD-H_2 profiles alone cannot determine catalytic behavior, the observed trends are consistent with the idea that hydrogen which is adsorbed in moderate-strength, reversible form is the most efficacious for catalysis.

- Nature of H_2 adsorption sites: We refrain from assigning specific hydride species or binding geometries to the observed TPD peaks in the absence of corroborating spectroscopic evidence. The present analysis is limited to distinguishing relatively strong vs. moderate adsorption sites. For example, we do not attempt to label the 600-770 °C desorption features as a particular Fe-H or spillover-hydrogen species, nor the 430-450 °C peak as a specific Cu-H complex, without literature evidence directly supporting such assignments. The key point is that our TPD-H_2 results can clearly differentiate between strongly retained hydrogen and readily desorbable hydrogen on

these hydrotalcite-derived catalysts. This level of resolution is sufficient for guiding interpretations: strong-site hydrogen is likely less accessible during reaction, whereas moderate-site hydrogen is available under operational temperatures. All further discussion will focus on these relative strengths of H_2 adsorption, rather than on conjecturing the exact chemical nature of the adsorbed hydrogen species on each catalyst. This careful, evidence-based approach ensures that any structure-function relationships proposed remain robust and avoid over-speculation.

4.3.5.2. Desorption Profiles and CO_2 Uptake

The total CO_2 uptake (per gram of catalyst) reflects the amount of basic oxides available. In the present series, the Zn-containing system retains the most CO_2 per gram, followed by the Co-based catalysts, with the Fe-based catalysts adsorbing the least. However, when these uptakes are normalized by BET surface area (to give a measure of *areal* basic site density), the picture changes markedly. Figure 4.62 illustrates the CO_2 uptake in μmol CO_2 per m^2 for each sample. The Fe and Co families prepared by ultrasound show moderate surface-normalized uptakes (on the order of 0.05-0.16 $\mu mol \cdot m^{-2}$), whereas their ball-milled counterparts are somewhat higher (especially in the Co45 case). The Zn-containing catalyst shows the highest basicity in both preparation modes. Table 4.19 below summarizes the surface-area-normalized CO_2 uptakes for the catalyst series:

Catalyst	CO_2 uptake ($\mu mol \cdot m^{-2}$)
Fe30 US	0.158
Fe30 BM	0.107
Fe40 US	0.118
Fe40 BM	0.093
Co33 US	0.035
Co33 BM	0.009
Co45 US	0.049
Co45 BM	0.117
FeZn US	0.345
FeZn BM	0.392

Table 4.19. CO_2 uptake (in $\mu mol \cdot m^{-2}$) for each catalyst, as measured by CO_2-TPD

Two major features stand out from the CO_2-TPD results:

- Synthesis route dominates accessible basicity. Across all compositions, the preparation method (ultrasound vs. ball-milling) has a larger effect on normalized CO_2 uptake than the metal identity. All ultrasound-derived Fe and Co samples cluster below ~0.16 $\mu mol \cdot m^{-2}$, indicating a relatively low density of basic sites per surface area. In contrast, ball-milled samples generally show higher values. Notably, the ball-milled Zn-containing catalyst (FeZn-BM) reaches ~0.39 $\mu mol \cdot m^{-2}$, far above the ultrasound range despite its lower BET surface area. The ball-milled Co45 sample also displays an elevated basic site density (more than double its ultrasound analog, Co45-US, as seen in Table 4.19). This trend suggests that mechanical treatment (milling) creates additional basic surface sites or defects, whereas ultrasound synthesis favors fewer, more uniformly distributed sites. Similar observations have been reported in literature for ultrasound-

assisted vs. conventional preparations of hydrotalcite-type oxides, where ultrasonic treatment tends to produce a higher proportion of accessible weak-to-moderate basic sites [42].

- Desorption peak positions distinguish "moderate" vs. "strong" basic sites. The CO_2 desorption profiles reveal that ultrasound-derived catalysts release CO_2 predominantly at intermediate temperatures, whereas ball-milled solids exhibit an additional high-temperature CO_2 release. For example, the CO_2-TPD traces of Fe30-US and Co33-US show main desorption peaks clustered in the 300-480 °C range. Desorption in this range is characteristic of medium-strength basic sites [44] strong enough to chemisorb CO_2 (as carbonate species) but still released well within typical reaction temperature windows (generally <~500 °C for CO_2 conversion processes [45]. By contrast, several ball-milled catalysts display a new CO_2-desorption feature at much higher temperatures. In particular, Fe40-BM and FeZn-BM exhibit broad desorption tails extending up to ~750-800 °C, indicating the presence of very strongly bound CO_2 species that decompose only at extreme temperatures. Such high-T CO_2 signals are attributed to strongly basic sites (e.g. low-coordination O^{2-} anions) that can form very stable carbonates [44]**.** In practical terms, CO_2 bound to these sites would not desorb until well above typical reaction conditions, remaining as residual carbonates on the surface. This delineation between moderate and strong basic sites is consistent with general CO_2-TPD analyses in the literature: peaks below roughly 500 °C correspond to medium-strength basic sites, whereas those emerging above ~600 °C signify strongly basic sites [44,46]**.**

Representative CO_2-TPD profiles for selected samples are provided in the figures below. These illustrate the qualitative differences between ultrasound and ball-milled preparations within each catalyst family. In the Fe family (Fig. 4.59), for instance, Fe40-US shows a single, symmetric CO_2 desorption peak in the 350-450 °C region, while Fe40-BM displays a broader release with an additional high-temperature tail.

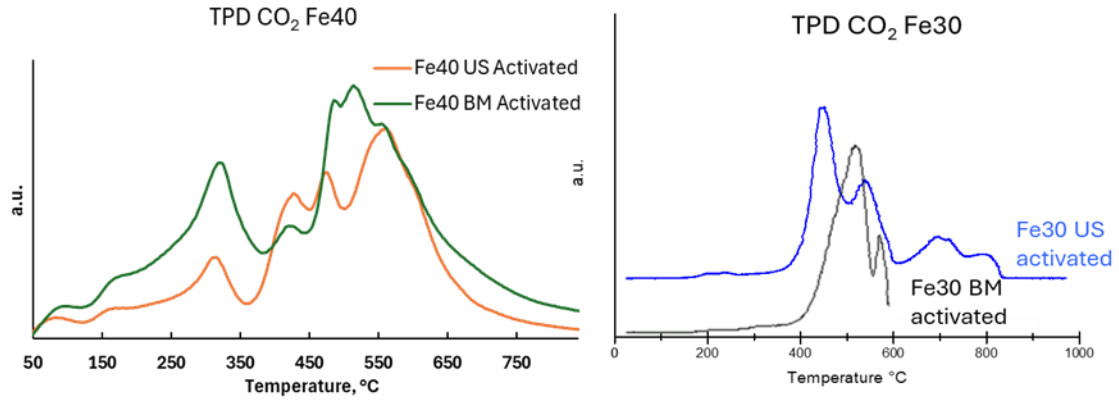

Figure 4.59. Activated Fe30 and Fe40 Temperature programmed desorption of CO_2.

The Co-based catalysts (Fig. 4.60) follow a similar pattern: both Co33 and Co45 ultrasound samples have relatively sharp desorption peaks centered ~400 °C, whereas their ball-milled counterparts broaden toward higher temperatures (Co45-BM in particular shows a pronounced extension above 600 °C).

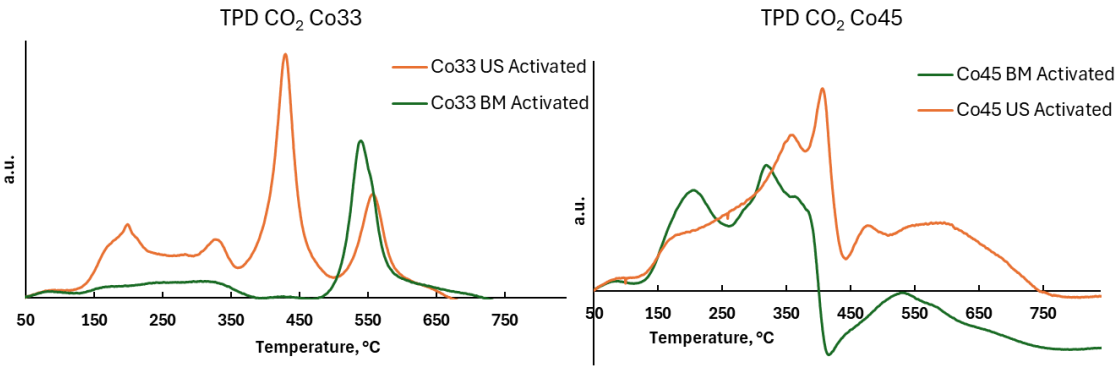

Figure 4.60. Activated Co33 and Co45 Temperature programmed desorption of CO_2.

Finally, the Zn-containing series (Fig. 4.61) highlights the extreme case: the ultrasound FeZn sample releases most CO_2 below 500 °C, whereas FeZn-BM exhibits substantial CO_2 retention up to ~800 °C. These profile differences underscore the creation of "deep" binding sites by ball-milling, as opposed to the "moderate" sites predominantly present in the ultrasound-prepared materials.

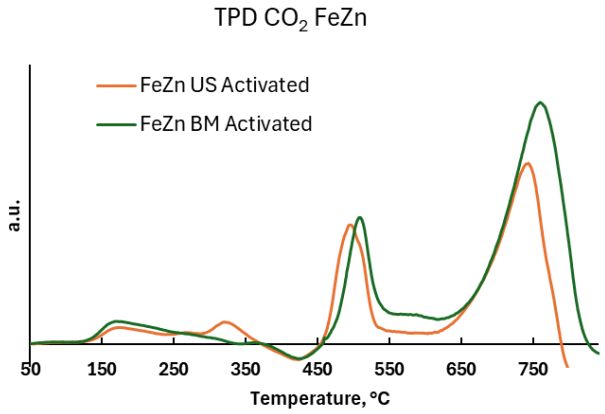

Figure 4.61. Activated FeZn Temperature programmed desorption of CO_2.

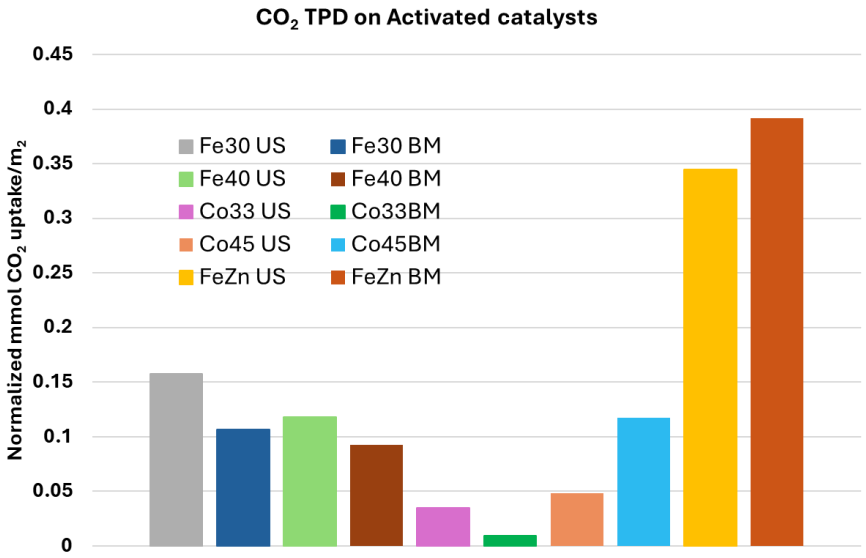

Figure 4.62. bar chart showing CO_2 uptake per unit surface area ($\mu mol \cdot m^{-2}$) for ultrasound (US) and ball-milled (BM) catalysts across the Fe, Co, and FeZn families.

Implications and Limitations of the CO_2-TPD Results

The CO_2-TPD analysis of these hydrotalcite-derived catalysts suggests clear trade-offs between the total CO_2 capacity and the practical usability of that capacity under reaction conditions. Ultrasound preparation yields a relatively uniform set of moderate basic sites: virtually all adsorbed CO_2 is released within a narrow ~120 °C window (roughly 300-420 °C for most samples). This uniform, mid-range basicity is advantageous for catalytic processes that require rapid adsorption-desorption cycling of CO_2 (or of intermediates like surface formates). In such cases, having all CO_2 binding sites able to take up and release CO_2 near the reaction temperature means that the catalyst can readily supply and remove CO_2 as the reaction progresses. Indeed, a narrow desorption profile centered in the 300-500 °C range is often associated with more effective CO_2 conversion performance [45], since the CO_2 can be mobilized on the surface under typical operating temperatures. The moderate basic sites in the ultrasound-treated catalysts should be sufficient to bind CO_2 (facilitating, for example, formate formation in hydrogenation mechanisms) but not so strong as to lock CO_2 on the surface.

Ball-milling, in contrast, generates a heterogeneous basicity landscape with an extended tail of strong sites. While this mechanical treatment increases the total number of basic sites (and thus the total CO_2 uptake capacity per gram), a significant fraction of these sites holds CO_2 so tenaciously that desorption only occurs above ~600 °C. Such strongly bound CO_2 (likely in the form of very stable carbonate species) would remain on the catalyst surface under typical reaction conditions, potentially *poisoning* those sites or converting them into inert carbonate reservoirs. In other words, ball-milled samples can store more CO_2, but much of it is in a form that is not readily exchangeable during a normal reaction cycle. This could lead to accumulation of carbonate intermediates on the surface during CO_2-involving reactions and might slow the steady-state turnover. An analogous effect was noted in the H_2-TPD profiles (Section 4.3.5.2, above), where ball-milling created deep hydrogen-trapping sites that released H_2 only at elevated temperatures, hinting that those sites contribute more to storage than to active reaction turnover. The present CO_2-TPD results reinforce that trend: mechanical activation (milling) introduces a population of basic sites that are strong but slow, whereas sonochemical preparation favors moderate and rapid sites.

Finally, it is noteworthy that the catalysts combining the highest surface-normalized CO_2 capacity with still-moderate desorption temperatures - for example, Co45-US within the Co series and FeZn-US within the Zn-containing series - are the ones that later exhibit the best catalytic performance in CO_2 conversion tests (see Chapter 5). This observation is qualitative and correlative in nature, but it supports the idea that a catalyst's efficacy is governed by the availability of readily exchangeable CO_2 (i.e. CO_2 that can adsorb and desorb near the operating temperature), rather than by the absolute maximum CO_2 that the material can store. Similar conclusions have been drawn by other researchers; for instance, a study in literature reported that a Ni/Y_2O_3 catalyst with predominantly medium-strength basic sites (CO_2 desorbing below ~400 °C) achieved superior CO_2 methanation rates at 350 °C, compared to catalysts that held CO_2 more strongly [45]**.** Considering this, an optimal catalyst would balance having enough basic sites

to activate CO_2 with ensuring that those sites are not so strong as to sequester CO_2 as unreactive carbonates.

No attempt is made here to deconvolute or assign each CO_2 desorption peak to specific carbonate species (e.g. monodentate vs. bidentate carbonates) on the surface the resolution of our TPD setup is sufficient to distinguish broad classes of moderate vs. strong binding, but not to identify every intermediate. In summary, CO_2-TPD provides a clear differentiation between moderate basic sites (adequate for reversible CO_2 binding under reaction conditions) and strong basic sites (which bind CO_2 too strongly to be released during reaction). This characterization complements the H_2-TPD and TPR results, building a comprehensive picture of how the synthesis method influences the distribution of active sites in hydrotalcite-derived catalysts and how these sites might function during catalytic operation.

4.3.6. ICP

ICP-MS confirms that the bulk composition of every catalyst remains essentially unchanged after CO/CO_2 hydrogenation testing, indicating negligible metal leaching under the applied conditions. For both Fe-rich hydrotalcites (Fe30, Fe40) the Mg, Fe and Cu contents are identical within experimental error (±1 wt %) before and after reaction. Ultrasound-derived samples are particularly stable, but even the mechanically ball-milled (BM) analogues retain >95 % of their initial Fe and Mg, evidencing that the harsher microstructure introduced by milling does not translate into significant metal loss.

	Fresh catalysts compositions (%)				
	Mg	Co	Cu	Fe	Zn
Fe30 US	60	-	6	34	-
Fe30 BM	62	-	6	32	-
Fe40 US	55	-	5	40	-
Fe40 BM	57	-	5	38	-
Co45 US	24	42	5	29	-
Co45 BM	43	29	5	24	-
Co33 US	32	33	5	30	-
Co33 BM	16	40	6	38	-
FeZn US	-	-	5	30	65
FeZn BM	-	-	5	33	62

Table 4.20. Catalysts composition from ICP measurement.

Cobalt-promoted solids behave similarly. Co45-US shows an invariant 42 wt % Co, while Co33-US decreases by only 1 wt % (33 → 32 wt %), well inside the typical reproducibility limits of the technique. The two BM cobalt samples exhibit the largest absolute changes (Co45-BM, Fe40-BM lose 1–2 wt % Fe), yet these variations correspond to <5 % of the starting metal quantity.

	Spent catalysts compositions (%)				
	Mg	Co	Cu	Fe	Zn
Fe30 US	60	-	6	34	-
Fe30 BM	**61***	-	6	**30***	-
Fe40 US	55	-	5	40	-
Fe40 BM	**56***	-	5	**36***	-
Co45 US	24	42	5	29	-
Co45 BM	43	29	5	24	-
Co33 US	32	**32***	5	30	-
Co33 BM	16	40	6	38	-
FeZn US	-	-	5	30	65
FeZn BM	-	-	5	33	62

Table 4.21. Catalysts composition after testing under CO_2/H_2 reaction. Variation is visible through.

Finally, the FeZn formulations display identical Fe, Zn and Cu levels (30/65 wt % for US; 33/62 wt % for BM) before and after testing, demonstrating that neither Zn volatilisation nor selective Fe migration occurred during long-term operation. Taken together, the ICP results corroborate that the hydrotalcite-derived samples effectively immobilise the active metals and promoters. Any slight deviations (≤2 wt %) are confined to ball-milled samples and most likely reflect minor particle-size dispersion.

References Chapter 4

[1] Bardestani R, Patience GS, Kaliaguine S. Experimental methods in chemical engineering: specific surface area and pore size distribution measurements BET, BJH, and DFT. Can J Chem Eng 2019; 97:2781–91. https://doi.org/10.1002/cjce.23632.

[2] Ke F, Yuan Y-P, Qiu L-G, Shen Y-H, Xie A-J, Zhu J-F, et al. Facile fabrication of magnetic metal–organic framework nanocomposites for potential targeted drug delivery. J Mater Chem 2011; 21:3843. https://doi.org/10.1039/c0jm01770a.

[3] Jung J-S, Kim SW, Moon DJ. Fischer–Tropsch Synthesis over cobalt based catalyst supported on different mesoporous silica. Catalysis Today 2012; 185:168–74. https://doi.org/10.1016/j.cattod.2012.02.002.

[4] Kinsela AS, Jones AM, Bligh MW, Pham AN, Collins RN, Harrison JJ, et al. Influence of Dissolved Silicate on Rates of Fe(II) Oxidation. Environ Sci Technol 2016; 50:11663–71. https://doi.org/10.1021/acs.est.6b03015.

[5] Bardestani R, Patience GS, Kaliaguine S. Experimental methods in chemical engineering: specific surface area and pore size distribution measurements BET, BJH, and DFT. Can J Chem Eng 2019; 97:2781–91. https://doi.org/10.1002/cjce.23632.

[6] Loh K-S, Lee YH, Musa A, Salmah AA, Zamri I. Use of Fe3O4 Nanoparticles for Enhancement of Biosensor Response to the Herbicide 2,4-Dichlorophenoxyacetic Acid. Sensors 2008; 8:5775–91. https://doi.org/10.3390/s8095775.

[7] Bertolucci E, Galletti AMR, Antonetti C, Marracci M, Tellini B, Piccinelli F, et al. Chemical and magnetic properties characterization of magnetic nanoparticles. 2015 IEEE International Instrumentation and Measurement Technology Conference (I2MTC) Proceedings, Pisa, Italy: IEEE; 2015, p. 1492–6. https://doi.org/10.1109/I2MTC.2015.7151498.

[8] Mangla O, Roy S. Monoclinic Zirconium Oxide Nanostructures Having Tunable Band Gap Synthesized under Extremely Non-Equilibrium Plasma Conditions. IOCN 2018, MDPI; 2018, p. 10. https://doi.org/10.3390/IOCN_2018-1-05486.

[9] Liu J-X, Wang P, Xu W, Hensen EJM. Particle Size and Crystal Phase Effects in Fischer-Tropsch Catalysts. Engineering 2017; 3:467–76. https://doi.org/10.1016/J.ENG.2017.04.012.

[10] Liu Y, Chen J-F, Zhang Y. The effect of pore size or iron particle size on the formation of light olefins in Fischer–Tropsch synthesis. RSC Adv 2015; 5:29002–7. https://doi.org/10.1039/C5RA02319J.

[11] Liu J-X, Wang P, Xu W, Hensen EJM. Particle Size and Crystal Phase Effects in Fischer-Tropsch Catalysts. Engineering 2017; 3:467–76. https://doi.org/10.1016/J.ENG.2017.04.012.

[12] Zhuang L, Zhang W, Zhao Y, Shen H, Lin H, Liang J. Preparation and Characterization of Fe_3O_4 Particles with Novel Nanosheets Morphology and Magnetochromatic Property by a Modified Solvothermal Method. Sci Rep 2015; 5:9320. https://doi.org/10.1038/srep09320.

[13] Husin H, Asnawi TM, Firdaus A, Husaini H, Ibrahim I, Hasfita F. Solid Catalyst Nanoparticles derived from Oil-Palm Empty Fruit Bunches (OP-EFB) as a Renewable

Catalyst for Biodiesel Production. IOP Conf Ser: Mater Sci Eng 2018; 358:012008. https://doi.org/10.1088/1757-899X/358/1/012008.

[14] Mandela E, Margellou AG, Kotsaridou A, Marnellos GE, Konsolakis M, Triantafyllidis KS. Layered Double Hydroxide (LDH)-Derived Mixed Oxides for Enhanced Light Hydrocarbon Production from CO_2 Hydrogenation. Catalysts 2025; 15:323. https://doi.org/10.3390/catal15040323.

[15] González MA, Trócoli R, Pavlovic I, Barriga C, La Mantia F. Capturing Cd(ii) and Pb(ii) from contaminated water sources by electro-deposition on hydrotalcite-like compounds. Phys Chem Chem Phys 2016; 18:1838–45. https://doi.org/10.1039/C5CP05235A.

[16] Thomas GS, Kamath PV. Line broadening in the PXRD patterns of layered hydroxides: The relative effects of crystallite size and structural disorder. J Chem Sci 2006; 118:127–33. https://doi.org/10.1007/BF02708774.

[17] Pimentel C, Hernández-Laguna A, Sainz-Díaz CI. Effect of Iron Isomorphic Substitution in Mg:Al and Zn:Al-Layered Double-Hydroxide Structures by Means of First Principle Calculations. ACS Earth Space Chem 2022; 6:2499–507. https://doi.org/10.1021/acsearthspacechem.2c00205.

[18] Zhao S, Yi H, Tang X, Gao F, Yu Q, Zhou Y, et al. Enhancement effects of ultrasound assisted in the synthesis of NiAl hydrotalcite for carbonyl sulfide removal. Ultrasonics Sonochemistry 2016; 32:336–42. https://doi.org/10.1016/j.ultsonch.2016.04.001.

[19] Grainca A, Boccalon E, Nocchetti M, Vivani R, Di Michele A, Longhi M, et al. Sonochemical and mechanochemical synthesis of iron-based nano-hydrotalcites promoted with Cu and K as catalysts for CO and CO_2 Fischer-Tropsch synthesis. Fuel 2024; 373:132303. https://doi.org/10.1016/j.fuel.2024.132303.

[20] Chang Q, Zhang C, Liu C, Wei Y, Cheruvathur AV, Dugulan AI, et al. Relationship between Iron Carbide Phases (ε-Fe_2 C, Fe_7 C_3 , and χ-Fe_5 C_2) and Catalytic Performances of Fe/SiO_2 Fischer–Tropsch Catalysts. ACS Catal 2018; 8:3304–16. https://doi.org/10.1021/acscatal.7b04085.

[21] Serhal CA, El Khawaja R, Labaki M, Mallard I, Poupin C, Cousin R, et al. Influence of Co/Fe molar ratio on hydrotalcite catalysts prepared with or without microwave. Journal of Solid State Chemistry 2022; 309:122943. https://doi.org/10.1016/j.jssc.2022.122943.

[22] Starukh G, Rozovik O, Oranska O. Organo/Zn-Al LDH Nanocomposites for Cationic Dye Removal from Aqueous Media. Nanoscale Res Lett 2016; 11:228. https://doi.org/10.1186/s11671-016-1402-0.

[23] American National Standard: Standard Guide for Forensic Analysis of Geological Materials by Powder X-Ray Diffraction. Designation: E3294 – 22.

[24] Liu LL, Zhu D, Cao LL, Stephan DW. N-Heterocyclic carbene stabilized parent sulfenyl, selenenyl, and tellurenyl cations (XH^+, X = S, Se, Te). Dalton Trans 2017; 46:3095–9. https://doi.org/10.1039/C7DT00186J.

[25] Okonye LU, Yao Y, Hildebrandt D, Meijboom R. Contributing to energy sustainability: a review of mesoporous material supported catalysts for Fischer–Tropsch synthesis. Sustainable Energy Fuels 2021; 5:79–107. https://doi.org/10.1039/D0SE01442G.

[26] Lykiema J, Sing KSW, Haber J, Kerker M, Wolfram E, Block JH, et al. Prepared for publication by the Subcommittee on Reporting Gas Adsorption Data Consisting of k. s. w. sing (uk, chairman); d. h. everett (uk); r. a. w. haul (frg); l. moscou (netherlands); r. a. pierotti (usa); j. rouquerol (france); t. siemieniewska (poland) n.d.

[27] Zhang C-H, Wan H-J, Yang Y, Xiang H-W, Li Y-W. Study on the iron–silica interaction of a co-precipitated Fe/SiO2 Fischer–Tropsch synthesis catalyst. Catalysis Communications 2006; 7:733–8. https://doi.org/10.1016/j.catcom.2006.03.018.

[28] Qing M, Yang Y, Wu B, Xu J, Zhang C, Gao P, et al. Modification of Fe–SiO2 interaction with zirconia for iron-based Fischer–Tropsch catalysts. Journal of Catalysis 2011; 279:111–22. https://doi.org/10.1016/j.jcat.2011.01.005.

[29] Li Z, Dong J, Zhang H, Zhang Y, Wang H, Cui X, et al. Sonochemical catalysis as a unique strategy for the fabrication of nano-/micro-structured inorganics. Nanoscale Adv 2021; 3:41–72. https://doi.org/10.1039/D0NA00753F.

[30] James OO, Chowdhury B, Maity S. Comparative TPR and TPD Studies of Cu and Ca Promotion on Fe-Zn- and Fe-Zn-Zr-Based Fischer-Tropsch Catalysts. Oil Gas Sci Technol – Rev IFP Energies Nouvelles 2015; 70:511–9. https://doi.org/10.2516/ogst/2013114.

[31] Parmaliana A, Arena F, Frusteri F, Giordano N. Temperature-programmed reduction study of NiO–MgO interactions in magnesia-supported Ni catalysts and NiO–MgO physical mixture. J Chem Soc, Faraday Trans 1990;86:2663–9. https://doi.org/10.1039/FT9908602663.

[32] Silva PH, Oliveira HS, Batista MS. Redox effects in Cu, Co or Fe in oxides nanocrystals with high catalytic activity for the acetonitrile combustion. SN Appl Sci 2020;2:649. https://doi.org/10.1007/s42452-020-2476-y.

[33] Alqassem B, Othman I, Abu Haija M, Banat F. Comparative catalytic activity of pure, mixed and P-modified $CoFe_2O_4$ nanoparticles for water treatment at neutral pH. Catalysis Communications 2021;150:106267. https://doi.org/10.1016/j.catcom.2020.106267.

[34] Chen X, Wu C, Guo Z. Synthesis of Efficient Cu/CoFe2O4 Catalysts for Low Temperature CO Oxidation. Catal Lett 2019; 149:399–409. https://doi.org/10.1007/s10562-018-2612-0.

[35] Lokteva ES, Golubina EV. Metal-support interactions in the design of heterogeneous catalysts for redox processes. Pure and Applied Chemistry 2019; 91:609–31. https://doi.org/10.1515/pac-2018-0715.

[36] Liang M, Kang W, Xie K. Comparison of reduction behavior of Fe_2O_3, ZnO and $ZnFe_2O_4$ by TPR technique. Journal of Natural Gas Chemistry 2009; 18:110–3. https://doi.org/10.1016/S1003-9953(08)60073-0.

[37] Rinaudo MG, Beltrán AM, Fernández MA, Cadús LE, Morales MR. Tailoring materials by high-energy ball milling: TiO_2 mixtures for catalyst support application. Materials Today Chemistry 2020; 17:100340. https://doi.org/10.1016/j.mtchem.2020.100340.

[38] Belthle KS, Martin WF, Tüysüz H. Synergistic Effects of Silica-Supported Iron−Cobalt Catalysts for CO_2 Reduction to Prebiotic Organics. ChemCatChem 2024;16: e202301218. https://doi.org/10.1002/cctc.202301218.

[39] Ning W, Li B, Wang B, Yang X, Jin Y. Enhanced Production of C5+ Hydrocarbons from CO_2 Hydrogenation by the Synergistic Effects of Pd and K on γ-Fe_2O_3 Catalyst. Catal Lett 2019;149:431–40. https://doi.org/10.1007/s10562-018-2622-y.

[40] Manzoli M, Bonelli B. Microwave, Ultrasound, and Mechanochemistry: Unconventional Tools that Are Used to Obtain "Smart" Catalysts for CO_2 Hydrogenation. Catalysts 2018;8:262. https://doi.org/10.3390/catal8070262.

[41] Huang C, Chen S, Fei X, Liu D, Zhang Y. Catalytic Hydrogenation of CO_2 to Methanol: Study of Synergistic Effect on Adsorption Properties of CO_2 and H_2 in CuO/ZnO/ZrO_2 System. Catalysts 2015;5:1846–61. https://doi.org/10.3390/catal5041846.

[42] Kalawoun H, Obeid M, Ciotonea C, Chaghouri M, Poupin C, Aouad S, et al. Review on the contribution of ultrasounds in layered double hydroxides synthesis and in their performances. Comptes Rendus Chimie 2023;26:167–79. https://doi.org/10.5802/crchim.249.

[43] Ooka H, Huang J, Exner KS. The Sabatier Principle in Electrocatalysis: Basics, Limitations, and Extensions. Front Energy Res 2021;9:654460. https://doi.org/10.3389/fenrg.2021.654460.

[44] Figueiredo A, Soria MA, Madeira LM, Rocha C. Preparation and Characterization of Materials for Low- to Intermediate-Temperature CO_2 Adsorption. Processes 2024;12:2403. https://doi.org/10.3390/pr12112403.

[45] Kuhaudomlap S, Srifa A, Koo-Amornpattana W, Fukuhara C, Ratchahat S. Insight and comprehensive study of Ni-based catalysts supported on various metal oxides for CO_2 methanation. Sci Rep 2024; 14:23149. https://doi.org/10.1038/s41598-024-73848-0.

[46] Bermejo-López A, Pereda-Ayo B, Onrubia-Calvo JA, González-Marcos JA, González-Velasco JR. Boosting dual function material Ni-Na/Al2O3 in the CO_2 adsorption and hydrogenation to CH4: Joint presence of Na/Ca and Ru incorporation. Journal of Environmental Chemical Engineering 2023; 11:109401. https://doi.org/10.1016/j.jece.2023.109401.

5. RESULTS

5.1. CO reaction

5.1.1. Metallosilicates

5.1.1.1. Unpromoted Fe-Based Metallosilicate Catalysts

The CO hydrogenation performance of iron catalysts supported on metallosilicate frameworks (SiO_2 doped with Ce, Zr, Ti, or V) shows strong dependence on the support composition. All tests were carried out after an initial activation ($H_2/CO = 2$ at 350 °C, 20 bar) followed by steady state runs at increasing temperatures under $H_2/CO = 2$. Each unpromoted catalyst exhibited the expected rise in CO conversion with temperature, but the absolute activity varied widely with support type. Fe/Ce-SiO_2 and Fe/Zr-SiO_2 achieved significantly higher conversions than Fe/Ti-SiO_2 and Fe/V-SiO_2. For example, Fe/Ce-SiO_2 reached ≈20% CO conversion at 250 °C, ≈50% at 300 °C, and up to 76% at 350 °C; Fe/Zr-SiO_2 similarly climbed from ≈10% at 250 °C to ≈52% at 300-350 °C. In contrast, the Ti- and V-containing catalysts remained below 20% conversion at 250 °C and only modestly improved by 350 °C (Fig. 5.2). Notably, Fe/V-SiO_2 was the least active, never exceeding roughly 15-20% conversion even at the highest temperature, whereas Fe/Ti-SiO_2 showed a somewhat greater increase. These trends highlight that the Ce- and Zr-silicate supports promote much higher FT activity than Ti or V under identical conditions.

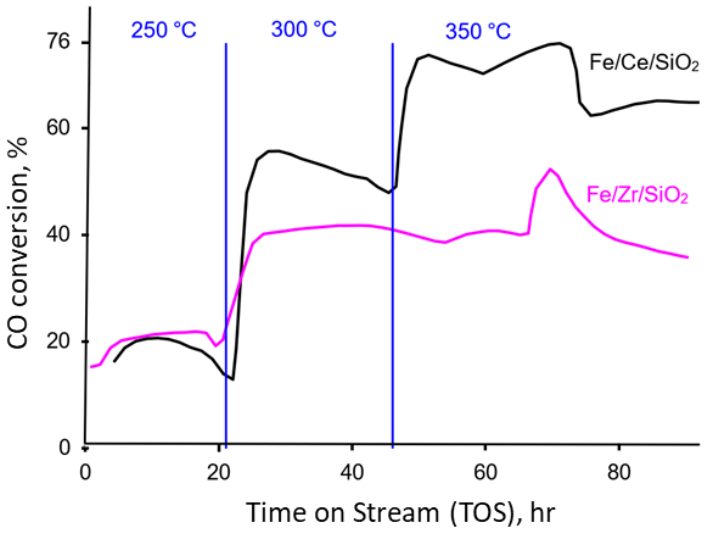

Figure 5.1. CO conversion of Fe/Ce-SiO_2 and Fe/Zr-SiO_2.

The time-on-stream behavior of the Ce- and Zr-supported catalysts also reflected their superior activity and reasonable stability. Both Fe/Ce-SiO_2 and Fe/Zr-SiO_2 maintained high conversions over ≈85 h of operation. Fe/Ce-SiO_2 stabilized around 68 % conversion and Fe/Zr-SiO_2 around 52 % by the end of the test. Fig. 5.1 illustrates the CO conversion profiles for these two catalysts during the temperature step increases. Apart from a transient drop, both showed sustained activity. Their higher conversions are partly due to the water-gas shift (WGS) activity of CeO_2 and ZrO_2 domains in the support, which convert produced H_2O to CO_2 and H_2 [1].

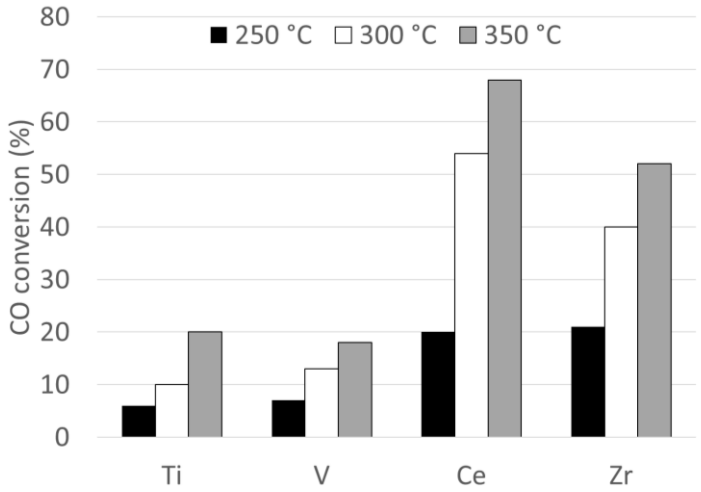

Figure 5.2. CO conversion of Fe/Ti-SiO_2 ***(Ti)*** *Fe/V-SiO_2* ***(V)****, Fe/Ce-SiO_2* ***(Ce)*** *FeZr-SiO_2* ***(Zr)****.*

Indeed, no separate liquid water phase was observed in the cold trap for these catalysts, as the water by-product was largely consumed by WGS to form CO_2. This led to considerable CO_2 selectivity, indicating that a portion of CO was diverted from Fischer-Tropsch synthesis into CO_2 formation. In summary, the Ce- and Zr-metallosilicate supports provided both high CO conversion and inherent WGS functionality, whereas the Ti- and V-based supports resulted in much lower FT activity with minimal WGS. The BET surface area trends correlate with these outcomes: Fe/Zr-SiO_2 had by far the highest surface area (335 m^2/g) among the fresh catalysts, and Fe/Ce-SiO_2 the lowest (54 m^2/g), while Fe/Ti-SiO_2 was intermediate (228 m^2/g) and Fe/V-SiO_2 extremely low (5.7 m^2/g). A low surface area severely limits the dispersion of active Fe sites, in the case of Fe/V-SiO_2 the support's pores collapsed into large voids (average pore diameter 21.2 nm) and bulk vanadium oxide crystallites [2], explaining its poor CO conversion. In contrast, the high surface area and porosity of the Zr- and Ti-silicate supports should favor dispersion; indeed Fe/Zr-SiO_2's strong initial activity can be ascribed to its large pore volume and surface, although other factors (discussed below) limit its ultimate performance. For Fe/Ce-SiO_2, the support's low surface area is offset by chemical promotion from Ce: CeO_2 can enhance oxygen exchange and CO adsorption, effectively acting as a structural promoter to Fe. The SEM-EDS analysis confirmed a more homogeneous distribution of Fe, K, and Cu on the Ce-silicate support compared to the Zr-silicate (which showed metal-rich agglomerates). A uniform metal distribution improves catalyst utilization by exposing more active sites to reactants [3], which helps explain why Fe/Ce-SiO_2 outperforms Fe/Zr-SiO_2 despite the latter's higher surface area [4].

Product selectivity over these unpromoted catalysts follows expected Fischer-Tropsch trends with temperature, with some variations among supports. At the lowest reaction temperature (200-220 °C), all catalysts were highly selective to long-chain hydrocarbons: C_{7+} selectivity was roughly 70 % for each, with the remainder being mostly C_2-C_6 hydrocarbons and minor CH_4. As temperature increased, the hydrocarbon distribution shifted toward lighter products for all compositions. In particular, the C_{7+} (heavy hydrocarbon) selectivity dropped substantially between 250 °C and 350 °C, while CH_4 and C_2-C_6 selectivities increased (Fig. 5.3). By the highest temperatures, the heavy hydrocarbon selectivity had decreased to roughly 30-40 %, varying slightly by catalyst, consistent with faster chain-termination at higher temperature. All four catalysts exhibited this same qualitative trend. Quantitatively, there were some differences: Fe/Zr-

SiO_2 tended to have the lowest C_{7+} selectivity at a given temperature, whereas Fe/Ce-SiO_2 maintained a somewhat higher fraction of heavy products. This is evidenced in the C_{2+} yield (the yield of C_2+ hydrocarbons, combining conversion and selectivity) for each catalyst (Fig. 5.4). Fe/Ce-SiO_2 achieved the highest C_{2+} yield across the temperature range, reflecting its superior CO conversion coupled with reasonably high heavy-product selectivity. In fact, by 350 °C Fe/Ce-SiO_2 showed a C_{2+} yield significantly above the others, whereas Fe/Zr-SiO_2, despite high conversion, had a lower yield due to its lighter product slate. Fe/Ti-SiO_2 and Fe/V-SiO_2 produced even less heavy product: for Fe/V-SiO_2 the C_{2+} yield remained around ≈7 % at all temperatures, the lowest of the group, attributable to its low conversion (very few hydrocarbons produced). The similar selectivity patterns among catalysts suggest that, in the absence of promoters, the chain-growth probability (α) is governed mainly by reaction temperature and the intrinsic properties of iron FT catalysis, with relatively minor modulation by the support. Still, the slightly higher heavy fraction on Fe/Ce-SiO_2 may indicate that cerium's promotional effect (perhaps via enhanced surface carbide formation or hydrogen moderation through WGS) favors longer chains [5]. Likewise, the lower heavy fraction on Fe/Zr-SiO_2 at high T could relate to its smaller pore size (~4 nm by BJH analysis, vs. 15 nm for Ce-SiO_2). Confinement in tiny pores can promote secondary reactions (cracking or olefin readsorption) that break long chains, thus yielding lighter products [6]. By contrast, the larger pores in the Ce-silicate support facilitate diffusion and reduce olefin readsorption, which helps preserve a higher C_{7+} selectivity [7]. Overall, Figure 5.3 confirms that all unpromoted metallosilicate catalysts experience a drop in C_{7+} selectivity from ≈70 % to ≈30-40 % as temperature rises, and Figure 5.4 highlights the superior heavy-product yields achieved by the Ce- and (to a lesser extent) Zr-based formulations relative to Ti and V.

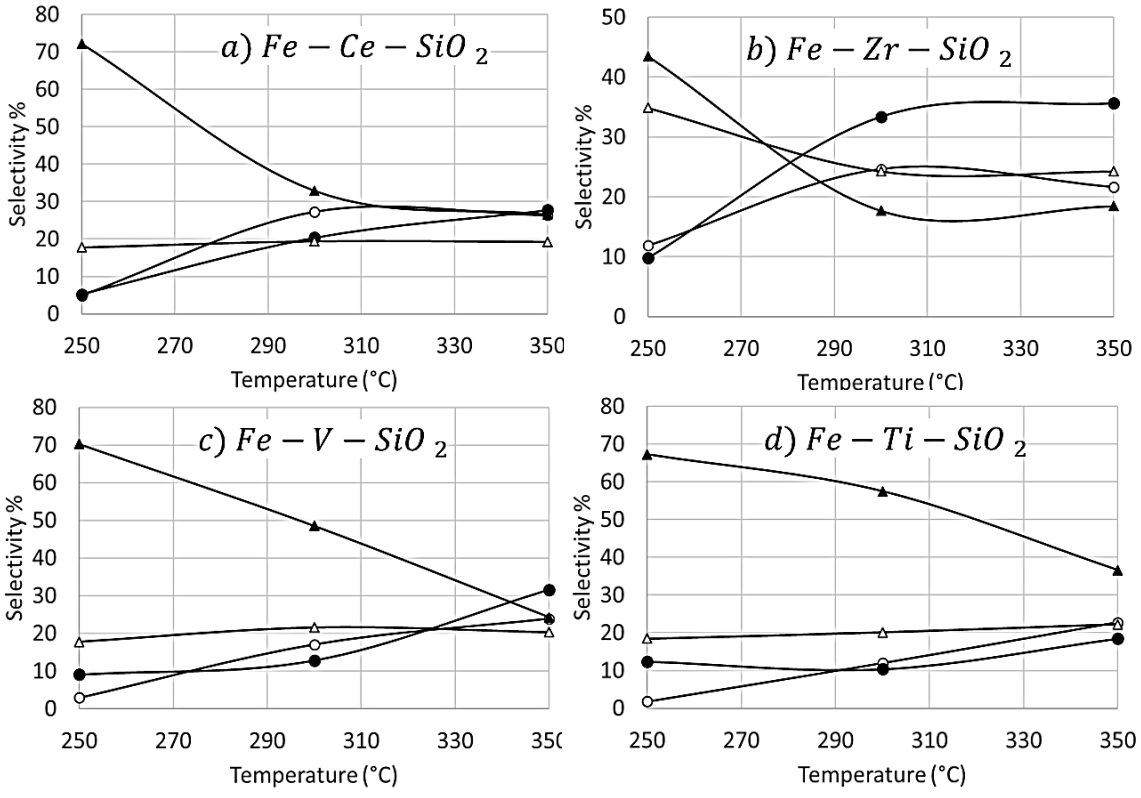

Figure 5.3. Selectivities in black triangles ▲: ≥C_7; white triangles ▵: <C_7; black circles •: CO_2; white circles ◦: CH_4

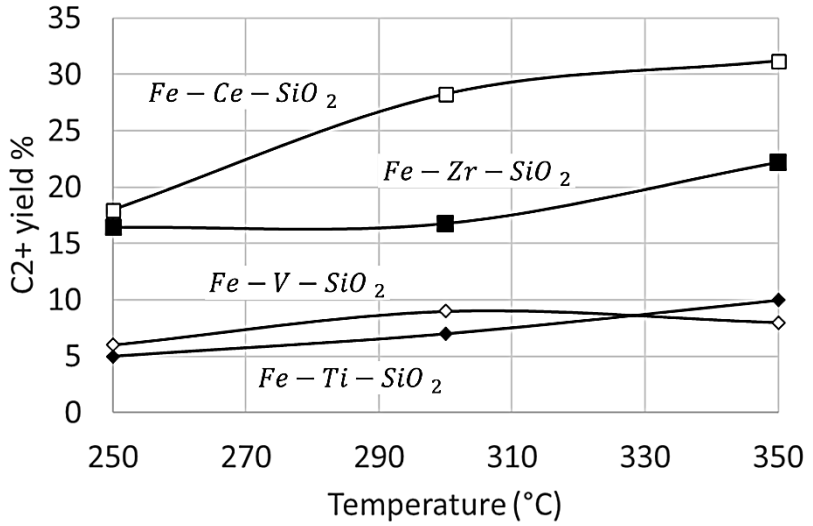

Figure 5.4. C2+ yield of Fe/Ce-SiO_2, Fe/Zr-SiO_2, Fe/V-SiO_2, and Fe/Ti-SiO_2 as a function of temperature.

The characterization data provide further insights into these performance differences. XRD phase analysis of the fresh catalysts showed that Fe was primarily present as hematite (Fe_2O_3) in all cases. However, the degree of crystallinity and the presence of other phases varied: Fe/Ce-SiO_2 exhibited well-defined CeO_2 and Fe_2O_3 reflections, giving the highest overall crystallinity (61.8 %). Fe/Zr-SiO_2 had the lowest crystallinity (34.3 %), with XRD suggesting that Zr was mostly incorporated into an amorphous silicate matrix rather than forming separate ZrO_2 crystals. In fact, EXPO analysis identified a zircon ($ZrSiO_4$) phase in this sample, indicating that the Zr dopant becomes part of a stable silicate structure. Such incorporation likely weakens metal-support interactions (as also evidenced by the larger Fe_2O_3 crystallite size of 16 nm in Fe/Zr-SiO_2), making Fe/Zr-SiO_2 more prone to Fe oxide particle growth during calcination. This could explain its slightly lower catalytic performance: a portion of the iron may be present as large Fe_2O_3 crystallites or Fe-Zr silicate domains that are less reducible and active in FT. By contrast, Fe/Ce-SiO_2 showed smaller Fe_2O_3 crystallites (≈7 nm), despite its lower surface area. It appears that CeO_2 in this sample helped structurally stabilize the silica framework and limit sintering of Fe oxide. The Ce likely also improves reducibility: CeO_2 can provide oxygen vacancies and facilitate the $Fe^{3+} \rightarrow Fe^{2+}$ reduction step, which might ease the formation of active Fe^0/Fe_3C during activation. In the case of Fe/Ti-SiO_2, XRD detected a Ti_2O_3 phase alongside Fe_2O_3, suggesting some strong interaction or even partial reduction of titania ($Ti^{4+} \rightarrow Ti^{3+}$) during synthesis. The crystallinity of Fe/Ti-SiO_2 was ≈37 %, similar to Fe/V-SiO_2 (≈48 %). Notably, Fe/V-SiO_2 showed reflections for V_6O_{13} (a vanadium oxide) and possibly an Fe-Si-V mixed phase, confirming that V forms bulk oxide aggregates. These large V-containing crystals led to the extremely low surface area observed and likely sequestered some iron in inactive forms.

5.1.1.2. Alumina supported and Promoted Fe-based Metallosilicates

The addition of potassium and copper promoters to the Fe/metallosilicate catalysts (Ce-SiO_2 and Zr-SiO_2 supports) improved their CO hydrogenation performance. Copper (5 wt% nominal in these formulations) serves to facilitate iron oxide reduction (by H_2 spillover) [8] and structural promotion, while potassium (2 wt%) is a well-known electronic promoter that enhances CO adsorption and chain-growth probability while suppressing hydrogenation [9]. Indeed, the K,Cu-promoted Fe/Ce-SiO_2 and Fe/Zr-SiO_2 catalysts showed higher conversions at lower temperatures

and much lower CH_4 selectivity compared to their unpromoted counterparts. As shown in Figure 5.5, the CO conversion over Fe/Ce-SiO_2-K,Cu increased with temperature from 13 % at 200 °C to 48 % at 275 °C and 86 % at 325 °C . Fe/Zr-SiO_2-K,Cu followed a similar trend, reaching 10 % at 200 °C, 40 % at 275 °C and 76 % at 325 °C. By 325 °C, both promoted catalysts far exceeded the maximum conversion observed for the unpromoted Fe/Ce-SiO_2 (≈68 % at 350 °C) and Fe/Zr-SiO_2 (≈52 %). The Ce-supported catalyst maintained a higher conversion than the Zr-supported one across all temperatures, but both exhibited the same general trend of sharply rising conversion with temperature. This underscores the effectiveness of the K/Cu promotion: even at 275 °C, the promoted Ce- and Zr-based catalysts were approaching or surpassing the performance that required 350 °C without promoters. Figure 5.5 compares the temperature-dependent conversion of Fe/Ce-SiO_2-K,Cu and Fe/Zr-SiO_2-K,Cu against their non-promoted counterparts.

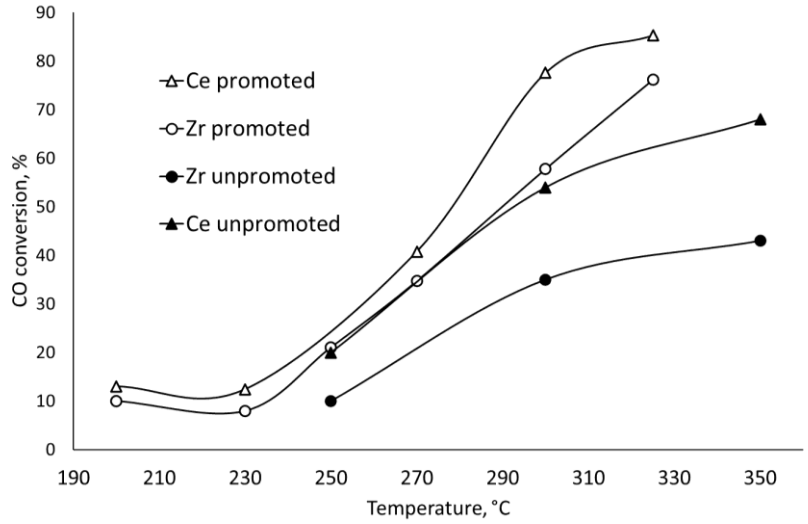

Figure 5.5. The CO conversion comparison over the increased temperature, for Fe/Ce-SiO_2-K,Cu and Fe/Zr/SiO_2-K,Cu with their non promoted versions of each catalyst.

Beyond higher activity, the promoted catalysts showed different selectivity patterns in particular, a strong suppression of methane and an increase in CO_2 production. Potassium is known to suppress hydrogenation of carbon intermediates, thereby lowering CH_4 and favoring longer-chain hydrocarbons, while also promoting the WGS reaction by increasing surface basicity and CO adsorption strength [10]. These effects were evident in the data. Fe/Ce-SiO_2-K,Cu exhibited an extremely low CH_4 selectivity of ≈1 % at 220 °C, rising gradually to 7 % at 300 °C and ≈13 % at 325 °C . By contrast, the unpromoted Fe/Ce-SiO_2 produced significantly more methane under similar conditions its CH_4 selectivity was ≈6 % at 250 °C, climbing to 15 % at 270 °C and as high as 27 % at 300 °C. A similar trend was observed for the Zr-supported catalysts: Fe/Zr-SiO_2-K,Cu had consistently lower CH_4 than unpromoted Fe/Zr-SiO_2 at each temperature. These comparisons are summarized in Figure 5.6. However, the carbon not appearing as CH_4 must go elsewhere, and in promoted iron catalysts a considerable fraction goes to CO_2 via the WGS reaction. For Fe/Ce-SiO_2-K,Cu, the CO_2 selectivity increased from ≈12 % (average from 200-220 °C) to ≈18 % (250-275 °C) and ≈36 % in the 300-325 °C range. This was significantly higher than the CO_2 levels for the non-promoted catalyst, indicating that K promotion shifted selectivity away from CH_4 (and possibly some C_2-C_6) toward CO_2. In essence, the K,Cu-promoted catalysts converted more of each CO feed into useful C_2+ hydrocarbons than the unpromoted ones, at the cost of converting

another portion of CO into CO_2 rather than additional hydrocarbon. From a mechanistic perspective, this trade-off reflects K's dual role in FTS: it enhances dissociative CO adsorption and chain growth, suppressing methane formation, but also facilitates removal of oxygen (via $CO \rightarrow CO_2$), especially in conjunction with iron which inherently performs WGS. The end result under our conditions was a net gain in heavy hydrocarbon production despite increased CO_2. It is noted in literature that optimizing K loading can minimize excessive CO_2 production, and that dual promotion with Cu improves Fe catalyst activity and stability synergistically [11,12].

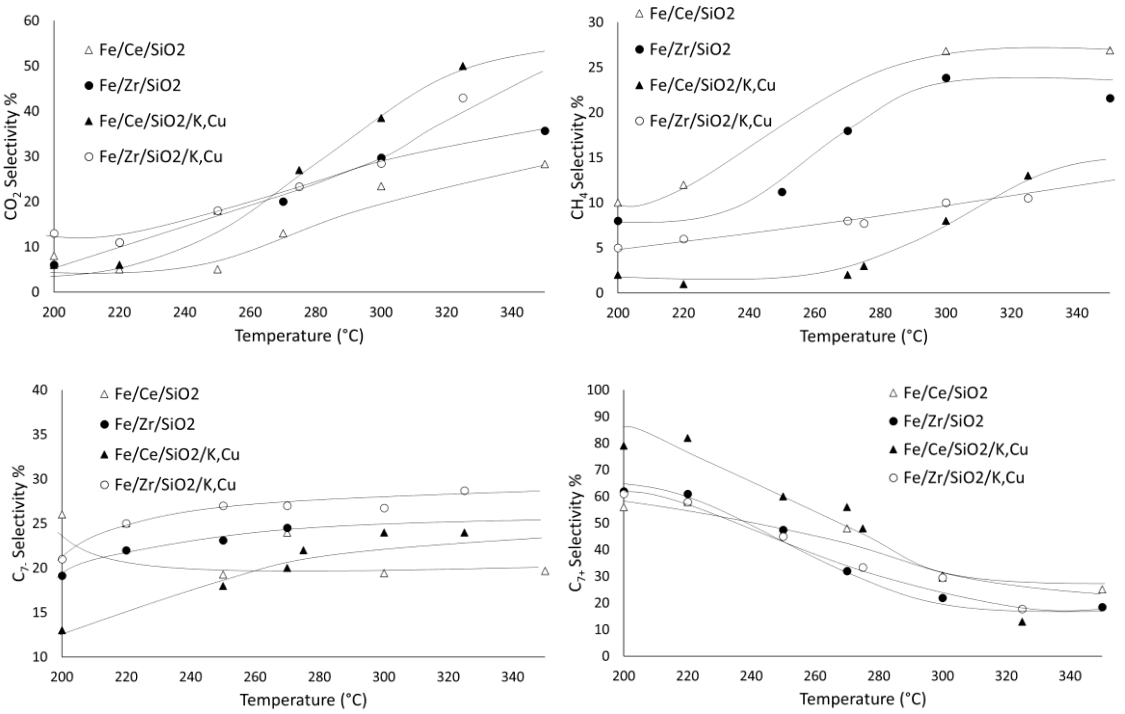

Figure 5.6. The selectivity comparison of CH_4, CO_2, C_{7-} and C_{7+} over increased temperature, unpromoted Fe/Ce/SiO_2 and Fe/Zr/SiO_2 vs Fe/Ce/SiO_2-K,Cu and Fe/Zr/SiO_2-K,Cu

Product selectivities for the K,Cu-promoted metallosilicate catalysts followed similar temperature trends to the unpromoted ones, but with generally more favorable values. Both Fe/Ce-SiO_2-K,Cu and Fe/Zr-SiO_2-K,Cu retained very high C_{7+} selectivity at lower temperatures: e.g. at 220 °C, the C_{7+} selectivity for Fe/Ce-SiO_2-K,Cu was about 90 %, comparable to cobalt-based catalysts on similar supports. As temperature increased, C_{7+} selectivity did decline, while CH_4 and CO_2 rose, but remained respectable. By 300 °C, Fe/Ce-SiO_2-K,Cu still had well over half of the carbon going to C_{2+} hydrocarbons, with only ≈7 % to CH_4. Fe/Zr-SiO_2-K,Cu showed a slightly lighter distribution,consistent with its smaller pore size and lack of crystalline domains but also produced the majority of products as C_{2+} hydrocarbons at all temperatures. In short, K and Cu promotion enabled the Fe/Ce-SiO_2 and Fe/Zr-SiO_2 catalysts to operate in a more desirable regime: high conversion with low methane yield and a product slate shifted toward longer chains. The enhanced performance is tied to characterization observations: TPR-H_2 profiles showed that the fresh K,Cu-promoted catalysts had most of their reduction peaks in the higher temperature region (300-500 °C), indicating strong metal-support interactions and fewer "easy-to-reduce" sites. After activation, only minor TPR signals remained, confirming that the syngas reduction had converted nearly all Fe to active phases. XRD of the promoted Fe/Ce-SiO_2-K,Cu and Fe/Zr-SiO_2-K,Cu

showed primarily hematite (Fe_2O_3) phases in the fresh state (with CuO and CeO_2 or $ZrSiO_4$ identifiable). Scherrer analysis revealed that Fe/Zr-SiO_2-K,Cu had larger Fe_2O_3 crystallites (≈16 nm) than Fe/Ce-SiO_2-K,Cu (≈7 nm), consistent with the idea that CeO_2 prevented excessive Fe oxide sintering whereas Zr did not. Despite this, Fe/Zr-SiO_2-K,Cu's activity was still high, the slightly larger Fe_2O_3 particles did not hinder its ability to generate active Fe^0/Fe_3C under reaction conditions, but they might contribute to its marginally lower conversion relative to Fe/Ce-SiO_2-K,Cu. Additionally, XPS confirmed that both Ce and Zr form stable surface silicate structures ($CeSiO_2$ and $ZrSiO_4$), rather than remaining as free oxides [3]. The Ce-silicate presumably provides oxygen buffers that facilitate WGS, whereas the Zr-silicate leads to a more inert support framework (explaining again the higher CO_2 and lower C_{7+} in Fe/Zr-SiO_2-K,Cu). Overall, the promoted Ce- and Zr-metallosilicate catalysts demonstrate how combining an active support with appropriate promoters yields excellent FT performance, with each component (support, K, Cu) contributing to activity and selectivity in distinct ways [13].

To benchmark the metallosilicate-supported catalysts against conventional supports, two additional K,Cu-promoted Fe catalysts were prepared on commercial alumina supports: Catalox (a high-purity γ-Al_2O_3 with ordered mesoporosity) and Dispal (a boehmite-derived alumina with a less ordered pore structure). These alumina-supported catalysts showed good performance but some notable differences from the metallosilicate-supported ones. Both Fe/Catalox-K,Cu and Fe/Dispal-K,Cu exhibited steadily increasing CO conversion with temperature (Fig. 5.7). At 275 °C, their conversions were already substantial (≈60-70 % range, similar to the metallosilicate catalysts at that temperature). By 325 °C, Fe/Catalox-K,Cu achieved 88 % CO conversion, while Fe/Dispal-K,Cu reached 77 % . These values are on par with the Fe/Ce-SiO_2-K,Cu (86 %) and Fe/Zr-SiO_2-K,Cu (76 %) results at 325 °C , indicating that the best alumina-supported catalyst (Catalox) can match the activity of the best metallosilicate-supported one (Ce-SiO_2). The Dispal-based catalyst, though slightly behind, was comparable to the Zr-SiO_2-supported catalyst in conversion. However, a key difference was observed in how the conversion evolved: the metallosilicate-supported catalysts tended to continuously increase in conversion with each temperature step, whereas the alumina-supported catalysts were "more stable at each temperature", i.e. they maintained their activity without sudden drops and possibly experienced less deactivation over the test duration. This could be related to stronger metal-support interactions in alumina (e.g. $FeAl_2O_4$ formation) which stabilize the active phase against sintering or attrition, as suggested in literature [14]. In fact, prior studies have shown iron on Al_2O_3 can be more stable and even more active than on SiO_2 for instance, one report found 51 % CO conversion on Fe/Al_2O_3 vs 26 % on Fe/SiO_2 (both unpromoted, 300 °C, 2 MPa), with higher C_{7+} selectivity on alumina as well (64 % vs 60 %) . The superior performance of alumina was attributed to the formation of iron aluminate species that prevent nanoparticle sintering [15]. On the other hand, the metallosilicate supports in our study likely owe their good activity to the incorporated metal acting as an internal promoter and to a robust mesoporous structure that remains intact during reaction [16]. Indeed, the Ce and Zr in the silicate framework appear to enhance activity while silica's high surface area supports many active sites; this combination led to the high conversions noted above. But the trade-off is possibly a lower long-term stability: because metal-silica interactions are relatively weak, iron particles on metallosilicates might detach or sinter more easily under reaction conditions, causing gradual deactivation [17]. In summary, Figure 5.7

compares the CO conversions of the promoted Sasol-supported (alumina) catalysts with those of the promoted metallosilicate-supported ones. All four are highly active, but the alumina systems show slightly lower peak conversion in this series, likely due to a fraction of iron being tied up in less-active aluminate structures, while offering robust stability.

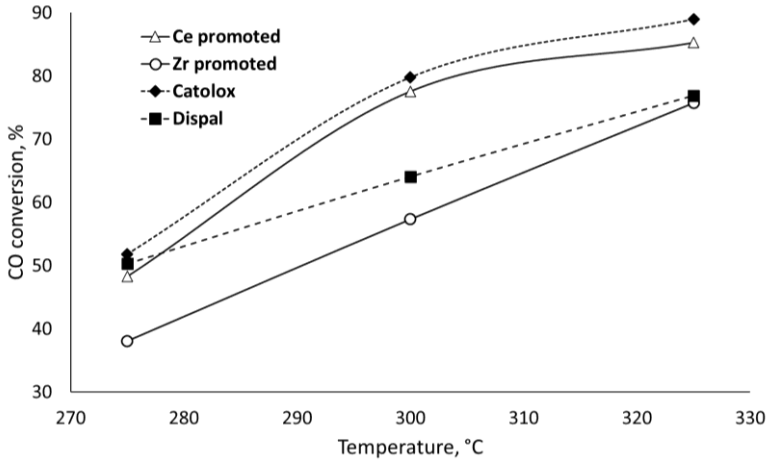

Figure 5.7. The conversion of CO conversion of Promoted Sasol supported and Metallosilicate supported iron catalysts.

Selectivity trends on the alumina-supported Fe catalysts were broadly similar to the metallosilicate catalysts, with low CH_4 and high heavy-hydrocarbon production, but with one difference: the C_{7+} selectivity exhibited a pronounced minimum at 300 °C for both Fe/Catalox-K,Cu and Fe/Dispal-K,Cu. At 275 °C, Fe/Catalox-K,Cu showed ≈76 % C_{7+} selectivity (with Fe/Dispal-K,Cu at ≈57 %). Upon increasing to 300 °C, the C_{7+} selectivity of the Catalox-based catalyst decreased to ≈24 %, and that of the Dispal-based catalyst to ≈16 %. Interestingly, when the temperature was raised further to 325 °C, the heavy product selectivity rebounded, C_{7+} increased to ≈48 % for Catalox and ≈36 % for Dispal at 325 °C. The CH_4 selectivities, meanwhile, remained very low in absolute terms. For Fe/Catalox-K,Cu, CH_4 was only ≈2 % at 275 °C, ≈7-8 % at 300-325 °C . Fe/Dispal-K,Cu showed slightly higher CH_4: ≈4 % at 275 °C, 9 % at 300 °C, and ≈11 % at 325 °C. The drop in C_{7+} was not due to methane but rather an increase in medium-weight (C_2-C_6 or "C_7^-") hydrocarbons and CO_2. This is confirmed by analysis of the product distribution and carbon balance. At 300 °C, the alumina-supported catalysts produced the highest amounts of C_2-C_6 (gasoline-range) hydrocarbons and also the highest CO_2 selectivity. Specifically, Fe/Catalox-K,Cu at 300 °C had CO_2 selectivity ≈43 % (versus 20 % at 275 °C) and C_7^- selectivity ≈28 %. Fe/Dispal-K,Cu at 300 °C had CO_2 ≈46 % (vs 24 % at 275 °C) and C_7^- ≈29 %. These values imply that at 300 °C a considerable portion of CO was being converted to CO_2, via WGS, and to lighter hydrocarbons, at the expense of C_{7+} production. This inverse relationship suggests a competitive interplay between the FT chain-growth pathway and the WGS, CO_2-forming, pathway. At 300 °C, conditions favored WGS strongly (high CO_2, low C_{7+}); by 325 °C, the WGS equilibrium shifted (since WGS is exothermic, higher temperature drives it backwards), resulting in lower CO_2 formation and more carbon available for chain growth. As a result, heavy hydrocarbon synthesis recovered. The net effect is that operating at 300 °C gave the highest yield of light products, and CO_2, whereas 325 °C shifted the product distribution back towards heavier fraction. This indicates the possibility of tuning the product spectrum by temperature in K-Cu-Fe catalysts on alumina: a slightly lower temperature favors gasoline-range

products and maximizes CO_2, whereas a higher temperature shifts towards heavier wax production. Importantly, CH_4 remained low across this range for both catalysts, meaning the selectivity shifts involved primarily the balance between C_{7+}, C_{7^-} and CO_2. Table 5.1 summarizes the C_{7+} and CH_4 selectivity trends for the Catalox and Dispal supported catalysts.

	Temperature, °C	CO_2	CH_4	C_{2-6}	$C_{\geq 7}$	C_{2+} yield
Fe/Catalox-K,Cu	275	20	5	14	61	44
	300	43	5	28	24	54
	325	35	7	10	48	49
Fe/Dispal-K,Cu	275	24	4	15	57	40
	300	46	9	29	16	41
	325	41	12	11	36	37

Table 5.1. Selectivities of Fe/Catalox-K,Cu and Fe/Dispal-K,Cu.

The differences between the Catalox- and Dispal-supported catalysts can be rationalized by their structural and compositional disparities. Catalox (Sasol's high-purity alumina) is known to have an ordered mesoporous structure and a uniform spherical particle morphology, often described as "donut"-shaped particles [18]. SEM images confirmed that our Fe/Catalox-K,Cu catalyst retained the spherical morphology of the Catalox support. N_2-physisorption showed a mesopore size ≈5 nm and BET surface area of 84 m^2/g for Fe/Catalox-K,Cu, versus a larger 15 nm pore size but higher area of 150 m^2/g for Fe/Dispal-K,Cu. Thus, the Dispal-supported catalyst had greater total surface area, but its porosity was less uniform. In fact, despite the lower surface area, Fe/Catalox-K,Cu exhibited better performance, indicating that pore architecture and metal dispersion were more crucial than sheer area. The Catalox support's ordered mesopores likely allowed a more homogeneous and accessible distribution of the iron and promoter species. EDS mapping showed Fe/Catalox-K,Cu had an even elemental distribution, whereas Fe/Dispal-K,Cu had regions with lower Fe, K, Cu concentrations (suggesting some segregation or poorer uptake). This translates to more active site accessibility in the Catalox-based catalyst, contributing to its higher CO conversion. Moreover, XRD and electron microscopy provided evidence of different Fe phases present: Fe/Catalox-K,Cu's fresh phase was mainly Fe_2O_3 (hematite) with some θ-Al_2O_3 reflections, whereas Fe/Dispal-K,Cu showed Fe_3O_4 (magnetite) as the dominant iron phase. The smaller crystallite size of iron oxide on Dispal (Scherrer crystallite ≈3 nm, vs ≈12 nm on Catalox) indicates higher dispersion of Fe on Dispal, yet much of it was already in the partially reduced magnetite state. Magnetite is a known active phase for WGS, which aligns with the higher CO_2 selectivity and lower C_{7+} on Fe/Dispal-K,Cu. In contrast, the larger Fe_2O_3 particles on Catalox were fully reduced *in situ* to the FT-active carbide phase without overly favoring WGS at 300 °C. In essence, the Dispal support seems to promote partial Fe reduction ($Fe_2O_3 \rightarrow Fe_3O_4$) even during calcination, yielding many small magnetite crystallites that boost WGS (CO_2 formation) at the expense of FT synthesis. Catalox, with slightly less reducible Fe_2O_3 initially, may transition to the carbide phase under syngas more directly, thus prioritizing hydrocarbon formation. Additionally, the metal-support interactions differ: Catalox's Fe likely interacts to form some $FeAl_2O_4$ (especially with 950 °C calcination), which can stabilize Fe but also moderate its reducibility. Dispal might interact differently, resulting in more Fe remaining free or in small clusters. These subtle differences in Fe phase and support interaction explain why Fe/Catalox-

K,Cu achieved higher conversion and heavier products, whereas Fe/Dispal-K,Cu, despite higher dispersion, leaned more towards WGS and lighter products. Nonetheless, both catalysts benefit from alumina's stabilizing effect: neither showed any abrupt deactivation, and their performance was reproducible and consistent across repeated tests. The textural stability of alumina supports under FT conditions is an advantage, as they do not significantly sinter or collapse; this contrasts with metallosilicate supports, which, although mesoporous, might undergo structural changes (silica phases can agglomerate or lose surface area in high-temperature, water-rich environments over long times). Indeed, it was observed that after reaction the BET surface areas of the metallosilicate catalysts dropped (e.g., Fe/Ce-SiO_2 fresh 54 → spent 33 m^2/g; Fe/Zr-SiO_2 335 → 287 m^2/g), while the alumina-supported ones maintained more of their structure (Fe/Catalox-K,Cu spent 84 m^2/g, Fe/Dispal-K,Cu 150 m^2/g, with only minor losses). This suggests the metallosilicates, while highly active, may have lower long-term stability than conventional alumina-supported catalysts, which aligns with general experience in FT catalysis [3].

5.1.2. Hydrotalcite: Fe30 US vs BM

5.1.2.1. Performance in Syngas Hydrogenation

This section discusses the Fischer-Tropsch performance of hydrotalcite-derived Fe30 catalysts prepared by ultrasound (Fe30 US) and ball milling (Fe30 BM). We focus on CO conversion trends, product selectivities (CH_4, C_2-C_6, C_{7+} fractions), and the overall C_{2+} hydrocarbon yields. A final section compares the Fe30 catalysts to the metallosilicate-supported catalysts from Chapter 5.1.1.

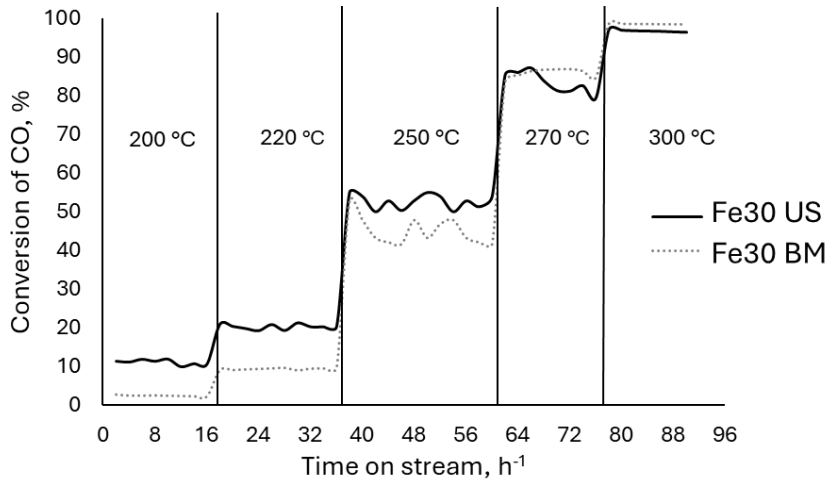

Figure 5.8. CO Conversion vs. Time on Stream for Fe30 US and Fe30 BM.

Both Fe30 catalysts showed active CO hydrogenation behavior, but with notable differences in conversion magnitude and activation profile. Fe30 US achieved higher CO conversion throughout the test, reaching steady-state levels approximately 10% above the ball-milled analogue. During initial hours on stream, Fe30 US exhibited a rapid rise in conversion, suggesting quick formation of the active iron carbide phase. In contrast, Fe30 BM displayed a more gradual activation, consistent with a slower reduction/carburization of iron when prepared by milling. This difference aligns with TPR-H_2 results, where the ultrasound-synthesized catalyst showed sharper, lower-temperature reduction peaks compared to the broader, higher-temperature reduction profile of the ball-milled sample. The easier reducibility of Fe30 US correlates with its faster attainment of high

activity, whereas Fe30 BM's stronger metal-support interactions (imparted by mechanical mixing) likely delay the reduction to Fe^0/Fe_3C, temporarily limiting its FT activity [19].

At reaction temperatures equal to 250°C, Fe30 US reached a stable CO conversion of ≈53% that remained nearly constant over the 24h on stream, indicating good stability. Fe30 BM ultimately approached a slightly lower plateau conversion (≈48%) under identical conditions. The ball-milled catalyst also maintained a steady conversion with only a marginal decline over the time-on-stream examined, suggesting that mechanical mixing did not introduce any rapid deactivation pathway beyond the slower initial activation.

The observed activity order Fe30 US > Fe30 BM is in line with the enhanced reducibility and crystallinity imparted by ultrasound synthesis. XRD and TEM characterization confirmed that Fe30 US contains well-defined oxide crystallites that convert readily to iron carbides, whereas Fe30 BM presents a more amorphous, interdispersed oxide structure. Such low-crystallinity, intimately mixed phases in the ball-milled catalyst can impede reduction a phenomenon similarly noted for other poorly crystalline Fe supports (e.g. Fe on amorphous Zr-silicate) which showed lower FT activity. In our case, Fe30 BM's intimate metal-oxide mixing likely forms Fe-Mg oxide compounds that require higher temperatures to reduce, resulting in a fraction of iron remaining as oxidic phase during FT. This residual oxide can still catalyze the water-gas shift reaction instead of Fischer-Tropsch hydrocarbon formation [20].

Consequently, Fe30 BM diverts a bit more CO to CO_2 byproduct via WGS, whereas Fe30 US, being more fully carburized, channels a greater proportion of CO into hydrocarbons. This contributes to Fe30 US's higher C_{2+} hydrocarbon yield (see Table 5.2). Additionally, ball-milling creates a broader distribution of strong adsorption sites on the catalyst surface, as evidenced by H_2-TPD and CO_2-TPD analyses (Chapter 4.3). These deep, high-strength sites can retain key reactants or intermediates (H_2, CO_2) more tightly, effectively slowing the turnover frequency by limiting reactant accessibility. In contrast, the ultrasound method yields a narrower range of moderate-strength sites, facilitating rapid adsorption-desorption cycles that sustain higher reaction rates. Overall, the superior CO conversion of Fe30 US is attributed to its more facile iron phase reduction and balanced adsorption properties, whereas Fe30 BM's lower activity stems from its strong metal-oxide interactions and heterogeneous surface sites introduced by mechanochemical synthesis.

5.1.2.2. Methane Selectivity and Chain Growth Probability

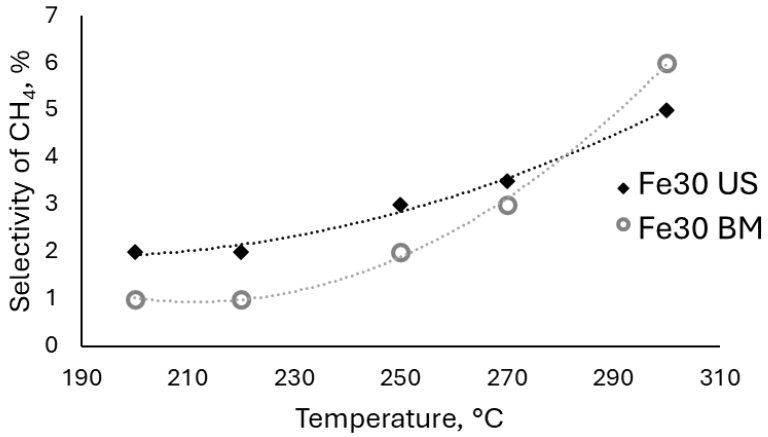

Figure 5.9. Selectivity to CH_4 for Fe30 US vs. Fe30 BM.

All Fe30 catalysts in this study were promoted with potassium (K) and copper (Cu), which are well-known additives in iron FT catalysts [21]. Potassium increases the intrinsic chain-growth probability (α) by enhancing CO chemisorption and dissociation on iron surfaces, thereby suppressing excessive methanation [22]. Copper, on the other hand, improves the reduction of iron oxide during activation, facilitating the Fe→Fe_3C transformation. Consistent with these roles, both Fe30 US and Fe30 BM exhibited low CH_4 selectivity relative to unpromoted iron catalysts [23]. During steady operation, methane accounted for only a minor fraction of the product. This reflects the strong effect of K in suppressing hydrogenation termination reactions. In literature, K-promoted Fe catalysts often show significantly lower CH_4 selectivity (sometimes <10%) compared to unpromoted counterparts [24], and our results fall in line with those trends.

Between the two preparation methods, no differences in CH_4 selectivity were observed, both catalysts produced similarly low methane fractions, indicating that chain growth remained favoured on both. At steady state, both catalysts achieved single-digit methane selectivities, with Fe30 US typically around ≈2-5%C (placeholder value) and Fe30 BM ≈1-8%C. These values underscore the effectiveness of our promotion strategy: the presence of K shifted the product spectrum away from methane toward longer chains [25]. Potassium increases the CO adsorption strength and reduces H_2 coverage on Fe, which disfavours the direct hydrogenation of surface C* to ethane [19]. Instead, carbon insertion into growing chains is promoted, raising α (the probability of chain propagation vs termination).

It is worth noting that Fe30 BM's slightly broader distribution of surface sites might lead to a bit more heterogeneity in active sites for FT. Some regions of the milled catalyst could have less K coverage or more defective Fe sites, which might locally produce more CH_4. Meanwhile, other regions with K presence produce mostly longer products. This could manifest as a marginally wider spread in CH_4 output under different conditions. Fe30 US, with a more uniform site landscape, likely offers more consistent behavior across its surface. Nonetheless, the overall methane selectivity remained low and comparable for both, confirming that the mechanochemical vs sonochemical preparation did not drastically alter the fundamental chain-growth propensity imparted by K promotion. Both catalysts behave as high-α iron FT systems.

5.1.2.3. Light vs. Heavy Hydrocarbon Selectivity and C_{2+} Yields

Both Fe30 catalysts exhibited a product slate dominated by C_{2+} hydrocarbons, with a clear emphasis on the heavier fraction (C_{7+}). This is a direct consequence of the high chain-growth probabilities discussed above. Under typical syngas reaction conditions, the C_{7+} fraction accounted for the largest share of the hydrocarbon products, while the intermediate C_2-C_6 fraction was moderate, and CH_4 was minimal. For instance, Fe30 US at 220 °C produced roughly 50 % C_{7+}, about 15 % C_{2-6}, and only a small remainder as CH_4. Fe30 BM showed a very similar distribution, with perhaps a slightly lower heavy fraction balanced by a slight increase in the C_2-C_6 portion. Overall, though, both preparation methods direct the majority of converted carbon into longer-chain products (C_{2+} *≈90%* of CO conversion), which is desirable for liquid fuel production.

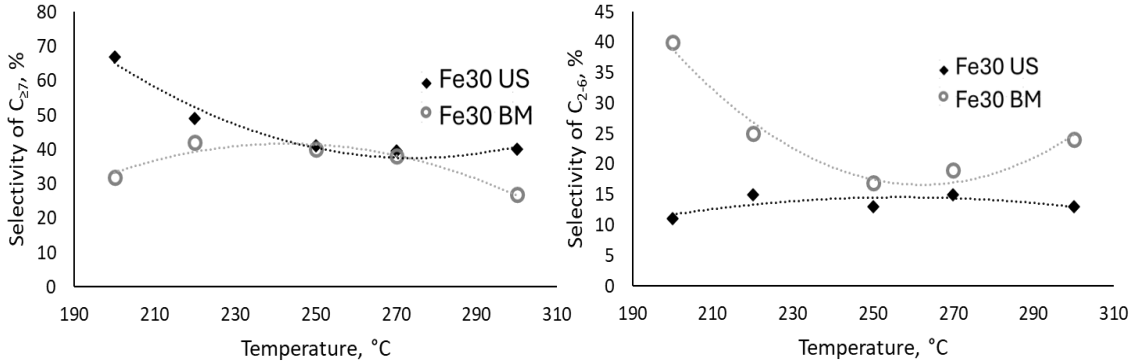

Figure 5.10. Product Selectivity Distribution (CH_4, C_2-C_6, C_{7+}) for Fe30 US and Fe30 BM.

The prominence of C_{7+} selectivity indicates robust chain growth on these catalysts, likely aided by the basic Mg-Fe-O support matrix derived from the hydrotalcite and the K promoter. Basic oxides can moderate secondary reactions like olefin readsorption/cracking, helping preserve higher molecular weight products. Indeed, prior studies on Fe catalysts supported on mixed MgO-Al_2O_3 (similar in composition to our hydrotalcite-derived support) found that increasing the base strength of the support increased the yield of heavier hydrocarbons by facilitating olefin polymerization while limiting over-hydrogenation [26]. Our Fe30 US catalyst, with uniformly moderate basic sites, appears well-suited for fostering continuous chain growth without prematurely terminating reactions. In contrast, Fe30 BM's heterogeneous surface includes some extra-strong basic sites; these might stabilize adsorbed intermediates or byproducts (e.g. formate, carbonate) very strongly, potentially hindering further chain propagation on those particular sites [27]. However, the net effect on product distribution is minor Fe30 BM still achieves a heavy-selectivity profile comparable to Fe30 US.

At 220 °C, Fe30 US converted 20 % of the CO feed and delivered a 13 % C_{2+} yield (≈65 % of the converted carbon). Fe30 BM, converting 12 %, produced a 9 % C_{2+} yield (≈75 % of its converted carbon). Moving to 270 °C, Fe30 US reached 83 % conversion with a 46 % C_{2+} yield (≈55 % of converted carbon), whereas Fe30 BM attained 86 % conversion and a 49 % C_{2+} yield (≈57 %). At the highest temperature tested, 300 °C, the two catalysts converged: Fe30 US gave 96 % conversion and 51 % C_{2+} yield (≈53 % of converted carbon), while Fe30 BM produced 98 % conversion with the same 51 % C_{2+} yield (≈52 %).

Integrated over the 200-300 °C window, Fe30 US therefore maintains a modest (≈8 % relative) advantage in cumulative C_{2+} yield, consistent with its slightly higher average conversion activity

across the temperature range. This difference is practically significant: it means the ultrasound-prepared catalyst produces more of the desirable longer-chain hydrocarbons from the same syngas input. The ball-milled catalyst, while still efficient at making C_{2+} products, loses a bit more carbon to unconverted CO (and to CO_2 via WGS), which slightly lowers its carbon efficiency towards fuels.

It is instructive to examine the light hydrocarbon (C_2-C_6) selectivity in context. Both catalysts showed moderate C_2-C_6 production (on the order of 30-40%C as noted). These light hydrocarbons include primarily C_2-C_4 gases and some C_5-C_6 gasoline-range liquids. The presence of a significant C_2-C_6 fraction alongside C_{7+} indicates an ASF-type distribution of products, as expected for FT chemistry. The slightly higher C_2-C_6 share on Fe30 BM could stem from its fraction of sites more H-rich due to the catalyst's retention of hydrogen. And also, If ball milling led to any regions of the catalyst with weaker K coverage, those regions might terminate chains earlier, increasing the C_2-C_6 output.

Catalyst	T(°C)	χCO	C_{2+} yield	SCH_4	SCO	SC_{2-6}	$SC_{\geq 7}$
Fe30 BM	200	6	4	1	27	40	32
	220	12	9	1	32	25	50
	250	48	30	2	41	17	40
	270	86	49	3	40	19	38
	300	98	51	6	43	24	27
Fe30 US	200	11	9	2	20	11	67
	220	20	13	2	34	15	49
	250	53	29	3	43	13	41
	270	83	46	4	42	15	40
	300	96	51	5	42	13	40

Table 5.2. Fischer-Tropsch Performance of Fe30 US and Fe30 BM - CO Conversion, CH_4 Selectivity, C_2-C_6 Selectivity, C_{7+} Selectivity, and C_{2+} Yield.

Additionally, the stronger adsorption sites on Fe30 BM might hold heavy hydrocarbon precursors so tightly that a portion cannot continue growing and instead desorb as mid-length molecules. Fe30 US, with more uniformly moderate sites, allows those intermediates to diffuse or migrate, continuing chain growth or at least desorbing in heavier form. These mechanistic differences could explain a marginal preference of lighter products on the milled sample. However, we emphasize that the overall selectivity trend, high C_{7+}, moderate C_2-C_6, low CH_4, holds for both catalysts.

5.1.2.4. Comparison with Metallosilicate-Supported Catalysts

In Chapter 5.1.1, the performance of Fe-based catalysts supported on metallosilicate frameworks (e.g. mesoporous Zr-silicate and Ce-silicate, with similar K-Cu promotion) was discussed. Both classes of catalysts exhibit high selectivity toward heavier hydrocarbons, but there are key differences in activity and stability. The metallosilicate-supported Fe catalysts, tested at somewhat lower temperatures (220-275 °C) in the earlier study, achieved very low methane outputs (≈7% CH_4) and very high C_{7+} selectivities often on the order of 80-90% under those conditions. For example, a K,Cu-promoted Fe catalyst on a Ce-silicate support showed ≈90%C_{7+} selectivity at 220 °C. These heavy-product selectivities are in the same qualitative range as observed for Fe30 US/BM in this chapter (which also produced ≈60-70%C_{7+} at 300-350 °C). Notably, the Fe30

catalysts maintain low CH_4 selectivity even at the higher temperature of our tests (≈300 °C), with CH_4 in single digits similar to the ≈7% reported for the silicate-supported Fe at 275-300 °C. This underscores the effectiveness of K promotion across different support systems.
In terms of CO conversion activity, the hydrotalcite-derived Fe30 catalysts show competitive to superior performance relative to the metallosilicate ones. In Chapter 5.1.1, it was noted that Fe catalysts on mesoporous Ce- and Zr-silicate supports required an increase in temperature to boost conversion, and even then, conversions were moderate (e.g. rising from ≈53% at 220 °C to 75% at 275 °C). The Fe30 US catalyst in this work, by contrast, achieved very satisfactory conversions. Furthermore, when comparing to Fe catalysts on traditional oxide supports: Chapter 5.1.1 described Fe/K/Cu on commercial alumina supports (Sasol's Catalox and Dispal) reaching 77-88% CO conversion at 325 °C. Our Fe30 US comes close to these figures at lower temperature, achieving robust activity. The hydrotalcite-derived mixed oxide support competes well with, and in some respects outperforms, conventional supports. One reason could be the homogeneous dispersion of metal in the HT-derived matrix, providing effective active phase distribution. Additionally, the basic nature of the HT-derived support (Mg-Fe-O) inherently promotes the WGS equilibrium, ensuring abundant in-situ H_2 for FT and removal of inhibiting surface carbon. The metallosilicate supports (especially Ce-silicate) also provided some oxygen donation and WGS activity, but the HT-derived support offers a different balance of acidity/basicity that appears favorable for sustained FT turnover.

A notable difference was observed in stability upon thermal changes. The Chapter 5.1.1 results indicated that Fe on a Ce-silicate support experienced some deactivation when temperature was raised (after long runs, activity dropped), whereas Fe on a Zr-silicate was more stable but exhibited a lower C_{7+} selectivity. In comparison, the Fe30 catalysts demonstrated excellent stability at their operating temperature no significant deactivation was seen over the test durations, and heavy hydrocarbon selectivity remained high. The metallosilicate supports (especially those that are partially amorphous) might undergo structural evolution or silica-iron interactions at elevated temperatures, affecting performance. Indeed, XRD in Chapter 4.3.1 showed the Fe/Ce-silicate catalyst was more crystalline and stable, whereas Fe/Zr-silicate was X-ray amorphous and delivered lower performance, suggesting that support crystallinity and stability were issues. Our HT-derived support calcines into a mixed $MgFe_2O_4$-like matrix that is quite refractory and thus provides a stable support up to the 350 °C range, likely contributing to the steady performance. In terms of product distributions, both families yield predominantly long-chain hydrocarbons with minimal methane. The silicate-supported Fe catalysts showed extremely high C_{7+} selectivities (often >80-90%). Our Fe30 catalysts, gave slightly lower heavy fraction (≈60-70%C_{7+}). Both catalysts are K-Cu-Fe systems that inherently favor low methane and high heavy products. This is supported by literature where promoted iron on diverse supports (silica, alumina, or mixed oxides) consistently shows chain-growth probabilities $\alpha \approx 0.7\text{-}0.9$, yielding ASF distributions rich in C_{7+} [9,28].

Finally, it's important to highlight the unique advantage of the Fe30 catalyst: the synthesis methods used here (ultrasound and ball milling) are "green" and scalable, and they produce catalysts that do not require exotic supports or templates. The metallosilicate supports require multi-step syntheses and structure-directing agents. In contrast, the hydrotalcite route offers a one-

pot co-precipitation approach, and the mechanochemical route avoids solvents altogether. The performance achieved by Fe30 US, in underscores the promise of sonochemical preparation. In conclusion, Fe30 US and Fe30 BM show performance on par with or exceeding that of earlier K-Cu-Fe catalysts on metallosilicate supports. They produce similarly low methane and high heavy product fractions, with the added benefits of robust stability and simpler synthesis. These findings position the hydrotalcite-derived Fe30 catalysts as a highly attractive option in the context of CO (and as will be seen, CO_2) hydrogenation, combining the selectivity advantages of classical alkali-promoted Fe catalysts with innovations in preparation that enhance activity and maintain durability. This comparison also highlights that the choice of support and preparation can be tuned to optimize results, but multiple routes can lead to the desired outcome of efficient, heavy-selective Fischer-Tropsch synthesis. The next section will explore how these catalysts perform in the hydrogenation of CO_2, further testing their versatility and stability under different reaction feeds.

5.2. CO_2 reaction

5.2.1. Promoted Fe-based Metallosilicates

Figure 5.11 compares the CO_2 conversion achieved over the two promoted Fe-based metallosilicates Fe/Ce-SiO_2-K,Cu and Fe/Zr-SiO_2-K,Cu as a function of reaction temperature. In all cases, conversion increased steadily with temperature from 270 °C up to 370 °C, as expected. Notably, the Ce-containing catalyst consistently exhibited higher activity than its Zr-based counterpart across this range. The conversion advantage of Fe/Ce-SiO_2-K,Cu averaged about ≈8% higher CO_2 conversion on average relative to Fe/Zr-SiO_2-K,Cu.

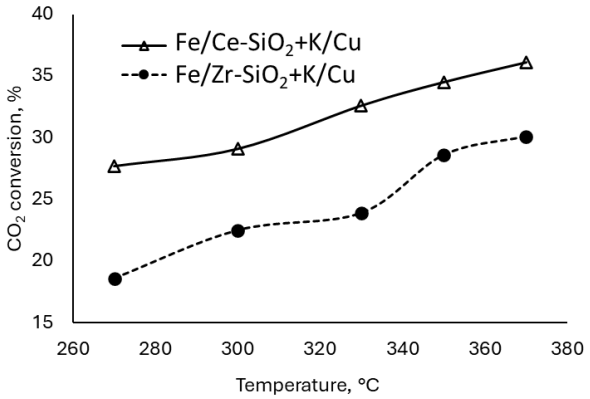

Figure 5.11. CO_2 conversion as a function of temperature over Fe-based metallosilicate catalysts promoted with Ce or Zr (each also K/Cu-promoted).

This superior activity of the ceria-promoted catalyst is evidence of ceria's beneficial role in CO_2 hydrogenation. Ceria can provide oxygen vacancies and labile oxygen storage capacity, which facilitate CO_2 adsorption/dissociation and enhance the *in situ* reverse water-gas shift (RWGS) step, which replicates the behaviour of the catalysts for the CO hydrogenation. Indeed, the addition of CeO_2 to Fe-based catalysts has been reported to boost CO_2 conversion, by ≈22% in one study, by creating more readily reducible oxide interfaces and by accommodating hydrogen in the ceria lattice [29]. In the present case, the Ce modifier likely improves the reduction and carburization of iron (via stronger metal-support interactions) [30] and offers basic oxygen vacancy sites for CO_2 activation, resulting in a higher intrinsic activity. By contrast, ZrO_2 (a

comparably less reducible, amphoteric oxide) appears to confer a lower density of such active sites, despite the Fe/Zr-SiO_2-K,Cu catalyst having a higher BET surface area than the Fe/Ce-SiO_2-K,Cu system. This suggests that mere surface area is not the governing factor; rather, the nature of the metal-support interaction and active phase dispersion is key. Post-reaction analyses (SEM-EDS) showed a much more homogeneous distribution of Fe and promoters in the Ce-SiO_2 supported catalyst, whereas the Zr-SiO_2 sample exhibited significant metal agglomeration [30,31]. Such homogeneous dispersion in the Ce-based catalyst ensures more accessible active Fe sites and better contact with reactant gases, which correlates with its higher CO_2 conversion. Another notable difference is the absence of any drastic CO_2 conversion with increasing temperature. In earlier CO hydrogenation runs on the same catalysts, Fe/Ce-SiO_2 showed a sharp jump in CO conversion above ≈250 °C (achieving >75% conversion by 350 °C), whereas under CO_2/H_2 this catalyst's conversion rises more gradually (reaching ≈36% at 370 °C). The smoother temperature-dependence observed here suggests that the kinetics of CO_2 hydrogenation are fundamentally limited by the initial CO_2-to-CO step and equilibria, rather than by mass transfer or rapid FT reaction kinetics. Both catalysts are active for the RWGS reaction (converting CO_2 to CO) due to the presence of Fe and the basic K promoter, so CO_2 conversion tends toward an equilibrium governed by RWGS at each temperature. As a result, no sudden rate surge is seen within the tested range, implying we did not reach a temperature threshold for significantly accelerated FT chain-growth activity (in contrast to the CO-only case).

The influence of reaction conditions on conversion was further tested by varying the contact time. When the gas hourly space velocity was halved, in other words doubling the contact time, the CO_2 conversions for both catalysts remained essentially unchanged, within ±1%, across all temperatures. Figure 5.11 shows that the conversion-temperature profiles at standard flow and half-flow overlap closely for each catalyst. This insensitivity to contact time suggests that the system is approaching equilibrium or a regime where RWGS and FT reactions reach a steady-state limit under the given conditions. In other words, simply providing longer residence time does not push CO_2 conversion higher, consistent with the notion that RWGS (which is fast and reversible) establishes an equilibrium CO/CO_2 ratio that limits further CO_2 consumption. It is likely that any additionally formed CO at longer contact times is preferentially converted back to CO_2 via the fast water-gas shift cycle (or consumed in methanation) rather than proceeding to form more C-C coupled products. We note that the RWGS equilibrium (and the inhibitory effect of by-product H_2O) can "freeze" the overall conversion at a maximum value. In practical terms, this result underscores that at 20 bar and $H_2/CO_2 = 3$, our reactor was already operating near the equilibrium-limited conversion for CO_2 hydrogenation. Similar observations of plateauing conversion at high space time have been reported in CO_2-FT studies, where beyond a certain point additional contact time yields mostly more CO (via RWGS) and H_2O rather than more hydrocarbons [32,33]. Thus, improving CO_2 conversion further would likely require either shifting equilibrium (e.g. by *in situ* H_2O removal or higher H_2 ratios) or increasing the intrinsic activity of FT chain growth.

5.2.1.1. C_{2+} Hydrocarbon Yields and Product Selectivity

Despite the moderate CO_2 conversions, the Ce-modified catalyst demonstrated a substantially higher yield of C_{2+} hydrocarbons than the Zr-based catalyst. The total C_{2+} yield, defined as the

fraction of CO_2 converted into C_{2+} hydrocarbon products, was about 13-14% for Fe/Ce-SiO_2-K,Cu across the tested temperatures, versus only 5-6% for Fe/Zr-SiO_2-K,Cu (Table 5.3 and Figure 5.12). Interestingly, for each catalyst the C_{2+} yield was relatively constant with temperature.

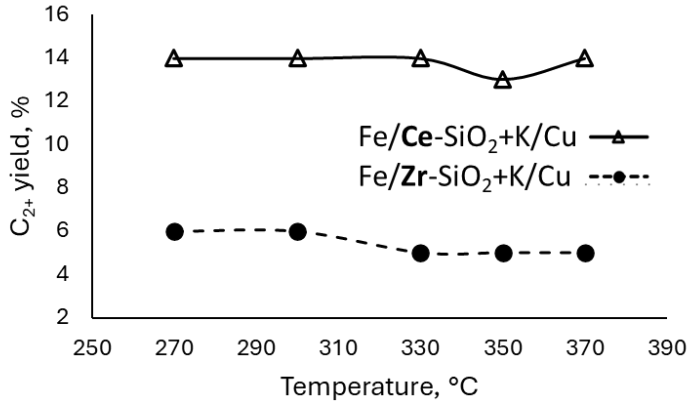

Figure 5.12. C_{2+} hydrocarbon yield (overall conversion × C_{2+} selectivity) as a function of temperature.

This behavior can be rationalized by opposing effects: increasing temperature raises the CO_2 conversion, but it also shifts the product selectivity away from heavier hydrocarbons, toward more CO and CH_4, as discussed below. For the Ce catalyst, these effects approximately cancelled, resulting in a near-constant C_{2+} yield. The Zr catalyst showed a slight maximum yield (≈6%) at the lowest temperature tested (270-300 °C), stabilizing at ≈5% at higher temperatures, indicating that the loss of hydrocarbon selectivity at high T slightly outweighed the gains in conversion in that case.

Catalyst	T(°C)	χCO	C_{2+} yield	SCH_4	SCO	SC_{2-6}	$SC_{\geq 7}$
	270	27.7	14	5	43	44	8
	300	29.1	14	5	46	42	7
Fe/Ce-SiO_2+K/Cu	330	32.6	14	6	50	33	11
	350	34.5	13	8	55	28	9
	370	36.1	14	10	51	25	14
	270	18.6	6	12	58	17	13
	300	22.5	6	10	63	14	13
Fe/Zr-SiO_2+K/Cu	330	23.9	5	12	67	14	7
	350	28.6	5	13	69	13	5
	370	30.1	5	14	70	11	5

Table 5.3. Dataset obtained from CO_2 tests.

The superior hydrocarbon yield of the Fe/Ce-SiO_2-K,Cu catalyst is mostly due to its higher selectivity toward C_{2+} products. While both catalysts were promoted with potassium and copper, which generally enhance Fischer-Tropsch chain growth, the Ce-based sample produced a higher fraction of hydrocarbons than the Zr-based sample at every temperature. Specifically, Fe/Ce-SiO_2-K,Cu converted a majority of the CO_2 (around 50-57% of converted carbon) into C_{2+} hydrocarbons, whereas Fe/Zr-SiO_2-K,Cu directed most of its converted carbon into CO (typically only ≈20-30% into C_{2+} hydrocarbon products, with the rest as CO/CH_4). For example, at 350 °C

the Ce catalyst's selectivity to C_{2+} was ≈36% of products, compared to only ≈18% for the Zr catalyst, which produced ≈70% CO by-product at that condition. Across the temperature range, the Ce catalyst maintained 50-55% selectivity to hydrocarbons, whereas the Zr catalyst's hydrocarbon selectivity was significantly lower, only ≈30-42%, with the balance being primarily CO. The higher hydrocarbon selectivity on Fe/Ce-SiO_2-K,Cu aligns with literature reports that rare-earth oxides like ceria promote Fischer-Tropsch chain growth when added to Fe catalysts [34,35]. Ceria can increase the population of surface carbon species (via enhanced CO_2→CO activation and CO adsorption) and mitigate hydrogen over-supply at active sites by temporarily storing hydrogen, both of which favor C-C coupling over methanation [29,33]. In contrast, zirconia, while it can provide some surface basicity and has been shown to synergize with alkali promoters in other studies [29], did not achieve comparable chain-growth efficiency in our SiO_2-based formulation. It is noteworthy that a Fe-K/ZrO_2 catalyst in prior work showed high selectivity to light olefins [29], but in that system ZrO_2 was the primary support. In our mixed SiO_2-ZrO_2 support, the Zr may be present as a dispersed oxide phase that is less effective at enhancing CO uptake or chain propagation, resulting in poorer overall hydrocarbon yields. Furthermore, the less homogeneous distribution of K and Fe in the Zr-containing catalyst (noted above) could mean that large Fe-K domains produce mostly CO, via RWGS and CH_4, rather than facilitating chain growth. In essence, the Ce-promoted catalyst not only converts more CO_2, but converts it more selectively into desirable hydrocarbons, whereas the Zr-promoted catalyst suffers from high selectivity toward undesired products.

5.2.1.2. Light vs. Heavy Hydrocarbon Distribution

Product selectivity was dominated by light hydrocarbons (C_2-C_6) in all cases, with very little formation of heavy waxes (C_{7+}). However, clear differences emerge between the two catalysts in the distribution of these hydrocarbon products. The Fe/Ce-SiO_2-K,Cu catalyst showed a strong tendency toward the C_2-C_6 fraction, whereas Fe/Zr-SiO_2-K,Cu produced a higher share of CH_4 and a somewhat greater fraction of CO and CH_4 at the expense of longer-chain products. At 270 °C, for instance, the Ce-based catalyst achieved ≈44% selectivity to C_2-C_6 hydrocarbons, compared to only ≈17% on the Zr catalyst. This tendency persists throughout the temperature range. Such a pronounced difference in C_{2+} selectivity directly explains the gap in C_{2+} yields noted above. Indeed, the ≈8% higher conversion of the Ce catalyst alone cannot account for its 3× greater hydrocarbon yield; it is the selectivity that further enhances that value. Prior characterization of these materials offers some clues: the Ce-containing sample, owing to its uniform metal/K distribution, likely creates a surface environment with strong CO adsorption and a high probability of C-C coupling (as K is known to enhance CO chemisorption and inhibit hydrogen termination). In fact, adding K promoter shifts the product spectrum toward heavier hydrocarbons by favoring chain growth over methane formation. Consistent with this, the Fe/Ce-SiO_2-K,Cu catalyst (with better dispersed K) showed a higher heavy-fraction selectivity at lower temperatures in CO-FT tests (e.g. 83% C_{7+} at 220 °C, versus 58% for Fe/Zr-SiO_2-K,Cu). In the CO_2 hydrogenation runs, the absolute heavy hydrocarbon yields were very small for both catalysts, but we do observe that Fe/Ce-SiO_2-K,Cu produces slightly more C_{7+} fraction than Fe/Zr-SiO_2-K,Cu (e.g. 14% vs 5% selectivity at 370 °C; Fig. 5.13).

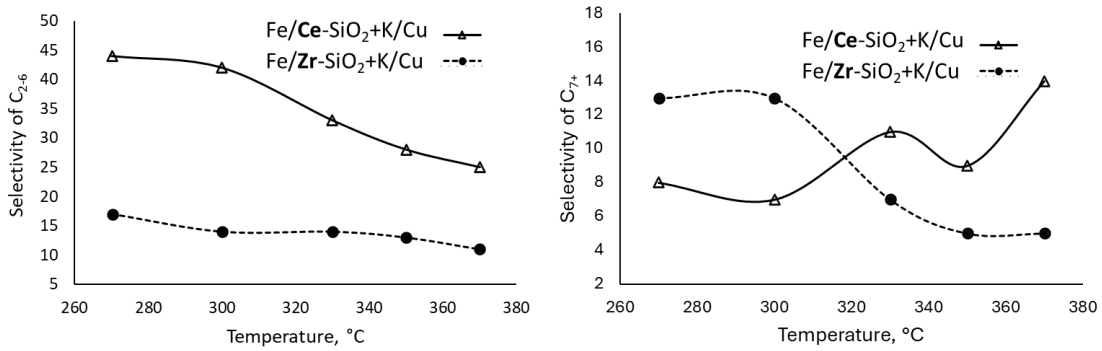

Figure 5.13. Selectivity to light hydrocarbons on the left and heavy hydrocarbons on the right as a function of temperature.

Additionally, the Ce catalyst's heavy-hydrocarbon selectivity showed a mild increasing trend with temperature (from ≈8% at 270 °C to ≈14% at 370 °C), whereas the Zr catalyst's already-low heavy fraction decreased further at higher temperatures (from ≈13% at 270 °C down to ≈5% at 370 °C). This opposite trend suggests that chain growth on the Zr catalyst becomes increasingly unfavorable at high temperature, whereas the Ce catalyst can still gradually build heavier molecules as temperature rises, possibly benefiting from ceria's ability to stabilize carbide iron phases at high T as mentioned before.

It must be noted that the "heavy hydrocarbon" selectivities recorded are very low and subject to considerable uncertainty. In fact, no separate liquid hydrocarbon phase was recovered in the cold trap at the end of these CO_2 hydrogenation tests only an aqueous phase was collected, which contained dissolved light oxygenates and had a hydrocarbon odor.

Both catalysts essentially produce predominantly *light hydrocarbons*, with the Ce-based catalyst favoring the C_2-C_6 range much more strongly. The heavy fraction is negligible under these conditions for both materials, which is not surprising given the high reaction temperature and the presence of abundant H_2O co-product. Any traces of heavy hydrocarbons formed may also remain dissolved in the water phase or be lost to cold sections of the apparatus, making their quantification unreliable. The key point, however, is that Fe/Ce-SiO_2-K,Cu directs a larger portion of carbon into the desired C_2-C_6 range, whereas Fe/Zr-SiO_2-K,Cu, even when it does form hydrocarbons, skews more toward C_1.

5.2.1.3. Selectivity to CH_4 and CO

The selectivity towards methane and carbon monoxide, shown in Figure 5.14 provides further insight into the differing performance of these catalysts. CO is the primary intermediate/by-product of CO_2 hydrogenation (via the RWGS reaction), and CH_4 is the most thermodynamically favoured hydrocarbon. Ideally, a CO_2-FT catalyst should minimize both to maximize liquid hydrocarbon output. In our results, Fe/Ce-SiO_2-K,Cu outperformed the Zr catalyst in this regard. CO selectivity was significantly lower on the Ce catalyst at all temperatures: for example, at 300 °C, Fe/Ce-SiO_2-K,Cu produced ≈45% CO whereas Fe/Zr-SiO_2-K,Cu produced ≈63% CO. At 370 °C, CO selectivity reached ≈51% for Ce vs ≈70% for Zr.

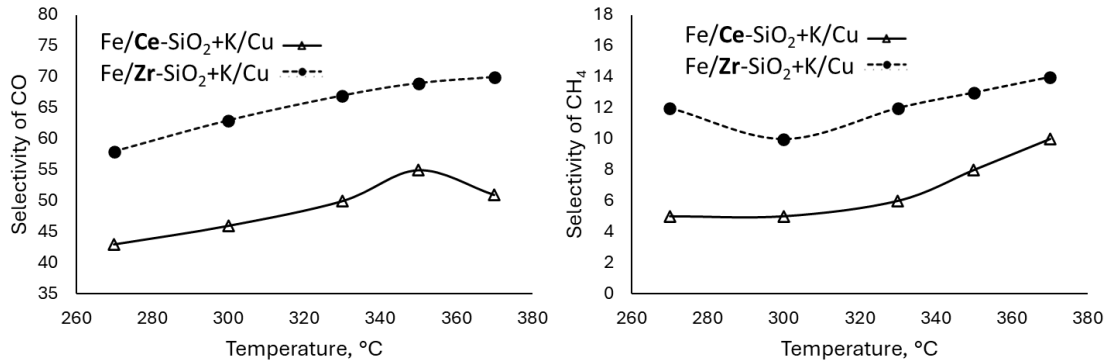

Figure 5.14. Selectivity to carbon monoxide on the left and methane on the right as a function of temperature.

The consistently lower CO fraction for the ceria-promoted catalyst indicates more effective conversion of the *in situ* generated CO into hydrocarbons. This observation agrees with the earlier point that ceria's oxygen vacancies and hydrogen-buffering ability facilitate CO consumption on the surface [29]. In contrast, the zirconia-based catalyst seems to let a larger portion of CO_2 slip through as CO, suggesting that once CO is formed (via RWGS), it is less efficiently polymerized on Fe/Zr-SiO_2-K,Cu. This could be due to fewer active carbide sites or a surface less conducive to CO chain-initiation (possibly related to K promoter not being as effectively utilized on that catalyst). High CO selectivity is a well-known challenge in CO_2 hydrogenation FT routes [33], it arises from the equilibrium and kinetic favourability of RWGS, especially at higher temperatures. Our Ce-promoted catalyst mitigates this to a degree, but even in the best case (Ce, 270 °C) CO still constituted ≈43% of products. This underlines that CO_2-to-hydrocarbon conversion inherently proceeds via CO formation, and a significant fraction of CO may desorb before converting to liquids.

Methane selectivity showed divergent behavior for the two catalysts as well. Fe/Zr-SiO_2-K,Cu consistently produced more CH_4 than Fe/Ce-SiO_2-K,Cu: at 270 °C, the methane selectivity was ≈12% for Zr vs ≈5% for Ce; at 370 °C it was ≈14% vs ≈10%, respectively. In other words, the Zr-containing catalyst yielded roughly double the methane of the Ce catalyst at lower temperatures, and still ≈40% higher CH_4 at the highest temperature. Notably, both catalysts exhibited only a mild increase in CH_4 selectivity with temperature. From 270 °C up to about 310 °C, CH_4 remained nearly constant (around 5-6% on Ce and 10-12% on Zr). Above ≈320 °C, a gradual rise in methane formation was observed, reaching the 10% (Ce) and 14% (Zr) at 370 °C. This trend is consistent with Fischer-Tropsch kinetics, wherein higher temperatures favor secondary hydrogenation and chain termination, boosting methane production [36]. The fact that Fe/Ce-SiO_2-K,Cu has a lower methane selectivity indicates a higher chain-growth probability (α) for that catalyst relative to Fe/Zr-SiO_2-K,Cu. Again, potassium promotion is crucial in suppressing methane by reducing hydrogen coverage; it appears the Ce-based catalyst leverages this promoter effect more effectively, likely due to better K dispersion and perhaps an intrinsically higher iron carbide population (supported by ceria's promotion of Fe carburization). The Zr-based catalyst, with its higher CH_4, suggests that a larger fraction of surface carbon species end up fully hydrogenated (C_1) rather than coupling to form longer chains. This aligns with its lower heavy fraction and overall C_{2+} selectivity, as discussed. It is worth noting that the absolute CH_4 selectivities we observe (5-14%) are relatively low for Fe catalysts at such high temperatures, reflecting the intentional addition of K as an anti-methanation promoter [29].

5.2.1.4. Effects of Contact Time and Reaction Environment

As noted above, doubling the contact time did not significantly alter the conversion or the general selectivity trends (Fig. 5.15).

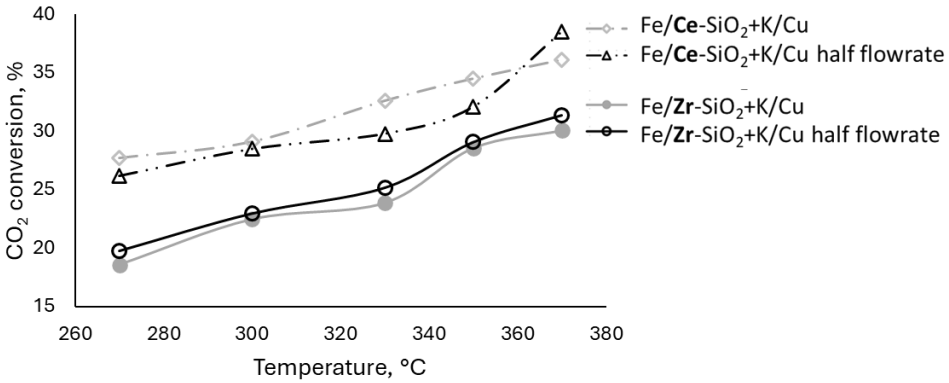

Figure 5.15. Effect of contact time on CO_2 conversion - comparison of standard flowrate vs. half flowrate for Ce-Fe and Zr-Fe catalysts.

Both Fe/Ce-SiO_2-K,Cu and Fe/Zr-SiO_2-K,Cu yielded essentially the same CO_2 conversion at a given temperature regardless of flow rate, indicating that under standard conditions the catalysts already approached a near-equilibrium conversion. Likewise, the product selectivities to CO, CH_4, and C_{2+} hydrocarbons remained nearly unchanged Figure 5.16 and 5.17. For instance, at 350 °C the Ce catalyst with half flow still showed ≈32% conversion, ≈55% CO selectivity and ≈12% C_{2+} yield values on par with the standard flow case, Table 5.4. The Zr catalyst at half flow gave ≈29% conversion with ≈68% CO selectivity, compared to ≈28.6% and ≈69% at standard flow. In other words, the same performance disparity between the catalysts persisted, and no improvement in hydrocarbon production was obtained by increasing residence time. This outcome reinforces the conclusion that the reaction was thermodynamically and/or equilibratively limited.

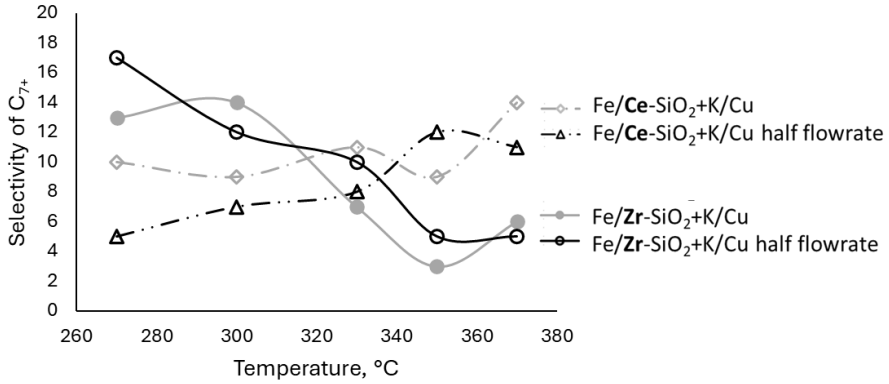

Figure 5.16. Selectivity to heavy hydrocarbons under standard vs. half flowrate conditions.

It appears that once a certain CO/H_2O ratio is reached in the reactor, additional contact merely shifts the RWGS equilibrium slightly without boosting net hydrocarbon formation. The catalysts likely operate in a regime where CO_2 is continually converted to CO and vice versa (via RWGS) at a fast rate, while the slower FT step siphons off a small fraction of CO into hydrocarbons. If the FT step does not intrinsically accelerate or if product inhibition (e.g. by water) occurs, then extending contact time yields diminishing returns. Indeed, the presence of abundant H_2O is a distinguishing aspect of CO_2 hydrogenation environments.

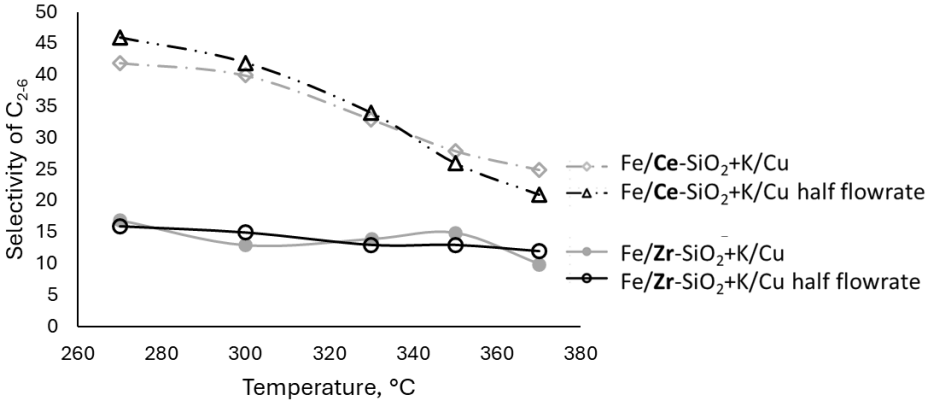

Figure 5.17. Selectivity to light hydrocarbons under standard vs. half flowrate conditions.

Water is known to adversely affect Fischer-Tropsch synthesis by shifting the equilibrium back to CO_2 and also by oxidizing active iron carbide phases [37]. In our tests, the amount of water collected in the condenser was nearly three times higher for CO_2 runs than for analogous CO-fed runs (average ≈17.5 g vs 6.1 g of water per test), confirming that water formation is significant. This water likely inhibits further conversion and could contribute to the stagnant performance at longer contact time. We note that the selectivity to heavier (C_{7+}) hydrocarbons tended to decrease with increasing temperature under both standard and extended contact time conditions, consistent with the idea that high temperatures and high H_2O partial pressures suppress wax formation.

Catalyst	T(°C)	χCO_2	C_{2+} yield	SCH_4	SCO	SC_{2-6}	SC≥7
Fe/Zr-SiO_2+K/Cu Half Flowrate	270	19.8	7	11	56	16	17
	300	23	6	11	62	15	12
	330	25.2	6	13	64	13	10
	350	29.1	5	14	68	13	5
	370	31.4	5	14	69	12	5
Fe/Ce-SiO_2+K/Cu Half Flowrate	270	26.2	13	5	44	46	5
	300	28.5	14	6	45	42	7
	330	29.8	13	7	51	34	8
	350	32.1	12	7	55	26	12
	370	38.5	12	10	58	21	11

Table 5.4. dataset obtained from CO_2 tests under double residence time conditions.

The light hydrocarbon (C_2-C_6) selectivity, on the other and, was essentially overlapping for standard vs. half flow runs. In fact, even with doubled contact time, the ceria-promoted catalyst maintained a dramatically higher C_2-C_6 selectivity than the zirconia catalyst (e.g. ≈46% vs ≈15% at 270 °C), which explains why the C_{2+} yields of the two did not converge. Overall, the invariance of performance with contact time indicates that under our conditions, kinetic limitations were secondary to thermodynamic/chemical equilibrium constraints. Achieving higher hydrocarbon yields from CO_2 would require altering the reaction environment (for example, by in situ water removal, as mentioned, or by using a dual-catalyst approach to shift equilibria), rather than simply increasing reactor volume or lowering space velocity.

Finally, it is informative to summarize the factors inherent to CO_2 hydrogenation that make it more challenging to achieve high yields of liquid hydrocarbons (compared to CO hydrogenation). Prior studies and our results concur on several points:

- Reverse Water-Gas Shift Competition: CO_2 hydrogenation proceeds via the RWGS reaction to form CO, which is equilibrium-limited and produces water. The presence of water drives the equilibrium back toward CO_2, reducing the amount of CO available for FT synthesis. In our system, water buildup likely capped the effective conversion and shifted selectivity toward CO (the *majority product* in all cases).
- CO_2 as a Reactive Diluent: CO_2 (and the resulting CO_2/CO mixture) acts as a diluent compared to a CO-only feed. The large excess of CO_2 can occupy catalytic sites (especially since CO_2 is acidic and our catalysts are promoted to be basic), competing with CO adsorption. This competitive adsorption can lower the rate of chain initiation and growth. Indeed, the zirconia catalyst, which likely had stronger CO_2 adsorption (due to more basic ZrO_2 sites), showed lower CO uptake into FT products (higher CO selectivity).
- High Temperature Requirement: CO_2 is thermodynamically more stable than CO, necessitating higher reaction temperatures to achieve appreciable conversion. Unfortunately, higher temperatures inherently favor methanation and light products in Fischer-Tropsch chemistry. Thus, operating at 350-370 °C (versus ≈270 °C for typical Fe-FT from CO) skews the product slate toward CH_4 and short chains. We observed this effect in both catalysts (increasing CH_4 at higher T), though the Ce catalyst managed to keep methane relatively low.
- Multi-step Reaction Sequence: The pathway from CO_2 to long-chain hydrocarbon involves at least two steps - $CO_2 \rightarrow CO$ (via RWGS) and then $CO \rightarrow C_1$ surface species $\rightarrow C_{2+}$ (via FT polymerization). The necessity of this sequential reaction means the overall process is a delicate interplay: the second step can only proceed as fast as CO is generated and remains on the surface, and any acceleration of RWGS without corresponding FT activity just produces more CO (as seen with the Zr catalyst). In essence, the catalyst must balance two reactions. Our Fe/Ce-SiO_2-K,Cu material appears to achieve a better balance (more of the CO from RWGS is consumed in FT), whereas Fe/Zr-SiO_2-K,Cu allows the two steps to remain largely decoupled (fast RWGS, slow C-C coupling).

5.2.1.5. Catalyst Stability under CO_2 Hydrogenation

An advantage observed for both promoted metallosilicate catalysts is their stability under reaction conditions. An isothermal durability test at 370 °C revealed that the Fe/Ce-SiO_2-K,Cu catalyst maintained a steady CO_2 conversion with no noticeable deactivation over the testing period (Fig. 5.18).

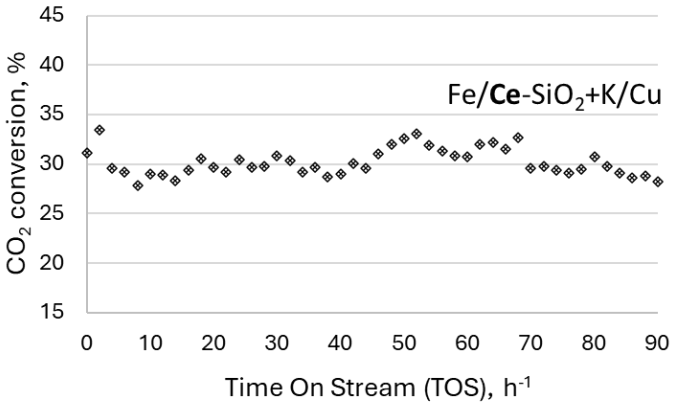

Figure 5.18. Time-on-stream stability of CO_2 conversion at 370 °C for the Fe/Ce-SiO_2+K/Cu catalyst.

This contrasts with the behavior in CO hydrogenation, where the same catalyst showed a slow deactivation trend over time, likely due to water-induced oxidation or carbon deposition in the CO-rich environment [38,39]. In the CO_2 runs, the lower overall reaction rate and the presence of excess H_2 may help avert rapid catalyst deactivation. The constant conversion indicates that active phase (iron carbide) was preserved throughout, suggesting that the catalyst's design, Fe nanoparticles anchored in a robust Ce-silicate matrix and stabilized by K/Cu - successfully resists sintering and oxidation at high temperature. The strong metal-support interactions in metallosilicates (Fe-O-Si bonds, and in this case Fe-O-Ce bridges) likely prevent metal migration even under harsh conditions [40]. Moreover, ceria's redox buffering capacity may mitigate oxidative damage from H_2O: CeO_2 can reversibly oscillate between Ce^{3+} and Ce^{4+}, potentially scavenging oxygen from iron when water is produced, thereby protecting the Fe^0/Fe_xC phase. This hypothesis is consistent with literature noting that appropriate promoters and supports (e.g. Ce, Cu) improve the stability of Fe catalysts by maintaining carburization and dispersity [33,29]. The Zr-promoted catalyst also did not exhibit abrupt deactivation in our short-term tests, but given its lower activity to begin with, any slight changes would be harder to discern. It is encouraging, however, that both catalysts showed the ability to operate at 20 bar and 350-370 °C for days without catastrophic loss of activity. The lack of heavy carbonaceous deposits (as implied by the negligible wax production) and the structural integrity of the silicate framework contribute to this stability.

5.2.2. Hydrotalcite catalysts

This section evaluates the CO_2 hydrogenation performance of five hydrotalcite-derived catalysts; Fe30, Fe40, Co33, Co45, and FeZn, tested in a lab-scale fixed-bed reactor under three different conditions.

- Test #1 is a baseline run at $H_2/CO_2 = 3$ and GHSV = 3200 h^{-1} (20 bar, temperature range 250-350 °C).
- Test #2 uses identical feed composition but half the GHSV (1600 h^{-1}), doubling the contact time.
- Test #3 returns to GHSV = 3200 h^{-1} but increases the H_2/CO_2 ratio to 4 (other conditions same).

These variations are made to study how residence time and hydrogen availability affect CO_2 conversion and product selectivity. The key performance metrics, CO_2 conversion and selectivities to CH_4, CO, and C_{2+} hydrocarbons, are analyzed for each test.

5.2.2.1. Test #1 - Standard Conditions (H_2/CO_2 = 3, GHSV 3200 h^{-1})

Under baseline conditions, all catalysts exhibit the expected rise in CO_2 conversion with increasing temperature (strongly endothermic activation in this range). Fig. 5.19 illustrates the conversion/temperature profiles for each catalyst. At 250 °C, the CO_2 conversions are modest (8-17%), with FeZn showing the highest conversion (≈17.6% at 250 °C) and Fe40 the lowest (≈8.8%). FeZn's superior low-temperature activity may be attributed to Zn promotion enhancing CO_2 adsorption/activation and providing additional active sites; Zn-Fe interactions are known to boost CO_2 conversion and favor CO formation, a necessary intermediate for chain growth [41,42].

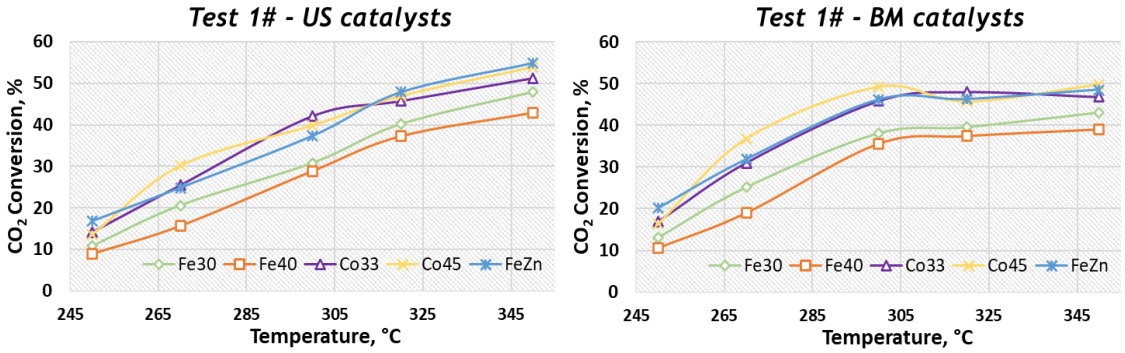

Figure 5.19. CO_2 Conversion in Test 1 (Standard 3:1 H_2/CO_2, GHSV 3200 h^{-1}).

As temperature increases to 350 °C, conversions improve substantially for all: Fe40 reaches ≈43%, Fe30 ≈48%, Co33 ≈51%, Co45 ≈54%, and FeZn ≈55% conversion at 350 °C. The Co45 and FeZn catalysts achieve the highest conversions in this test, closely followed by Co33, while Fe30 is moderate and Fe40 consistently underperforms. This ranking correlates with catalyst composition and dispersion, e.g., Co45 (higher Co content) provides more active metal surface than Co33, and Fe40 (highest Fe loading) likely suffers from larger crystallites or lower surface area (as seen in XRD/BET from Chapter 4), limiting its activity. Notably, FeZn nearly matches Co45 in conversion by 350 °C despite a lower Fe content than Fe40, underscoring the positive influence of Zn in creating an effective active phase (possibly via formation of ZnO-Fe interfaces or improved Fe carbide formation). The Ultrasound vs. Ball-Milled preparation had a measurable impact on activity: at lower temperatures (250-300 °C), the BM catalysts reached higher conversions than their US counterparts (e.g., at 270 °C Fe30-BM converted ≈13% vs. ≈11% for Fe30-US). By contrast, at the highest temperatures the US samples surpassed BM (at 350 °C Fe30-US ≈47.9% vs. Fe30-BM ≈43.1%). This crossover suggests that ball milling creates catalysts that are more active in the kinetically limited low-T regime, perhaps due to smaller initial particle size or defect sites that favor CO_2 chemisorption, whereas the ultrasound-derived catalysts attain full activity only at higher T. However, both forms follow the same qualitative trends and reach comparable maximum conversions, indicating that the preparation method does not drastically change the intrinsic activity, it mainly shifts the temperature needed to achieve it. In terms of product selectivity, in Figure 5.20, clear differences emerge among the catalysts. The Fe-based catalysts tend to produce a significant amount of CO via RWGS at the lower

temperatures, whereas the Co-based catalysts, which have negligible RWGS activity, predominantly hydrogenate CO_2 directly to methane and subsequently to higher hydrocarbons as temperature rises. For instance, at 250 °C Fe40 shows only ≈45% of converted CO_2 appearing as C_{2+} hydrocarbons, consistent with Fe's tendency to favor RWGS at low conversion[47].

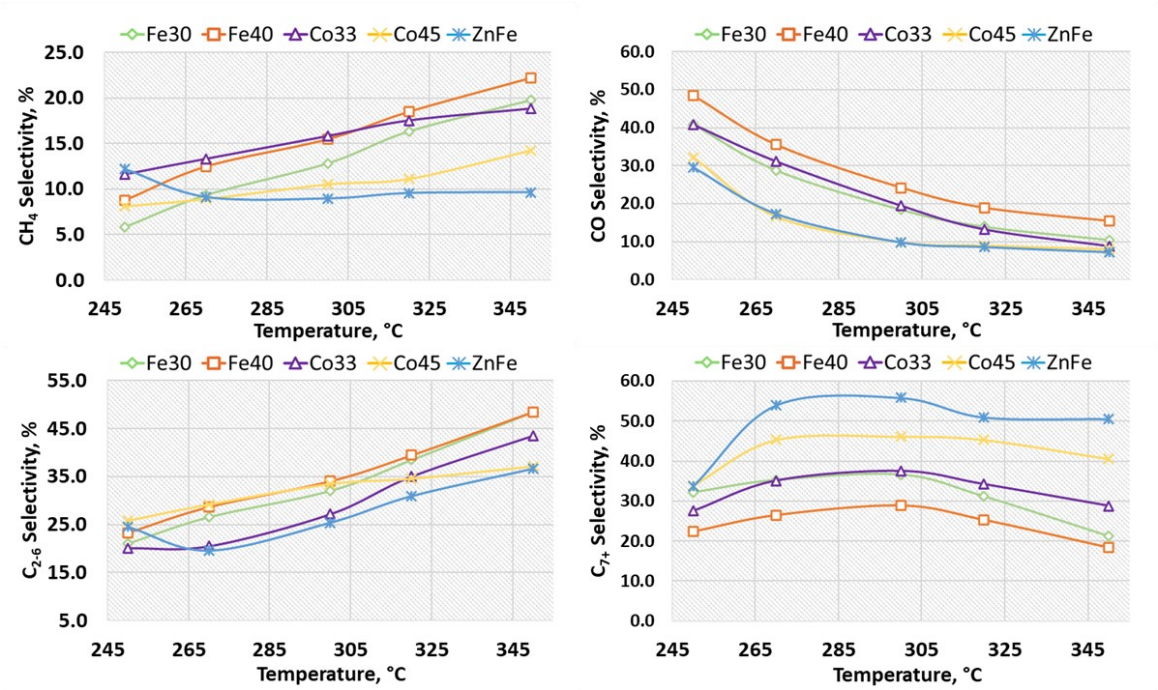

Figure 5.20. Product selectivities during test 1# of US catalysts.

In contrast, Co45 at 250 °C gives ≈60% of products as C_{2+}. Fe30 and FeZn fall in between: Fe30 yields ≈44% C_{2+} at 250 °C, while FeZn reaches ≈58% C_{2+}, reflecting Zn's ability to suppress the methanation pathway in favor of longer-chain products [43,44]. As temperature increases, all catalysts show a marked shift toward hydrocarbon production and in some cases also more CH_4. By 350 °C, the C_{2+} selectivity rises to ≈60-68% for Fe30/Fe40, ≈73% for Co33, ≈76% for Co45, and ≈80% for FeZn. In other words, FeZn achieves the lowest CH_4 selectivity of the group (<15% CH_4 at 350 °C), demonstrating strong chain-growth propensity. This can be linked to Zn promotion: literature reports Zn-Fe catalysts attaining C_{2-12} olefin selectivities on the order of 80% [42], as ZnO sites may facilitate CO formation and inhibit over-hydrogenation of intermediates. Co45 also exhibits relatively low CH_4 selectivity (≈14% CH_4 at 350 °C, vs. ≈18% for Co33), indicating that the higher Co loading in Co45 favors chain propagation. Fe30, reaches about 19% CH_4 at full conversion; Fe40 is higher (≈23% CH_4) due to its overall lower chain productivity. These findings align with general FT kinetics: for cobalt-based catalysts, methane selectivity tends to *decrease* as CO conversion increases [45,46]. It is noteworthy that US vs. BM preparations showed virtually no difference in selectivity patterns in Test 1, at a given temperature, both forms of a given catalyst had nearly identical CH_4/C_{2+} ratios. For example, Fe30-US and Fe30-BM both exhibited ≈68% C_{2+} selectivity at 350 °C. This suggests that while the preparation method influences the rate of achieving conversion, it does not fundamentally alter the product distribution.

5.2.2.2. Test #2 - Doubled Contact Time ($H_2/CO_2 = 3$, GHSV 1600 h^{-1})

In the second test, the feed composition remains the same as Test 1, but the gas hourly space velocity is halved, allowing CO_2 and intermediates a longer residence time over the catalyst bed. This change produces a pronounced increase in CO_2 conversion across all catalysts, as shown in Figure 5.21.

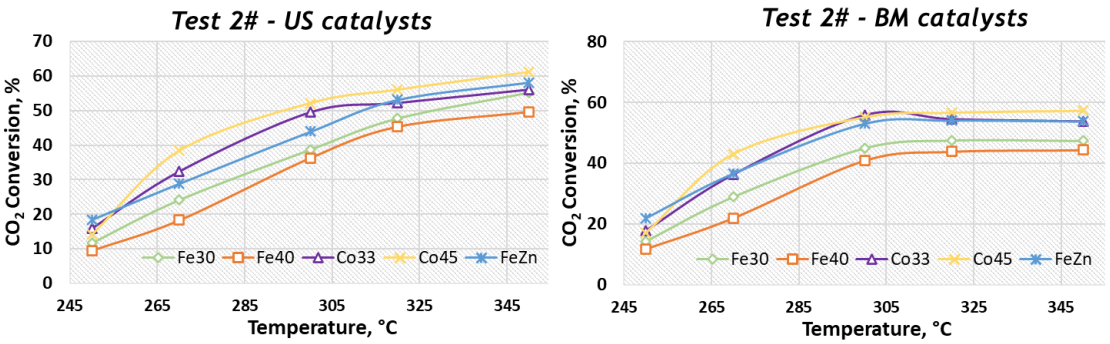

Figure 5.21. CO_2 Conversion in Test 2 (3:1 H_2/CO_2, GHSV 1600 h^{-1} - doubled contact time.

At the high end (350 °C), Co45 reaches ≈61% conversion (vs. ≈54% in Test 1), the highest of the group. FeZn follows at ≈58% (slightly above its Test 1 value of 55%), and Co33 and Fe30 each attain ≈56-55% (up from ≈51% and 48%, respectively). Even the least active catalyst, Fe40, improves to ≈50% conversion at 350 °C (compared to ≈43% prior). The magnitude of conversion gain is more pronounced at intermediate temperatures: for instance, at 300 °C Co45 converts ≈52% (versus ≈40% in Test 1) and Fe30 ≈39% (vs. ≈31% in Test 1). Such improvements confirm that kinetic limitations rather than thermodynamic equilibrium were restricting conversion in the test 1, by doubling contact time, CO_2 has more opportunity to react, pushing conversions higher at each temperature. All catalysts still show the same rank order by activity, Co45 ≈ FeZn > Co33 ≈ Fe30 > Fe40 at most temperatures, indicating that the intrinsic activity advantages conferred by composition persist under longer residence. The US vs. BM behavior also remains consistent: BM samples lead in conversion at low T, while US catches up by ≈320-350 °C. The effect of longer contact time on selectivity, in Figure 5.22, is quite interesting to study: here, with more residence time, the production shifts *away* from CH_4 and towards higher hydrocarbons for all catalysts.

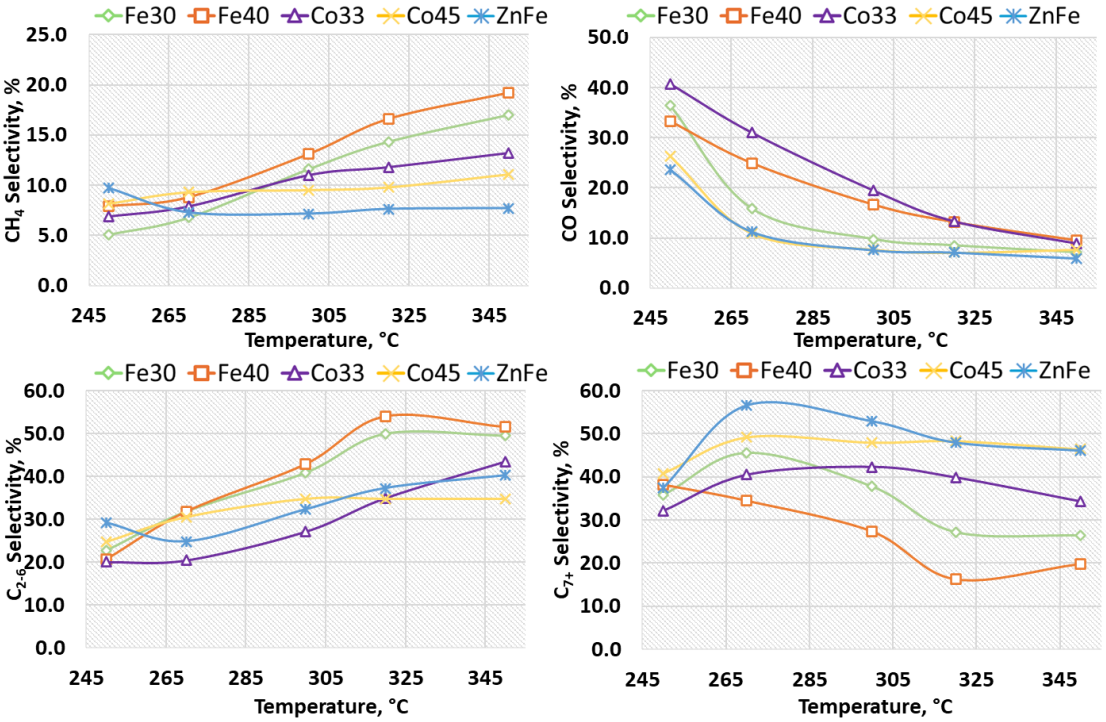

Figure 5.22. Selectivities of US catalysts among different temperatures.

Essentially, secondary reactions (further CO hydrogenation, chain growth on surface) become more complete. Methane selectivity is suppressed relative to Test 1 at the same temperatures, as additional hydrogenation steps convert what would have been CH_4 or CO into larger molecules. For instance, at 300 °C Fe30's C_{2+} selectivity climbs to ≈75% in Test 2, up from ≈68% in Test 1 at that temperature. Fe40's heavy product selectivity remains almost the same from ≈28% → ≈29% while Co33 goes from ≈37% → ≈42%, and Co45 from ≈45% → ≈49%. Huge change is seen in the Fe catalysts at lower temperatures: Fe30 at 270 °C jumps from ≈60% C_{2+} (Test 1) to ≈74% in Test 2, and Fe40 from ≈55% → ≈66%. This indicates that under the short contact of Test 1, a substantial fraction of CO_2 on Fe catalysts was being converted only to CO (RWGS) or short products, but with more time that intermediate CO can undergo Fischer-Tropsch steps on Fe active sites, yielding additional C-C coupling. Indeed, Fe catalysts are bifunctional in CO_2 hydrogenation (both RWGS-active and FT-active), and longer residence encourages the FT pathway to consume CO that would otherwise exit. As a result, Fe30 and Fe40 produce far less CO byproduct in Test 2, confirmed by higher C_{2+} yields and lower CO selectivity. Co-based catalysts experience also the same phenomena of increasing hydrocarbon production. This phenomenon is consistent with FT literature: increasing conversion (by lowering space velocity) generally leads to a lower methane fraction especially on Co catalysts [47]. Additionally, water formed in the reactions might accumulate slightly more at higher conversion and could suppress methanation kinetics while favoring chain growth on Co [48] (an effect noted for Co FT catalysts at high conversion [49]).

Quantitatively, by 350 °C in Test 2 the heavy hydrocarbon selectivities are impressive: FeZn still leads with ≈86% of converted carbon as C_{2+}, Co45 follows (≈81%), then Co33 (≈78%) ≈ Fe30 (≈76%), and Fe40 is lowest (≈71%). Compared to Test 1, each catalyst's CH_4 selectivity at 350

°C drops by ≈3-7 percentage points, and CO selectivity drops as well, often below 5%. The trend confirms that extended contact time is an effective strategy to maximize chain-growth products in CO_2 hydrogenation on these catalysts. It is worth noting that Fe40, while still the poorest performer, benefited proportionally from the longer contact almost as much as Fe30 - suggesting that Fe40's low baseline C_{2+} yield was largely due to kinetic limitations (short contact exacerbating its slow FT step) rather than an inability to form heavier products per se. Meanwhile, FeZn and Co45, which were already efficient at chain growth, show more modest selectivity gains, since they were already near their optimal chain-length distribution under shorter contact. The preparation method again does not significantly alter the selectivity outcome in Test 2. This reinforces that the fundamental selectivity patterns are governed by the catalyst's composition and active phases.

5.2.2.3. Test #3 – Increased H_2 content (H_2/CO_2 = 4:1, GHSV 3200 h^{-1})

In the third variant, the hydrogen feed is increased to a 4:1 molar ratio with CO_2. The space velocity is returned to 3200 h^{-1}, isolating the effect of hydrogen partial pressure. Generally, adding H_2 drives CO_2 conversion higher, as the reactions are hydrogen-limited. Indeed, we observe slight to moderate conversion boosts in Test 3 relative to Test 1. Figure 5.23 shows that at 350 °C, Fe30 reaches ≈50% (vs 48% in Test 1), Fe40 ≈45% (vs 43%), Co33 ≈54% (vs 51%), Co45 ≈58% (vs 54%), while FeZn remains ≈54% (virtually unchanged from 53%). The gains are more evident at intermediate temperatures: e.g., at 300 °C Co45 converts ≈50.0% (over ≈40% in Test 1), highlighting how additional H_2 can accelerate the kinetic rate of CO_2 consumption. This agrees with expectations and prior studies showing that higher H_2/CO_2 feeds increase CO_2 conversion rates and CH_4 yields [50,51]. However, the increased hydrogen availability also profoundly alters the selectivity, in the undesirable direction for chain growth. In contrast to Test 2, here methane formation is promoted at the expense of C_{2+} products. Additional H_2 tends to terminate growing hydrocarbon chains more readily and hydrogenate carbon intermediates fully to CH_4. Thus, all catalysts exhibit lower C_{2+} selectivities in Test 3 compared to the 3:1 baseline. In practical terms, FeZn in Test 1 produced relatively little CH_4, but in Test 3 its CH_4 selectivity roughly doubles, from ≈13% to ≈28%. The Fe30 and Fe40 catalysts, which already had higher CH_4 fractions, see those increase further, Fe40 for example goes from ≈33% CH_4 in Test 1 to ≈45% CH_4 in Test 3. These trends confirm that a hydrogen-rich feed pushes the reaction network toward the most hydrogen-saturated product, CH_4, at the cost of chain growth, consistent with known FT mechanism sensitivities, where a higher H_2/CO ratio yields lower average hydrocarbon chain length [51].

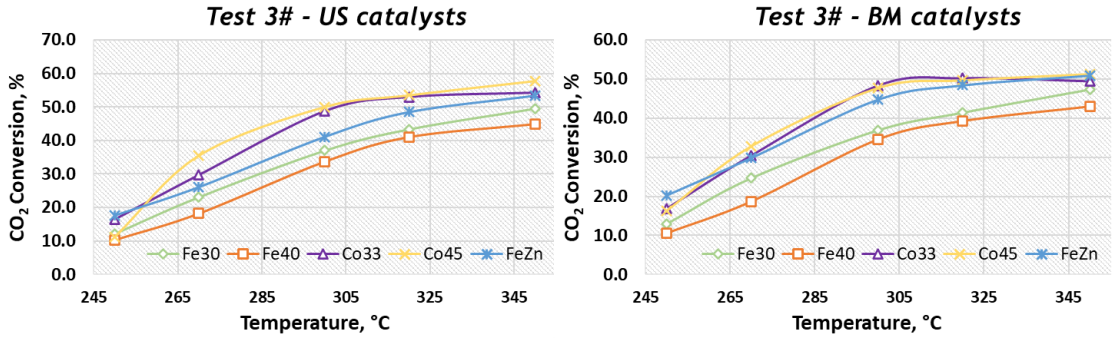

Figure 5.23. CO_2 Conversion in Test 3 (4:1 H_2/CO_2, GHSV 3200 h^{-1}).

In one study on CO_2-FT, it was observed that low H_2:CO_2 ratios favor heavier hydrocarbons, whereas higher ratios produce more methane [51]. Abundance of H_2 may also shift the equilibrium of RWGS: with excess H_2, any CO formed is quickly converted to CH_4 rather than accumulating or desorbing. Accordingly, in Test 3 we find that CO selectivity is extremely low for all catalysts. The main carbon products are CH_4 and whatever C_{2+} fraction can form before hydrogenation stops growth.

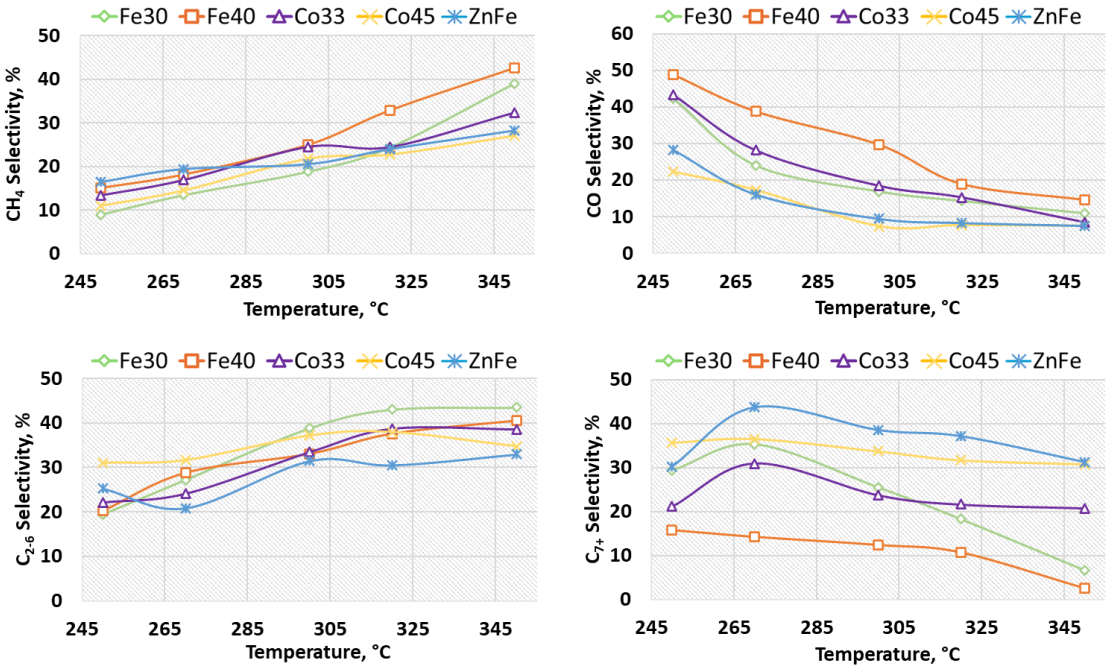

Figure 5.24. Selectivities of BM catalysts among different temperatures.

Interestingly, the relative ordering of catalysts in terms of heavy selectivity persists. Co45 and FeZn remain the top performers for C_{2+} production under 4:1 feed, each ≈70-72% C_{2+} at 350 °C. This suggests that Co45's inherently strong FT chain-growth ability is more robust against H_2-rich conditions than FeZn's, which was largely overcoming a kinetic limitation in H_2-poor conditions. Co33 and Fe30 follow (around 68-61% C_{2+} at 350 °C, respectively), and Fe40 is lowest (≈55%). These gaps are similar to Test 1, just shifted downward in heavy selectivity. The US vs. BM preparation difference again primarily appears in the activity, BM catalysts still achieve slightly higher conversion at the lower temperatures in Test 3. For example, at 300 °C Fe30-BM converts ≈37% vs. Fe30-US ≈34%; at 350 °C Fe30-US ≈50%, BM ≈47%. But critically, both US and BM forms of each catalyst suffer the same decline in C_{2+} selectivity when going to H_2:CO_2 = 4. Thus, the deleterious effect of excess H_2 on chain growth is an intrinsic catalytic phenomenon not mitigated by preparation method.

5.2.2.4. Synthesis of Results and Catalyst Trends

Across the three tests, several consistent patterns emerge, alongside some noteworthy deviations, which have implications for catalyst selection and process optimization. First, the Co45 and FeZn catalysts distinguish themselves as the most promising formulations. Co45 achieved the highest CO_2 conversions in all scenarios while also maintaining among the lowest methane selectivities. Its superior performance can be attributed to a high density of active Co sites (given its ≈45% Co content) combined with the favorable oxide support from the hydrotalcite, which likely provides

structural stability and maybe some CO adsorption capacity. FeZn, on the other hand, demonstrates one of the highest performances among different test conditions: compared to the Fe30 and Fe40, the ZnFe catalyst exhibits higher activity and productivity of longer hydrocarbons (e.g., 87% C_{2+} selectivity at 350 °C in Test 1). Zn likely facilitates the formation of a partly reduced FeOx-ZnO composite or $ZnFe_xOy$ phase that modifies the catalyst's adsorption properties, encouraging CO_2 to be converted to CO (via RWGS) and concurrently suppressing excessive hydrogenation of that CO to CH_4 [52,44]. External studies have similarly found that adding Zn to Fe catalysts boosts heavy olefin/hydrocarbon output (for example, Zn-Fe catalysts have achieved ≈80% hydrocarbon selectivity with minimal CH_4)[53]. In our tests, FeZn consistently yielded the lowest CH_4 fraction in every condition [54]. It is worth mentioning that Fe30 outperformed Fe40 in both conversion and heavy product selectivity. This indicates that more metal is not necessarily better for these hydrotalcite-derived catalysts; Fe40 may have suffered from agglomeration or diffusion limitations. Indeed, earlier characterization showed Fe40 had a lower BET surface area and larger Fe-oxide crystallites than Fe30, due to the higher Fe loading. As a result, Fe40 likely has fewer accessible active sites and less optimal metal-support interaction. It also may reduce less completely during activation (some Fe remains in inactive oxide form), as hinted by TPR profiles, Fe40's reduction peaks were shifted to higher temperature, implying less reducible species. These factors contribute to Fe40's consistently poorer performance and higher CH_4 selectivity, since large Fe_3O_4 particles can favor direct methanation.

From a process perspective, the comparisons between tests highlight two controllable parameters for selectivity: contact time vs. H_2 ratio. Extending contact time, lower GHSV, proved to be a *favorable* for heavier products: it pushed all catalysts toward higher C_{2+} selectivity, essentially allowing each catalyst to operate by converting intermediate CO/C-C to longer chains. Fe catalysts benefited greatly implying that in industrial practice, Fe-based CO_2 hydrogenation catalysts should be run at sufficiently low space velocities or with product recycling to maximize chain growth. On the other hand, increasing the H_2/CO_2 ratio (beyond stoichiometric 3:1) was found to *increase conversion but at the cost of selectivity*. The results clearly demonstrate that a 4:1 ratio, while thermodynamically optimal for methanation, is suboptimal for liquid fuel generation. This aligns with reports that high H_2/CO_2 (or H_2/CO) feeds produce mainly CH_4, whereas slightly H_2-lean conditions favor chain growth [51]. Therefore, to suppress methane, it may be advantageous to use H_2/CO_2 ratios at or even below 3 even accepting some CO output that can be recycled. In summary, if the goal is liquid hydrocarbons, Test #2 conditions (longer contact, stoichiometric H_2) appear far more favorable than Test #3. Conversely, if methane is the desired product, the opposite is true [55,50]. These insights will be important when designing the integrated process and are supported by similar observations in recent studies of CO_2 methanation and Fischer-Tropsch synthesis (e.g., [47] showing lower CH_4 at higher conversion, and [51], noting the effect of H_2/CO_2 ratio on product distribution). Finally, the preparation method (US vs. BM) can be considered. Although it did not drastically change what products are formed, it did influence the temperature-dependent activity. The BM catalysts consistently showed higher conversions at lower temperatures, suggesting they have either a higher density of readily reducible active sites or better initial dispersion. Ultrasound-derived catalysts required slightly higher temperatures to reach the same conversion, but often achieved equal or slightly greater

conversions at high range temperatures (300°C and above) hinting at possibly higher stability or a more robust structure at high T. These differences might translate to varying apparent activation energies - something that will be quantified in Section 5.2.3 when we discuss kinetic parameters. For now, the key point is that both preparation routes yield catalysts that follow the same qualitative trends and ultimate performance limits. Thus, the choice between US and BM may come down to practical factors (e.g., ease of synthesis, catalyst attrition, scale-up considerations) rather than fundamental performance differences.

5.2.3. Macrokinetic Trends in CO_2 Hydrogenation over Fe-Based Catalysts

5.2.3.1. Activation Energies and Dual Arrhenius Behavior

Dual Arrhenius Regimes: All the Fe-based catalysts exhibit two distinct Arrhenius regimes, with a higher apparent activation energy (Ea_1) at low temperatures and a much lower Ea_2 at high temperatures. This inflection in the Arrhenius plot indicates a transition from kinetic control to transport or thermodynamic limitations as temperature rises [56]. For example, Arrhenius plots for Fe-MgO catalysts (Fe30, Fe40) show an initial linear region up to ≈300 °C, followed by a plateau/flattening above ≈320-350 °C (Fig. 5.25). In the low-T regime, Ea_1 values are on the order of 50-60 kJ·mol^{-1} for unpromoted Fe catalysts, whereas at high T the apparent Ea_2 drops to ≈10-20 kJ·mol^{-1} (or even approaches zero/negative for some samples, as discussed below).

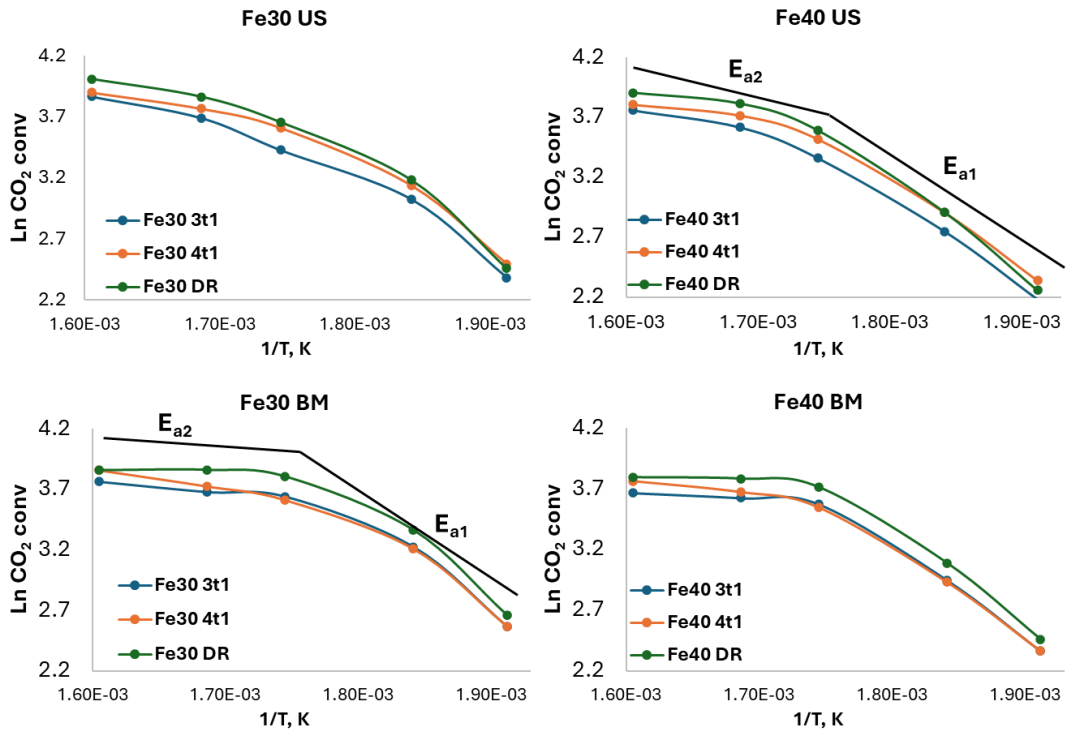

Figure 5.25. Schematic Arrhenius plots (ln Rate vs. 1/T) for a Fe-MgO catalyst prepared by Ultrasound (US) vs. Ball-Milling (BM). Two linear regimes are evident: a steeper low-T slope (Ea_1) and a flattened high-T slope (Ea_2).

This drop in slope suggests that above ≈320 °C the reaction rate no longer increases steeply with temperature, consistent with approach to equilibrium in the $CO_2 + H_2 \rightleftharpoons CO + H_2O$ (RWGS) and CH_4 formation reactions [57,56]. Similar dual-regime behavior has been reported for CO_2 methanation on Ni catalysts, where the apparent Ea falls from ≈89 to 39 kJ·mol^{-1} at higher T due to diffusion and equilibrium constraints [56].

- Relation to Performance: The magnitude of Ea_1 correlates with low-temperature activity: catalysts with lower Ea_1 initiate CO_2 conversion more readily at mild temperatures. Notably, the Fe-Zn-Cu catalyst (Fe-Zn) shows the lowest Ea_1 (≈40-45 kJ·mol^{-1}, vs. ≈55 kJ·mol^{-1} for Fe-only), reflecting an easier CO_2 activation pathway due to the ZnO (and Cu) promoter [58]. In contrast, the Co catalysts have Ea_1 in a similar range as Fe (≈50-60 kJ·mol^{-1}), indicating that the initial CO_2 activation barrier is still governed largely by Fe sites. However, because Co facilitates hydrogenation steps, the effective barrier for CH_4 formation can be lower than for CO formation; literature reports for Fe-based catalysts show Ea for CH_4 (Sabatier) ≈59 kJ·mol^{-1} vs. 81 kJ·mol^{-1} for RWGS [57]. Thus, in Co catalysts, the methane pathway can dominate at low T, yielding high activity even if Fe's intrinsic CO_2→CO step is unchanged.

In the high-temperature regime, a small Ea_2 (approaching zero) is actually a symptom of a high-performance catalyst reaching external limits. For instance, Fe30-US maintains Ea_2 ≈15-18 kJ/mol under baseline conditions, while Fe30-BM drops to ≈0-9 kJ/mol (Table 5.5). The near-zero Ea_2 for ball-milled samples suggests that above 320 °C the reaction is no longer chemically rate-limited - consistent with either internal diffusion limits in the catalyst pores or thermodynamic saturation of CO_2 conversion (especially for exothermic CH_4 formation). Indeed, ball-milled catalysts often feature smaller crystallites and stronger metal-support interactions, which can create diffusion constraints and overly strong binding sites. Such effects manifest as a flattened Arrhenius slope at high T. In summary, the more active a catalyst is, the sooner it encounters transport/thermodynamic limits: the most active formulations show an earlier and more pronounced downward deviation in the Arrhenius plot (lower Ea_2), whereas less active ones continue in the kinetics- controlled regime longer (higher Ea_2).

- Influence of Preparation Method: Ultrasound vs. Ball-Milling

Low- vs High-Temperature Activity: Ultrasound (US) and ball-milled (BM) versions of each catalyst show different macrokinetics. Ball-milled samples exhibit higher CO_2 conversions at low temperatures (e.g. at 250 °C, BM conversions are ≈2-5% absolute higher than US for all catalysts), indicating that BM creates a greater density of active sites or dispersion (higher BET surface area). Consequently, Ea_1 values for BM are often slightly lower or comparable to US in the low-T regime (Table 1), facilitating better initial kinetics. For example, Fe30-BM has Ea_1 ≈52 kJ/mol vs. 51 kJ/mol for Fe30-US, and Co33-BM shows Ea_1 ≈49 kJ/mol vs. 54 kJ/mol for Co33-US - consistent with BM enhancing low-T activity by exposing more active Fe sites. However, at high temperatures the trend reverses. US-prepared catalysts outperform BM in conversion above ≈320 °C, corresponding to a higher Ea_2 (still positive slope) than BM. Ball-milled catalysts often plateau or even decrease in conversion beyond 320-350 °C, giving near-zero or negative Ea_2 (Table 1). This is attributed to BM creating stronger binding sites and potential diffusional constraints: CO_2 and H_2 chemisorb very strongly on BM samples (as evidenced by broad, high-temperature TPD peaks), which can lead to product inhibition or slow desorption at high T. In contrast, US samples have more moderate adsorption strengths and accessible pores, allowing reaction rates to continue increasing with temperature. For instance, Fe30-US still shows a measurable Ea_2 ≈15 kJ/mol under baseline conditions, whereas Fe30-BM's Ea_2 ≈0-5 kJ/mol (essentially temperature-independent rate) suggests it has hit a mass-transfer or equilibrium ceiling. Thus, ultrasound preparation yields catalysts with better high-temperature efficacy and

resistance to transport limitations, whereas ball-milling sacrifices high-T performance (and long-term turnover) for a boost in low-T activity.

- Effect of Reaction Conditions: GHSV and H_2/CO_2 Ratio

Baseline vs Low GHSV (Test #2): Reducing the gas hourly space velocity (from 3200 to 1600 h^{-1}) increases contact time, leading to higher CO_2 conversions at each temperature. Under Test #2, all catalysts reach higher conversion levels by 350 °C (often 5-10% higher absolute conversion than baseline). This accelerated approach to equilibrium causes the high-temperature regime to flatten more severely. Accordingly, apparent Ea_2 values drop under low GHSV conditions (see Table 1). For example, Fe40-US has Ea_2 ≈14 kJ/mol at baseline but only ≈9 kJ/mol in Test #2, and Fe40-BM falls from ≈4 kJ/mol to ≈1 kJ/mol. Several BM catalysts (Fe30-BM, Co33-BM, FeZn-BM) even show *slightly negative* Ea_2 in Test #2, meaning the conversion at 350 °C was marginally lower than at 320 °C - a clear indication of equilibrium limitation (exothermic reactions shifting backwards at higher T) or water inhibition. In contrast, Ea_1 in the low-T regime tends to remain similar or increase slightly at lower GHSV (since early-temperature data are less affected by equilibrium). Overall, lower GHSV accentuates dual-regime behavior, pushing catalysts into the transport/thermodynamic-limited regime sooner.

Higher H_2/CO_2 ratio (Test #3, H_2/CO_2 = 4): Increasing the hydrogen partial pressure generally promotes the forward hydrogenation reactions. Under Test #3, CO_2 conversions at high T (350 °C) are higher for most catalysts (especially those prone to CH_4 formation). For instance, Co45-US reaches ≈58% conversion at 350 °C with H_2/CO_2=4, versus ≈54% at H_2/CO_2=3. This suggests the extra H_2 drives methane formation forward (mitigating the equilibrium penalty to some extent) [50]. Consequently, some catalysts show a slightly larger Ea_2 under Test #3 compared to baseline (recovering some temperature-dependence of rate). For example, Fe30-BM, which had essentially Ea_2≈0 in baseline, exhibits Ea_2 ≈14 kJ/mol in Test #3 (Table 1), as the higher H_2 ratio allows continued rate increases up to 350 °C. Likewise, Co45-BM's Ea_2 rises to ≈3-5 kJ/mol (from ≈0). Notably, Co33-US in Test #3 becomes nearly equilibrium-limited by 320-350 °C (Ea_2 ≈0-3 kJ/mol), likely because its CH_4-selective sites drive conversion so high that methane equilibrium is approached. On the low-temperature side, Ea_1 can shift due to H_2/CO_2 changes: a higher H_2 fraction can lower the apparent Ea if H_2 adsorption/activation was rate-limiting. In practice, Ea_1 values in Test #3 are similar to or slightly higher than baseline for most catalysts (Table 1), with no systematic large change. One exception is Co45-US, which shows a somewhat higher Ea_1 in Test #3 (≈65-70 kJ/mol vs ≈52 kJ/mol baseline). This anomaly is explained by its unusually lower 250 °C conversion at H_2/CO_2=4 (dilution of CO_2 partial pressure outweighed the kinetic benefit of extra H_2 at the lowest temperature). In summary, raising H_2/CO_2 = 4 improves high-T performance (delaying the Arrhenius "bend") but yields comparable Ea_1 in the intrinsic kinetics regime.

- Metal loading effects on Kinetics and Selectivity (Zn vs Co)

FeZn: The Zn (and Cu) profoundly influences the reaction pathway. Fe-Zn exhibits the lowest Ea_1 among all catalysts (≈35-45 kJ/mol in most conditions, versus ≈50-60 kJ for others; see Table 1). This indicates that ZnO/Cu sites provide an additional low-barrier route for CO_2 activation - likely via a formate or CO intermediate on Cu-ZnO, akin to methanol synthesis or

low-temperature WGS chemistry [59,58]. As a result, Fe-Zn achieves superior CO_2 conversion at the lowest temperatures (e.g. ≈16-18% at 250 °C, whereas Fe-only catalysts manage ≈9-14%). The high-temperature Ea_2 for Fe-Zn is also relatively low (often approaching 0 in BM form under high conversion conditions), suggesting that once the facile Zn/Cu-assisted route is maximized, the rate becomes limited by CO_2 supply or product removal. In terms of products, Zn promotion (especially when combined with Cu) tends to suppress excessive methanation in favor of CO and higher hydrocarbons. Indeed, the Fe-Zn catalyst shows a high C_{2+} hydrocarbon yield (Table 1, C_{2+} yield columns) and literature reports that adding Zn to Fe shifts selectivity toward olefinic hydrocarbons by stabilizing iron carbide and moderating hydrogenation activity [60,61]. Our data support this: Fe-Zn achieves ≈80% of carbon converted ending up as C_{2+} products, the highest among the tested catalysts (e.g. 37-39% C_{2+} yield out of ≈48% conversion). ZnO's basic sites also enhance CO_2 adsorption [62], which, however, can lead to water inhibition at high conversion (water produced from RWGS/FT can adsorb on ZnO, slowing further CO_2 activation [41]). Overall, Zn (with Cu) acts as a structural and electronic promoter that lowers activation barriers and boosts chain-growth selectivity to light olefins [60].

Fe-Co 33 and 45: Cobalt addition does not significantly lower the initial CO_2 activation barrier (Ea_1) - these remain in the ≈50-60 kJ/mol range - but it provides additional H_2 dissociation and hydrogenation sites. Consequently, Co-doped catalysts have high activity in converting intermediates (CO or surface carbides) to methane and saturated hydrocarbons. Co45 (the higher Co fraction) in particular shows the highest CO_2 conversion among unpromoted and promoted samples at most temperatures. For instance, Co45-US reaches ≈54% conversion at 320 °C (versus ≈46-48% for Fe-only and Fe-Zn at 320 °C under baseline). The presence of Co thus accelerates the overall rate, especially in H_2-rich conditions, by facilitating the rate-limiting C-O bond hydrogenation steps. In terms of high-T kinetics, Co-promoted catalysts also hit a transport/thermodynamic ceiling: e.g., Co33-BM and Co45-BM have Ea_2 ≈0 (or negative) under baseline and Test #2, reflecting early methane equilibrium limitations (CH_4 formation being highly exothermic and unfavorable at high T [50]). Adding more H_2 (Test #3) partly alleviates this, as noted, allowing Co45 to continue reacting (Ea_2 ≈3-9 kJ/mol instead of ≈0).

Product Selectivity: Co noticeably shifts the product distribution towards more saturated hydrocarbons and methane, at the expense of olefins. Iron-based FT catalysts inherently favor olefin formation (especially when promoted by K) [61], but Co provides a hydrogenation function that tends to saturate those olefins into paraffins. In our experiments, Fe-Co catalysts show slightly lower C_{2+} yields than Fe-Zn at equivalent conversion, implying a higher fraction of CH_4. For example, at 350 °C baseline, Co33-US and Co45-US achieve ≈51-54% conversion with C_{2+} yields of 33-36%, whereas Fe-Zn-US at 55% conversion gives 37.8% C_{2+} (suggesting Co-catalysts made ≈15-20% of product as CH_4 vs. ≈10% for Fe-Zn). Moreover, the hydrocarbons produced on Co-Fe are more saturated. This aligns with literature observations that Fe sites contribute to C-C coupling and olefin production, while Co promotes further hydrogenation to alkanes [61]. Indeed, Co45 (with more Co) produces the highest CH_4 selectivity. Under baseline conditions ≈12% of CO_2 ends as CH_4 on Co45-US (derived by difference, not shown in table), roughly double that on Fe-Zn. Despite this, Fe-Co catalysts still generate substantial C_{2+} hydrocarbons (up to ≈35-39%C yield), indicating that the bimetallic system integrates both FT chain growth (via Fe carbides) and

methanation (via Co sites) [63]. Interestingly, adding Co also seems to enhance the extent of CO_2 conversion into liquids: Co45-BM achieved the highest C_{2+} yield of ≈39% (at 49.8% conversion), possibly because Co improved overall CO_2 conversion without completely terminating chain growth. In summary, Zn and Co promoters both increase CO_2 conversion but with different selectivity profiles: Zn promotes CO formation and olefinic C_{2+} products via lower-barrier CO_2 activation, whereas Co boosts total conversion and tends toward CH_4/alkane products by increasing hydrogenation rates [61]. The optimal promoter depends on the desired product spectrum - Zn for maximizing olefins (and lowering Ea), Co for maximizing throughput and methane (or saturated fuels).

Fe30 US

		first region Ea1	second region Ea2
3t1	Ea	46.4	18
	A	5.16E+05	1.56E+03
4t1	Ea	75.8	17.1
	A	4.49E+08	1.35E+03
3t1 DR	Ea	58.5	20.7
	A	8.93E+06	3.06E+03

Fe30 BM

		first region Ea1	second region Ea2
3t1	Ea	77.7	7.4
	A	7.54E+08	178.3
4t1	Ea	75.8	14.6
	A	4.81E+08	802.8
3t1 DR	Ea	55.9	2.9
	A	5.92E+06	84

Fe40 US

		first region Ea1	second region Ea2
3t1	Ea	58.5	14.5
	A	6.36E+06	7.07E+02
4t1	Ea	58.5	9.2
	A	7.44E+06	2.68E+02
3t1 DR	Ea	66	9.2
	A	3.88E+07	2.93E+02

Fe40 BM

		first region Ea1	second region Ea2
3t1	Ea	59.9	5.4
	A	1.06E+07	1.11E+02
4t1	Ea	58.5	12.7
	A	7.63E+06	5.02E+02
3t1 DR	Ea	61.9	1.2
	A	1.86E+07	5.60E+01

Co33 US

		first region Ea1	second region Ea2
3t1	Ea	69.4	11.6
	A	1.22E+08	4.84E+02
4t1	Ea	53.3	2.4
	A	3.66E+06	8.69E+01
3t1 DR	Ea	84.3	7.4
	A	4.14E+09	2.33E+02

Co33 BM

		first region Ea1	second region Ea2
3t1	Ea	71.4	1
	A	2.29E+08	5.74E+01
4t1	Ea	51.6	1.1
	A	2.54E+06	6.22E+01
3t1 DR	Ea	84.2	-2.2
	A	4.55E+09	3.50E+01

Co45 US

		first region Ea1	second region Ea2
3t1	Ea	94.3	17.6
	A	3.54E+10	1.64E+03
4t1	Ea	137.1	8.5
	A	5.46E+14	2.99E+02
3t1 DR	Ea	118.2	9.4
	A	8.96E+12	3.77E+02

Co45 BM

		first region Ea1	second region Ea2
3t1	Ea	96.2	1.2
	A	6.65E+10	6.11E+01
4t1	Ea	83	4.2
	A	3.16E+09	1.16E+02
3t1 DR	Ea	109	2.2
	A	1.32E+12	8.79E+01

		FeZn US				FeZn BM	
		first region Ea1	second region Ea2			first region Ea1	second region Ea2
3t1	Ea	39.6	14.1	**3t1**	Ea	40.7	3.1
	A	1.54E+05	8.28E+02		A	2.46E+05	8.77E+01
4t1	Ea	42	9.9	**4t1**	Ea	39.6	9.9
	A	2.80E+05	3.59E+02		A	1.85E+05	3.59E+02
3t1 DR	Ea	42.8	9.2	**3t1 DR**	Ea	43.3	0.8
	A	3.59E+05	3.46E+02		A	4.84E+05	6.30E+01

Table 5.5. Apparent Activation Energies (Ea_1, Ea_2) under Various Conditions and Catalyst Preparations. Ea values ($kJ \cdot mol^{-1}$) were obtained from Arrhenius fits in low- and high-T ranges (250-300 °C and 320-350 °C, respectively).

5.2.4. CO_2 Hydrogenation on Bench-Scale

The catalytic performance of Fe30US and FeZnUS was evaluated in a bench-scale fixed-bed reactor over a range of temperatures (250-365 °C) and pressures (20, 25, 30 bar). Key results are summarized in Figure 5.26 (CO_2 conversion) and Figure 5.27 (product selectivities for CH_4, CO, C_2-C_6, and C_{7+}) for Fe30US, with analogous trends for FeZnUS shown in Figure 5.28 and 5.29. In general, increasing reaction temperature accelerated CO_2 conversion for both catalysts, while changes in pressure had a profound influence on product selectivity. Below, the effects of temperature and pressure are analyzed separately for each catalyst, highlighting how elevated pressure suppresses methanation and promotes long-chain hydrocarbon formation.

5.2.4.1. Fe30US Catalyst: Effect of Temperature and Pressure

CO_2 Conversion: Fe30US exhibited steadily increasing CO_2 conversion with rising temperature at all pressures (Fig. 5.26). At 20 bar, conversion climbed from ≈15% at 255 °C to ≈50% by 355 °C. Higher pressure enhanced the conversion across the temperature range: for example, at 315 °C CO_2 conversion was ≈35% at 20 bar, compared to ≈47% at 30 bar (Fig. 5.26).

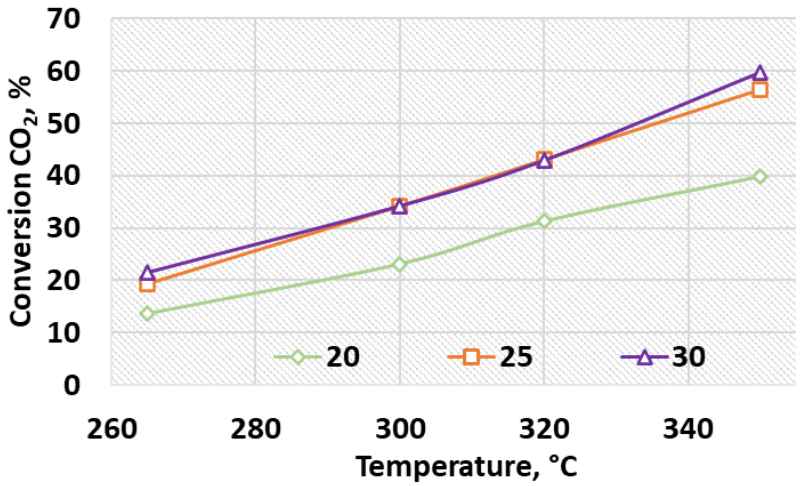

Figure 5.26. Conversion of CO_2 at different pressure conditions.

This positive pressure effect is consistent with the general understanding that high synthesis pressure drives the CO_2/CO hydrogenation equilibrium toward hydrocarbon products, effectively increasing reactant utilization [64,65]. The trend also aligns with Le Chatelier's principle for

Fischer-Tropsch reactions, where forming long-chain hydrocarbons (condensed/liquid at reaction conditions) consumes gaseous reactants and is favored by elevated pressure [65]. Indeed, literature on CO hydrogenation (FTS) notes that increasing total pressure enhances CO conversion while shifting the product spectrum toward heavier hydrocarbons [64]. The Fe30US catalyst follows this pattern: at 30 bar it achieved the highest CO_2 conversions and, as discussed below, produced a greater fraction of heavy products.

Product Selectivity vs. Temperature (20 bar): At the baseline pressure of 20 bar, Fe30US showed a distribution typical of a combined Reverse Water-Gas Shift (RWGS) + FTS pathway. At low temperature (250-260 °C), a significant portion of CO_2 was converted to CO (RWGS product): CO selectivity was ≈40% at 255 °C (Fig. 5.27). Methane accounted for another ≈30% of products at this temperature (Fig. 5.27), indicating that direct methanation was also active. The remainder (≈30%) comprised hydrocarbons in the C_2-C_6 and C_{7+} ranges, with C_2-C_6 slightly exceeding C_{7+} (Fig. 5.27). As temperature increased to ≈300 °C, the selectivity profile shifted markedly. CO selectivity dropped to <10% by 315 °C, implying that most of the intermediate CO was further converted to hydrocarbons rather than exiting as CO byproduct. Concomitantly, C_2-C_6 and C_{7+} hydrocarbon selectivities increased. Notably, at 295-315 °C the C_{7+} fraction on Fe30US reached ≈30-35% (Fig. 5.27), surpassing the CH_4 fraction, which reached a minimum of ≈20-22% in this mid-temperature range (Fig. 5.27). This suggests that intermediate temperatures favor chain growth: the Fischer-Tropsch synthesis activity becomes significant, converting CO (from RWGS) and CO_2 into long-chain hydrocarbons, while excessive methanation is limited. By 335-355 °C, however, the selectivity trends began to reverse. At 355 °C and 20 bar, CH_4 selectivity rose sharply to ≈33% - the highest of any temperature at this pressure - whereas C_{7+} selectivity declined to ≈20% (nearly as low as it had been at 255 °C). The C_2-C_6 fraction at 20 bar peaked at ≈32% around 355 °C (Fig. 5.27). These observations are in line with the known temperature-dependence of Fischer-Tropsch: higher reaction temperatures accelerate chain-termination reactions (favoring lighter products like CH_4 and light olefins) at the expense of chain propagation to heavy waxes [66]. In other words, low-temperature FT tends to produce high molecular mass waxes, whereas high-temperature operation (≥ ≈330 °C) produces more low-boiling products (gasoline-range and lighter) [66]. The Fe30US data reflect this behavior - an intermediate temperature (≈300 °C) “sweet spot” where heavy product formation is maximized, bounded by low-temperature conditions limited by kinetics/RWGS and high-temperature conditions that favor methane and short hydrocarbons.

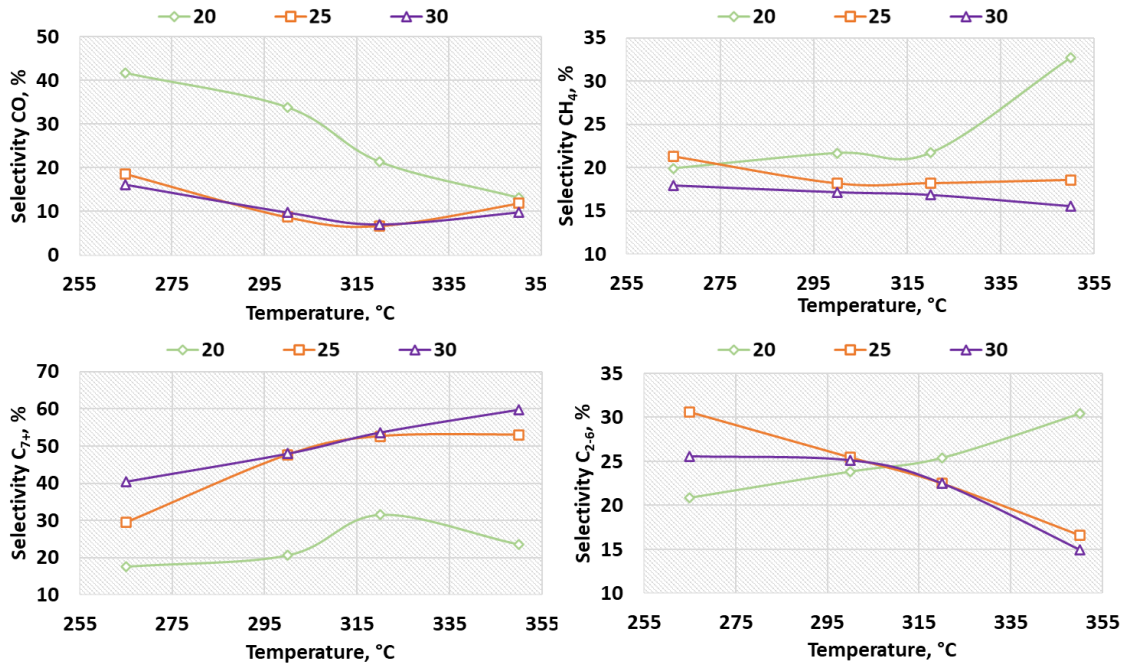

Figure 5.27. Fe30 US Bench scales selectivity of CO (top left), CH_4 (top right), C_{2-6} (bottom right), C_{7+} (bottom left).

Effect of Pressure on Product Selectivity: Changing the pressure from 20 bar to 25 bar and 30 bar had a pronounced effect on product selectivities for Fe30US. Higher pressure consistently suppressed methane formation and enhanced heavy hydrocarbon formation across the temperature range. For example, at 255 °C CH_4 selectivity was ≈30% at 20 bar, but only ≈22% at 25 bar and ≈18% at 30 bar (Fig. 5.27). This inverse relationship between pressure and CH_4 selectivity held true at the other temperatures as well - at 315 °C, raising pressure from 20 → 30 bar cut the CH_4 selectivity from ≈24% down to ≈16%. Such methane suppression by pressure is well documented in FTS literature: high pressures tend to reduce the probability of chain termination by hydrogenation to CH_4, instead favoring chain growth to longer products [65]. In fact, operating at 25-30 atm has been reported to favor the formation of waxy hydrocarbons (C_{20+}) over lighter fractions, whereas moderate pressures (≈20 atm) yield more gasoline/diesel-range products [65]. Consistent with this, the Fe30US catalyst at 30 bar showed a substantial boost in C_{7+} selectivity alongside the drop in CH_4. At 255 °C, C_{7+} selectivity nearly doubled from ≈20% (20 bar) to ≈40% (30 bar) (Fig. 5.27). At 315 °C, the C_{7+} fraction reached ≈55-60% at 25-30 bar, compared to ≈30% at 20 bar. Even at 355 °C - a temperature where heavy product formation was diminishing at low pressure - the C_{7+} selectivity at 30 bar remained ≈65%, in stark contrast to the ≈21% at 20 bar. The C_2-C_6 fraction showed an intermediate behavior: at low temperature (255 °C), 25 bar gave the highest C_2-C_6 selectivity (≈30%, vs. 25% at 30 bar and 28% at 20 bar), but at higher temperatures the ranking inverted, with 20 bar showing the most C_2-C_6 (as 30 bar diverted more carbon into the C_{7+} category). For instance, by 355 °C the C_2-C_6 selectivity at 20 bar was ≈32%, roughly double that at 30 bar (≈15-18%). In summary, increasing pressure shifted the Fe30US product slate away from CO and CH_4 and towards heavier hydrocarbons.

Mechanistically, the pressure-induced selectivity shifts can be rationalized by Fischer-Tropsch kinetics and thermodynamics. Higher pressure increases the surface coverage of reactants (CO_2/CO and H_2) on iron sites, which promotes the chain growth probability (α in the Anderson-Schulz-Flory distribution). Simultaneously, elevated pressure likely accelerates the conversion of

CO (from RWGS) into longer-chain surface intermediates, thereby reducing the net CO observed in products. Indeed, at 30 bar Fe30US exhibited very low CO selectivity (<5% in the 295-315 °C range; Figure 5.27), implying near-complete incorporation of CO into hydrocarbons. This is consistent with studies noting that Fe-based catalysts can achieve low CO selectivity in CO_2 hydrogenation when reaction conditions favor the FT route over RWGS [67]. The suppression of CH_4 at high pressure suggests that termination via hydrogenation of surface C_1 species becomes less competitive; instead, chain propagation steps (C-C coupling) proceed further to form C_{2+} fragments before termination. The net result is an enhanced yield of long-chain (C_{7+}) products at high pressure, as observed. This behavior parallels that of classic FTS: low-pressure operation tends to produce more light gases (including CH_4), whereas high-pressure operation favors heavy waxes [65]. Overall, Fe30US demonstrates that simply increasing pressure can shift CO_2 hydrogenation from a pseudo-Sabatier/RWGS-dominated regime (high CH_4 + CO) into a true Fischer-Tropsch regime producing predominantly liquid-range hydrocarbons.

5.2.4.2. FeZnUS Catalyst: Effect of Temperature and Pressure

Incorporating Zn (FeZnUS) altered the catalyst performance, leading to higher activity and a strong intrinsic bias toward heavier hydrocarbons.

CO_2 conversion on FeZnUS was uniformly higher than on Fe30US under comparable conditions (Figure 5.28).

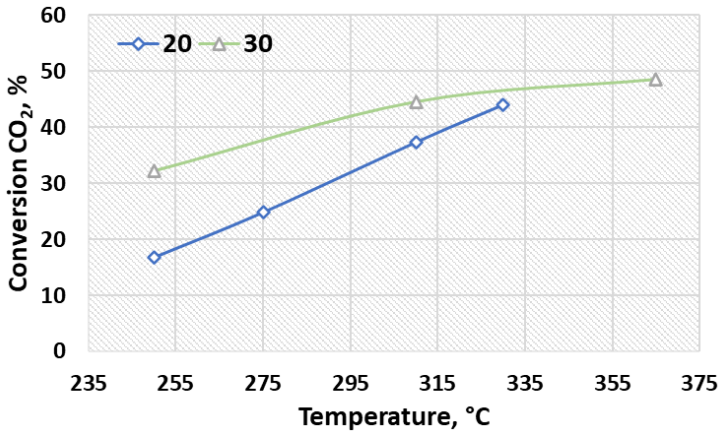

Figure 5.28. FeZn US conversion of CO_2 at different pressure conditions.

For instance, at 255 °C and 20 bar, FeZnUS achieved ≈18% conversion (vs. ≈15% for Fe30US), and at 315 °C conversion reached ≈40% (versus ≈35% on the unpromoted catalyst).This improvement can be attributed to Zn's promotional effects on iron: Zn is known to facilitate CO_2 activation and CO adsorption on iron sites, as well as to enhance H_2 dissociation [62]. Additionally, Zn increases the dispersion of iron (by forming a Zn-Fe oxide solid solution or spinel) and stabilizes the Fe carbide phase under reaction conditions [62]. These factors effectively generate more active sites and maintain them in the carbidic state needed for CO_2 conversion via the FTS pathway. The result is a higher apparent reaction rate and CO_2 turnover for the Zn-promoted catalyst, in line with literature reports of Zn-enhanced CO_2 hydrogenation activity [68].

Selectivity and the Role of Zn: Perhaps the most striking effect of Zn promotion is the shift in baseline selectivity towards long-chain hydrocarbons even at lower pressure. Compared to

Fe30US, FeZnUS produced significantly less CH_4 and much more C_{7+} under all conditions examined. At 20 bar and 255 °C, CH_4 selectivity on FeZnUS was only ≈12% (Fig. 5.29), which is about one-third of the value on Fe30US at the same condition (≈30%). Correspondingly, the C_{7+} selectivity on FeZnUS (20 bar, 255 °C) was ≈35-40% (Fig. 5.29), roughly double that of Fe30US (≈20%). In fact, the product distribution on FeZnUS at 20 bar resembles that of Fe30US at 30 bar - indicating that Zn provides an effect analogous to a pressure increase in terms of steering the reaction toward heavier products. This behavior is supported by literature: transition metal promoters like Zn have been found to enhance carbon-carbon coupling on iron catalysts, likely by promoting the formation of Hägg carbide (Fe_5C_2) and strengthening the Fe-C bond, which in turn raises the chain-growth probability [62]. Zn also creates a more electron-rich (basic) surface that can suppress hydrogenation of intermediates [62], thereby mitigating the tendency to form CH_4 and other fully hydrogenated light products. The net effect is a catalyst that intrinsically favors the assembly of longer hydrocarbon chains.

Temperature Trends (FeZnUS): The influence of temperature on FeZnUS mirrored the general pattern observed with Fe30US, but the extent of change in selectivity was less extreme due to the already heavy-biased product slate. As temperature increased from 250 °C to ≈330 °C at 20 bar, CH_4 selectivity, already low, decreased further (from ≈12% to below 5%; Figure 5.29). CO selectivity also plummeted with rising temperature on FeZnUS. At 255 °C and 20 bar, CO accounted for ≈25-30% of products (still lower than the 40% on Fe30US). By 315 °C, CO selectivity on FeZnUS was under 10% at 20 bar (Fig. 5.29), indicating efficient conversion of most CO_2 to hydrocarbons at higher temperatures. Meanwhile, the C_{7+} fraction grew with temperature: at 20 bar it rose from ≈35% at 255 °C to ≈65-70% at 315-335 °C (Fig. 5.29). This trend confirms that once sufficient temperature is reached to activate FT synthesis on FeZnUS, the catalyst channels a majority of the carbon into heavy hydrocarbon chains. Notably, even at the highest temperatures tested, FeZnUS did not exhibit the same pronounced methane upsurge that Fe30US did. For example, at ≈335 °C and 20 bar, CH_4 remained below ≈6-8% on FeZnUS (whereas Fe30US at 355 °C, 20 bar had >30% CH_4).

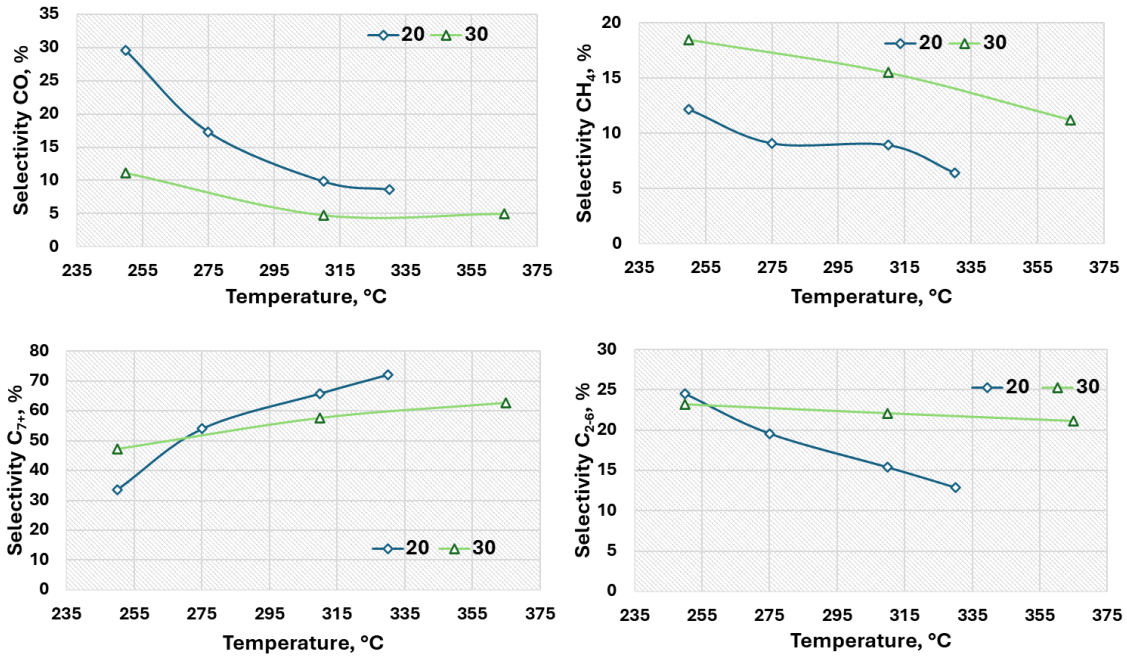

Figure 5.29. FeZn US selectivity of CO (top left), CH_4 (top right), C_{2-6} (bottom right), C_{7+} (bottom left).

This suggests that Zn promotion raises the thermal tolerance for maintaining a heavy product selectivity - likely because the promoted catalyst can sustain a high surface coverage of carbon intermediates (carbide phase) even as temperature increases, thus continuing to favor chain propagation over termination. Indeed, Zn has been shown to stabilize iron carbides against oxidation by H_2/H_2O at reaction conditions [62], which could help preserve the FT-active phase at higher temperatures.

Pressure Effects (FeZnUS): Increasing pressure from 20 bar to 30 bar on the FeZnUS catalyst further enhanced CO_2 conversion and somewhat modified the selectivity, though the relative impact was smaller than on Fe30US (because FeZnUS was already highly selective to C_{7+} at 20 bar). CO_2 conversion at 30 bar was ≈10 percentage points higher than at 20 bar across the temperature range (Fig. 5.28), similar to the trend on Fe30US. In terms of products, raising the pressure to 30 bar did reduce the CH_4 selectivity slightly (Fig. 5.29) - but given that CH_4 was <15% even at 20 bar, the absolute change was modest. For example, at 275 °C CH_4 was ≈10% at 20 bar and ≈16% at 30 bar; by 315 °C both pressures yielded CH_4 in the single digits. (Within experimental uncertainty, the CH_4 levels at 25-30 bar on FeZnUS were very low across the board, making it difficult to discern a strong pressure trend for methane). The major product on FeZnUS at all pressures was the C_{7+} fraction. At 255 °C, increasing pressure from 20 to 30 bar raised the C_{7+} selectivity from ≈35% to ≈45% (Fig. 5.29). This indicates that, as expected, higher pressure still favors longer-chain formation even on the promoted catalyst. At intermediate temperatures (295-315 °C), both 20 bar and 30 bar runs yielded a very high heavy fraction (≈50-60% or more). Interestingly, at the highest temperature examined (≈335 °C), the 20 bar FeZnUS run showed a slightly higher C_{7+} selectivity (≈72%) than the 30 bar run (≈65%). This minor inversion may suggest that beyond a certain point, additional pressure does not further increase heavy product yield and could even be counteracted by secondary factors - for instance, increased water partial pressure at 30 bar might inhibit further chain growth or alter the catalyst surface. However, the difference is small, and both pressures clearly produce predominantly heavy hydrocarbons (with

C_{7+} making up well over half of the products). The C_2-C_6 fraction on FeZnUS was comparatively low: ≈20-25% at 255 °C (slightly higher at 30 bar) tapering to ≈10-15% at 315 °C (Fig. 5.29). Pressure had a mild effect on this mid-range fraction; e.g. at 335 °C, C_2-C_6 selectivity was ≈10% at 20 bar versus ≈16% at 30 bar, reflecting that 30 bar produced a bit more medium liquids while 20 bar pushed an even larger share into C_{7+}. Overall, Zn promotion diminished the sensitivity of selectivity to pressure: FeZnUS gave a heavy product slate even at low pressure, and while higher pressure still reinforced the trend (especially at lower temperatures), the catalyst achieved "high-pressure performance" (low CH_4, high C_{7+}) even at 20 bar.

Comparison and Mechanistic Links: The contrast between Fe30US and FeZnUS highlights how catalyst composition and reaction pressure both govern the reaction pathway. Fe30US required a high pressure (25-30 bar) to curtail methanation and boost heavy product formation, whereas FeZnUS inherently exhibited those desirable traits due to the promoter. In essence, Zn promotion shifted the product selectivity in the same direction as increasing pressure, favoring longer-chain hydrocarbons at the expense of CH_4, which concurs with previous studies on Zn- or metal-promoted iron catalysts [62]. The underlying mechanism is likely the stabilization of the iron carbide phase (Fe_5C_2) and an increase in active carbon intermediates on the surface. Mössbauer and IR studies have shown that adding Zn can facilitate the formation and maintenance of Fe_5C_2 during CO/CO_2 hydrogenation [62]. This carbide is the key active phase for Fischer-Tropsch chain growth; thus, its presence correlates with higher chain growth probability and heavier products. Zn may also act as an electronic promoter - creating a more alkaline surface that enhances CO_2 adsorption and dissociation [62] - effectively accelerating the initial RWGS step to produce CO and carbon species that enter the FT cycle [62]. Once those species are on the surface, the strong Fe-C bonds (further strengthened by Zn's electron donation [62]) favor carbon-carbon coupling over hydrogenation, thereby suppressing CH_4 formation. The end result is a catalyst that, even at moderate pressures, converts CO_2 predominantly into heavier hydrocarbons. Notably, FeZnUS achieved >60% selectivity to C_{7+} (here C_{7+}) hydrocarbons at just 20 bar and ≈320 °C - a performance level that typically would require much higher pressure or additional promoters in a conventional Fe catalyst [65].

5.2.5. Performance of Fe30 in Lab-Scale vs. Bench-Scale Reactors

5.2.5.1. Reactor and Catalyst Overview

In this section, we compare CO_2 hydrogenation results over the Fe30 catalyst in two reactor setups: a lab-scale fixed-bed (BUNKER) and a bench-scale fixed-bed (CNR). Both operated at 20 bar with identical feed compositions ($H_2/CO_2 = 3$), but the catalyst was used in different forms. BUNKER employed Fe30 in a powder form (high dispersion, BET ≈87 m^2/g), whereas CNR used Fe30 in a pelletized form (larger particles, BET ≈67 m^2/g). These textural differences (surface area and particle size) are expected to influence catalytic performance. Table 5.6 summarizes the CO_2 conversion and product selectivities for both systems at various temperatures, and Fig. 5.30 illustrates the trends in conversion and C_{2+} yield with temperature. In general, the lab-scale powder catalyst exhibits higher activity and a heavier product slate, while the bench-scale pellet shows lower overall conversion and a lighter product distribution, as detailed below.

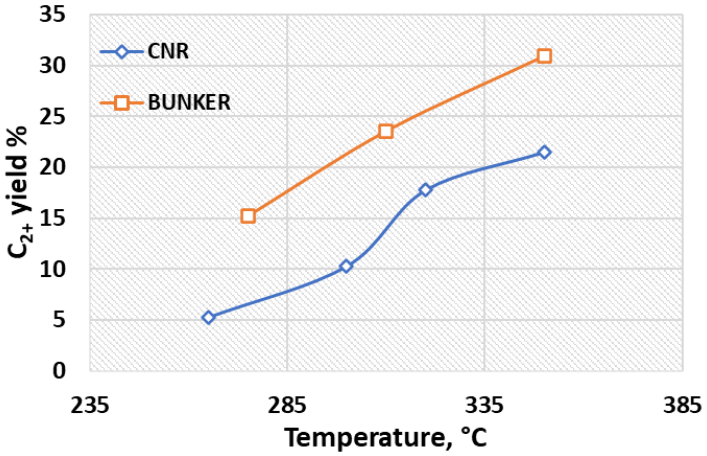

Figure 5.30. C2+ yield representation of Fe30 in lab scale (BUNKER) and bench scale (CNR) set ups.

CNR	CO_2 conv %	S C_2	S C_3	S CO	S CH_4	S C_{4+}	C_{2+} yield
265	13.6	11.0	9.8	41.6	19.9	17.7	5.2
300	23.1	12.0	11.9	33.8	21.7	20.7	10.3
320	31.2	11.8	13.6	21.4	21.7	31.5	17.8
350	39.8	13.5	17.0	13.2	32.7	23.6	21.5

BUNKER	CO_2 conv %	S C_2	S C_3	S CO	S CH_4	S C_{4+}	C_{2+} yield
275	21.7	12.9	8.9	20.5	9.3	48.4	15.2
300	34.3	14.2	6.6	18.5	12.8	48.0	23.5
350	43.1	18.6	7.2	10.5	17.8	46.0	30.9

Table 5.6. Summary of performances of Fe30 in two different plant set ups.

5.2.5.2. CO_2 Conversion Trends

The Fe30 powder in BUNKER achieved consistently higher CO_2 conversions than the pellet in CNR at equivalent temperatures. For example, at 300 °C the lab reactor converted about 34% of CO_2, versus ≈23% in the bench reactor. The difference narrowed at higher temperature: by 350 °C, BUNKER reached ≈43% conversion compared to ≈40% in CNR. Overall, however, the powder form clearly outperformed the pellet form in CO_2 conversion at most conditions. The lower conversion in the pelletized catalyst can be attributed to its lower accessible surface area and internal mass transfer resistance. Larger catalyst pellets are known to suffer from intraparticle diffusional limits [69], which reduce the effective utilization of active sites (low "effectiveness factor") in fixed-bed reactors [70]. This is consistent with literature reports that smaller catalyst particles or larger pore structures yield higher CO_2 conversion due to better mass transfer [71].

5.2.5.3. Selectivity: CH_4 vs. CO (RWGS vs. FT Pathways)

Along with activity differences, the two systems showed different selectivity patterns for methane and carbon monoxide. The lab-scale favored lower CO selectivity. At 300 °C, the powder's CO selectivity was ≈18% of carbon products, significantly lower than the pellet's ≈34%. Even at 265-275 °C, the powder produced only ≈20% CO while the pellet released over 40% of CO_2 as CO, indicating that the pellet catalyst initially converted a larger fraction of CO_2 into the one-step RWGS reaction rather than the subsequent FT synthesis. This implies the FT chain-growth step was less active in the pellet at low temperature. As temperature increased, CO selectivity dropped in both systems. By 350 °C, CO selectivity fell below ≈13% in CNR and ≈10% in BUNKER,

suggesting that most of the CO_2 converted was further transformed into hydrocarbons in both cases. Notably, the powder consistently showed a lower CH_4 selectivity than the pellet. At 300 °C, CH_4 accounted for only ≈12.8% of the powder's products versus ≈21.7% for the pellet. This gap widened at higher temperature at 350 °C the pellet generated ≈33% methane, almost double the powder's ≈18%. One explanation is that the pellet's larger diffusion distance leads to hydrogen-rich zones near the exterior that promote methanation, while its interior may be under-utilized or subject to water inhibition [72,73]. Additionally, any differences in catalyst promotion could play a role, if pelletizing led to a less effective dispersion of K-promoter on the surface, the catalyst would exhibit higher CH_4 selectivity, since potassium is known to suppress methane formation on Fe catalysts [74]. The powder's combination of better dispersion and mass transfer likely facilitated more CO insertion and chain growth relative to methanation [74], resulting in a lower CH_4/CO ratio.

5.2.5.4. Light (C_2-C_6) vs. Heavy (C_{7+}) Hydrocarbon Distribution

The disparity in product yield between powder and pellet is further highlighted by the distribution of hydrocarbon chain lengths. The Fe30 powder produced a significantly heavier product spectrum. Even at 275 °C, BUNKER showed nearly 50% selectivity toward C_4^+ hydrocarbons. At 300 °C and 350 °C, the C_{4+} fraction in the powder remained around 46-48% of the total hydrocarbons. In contrast, the pelletized catalyst in CNR shifted much more towards light hydrocarbons (C_2-C_3). The total C_{4+} selectivity for the pellet peaked at only ≈31%, at 320 °C, and was ≈24% at 350 °C, about half that of the powder. This suggests the heavy C_{7+} fraction was comparatively small in the bench-scale output, with most of the hydrocarbons being C_2-C_3 gases and liquids. For instance, at 350 °C the pellet yielded ≈17% C_3 products (propane/propene) versus only ≈7% from the powder, indicating shorter chains were terminating around C_3 in the pellet reactor rather than growing into heavy waxes. These trends are visualized in Table 5.6, which compares the product selectivity breakdown for both reactors. The lighter product slate from the pellet can be explained by diffusion and kinetic effects: in large pellets, olefin intermediates are more likely to escape the catalyst before further chain growth, and internal regions may experience lower reactant concentrations or deactivating by-products (water, coke) that cap the attainable chain length [75]. By contrast, the powder's open, high-surface-area structure allowed olefins to readsorb and continue chain propagation, yielding a higher probability of long-chain formation (high C_{7+} selectivity). This aligns with general Fischer-Tropsch behavior where enhanced pore diffusion can shift the Anderson Schulz Flory chain-growth probability, often increasing the heavy hydrocarbon fraction [75].

Fe30 powder outperforms pellets because pelletization reduces accessible surface area and pore volume (Fig. 5.31), limiting active sites for CO_2 conversion [76,77]. The large Fe30 pellets suffer severe intraparticle diffusion resistance, so much of the catalyst interior is under-utilized [78].

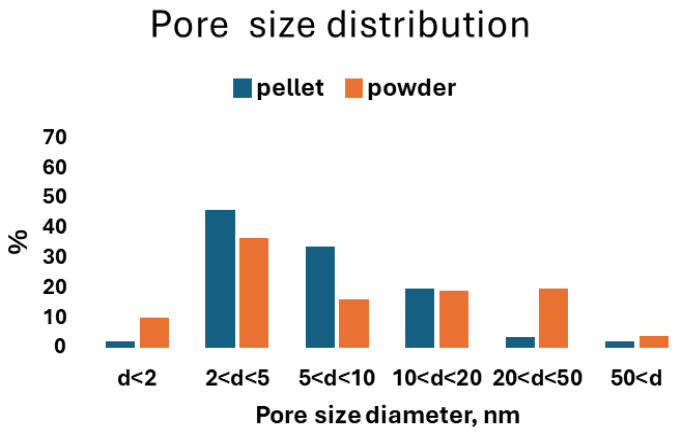

Figure 5.31. Pore size distribution among the two Fe30 used catalysts during tests in lab and bench scale plant.

Consequently, reactant gradients form inside pellets: a high H_2 concentration near the pellet exterior drives excessive methanation, while H_2-depleted cores favor the reverse water-gas shift (yielding more CO) [79]. This shifts product selectivity - pellets show higher CH_4 and CO (or CO_2 by-product) selectivity and lower heavier hydrocarbon yields compared to powder catalysts [80]. Finally, the mechanical shaping can redistribute or leach promoters like K, diminishing its CH_4-suppressing, olefin-promoting effect. Indeed, literature shows that without K, CO_2 conversion plummets while CH_4 and CO selectivities surge [81]. Hence the Fe30 powder, with greater porosity, minimal diffusion limitations, and intact promoter function, achieves higher CO_2 conversion and C_{2+} hydrocarbon yield than its pellet form.

5.3. Conclusion

In this work, a comprehensive investigation of CO_2 hydrogenation catalysis was undertaken, encompassing catalyst synthesis, detailed characterization, performance evaluation at laboratory and bench scales, kinetic analysis, and macro-level machine learning assessment of the process. The primary goal was to develop an efficient catalyst for converting CO_2 into valuable products and to understand its behavior across scales, while employing data-driven tools to interpret and optimize performance. Through this multifaceted approach, several key findings and contributions have emerged, reflecting advancements in both fundamental understanding and practical application.

Novel iron-based catalysts, both metallosilicate supported and hydrotalcites, were successfully synthesized to facilitate CO/CO_2 hydrogenation. Regarding the hydrotalcitic ones, the chosen synthesis method yielded catalysts with enhanced structural and surface properties. Extensive characterization confirmed that the catalyst possessed the desired active phases and morphology. X-ray diffraction revealed the formation of iron carbide phases known active sites for CO_2 conversion while electron microscopy showed a high dispersion of the iron-based active component on the support. These features imply a high density of accessible active sites and strong metal-support interactions, which are directly linked to the catalyst's outstanding activity. Indeed, the tailored structural properties stemming from the synthesis are crucial, as they promote efficient CO_2 adsorption and activation, laying the groundwork for superior catalytic performance.

Performance testing in a laboratory-scale reactor demonstrated the catalyst's excellent efficacy for CO/CO_2 hydrogenation. Under optimized conditions, the catalyst achieved high CO/CO_2 conversion with a favorable selectivity toward the desired products and minimal formation of side-products. It also maintained stable activity over prolonged operation, indicating robust durability of the catalyst under reaction conditions. This superior lab-scale performance confirms that the rational design and synthesis of the catalyst translated into tangible improvements in reaction outcomes. The findings at this scale provided a strong proof-of-concept that the new catalyst can drive the hydrogenation reactions efficiently towards the target products, validating the approach of enhancing active site availability and stability.

Importantly, when the process was scaled up to a bench-scale plant, the catalyst's performance remained high and consistent. The CO_2 conversion and product distribution observed in the bench-scale reactor closely mirrored the laboratory results, demonstrating that the intrinsic catalytic activity was retained in a larger-scale system. This outcome is significant because it confirms the scalability of both the catalyst and the process conditions. Any minor deviations observed at the bench scale for instance, slight temperature gradients or mass transfer limitations due to the larger reactor volume did not significantly impede overall performance. Such issues were mitigated through appropriate reactor design and operating adjustments (e.g. enhanced heat removal and improved flow distribution), ensuring the process remained efficient at scale. Overall, the bench-scale trials validated that the developed catalyst and the optimized operating conditions can be practically applied beyond the lab, effectively bridging the gap toward industrial implementation of CO_2 hydrogenation.

Detailed kinetic analysis of the CO_2 hydrogenation reaction provided fundamental insight into the reaction mechanism on the developed catalyst. The reaction rate behavior was well described by an appropriate kinetic model, and key kinetic parameters were determined. The apparent activation energy for CO_2 conversion was found to be in a moderate range, consistent with surface reaction-limited kinetics rather than diffusion limitation. Furthermore, the reaction orders with respect to CO_2 and H_2 were quantified, indicating how changes in reactant concentrations influence the rate. These kinetic parameters were remarkably consistent between the lab-scale and bench-scale experiments, suggesting that the performance was governed by intrinsic reaction kinetics under the conditions studied. This consistency underscores that external mass transfer or heat transfer limitations were negligible, meaning the kinetic data truly reflect the catalyst's activity. The validated kinetic model, supported by data across scales, provides a valuable tool for reactor design and scale-up, as it can reliably predict reactor behavior under various conditions. In essence, the kinetic study not only reinforces the mechanistic understanding of CO_2 hydrogenation on this catalyst but also gives confidence that the catalyst will behave predictably as the process scales further.

Reference Chapter 5

[1] Chou W, Wu P, Luo M, Li W, Li S. Effects of Al, Si, Ti, Zr Promoters on Catalytic Performance of Iron-Based Fischer–Tropsch Synthesis Catalysts. Catal Lett 2020;150:1993–2002. https://doi.org/10.1007/s10562-020-03104-3.

[2] Mendoza Mesa JA, Robijns S, Khan IA, Rigamonti MG, Bols ML, Dusselier M. Support effects in vanadium incipient wetness impregnation for oxidative and non-oxidative propane dehydrogenation catalysis. Catalysis Today 2024;430:114546. https://doi.org/10.1016/j.cattod.2024.114546.

[3] Eran TN, Galli F, Mazzoni F, Longhi M, Grainca A, Patience G, et al. Metallosilicates as an iron support to catalyze Fischer-Tropsch synthesis. Catalysis Today 2022;404:132–41. https://doi.org/10.1016/j.cattod.2022.04.008.

[4] Zhang H, Ma H, Zhang H, Ying W, Fang D. Effects of Zr and K Promoters on Precipitated Iron-Based Catalysts for Fischer–Tropsch Synthesis. Catal Lett 2012;142:131–7. https://doi.org/10.1007/s10562-011-0739-3.

[5] Reina TR, Ivanova S, Centeno MA, Odriozola JA. Boosting the activity of a $Au/CeO_2/Al_2O_3$ catalyst for the WGS reaction. Catalysis Today 2015;253:149–54. https://doi.org/10.1016/j.cattod.2015.01.041.

[6] Huang Y, Ma H, Xu Z, Qian W, Zhang H, Ying W. Direct Conversion of Syngas to Light Olefins over a $ZnCrO_x$ + H-SSZ-13 Bifunctional Catalyst. ACS Omega 2021;6:10953–62. https://doi.org/10.1021/acsomega.1c00751.

[7] Keunecke A, Dossow M, Dieterich V, Spliethoff H, Fendt S. Insights into Fischer–Tropsch catalysis: current perspectives, mechanisms, and emerging trends in energy research. Front Energy Res 2024;12:1344179. https://doi.org/10.3389/fenrg.2024.1344179.

[8] Cano LA, Garcia Blanco AA, Lener G, Marchetti SG, Sapag K. Effect of the support and promoters in Fischer-Tropsch synthesis using supported Fe catalysts. Catalysis Today 2017;282:204–13. https://doi.org/10.1016/j.cattod.2016.06.054.

[9] Wan H, Wu B, Zhang C, Xiang H, Li Y. Promotional effects of Cu and K on precipitated iron-based catalysts for Fischer–Tropsch synthesis. Journal of Molecular Catalysis A: Chemical 2008;283:33–42. https://doi.org/10.1016/j.molcata.2007.12.013.

[10] Li S, Li A, Krishnamoorthy S, Iglesia E. Effects of Zn, Cu, and K promoters on the structure and on the reduction, carburization, and catalytic behavior of iron-based Fischer–Tropsch synthesis catalysts n.d.

[11] Chang H, Lin Q, Cheng M, Zhang K, Feng B, Chai J, et al. Effects of Potassium Loading over Iron–Silica Interaction, Phase Evolution and Catalytic Behavior of Precipitated Iron-Based Catalysts for Fischer-Tropsch Synthesis. Catalysts 2022;12:916. https://doi.org/10.3390/catal12080916.

[12] Trépanier M, Tavasoli A, Dalai AK, Abatzoglou N. Co, Ru and K loadings effects on the activity and selectivity of carbon nanotubes supported cobalt catalyst in Fischer–Tropsch synthesis. Applied Catalysis A: General 2009;353:193–202. https://doi.org/10.1016/j.apcata.2008.10.061.

[13] Kamath G, Badoga S, Dalai AK. Synthesis and Application of Metallosilicate Supports for Cobalt-Based Fischer–Tropsch Synthesis Catalysts. Energy Fuels 2019;33:551–60. https://doi.org/10.1021/acs.energyfuels.8b03209.

[14] Lu J, Lei Y, Wan G, Mei Z, Yu J, Zhao Y, et al. Weakening the metal-support strong interaction to enhance catalytic performances of alumina supported Ni-based catalysts for producing hydrogen. Applied Catalysis B: Environmental 2020;263:118177. https://doi.org/10.1016/j.apcatb.2019.118177.

[15] Said S, Mikhail S, Riad M. Recent processes for the production of alumina nano-particles. Materials Science for Energy Technologies 2020;3:344–63. https://doi.org/10.1016/j.mset.2020.02.001.

[16] Ahmad Zamri MFM, Hassan SHA, Tiong SK, Milano J, Bahru R, Fattah IMR, et al. Progress and challenges of mesoporous catalysts in upgraded pyrolysis of biomass for biofuel production. Journal of Analytical and Applied Pyrolysis 2024;182:106651. https://doi.org/10.1016/j.jaap.2024.106651.

[17] Eran TN, Galli F, Guyot J, Lefebvre J, Grainca A, Patience G, et al. Copper, potassium promoted iron on metallosilicate and aluminum oxide supports synthesized via a non-hydrolytic sol-gel for Fischer-Tropsch. Catalysis Today 2024;433:114655. https://doi.org/10.1016/j.cattod.2024.114655.

[18] First Annual Topical Report: Sensitivity of Fischer-Tropsch synthesis and water-gas shift catalysts to poisons from high-temperature high-pressure entrained-flow (EF) oxygen-blown gasifier gasification of coal/biomass mixtures n.d.

[19] Shafer W, Gnanamani M, Graham U, Yang J, Masuku C, Jacobs G, et al. Fischer–Tropsch: Product Selectivity–The Fingerprint of Synthetic Fuels. Catalysts 2019;9:259. https://doi.org/10.3390/catal9030259.

[20] Ozbek MO, Niemantsverdriet JW (Hans). Elementary reactions of CO and H_2 on C-terminated χ-Fe_5C_2(0 0 1) surfaces. Journal of Catalysis 2014;317:158–66. https://doi.org/10.1016/j.jcat.2014.06.009.

[21] Herzog K. Kinetic studies for elucidation of the promoter effect of alkali in Fischer-Tropsch iron catalysts. Journal of Catalysis 1989;115:337–46. https://doi.org/10.1016/0021-9517(89)90038-9.

[22] Bukur DB, Mukesh D, Patel SA. Promoter effects on precipitated iron catalysts for Fischer-Tropsch synthesis. Ind Eng Chem Res 1990;29:194–204. https://doi.org/10.1021/ie00098a008.

[23] Jacobs G, Ji Y, Davis BH, Cronauer D, Kropf AJ, Marshall CL. Fischer–Tropsch synthesis: Temperature programmed EXAFS/XANES investigation of the influence of support type, cobalt loading, and noble metal promoter addition to the reduction behavior of cobalt oxide particles. Applied Catalysis A: General 2007;333:177–91. https://doi.org/10.1016/j.apcata.2007.07.027.

[24] An X, Wu B, Wan H-J, Li T-Z, Tao Z-C, Xiang H-W, et al. Comparative study of iron-based Fischer–Tropsch synthesis catalyst promoted with potassium or sodium. Catalysis Communications 2007;8:1957–62. https://doi.org/10.1016/j.catcom.2007.03.016.

[25] Rao Pendyala VR, Jacobs G, Mohandas JC, Luo M, Ma W, Gnanamani MK, et al. Fischer–Tropsch synthesis: Attempt to tune FTS and WGS by alkali promoting of iron

catalysts. Applied Catalysis A: General 2010;389:131–9. https://doi.org/10.1016/j.apcata.2010.09.018.

[26] Wang Y, Li H-X, Li X-G, Chen D, Xiao W-D. Effective Iron Catalysts Supported on Mixed MgO–Al_2 O_3 for Fischer–Tropsch Synthesis to Olefins. Ind Eng Chem Res 2020;59:11462–74. https://doi.org/10.1021/acs.iecr.0c01603.

[27] Grainca A, Boccalon E, Nocchetti M, Vivani R, Di Michele A, Longhi M, et al. Sonochemical and mechanochemical synthesis of iron-based nano-hydrotalcites promoted with Cu and K as catalysts for CO and CO_2 Fischer-Tropsch synthesis. Fuel 2024;373:132303. https://doi.org/10.1016/j.fuel.2024.132303.

[28] Wang Y-N, Ma W-P, Lu Y-J, Yang J, Xu Y-Y, Xiang H-W, et al. Kinetics modelling of Fischer –Tropsch synthesis over an industrial Fe – Cu – K catalystq n.d.

[29] Gao Y, Liu S, Zhao Z, Tao H, Sun Z, 100029, State Key Laboratory of Organic-Inorganic Composites, Beijing University of Chemical Technology, Beijing 100029, P. R. China. Heterogeneous Catalysis of CO_2 Hydrogenation to C_{2+} Products. Acta Physico-Chimica Sinica 2018;34:858–72. https://doi.org/10.3866/PKU.WHXB201802061.

[30] Guo Y, Jia L, Zhang Z, Gong M, Dang S, Huang Y, et al. Revealing the mechanism of Ce promoter in modulating product distribution of CO_2 hydrogenation over Fe-based catalysts. Chemical Engineering Journal 2024;491:151964. https://doi.org/10.1016/j.cej.2024.151964.

[31] Zhang H, Ma H, Zhang H, Ying W, Fang D. Effect of incorporation manner of Zr promoter on precipitated iron-based catalysts for Fischer-Tropsch synthesis. J Coal Sci Eng China 2012;18:182–7. https://doi.org/10.1007/s12404-012-0213-x.

[32] Meng W, Jong BCAD, Bovenkamp HVD, Boer G-J, Leendert Bezemer G, Iulian Dugulan A, et al. Selectivity control between reverse water-gas shift and fischer-tropsch synthesis in carbon-supported iron-based catalysts for CO_2 hydrogenation. Chemical Engineering Journal 2024; 489:151166. https://doi.org/10.1016/j.cej.2024.151166.

[33] Wang Q, Hu K, Gao R, Zhang L, Wang L, Zhang C. Hydrogenation of Carbon Dioxide to Value-Added Liquid Fuels and Aromatics over Fe-Based Catalysts Based on the Fischer–Tropsch Synthesis Route. Atmosphere 2022; 13:1238. https://doi.org/10.3390/atmos13081238.

[34] Han Z, Qian W, Zhang H, Ma H, Sun Q, Ying W. Effect of Rare-Earth Promoters on Precipitated Iron-Based Catalysts for Fischer–Tropsch Synthesis. Ind Eng Chem Res 2020; 59:14598–605. https://doi.org/10.1021/acs.iecr.9b06760.

[35] He L, BotaoTeng, Zhang Y, Fan M. Development of composited rare-earth promoted cobalt-based Fischer–Tropsch synthesis catalysts with high activity and selectivity. Applied Catalysis A: General 2015; 505:276–83. https://doi.org/10.1016/j.apcata.2015.07.041.

[36] Teimouri Z, Abatzoglou N, Dalai AK. Kinetics and Selectivity Study of Fischer–Tropsch Synthesis to C_{5+} Hydrocarbons: A Review. Catalysts 2021; 11:330. https://doi.org/10.3390/catal11030330.

[37] Amin M, Usman M, Kella T, Khan WU, Khan IA, Hoon Lee K. Issues and challenges of Fischer–Tropsch synthesis catalysts. Front Chem 2024; 12:1462503. https://doi.org/10.3389/fchem.2024.1462503.

[38] Vogt ETC, Fu D, Weckhuysen BM. Carbon Deposit Analysis in Catalyst Deactivation, Regeneration, and Rejuvenation. Angew Chem Int Ed 2023;62: e202300319. https://doi.org/10.1002/anie.202300319.

[39] Ruiz E, Villuendas M, Morales Á, Farchado M, Sánchez JM. Catalytic CO_2 hydrogenation to hydrocarbon fuels in a potassium ion-conducting reactor. Catalysis Today 2024; 437:114777. https://doi.org/10.1016/j.cattod.2024.114777.

[40] Kosinov N, Liu C, Hensen EJM, Pidko EA. Engineering of Transition Metal Catalysts Confined in Zeolites. Chem Mater 2018; 30:3177–98. https://doi.org/10.1021/acs.chemmater.8b01311.

[41] Zhang Z, Huang G, Tang X, Yin H, Kang J, Zhang Q, et al. Zn and Na promoted Fe catalysts for sustainable production of high-valued olefins by CO_2 hydrogenation. Fuel 2022; 309:122105. https://doi.org/10.1016/j.fuel.2021.122105.

[42] Liu J, Zhang Y, Peng C. Recent Advances Hydrogenation of Carbon Dioxide to Light Olefins over Iron-Based Catalysts via the Fischer–Tropsch Synthesis. ACS Omega 2024; 9:25610–24. https://doi.org/10.1021/acsomega.4c03075.

[43] Evdokimenko ND, Kapustin GI, Tkachenko OP, Kalmykov KB, Kustov AL. Zn Doping Effect on the Performance of Fe-Based Catalysts for the Hydrogenation of CO_2 to Light Hydrocarbons. Molecules 2022; 27:1065. https://doi.org/10.3390/molecules27031065.

[44] Ren H, Yang H, Xin J, Wu C, Wang H, Zhang J, et al. Direct carbon dioxide hydrogenation to long-chain α-olefins over FeMnK catalysts. Applied Catalysis B: Environment and Energy 2024; 358:124440. https://doi.org/10.1016/j.apcatb.2024.124440.

[45] Ma W, Jacobs G, Sparks DE, Todic B, Bukur DB, Davis BH. Quantitative comparison of iron and cobalt based catalysts for the Fischer-Tropsch synthesis under clean and poisoning conditions. Catalysis Today 2020; 343:125–36. https://doi.org/10.1016/j.cattod.2019.04.011.

[46] Chen Z, Du J, Chen D, Gong F, Gao Y, Huang Z, et al. Revisiting the Impact of CO_2 on the Activity and Selectivity of Cobalt-Based Catalysts for Fischer–Tropsch Synthesis Under Industrial-Relevant Conditions. Catalysts 2025; 15:329. https://doi.org/10.3390/catal15040329.

[47] Wang P, Chiang F-K, Chai J, Dugulan AI, Dong J, Chen W, et al. Efficient conversion of syngas to linear α-olefins by phase-pure χ-Fe_5C_2. Nature 2024; 635:102–7. https://doi.org/10.1038/s41586-024-08078-5.

[48] Lykaki M, Mandela E, Varvoutis G, Lampropoulos A, Marnellos GE, Konsolakis M. State-of-the-art thermocatalytic systems for CH_4 and CO production via CO_2 hydrogenation: critical comparison, mechanistic considerations and structure-performance insights. Discov Chem Eng 2024; 4:11. https://doi.org/10.1007/s43938-024-00048-7.

[49] Fan WK, Tahir M. Recent developments in photothermal reactors with understanding on the role of light/heat for CO_2 hydrogenation to fuels: A review. Chemical Engineering Journal 2022; 427:131617. https://doi.org/10.1016/j.cej.2021.131617.

[50] Tommasi M, Degerli SN, Ramis G, Rossetti I. Advancements in CO_2 methanation: A comprehensive review of catalysis, reactor design and process optimization. Chemical

Engineering Research and Design 2024; 201:457–82. https://doi.org/10.1016/j.cherd.2023.11.060.

[51] Baraj E, Vagaský S, Hlinčik T, Ciahotný K, Tekáč V. Reaction mechanisms of carbon dioxide methanation. Chemical Papers 2016;70. https://doi.org/10.1515/chempap-2015-0216.

[52] Liu X, Xu M, Cao C, Yang Z, Xu J. Effects of zinc on χ-Fe_5C_2 for carbon dioxide hydrogenation to olefins: Insights from experimental and density function theory calculations. Chinese Journal of Chemical Engineering 2023; 54:206–14. https://doi.org/10.1016/j.cjche.2022.03.027.

[53] Liu J, Zhang Y, Peng C. Recent Advances Hydrogenation of Carbon Dioxide to Light Olefins over Iron-Based Catalysts via the Fischer–Tropsch Synthesis. ACS Omega 2024;9:25610–24. https://doi.org/10.1021/acsomega.4c03075.

[54] Krausser L, Yang Q, Kondratenko EV. CO_2 Hydrogenation to Hydrocarbons over Fe-Based Catalysts: Status and Recent Developments. ChemCatChem 2024;16: e202301716. https://doi.org/10.1002/cctc.202301716.

[55] Yarbaş T, Ayas N. A detailed thermodynamic analysis of CO_2 hydrogenation to produce methane at low pressure. International Journal of Hydrogen Energy 2024; 49:1134–44. https://doi.org/10.1016/j.ijhydene.2023.06.223.

[56] Weatherbee G, Bartholomew C. Hydrogenation of CO_2 on Group VIII Metals. Journal of Catalysis 77, 460-472; 1982.

[57] Ye R-P, Ding J, Gong W, Argyle MD, Zhong Q, Wang Y, et al. CO_2 hydrogenation to high-value products via heterogeneous catalysis. Nat Commun 2019;10:5698. https://doi.org/10.1038/s41467-019-13638-9.

[58] Ababneh H, Hameed BH. Electrofuels as emerging new green alternative fuel: A review of recent literature. Energy Conversion and Management 2022;254:115213. https://doi.org/10.1016/j.enconman.2022.115213.

[59] Orege JI, Wei J, Ge Q, Sun J. Spinel-structured nanocatalysts: New opportunities for CO_2 hydrogenation to value-added chemicals. Nano Today 2023;51:101914. https://doi.org/10.1016/j.nantod.2023.101914.

[60] Wang C, Zhang J, Gao X, Ma Q, Fan S, Zhao T-S. CO_2 hydrogenation to linear α-olefins on FeCx/ZnO catalysts: Effects of surface oxygen vacancies. Applied Surface Science 2023;641:158543. https://doi.org/10.1016/j.apsusc.2023.158543.

[61] Liang J, Liu J, Guo L, Wang W, Wang C, Gao W, et al. CO_2 hydrogenation over Fe-Co bimetallic catalysts with tunable selectivity through a graphene fencing approach. Nat Commun 2024;15:512. https://doi.org/10.1038/s41467-024-44763-9.

[62] Jia J-Y, Shan Y-L, Tuo Y-X, Yan H, Feng X, Chen D. Review of Iron-Based Catalysts for Carbon Dioxide Fischer–Tropsch Synthesis. Trans Tianjin Univ 2024;30:178–97. https://doi.org/10.1007/s12209-024-00392-3.

[63] Wang W, Toshcheva E, Ramirez A, Shterk G, Ahmad R, Caglayan M, et al. Bimetallic Fe–Co catalysts for the one step selective hydrogenation of CO_2 to liquid hydrocarbons. Catal Sci Technol 2023;13:1527–40. https://doi.org/10.1039/D2CY01880B.

[64] Todic B, Nowicki L, Nikacevic N, Bukur DB. Fischer–Tropsch synthesis product selectivity over an industrial iron-based catalyst: Effect of process conditions. Catalysis Today 2016;261:28–39. https://doi.org/10.1016/j.cattod.2015.09.005.

[65] Gorimbo J, Muleja A, Liu X, Hildebrandt D. Fischer–Tropsch synthesis: product distribution, operating conditions, iron catalyst deactivation and catalyst speciation. Int J Ind Chem 2018;9:317–33. https://doi.org/10.1007/s40090-018-0161-4.

[66] Mahmoudi H, Mahmoudi M, Doustdar O, Jahangiri H, Tsolakis A, Gu S, et al. A review of Fischer Tropsch synthesis process, mechanism, surface chemistry and catalyst formulation. Biofuels Engineering 2017;2:11–31. https://doi.org/10.1515/bfuel-2017-0002.

[67] Karakaya C, Parks J. Thermochemical processes for CO_2 hydrogenation to fuels and chemicals: Challenges and opportunities. Applications in Energy and Combustion Science 2023;15:100171. https://doi.org/10.1016/j.jaecs.2023.100171.

[68] Evdokimenko ND, Kapustin GI, Tkachenko OP, Kalmykov KB, Kustov AL. Zn Doping Effect on the Performance of Fe-Based Catalysts for the Hydrogenation of CO_2 to Light Hydrocarbons. Molecules 2022;27:1065. https://doi.org/10.3390/molecules27031065.

[69] Sie ST. Intraparticle diffusion and reaction kinetics as factors in catalyst particle design. The Chemical Engineering Journal and the Biochemical Engineering Journal 1993;53:1–11. https://doi.org/10.1016/0923-0467(93)80002-E.

[70] Brunner KM, Perez HD, Peguin RPS, Duncan JC, Harrison LD, Bartholomew CH, et al. Effects of Particle Size and Shape on the Performance of a Trickle Fixed-Bed Recycle Reactor for Fischer–Tropsch Synthesis. Ind Eng Chem Res 2015;54:2902–9. https://doi.org/10.1021/ie503174v.

[71] Ding, M., Liu, X., Ma, P., & Yao, J. (2022). Porous materials for capture and catalytic conversion of CO_2 at low concentration. Coordination Chemistry Reviews, 465, 214576.

[72] Schumacher J, Meyer D, Friedland J, Güttel R. 1 Methanation of CO/CO_2 mixtures: Evaluation of pellet size 2 effect on methane formation rate and reactant selectivity n.d.

[73] Yang Lim J, McGregor J, Sederman AJ, Dennis JS. Kinetic studies of CO_2 methanation over a Ni/γ-Al_2O_3 catalyst using a batch reactor. Chemical Engineering Science 2016;141:28–45. https://doi.org/10.1016/j.ces.2015.10.026.

[74] Bradley M, Ananth R, Willauer H, Baldwin J, Hardy D, Williams F. The Effect of Copper Addition on the Activity and Stability of Iron-Based CO_2 Hydrogenation Catalysts. Molecules 2017;22:1579. https://doi.org/10.3390/molecules22091579.

[75] Yang JH, Kim H-J, Chun DH, Lee H-T, Hong J-C, Jung H, et al. Mass transfer limitations on fixed-bed reactor for Fischer–Tropsch synthesis. Fuel Processing Technology 2010;91:285–9. https://doi.org/10.1016/j.fuproc.2009.10.010.

[76] Vajglová Z, Kumar N, Mäki-Arvela P, Eränen K, Peurla M, Hupa L, et al. Effect of Binders on the Physicochemical and Catalytic Properties of Extrudate-Shaped Beta Zeolite Catalysts for Cyclization of Citronellal. Org Process Res Dev 2019;23:2456–63. https://doi.org/10.1021/acs.oprd.9b00346.

[77] Yeskendir B, Dacquin J-P, Lorgouilloux Y, Courtois C, Royer S, Dhainaut J. From metal–organic framework powders to shaped solids: recent developments and challenges. Mater Adv 2021;2:7139–86. https://doi.org/10.1039/D1MA00630D.

[78] Hubble R, York APE, Dennis JS. Modelling reaction and diffusion in a wax-filled hollow cylindrical pellet of Fischer Tropsch catalyst. Chemical Engineering Science 2019;207:958–69. https://doi.org/10.1016/j.ces.2019.06.051.

[79] Zamaniyan A, Mortazavi Y, Khodadadi AA, Pour AN. Effect of mass transfer limitations on catalyst performance during reduction and carburization of iron based Fischer-Tropsch synthesis catalysts. Journal of Energy Chemistry 2013;22:795–803. https://doi.org/10.1016/S2095-4956(13)60106-0.

[80] Mhinga M. Comparing the performance of different catalyst packing for Fischer-Tropsch synthesis. Department of Chemical Engineering, University of Cape Town 2019.

[81] Bradley M, Ananth R, Willauer H, Baldwin J, Hardy D, Williams F. The Effect of Copper Addition on the Activity and Stability of Iron-Based CO_2 Hydrogenation Catalysts. Molecules 2017;22:1579. https://doi.org/10.3390/molecules22091579.

6. SAFETY AND OPERABILITY FRAMEWORKS

The lack of a well-developed safety culture is the leading cause of accidents in academic laboratories during research and development activities. Differently from the industrial framework, research laboratories are characterized by various additional vulnerabilities, including variable operating conditions and equipment setup, high impact of human error, and improper training and determination of emerging risk scenarios. This has determined a high-frequency environment for near misses, incidents and accidents, also resulting in severe outcomes. Although a portfolio of dedicated risk assessment techniques is available, a generalized underestimation of hazards and risks emerges. A risk assessment should identify potential hazards and implement controls to eliminate or reduce risks to people, operations or property. Moreover, a new risk assessment should be completed and documented each time a new potentially hazardous experiment is planned. This aspect is often overlooked, leading to risk misperception or inadequate risk-reduction measures. Consequently, experiment participants can face associated tasks with imperfect operating procedures or without available or up-to-date documentation. Current statistics show that academic laboratories share the majority of accidents. This poses a serious concern that urges robust, extensive and comprehensive actions. Unfortunately, research hazard analysis and risk assessment is more complex than in industrial settings.

This work conducts a risk assessment for a Fischer-Tropsch pilot plant in an academic lab. Various techniques, including interaction matrix and HAZOP analysis, identify material incompatibility and potential hazards. Results are analyzed by risk class, and a Layer of Protection Analysis (LOPA) is done to define protective measures for high-risk events.

6.1. Hazard evaluation procedures

A complete hazard evaluation is the critical aspect of a successful risk assessment, but it has many limitations, such as completeness, reproducibility, inscrutability, relevance of experience and subjectivity [1]. It means that the experience of the analyst influences the risk assessment, so it is not objective and may be incomplete or difficult to understand. The risk assessment depends on the objective of the process under consideration and its lifetime. For pilot plants, the objective is usually to investigate toxic waste management and to increase the knowledge of a specific reactive system (e.g., catalyst deactivation and behavior of the reactions involved) [1]. The pilot plants have peculiar features, including prominent manual operations, variable operating conditions, and issues due to documenting and addressing hazards, risks, and procedures.

To address a risk assessment study, different methodologies can be applied, such as:

- Interaction matrix;
- Checklist analysis;
- What-if analysis;
- FMEA (Failure Modes and Effects Analysis);
- HAZOP (Hazard and Operability Analysis);
- LOPA (Layer of Protection Analysis);

- Event tree analysis;
- Fault tree analysis.

While the tree-based techniques are quantitative, the other strategies above are qualitative and used to identify proper scenarios. Typically, more than one of these techniques provide a robust and exhaustive hazard and risk assessment, including hazard identification methods and hazard assessment techniques based or non-based on scenarios [1].

6.2. Interaction matrix

The interaction matrix is a hazard identification method that analyzes the interaction between different chemicals, materials and operating conditions. The interaction matrix is a 2D matrix where one axis consists of all chemicals, utilities and intermediates involved in the process. In the other axes, all the previously listed chemicals must be indicated, and, in addition, normal and abnormal operating conditions that could lead to a hazardous scenario must be analyzed [1].

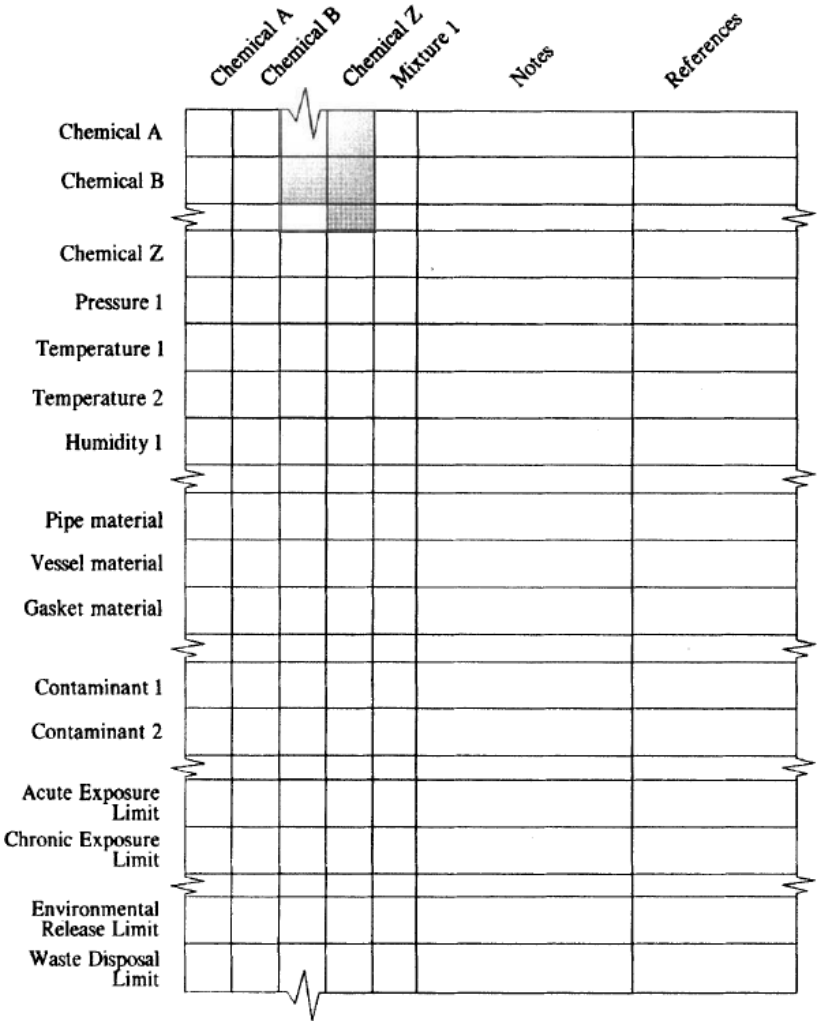

Figure 6.1. Example of the structure of an interaction matrix [1].

There are three main methods for determining whether or not the various interactions are compatible: personal knowledge, literature, and appropriate tools [2]. If incompatibilities are observed, the analyst should determine the better way to avoid or minimize them to work under safe conditions [1]. It is possible that the interaction between two chemicals or a chemical and an operating condition may not be reported in the literature. This could occur if the interaction is safe

or if this combination has never been studied. The analyst's knowledge is crucial to recognize which of these two cases is being considered. If the interaction studied between two chemicals or between a chemical and an operating condition can be called new, a compatibility analysis should be performed, this only if it can be done safely; if this is not possible, the interaction should be avoided. If the interaction under study is between a chemical and a building material, the equipment manufacturer should be consulted.

Peculiar to pilot plants and research and development experimental apparatus is that molecules, materials and operating conditions can change in relation to different experimental campaigns performed. Moreover, variable boundary conditions can lead to new risk scenarios, especially when performing transient operations or modifying the experimental apparatus for research purposes.

6.3. Hazard and Operability Analysis (HAZOP)

The HAZOP analysis is one of the most commonly used techniques to analyze the chemical process and the possible hazards in a systematic way [3]. The main objective of the hazard and operability analysis is to define the risks associated with a specific operation and maintenance of the equipment [4]. In addition, the sources of deviation from the design intent are identified through HAZOP analysis. This technique can also be used to assess written procedures [1].

The HAZOP is usually applied during the review step [3]. Therefore, detailed plant information is necessary to obtain a complete risk assessment of the process. In addition to the process schematic in the form of a P&ID, the manuals for the equipment involved and the logic solvers for the controllers and programs used to manage the process should be provided [1]. The HAZOP study should be reviewed periodically to determine if the analysis needs to be updated with new comments. The analysis must also be reviewed when part of the process is changed to analyze whether new hazards can be observed or an initiating event can no longer occur [4].

6.3.1. Roles during the HAZOP

The HAZOP analysis is performed by a multidisciplinary team [1]. This analysis is usually initiated by a HAZOP leader responsible for governing the HAZOP. The study leader is responsible for many aspects of the study, such as the definition of the study team, the timing of the analysis, communication between the HAZOP team and the manager, and the proper application of the technique [4].

- The study leader should identify different roles. In addition to the study leader, the list of possible roles in a team study is as follows:
- Specialists with extensive knowledge of the system. This role has limited participation.
- A designer who knows the design and process representation. Someone who can explain how the node and its systems should behave if a deviation occurs.
- A recorder (the study leader can cover this role). The recorder helps the study director to schedule meetings and manage administrative tasks.
- The user with knowledge of the operating conditions and consequences of a deviation from the design intent.
- Maintainer: someone responsible for the maintenance of the process equipment.

In addition to these roles, other people may be present during the meetings, such as stakeholders and suppliers [4].

6.3.2. Performing the HAZOP analysis

The HAZOP study can be divided into three steps: collecting all the necessary information for the review, performing the analysis, and documenting the results [1]. The study leader usually takes the first step [4] (Figure 6.2).

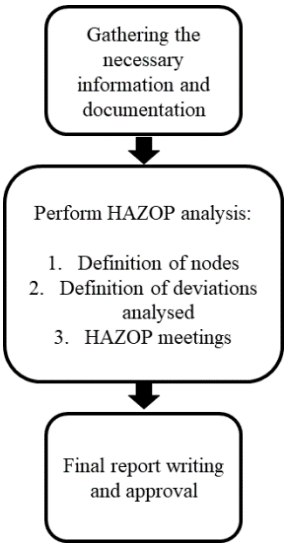

Figure 6.2. HAZOP procedure.

The third step is also carried out by the study leader with the help of the recorder. The time required to carry out all these steps depends on the complexity of the plant being studied. Small processes may require within 4-12 days to carry out both steps two and three, the first step usually requiring less than 12 hours. On the other hand, complex processes may require more than 12 weeks, as each step requires 2-4 days, 2-6 weeks and 2-6 weeks respectively [1].

A HAZOP analysis is based on the definition of all the deviations from the ideal behavior of the plant (also defined as design intent), where a deviation is composed of a guideword and a parameter (Table 6.1) [3].

Guideword	Parameter	Deviation
No	Flow	No Flow
Less	pressure	Less pressure
More	Temperature	More temperature
Reverse	Flow	Reverse flow
Before/After	Mixing	Before/After mixing

Table 6.1. Example of guidewords, parameters and resulting deviations.

The first step of the HAZOP analysis is to divide the process into different nodes. A node is a plant section comprising one or more streams and equipment. Each node is analyzed chronologically [3]. In a node, an operation on a stream or substance is performed. The analysis report is written, where all considerations about possible risk scenarios and their management

must be discussed and recorded. The first step of the technique is the definition of the required guidewords, supervised by the study leader [4]. The HAZOP analysis is then performed.

Each node is analyzed, and the deviations are reported in a worksheet. This worksheet is not unique to all processes, but some common points are usually observed. The worksheet header usually consists of the following elements: title of study, sheet number, date of study, team members, section of plant/node, description of design intent and page number [4]. The table of the worksheet can be composed of the following minimum elements:

- Deviation number;
- Guide word;
- Parameter;
- Material involved;
- Deviation;
- Deviation causes;
- Deviation consequences;
- Presence of specific controls
- Comments;
- Safeguards.

In addition, some other information can be described, such as who defines the specific deviation [4] and the likelihood and severity of the specific deviation.

STUDY TITLE: PROCESS EXAMPLE								**SHEET:** 1 of 4	
Drawing No.:	**REV. No.:**							**DATE:** December 17, 1998	
TEAM COMPOSITION:	LB, DH, EK, NE, MG, JK							**MEETING DATE:** December 15, 1998	
PART CONSIDERED:	**Transfer line from supply tank A to reactor**								
DESIGN INTENT:	**Material:** A **Activity:** Transfer continuously at a rate greater than B **Source:** Tank for A **Destination:** Reactor								
No.	**Guide word**	**Element**	**Deviation**	**Possible causes**	**Consequences**	**Existing controls**	**Comments**	**Actions required**	**Action allocated to**
1	NO	Material A	No material A	Supply tank A is empty	No flow of A into reactor Explosion	None shown	Situation not acceptable	Consider installation on tank A of a low-level alarm plus a low-level trip to stop pump B	MG
2	NO	Transfer A (at a rate > B)	No transfer of A takes place	Pump A stopped, line blocked	Explosion	None shown	Situation not acceptable	Measurement of flow rate for material A plus a low flow alarm and a low flow which trips pump B	JK
3	MORE	Material A	More material A: supply tank over full	Filling of tank from tanker when insufficient capacity exists	Tank will overflow into bounded area	None shown	Remark: This would have been identified during examination of the tank	Consider high-level alarm if not previously identified	EK
4	MORE	Transfer A	More transfer of A Increased flow rate of A	Wrong size impeller Wrong pump fitted	Possible reduction in yield Product will contain large excess A	None		Check pump flows and characteristics during commis-sioning Revise the commissioning procedure	JK

Figure 6.3. Example of a HAZOP table [4].

The study ends when all the nodes and their deviations have been analyzed and reported on the specific worksheet. Usually, all the information needed for the final report is given in the HAZOP worksheets. When the final report is written, it is reviewed by all the team members and should then be validated by them. If not all team members agree with the final report, this must be

recorded. Then, the study leader and the manager must formally approve and sign off the final documents [4].

6.3.3. HAZOP drawbacks

HAZOP technique is used to study small and large processes. The results obtained from this analysis are related to the knowledge and experience of the study leader and the HAZOP team. There is no guarantee that all deviations and hazardous scenarios will be identified and analyzed. Deviations in one node can lead to consequences in downstream sections, which can not be analyzed when the process is complex. In addition, HAZOP analysis could be limited if only graphical representations are considered. The analysis does not consider actions and operations not reported in P&ID. Finally, when the resulting deviation scenario is too dangerous, the HAZOP study is not enough and other techniques are necessary, such as fault and event tree analysis, to provide quantitive information [4]. These last techniques are graphical models. FTA indicates the frequency of a top event when a system failure occurs.

ETA indicates the frequency of possible scenarios resulting from an initiating event, taking into account the probability of failure of specific layers of protection in the system [1].

In addition, HAZOP analysis requires in-depth knowledge of the process, and this could be a disadvantage when analyzing a pilot plant as all the necessary information may not be available. Another technique should be used, such as what-if analysis or the checklist method [5].

6.4. Functional safety and Layer of Protection Analysis (LOPA)

Many hazardous scenarios can occur in a process, but not all are unacceptable. The risk class must be defined and assigned to assess whether the resulting scenario is acceptable. Risk class is related to the severity of the outcoming scenario and its likelihood [6]. These parameters are studied and managed by functional safety discipline. The main objective of functional safety is to reduce the risk of hazardous scenarios by using safety systems called SIS (Safety Instrumented Systems), which are required to perform safety instrumented functions. (SIFs) [7]. All these systems are applied to obtain a final tolerable risk since zero risk can never be obtained [6]. The concept of tolerable risk is defined by a specific standard (as IEC 61511 [6,7]). It is a function of the severity (classified as major, severe or minor) and of tolerable frequency, which is defined in terms of (undesired) events per year (Table F.8 in [8]). The international standards for functional safety are the IEC 61508 and 61511 [6,7].

The Layer of Protection Analysis (LOPA) is a quantitative method to define the SIL required for a specific initiating event [6]. The list of initiating events is typically produced in a previous hazard identification step, e.g., using a HAZOP analysis.

6.4.1. Definitions

Many different definitions must be known in order to describe functional safety. The following definitions refer to safety systems within the functional safety framework:

- SIS: it is a safety instrumented system used to execute a safety function SIF [7].
- SIL: it is a safety integrity level that can be classified from 1 to 4. The level is assigned to the SIF in order to specify the SIS integrity requirement [7]. In essence, each order of

magnitude of risk reduction that is required correlates with an increase in SIL, up to a maximum of SIL 4.

- SIF: it is a safety instrumented function performed by an SIS [7].
- IPL: it is an independent protection layer. The main objective of a protective layer is to decrease the likelihood of an undesired event. The protective layer has to be specific, auditable, independent, and reliable [9,6]. If at least one of these criteria is not met, it cannot be intended as an IPL.
- Safety interlock: it is a subclass of SISs. It consists of a SIF that protects against one or more specified harmful scenarios [6].
- BPCS: it is a basic process control system used to control and guide the response of the system. Usually, the final control element is a pneumatic, electronic or electrical system or a PES (Programmable Electronic System) [10].
- MooN (logic): it is an SIS composed of N independent detectors, with a minimum of M channels required to initiate the SIF operation [7]. This system is usually used when a redundant system is applied. It can have different configurations [6,11].
- In addition, other definitions are used to define how much the safety system is reliable and terms related to LOPA, such as:
- ALARP: it is the acronym for As Low As Reasonably Practicable, and it is useful to define when a risk is tolerable or not [6].
- PFD: it is the probability of failure on demand [6,7,10]. It is a value that indicates the reliability of the equipment used, so the probability that the safety system does not respond when the hazardous scenario occurs [11]. It can also be given as PFDavg, which is the average over the life of the SIF [6].
- MTTF: it is the mean time to failure [6]. It is a value that indicates the reliability of the equipment used.
- RRF: it is the risk reduction factor [6,11].
- UEF: unmitigated event frequency (UEL in [6]).

These definitions will be useful in understanding the LOPA analysis.

6.4.2. The procedure of LOPA

The LOPA analysis is a quantitative method to define the SIL required to obtain a final frequency equal to or less tolerable [6].

Figure 6.4 shows the conventional procedure for carrying out a LOPA analysis. An H&RA carries out the first step, usually the HAZOP analysis [8]. When an initiating event is identified, its frequency should be defined by different available data in the literature [6]. Example data can be retrieved in [9] and [12]. The IPLs present must then be identified. These protective systems must have the four characteristics listed in §6.4.1, and the PFD is usually provided in the literature or by the manufacturer [9]. Conditional modifiers (Table 5.23 in [6]) are conditions, such as the ignition of a chemical with a low flash point, that should be considered to adjust the final frequency of the scenario [6].

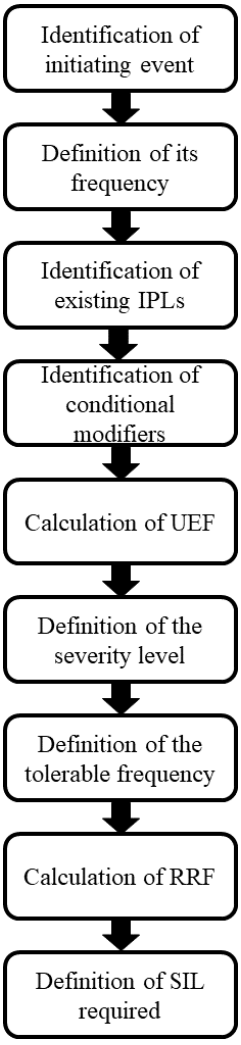

Figure 6.4. Structured procedure of LOPA (adjusted from [6]).

The UEF is defined by knowing the frequency of the initiating event. If there are IPLs, the initial frequency is multiplied by the different PFDs of the IPLs present and the final frequency is defined as the UEF. If no IPLs are present, the UEF is equal to the frequency of the initiating event. The definition of the severity class (Table C.2 in [9]) and of the tolerable frequency is crucial to obtaining the value of the desired RRF and, consequently, the required SIL according to Eq. 1 [6].

$$RRF = \frac{UEF}{Tolerable\ frequency} \tag{1}$$

Tolerable frequency is a function of the final scenario severity (Table F.8 in [8]). Different tables can be consulted [5] to define the SIL required, as reported in Table 6.2 and Table 6.3.

N. of existing PLs	**Required SIL**								
3								**1**	**1**
2			**1**		**1**	**2**	**1**	**2**	**3**
1		**1**	**2**	**1**	**2**	**3**	**3**	**3**	**3**
Hazardous event likelihood	Low	Medium	High	Low	Medium	High	Low	Medium	High
	Minor			***Serious***			***Extensive***		
Hazardous event severity rating									

Table 6.2 Allocation of the SIL as a function of likelihood and severity of a hazardous event and existing protection layers (adapted from [8]).

SIL target	Risk reduction factor (RRF)
No SIF [1]	UEF ≤ tolerable frequency
SIL 'a' [2]	RRF ≤ 10
SIL 1	10 < RRF ≤ 100
SIL 2	100 < RRF ≤ 1000
SIL 3	1000 < RRF ≤ 10000

Table 6.3. SIL targets expressed in terms of risk reduction factor (RRF) (adapted from [6]).

To determine if the SIL complies with the IEC 61511, Tables 4 and 5 of Ref. [7] have to be consulted. Once the required SIL has been determined, an appropriate IPL must be selected to reduce the final frequency of the event. If the IPL does not provide the same RRF indicated by the SIL classification, more than one IPL should be applied to achieve the required final risk reduction [7]. The risk reduction can be the required or the actual risk reduction. The required risk reduction is the one specified to achieve the tolerable frequency. The actual risk reduction is the one that gives a final frequency lower than the tolerable frequency, taking into account all possible layers of protection [9]. The LOPA analysis for the specific initiating event is terminated if the frequency of the hazard scenario is less than tolerable.

6.4.3. Limitations of LOPA

As HAZOP analysis, LOPA analysis presents some limitations [10]. These limitations are related to the fact that the LOPA technique must be used with an identification tool and is more time-consuming than qualitative methods such as HAZOP and what-if analysis [1]. Another limitation is the definition of the risk class. There are guidelines for defining the severity class of hazardous scenarios (Table C.2 in [9]). However, the experience and the interpretation of the analyst are crucial to obtaining robust and correct results. In addition, two PFD values for a particular IPL may not be the same because the IPL manufacturer may be different, or the data may not be from the same reference. So, the same LOPA analysis performed by two analysts could be different [1].

[1] Table 5.13-5.14 in [6].
[2] The safety function does not need to be a SIF and need not comply with IEC 61508 and 61511 (Table 5.13 in [6]).

6.4.4. Human factor

In LOPA techniques, the human factor can be considered an IPL, but it has some limitations [6]. Human error is a possible initiating event in the LOPA and HAZOP analysis. The frequency of this type of event depends on how often the task is to be performed [9,10].

Frequency of the task	IEF (yr^{-1})
Once per week (or more often)	1
Once per month (or more often)	0.1
Less than once per month	0.01

Table 6.4. The initiating event frequency (IEF) for a task performed by an operator [10].

When the studied initiating event is due to a human operation, the human response from an alarm cannot be considered as an IPL [6].

The operator response to an alarm can be considered an independent layer of protection when two conditions are present. Firstly, the triggering event is not due to human error. Second, the triggering event is not due to a failure of the alarm system. In addition, several other conditions are required to define the operator response to an alarm as an IPL. One of these additional conditions is that the plant must be continuously monitored to respond to the specific alarm with sufficient time. The task required of the operator must not place the worker in a hazardous situation. If equipment shutdown is required, the operation should be autonomous from any other SIF that is shutting down the same equipment [6].

Figure 6.5 is helpful in understanding when an operator response may or may not be considered an IPL (this is also true for other types of possible IPLs). The alarm starts when the MSP is reached. If the operator's response is not faster than the time indicated as IRT, it cannot be considered an IPL. The process does not react immediately to the operator's corrective action but requires a certain amount of time. IRT is the time available to correct the process parameter because if it is not corrected within this time, it will exceed the Never Exceed value. PLT is the time the process requires to change the trend of the process parameter to return to “normal” operative conditions [6,10].

The effectiveness of the operator response depends on the level of experience of the operator itself [9]. An operator can be considered as an IPL only if he is trained. In addition, if the task is carried out once a day or once a week, the MTTF can be reduced from 1 per year to 1 per 10 years, depending on the operator's experience (Table G.3 in [9]).

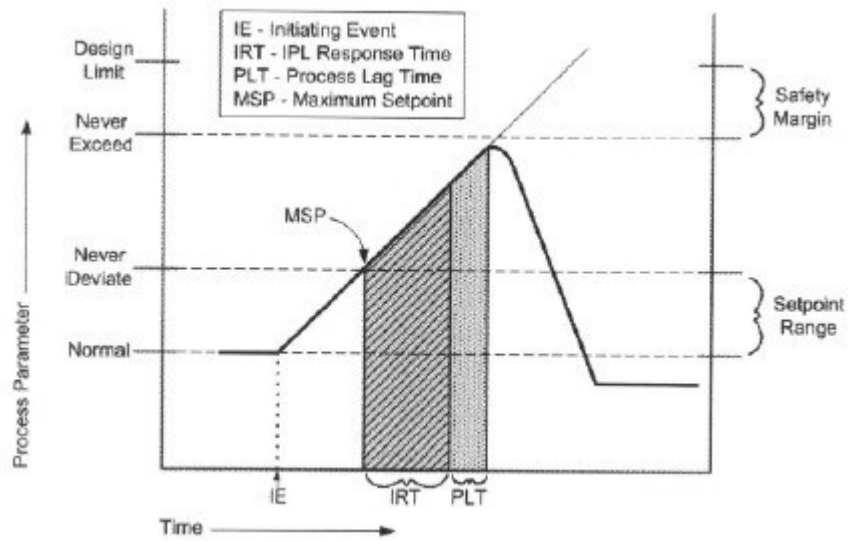

Figure 6.5. Trend of the process parameter when the initiating event occurs (Figure 3.1 in [10]).

In conclusion, the human factor is closely related to the plant's safety, as it can be fundamental to the execution of some key safety procedures. However, it can also be the initiating event of hazardous scenarios. Training the operator is the only way to observe more advantages than disadvantages of a human operation. This holds, especially in manual operations-rich settings where the operator is frequently asked to act on the equipment or procedures partially or totally rely on human actions. Academic research settings and related research infrastructures can be characterized by non-automatized contexts where the PI, researchers or students can be frequently asked to perform manual tasks. Moreover, routine and safety procedures can include relevant manual steps whose success strongly correlates with training and knowledge. Frequent manual operations and a framework with limited automatic supervision safety systems can lead to frequent and even severe undesired scenarios caused or concurrently caused by human error.

6.4.5. Equipment for pressure relief

One of the most common IPLs when the internal pressure of equipment increases or decreases are pressure relief devices, such as rupture disks, relief valves and vacuum breakers [10]. Pressure devices are useful to prevent the consequences of high or low pressures in the pilot plant. If a pressure increase is suffered, the consequences can include rupture, leakage, exposure to toxic or flammable substances, explosion and impact on a human target. This last consequence is usually due to an explosion, exposure to hazardous chemicals or fragment projections in the case of loss of equipment integrity. If the pressure is too low, especially when associated with vacuum conditions, the consequences could be the collapse of the equipment with possible ruptures, leaks and loss of containment. Sometimes, reverse flow is also a credible consequence determining contact between incompatible materials or uncontrolled flow to undesired locations. These two opposite behaviours result in hazardous scenarios that should be avoided. In addition, if one part of the system operates at low pressure and another is expected to operate at high pressure, a check valve (PFD = 0.1 [6]) should be added to prevent reverse flow [10].

The effectiveness of pressure relief systems depends on their sizing and fouling [6]. If a pressure relief device is to function as an IPL, it must be sized for the expected discharge scenario (API 520 [14,15]). It should be independent of other devices in the plant section under consideration.

In addition, the material of the safety devices must be compatible with the chemicals involved, and the release of the substances must not result in hazardous conditions such as explosive and flammable mixtures in the atmosphere [6,10]. In this regard, the R&D setting can pose issues since the exact nature and composition of the stream can be unknown, especially when innovative experimental campaigns are performed or deviated process conditions are established, pushing side or unknown reactions.

The PFD of pressure relief devices can be considered between 0.1 and 0.01, depending on the number of devices installed. If more devices are required to manage the resultant scenario, the final PFD will have to be calculated with reference to the layout of the devices. Typically, a good PFD approximation when more than one pressure relief device is present is to consider the PFD equal to 0.1 [6,10].

6.4.6. Control loop, BPCS and safety interlock

The primary safety systems for a chemical plant are a control loop, BPCS and safety interlock. BPCS are basic process control systems; their definition is given in §6.4.1. BPCSs have previously been used as a synonym for control loop as they apply a defined control function. This safety system can apply its corrective action automatically or by operator action. This system comprises three components: an initiator, a control system embedding the SIF, and an actuator. The initiator measures the operating condition and sends a corresponding signal to the control system, which applies a corrective action only if the incoming signal indicates an abnormal condition. The corrective action is performed by an electrical or pneumatical system [10].

The control loops can be installed to obtain the best product quality and maintain safe working conditions in the plant. The control loop related to safety conditions can work continuously or in demand mode. The control loop is a subclass of the BPCS and can be classified as an IPL if it is independent of other BPCSs and the cause of the initiating event [6,10].

Interlocks are safety systems, such as BPCS interlocks, whose corrective action is to shut down a specific piece of equipment. Safety interlocks can have one or more SIFs, as different initiating events can activate them. The importance of the different SIFs could be related to the resulting hazardous scenario of the corresponding initiating event [6].

All these systems can be considered IPLs if they comply with IEC 61511 and the time required for the corrective action is so short that it does not lead to a hazardous scenario. All their PFDs are equal to 0.1 [6].

6.4.7. MooN structure

One of the strategies to improve the reliability of safety systems is based on a MooN structure. MooN systems consist of N detectors in contact with the desired SIF. If at least M detectors fail, the SIF is activated, and the safety function is initiated. Not all systems have the same target or the same PFD. Some examples are given in Table 6.5 [6,7,11].

Redundant architecture	Objective	PFD
1oo1	Base unit	0.001
1oO₂	High-level of Safety	0.00002
2oO₂	Maintaining output	0.002
2oo3	Safety and Availability	0.00007

Table 6.5. Examples of MooN structures: objectives and PFDs (derived from Appendix F of [16]).

The structure of these systems can vary according to the number of detectors and initiators required, but not all of them have the same weight in the final operation. Some sensors are more important than others because of their position. Therefore, when defining the MooN structure, the analyst must also consider the position and importance of the different initiators [6].

6.4.8. Ventilation system: Hood

The ventilation system is one of the most critical layers of protection in a chemical laboratory and pilot plant. Ventilation systems can be classified according to their operating principle:

- Continuous ventilation systems can be divided into two sub-classes: those without performance monitoring (PFD = 0.1) and those with performance monitoring (PFD = 0.01).
- Discontinuous ventilation system: emergency ventilation triggered by safety controls, alarms and interlocks, known as SCAI (PFD = 0.1).

The difference between the first and second ventilation systems is the ability to define the hood performance. The system measuring the hood's performance helps determine whether the ventilation system works properly. A hood with such a system is connected to a safety interlock or an alarm to prevent dangerous scenarios and not put the operators at risk. SCAI, considered a BPCS, is a discontinuous ventilation system connected to toxic or combustible gas detectors. When the detection system detects at least one of the hazardous gases, the ventilation system is activated to reduce the gas concentration below the safety limit. These systems may be unreliable during a power failure unless provided with a backup utility supply [10].

In R&D settings and academic laboratories, a hood is typically present in chemical or biological laboratories and used when operations occur. It is always continuous and typically without performance monitoring, while discontinuous safety ventilation (SCAI) is rare.

6.4.9. Useful IPLs: AutoStart of standby equipment and Backup utility supplies

If a power failure occurs and the existing protective layers are not sufficient to reduce the frequency of the scenario, two possible IPLs can contribute to the required risk reduction target:

- Automatic start of standby equipment (such as a standby generator or standby pumps);
- Backup utility supplies.

These two systems are used for voltage drop and other scenarios such as utility loss or equipment inefficiency. Certain conditions must be met for the AutoStart system to work as expected. Firstly, the equipment must be maintained in the conditions required to operate as expected and in automatic mode. The standby equipment starts working when the specific signal is received. Some

examples of this type of signal are an increase in voltage and high or low pressure. When all these conditions are present, the system can be considered an IPL [6]. The second IPL is a backup utility supply usually associated with a LESS deviation, such as a decrease in voltage or less flow rate of a utility stream. It can be considered independent if activated autonomously and not by operator action, i.e., manual activation is not contemplated. In addition, this system must be able to manage the scenario, and the time required to be online is short enough and less than the IRT. The PFDs of these two IPLs are equal to 0.1 [6].

6.5. Case study: the Fischer-Tropsch synthesis

This chapter discusses the risk assessment of the Fischer-Tropsch (FT) lab scale plant for research. The main objective of this plant is to study the production and composition of liquid fuels obtained from hydrogen and carbon monoxide or carbon dioxide via FT synthesis. The P&ID and detailed information on the equipment used and the operating conditions are given in the Appendix (§A.1-5). The introduction of FT synthesis is discussed in Chapter 1.4.2 therefore this chapter aims at evaluating the results obtained from the three different techniques used, namely the interaction matrix, the HAZOP and the LOPA analysis.

6.5.1. Description of the FT pilot plant

The pilot plant considered in this study is shown in Figure 6.6 and is located in an academic laboratory. All the pieces of the equipment are under a fume hood, but others are not, i.e. T-01 to T-04 and valves 1-5, which are located in a separate room.

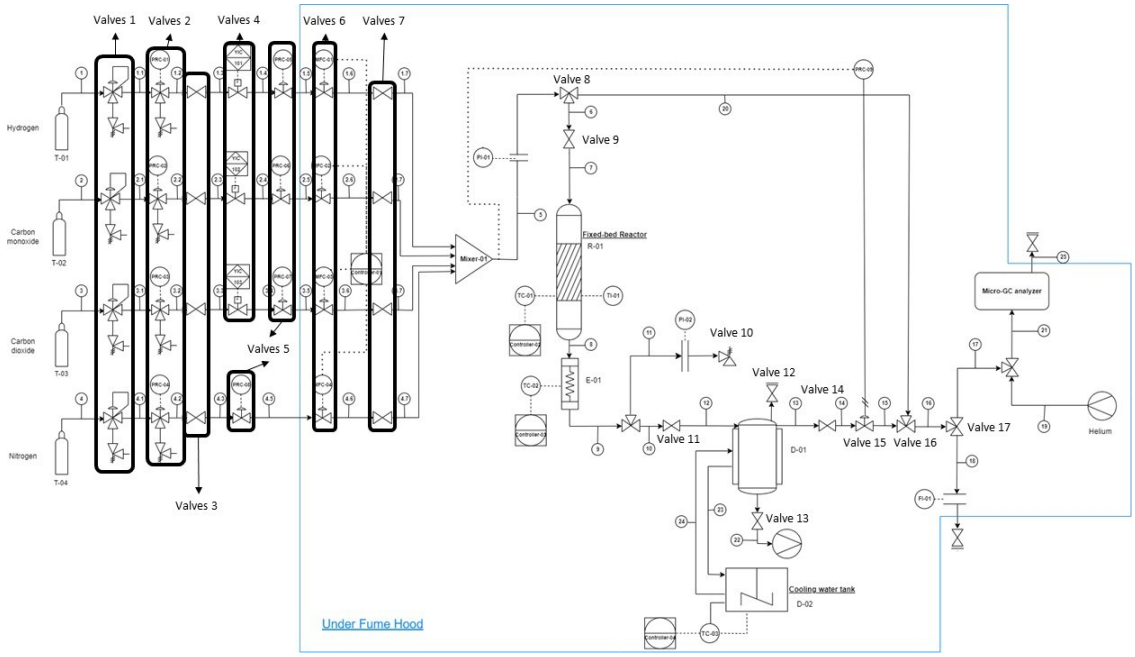

Figure 6.6. Instrumented process flow diagram of the pilot plant for Fischer-Tropsch synthesis (see §A.1 for a full-page view).

The equipment is usually run by one or two people (PhD and undergraduate students) under the supervision of a PI or professor. Pilot plants can have several intrinsically hazardous properties, and in the plant under consideration, these properties are:

- Chemicals involved, which are toxic and flammable (§A.5, §A.8);

- Manual operations (e.g.; start-up and shut-down, §A.4);
- Second-hand equipment (§A.2-3);
- No written procedures available for the entirety of the operations performed;
- Variability in operating conditions which depend on the experimental campaign performed (e.g., temperature, pressure, composition of reactant mixture and catalyst);
- Series of valves (see §A.2, discussed later).

Different precautions should be taken to manage these properties. As the chemicals involved are both toxic and flammable, in-depth knowledge is required to manage these substances safely (§A.8). In addition, a compatibility analysis between the chemicals and the materials involved is essential (§6.5.2, §A.6-7) in order to avoid dangerous scenarios such as irreversible damage to the equipment. Unfortunately, this is not always possible because the equipment used is "second-hand", and the technical specifications may no longer be available or may be altered.

This compatibility analysis should also be carried out between the different chemicals and operating conditions, as discussed in §6.2. It should be noted that the valves' series could lead to abnormal pressure conditions since if one of them fails, the pressure in the downstream sections will be modified, and different consequences can be led (see §A.9 to understand which are the main consequences).

One of the most critical aspects of the pilot plant under consideration is the lack of written procedures that could affect good operator performance in manual operations. The most common manual operations required for this pilot plant are:

- Start-up (see Table A.4.2 in §A.4);
- Shut-down (see Table A.4.2 in §A.4);
- Cleaning of R-01 and D-01.

The start-up and shut-down procedures of the system require the manual setting of the PRC-09 and various controllers (Controllers -01 and -02). In addition, during start-up, the operator must close the shut-off valves (valves 7) in order to open and clean R-01 and D-01. Typically, the operator carries out the cleaning of R-01 and D-01 autonomously, as well as the start-up and shut-down operations. The frequency of these operations is the main problem of the pilot plant since the probability of a human error for a task performed once a week is equal to 1 time a year [10]. The consequences of possible mistakes in these procedures are analyzed and discussed in §6.5.3 and §6.5.4.

6.5.2. Interaction matrix

The interaction matrix is helpful in identifying hazardous situations due to incompatibilities between chemicals, materials and operating conditions (normal and abnormal). In this study, the interaction matrix was divided into two different matrices:

- Chemicals vs. Materials;

- Interaction matrix without materials.

Therefore, the compatibility is assessed not only among chemicals but also with construction materials of the experimental setup.

6.5.2.1. Compatibility between Chemicals and Materials

Table A.6.1 (§A.6) and Table 6.6 show the interaction matrix between chemicals and materials. The materials considered are those of the leading equipment such as pipes, valves, seals, gaskets, M-01, R-01, E-01, D-01, pressure and flow indicators.

Two standards are used to analyze the compatibility between gases and equipment materials: EN ISO 11114-1:2020 [17] and EN ISO 11114-2:2021 [18]. The remaining interactions have been analyzed from other sources [19][20][21].

	SS316	SS304	Brass	PCTFE	Elastomer	PTFE	FKM	BunaN	Aluminum	Glass
H_2										
CO										
CO_2										
N_2										
SiO_2										
Mineral wool										
Catalyst										
Water										
CFC										
He										
Acetone				T < 37°C						
C_7-C_{30}										
C_2-C_6										
Incondensable gases										
Oxygen compounds										

Table 6.6. Compatibility between chemicals and materials (white: not found; green: compatible; red: incompatible; orange: could be incompatible). Further details are provided in Table A.6.1.

Table A.6.1 and Table 6.6 show that elastomer materials could not be compatible with different chemicals, depending on the elastomeric material. To avoid this margin of error, it is necessary to consult the manufacturer to know the material in question and its compatibility. In addition, FKM (fluorinated elastomers) and Buna N (nitrile rubber) should be avoided since they are incompatible with carbon dioxide.

6.5.2.2. Compatibility among Chemicals

Table A.7.1 (§A.7) analyses the compatibility between the different chemicals, but also the compatibility between chemicals, environment, and deviated operating conditions, such as:

- Very high (MORE) temperature;
- Very high (MORE) pressure.

The incompatibilities are due to the presence of flammable gases, pyrophoric catalysts and the formation of corrosive materials. Altered process conditions leading to undesired temperature values can provide additional risk scenarios mainly related to the ignition of flammable mixtures

and the effect on the flammability limits. Moreover, the pressure affects the flammability limits as well, enlarging the potential flammable range. The correct management of the substances and setting proper operating conditions to ensure an experimental run out of the flammability limits is fundamental to avoid incompatibilities and hazardous consequences [22,23].

6.5.3. Hazard and Operability Analysis (HAZOP)

To develop the HAZOP analysis, the pilot plant has been divided into four nodes, which are shown in Figure 6.7.

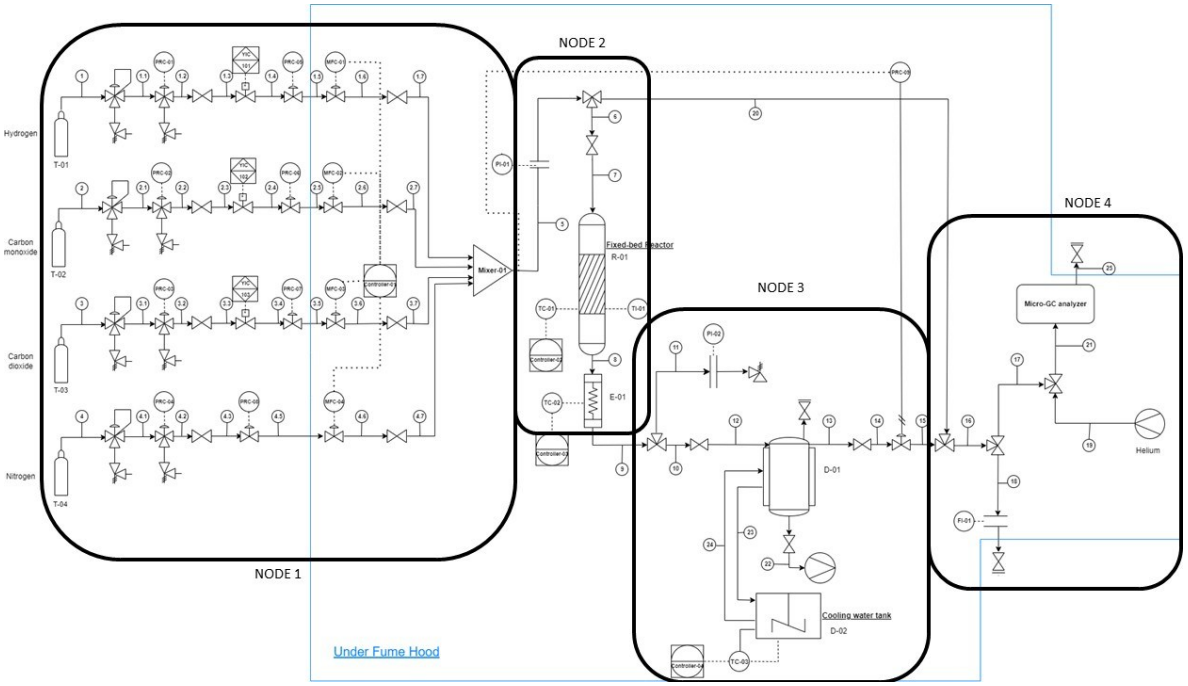

Figure 6.7. Definition of the four nodes for the HAZOP analysis.

The different sections have different objectives, which can be summarized as follows:

- Node 1: Feeding section, where four feeding lines are mixed.
- Node 2: Reaction section, where the synthesis occurs in a dedicated reactor.
- Node 3: Separation section, where the products are separated from the mixture.
- Node 4: Gas phase analysis, where the quality of the products is assessed.

Once the nodes have been defined, the deviations to be analyzed along the HAZOP have been defined (Tables A.9.1-2). The plant runs continuously for five days per week, and it is stopped for cleaning and emptying operations on R-01 and D-01. The frequent start-ups and shut-downs require a HAZOP study with respect to both continuous and transient states of the process. The transient analysis is limited to the procedure regarding the start-up and shutdown of the process. Table A.9.1 shows the deviations studied when the plant is operating as a continuous process. On the other hand, Table A.9.2 shows the deviations that an incorrect start-up or shut-down of the plant can cause.

Deviations with a high-risk classification (i.e. risk classes A, B, C) are listed in Table 6.7. They are further discussed and analyzed in §6.5.4.

Node	Initiating event	Characteristics of the basic event	Deviation	S	L	RC
1	Set a wrong set point in at least one of MFC-01/02/03/04	Human error	MORE pressure or flow rate	E3	W4	C
	A power outage	System failure	NO/LESS electric voltage-current	E3	W4	C
2	Wrong value at PI-01	System failure	MORE pressure	E3	W4	C
	Reactor too packed	Human error	MORE pressure	E3	W4	C
	Wrong set point in PRC-09	Human error	MORE pressure or flow rate	E3	W4	C
	Wrong set point in TC-01	Human error	MORE temperature/reaction rate	E3	W4	C
	Wrong set point of temperature (start-up)	Human error	MORE temperature	E3	W4	C
	Leakage/defective connection	System failure	LESS pressure, LESS/NO flow	E4	W3	C
	Reactor opening before closing the feed line(s)	Human error	TOO EARLY opening of the reactor	E3	W4	C
	Reactor closing after opening the feed line(s)	Human error	TOO LATE closing of the reactor	E3	W4	C
	A power outage	System failure	LESS/NO electric current/voltage	E3	W4	C
	Catalyst poisoning (not required)	System failure/human error	LESS/NO reaction rate or catalytic activity	E4	W3	C
3	Wrong set point in PRC-09	Human error	MORE pressure or flow	E3	W4	C
	PI-02 failure	System failure	MORE pressure	E3	W4	C
	Power outage	System failure	LESS/NO electric voltage	E3	W4	C

Table 6.7. Main hazardous events emerged from the HAZOP analysis (L: likelihood; S: severity; R.C.: risk class).

Deviation name: Increasing Flow
Node description (design intent): feeding of reactants and mixing to the desired composition (which couldchange depending on the experimental test performed).

Cause	Consequence	Safeguards	Recommendations	S	L	RC
1.Wrong set point at the mass flow controller	Potential increase in pressure [3] and changes in the final composition with loss of the experimental test.	Hood. Sensor for leakages. Sensors for pressure. Alarmed high-pressure sensor (PIAH).	Periodic check of the set-point of the mass flow controller. Proper procedures.	E2/E3	W4	D/C
2.…						

Table 6.8. Example of a HAZOP table based on the deviation MORE flow rate in Node 1 (feed section).

[3] Refer to the associated deviation MORE pressure in the HAZOP analysis.

All HAZOP deviations analyzed are reported in §A.9, and the structure of the tables is the same as Table 6.8. The definitions of severity (S), likelihood (L) and risk class (R) are reported in Tables 6.11-14.

Severity class (S)	Description
E1	**NOTICEABLE** People: Recoverable injuries for which FIRST AID is necessary. No sick leave. Environment: No significant environmental damage.
E2	**GREAT** People: Recoverable injuries with sick leave. Environment: Environmental damage without lasting effects.
E3	**SERIOUS** People: Irreparable injuries involving one individual. Possibly minor release of hazardous material. However, the effects on people manifest only in the place where the calamity occurs. Environment: There is a significant release of a dangerous product, environmental damage noticeable in the immediate surroundings of the calamity, with possible permanent local effects.
E4	**VERY SERIOUS** People: Irreparable injuries for multiple individuals within the plant. Possibly significant releaseof hazardous product. However, the effects on individuals manifest only within the plant. Environment: There is a significant release of hazardous material and environmental damage in the wide surroundings of the calamity within the plant, with possible permanent local effectswithin the plant.
E5	**CATASTROPHIC** People: Irreparable injuries for multiple individuals within the plant. Possibly significant release of a hazardous material. Effects on individuals may also manifest outside the plant. Environment: There is a significant release of hazardous material and environmental damage in the surrounding area outside the plant, with potential permanent effects outside the plant.

Table 6.9. Classification of severity (S) for evaluating the risk R of a scenario.

Likelihood class (L)	Description
W1	**UNLIKELY** Since the start of the exploitation of the installation, a record of all accidents was kept in an incident-accident system. As no accidents have occurred in the last 20 years, it seems unlikely that an accident will occur during the further exploitation of this installation.
W2	**RARE** This cause is unlikely but not excluded during the period of exploitation. However, the situation has not yet occurred in this installation.
W3	**PROBABLE** This cause might occur during the period of operation and has already occurred in the past in installations in the company or similar installations elsewhere.
W4	**EXPECTED** No experience with the installation, e.g., new installations, or no assessment possible. For existing installations, this cause has already occurred frequently.

Table 6.10. Classification of likelihood (L) for evaluating the risk R of a scenario.

		1 per 1000 years **W1** *Unlikely*	1 per 100 years **W2** *Rare*	1 per 10 years **W3** *Probable*	1 per 1 years **W4** *Expected*
E1	*Noticeable*	F	F	F	E
E2	*Great*	F	F	E	D
E3	*Serious*	F	E	D	C
E4	*Very serious*	E	D	C	B
E5	*Catastrophic*	D	C	B	A

Table 6.11. Matrix for evaluating the risk class (RC) of a scenario, combining the likelihood (L) and severity (S) classes.

Risk class (RC)	Description
F	**Noticeable Risk** No additional risk measures are required.
E	**Moderate Risk** Technical or organisational risk-reducing measures may be required.
D	**Severe Risk** Active or passive barriers as risk-reducing measures may be required.
C	**Very severe Risk** Active or passive barriers as risk-reducing measures are required.
B	**Catastrophic Risk** Active or passive barriers as risk-reducing measures are required.
A	**Extreme Risk** Passive barriers as risk-reducing measures are required. Redesign is recommended.

Table 6.12. Risk classification.

In order to determine the likelihood of the different initiating events (indicated as causes in Table 6.8), values from the literature have been used [9,6,8,10,24]. In Table 6.8, it can be observed that the severity class, and consequently the risk class, is not always unique. This is because the final scenario could be classified in both classes. However, during the LOPA analysis (§6.5.4), the conservative approach was used (e.g., the risk class of cause 1 in Table 6.8 is considered equal to C).

6.5.4. Case study: LOPA

In the present work, the risk classification involves three different classes:

- Risk class A (extreme risk): risk-reducing measures can only be passive technical measures where redesign is strongly recommended.
- Risk class B (very big risk): risk-reducing measures can only be active or passive technical measures with a slight preference for the use of passive measures.
- Risk class C (big risk): risk-reducing measures can only be active or passive technical measures with a slight preference for the use of passive measures.

This classification can be obtained by combining the likelihood and severity of the final events, i.e. the Top Events, that emerged from the HAZOP analysis. The relevant Top Events are discussed in the following sections, and the functional safety approach (discussed in §6.4) is implemented to identify and quantify proper protective measures and recommendations. These

sections are structured to provide a clear analysis of the initiating events and how adding specific protective layers can reduce their frequency of occurrence.

The possible initiating events have been obtained from the HAZOP analysis (see §A.9). Top Events listed in Table A.10.1 are the initiating events with a high probability and a risk class higher than C, i.e. at least very severe risk scenarios.

It can be noted that the majority of Top Events occur in Node 2 and are primarily due to human error. Incidentally, operating on the reactor is critical, and many actions on the pilot plant are performed manually. Other initiating events are due to system failures, which are described in §6.5.4.2.

The LOPA is performed according to BS EN 61511-1:2017+A1 [7], BS EN 61511-2:2017 [8] and BS EN 61511-3:2017 [9]. According to Table F.8 of [8], the tolerable frequency of a hazardous event (expressed in events/year) is defined. Since the resulting risk class is C (very severe) for all the considered events, the tolerable occurrence frequency [4] is equal to 10-4 yr-1. The procedure discussed in Fig. 6.4 has been followed to perform the analysis. When the intermediate frequency is lower than the tolerable frequency, the procedure is finished.

When this final frequency is calculated, the resulting reduced final risk class is represented in a contour plot and compared to the initial state (Figure 6.8 [25]). Equations 2 and 3 define the mean probability of failure (Pf) and the severity (D, It has a different definition than S in HAZOP) of the specific event [25]. The time assumed for the analysis (t) is 10 years, which is considered consistent with the lifetime of an experimental setup for academic research, and the frequency is specified for each event. The C (cost of damage) is estimated to calculate the severity using the values given in Table 6.13 [25].

$$P_f = \frac{\mathrm{t} - 1/\mathrm{f}(1 - \exp(-\mathrm{ft}))}{t} \tag{2}$$

$$D = \frac{\log(c)}{\log(cmax)} \tag{3}$$

Rank	Assets	C [€]	D [-]
1	No damage	1	0
2	Slight (< 100 €)	10	0.2
3	Minor (> 100 € and < 1,000 €)	10^2	0.4
4	Localized (> 1,000 € and < 10,000 €)	10^3	0.6
5	Major (> 10,000 € and < 100,000 €)	10^4	0.8
6	Extensive (> 100,000 €)	10^5	1

Table 6.13. Classification of the severity of a given hazardous initiating event, considering the cost of damage (C) and the severity (D) [25].

[4] The correction factor required from Note 1 of Table F.8 [8] is already considered.

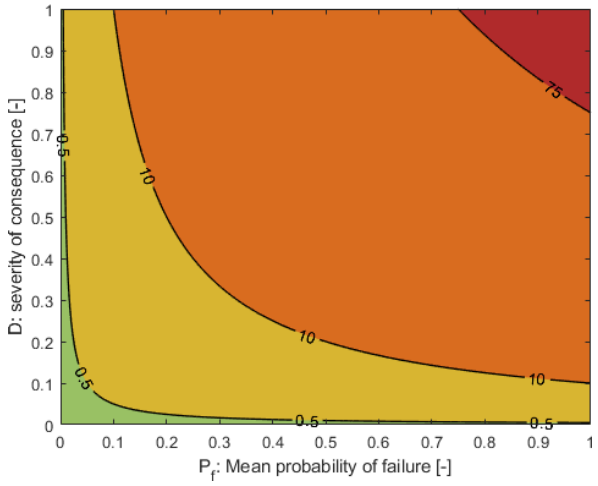

Figure 6.8. Contour plot to define the risk class of the scenario (adjusted from [25]).

The contour plot reported in Fig. 6.8 is useful to understand the classification of the risk class for each considered event. The risk class is classified as reported in Table 6.14, and the value of the resulting risk R is calculated by Eq. 4.

$$R = 100 \cdot D \cdot P_f \tag{4}$$

Risk level	Classification
$0 \leq R < 0.5$	*Low*
$0.5 \leq R < 10$	*Moderate*
$10 \leq R < 75$	*High*
$75 \leq R \leq 100$	*Unacceptable*

Table 6.14. Risk classification criterion.

Since the risk assessment is based on the experience of the analyst, the classification shown in Table 6.14 may be different depending on alternative criteria decided by the HAZOP and LOPA team. The events analyzed in the present work are classified as unacceptable or high.

6.5.4.1. Deviations due to human error

The primary deviations induced by human error are the following:

- MORE pressure,
- MORE flow,
- MORE temperature or reaction rate (higher reaction magnitude),
- TOO EARLY opening of the reactor,
- TOO LATE closing of the reactor.

MORE pressure is usually combined with MORE flow. This can be explained by the fact that an increase in flow accompanies an increase in pressure, as the reactants are gases in isothermal conditions.

MORE pressure or flow can induce various consequences, including:

- MORE conversion of CO and consequent loss of an experimental test;
- LESS separation in D-01 and consequent loss of an experimental test;

- Establishment of the maximum pressure of the equipment, i.e., in pipes, in the mixer, in the reactor;
- Basic damage to sealings and fittings;
- Leakages and ruptures from the pilot plant equipment;
- Loss of containment of flammable or toxic material(s);
- Fire, explosion or exposure to toxic.

It is worth noting that a deviation of MORE flow affects the final composition of the mixture, leading to the loss of the experimental test. Increasing the flow in streams 5, 6 or 7 will not change the final composition of the mixture but will change the flow rates of the streams after R-01 (streams 8 to 17), resulting in possible condensation of products in streams 9, 10 and 11 and less separation in D-01. If the flow rate is changed by only one of the reactants, the final composition will change as reported in §6.5.4.3 (1).

The substances involved are flammable and poisoning, and some protection layers are required in the case of a loss of containment, as will be discussed later in the section.

In the HAZOP analysis, the safeguards indicated for these deviations are:

- hood;
- pressure sensor(s);
- leakage monitoring system;
- high-pressure indicator and alarm (PIAH), i.e., a sensor providing an alarm once the pressure is above a set threshold.

According to the functional safety approach, the effectiveness of the layers of protection needs to be assessed according to the risk reduction criteria.

Concerning the consequences of the initiating event these are classified into three categories: acceptable, undesired and unacceptable (Table 6.15). Acceptable consequences also refer to minor consequences which are related to operational issues or transient scenarios. Unacceptable consequences can involve an effect on a human target.

Classification	Consequences
Acceptable	MORE conversion LESS separation Loss of an experimental test
Undesired	Establishment of the maximum pressure Damage to sealings and fittings General leakages and ruptures
Unacceptable	Loss of containment of flammable or toxic material(s) Fire, explosion or exposure to toxics.

Table 6.15. Categories of consequences.

For each undesired or unacceptable consequence, Table 6.16 indicates which are the possible preventive or mitigative actions or systems.

Classification	Consequences	Preventive/mitigative actions
Undesired	Establishment of the maximum pressure	BPCS, safety devices (pressure relief devices)
	Damage to sealings or fittings	Hood, leakage monitoring system acting on isolation valves
	Leakages and ruptures	Hood, leakage monitoring system acting on isolation valves
Unacceptable	Loss of containment of flammable or toxicmaterial(s)	Hood, leakage monitoring system acting onisolation valves
	Fire, explosion, exposure to toxics	No ignition sources, hood, or leakage monitoring system acting on isolation valves reducing the amount released

Table 6.16. Preventive or mitigative actions in the case of undesired or unacceptable consequences associated with an initiating event.

The pressure relief devices should be compliant with the regulations, such as API 520 [14,15] or EN 764-7:2002 [25].

A deviation of MORE temperature is usually correlated to MORE reaction rate, and the main consequences of these deviations are classified in Table 6.17.

Classification	Consequences
Acceptable	Altered final composition of the mixture Loss of the experimental test
Undesired	Pressure increase Damage to the catalyst Leakages and ruptures
Unacceptable	Major loss of containment, fire, explosion or exposure to toxics

Table 6.17. Deviation of MORE temperature or reaction rate: classification of consequences.

These safeguards are similar to those assigned to the deviation of MORE pressure deviation since the temperature is strictly correlated to the system's pressure. As the temperature increases, so does the reaction rate of R.1-5, and a higher carbon deposition can be expected. If the carbon deposition fouls the catalyst, hot spots can also arise. Moreover, the internal pressure in the system may increase, with the associated consequences since an increase in temperature increases the volume of the gaseous phases and the final pressure.

The pilot plant operates continuously but is stopped every week for cleaning and emptying operations on the main equipment (R-01 and D-01). The start-up and shut-down of the plant require to change the set-point of the following controllers:

- PRC-09;
- MFC-01; -02; -03; -04;
- TC-01; -02;

When the flow in the system is zero, R-01 and D-01 are opened by the operator and cleaned with acetone. The shut-down and the start-up of the system are performed manually by a single operator (no written procedure is available), so it is reasonable to consider a high frequency of

human error (§6.4.4). In this regard, two credible hazardous scenarios can be obtained when the procedure is not applied correctly:

- the reactor is opened TOO EARLY;
- the reactor is closed TOO LATE.

Independently on the scenario, the following consequences can occur: loss of containment of flammable or toxic materials, fire, or explosion (upon effective ignition source and provided the quantity of released material can sustain an explosion). Such a set of consequences is unacceptable, and proper layers of protection are required. These include suitable sensors (as detectors for hazardous gases) and the hood.

6.5.4.2. System failure

The system failure considered in this analysis includes:

- a power outage,
- a failure of a sensor or an indicator of a process variable,
- leakages or defective connections.

These initiating events can lead to hazardous scenarios, and the associated deviations are the following:

- MORE or LESS pressure (§6.5.4.1);
- MORE or LESS flow (§6.5.4.1);
- LESS or NO voltage.

If there is LESS or NO voltage, the equipment (such as R-01, D-01, controllers -01 to -04) may not respond as it should. In this scenario, the solenoid valves (valves 4, Figure A.1.1) will fail closed, and the process will no longer be supplied with reactants (all the valves in the plant behave as FC). The reactor (R-01) will stop running appropriately as its temperature control (Control-02) will stop working. Control-02 is a feedback controller with a temperature indicator. It adjusts the furnace power as the temperature inside R-01 rises. If the power is switched off, valves will fail close, and some reactants may remain in the reactor, which will take some time to reduce its temperature. During this time, the temperature inside the reactor is no longer controlled, and the residues inside R-01 could lead to some hot spots and consequently increase the reaction rate (§6.5.4.1), potentially damaging the catalyst bed. Finally, in the event of a power failure, controllers -03 and -04 will also stop working, resulting in the following:

- LESS separation in D-01 because the temperature in D-01 is not equal to 5°C, and not all heavy products could condensate;
- Blockage of E-01 because the temperature can be lower than 60÷80°C, and some products, including waxes, can condense before D-01.

Such scenarios can be prevented by adopting an independent emergency power supply with the characteristics described in §6.4.9.

6.5.4.3. Deviations in Node 1: Feeding section

The purpose of Node 1 is to feed the process and maintain the composition of the mixture fed to the reactor. The node consists of four streams carrying respectively hydrogen, carbon monoxide, carbon dioxide and nitrogen. All these chemicals are pure, and the equipment is listed in Table A.10.2. It can be seen from Figure 4.1 that the valves of each stream have the same number. This does not mean that the same valve manages four different streams but that these valves have the same characteristics for each stream (e.g., valve 1 for the hydrogen stream has the same characteristics as valve 1 for the CO stream).

The hazardous initiating events of Node 1 reported in Table A.10.1 are the following:

- Wrong set point in at least one of MFC-01, 02, 03 or 04;
- A power outage.

These initiating events are analyzed respectively in Sections §6.5.4.3(1)-(2).

1. Mass flow controllers: MFC-01, -02, -03, -04

Setting the MFC-01/02/03/04 is a manual operation done by a student or a researcher every week, so the possibility of incorrect setting has a frequency of 1 per year [10]. When at least one set point is wrong, a deviation of MORE pressure or flow can occur (§6.5.4.1). The safeguards indicated in the HAZOP analysis are the adoption of the hood, a sensor for leakages and a high-pressure alarm and indicator (PIAH). In this regard, the hood and detectors for reactants and methane are already installed. The increasing pressure will be expected downstream of valve 6, so the existing protection layers are the hood and valve 4. As the nitrogen stream (stream 4) does not have a solenoid valve (valve 4 in the other streams), this valve cannot be considered for managing an incorrect nitrogen set-point. When at least one of the flow rates is set incorrectly, the ratio between the reactants and the inert fed to the pilot plant changes. The resulting scenarios are illustrated in Table 6.18.

Substance	Deviation	Consequence
Hydrogen	MORE flow rate	Altered selectivity and conversion, i.e., a higher quantity of short-chained products is produced (e.g., liquefied petroleum gas)
	LESS flow rate	Altered selectivity and conversion, i.e., a higher quantity of long-chained products is produced (e.g., waxes)
	NO flow rate	R.1-4 do not occur
	LESS ratio with CO or CO_2 (< 1)	No reactions occur
Carbon monoxide	MORE flow rate	Altered selectivity and conversion, i.e., a higher quantity of long-chained products is produced (e.g., waxes)
	LESS flow rate	Altered selectivity and conversion, i.e., a higher quantity of short-chained products is produced (e.g., liquefied petroleum gas)
	NO flow rate	R.1-5 do not occur
Carbon dioxide	MORE flow rate	Altered selectivity and conversion, i.e., a higher quantity of long-chained products is produced (e.g., waxes)
	LESS flow rate	Altered selectivity and conversion, i.e., a higher quantity of short-chained products is produced (e.g., liquefied petroleum gas)
	NO flow rate	R.1-5 do not occur
Nitrogen	NO flow rate	GC composition measurement not correct

Table 6.18. Deviations induced by errors in the setting of mass flow controllers.

Table 6.18 shows that a change in the initial composition affects the final composition of the mixture resulting from the FT synthesis. More in detail, an altered quantity of H_2, CO or CO_2 will affect selectivity towards short of long chain products.

Another possible operator error is the swapping of carbon monoxide operating conditions for carbon dioxide in MFC-01, -02, -03 and -04. The consequences are illustrated in Table 6.19.

Deviation	Consequence
AS WELL AS flow rate of CO (CO fed instead of CO_2)	If CO is fed instead of CO_2, a higher conversion of CO will be observed since CO is more reactive than CO_2. The product mixture will be rich in long-chain hydrocarbons. Faster FT catalyst deactivation.
AS WELL AS flow rate of CO_2 (CO_2 fed instead of CO)	If CO_2 is fed instead of CO, a lower conversion of CO_2 will be observed as CO is more reactive than CO_2, and the temperature of R-01 is lower than that required for CO_2. The product mixture will be rich in short-chain hydrocarbons.

Table 6.19. Deviations induced by substitution of substances. Details on the consequences.

In summary, if the wrong reactant is added, an experimental test is lost.

To control the eventual consequences of deviations related to the hydrogen feed line (e.g., leakages), the following IPLs are provided:

1. Valve 4: This solenoid valve is connected to detectors of CO, CO_2, CH_4 and H_2. This valve acts as FC, i.e., if any detector detects at least one of the abovementioned chemicals

or when there is a decrease in the voltage of supplied equipment, the valve will block the flow.

2. Hood, which can be considered as an IPL since the increase in pressure starts from stream 1.5;

The effect of these protection layers on the frequency of events is reported in Table 6.20.

Initiating event	Frequency (yr^{-1})	Independent protection layer 1 Solenoid valve	Independent protection layer 2 Hood (Passive IPLs)	Intermediate frequency (yr^{-1})	Tolerable frequency (yr^{-1})
Wrong set point (MORE pressure or flow)	1 [5,6]	0.028	0.1	$2.8 \cdot 10^{-3}$	$1 \cdot 10^{-4}$

Table 6.20. Existing independent protection layers (IPLs) to manage a deviation induced by a wrong set-point in MFC-01/-03.

This intermediate frequency is higher than tolerable, so additional IPLs are required. The risk reduction factor (RRF) obtained by eq. 1 equals 28, and a SIL 1 is required. The SIL 1 IPL needs to be added to the existing protection layers, i.e., the solenoid valve and hood.

Initiating event	Frequency (yr^{-1})	IPLs 1 SIL 1	2 Solenoid valve	3 Hood (Passive IPLs)	Intermediate frequency (yr^{-1})	Tolerable frequency (yr^{-1})
Wrong set point (MORE pressure or flow)	1	0.1 [7]	0.028	0.1	$2.8 \cdot 10^{-4}$	$1 \cdot 10^{-4}$

Table 6.21. Additional independent protection layer (IPL) to manage a deviation induced by a wrong set-point in MFC-01/-03.

The resulting intermediate frequency is higher than the tolerable threshold, and additional layers of protection are required. However, the necessary reduction factor is RRF = 2.8. Hence, a SIL "a" (RRF < 10) is required. It does not need to be a SIF, and it is not necessary to comply with IEC 61508 and 61511. In this regard, maintenance practice and control of equipment wear out are helpful to reduce further and control the frequency. In any case, provided that the initiating event is due to a human error, the operator response cannot be considered an IPL, as the same person who initiated the event is likely to respond to an alarm [6].

Initiating event	Frequency (yr^{-1})	IPLs 1 Safety device	2 Pressure relief device	3 Solenoid valve	4 Hood (Passive IPLs)	Intermediate frequency (yr^{-1})	Tolerable frequency (yr^{-1})
Wrong set point (MORE pressure or flow)	1	$1 \cdot 10^{-4}$ [8]	0.1 [9]	0.028	0.1	$2.8 \cdot 10^{-8}$	$1 \cdot 10^{-4}$

Table 6.22. Safety and pressure relief device as independent protection layers (IPLs) to manage a deviation induced by a wrong set-point in MFC-01/-03.

[5] From Table 4.3 of [10].
[6] From Table G.3 of [9].
[7] From Table 5.14 of [10].
[8] http://silsafedata.com/ [12], expressed as a digital input channel.
[9] From Table 4.5 of [6].

Adding a safety device and a pressure relief device decreases the frequency of the hazardous event to a value of < 10-4. The safety device indicated as IPL 1 is an I/O system and is a digital input channel used to limit the possible setpoint range. In particular, this device can be classified as a "maximum physical value limiter", where a maximum value for the flowrate is set by anauthorized operator, in this case, the principal investigator of the pilot plant or the maintenance manager [27].

The pressure relief device should be placed before valve 7 (stream 1.6) (Fig. 6.9) since Node 1 can be isolated via valve 7 if the pressure or flow is higher than the design intent. The safety device is implemented such as to fix an operating range that an operator can not modify.

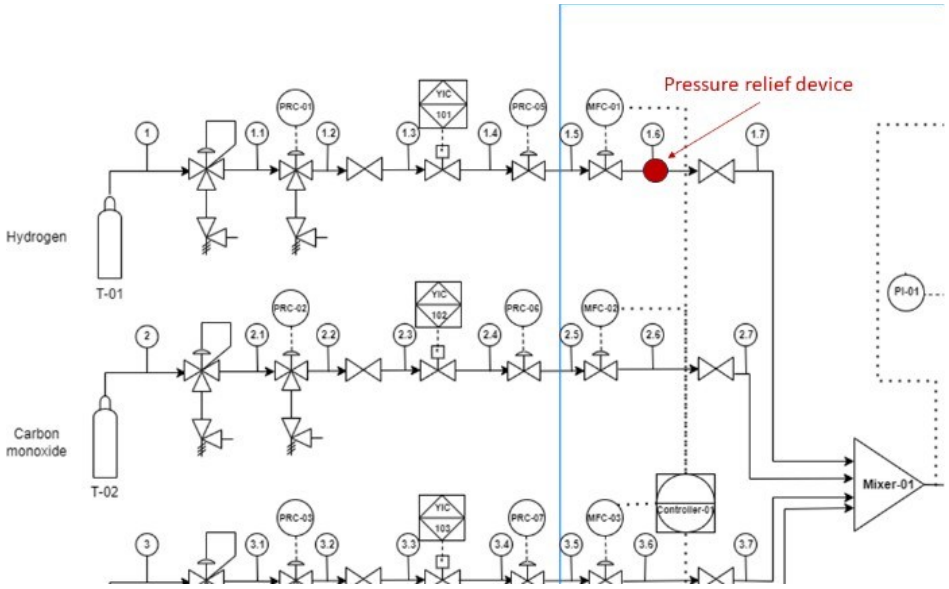

Figure 6.9. Position of the pressure relief device along the hydrogen stream.

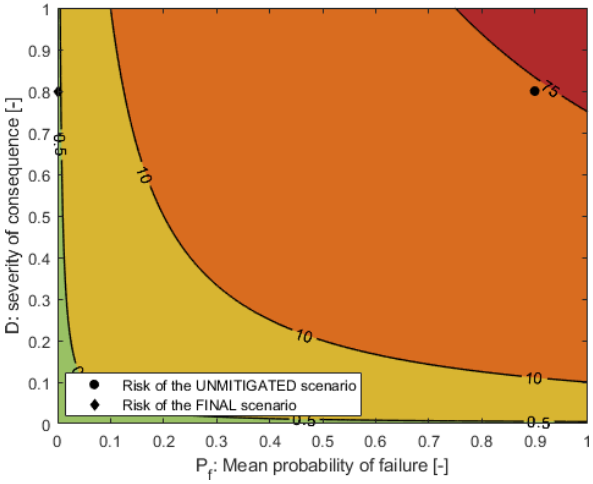

Figure 6.10. Risk class when the set-point of MFC-01/-03 is incorrect (Node 1) (D = 5).

The final risk class of the present scenario for the hydrogen stream is reduced to low after implementing the proposed independent protection layers. The considerations made for hydrogen streams can also be implemented for carbon monoxide and carbon dioxide streams since the existing protection layers used to manage the resulting scenarios are the same. So, the additional IPLs required are the safety device and the pressure relief device.

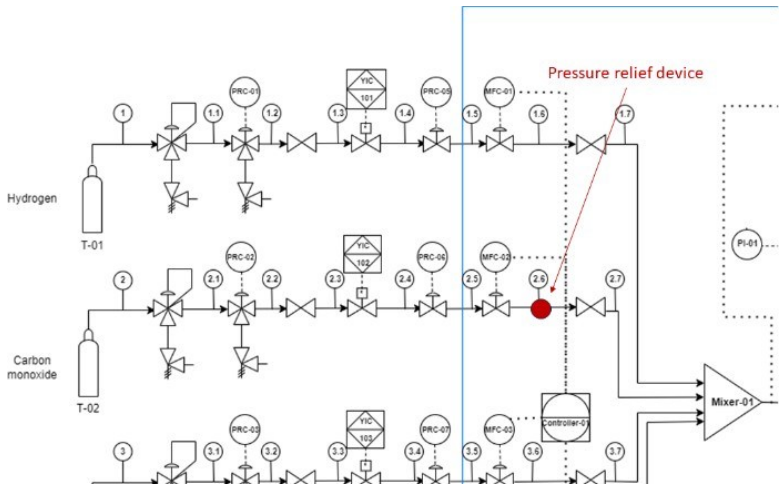

Figure 6.11. Position of pressure relief device along the carbon monoxide stream.

Figures 6.11 and 6.12 indicate the position of the pressure relief device to accommodate eventual deviations as emerged from the HAZOP analysis. The final and the initial risk classes are equal to the one represented in Figure 4.5, so the final classification is equal to low for both the considered streams.

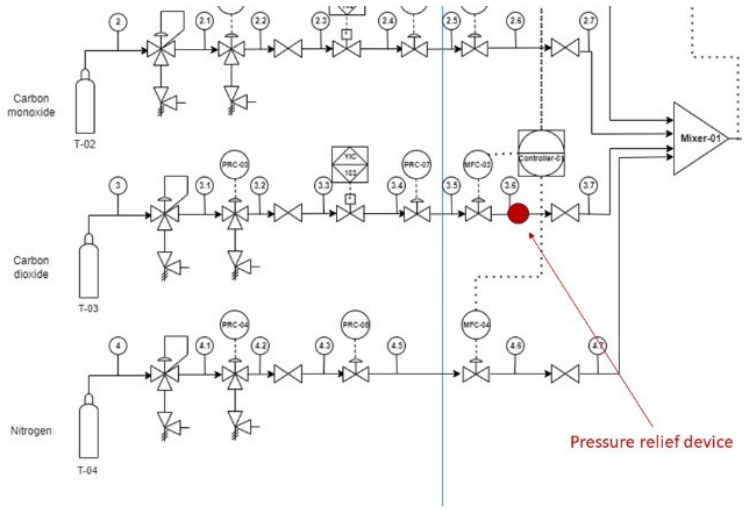

Figure 6.12. Position of pressure relief device along the carbon dioxide stream.

The nitrogen stream has a similar structure to the previous streams but does not have the solenoid valve. The properties of N2 are less hazardous than H_2 and CO, so the classification of the HAZOP risk class is D, and the LOPA analysis is not required.

However, a possible final configuration of the IPLs is shown in Table 6.23, where the assumptions of the two additional protective layers (IPLs 1 and 2) are the same as the one discussed for the hydrogen stream.

Initiating event	Frequency (yr^{-1})	IPLs			Intermediate frequency (yr^{-1})
		1	2	3	
		Safety device	Pressure relief device	Hood (Passive IPLs)	
Wrong set point (MORE pressure or flow)	1 [10,11]	$1 \cdot 10^{-4}$ [12]	0.1[13]	0.1 [14]	$2.8 \cdot 10^{-6}$

Table 6.23. Independent protection layers required to manage a wrong set-point in MFC-04.

The position of the pressure relief device is reported in Fig. 6.13.

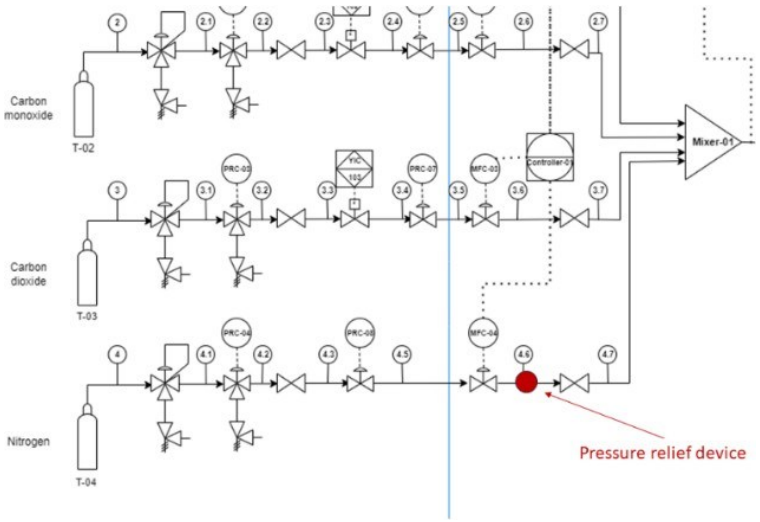

Figure 6.13. Position of pressure relief device in Nitrogen stream.

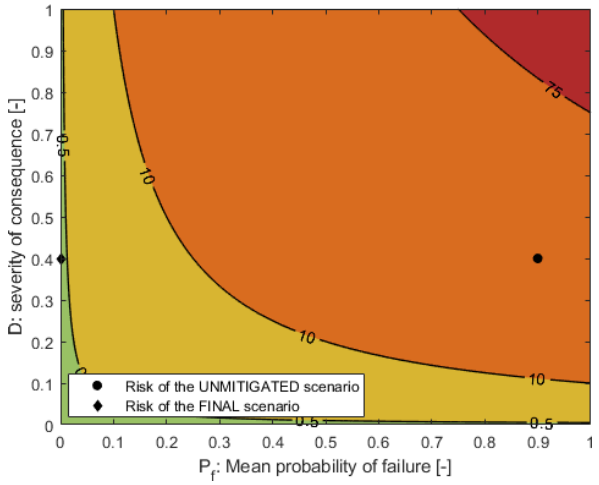

Figure 6.14. Risk class when the set-point of MFC-04 is incorrect (Node 1) (D = 3), before and after implementing the protection layers.

From Figure 6.14, the initial risk class (the existing IPLs are not considered) is high, and the final risk class (considering the existing and the additional IPLs) is low.

[10] From Table 4.3 of [10]
[11] From Table G.3 of [9]
[12] http://silsafedata.com/ [12]: Digital input channel
[13] From Table 4.5 of [6]
[14] From Table 5.37 of [10]

2. Electrical system: a power outage

A power outage, intended among the different initiating events, can determine a trip scenario leading to undesired outcomes. Other causes inducing such an occurrence include a short circuit and a spurious trip of electrical protective systems.

If there is a power outage, the solenoid valves will act fail close (FC). Without proper management of the inflow, this gives a possible increase in the pressure upstream of valve 4, especially if this is a manual step requiring monitoring. Other expected consequences affecting the downstream nodes include a pressure decrease, decreasing/no flow to the reactor and the loss of an experimental test (see §6.5.4.2). The hazardous scenario is related to the increasing pressure consequences. The existing protection layers are the hood, solenoid valve, and two pressure relief valves connected to valves 1 and 2.

Initiating event	Frequency (yr^{-1})	IPLs				Intermediate frequency (yr^{-1})	Tolerable frequency (yr^{-1})
		1 Pressure relief valve	2 Pressure relief valve	3 Solenoid valve	4 Hood (Passive IPLs)		
Power outage (LESS/NO electric voltage)	1 [15]	0.01 [16]	0.01	0.028	0.1	$2.8 \cdot 10^{-7}$	$1 \cdot 10^{-4}$

Table 6.24. Existing independent protection layers required to manage a power outage in Node 1.

The resulting scenario is classified with severe consequences, so the tolerable frequency is equal to 10-4 yr-1, higher than the intermediate frequency.

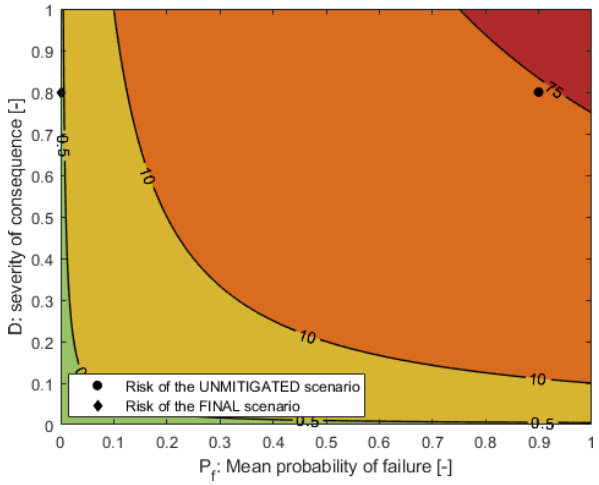

Figure 6.15. Risk class for the event power outage in Node 1 (D = 5).

In conclusion, no additional protection layers are required, and the risk classification is low.

[15] From personal communication with the operators of the pilot plant. Such a scenario has been experienced statistically one time per year.
[16] Table G.7 of [9]

6.5.4.4. Deviations in Node 2: the reaction section

Node 2 converts the reactants to products according to the desired conversion and selectivity. The aim is to obtain a heavy phase consisting of C7-C30. A by-product of the main reaction is water. The E-01 is the heat exchanger downstream of the reactor, and it keeps stream 8 in a gaseous phase. The composition of stream 8 depends on the composition of stream 7, where the ratios between the different reactants are fundamental to the occurrence of R.1 and R.2 (Tables 6.21-22).

The solenoid valves (valve 4) connected to the detectors (Node 1) fail close and act if at least one of CO, CO_2, CH_4 or H_2 is detected in the laboratory. However, for the LOPA analysis of Node 2, Valve 4 is not considered an IPL as it is equipment of node 1.

1. Failure of PI-01

If PI-01 fails or malfunctions, the pressure indicated can be wrong. The pressure inside the pilot may increase without supervision by the operator. Additionally, an increasing flow is possible. The consequences of these deviations are listed in Table 6.25.

Deviation	Possible Safeguards	Comments
MORE conversion of carbon monoxide	Temperature control loop, pressure control loop	In the case of PI-01 failure, the operator can wrongly set the pressure. If the resulting deviationis LESS pressure, the resulting consequence is LESS conversion, and the system is more prone tolight products. On the contrary, MORE pressure pushes the conversion to long-chain hydrocarbons.
AS WELL AS outlet composition	Temperature control loop, pressure control loop	See Table 6.19
MORE Temperature in E-01 and R-01	Temperature control loop Sensors for pressure	See §6.5.4.1
Leakages or rupture	Sensors for leakages Sensors for pressure Hood	There is a release of toxic or flammable materials, so additional protective layers are required.
Loss of containment and additional final events	Sensors for leakages Sensors for pressure Hood	There is a release of toxic and flammable materials, so additional protective layers are required.

Table 6.25. Deviations of MORE pressure or flow in the pilot plant and associated safeguards.

The safeguards indicated in the HAZOP analysis are a hood, a sensor for leakages, a sensor for pressure and an alarmed high-pressure indicator (PIAH). Two existing protection layers are present, i.e., the hood and valve 10. Valve 10, although related to node 3, can handle a deviation of MORE pressure originating in node 2.

Initiating event	Frequency (yr^{-1})	IPLs 1 Valve 10 (Rupture disk)	IPLs 2 Hood (Passive IPLs)	Intermediate frequency (yr^{-1})	Tolerable frequency (yr^{-1})
PI-01fails (MORE pressure)	~ 1 [17]	0.01 [18]	0.1	$1 \cdot 10^{-3}$	$1 \cdot 10^{-4}$

Table 6.26. Existing independent protection layers to manage the failure of PI-01 in Node 2.

Intermediate frequency is higher than tolerable. The risk reduction factor equals 10, so a SIL 1 is required.

Initiating event	Frequency (yr^{-1})	IPLs 1 SIL 1	IPLs 2 Valve 10 (Rupture disk)	IPLs 3 Hood (Passive IPLs)	Intermediate frequency (yr^{-1})	Tolerable frequency (yr^{-1})
PI-01fails (MORE pressure)	≈ 1	0.1	0.01	0.1	$1 \cdot 10^{-4}$	$1 \cdot 10^{-4}$

Table 6.27. Additional independent protection layers required to manage the failure of PI-01 in Node 2.

Since the initiating event is not related to a human error but is due to misoperations, the alarmed high-pressure indicator with an operator response could be considered an independent layer of protection if the operator has been trained to act upon an alarm. Alarms with operator response can be assigned PFD = 0.1 if the independence requirements are met. More in detail, the alarmed system must be independent of the BPCS (i.e., the hardware associated with the initiating cause is not associated with the alarm), and the initiating cause does not involve an operator error.

Concerning this topic, it is worth noting that the operator's response to the alarm must be feasible and independent (see §6.4.4). The pilot plant is not continuously monitored. Therefore, the operator action coupled with the alarm cannot be considered an independent protection layer.

Initiating event	Frequency (yr^{-1})	IPLs 1 2oo3 Redundant scheme	IPLs 2 Valve 10 (Rupture disk)	IPLs 3 Hood (Passive IPLs)	Intermediate frequency (yr^{-1})	Tolerable frequency (yr^{-1})
PI-01fails (MORE pressure)	≈ 1	$3.5 \cdot 10^{-5}$ [19]	0.01	0.1	$3.5 \cdot 10^{-8}$	$1 \cdot 10^{-4}$

Table 6.28. Independent protection layers required to manage PI-01 failure in Node 2.

The additional layer of protection can be a redundant pressure sensor with a suitable MooN scheme, such as 2oo3 (discussed in §6.4.7), where the three initiators should be placed at streams 5, 7 and 8 (Figure 4.11). This scheme is a symmetrical architecture that successfully tolerates a short circuit or an open circuit failure. If a short circuit occurs, the 2oo3 structure becomes a $2oO_2$

[17] Table 11-1 of [24]
[18] Table 5.21 of [10]
[19] Table F-10 of [11]

system. On the other hand, if a unit fails as an open circuit, the redundant scheme goes from a 2oo3 structure to a 1oO₂ structure [11].

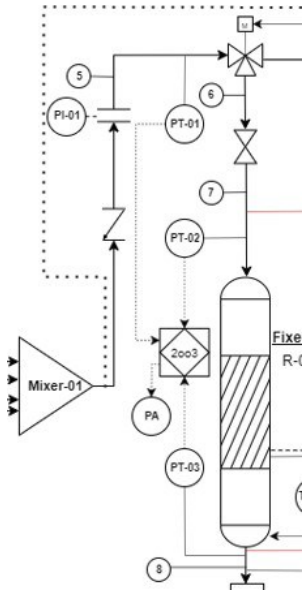

Figure 6.16. Independent protection layer based on 2oo3 redundant scheme working on 20 bar sensors (PT-01, PT-02, PT-03, SIL3 2oo3, PA). When the pressure is above 20 bar, the alarm is provided.

The 2oo3 architecture will fail dangerously only if two units fail simultaneously [11]. In this case, when two sensors fail, an alarm is provided.

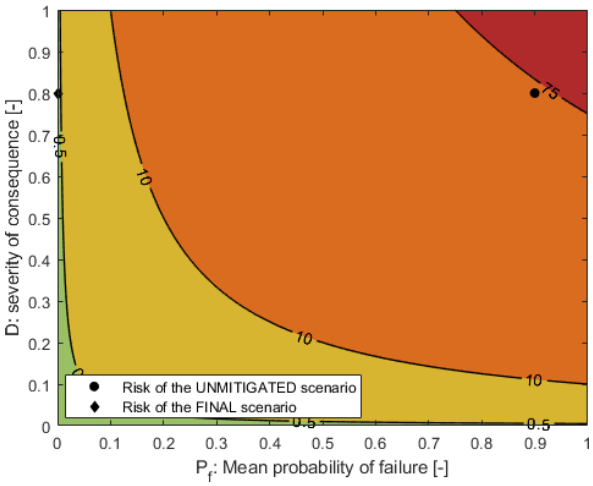

Figure 6.17. Risk class for the event PI-01 failure in Node 2 (D = 5).

Use the 2oo3 scheme instead of PI-01 to reduce the risk class from high to low.

2. Incorrect reactor packing (R-01)

When the pilot plant is shut down, the reactor is emptied, and the catalyst is entirely replaced. Previous tests showed that if the catalyst is too fine or active, the pressure inside R-01 will increase, and the equipment undergoes dangerous vibration. Possible leakages from the inlet or outlet connections can occur. In order to avoid this scenario, the following catalyst's

characteristics are already adjusted:

- Catalyst size (100-150 μm);
- Addition of an inert to the catalyst, such as SiO_2 or mineral hood.

The consequences listed in the HAZOP analysis for an incorrect reactor packing are classified as reported in Table 6.29.

Classification	Consequences
Acceptable	More conversion of CO Altered composition of products Loss of a test
Undesired	Leakages Rupture of the reactor (the reactor no longer works as expected)
Unacceptable	Explosion, injury or death

Table 6.29. Classification of consequences for the event of reactor overpacking.

Since the hazardous scenario is related to an increase in pressure, the safeguards are the following: hood, sensor for leakages, sensors for pressure, alarm sensor set at high pressure (PIAH).

The PIAH cannot be used as an independent layer of protection since the initiating event is related to a human error (§6.4.4). Since the existing protection layers are the same as in §6.5.4.4 (1) (hood and valve 10) and the classification of the hazardous scenario is preserved, final calculations are reported in Table 6.30.

		IPLs				
		1	2	3		
Initiating event	**Frequency (yr^{-1})**	**Basic process control system (BPCS)**	**Valve 10 (Rupture disk)**	**Hood (Passive IPLs)**	**Intermediate frequency (yr^{-1})**	**Tolerable frequency (yr^{-1})**
Incorrect reactor packing: overpacked reactor (MORE pressure)	1 [20,21]	0.1	0.01	0.1	$1 \cdot 10^{-4}$	$1 \cdot 10^{-4}$

Table 6.30. Independent protection layers required to manage an incorrect reactor packing in Node 2.

Without the independent layer of protection, the intermediate frequency is higher than the tolerable frequency. A control loop (BPCS) has to be added in order to decrease the frequency of the resulting scenario. The control loop should be composed of a pressure sensor measuring the process variable in stream 8, which is connected to a motorized three-way valve, as in Figure 6.18 (valve 8 should be changed with a motorized three-way valve).

[20] From Table 4.3 of [10]
[21] From Table G.3 of [9]

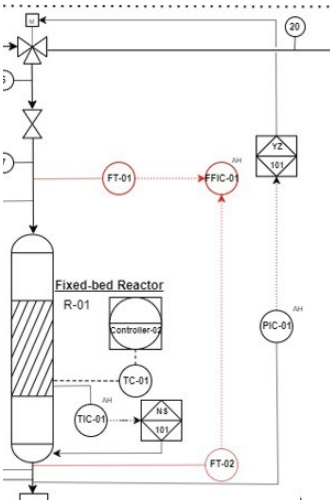

Figure 6.18. Independent protection layer based on a BPCS (PIC-01, YZ-101, motorized three-way valve). When the pressure is above 20% of the operating pressure, the motorized three-way valve changes the direction of the flow from stream 6 to stream 20.

When the pressure in stream 8 is higher than the one fixed for safety reasons, the new valve 8 automatically deviates the feeding mixture to the by-pass line.

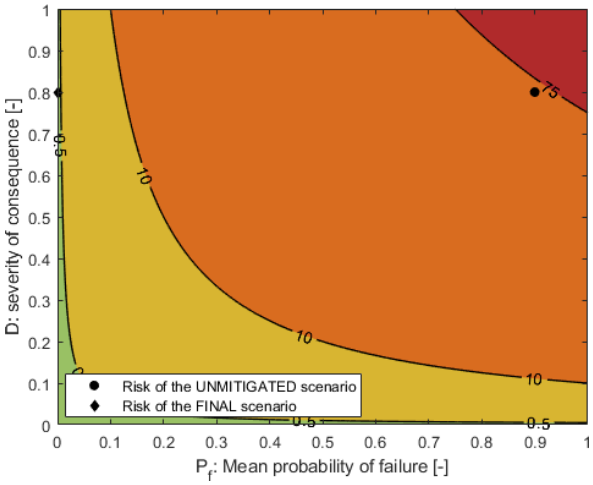

Figure 6.19. Risk class for the event of reactor overpacking in Node 2 (D = 5).

The final risk class is low when adding the BPCS as an independent layer of protection.

3. Incorrect setting of PRC-09

Selecting the set-point of PRC-09 is a manual operation done weekly. Periodic checking and recording of the setpoint should be done at least twice daily.

If the set-point is wrong, two primary deviations can be observed from R-01: MORE or LESS pressure. If the pressure increases, the flow will have the same trend (MORE flow rate), and the same is true for decreasing pressure (NO or LESS flow). When there is a decrease in pressure, the conversion of CO decreases. The main deviations are MORE flow and pressure (discussed in §6.5.4.1).

The existing independent protection layers (IPLs) are the following:

- Valve 10;
- Hood.

The intermediate frequency of the initiating event without additional IPLs is higher than the tolerable one, so a SIL1 is required. Table 6.31 provides the final analysis related to an increase in pressure and flow due to a wrong set-point of PRC-09.

Initiating event	Frequency (yr^{-1})	IPLs 1	IPLs 2	IPLs 3	Intermediate frequency (yr^{-1})	Tolerable frequency (yr^{-1})
		Basic process control system (BPCS)	Valve 10 (Rupture disk)	Hood (Passive IPLs)		
Wrong set point of PRC-09 (MORE pressure or flow)	1 [22,23]	0.1	0.01	0.1	$1 \cdot 10^{-4}$	$1 \cdot 10^{-4}$

Table 6.31. IPLs required to manage a wrong set-point of PRC-09.

The additional control system has the same characteristics as discussed in §6.5.4.4 (2), and it is represented in Figure 6.18. The resulting risk class is low.

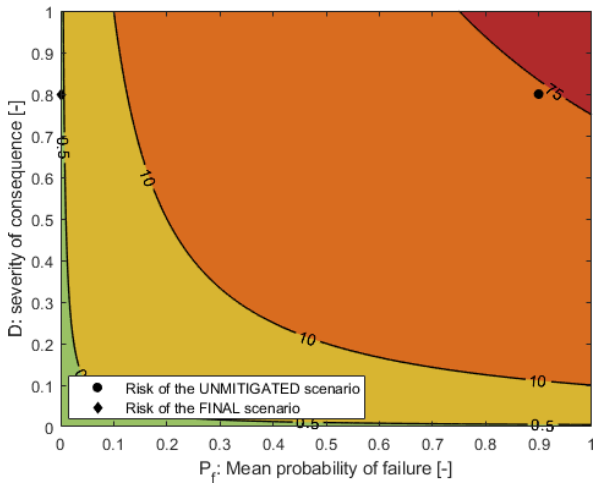

Figure 6.20. Risk class when the set-point of PRC-09 is wrong in Node 2 (D = 5).

4. Incorrect setting of TC-01

Set the set-point of TC-01 is a manual operation done almost daily, with an estimated failure frequency of 1 yr-1. The temperature inside the reactor follows a ramp, which is already defined (Fig. 6.21). The resulting hazardous scenarios are related to a higher set-point of TC-01.

[22] From Table 4.3 of [10]
[23] From Table G.3 of [9]

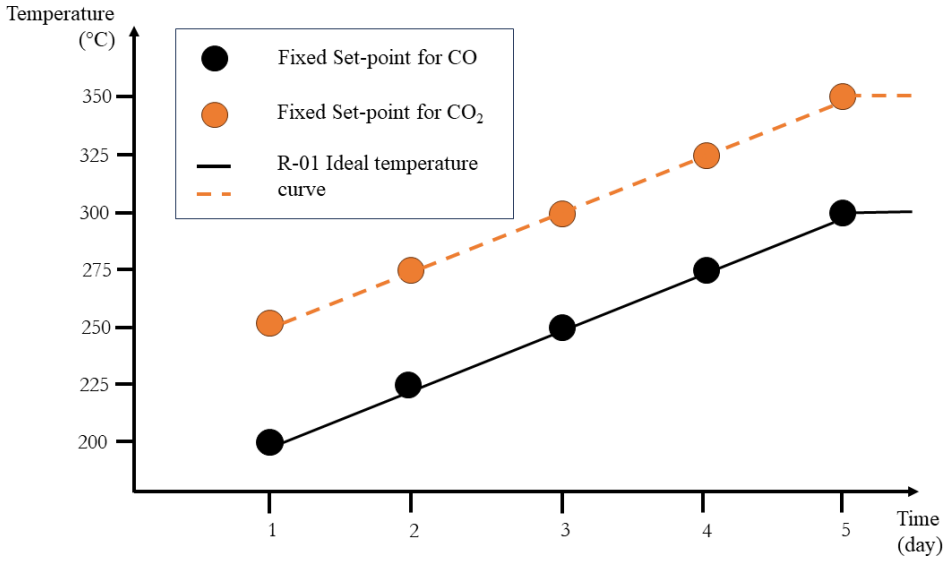

Figure 6.21. Temperature ramp in R-01 for CO and CO_2.

The consequences related to this occurrence are reported below and discussed in §6.5.4.1:

- MORE temperature, i.e., a higher amount of energy and a higher temperature than required, variation in the final composition, loss of the experimental test, higher pressure, possible leakages or ruptures, loss of containment and subsequent release of a flammable/toxic mixture, and damage to the catalyst.
- MORE reaction rate, i.e., a higher temperature, variation in the composition of the reactive mass, loss of the experimental test, increase in the heavy phase, and damage to the catalyst.

The protective layers already present are the hood and valve 10.

Initiating event	Frequency (yr^{-1})	IPLs		Intermediate frequency (yr^{-1})	Tolerable frequency (yr^{-1})
		1 Valve 10 (Rupture disk)	2 Hood (Passive IPLs)		
Wrong set point of TC-01 (MORE temperature)	1 [24,25]	0.01	0.1	$1 \cdot 10^{-3}$	$1 \cdot 10^{-4}$

Table 6.32. Existing independent protection layers to manage an incorrect setting of TC-01.

The most critical scenario is related to increased pressure and temperature, which are correlated since the mixture is in the gaseous phase. The SIL required to reduce the frequency of this peak event is 1. The possible protection layer is a safety interlock consisting of a temperature sensor connected to the reactor furnace. This sensor detects the temperature inside the reactor, and if the temperature is higher than the safety set-point (such as 400°C), the furnace is shut down.

[24] From Table 4.3 of [10]
[25] From Table G.3 of [9]

Initiating event	Frequency (yr^{-1})	IPLs			Intermediate frequency (yr^{-1})	Tolerable frequency (yr^{-1})
		1	2	3		
		Safety interlock	Valve 10 (Rupture disk)	Hood (Passive IPLs)		
Wrong set point of TC-01 (MORE temperature)	1	0.1[26]	0.01	0.1	$1 \cdot 10^{-4}$	$1 \cdot 10^{-4}$

Table 6.33. Independent protection layer required to manage an incorrect setting of TC-01.

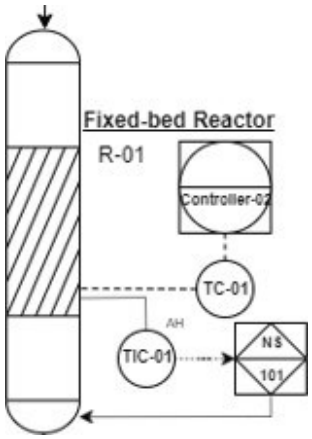

Figure 6.22. Independent protection layer based on a safety interlock (TIC-01, NS-101). The safety interlock shuts-down the furnace when the temperature measured in R-01 is above 400°C.

The resulting intermediate frequency is smaller than the tolerable one.

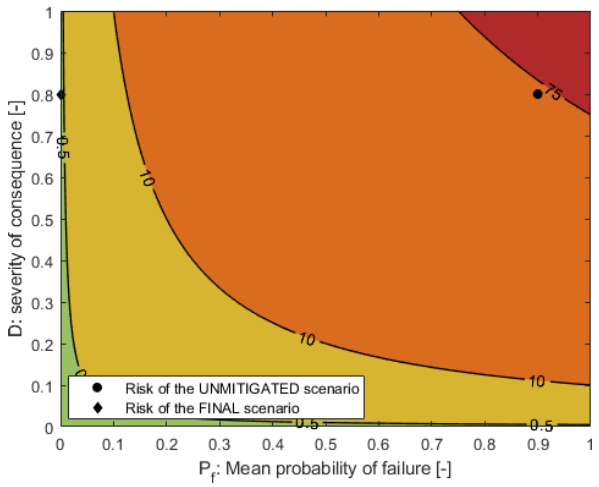

Figure 6.23. Risk class when the setting of TC-01 is incorrect in Node 2 (D = 5).

The existing independent protection layer and the addition of the safety interlock results in a low-risk classification.

[26] From Table 5.13 of [10]

5. Incorrect setting in R-01 and TC-01 during start-up

During the start-up, the temperature inside the reactor increases following a defined temperature ramp (Figure 6.24, Table 6.34).

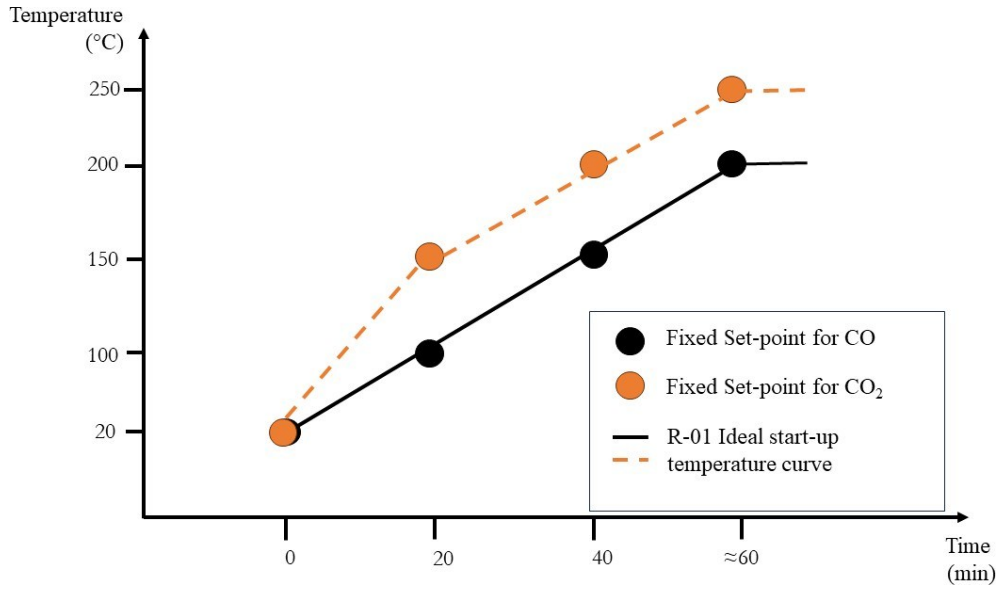

Figure 6.24. Temperature ramp during the start-up of the reactor (graphical profile).

Set point of temperature (CO)	Set point of temperature (CO_2)	Duration of the temperature step
20°C (ambient temperature)	20°C (ambient temperature)	Initial step
100°C	150°C	0
150 °C	200 °C	20 min
200°C	250°C	40 min[27]

Table 6.34. Temperature ramp during the start-up of the reactor.

The temperature profile is adjusted through a manual operation every week. Provided this time frame, the frequency of setting the wrong temperature set point is set to 1 yr-1.

This occurrence can lead to a deviation of MORE temperature inside the reactor, inducing possible damage to the catalyst (the catalyst loses its structure at temperatures above 400°C), MORE pressure, different product composition and the loss of the experimental test. According to the HAZOP analysis, the safeguards indicated are the following: a hood, a sensor for leakages, a sensor for pressure, and an alarmed high-pressure indicator (PIAH).

[27] When the set-point is achieved the operative steady-state condition starts.

Initiating event	Frequency (yr^{-1})	IPLs			Intermediate frequency (yr^{-1})	Tolerable frequency (yr^{-1})
		1	2	3		
		Safety interlock	Valve 10 (Rupture disk)	Hood (Passive IPLs)		
Set wrong temperature during the start-up (MORE temperature)	1	0.1[28]	0.01	0.1	$1 \cdot 10^{-4}$	$1 \cdot 10^{-4}$

Table 6.35. Independent protection layer required to manage an incorrect setting of TC-01 during the start-up.

The safety interlock has the same characteristics as the one discussed in §6.5.4.4 (4) (Figure 6.22). The risk of the mitigated event is classified as low (Figure 6.23).

6. Failure of R-01 connections

Two primary connections are present on R-01, which could represent a source of leakage. The safeguards include a hood and a sensor for leakages. Only a single protection layer is provided (hood). According to Table 6.36, the resulting intermediate frequency is unacceptably high.

Initiating event	Frequency (yr^{-1})	IPLs	Intermediate frequency (yr^{-1})	Tolerable frequency (yr^{-1})
		1		
		Hood (Passive IPL)		
Leakages/defective connections (LESS/NO pressure or flow)	1[29]	0.1	$1 \cdot 10^{-1}$	$1 \cdot 10^{-4}$

Table 6.36. Existing independent protection layers to manage potential leakages from R-01 junctions.

To achieve the tolerable frequency (10-4), SIL 3 is required (Table 6.37). In this regard, it should be noted that such a SIL performance is pretty high, requiring sophisticated strategies. Moreover, more than one layer of protection can be assigned, provided such layers of protection are independent.

Initiating event	Frequency (yr^{-1})	IPLs		Intermediate frequency (yr^{-1})	Tolerable frequency (yr^{-1})
		1	2		
		SIL 3	Hood (Passive IPL)		
Leakages/ defective connections (LESS/NO pressure or flow)	1	10^{-3}	0.1	$1 \cdot 10^{-4}$	$1 \cdot 10^{-4}$

Table 6.37. Additional independent protection layers required to manage potential leakages from R-01 junctions.

A suitable device could be a ratio control loop connected to a high alarm. The ratio control loop consists of two mass flow transmitters arranged across R-01 and connected to a ratio controller. The ratio controller compares the two flow rate signals, and if the ratio is greater than 1.2, the

[28] From Table 5.13 of [10].
[29] No data are found (conservative approach).

signal is activated, and the operator must initiate an appropriate procedure to shut down the equipment. An increasing differential value measured is indicative of a leakage from the plant section. This control loop should be switched on and off every week, as it must only be active when the process is in continuous operation. In fact, during transients (i.e. start-up and shut-down) can be detrimental.

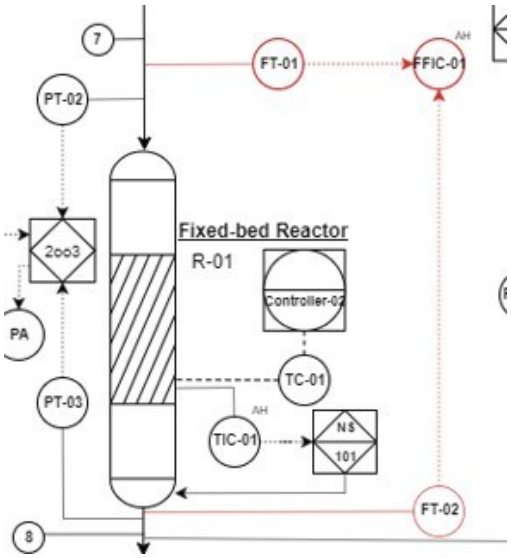

Figure 6.25. Protection layer based on a ratio controller with a high alarm (FT-01, FT-02, FFIC-01). The alarm is activated when the ratio between the signal from FT-01(mass-flowrate) and the signal from FT-02 (mass-flowrate) is above 1.2.

According to the proposed features, this control loop and operator response cannot be considered an independent protection layer since the operation is not monitored 24 hours a day. In addition, there could be an additional source of human error when activating the proposed procedure. According to the LOPA approach, the initiating event discussed can not be adequately managed under the current framework, and the resulting frequency is above the tolerability limit (Table 6.36).

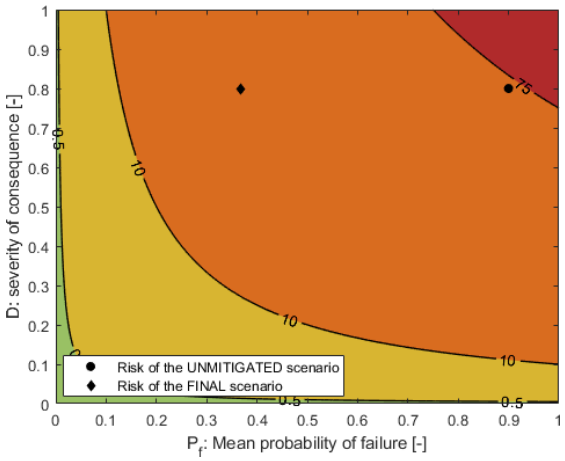

Figure 6.26. Risk class in the case of the failure of R-01 primary connections in Node 2 (D = 5). According to the LOPA analysis, in the current framework the scenario is still unprotected.

7. Deviations related to transients of R-01 (start-up or shut-down)

The experimental apparatus is shut down weekly. On that occasion, the reactor is emptied to replace the deactivated catalyst with a new one. The following two hazardous events could result from a human error in performing the requested tasks:

- TOO EARLY reactor opening before the feed is closed. This can lead to a loss of containment with subsequent severe final scenarios, including releasing a flammable or toxic material.
- TOO LATE reactor closure after the feed is opened. Similarly to the previous event, this induces a loss of containment of hazardous materials.

These two events can only be ascribed to a human error. The occurrence frequency is equivalent since the two events are correlated. In addition, both scenarios give a loss of containment, so they are analyzed similarly. According to the HAZOP analysis, possible safeguards include a hood and a sensor system. A single independent protection layer is already provided, i.e., the hood.

Initiating event	Frequency (yr^{-1})	IPLs	Intermediate frequency (yr^{-1})	Tolerable frequency (yr^{-1})
		1		
		Hood (Passive IPL)		
TOO EARLY reactor opening/ TOO LATE reactor closure [30]	1	0.1	$1 \cdot 10^{-1}$	$1 \cdot 10^{-4}$

Table 6.38. Existing independent protection layers to manage leakages during transients of R-01 (start-up or shut-down)

The resulting RRF is equal to 1000, so a SIL3 is required.

Initiating event	Frequency (yr^{-1})	IPLs		Intermediate frequency (yr^{-1})	Tolerable frequency (yr^{-1})
		1	2		
		SIL 3	Hood (Passive IPL)		
TOO EARLY reactor opening/ TOO LATE reactor closure	1	10^{-3}	0.1	$1 \cdot 10^{-4}$	$1 \cdot 10^{-4}$

Table 6.39. Additional independent protection layers to manage leakages during transients of R-01 (start-up or shut-down).

Under the current configuration, it is impractical to add independent protection layers to manage leakages during transient operations. The resulting risk class is equivalent to that reported in Figure 6.26. It should be considered that there are detectors connected to solenoid valves (valves 4) in the same room, which are FC (fail closed) when at least one of the following gases is detected: H_2, CO, CO_2 or CH_4. The detection system can be intended as the sole protection layer able to manage the initiating events under consideration. According to what is stated in §6.5.4.4 , it can not be considered an independent layer of protection.

[30] Too early refers to opening the reactor R-01 without interrupting the feeds to the experimental setup. Too late refers to closing the reactor R-01 after the feeds have been opened.

8. Deviations related to an electrical power outage

When there is a power outage, the process could behave differently than expected. As said in §6.5.4.2 and §6.5.4.3 (2), when a voltage or power variation is experienced, valves 4 close, and the consequences listed in Table 6.40 can be observed.

Equipment	Consequences
Streams: 1.3, 2.3, 3.3	MORE pressure (§6.5.4.1).
Streams from: 1.4, 2.4 and 3.4	LESS pressure (R-01, E-01, D-01).
Reactor R-01	LESS pressure and temperature: the furnace of R-01 does not work. LESS reaction rate is an associated consequence.
Heat exchangerE-01	LESS pressure and temperature: E-01 does not heat the product mixture.Partial condensation of streams 8, 9, 10, 11 and 12 is an associated consequence. Moreover, a blockage in the piping can be expected. An escalating scenario involves a credible loss of containment.
D-01 (Node 3)	LESS pressure and temperature: the temperature of 5°C is not maintained. Partial condensation of hydrocarbons is an associated consequence (poor separation during an experimental test).

Table 6.40. Equipment involved and primary consequences in the case of a power outage.

Since one of the possible consequences is the loss of containment, especially when the power outage affects the heat exchanger E-01, the hood can be considered an independent protection layer.

Initiating event	Frequency (yr^{-1})	IPLs 1 Hood (Passive IPL)	Intermediate frequency (yr^{-1})	Tolerable frequency (yr^{-1})
Power outage (LESS/NO electric voltage)	1 [31]	0.1	$1 \cdot 10^{-1}$	$1 \cdot 10^{-4}$

Table 6.41. Existing independent protection layers to manage a scenario of power outage.

The SIL required to decrease the frequency of the initiating event is SIL 3. Therefore, a high-performance strategy is required.

Initiating event	Frequency (yr^{-1})	IPLs 1 SIL 3	IPLs 2 Hood (Passive IPL)	Intermediate frequency (yr^{-1})	Tolerable frequency (yr^{-1})
Power outage (LESS/NO electric voltage)	1	0.001	0.1	$1 \cdot 10^{-4}$	$1 \cdot 10^{-4}$

Table 6.42. Additional independent protection layers to manage a scenario of power outage.

[31] From personal communication with the operators of the pilot plant. Such a scenario has been experienced statistically one time per year.

Possible protective layers can include the following:

- Backup utility supplies;
- AutoStart of standby equipment. These are discussed in Section §6.4.9.

Initiating event	Frequency (yr^{-1})	IPLs			Intermediate frequency (yr^{-1})	Tolerable frequency (yr^{-1})
		1	2	3		
		Backup utility supplies	AutoStart of standby equipment	Hood (Passive IPL)		
Power outage (LESS/NO electric voltage)	1	0.1 [32]	0.1 [33]	0.1	$1 \cdot 10^{-3}$	$1 \cdot 10^{-4}$

Table 6.43. Required independent protection layers to manage a scenario of power outage.

The final frequency is higher than the tolerable one, but no additional protection layer can be added. So, the event of a power outage and associated consequences is a partially protected scenario. Further strategies are required, including a variation of the design of the experimental setup.

The final risk class of the scenario, once the proposed independent layers are added, is low (Fig. 6.27).

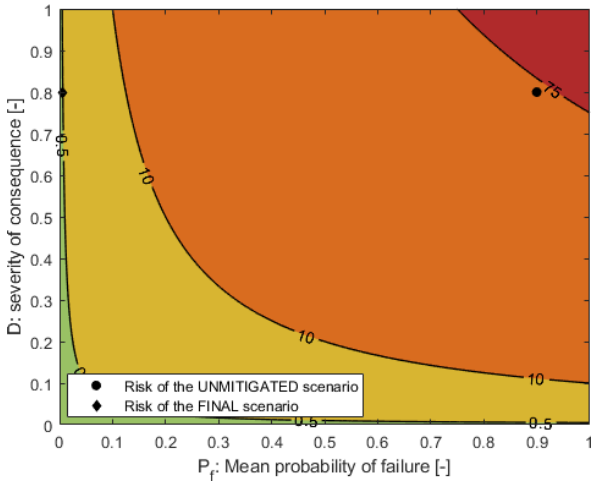

Figure 6.27. Risk class when there is a power outage in Node 2 (D = 5). According to the LOPA analysis, in the current framework the scenario is still unprotected.

9. Deviations related to catalyst poisoning in R-01

According to the design intent, the reactants fed to the process are pure, so no catalyst poisoning exists. A variation in the feed quality can modify the experimental run by introducing poisonous compounds, including:

- Sulphur: formation of stable sulfuric compounds;
- Phosphorus: formation of stable compounds;

[32] §4.6.12 of [6]
[33] §4.6.4 of [6]

- Halogens: inhibition of active sites (increased danger: iodine, bromine, chlorine, fluorine);
- Heavy hydrocarbons: formation of carbon residues.

Table 4.39 illustrates the classification of the consequences. According to Table 4.39, unacceptable consequences are not expected, and the primary concern is due to the increase of the internal pressure in the experimental equipment. The main effects of introducing poisons in the catalytic reactive system are related to a loss of the experimental test because of an altered composition of the products.

Classification of consequences	Detail of consequences
Acceptable	AS WELL AS final composition, i.e., altered product mixture.MORE flow rate of gaseous components. Loss of an experimental test.
Undesired	MORE pressure (see §6.5.4.1)
Unacceptable	-

Table 6.44. Classification of the consequences in the case of catalyst poisoning.

For the scenario concerning the poisoning of the catalyst, the LOPA analysis is not carried out since the presence of toxic compounds cannot be prevented or managed unless a prior control of the composition of the reactants is carried out (composition of T-01, T-02, T-03, T-04).

6.5.4.5. Deviations in Node 3: the separation section

Node 3 purpose is to separate the heavy phase from the light phase. The stream from E-01 is made of a gaseous phase where different substances are present: C2-C6, water, C7-C30 and incondensable gases (CO, CO_2, H_2 and N2). Table 6.45 shows which are the usual composition of stream 8 (R-01 outlet stream).

Component	mol. %	Component	mol. % dry basis
Methane	5	Methane	2
Carbon dioxide	15	Carbon dioxide	41
Water	50	C_2-C_6	17
Hydrocarbons (C_2-C_{30})	30	C_7-C_{30}	40

Table 6.45. Composition of stream 8 according to the design intent. Total flowrate: 40-50 ml/min.

The light phase is composed of C2-C6 and incondensable gases fed to Node 4. The heavy phase condenses inside D-01, consisting of water and C7-C30.

1. **Deviations related to PRC-09**

PRC-09 is already analyzed in §6.5.4.4 (3) but is connected to valve 15 of Node 3. If the pressure set point exceeds the intended operating condition, pressure and flow may increase.

The additional independent protection layer designed to manage the outcoming scenario is reported in Table 6.31. An additional protection layer is valve 12, a flanged valve (pressure relief device, §6.4.5) managing the increase in pressure in D-01.

2. Deviations related to PI-02

The comments are similar to those reported in §6.5.4.4 (1).

Deviation	Primary safeguard	Comments
MORE pressure in D-01	Basic process controlsystem (BPCS) of pressure	If PI-02 is not working properly, the actual pressure can be higher than the design intent. A direct consequence is the poor performance ofthe separation. A redundant pressure indicator is a suggested IPL for managing this deviation.
AS WELL AS product composition (altered outlet composition due to poor separation)	-	A deviation of MORE pressure in D-02 reduces the performance of the separation of stream 12.
Loss of the experimentaltest	-	-
Leakages or rupture Loss of containment andadditional final events	Sensors for leakages Sensors for pressure Hood	Flammable or toxic materials can be released. If the unprotected frequency is higher than tolerable, additional IPLs are required.

Table 6.46. Consequences related to the event of pressure increases due to PI-02 not working properly.

Considering the deviation of MORE pressure, the existing protection layers are Valve 10, 12 and the hood, respectively. The corresponding mitigation performance on the initiating event frequency is reported in Table 6.47.

Initiating event	Frequency (yr^{-1})	IPLs			Intermediate frequency (yr^{-1})	Tolerable frequency (yr^{-1})
		1	2	3		
		Valve 10 (Rupturedisk)	Valve 12	Hood (Passive IPLs)		
PI-02 fails (MORE pressure)	≈ 1 [34]	0.01	0.01 [35]	0.1	$1 \cdot 10^{-5}$	$1 \cdot 10^{-4}$

Table 6.47. Independent protection layers required to manage a PI-02 failure.

As indicated, the actual protection layers are sufficient to manage the event, provided the resulting frequency is lower than the tolerable threshold assigned to the expected consequences class.

[34] Table 11-1 of [24]
[35] Table G.7 of [9]

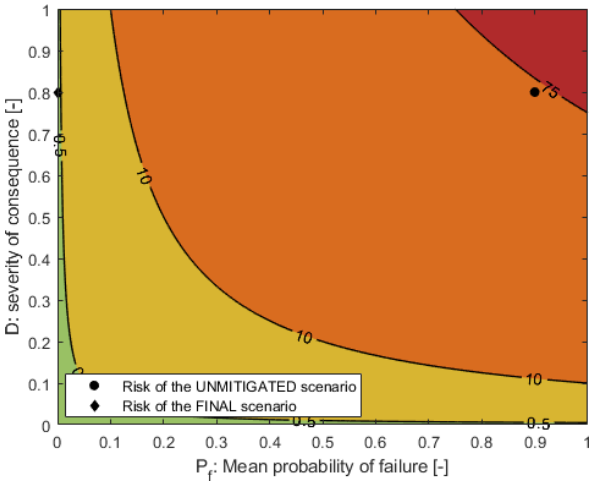

Figure 6.28. Risk class in the case of an event related to a failure of PI-02 in Node 3 (D = 5).

The resulting risk class is low (Figure 6.28).

3. Deviations related to an electrical power outage

The consequences of a power outage for Node 3 are reported in Table 6.40.

Initiating event	Frequency (yr^{-1})	IPLs 1 — Pressure relief device (valve 12)	IPLs 2 — Hood (Passive IPLs)	Intermediate frequency (yr^{-1})	Tolerable frequency (yr^{-1})
Power outage (LESS/NO electric voltage)	1	0.01	0.1	$1 \cdot 10^{-3}$	$1 \cdot 10^{-4}$

Table 6.48. Existing independent protection layers to manage a power outage in Node 3.

From Table 6.48, the resulting RRF equals 10, so a SIL 1 is required, provided that the existing layers of protection are insufficient to provide the required safety level. Among the possible protective layers, the following are considered (as in §6.5.4.4 (8)):

- Backup utility supplies;
- AutoStart of standby equipment.

Initiating event	Frequency (yr^{-1})	IPLs 1 — SIL 1	IPLs 2 — Valve 12	IPLs 3 — Hood (Passive IPLs)	Intermediate frequency (yr^{-1})	Tolerable frequency (yr^{-1})
Power outage (LESS/NO electric voltage)	1	0.1	0.01	0.1	$1 \cdot 10^{-4}$	$1 \cdot 10^{-4}$

Table 6.49. Additional independent protection layers required to manage a power outage in Node 3.

Initiating event	Frequency (yr^{-1})	IPLs				Intermediate frequency (yr^{-1})	Tolerable frequency (yr^{-1})
		1	2	3	4		
		Backup utility supplies	AutoStart of standby equipment	Valve 12	Hood (Passive IPLs)		
Power outage (LESS/NO electric voltage)	1	0.1 [36]	0.1 [37]	0.01	0.1	$1 \cdot 10^{-5}$	$1 \cdot 10^{-4}$

Table 6.50. Independent protection layers required to manage a power outage in Node 3.

The final frequency is lower than the tolerable one. The risk class of the mitigated scenario is low.

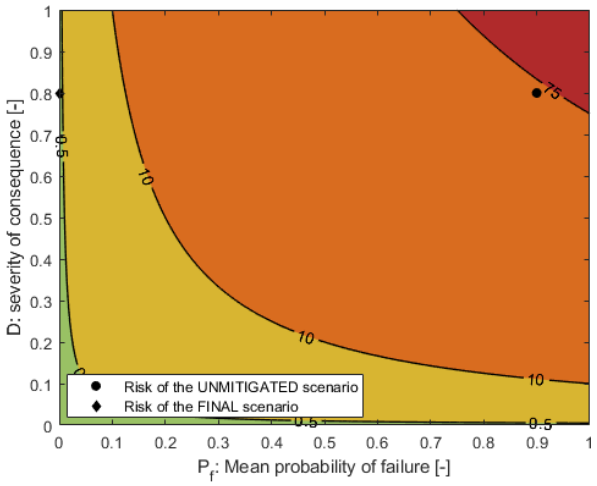

Figure 6.29. Risk class when there is a power dip (Node 3) (D rank= 5).

6.5.4.6. Deviations in Node 4: the analysis of the gaseous phase.

Node 4 purpose is to define the composition of the light phase from the cold trap. The equipment used is a Micro CG, which works under isothermal conditions (60°C), and the time required for the analysis cycle is around 3 minutes.

This node is not related to initial events with a risk classification of A, B or C. Therefore, no LOPA is required, and the scenarios associated with Node 4 are minor.

6.5.5. Final comments on the protection layers

According to the HAZOP analysis, the experimental setup for Fischer-Tropsch synthesis has been divided into four nodes. A set of deviations and credible consequences and recommendations have been identified. Moreover, the HAZOP has shown that a specific set of deviations is characterized by a moderate-to-severe risk, requiring proper layers of protection. In the case of risk classes A-C, a subsequent LOPA has been established to quantify the risk reduction target.

Figure 6.30 provides the improvements proposed by the combined HAZOP-LOPA, in which specific sets of IPLs are provided to manage unprotected or insufficiently protected events.

[36] For further details refer to §4.6.12 of [6].
[37] For further details refer to §4.6.4 of [6].

The primary concern is related to a prominent set of manual operations, in which misoperations or errors can lead to relevant deviations in the process parameters. Moreover, releasing material from the apparatus is always an undesired event, even if proper protection layers are already in place.

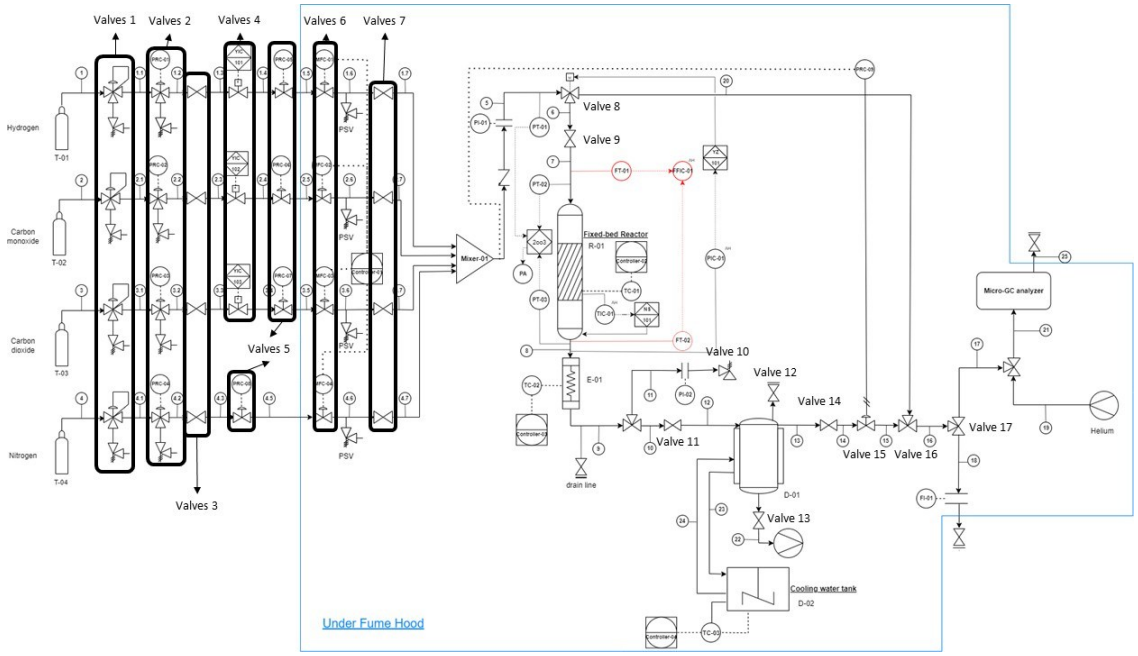

Figure 6.30. Improved process diagram of the experimental setup following the recommendations emerged from the combination HAZOP-LOPA.

Additional components	**Notes**
Pressure safety valves (PSVs) between valves 6 and 7	The scenario managed concerns the pressure increase after valves 5.
2oo3 redundant scheme of PI-01/02	This accommodates a SIL 3 requirement for managing failures of the pressure indicators. The strategy is also helpful in avoiding manual misoperations induced by a hardware error in indicating the pressure tothe operator.
TIC-01 interlocked	This architecture shuts down the furnace if the temperature in R-01 isabove the safe threshold (400°C).
PIC-01 automatic pressure control	This automatic control loop acts when the pressure in stream 8 is above the threshold (> 20% of the operating pressure). Valve 8 changes direction from stream 6 to stream 20 (bypass line)
FFIC-01 ratio control	This control cannot be considered as an IPL. It compares the two signals from FT-01 and FT-02, which measures the mass flowrate respectively before and after R-01. When the ratio between the twosignals is above 1.2, the alarm starts.
Drain line	The drain line is essential to remove liquid residues in stream 9.
NRV in stream 5	The non-return valve avoids reverse flow downstream of the mixing of reactants.

Table 6.51. Additional equipment, systems and layers of protection required for the experimental setup.

The main modifications on the experimental setup, driven by the structured quantitative risk assessment, are listed in Table 6.51.

As there are multiple connections and valves in the system, an additional consideration can be made for leaks. When leaks occur, a difference in mass flow rates can be observed. This difference in flow rates cannot be considered across reactor R-01 since volumetric data can change due to chemical reactions. Figure 6.31 shows an option for arranging the flow indicators (FI) in Node 2. If the coupled flow rates measured in 1-2 or 3-4 are significantly different, a leakage can be expected in the monitored section. Periodic soapy testing along the piping and periodic inspection of seals, gaskets, and joints should be performed to avoid potential sources of leakage.

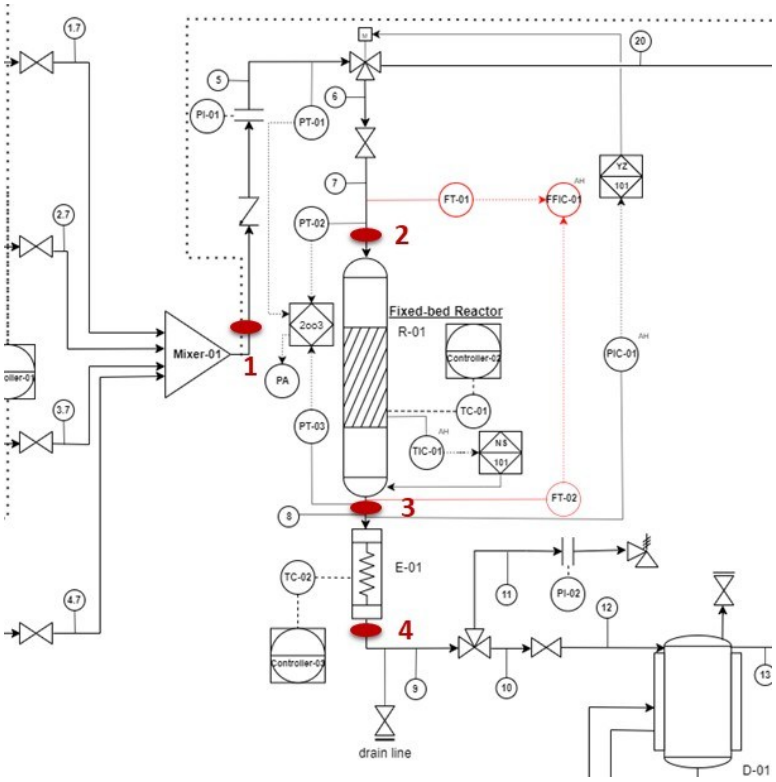

Figure 6.31. Arrangement of mass flow indicators (FIs) to detect eventual leakage occurring in node 2. A relevant variation of data provided by the sensors is representative of leakages affecting the monitored sections of the experimental setup.

Finally, the numbering of the valves and, more generally, of the equipment should be updated to avoid mistakes due to the non-unique labeling of process equipment.

6.5.6. Conclusions

This work discussed safety engineering and management in an academic environment, specifically in relation to the risk assessment of an experimental setup used for Fischer-Tropsch synthesis. Due to the unique nature of experimental setups and academic settings, a combined Hazard and Operability Analysis (HAZOP) and Layers of Protection Analysis (LOPA) were implemented. This allowed for the inclusion of specific features that characterize these frameworks, such as the impact of manual procedures and transient operations.

The first section of the work focused on the analysis of the frameworks while discussing accident statistics and the leading factors that contribute to hazards and risks in pilot plants and academic settings.

The experimental setup used for Fischer-Tropsch synthesis was then analyzed in terms of operability issues through a structured HAZOP analysis. High-risk deviations and related scenarios were identified, some of which were not sufficiently protected against the associated consequences. The Fischer-Tropsch reactor and the feeding section were identified as the most critical nodes, in relation to which different manual procedures were expected.

A subsequent LOPA analysis was conducted, which allowed for the identification of proper preventive and mitigative strategies while assessing the features of protection layers, both automatic and human-action-based. Recommended measures included the automation of the experimental setup, embedding safety interlocks and devices, automatic control loops, and redundant schemes. Special attention was given to the impact of manual operations and settings on the establishment of hazardous or risk scenarios and specific hazardous frameworks that may be present in experimental apparatus like that analyzed. Unlike usual risk assessment approaches, the presence of laboratory infrastructures and equipment (e.g. hood, ventilation, and procedures) was included when assessing the functionality of specific risk reduction measures.

APPENDIX

A.1 Instrumented diagram of the experimental setup

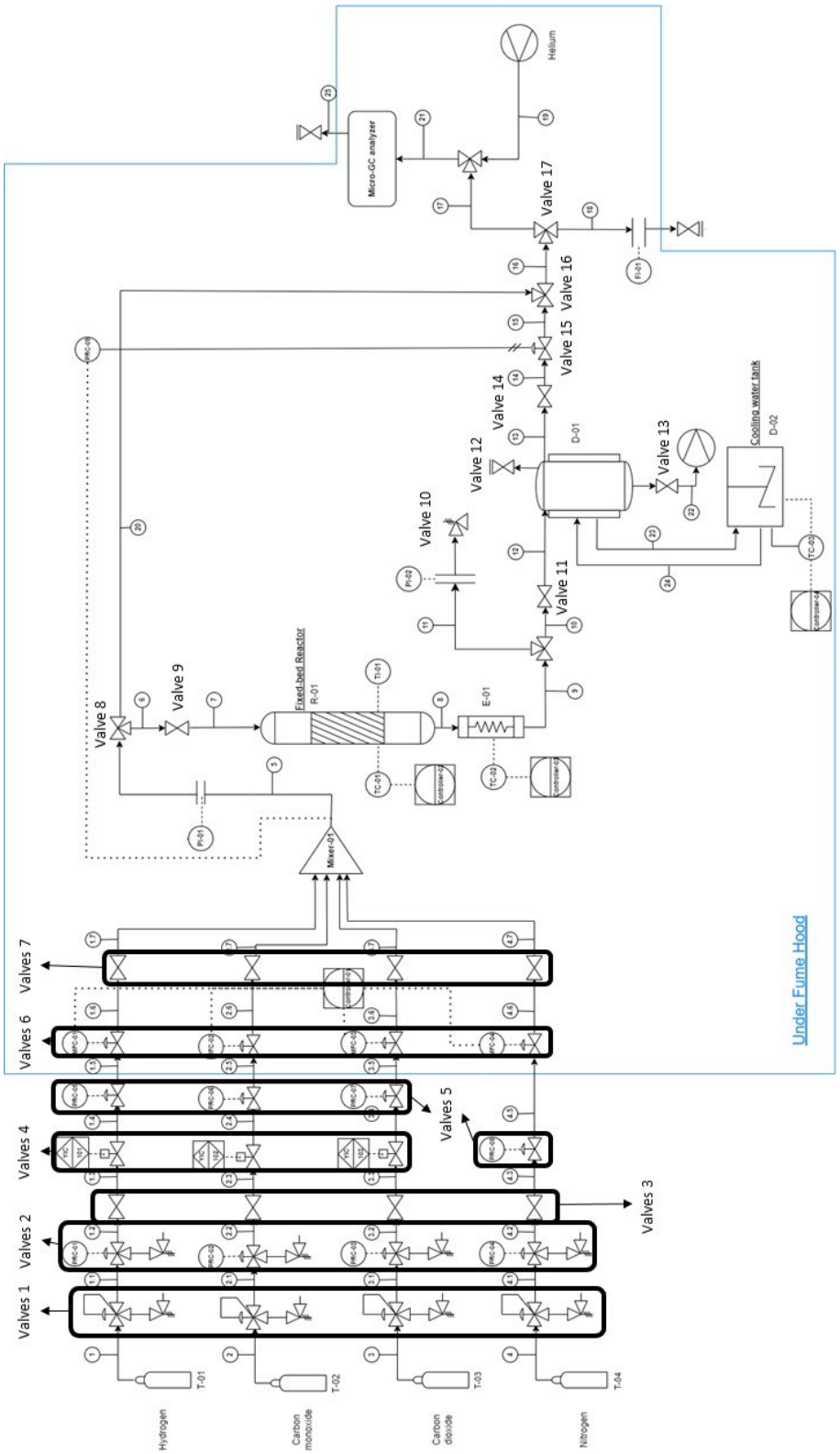

Figure A.1.1: Instrumented diagram of FT pilot plant with details on thevalve systems.

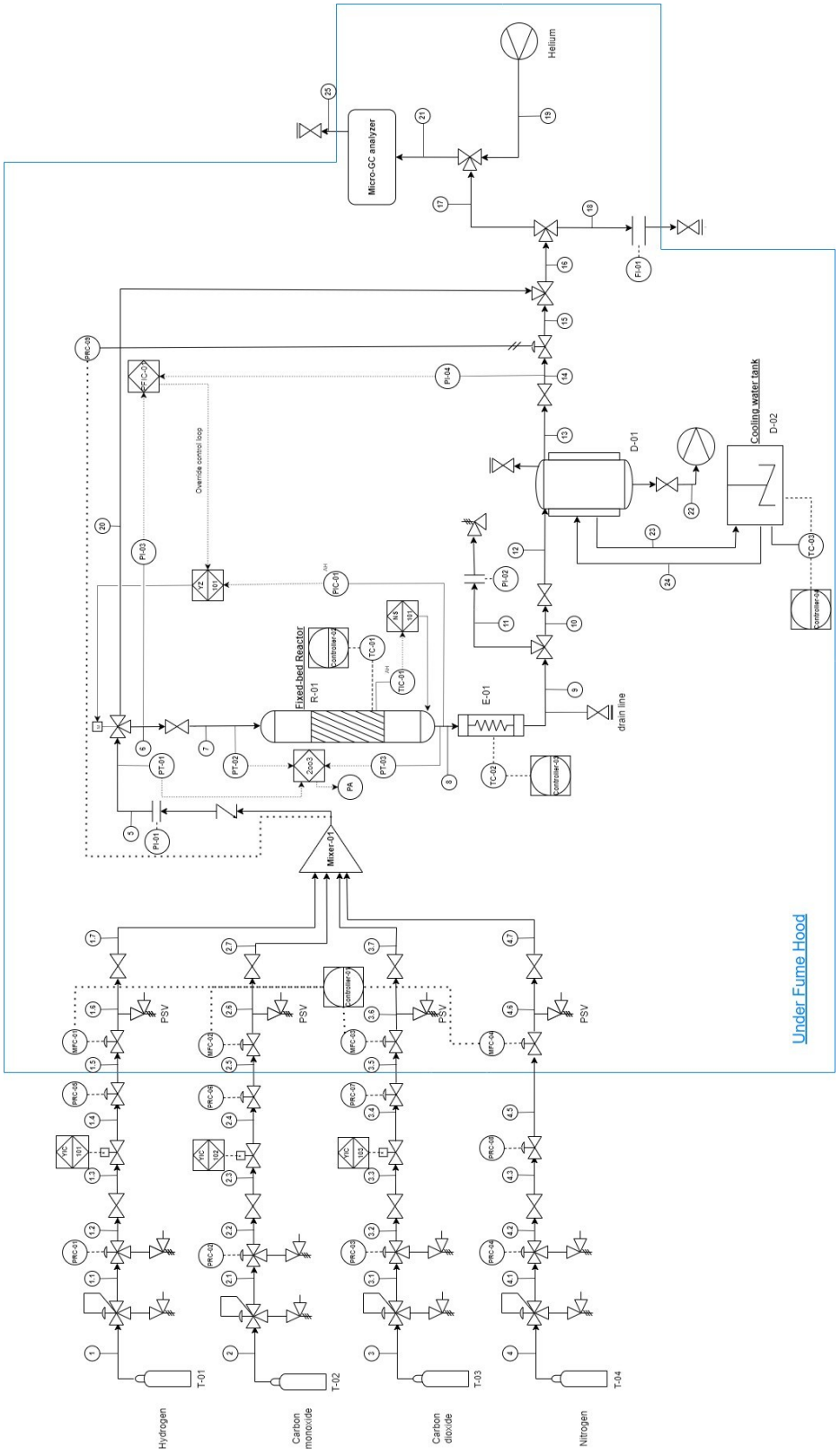

Figure A.1.2: Instrumented diagram of FT pilot plant

A.2 Specifications of the valves used in the experimental setup

Valve	Description	Fail open (FO) or fail close (FC)	Number of times the valve is touched (month^{-1})
01	Self-regulating valve and pressure safety valve with the function of avoiding the MAWP. Safety valve size: 6 x 3 cm (length x width)	FC	0
02	Control valve (PRC and three-way) and pressure safety valve with the function of decreasing the pressure from 180 to 40 bar and avoiding the MAWP. Safety valve size: 7 x 3 cm (length x width)	FC	0
03	Ball-valve (open manual isolation valve) with the function of isolation	FC	0
04	Solenoid valve (with a gas detection system) with the function of shutting off the plant in the case of a leakage	FC	0
05	Pressure regulator (control valve with PRC), i.e. pressure reduction from 40 to 5-10 bar	FC	1
06	Mass flow meter (control valve with MFC), with the function of realizing the correct composition in Mixer-01	FC	5
07	Open-close valve with the function of isolation	FC	5
08	Three-way valve (open manual isolation valve) with the function of isolation	FC	1
09	Open manual isolation valve with the function of isolation	FC	10
After E-01 (three-way valve)	It is a tee junction serving the safety valve 10	-	0
10	Pressure relief valve working at 51.7 bar Size: 2.5 x 2 cm (length x width)	Rupture disk valve	0
11	Open manual isolation valve with the function of isolation	FC	10
12	Nupro gas shut-off valves with the function of relief	FC	0
13	Nupro gas shut-off valves with the function of sampling	FC	5
14	Open manual isolation valve with the function of isolation	FC	10
15	Back pressure regulator valve with the function of pressure regulation	FC	0
16-17	Three-way valve and open manual isolation valve, i.e. a tee junction and a valve driving to the analyzer section	FC	10
After the rotameter	Flanged valve with the function of relief (out of the hood)	FC	0
Before GC	Three-way valve with the function of isolating the analyzer section	FC	20
After GC	Flanged valve with the function of relief (out of the hood)	FC	0

Table A.2.1: List and specifications of the valves.

A.3 Main equipment of the experimental setup

Equipment	Description
Pipes	Material: SS316 MAWP (maximum allowable working pressure): 80 bar
H_2 Detector	Valve-04 communicates with the gas detector Detection range: 0-100% LFL Alarm: 10% max detection value
CO Detector	Valve-04 communicates with the gas detector Detection range: 0-500 ppm Alarm: 10% max detection value
CO_2 Detector	Valve-04 communicates with the gas detector. Detection range: 0-500 ppm Alarm: 10% max detection value
CH_4 Detector	Valve-04 communicates with the gas detector. Detection range: 0-100%LFL Alarm: 10% max detection value
H_2 Mass flow meter	Product: Mass flow meter SLA5860 Manufacturer: Brooks instruments Flow range: 0.003-50 slpm P max: 1500 psi/103 bar Accuracy: ± 0.6% of SP T limits: 0-65°C Seal material: elastomeric Wetted parts: SS with Viton
CO Mass flow meter	Product: Mass flow meter SLA5860 Manufacturer: Brooks instruments Flow range: 0.003-50 slpm P max: 1500 psi/103 bar Accuracy: ± 0.6% of SP T limits: 0-65°C Seal material: elastomeric Wetted parts: SS with Viton
CO_2 Mass flow meter	Product: Mass flow meter SLA5860 Manufacturer: Brooks instruments Flow range: 0.003-50 slpm P max: 1500 psi/103 bar Accuracy: ± 0.6% of SP T limits: 0-65°C Seal material: elastomeric Wetted parts: SS with Viton
N2 Mass flow meter	Product: Mass flow meter SLA5860 Manufacturer: Brooks instruments Flow range: 0.003-50 slpm P max: 1500 psi/103 bar Accuracy: ± 0.6% of SP T limits: 0-65°C Seal material: elastomeric Wetted parts: SS with Viton
Flow input controller (Controller-01A): CO_2	Gas and liquid mass flow secondary electronics Controller 0254 Manufacturer: Brooks instruments

	Power input: Voltage: 12-24 Vdc required, -15 Vdc permitted Current: 400 mA max current per channel Instrument power draw: 0.8 Watts Power Output: +15V/2.0 A, -15 V/1.0 A or 12-24 Vdc/2.0 A Signal Input/Output: 0(1)-5 V, 0(2)-10 V, 0(4)-20 mA Operating T: 0-50°C, 0-95% non-condensing
Flow input controller (Controller-01B): H_2, CO, N2	Gas and liquid mass flow secondary electronics Controller 0154 Manufacturer: Brooks instruments Power Input: 0-260 Vac, 50/60 Hz 70 W Power Output: +15V/2.9 A, -15 V /1.4 A max or 24 Vdc/2.5 A max Signal Input/Output: 0(1)-5 V, 0(4)-20 mA Operating T: 0-50°C
Mixer (Mixer-01)	Mixing chamber up to 4 gaseous Material: SS 316
Pressure indicator (PI-01)	Differential Bourdon manometer Manufacturer: Tagliabue manometri Material: 304 SS T max: 100°C Degree of protection: IP65 Operating pressure: max 90% of full-scale value
Reactor furnace (R-01)	Tubular wired heating furnace Manufacturer: Fornomab Srl T max: 900°C Power: 900 Watt Electric potential: 230 V
Temperature indicator and temperature controller of reactor furnace (respectively: TI-01 and TC-01)	P108- Temperature/ Process Controllers, Temperature indicator Manufacturer: Eurotherm ltd Operating temperature: 0 to 55°C 24 V ac/dc supply voltage Sample rate: 4 Hz (250 ms) Protection class: IP66, IP65 Coupled with two K-type thermocouples
Electric heater (E-01)	Wired electric heater Manufacturer: Colaver srl Material: fiberglass
Temperature controller of electric heater (TC-02)	-
Pressure indicator (PI-02)	Pressure gauge ind PGI-63B Manufacturer: Swagelok Material: SS316 T max: 60°C P min: 0 bar P max: 60 bar T min: -40°C Lens gasket: Buna N
Cold trap (D-01)	Flanged cooling jacket reservoir Manufacturer: Sofferia Sestese Material: SS316 V: 192 ml Equipped with valve 12 and 13 and flanged via 4 screws

Water tank (D-02)	CRIOTERM 190 ISCO Manufacturer: ISCO Material: Aluminium
Temperature controller (TC-03)	ISCO GTR 90 Manufacturer: ISCO T range: -9.9°C to +104.9°C Heating power: 1.05 kW to 230 V Pump capacity: 1.7 m Pump flow: 8 l/min Temperature stability: 0.05°C
Bubble flow-meter: rotameter (F-01)	Material: glass Capacity: 120 ml Tightness: O-ring Junction with the plant through a plastic tube clamped on the joints
Micro-GC	Micro-GC 3000 A Manufacturer: Agilent

Table A.3.1: Main equipment of the experimental setup.

A.4 Operative conditions of the experimental setup

Part of the plant	Operative conditions
T-01, T-02, T-03, T-04	Gas cylinders: respectively H_2, CO, CO_2, N2 P =180 bar Sizes (each, G2 classified cylinder tank): 10.2 m^3 T = ambient
Gas detectors	Respectively: H_2, CO, CO_2, CH_4 Detection range H_2: 0-LEL ppm (LEL: 4%) Detection range CO: 0-500 ppm (LEL: 12%) Detection range CO_2: 0-500 ppm (IDLH: 40000 ppm) Detection range CH_4: 0-LEL ppm (LEL: 5%) Alert sound (for all the detectors): 10% of the maximum detection range value
PRC-01, PRC-02, PRC-03,PRC-04	Pressure control from 180 bar to 40 bar
PRC-05, PRC-06, PRC-07,PRC-08	Pressure control from 40 bar to 5-10 bar
MFC-01, MFC-02, MFC-03,MFC-04	The MFCs are connected to controller-01, which has a panel control where the operator sets the fluxes of each substance. The total flux is equal to 50 ml. 1. H_2/CO/N2: 30/15/5 ml/min (H_2/CO=2) 2. H_2/CO_2/N2: 30/10/5 ml/min (H_2/CO_2=3)
Mixer	All the streams are mixed
PI-01, PRC-09	The line works under P =20 bar
Reactor	The reactor is made of (external) stainless steel, (internal) unknown (probably ceramicfiber). Temperatures: 1. With CO: 200-300°C @ 20 bar 2. With CO_2: 250-350°C @ 20 bar A ramp is applied starting from the lowest temperature reported (respectively 200 and250°C) for day one. On the following days, 25°C/day are added to obtain the final temperature during the 5^{th} day (Figures A.4.1-2). The furnace of the reactor is electrical.
TC-01, TI-01, Controller-02	TI-01 is a thermocouple, and the signal received by Controller-02 coupled with TC-01that governs the reactor temperature. The reactor SP temperature is manually set on a daily basis.
E-01	Wired electric heater made of fiberglass T=60÷80°C The main purpose is to maintain the products in the gas phase

TC-02, Controller-03	The temperature is indirectly set by an operator, acting on the power of E-01 through Controller-03. The controller sends a signal to TC-02 in order to obtain a temperature within 60-80°C.
PI-02	Pressure gauge. P = 20 bar.
D-01: Cold trap	Flanged cooling jacket reservoir. T = 5°C.
D-02: Cooling water tank(cryostat)	The water used in D-01 is cooled down with CFC
TC-03, Controller-04	The temperature is set manually to 5°C, and the controller sends a signal to TC-03
FI-01	The bubble flowmeter is made of glass and the junction with the plant is through aplastic tube To obtain an adequate flow to the GC
Micro-GC	Carrier: Helium T is set equal to 60°CP is equal to 20 psi Analysis time is 2-3 minutes The analysis is automatic

Table A.4.1: Operative conditions of the experimental setup according to the design intent.

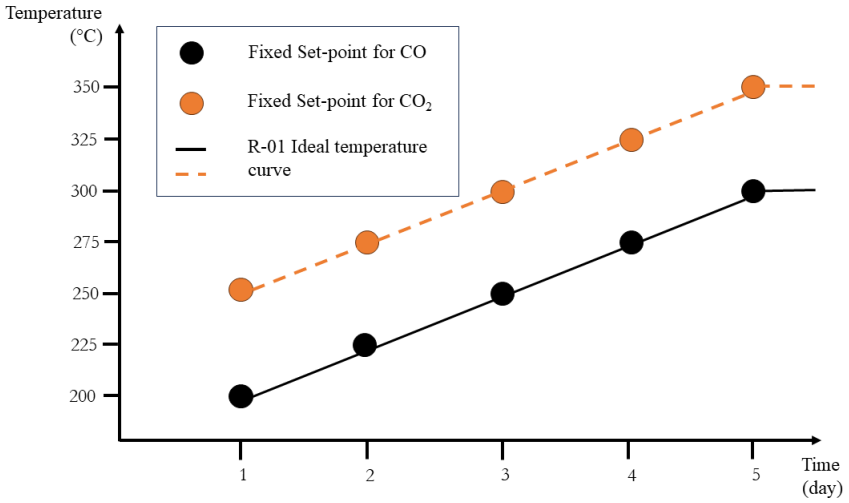

Figure A.4.1: Temperature ramp in R-01 when CO or CO_2 are used as feed.

Shut-down basic procedure	Start-up basic procedure
Decrease the temperature inside the reactor (Controller-02)in order to obtain an ambient temperature (20°C) (this steprequires almost 2 hours). Close input valves (valves 07) of the reactants (this step canbe done when the temperature inside the reactor is 20°C). Set to 0 the volume flow rate of Controller-01. Decrease the pressure (in PRC-09) in order to guaranteeatmospheric conditions in the experimental setup.	Open input valves (valves 07). Set volume flow rates at Controller-01.Set the operative pressure at PRC-09. Increase the temperature of the reactor (Controller-02) according to three different steps (as a ramp): 20-150°C;150-200°C; 200°C-operative temperature.

Table A.4.2: Procedures for start-up and shut-down.

A.5 Chemicals used or produced while operating the process

Classification	Substance	Section involved
Reactants	Hydrogen Carbon monoxide Carbon dioxide	Feeding Mixer R-01 E-01 D-01 Micro-GC
Inert	Nitrogen	Feeding Mixer R-01 E-01 D-01 Micro-GC
	SiO_2 Mineral wool	R-01
Catalyst	Iron-based Mg-Cu-Fe-K, Mg-Cu-Co-Fe-K, Zn-Cu-Fe	R-01
Utilities	Water	D-01 D-02
	Electricity	Feeding Mixer R-01 E-01 D-01 Micro-GC
	CFC (with F)	D-01 D-02
	Helium	Micro-GC
	Acetone	R-01 D-01
Contaminants	-	-
Products	Heavy phase: C_7-C_{30} Light gaseous phase: C_2-C_6 Oxygen compounds: long-chain alcohols	R-01 E-01 D-01
	Incondensable gases: CO, H_2, CO_2, CH_4	R-01 E-01 D-01 Micro-GC

Table A.5.1: Chemicals used or involved while operating the process.

A.6 Interaction matrix: chemicals and materials

Table A.6.1: Interaction matrix between chemicals and materials.

Legend:

- Compatible
- Can be compatible, depending on the elastomeric material used
- Unknown/no data
- Not compatible

[41] Not compatible: N (not compatible for use under normal service conditions), S (swelling), M (change of mechanical properties) .

[42] Not compatible: N (not compatible for use under normal service conditions), S (swelling), M (change of mechanical properties).

[43] Probably incompatible.

[44] Not compatible.

A.7 Interaction matrix: chemicals

Table A.7.1: *Interaction matrix among chemicals.*

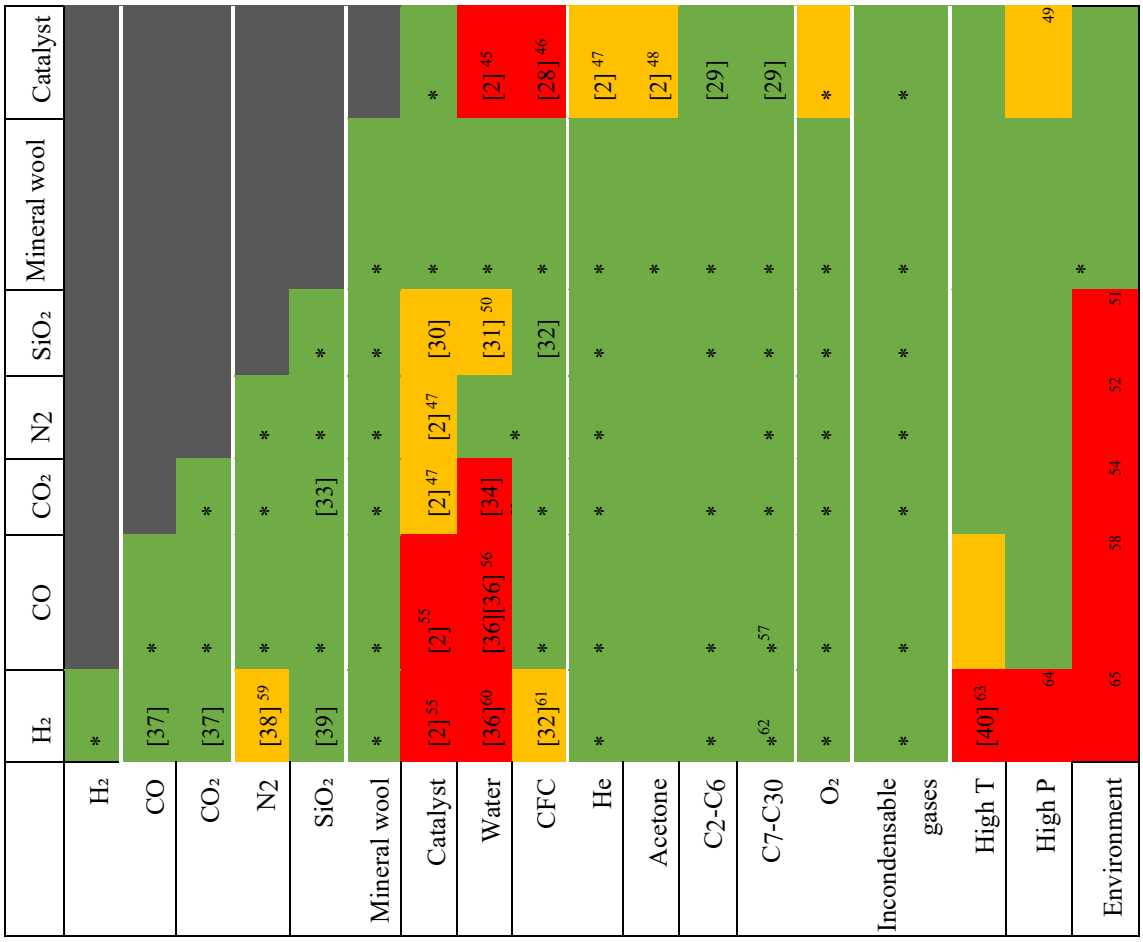

[45] Reaction products may be flammable. The reaction generates gaseous products and may cause pressurization. Exothermic reaction and the products may be toxic.

[46] Possible CFC degradation. Reaction products may be corrosive. The reaction generates gaseous products (which could be toxic) and may cause pressurization. Exothermic reaction at ambient temperature. The reaction may be particularly intense, violent or explosive.

[47] Reaction products may be flammable. Exothermic reaction at ambient temperatures (releases heat)

[48] Reaction products may be flammable. Reaction liberates gaseous products and may cause pressurization. Exothermic reaction at ambienttemperatures (releases heat)

[49] Pyrophoric material.

[50] H_2SiO_3 formation.

[51] If silica is present as powder.

[52] Possible problem related to asphyxiation.

[53] H_2CO_3 formation.

[54] Toxic material.

[55] Reaction products may be flammable. Exothermic reaction at ambient temperatures (releases heat). Reaction products may be unstable above ambient temperatures. Reaction may be particularly intense, violent, or explosive.

[56] CO is highly flammable in contact with water and air, Water Gas Shift reactions.

[57] Possible CO addition in order with Fischer Tropsch synthesis.

[58] Flammable and toxic material.

[59] NH_3 formation: if the pressure increases (above 100 bar).

[60] H_2 is highly flammable in contact with water and air.

[61] Possible hydrochlorination and dimerization (operative condition unknown).

[62] Saturation of the double bond (if there is any double bond).

[63] HTHA (high-temperature hydrogen attack).

[64] Embrittlement.

[65] Flammable material.

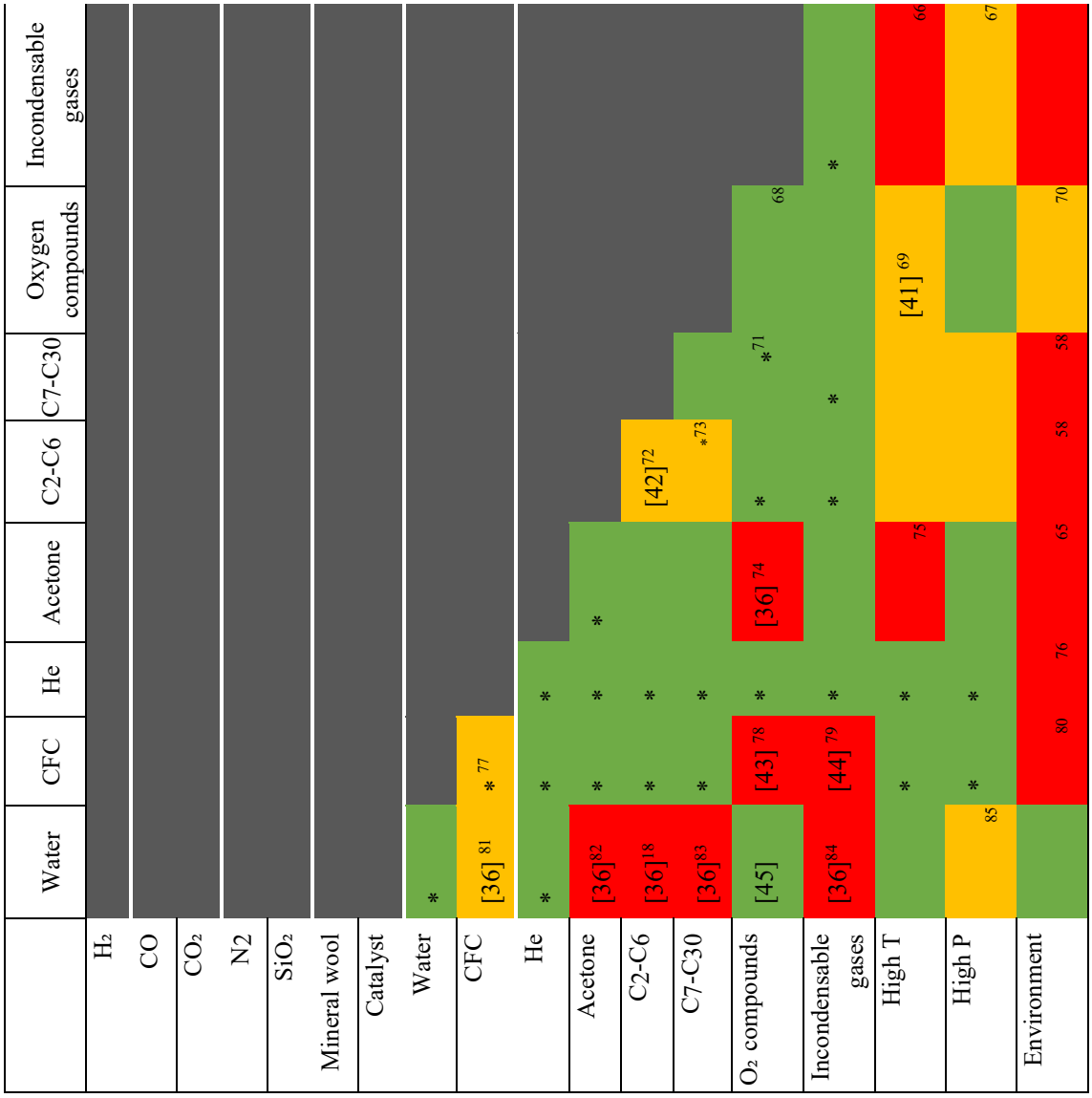

Table A.7.1: Interaction matrix among chemicals.

[66] Flammable gases.
[67] Possible material stresses.
[68] Aldehydes, alkenes, -COOH formation.
[69] Possible thermal composition.
[70] Possible health problems related to alcohol dispersion.
[71] Ether formation.
[72] Possible polymerization.
[73] Possible polymerization.
[74] Acetone with Ethanol can burn with an invisible flame.
[75] Acetone decomposition.
[76] Problems related to asphyxiation.
[77] Possible F_2 formation.
[78] HF formation.
[79] HCl formation.
[80] Health problems related to CFC dispersion.
[81] It could be flammable (type of CFC is unknown)
[82] Highly flammable.
[83] Highly flammable.
[84] Highly flammable mixture. Steam reforming reactions can occur.
[85] Possible material stresses

Legend of Table A.7.1:

Compatible

* Probably compatible (no data available)

Probably not compatible

* Probably not compatible (no data available)

Not compatible

A.8 Properties of hazardous chemicals ([36][46])

Chemical | **Hazardous properties**

Hydrogen [46]

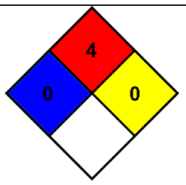

Flammable Gas
LEL: 4.1
UEL: 74.2%
Autoignition T: 400°C
Melting point: -259.18°C
Boiling point: -252.8°C

IDLH: -

AEGLs (Acute Exposure Guideline Levels): -
PACs (Protective Action Criteria): Hydrogen (1333-74-0) [12]

PAC-1	PAC-2	PAC-3	LEL
65000 ppm	230000 ppm	400000 ppm	40000 ppm

Carbon monoxide [36][46]

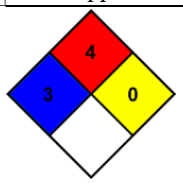

Flammable Gas; Poison Gas
LEL: 12.5%
UEL: 74.2%
Autoignition T: 608.9°C
Melting point: -213°C
Boiling point: -190°C
Water Solubility: 2%
Vapor pressure: >35 atm
IDLH: 1200 ppm
LCLo (ihl-man): 4000 ppm/ 30M
LC50 (ihl-rat): 1807 ppm/4H
AEGLs (Acute Exposure Guideline Levels):

Exposure period	AEGL-1	AEGL-2	AEGL-3
10 min	NR	420 ppm	1700 ppm
30 min	NR	150 ppm	600 ppm
60 min	NR	83 ppm	330 ppm
4 hours	NR	33 ppm	150 ppm
8 hours	NR	27 ppm	130 ppm

NR= not recommended

PACs (Protective Action Criteria): Carbon monoxide (630-08-0)

PAC-1	PAC-2	PAC-3	LEL
75 ppm	83 ppm	330 ppm	125000 ppm

Carbon dioxide [36][46]

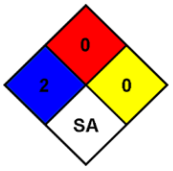

Non-Flammable Gas
Melting point: 57°C (sublimes @-78.5°C)
Boiling point: -
Water Solubility: 0.2% (21.1°C)
Vapor pressure: 56.5 atm
IDLH: 40000 ppm
LCLo (ihl-human): 9 pph/ 5M
LC50: -

	AEGLs (Acute Exposure Guideline Levels): - **PACs** (Protective Action Criteria): -
Nitrogen [36]	**Non-Flammable Gas** **Melting point:** -214.4°C **Boiling point:** -195.6°C **IDLH:** - **AEGLs** (Acute Exposure Guideline Levels): - **PACs** (Protective Action Criteria): -
Catalyst (Fe) [36][46]	**Flammable solid; Strong Reducing Agent; Known Catalytic Activity; Water-Reactive; Pyrophoric.** **Melting point:** 1535°C **Boiling point:** 27°C (@3000 mm) **IDHL:** - **AEGLs** (Acute Exposure Guideline Levels): - **PACs** (Protective Action Criteria): Iron (7439-89-6) PAC-1: 3.2 mg/m^3 | PAC-2: 35 mg/m^3 | PAC-3: 150 mg/m^3
Water [36]	**Boiling point:** 100°C (60 mmHg) **Melting point:** 0°C **IDLH:** - **AEGLs** (Acute Exposure Guideline Levels): - **PACs** (Protective Action Criteria): -
SiO_2 [36][46]	**Boiling point:** 2230°C (60 mmHg) **Melting point:** 1716-1736°C **Water solubility:** Insoluble (soluble in HF) **Vapor pressure:** 0 mmHg **IDLH:** 3000 mg/m^3 **AEGLs** (Acute Exposure Guideline Levels): - **PACs** (Protective Action Criteria): Silica amorphous hydrated (7631-86-9) PAC-1: 18 mg/m^3 | PAC-2: 740 mg/m^3 | PAC-3: 4500 mg/m^3
Alcohol with a long chain (e.g.; 2-heptanol) [46]	**Poison** **Boiling point:** 160.4°C **Melting point:** - **Flash point:** 71.1°C **IDLH:** - **LD50 (orl-rat):** 2580 mg/kg **LD50 (skn-rbt):** 1780 mg/kg **AEGLs** (Acute Exposure Guideline Levels): - **PACs** (Protective Action Criteria): -
C7-C30 (e.g.n-heptane) [36][46]	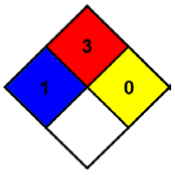 **Flammable liquid** **LEL**: 1.05% **UEL**: 6.7% **Autoignition T**: 223°C **Flash point:** -3.9°C **Melting point:** -91.61°C **Boiling point:** 98.52°C

Water Solubility: 0.0003%
Vapor pressure: 40 mmHg (22.3°C)
IDLH: 750 ppm
TCLo (ihl-human): 1000 ppm/ 6M:CNS
LC50 (ihl-rat): 103 g/m^3 /4H
AEGLs (Acute Exposure Guideline Levels): -
PACs (Protective Action Criteria): Heptane (142-82-5)

PAC-1	PAC-2	PAC-3	LEL
500 ppm	830 ppm	5000 ppm	10500 ppm

C_2-C_6 (e.g.; propane)
[36][46]

Flammable Gas
LEL: 2.3%
UEL: 9.5%
Autoignition T: 450°C
Flash point: -104.4°C
Melting point: -187.7°C
Boiling point: -44.5°C
Water Solubility: 0.01%
Vapor pressure: 9823 mmHg
IDLH: 2100 ppm (Based on 10% of the lower explosive limit)
AEGLs (Acute Exposure Guideline Levels):

Exposure period	AEGL-1	AEGL-2	AEGL-3
10 min	10000 ppm	17000 ppm	33000 ppm
30 min	6900 ppm	17000 ppm	33000 ppm
60 min	5500 ppm	17000 ppm	33000 ppm
4 hours	5500 ppm	17000 ppm	33000 ppm
8 hours	5500 ppm	17000 ppm	33000 ppm

PACs (Protective Action Criteria): Propane (74-98-6)

PAC-1	PAC-2	PAC-3	LEL
5500 ppm	17000 ppm	33000 ppm	23000 ppm

Methane (inside incondensable gases)
[36][46]

Flammable Gas; Strong Reducing Agent.
LEL: 5.3%
UEL: 15%
Autoignition T: 650°C
Flash point: -183.2°C
Melting point: -182.6°C
Boiling point: -161.5°C (760 mmHg)
Water Solubility: 3.5 mL/100 mL (17.2°C)
Vapor pressure: 258574 mmHg (37.8°C); 760 mmHg (-161.5°C)
IDLH: -
AEGLs (Acute Exposure Guideline Levels): -
PACs (Protective Action Criteria): Methane (74-82-8)

PAC-1	PAC-2	PAC-3	LEL
65000 ppm	230000 ppm	400000 ppm	50000 ppm

Acetone [36][46]

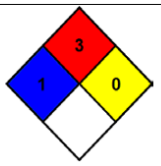

Flammable Liquid
LEL: 2.6%
UEL: 12.8%
Autoignition T: 465°C
Flash point: -17.8°C
Melting point: -94.6°C
Boiling point: 56.2°C
Water Solubility: greater than or equal to 100 mg/mL (22.2°C)
Vapor pressure: 180 mmHg (20°C); 270 mmHg (30°C)
IDLH: 2500 ppm; based on 10% of the lower explosive limit
AEGLs (Acute Exposure Guideline Levels):

Exposure period	AEGL-1	AEGL-2	AEGL-3
10 min	200 ppm	9300 ppm	16000 ppm
30 min	200 ppm	4900 ppm	8600 ppm
60 min	200 ppm	3200 ppm	5700 ppm
4 hours	200 ppm	1400 ppm	2500 ppm
8 hours	200 ppm	950 ppm	1700 ppm

PACs (Protective Action Criteria): Acetone (67-64-1)

PAC-1	PAC-2	PAC-3	LEL
200 ppm	3200 ppm	5700 ppm	26000 ppm

Helium [36][46]

Boiling point: -268.9°C
Melting point: -272.2°C
Water solubility: -
Vapor pressure: -
IDLH: -
AEGLs (Acute Exposure Guideline Levels): -
PACs (Protective Action Criteria): Helium (7440-59-7)

PAC-1	PAC-2	PAC-3
65000 ppm	230000 ppm	400000 ppm

CFC (e.g.; Chlorodifluoromethane) [36][46]

Gas
Autoignition T: 632.2°C
Flash point: -160°C
Boiling point: -40.8°C
Melting point: -146°C
Water solubility: 0.3% (25°C)
Vapor pressure: 10991.42 mmHg
IDLH: -
LCLo (ihl-dog): 70 pph
LC50 (ihl-rat): 35pph/ 15M
AEGLs (Acute Exposure Guideline Levels): -
PACs (Protective Action Criteria):
Chlorodifluoromethane (75-45-6)

PAC-1	PAC-2	PAC-3
1250 ppm	2400 ppm	14000 ppm

A.9 HAZOP analysis

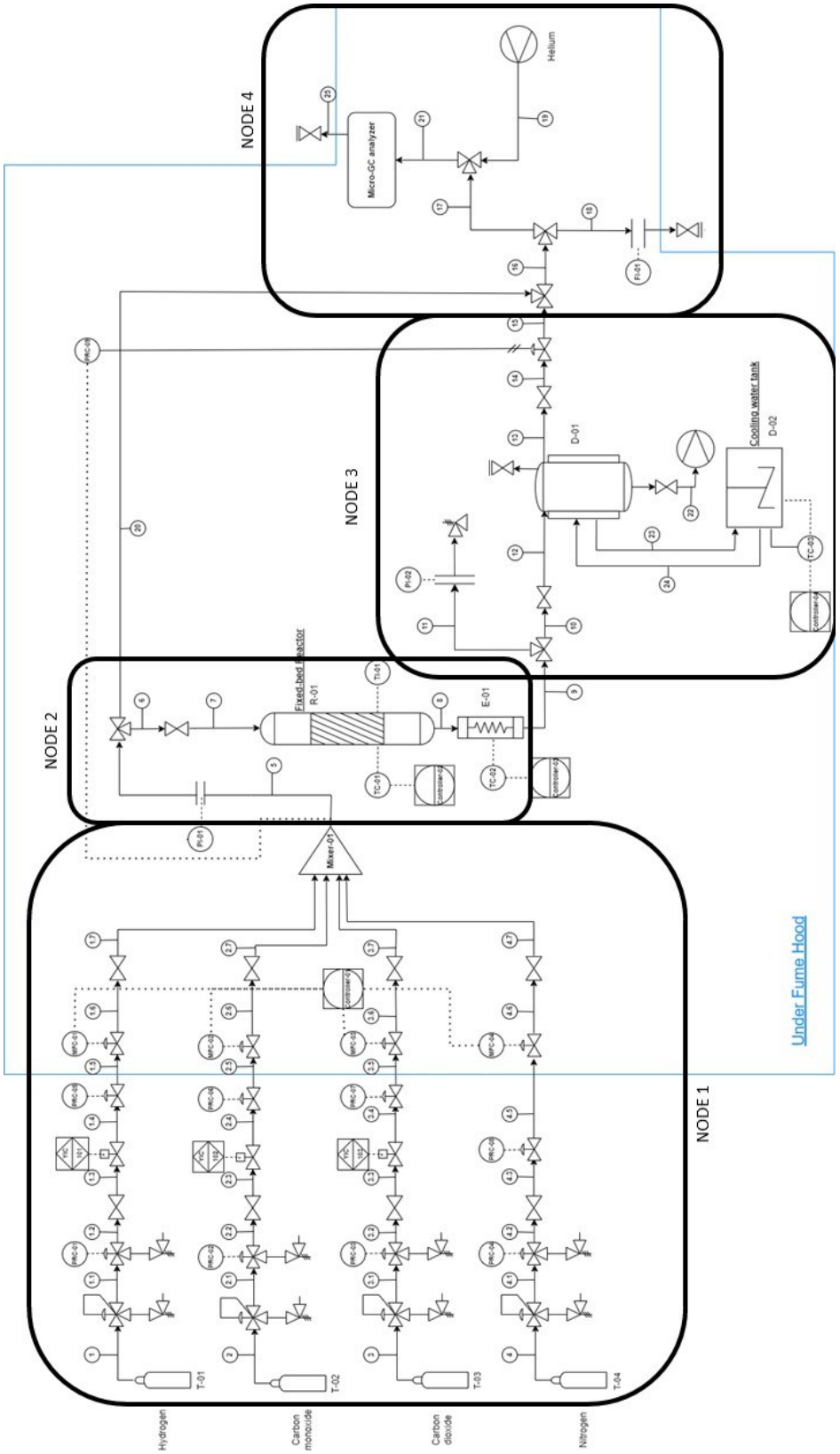

Figure A.9.1: HAZOP analysis: nodes based on the experimental setup for Fischer-Tropsch synthesis.

NODE	GUIDE WORD	PARAMETER
Node 1	MORE	Flow Pressure Temperature Voltage
	LESS	Pressure Temperature
	NO/LESS	Flow Voltage
	AS WELL AS	Material
Node 2	MORE	Flow Pressure Temperature Voltage
	LESS	Pressure Temperature Voltage Reaction rate
	NO/LESS	Flow Reaction rate Voltage
	AS WELL AS	Material
	TOO EARLY	Open reactor
	TOO LATE	Close reactor
	Operation	
Node 3	MORE	Flow Pressure Temperature Voltage
	LESS	Pressure Temperature Separation
	NO/LESS	Flow Voltage
Node 4	MORE	Flow Pressure Temperature Voltage Concentration
	LESS	Pressure Temperature Concentration
	NO/LESS	Flow Voltage Concentration

Table A.9.1: Deviations considered in the HAZOP analysis.

Node	Deviation
Node 1	Close input valves before the reactor's temperature is equal to 20°C
Node 2	Close input valves before the reactor's temperature is equal to 20°C NO/LESS conversion

Table A.9.2: Deviations considered in the HAZOP analysis for transient states.

For each deviation, the following points are analysed: causes, consequences, safeguards, recommendations, severity (S), likelihood (L), and risk class (RC).

A.9.1 HAZOP analysis: Node 1, feeding section

Deviation name: MORE (increasing) pressure **Node description (design intent): reactants' feeding and mixing in the right composition (which could change from one experimental test to another)**						
Cause	**Consequence**	**Safeguards**	**Recommendations**	**S**	**L**	**R**
1. The pressure-drop in valve 02 is not enough	The down-stream sections are not with the correct pressure, the valve can break, possible leakages, failures, ruptures, explosions and death.	Hood, sensor for leakages, Sensors for pressure, alarmed high-pressure sensor (PIAH)	Correct valve sizing, maintenance of the pipes and the valve.	E3	W3	D
2. The pressure-drop in valve 05 is not enough	As above	As above	As above	E3	W3	D
3. The control pressure fails (PRC-01 to PRC-08)	The pressure can reach the MAWP of the pipes (or Pmax of the operation units). Possible ruptures, leakages and loss of containment of toxics or flammables.	Hood, sensor for leakages, Sensors for pressure, alarmed high-pressure sensor (PIAH)	Maintenance of the pipes, the valves and the mixer.	E3	W3	D
4. The control pressure set point is wrong (for PRC-01 to PRC-04)	As above	As above	Checklist	E3	W3	D
5. The control pressure set point is wrong (for PRC-05 to PRC-08)	As above	As above	Checklist	E3	W3	D
6. Valve-03 closes	As above	As above	Maintenance of the pipes and the valves.	E3	W3	D
7. Valve-07 closes	As above	As above	Maintenance of the pipes and the valves.	E3	W3/ W2	E/ D
8. Relief valves fail (the ones connected to valve-01 and 02)	As above	As above	As above	E3	W2	E
9. Wrong set point at least one of MFC-01, 02, 03 and 04	As above	As above	As above	E3	W4	C
10. Controller-01 fails	As above	As above	As above	E3	W3	D
11. At least one of the MFCs fail	As above	As above	As above	E3	W3	D

Table A.9.3: MORE pressure (Node 1)

Deviation name: LESS (decreasing) pressure **Node description (design intent): reactants' feeding and mixing in the right composition (which could change from one experimental test to another)**						
Cause	**Consequence**	**Safeguards**	**Recommendations**	**S**	**L**	**RC**
12. Higher pressure-drop in valve-02	Less pressure in the reactor and the outlet composition will change. Loss of the experimental test. Possible problems related to low temperature in CO_2 line.	Sensor for pressure	Correct sizing	E2	W3	E
13.Higher pressure-drop in valve-05	As above	As above	As above	E2	W3	E
14.Wrong set point for pressure controllers	As above	As above	Periodic check of the SP	E2	W4	D
15.Wrong set point on the mass flow controller	As above	As above	Periodic check of the SP	E2	W4	D
16. Leakages (gaskets' rupture)	Less pressure in the reactor and the outlet composition will change. Loss of the test. Dispersion of dangerous chemicals (toxic and flammable).	Hood, Sensor for leakages, Sensor for pressure	Periodic maintenance.	E3	W3	D
17. Controller-01 fails	Less pressure in the reactor and the outlet composition will change. Loss of the test.	Sensor for pressure	Periodic maintenance.	E2	W3	E
18. At least one of the MFCs fail	As above	As above	As above	E2	W3	E

Table A.9.4: LESS pressure (Node 1)

Deviation name: MORE (increasing) flow **Node description (design intent): reactants' feeding and mixture them with the right composition (which could change from one experimental test to another)**						
Cause	**Consequence**	**Safeguards**	**Recommendations**	**S**	**L**	**RC**
19. Wrong set point in the mass flow controller	Possible increase in pressure (refer to MORE - increasing pressure) and changes in the final composition with loss of the experimental test.	Hood, sensor for leakages, sensors for pressure, alarmed high pressure sensor (PIAH)	Periodic check of the SP	E2/ E3	W4	D/C
20. At least one of the Mass flow controllers (MFC-01 to MFC-04) fails	As above	As above	Periodic maintenance	E2/ E3	W4	D/C
21. At least one of the pressure controllers fails (PRC-01 to PRC-08)	As above	As above	Periodic maintenance	E2/ E3	W3	E/D

Table A.9.5: MORE flow (Node 1)

Deviation name: LESS/NO Flow **Node description (design intent): reactants' feeding and mixture them with the right composition (which could** **change from one experimental test to another)**						
Cause	**Consequence**	**Safeguards**	**Recommendations**	**S**	**L**	**RC**
22. Electricity shut-down	The safety valve closes, No flow in the reactor, No reaction, Exposure to reactants.	Hood, Sensor for leakages.		E2	W3	E
23.One or more tanks are empty	No reaction, different composition and loss of the test.	Sensor for pressure	Periodic check	E2	W4	D
24.Valves close (at least one)	Increasing pressure, leakages, explosion, death.	Hood, Sensor for leakages, Sensor for pressure.	Periodic maintenance	E3	W3	D
25.Failure of pressure controller	As above	As above	Periodic maintenance	E3	W3	D
26.Failure of mass flow controller	As above	As above	Periodic maintenance	E3	W3	D
27.Leakages	Loss of reactants, which are toxic and flammable. Subsequent fire or explosion.	Hood, Sensor for leakages	Periodic maintenance	E3	W3	D
28.Plug in the pipes	Increase in pressure, loss of containment of material.	As above	Periodic maintenance	E3	W2/W3	E/D
29.Set flowrates equal to zero before closing input valves (Shutdown)	Decreasing in pressure, less conversion inside the reactor, loss of the experimental test.	-	Checklist, procedures.	E2	W4	D

Table A.9.6: LESS/NO flow (Node 1)

Deviation name: MORE Temperature **Node description (design intent): reactants' feeding and mixture them with the right composition (which could change from one experimental test to another)**						
Cause	**Consequence**	**Safeguards**	**Recommendations**	**S**	**L**	**RC**
30.High external environmental temperature	Moles of the substances decrease, and the final composition can change.	-	Work in a temperature-controlled environment	E2	W4	D

Table A.9.7: MORE temperature (Node 1)

Deviation name: LESS Temperature **Node description (design intent): reactants' feeding and mixture them with the right composition (which could change from one experimental test to another)**						
Cause	**Consequence**	**Safeguards**	**Recommendations**	**S**	**L**	**RC**
31.Low external environmental temperature	Increasing moles of the substances and change in the final composition	-	Work in a temperature-controlled environment	E2	W4	D

Table A.9.8: LESS temperature (Node 1)

Deviation name: OTHER THAN material/substance **Node description (design intent): reactants' feeding and mixture them with the right composition (which could change from one experimental test to another)**						
Cause	**Consequence**	**Safeguards**	**Recommendations**	**S**	**L**	**RC**
32.Wrong opening of valves/stream (e.g., use of CO instead of CO_2 or vice versa)	Wrong composition and loss of the experimental test.	Detection system	Checklist, Labelling	E2	W3/W4	E/D
33.At least one pressure or mass flow controller with a wrong set point	Wrong composition and loss of the experimental test.	-	Checklist	E2	W4	D

Table A.9.9: OTHER THAN MATERIAL (Node 1)

Deviation name: MORE voltage **Node description (design intent): reactants' feeding and mixture them with the right composition (which could change from one experimental test to another)**						
Cause	**Consequence**	**Safeguards**	**Recommendations**	**S**	**L**	**RC**
34.Electrical current overload	Electrical short circuit. Fire. Damage to equipment.	Compliance of the electrical system with regulations. Fire protection systems.	Maintenance.	E4	W2	D
35.Defective grounding of equipment	Circulating currents. Uncontrolled ignition sources.	-	Inspection and regular check of grounding.	E4	W2	D

Table A.9.10: MORE voltage (Node 1)

Deviation name: LESS/NO voltage **Node description (design intent): reactants' feeding and mixture them with the right composition (which could change from one experimental test to another)**						
Cause	**Consequence**	**Safeguards**	**Recommendations**	**S**	**L**	**RC**
36.Shut-down electricity	Wrong composition to the reactor, wrong/no flowrate to the reactor (valves are FC), decreasing pressure, increasing pressure before valve 4.	Safety valve	-	E2	W3	E
37.Power outage	As above	Compliance of the electrical system with regulations. Hood, sensors for leakages.	Maintenance.	E3	W4	C

Table A.9.11: LESS/NO voltage (Node 1)

Deviation name: Close input valves before the reactor's temperature is equal to 20°C (TOO EARLY closure) Node description (design intent): reactants' feeding and mixture them with the right composition (which could change from one experimental test to another)						
Cause	**Consequence**	**Safeguards**	**Recommendations**	**S**	**L**	**RC**
38.TI-01 fails	Possible damage to the catalyst, different final composition, loss of the experimental test.	Hood, sensors for pressure.	Checklist, procedure.	E2	W4	D
39.Wrong reading of TI-01	As above	As above	As above	E2	W4	D

Table A.9.12: Close input valves BEFORE required - TOO EARLY (Node 1)

A.9.2 HAZOP analysis: Node 2, reaction section

Deviation name: MORE Pressure **Node description (design intent): Establish the intended conversion inside the reactor and maintain the product stream in a gas phase after exchanging heat.**						
Cause	**Consequence**	**Safeguards**	**Recommendations**	**S**	**L**	**RC**
40.Pressure controller fails (PRC-09)	Higher conversion of CO. Different final composition. Loss of the experimental test. Leakages (from reactor or pipes). Rupture of the reactor.	Hood, sensor for leakages, sensors for pressure, alarmed high-pressure sensor (PIAH)	Maintenance	E3	W3	D
41.Wrong SP of PRC-09	As above	As above	Maintenance. Checklist, double check (> 2 people)	E3	W4	C
42.PI-01 fails (The displayed pressure is incorrect, and there is no perception from the operator of the error)	As above	As above	Periodic maintenance. Checklist.	E3	W4	C
43.Valve 08 closes	No reaction, uncontrolled leakages from the pipes.	As above	As above	E3	W3	D
44.Valve 09 closes	As above	As above	As above	E3	W3	D
45.Higher P in the previous section	Higher conversion of CO. Different final composition. Loss of the experimental test. Leakages (from reactor or pipes). Rupture of the reactor.	As above	Maintenance.	E3	W3	D
46.Overpacked reactor	As above	As above	As above	E3	W4	C

Table A.9.13: MORE pressure (Node 2)

Deviation name: LESS Pressure **Node description (design intent): Establish the intended conversion inside the reactor and maintain the product stream in a gas phase after exchanging heat.**						
Cause	**Consequence**	**Safeguards**	**Recommendations**	**S**	**L**	**RC**
47.Wrong SP in PRC-09	Less conversion of CO. Different final composition. Loss of experimental test.	Pressure sensor	Periodic check.	E2	W4	D
48.Wrong SP in the previous valves	As above	Pressure sensor		E2	W3	E
49.Leakages	Release of flammable or toxic materials. Uncontrolled ignition with final events of fire/explosion.	Hood, Sensors for leakages, Sensors.	Periodic maintenance.	E4	W3	C
50.Not adequately packed reactor	Less conversion, different final composition, loss of the test	As above	As above	E2	W3	E
51.More pressure drops at least in valve 08 or 09	Less conversion, Different final composition, loss of test. Leakages, death.	As above	As above	E2	W3	E

Table A.9.14: LESS pressure (Node 2)

Deviation name: MORE Temperature **Node description (design intent): Establish the intended conversion inside the reactor and maintain the product stream in a gas phase after exchanging heat.**						
Cause	**Consequence**	**Safeguards**	**Recommendations**	**S**	**L**	**RC**
52.Wrong SP in TC-01	More energy and higher temperature than required. Different final composition. Loss of the experimental test. Increasing pressure, possible leakages or ruptures. Damage to the catalyst.	Hood, Sensors for leakages, Sensors.	Periodic check.	E3	W4	C
53.TI-01 fails	As above	As above	As above	E3	W3	D
54.Controller-02 fails	As above	As above	As above	E3	W3	D
55.Set the wrong temperature in the temperature ramp for the start-up	Damage to the catalyst. Increasing pressure. Altered final composition. Loss of the experimental test.	Hood, sensor for leakages, sensors for pressure, alarmed high-pressure sensor (PIAH)	Checklist, procedure (double check)	E3	W4	C
56.Set the volume flowrates after starting the temperature ramp	Possible damage to the catalyst. Different final composition. Loss of the experimental test.	-	As above	E2	W4	D

Table A.9.15: MORE temperature (Node 2)

Deviation name: LESS Temperature **Node description (design intent): Establish the intended conversion inside the reactor and maintain the product stream in a gas phase after exchanging heat.**						
Cause	**Consequence**	**Safeguards**	**Recommendations**	**S**	**L**	**RC**
57.Wrong SP in TC-01	Less energy and lower temperature than required. Different final composition (less reaction). Possible issues in the heat exchanger with partial evaporation of the products.	Temperature sensor	Periodic check.	E2	W4	D
58.TC-01 fails	Different final composition. Loss of the experimental test. Possible plugs of the pipes by heavy hydrocarbons. Increasing pressure. Leakages, loss of containment.	Hood, Sensors for leakages, Sensors.	Maintenance.	E3	W3	D
59.Electricity shut-down	No energy, no reaction. Loss of the experimental test. Possible plugs of the pipes. Increasing pressure. Leakages, loss of containment.	As above	Maintenance.	E3	W3	D
60.TC-02 fails	Plugs in the lines by heavy hydrocarbons. Increasing pressure. Leakages, loss of containment.	As above	Maintenance.	E3	W3	D

Table A.9.16: LESS temperature (Node 2)

Deviation name: MORE Flow Node description (design intent): Establish the intended conversion inside the reactor and maintain the product stream in a gas phase after exchanging heat.						
Cause	Consequence	Safeguards	Recommendations	S	L	RC
61.PI-01 fails	Higher pressure in the reactor with possible failures. Leakages and loss of containment. Different final composition. Loss of the experimental test. Issues when exchanging heat to achieve the final temperature in E-01 and R-01.	Hood, sensor for leakages, sensors for pressure, alarmed high-pressure sensor (PIAH)	Periodic maintenance.	E3	W3	D
62.PRC-09 fails	As above	As above	As above	E3	W3	D
63.Wrong SP of PRC- 09	As above	As above	Maintenance, checklist, double check (> 2 people)	E3	W4	C
64.Deviations in Node 1	As above	As above	As above	E3	W3	D
65.Less pressure drops at least in valve-08 and/or in valve-09	As above	As above	Periodic maintenance, proper sizing of equipment.	E3	W3	D

Table A.9.17: MORE flow (Node 2)

Deviation name: LESS/NO Flow **Node description (design intent): Establish the intended conversion inside the reactor and maintain the product stream in a gas phase after exchanging heat.**						
Cause	**Consequence**	**Safeguards**	**Recommendations**	**S**	**L**	**RC**
66.Deviations in Node 1	Less pressure in the reactor. Less conversion. Loss of the experimental test. Leakages and loss of containment.	Hood, Sensors for leakages, Sensors.	Periodic maintenance.	E2	W3	E
67.PI-01 fails	Increasing pressure in the pipes. Leakages and loss of containment. Less pressure in the reactor. Less conversion. Loss of the experimental test.	As above	As above	E2	W3	D
68.Closure of valves 08 or 09	Increasing in pressure. Leakages and loss of containment. No reaction. Loss of the experimental test.	As above	As above	E2	W3	D
69.PRC-09 fails	Less pressure in the reactor. Less conversion. Loss of the experimental test.	As above	As above	E2	W3	E
70.Wrong SP of PRC-09	As above	As above	As above	E2	W3	E
71.Use of the by-pass	No reaction. Loss of the experimental test. Increasing pressure in the by- pass line. Leakages and loss of containment.	As above	As above	E3	W3	D
72.Leakage/defect connection	No or reduced circulating flow. No reaction. Leakages and loss of containment.	No safeguards.	Environmental sensor system.	E4	W2/ W3	D/C

Table A.9.18: LESS/NO flow (Node 2)

Deviation name: MORE voltage **Node description (design intent): Establish the intended conversion inside the reactor and maintain the product stream in a gas phase after exchanging heat.**						
Cause	**Consequence**	**Safeguards**	**Recommendations**	**S**	**L**	**RC**
73.Electrical current overload	Electrical short circuit, fire. Damage to equipment.	Electrical system compliant with regulations, fire protection systems.	Maintenance.	E4	W2	D
74.Defective grounding of equipment	Circulating currents. Uncontrolled ignition sources.		Inspection and regular check of grounding.	E4	W2	D

Table A.9.19: MORE voltage (Node 2)

Deviation name: LESS/NO voltage **Node description (design intent): Establish the intended conversion inside the reactor and maintain the product stream in a gas phase after exchanging heat.**						
Cause	**Consequence**	**Safeguards**	**Recommendations**	**S**	**L**	**RC**
75.Shut-down electricity	No reaction. No vaporization in E-01.	Safety valve, i.e. if there is no electricity, the reactor will have a mixture of unreacted material and products (valves: FC). The reaction inside the reactor will continue, but the operative conditions are not controlled.	Checklist for the following start-up	E2	W3	E
76.Power outage	Less or no reaction, problems related to the vaporization in E-01. Plugs in pipelines due to heavy hydrocarbons. Leakages and loss of containment.	Electrical system compliant with regulations, hood, sensors for leakages.	Maintenance.	E3	W4	C

Table A.9.20: LESS/NO voltage (Node 2)

Deviation name: MORE Reaction rate **Node description (design intent): Establish the intended conversion inside the reactor and maintain the product stream in a gas phase after exchanging heat.**						
Cause	**Consequence**	**Safeguards**	**Recommendations**	**S**	**L**	**RC**
77. Higher temperature (Wrong SP in TC-01)	Increasing in temperature (see MORE Temperature). Different composition. Loss of the experimental test. More quantity of heavy-phase. Damage to catalyst.	Hood, sensor for leakages, Sensors for pressure, alarmed high-pressure sensor (PIAH)	Checklist, double check (> 2 people)	E3	W4	C

Table A.9.21: MORE reaction rate (Node 2)

Deviation name: Decreasing Reaction rate **Node description (design intent): Establish the intended conversion inside the reactor and maintain the product stream in a gas phase after exchanging heat.**						
Cause	**Consequence**	**Safeguards**	**Recommendations**	**S**	**L**	**RC**
78. Catalyst poisoning	Different composition. Loss of the experimental test. Increasing gaseous components. Increasing pressure (see MORE pressure)	Hood, sensor for leakages, Sensors for pressure, alarmed high-pressure sensor (PIAH)	Periodic change of the catalyst	E4	W3	C
79.Wrong SP of TC-01	Less conversion. Different final composition. Loss of the experimental test. Increasing in pressure.	As above	As above	E2	W4	D

Table A.9.22: LESS reaction rate (Node 2)

Deviation name: LESS/NO Reaction rate **Node description (design intent): Establish the intended conversion inside the reactor and maintain the product stream in a gas phase after exchanging heat.**						
Cause	**Consequence**	**Safeguards**	**Recommendations**	**S**	**L**	**RC**
80.Catalyst poisoning	Different composition. Loss of the experimental test. Increasing gaseous components. Increasing pressure (see MORE pressure)	Hood, sensor for leakages, Sensors for pressure, alarmed high-pressure sensor (PIAH)	Periodic change of the catalyst	E4	W3	C
81.Wrong SP of TC-01	Less conversion. Different final composition. Loss of the experimental test. Increasing pressure.	As above	As above	E2	W4	D

Table A.9.23: LESS/NO reaction rate (Node 2)

Deviation name: OTHER THAN material **Node description (design intent): Establish the intended conversion inside the reactor and maintain the product stream in a gas phase after exchanging heat.**						
Cause	**Consequence**	**Safeguards**	**Recommendations**	**S**	**L**	**RC**
82.Opening of the wrong equipment (from Node 1) (CO instead of CO_2 or vice versa)	LESS/MORE reaction rate. Loss of the experimental test.		Checklist. Labelling. Double-check (> 2 operators)	E3	W3	D

Table A.9.24: OTHER THAN material (Node 2)

Deviation name: TOO EARLY reactor opening (before the feed is closed) **Node description (design intent): Establish the intended conversion inside the reactor and maintain the product stream in a gas phase after exchanging heat.**						
Cause	**Consequence**	**Safeguards**	**Recommendations**	**S**	**L**	**RC**
83.Open the reactor before the feeding stream is closed	Possible release of toxic and flammable gases. Uncontrolled ignition. Final events of fire/explosion.	Sensors, hood.	Procedure to open and close the reactor, no ignition sources.	E3	W4	C

Table A.9.25: TOO EARLY reactor opening (Node 2)

Deviation name: TOO LATE reactor closure (after the feed is opened) Node description (design intent): Establish the intended conversion inside the reactor and maintain the product stream in a gas phase after exchanging heat.						
Cause	**Consequence**	**Safeguards**	**Recommendations**	**S**	**L**	**RC**
84.Close the reactor after opening the feeding stream (Start-up)	Possible release of toxic and flammable gases. Uncontrolled ignition. Final events of fire/explosion.	Sensors, hood.	Procedure to open and close the reactor, no ignition sources.	E3	W4	C

Table A.9.26: TOO LATE reactor closure (Node 2)

Deviation name: LESS/NO electrical insulation Node description (design intent): Establish the intended conversion inside the reactor and maintain the product stream in a gas phase after exchanging heat.						
Cause	**Consequence**	**Safeguards**	**Recommendations**	**S**	**L**	**RC**
85.Damage to the electrical insulation of the reactor	Contact with electricity, possible electrocution, damage to the operator.	Grounding system, insulation.	Periodic maintenance	E3	W3	D
86.Damage to the electrical insulation of the heat exchanger	As above	Grounding system.	As above	E3	W3	D

Table A.9.27: LESS/NO electrical insulation (Node 2)

Deviation name: Operation Node description (design intent): Establish the intended conversion inside the reactor and maintain the product stream in a gas phase after exchanging heat.						
Cause	**Consequence**	**Safeguards**	**Recommendations**	**S**	**L**	**RC**
87.Cleaning the reactor	Damage to the reactor.		Proper procedure to clean the reactor.	E1	W4	E

Table A.9.28: Deviation during cleaning operations (Node 2)

Deviation name: Close input valves before the temperature in the reactor is 20°C Node description (design intent): Establish the intended conversion inside the reactor and maintain the product stream in a gas phase after exchanging heat.						
Cause	**Consequence**	**Safeguards**	**Recommendations**	**S**	**L**	**RC**
88.TI-01 fails (Shutdown)	Possible damage to the catalyst. Different final composition. Loss of the experimental test.	Hood, sensors for pressure.	Checklist, procedure.	E2	W4	D
89.Wrong reading of TI-01 (Shutdown)	As above	As above	As above	E2	W4	D

Table A.9.29: Close input valves BEFORE required (Node 2)

Deviation name: LESS/NO conversion Node description (design intent): Establish the intended conversion inside the reactor and maintain the product stream in a gas phase after exchanging heat.						
Cause	**Consequence**	**Safeguards**	**Recommendations**	**S**	**L**	**RC**
90.Decreasing pressure inside the plant before setting the flowrate equal to zero. (Shutdown)	Pressure decreases inside the reactor. LESS/NO conversion. Loss of the experimental test.	-	Checklist and procedure (double check)	E2	W4	D
91.Decreasing pressure inside the plant before closing the input valves. (Shutdown)	As above	-	As above	E2	W4	D

Table A.9.30: LESS/NO conversion (Node 2)

A.9.3 HAZOP analysis: Node 3, separation section

Deviation name: MORE Pressure **Node description (design intent): Condensation of the heavy phase (C7-C30) and the water to separate from condensable gases and the light phase (C2-C6).**						
Cause	**Consequence**	**Safeguards**	**Recommendations**	**S**	**L**	**RC**
92.PI-02 fails	Achieve the maximum pressure of the pipes/equipment. Less separation. Ruptures and leakages.	Hood, sensor for leakages, sensors for pressure, alarmed high-pressure sensor (PIAH)	Periodic maintenance.	E3	W4	C
93.Valve 10 fails	As above	As above	As above	E3	W2	E
94.Valve 11 closes (three-way valve)	As above	As above	As above	E3	W3	D
95.PRC-09 fails	As above	As above	As above	E3	W3	D
96.Wrong SP of PRC- 09	As above	As above	Periodic maintenance, periodic check of SP.	E3	W4	C
97.Valve 14 closes	As above	As above	Periodic maintenance.	E3	W3	D
98.Valve 13 closes	As above	As above	As above	E3	W3	D
99.Valve 12 closes	As above	As above	As above	E3	W3	D
100.Higher pressure from the previous nodes	Less condensation. Less separation. Loss of the experimental test. Plugs in the external tubes.	Temperature indicator		E3	W3	D
101.Higher water temperature in the jacket of D-01	Less condensation. Less separation. Loss of the experimental test. Plugs in the external tubes. Rupture, leakages with loss of containment.	Temperature indicator. Hood. Sensors for leakages. Sensors.	Periodic maintenance. Checklist. Periodic check of TC-03.	E3	W3	D

Table A.9.31: MORE pressure (Node 3)

Deviation name: LESS Pressure **Node description (design intent): Condensation of the heavy phase (C7-C30) and the water to separate from condensable gases and the light phase (C2-C6).**						
Cause	**Consequence**	**Safeguards**	**Recommendations**	**S**	**L**	**RC**
102.Lower temperature in the jacket	More condensed phase. Plugs in the pipes. Plug in D-01. Loss of containment of heavy and light phases.	Temperature indicator. Hood. Sensor for leakages. Sensors.	Maintenance, periodic check of the temperature controller set point	E2	W3	E
103.Wrong SP of PRC-09	More condensation. More separation. Loss of the experimental test.	Pressure sensor.	Periodic check.	E2	W4	D
104.Valve 12 completely open	Loss of the experimental test. Loss of the experimental test.	Hood, Sensors.	Periodic maintenance.	E2	W3	E
105.Valve 13 completely open	Partial condensation. Loss of containment of incondensable gases. Loss of the experimental	Hood, Sensors.	As above.	E2	W3	E

	test.					

Table A.9.32: LESS pressure (Node 3)

Deviation name: MORE Flow **Node description (design intent): Condensation of the heavy phase (C7-C30) and the water to separate from condensable gases and the light phase (C2-C6).**						
Cause	**Consequence**	**Safeguards**	**Recommendations**	**S**	**L**	**RC**
106.Higher flow from previous nodes	More quantity to condensate. Less separation. Loss of the experimental test. Increasing pressure. Leakages, loss of containment.	Hood, Sensors for leakages, Sensor of pressure, PIAH.	Periodic maintenance and periodic check of the operative conditions.	E3	W3	D
107.Less pressure drops in valves 11 or three-way before D-01	As above.	As above.	As above.	E3	W3	D
108.Wrong SP of PRC-09	Increasing pressure. Less separation. Leakages, loss of containment.	As above.	Periodic check, checklist.	E3	W4	C

Table A.9.33 MORE flow (Node 3)

Deviation name: LESS/NO Flow **Node description (design intent): Condensation of the heavy phase (C7-C30) and the water to separate from condensable gases and the light phase (C2-C6).**						
Cause	**Consequence**	**Safeguards**	**Recommendations**	**S**	**L**	**RC**
109.Plug in the reactor	Increasing pressure. Ruptures, leakages and loss of containment.	Hood, Sensors for leakages, Sensors.	Periodic maintenance.	E3	W3	D
110.Decreased/no flow from previous nodes	Loss of the test.	-	-	E1	W3	F
111.Plugs in the pipes	Increasing pressure. Ruptures, leakages and loss of containment.	Hood, Sensors for leakages, Sensors.	Periodic maintenance.	E3	W3	D
112.Leakages	Release of toxic, flammable or condensable gases. Possible fire or explosion.	Hood, Sensors for leakages, Fire protection systems.	Work far from possible sources of fire.	E3	W3	D
113.Valve 11 closes	Increasing pressure. Plugs in the pipes. Ruptures, leakages and loss of containment.	Hood, Sensors for leakages, Sensors.	Periodic maintenance.	E3	W3	D
114.Valve 10 fails	Ruptures, leakages and loss of containment of flammables/toxics.	As above	As above	E3	W3	D
115.No Flow of CFC	Higher water temperature. No/less separation. Plugs in the pipes. Increasing pressure. Ruptures, leakages and loss of containment.	Temperature indicator, Hood, Sensors for leakages, Sensors.	Checklist.	E3	W3	D
116.No water	No/less separation. Plugs in the pipes. Increasing pressure. Ruptures, leakages and loss of containment.	As above	As above	E3	W3	D

Table A.9.34: LESS/NO flow (Node 3)

Deviation name: MORE Temperature **Node description (design intent): Condensation of the heavy phase (C7-C30) and the water to separate from condensable gases and the light phase (C2-C6).**						
Cause	**Consequence**	**Safeguards**	**Recommendations**	**S**	**L**	**RC**
117.TC-02 fails	More difference in temperature than required. Less separation. Increasing pressure. Ruptures, leakages and loss of containment.	Hood, sensor for leakages, sensors for pressure, alarmed high-pressure sensor (PIAH)	Periodic maintenance, periodic check.	E3	W3	D
118.TC-03 fails	Less separation. Increasing pressure. Ruptures, leakages and loss of containment.	As above.	As above.	E3	W3	D
119.Controller 4 fails	As above.	As above.	As above.	E3	W3	D
120.Fouling in the jacket	As above.	As above.	As above.	E3	W3	D

Table A.9.35: MORE temperature (Node 3)

Deviation name: LESS Temperature **Node description (design intent): Condensation of the heavy phase (C7-C30) and the water to separate from condensable gases and the light phase (C2-C6).**						
Cause	**Consequence**	**Safeguards**	**Recommendations**	**S**	**L**	**RC**
121.Lower temperature from E-01	Plug in the pipe. Increasing pressure. Ruptures, leakages and loss of containment.	Temperature indicator, Hood, Sensors for leakages, Sensors.	Periodic check and maintenance.	E3	W3	D
122.TC-03 has a wrong SP	More condensation. More separation. Plugs in the pipes. Loss of the experimental test.	Temperature indicator, Hood, Sensors for leakages, Sensors.	Periodic check and maintenance.	E2	W4	D
123.Controller 4 fails	As above.	As above.	As above.	E2	W3	E

Table A.9.36: LESS temperature (Node 3)

Deviation name: LESS Separation **Node description (design intent): Condensation of the heavy phase (C7-C30) and the water to separate from condensable gases and the light phase (C2-C6).**						
Cause	**Consequence**	**Safeguards**	**Recommendations**	**S**	**L**	**RC**
124.Higher Temperature in D- 01	Increasing pressure. Ruptures, leakages and loss of containment.	Temperature indicator, Hood, Sensors for leakages, Sensors.	Periodic maintenance, periodic check.	E3	W3	D
125.Higher flow in D-01	Ruptures, leakages and loss of containment. Loss of the experimental test.	Hood, Sensors for leakages, Sensors.	As above.	E3	W3	D

Table A.9.37: LESS separation (Node 3)

Deviation name: MORE voltage **Node description (design intent): Condensation of the heavy phase (C7-C30) and the water to separate from condensable gases and the light phase (C2-C6).**						
Cause	**Consequence**	**Safeguards**	**Recommendations**	**S**	**L**	**RC**
126.Electrical current overload	Electrical short circuit. Possibility of fire. Damage to equipment.	Electrical system compliant with regulations. Fire protection systems.	Maintenance.	E4	W2	D
127.Defective grounding of equipment	Circulating currents. Uncontrolled ignition sources.		Inspection and regular check of grounding.	E4	W2	D

Table A.9.38: MORE voltage (Node 3)

Deviation name: LESS/NO voltage **Node description (design intent): Condensation of the heavy phase (C7-C30) and the water to separate from condensable gases and the light phase (C2-C6).**						
Cause	**Consequence**	**Safeguards**	**Recommendations**	**S**	**L**	**RC**
128. Shut-down of electricity	Decreasing in separation at D-01. Increasing pressure. Loss of the experimental test.	Safety valve. Hood. Sensor for leakages.		E2	W3	E
129. Power outage	As above.	Electrical system compliant with regulations, hood, sensors for leakages, sensors for pressure, PIAH, and safety valve.	Maintenance.	E3	W4	C

Table A.9.39: LESS/NO voltage (Node 3)

A.9.4 HAZOP analysis: Node 4, analysis of the gas phase

Deviation name: MORE Pressure **Node description (design intent): Analysis of the light phase after the reaction section.**						
Cause	**Consequence**	**Safeguards**	**Recommendations**	**S**	**L**	**RC**
130.Valve 16 closes	Leakages and loss of containment. Possible fire or explosion.	Hood, sensor for leakages, sensors for pressure, alarmed high-pressure sensor (PIAH)	Maintenance	E3	W3	D
131.Valve 17 closes	As above	As above	As above	E3	W3	D
132.Flanged valves close	As above	As above	As above	E3	W3	D

Table A.9.40: MORE pressure (Node 4)

Deviation name: LESS Pressure **Node description (design intent): Analysis of the light phase after the reaction section.**						
Cause	**Consequence**	**Safeguards**	**Recommendations**	**S**	**L**	**RC**
133.Lower pressure from previous nodes	Less quantity. Different final composition. Loss of the experimental test.	Hood. Sensors for leakages. Sensors.	Maintenance	E3	W3	D
134.Leakages	Release of flammable or toxic material(s).	Hood. Sensors.	Maintenance	E3	W1	F

Table A.9.41: LESS pressure (Node 4)

Deviation name: MORE Flow **Node description (design intent): Analysis of the light phase after the reaction section.**						
Cause	**Consequence**	**Safeguards**	**Recommendations**	**S**	**L**	**RC**
135.Higher flow from previous nodes	Different composition. Loss of the experimental test. Leakages and loss of containment.	Hood, sensor for leakages, sensors for pressure, alarmed high-pressure sensor (PIAH)	Maintenance	E3	W3	D
136.FI-01 fails	Erroneous quantity in the Micro-GC. Loss of the experimental test.	As above	Periodic check	E2	W4	D

Table A.9.42: MORE flow (Node 4)

Deviation name: LESS/NO flow **Node description (design intent): Analysis of the light phase after the reaction section.**						
Cause	**Consequence**	**Safeguards**	**Recommendations**	**S**	**L**	**RC**
137.Lower flow from previous nodes	Changes in the composition. Loss of the experimental test.	Hood, Sensors for leakages, sensors	Maintenance	E2	W3	E
138.Valve 16 closes	Increasing pressure. Leakages and loss of containment. Loss of the experimental test.	Hood, Sensors for leakages, sensors	Maintenance	E3	W3	D
139.Valve 17 closes	Increasing pressure. Leakages and loss of containment. Loss of the experimental test.	As above.	Maintenance	E3	W3	D
140.FI-01 fails	Erroneous quantity to the Micro-GC. Loss of the experimental test.	As above.	Maintenance, periodic check.	E2	W3	E
141.Valve before Micro-GC closes (three-way valve)	No carrier into the Micro-GC. Loss of the experimental test.		Check list, periodic check	E1	W3	F

Table A.9.43: LESS/NO flow (Node 4)

Deviation name: MORE Temperature **Node description (design intent): Analysis of the light phase after the reaction section.**						
Cause	**Consequence**	**Safeguards**	**Recommendations**	**S**	**L**	**RC**
142.Wrong setting of the temperature ramp.	Loss of the experimental test.		Checklist, procedure.	E1	W3	F
143.Thermostat failure in the Micro-GC.	Loss of the experimental test. Leakage and loss of containment.	Hood. Sensors.	Maintenance.	E3	W3	D

Table A.9.44: MORE temperature (Node 4)

Deviation name: LESS Temperature **Node description (design intent): Analysis of the light phase after the reaction section.**						
Cause	**Consequence**	**Safeguards**	**Recommendations**	**S**	**L**	**RC**
144.Wrong setting of the temperature ramp.	Loss of the experimental test.	-	Checklist, procedure.	E1	W3	F
145.Thermostat fails in the Micro-GC.	Loss of the experimental test.	-	Periodic maintenance.	E1	W3	F

Table A.9.45: LESS temperature (Node 4)

Deviation name: LESS/NO voltage Node description (design intent): Analysis of the light phase after the reaction section.						
Cause	**Consequence**	**Safeguards**	**Recommendations**	**S**	**L**	**RC**
146.Shut down of the electricity.	No analysis. Loss of the experimental test.	-	-	E1	W3	F
147.Micro-GC is not connected to electricity.	No analysis. Loss of the experimental test.	-	Periodic check	E1	W3	F
148. Power outage.	As above	-	-	E1	W3	F

Table A.9.46: LESS/NO voltage (Node 4)

Deviation name: MORE Concentration Node description (design intent): Analysis of the light phase after the reaction section.						
Cause	**Consequence**	**Safeguards**	**Recommendations**	**S**	**L**	**RC**
149. Detector fails	Loss of the experimental test.	-	Periodic maintenance	E1	W4	E

Table A.9.47: MORE concentration (Node 4)

Deviation name: LESS Concentration Node description (design intent): Analysis of the light phase after the reaction section.						
Cause	**Consequence**	**Safeguards**	**Recommendations**	**S**	**L**	**RC**
150. Detector fails	Loss of the experimental test.	-	Periodic maintenance	E1	W4	E

Table A.9.48: LESS concentration (Node 4)

Deviation name: LESS/NO Concentration Node description (design intent): Analysis of the light phase after the reaction section.						
Cause	**Consequence**	**Safeguards**	**Recommendations**	**S**	**L**	**RC**
151. Detector fails	Loss of the test		Periodic maintenance	E1	W4	E

Table A.9.49: LESS/NO concentration (Node 4)

Deviation name: MORE voltage Node description (design intent): Analysis of the light phase after the reaction section.						
Cause	**Consequence**	**Safeguards**	**Recommendations**	**S**	**L**	**RC**
152.Electrical Current overloading	Electrical short circuit. Possible fire scenario.	Electrical system compliant with regulations. Fire protection systems.	Maintenance.	E4	W2	D

Table A.9.50: MORE voltage (Node 4)

A.10 Supplementary material for LOPA analysis

Node	Initiating event	Characteristics of the basic event	Deviation	L	S	RC
1	Set a wrong set point in at least one of MFC-01/02/03/04	Human error	MORE pressure or flow	E3	W4	C
	A power outage	System failure	NO/LESS electric voltage-current	E3	W4	C
2	Wrong value at PI-01	System failure	MORE pressure	E3	W4	C
	Reactor too packed	Human error	MORE pressure	E3	W4	C
	Wrong set point in PRC-09	Human error	MORE pressure or flow	E3	W4	C
	Wrong set point in TC-01	Human error	MORE temperature/reaction rate	E3	W4	C
	Wrong set point of temperature (start-up)	Human error	MORE temperature	E3	W4	C
	Leakage/defective connection	System failure	LESS pressure, LESS/NO flow	E4	W3	C
	Reactor opening before closing the feed line(s)	Human error	TOO EARLY opening of the reactor	E3	W4	C
	Reactor closing after opening the feed line(s)	Human error	TOO LATE closing of the reactor	E3	W4	C
	A power outage	System failure	LESS/NO electric current/voltage	E3	W4	C
	Catalyst poisoning (not required)	System failure/human error	LESS/NO reaction rate or catalytic activity	E4	W3	C
3	Wrong set point in PRC-09	Human error	MORE pressure or flow	E3	W4	C
	PI-02 failure	System failure	MORE pressure	E3	W4	C
	Power outage	System failure	LESS/NO electric voltage	E3	W4	C

Table A.10.1: Hazardous events emerged from the HAZOP analysis (L: likelihood; S: severity; RC: risk class).

Stream	Equipment
Hydrogen	T-01 Valve 1 Valve 2 connected to PRC-01 Valve 3 Valve 4 connected to gas detectors (CO, CH_4, H_2 and CO_2) Valve 5 connected to PRC-05 Valve 6 connected to MFC-01 Valve 7 Mixer-01
Carbon monoxide	T-02 Valve 1 Valve 2 connected to PRC-02 Valve 3 Valve 4 connected to gas detectors (CO, CH_4, H_2 and CO_2) Valve 5 connected to PRC-06 Valve 6 connected to MFC-02 Valve 7 Mixer-01
Carbon dioxide	T-03 Valve 1 Valve 2 connected to PRC-03 Valve 3 Valve 4 connected to gas detectors (CO, CH_4, H_2 and CO_2) Valve 5 connected to PRC-07 Valve 6 connected to MFC-03 Valve 7 Mixer-01
Nitrogen	T-04 Valve 1 Valve 2 connected to PRC-04 Valve 3 Valve 5 connected to PRC-08 Valve 6 connected to MFC-01 Valve 7 Mixer-01

Table A.10.2: Streams and associated equipment involved in Node 1.

Node	Initiating event	Initial *Pf* [-]	Initial Severity [-]	Final *Pf* [-]	Final Severity [-]
	Set a wrong set point in at least one of MFC-01/02/03	0.9	0.8	$1.4 \cdot 10^{-7}$	0.8
1	Set a wrong set point in MFC-04	0.9	0.4	$1.4 \cdot 10^{-5}$	0.4
	A power outage	0.9	0.8	$1.4 \cdot 10^{-6}$	0.8
	Wrong value at PI-01	0.9	0.8	$1.8 \cdot 10^{-7}$	0.8
	Incorrect reactor packing	0.9	0.8	$5.0 \cdot 10^{-4}$	0.8
	Wrong set point in PRC-09	0.9	0.8	$5.0 \cdot 10^{-4}$	0.8
	Wrong set point in TC-01	0.9	0.8	$5.0 \cdot 10^{-4}$	0.8
2	Wrong set point of temperature (start-up)	0.9	0.8	$5.0 \cdot 10^{-4}$	0.8
	Leakage/defective connection	0.9	0.8	$3.7 \cdot 10^{-1}$	0.8
	Reactor opening before closing the feed line(s)	0.9	0.8	$3.7 \cdot 10^{-1}$	0.8
	Reactor closing after opening the feed line(s)	0.9	0.8	$3.7 \cdot 10^{-1}$	0.8
	A power outage	0.9	0.8	$5.0 \cdot 10^{-3}$	0.8
	Wrong set point in PRC-09	0.9	0.8	$5.0 \cdot 10^{-4}$	0.8
3	PI-02 failure	0.9	0.8	$5.0 \cdot 10^{-5}$	0.8
	A power outage	0.9	0.8	$5.0 \cdot 10^{-5}$	0.8

Table A.10.3: LOPA analysis. Initial failure probability Pf and severity of the different initiating events.

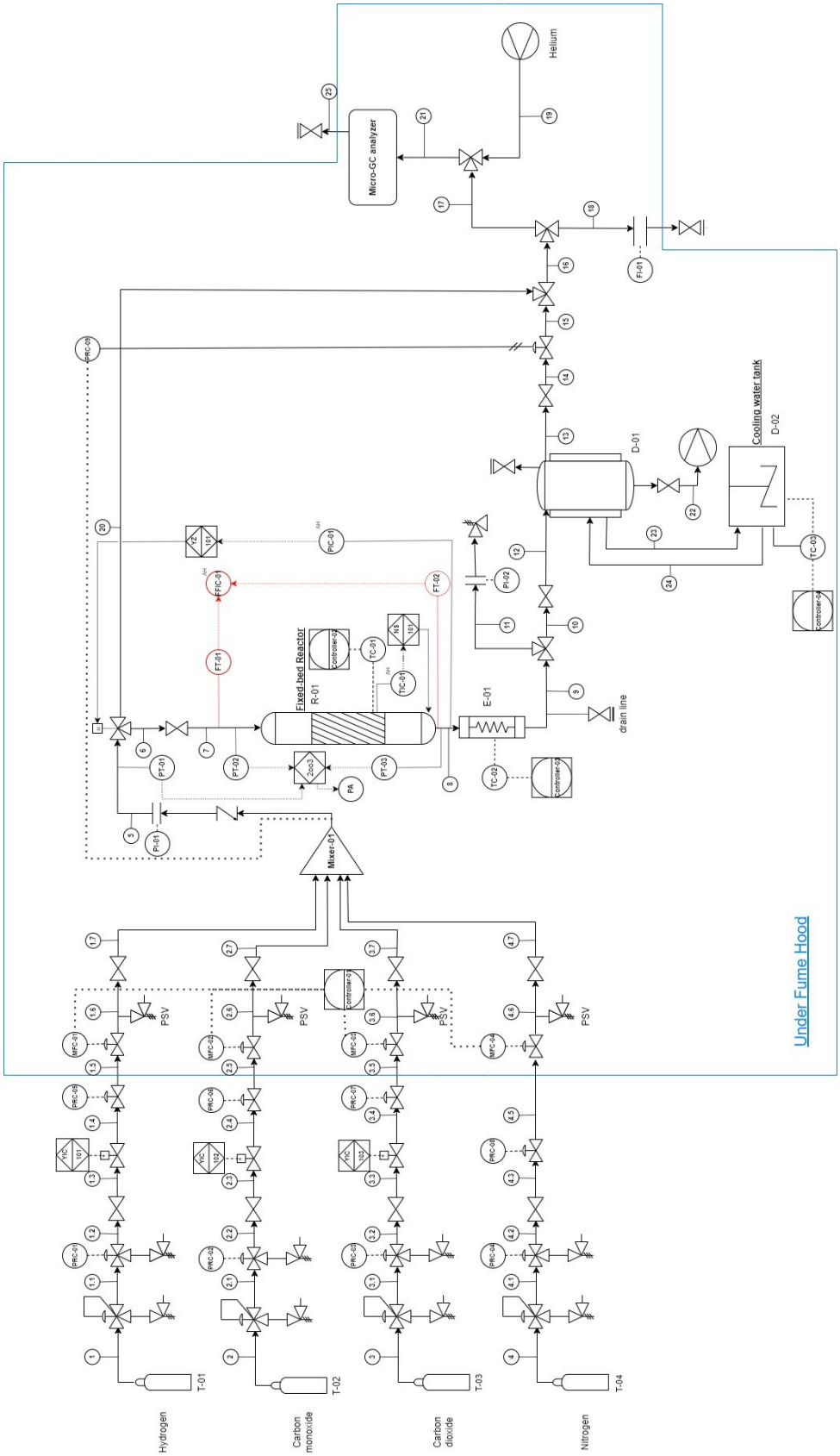

Figure A.10.1: Improved P&ID of the pilot plant embedding modification from the combined HAZOP and LOPA analyses.

Nomenclature

C	=	Cost of damage (€)
C_{max}	=	Maximum cost of damage (€)
D	=	Severity (-)
E_{TNT}	=	Explosive energy of TNT (4686 kJ/kg)
f	=	Frequency of the event (yr-1)
H_i	=	Heat of formation of species i (kJ/mol)
L	=	Likelihood (-)
m	=	Mass of the flammable substance (kg)
m_{TNT}	=	Equivalent mass of TNT (kg)
P_f	=	Mean probability of failure (-)
R	=	Risk (-)
RC	=	Risk Class (-)
S	=	Severity (-)
t	=	Time (years)

Greek letters

$\Delta H°_{298}$	=	Standard enthalpy of reaction at 298 K (kJ/mol)
ΔH_R	=	Heat of reaction (kJ/mol)
ΔP	=	Difference between outlet and inlet pressures (bar)
η	=	Reactivity coefficient (-)
ν_i	=	Stoichiometric coefficient (-)

Acronyms

ACS	=	American Chemical Society
ALARP	=	As Low As Reasonably Practicable
ATEX	=	Atmosphere Explosible
BPCS	=	Basic Process Control System
BST	=	Baker-Strehlow-Tang method
DDT	=	Deflagration to detonation transition
DSC	=	Differential Scanning Calorimeter
ETA	=	Event Tree Analysis
FC	=	Fail to close
FKM	=	Fluorine Kautschuk Material
FMEA	=	Failure Modes and Effects Analysis
FO	=	Fail to open
FT	=	Fischer Tropsch
FT	=	Flow Transmitter (equipment)
FTA	=	Fault Tree Analysis
FTIR	=	Fourier Transform Infrared
GC	=	Gas Chromatography
HAZOP	=	Hazard and Operability
H&RA	=	Hazard and Risk Assessment
IE	=	Initiating Event
IEF	=	Initiating Event Frequency
IPL	=	Independent Protection Layer
IRT	=	IPL Response Time
LEL	=	Lower Explosive Limit
LFL	=	Lower Flammable Limit
LOPA	=	Layer of Protection Analysis
MA FACE	=	Massachusetts Fatality Assessment and Control Evaluation

MAWP	=	Maximum Allowable Working Pressure
MFC	=	Mass-Flow Controller
MMC	=	Multiple Module Calorimeter
MOC	=	Management of Change
MooN	=	M out of N channel architecture
MSDS	=	Material Safety Data Sheet
MSP	=	Maximum Setpoint
MTTF	=	Mean time to failure
NFPA	=	The National Fire Protection Association
NGAP	=	Next Generation Advanced Procedures
OSHA	=	Occupational Safety and Health Administration
PA	=	Pressure Alarm
P&ID	=	Piping and Instrumentation Diagram
PCTFE	=	Polychlorotrifluoroethylene
PFD	=	Process Flow Diagram (Chapter 1 and 2)
PFD	=	Probability of Failure on Demand (Chapter 3 and 4)
PhD	=	Doctor of Philosophy
PI	=	Principal Investigator
PI	=	Pressure Indicator (equipment)
PIAH	=	High-Pressure Indicator and Alarm
PIC	=	Pressure Indicator Controller
PLT	=	Process Lag Time
PSV	=	Pressure Safety Valve
PRC	=	Pressure Recording Controller
PT	=	Pressure Transmitter
PTFE	=	Polytetrafluoroethylene
RAMP	=	Recognize hazards, Assess risk of hazard, Minimize risk of hazards, Prepare for emergencies
RC	=	Risk class
R&D	=	Research and Development
RRF	=	Risk Reduction Factor
SCAI	=	Safety controls, alarms and interlocks
SDSs	=	Safety Data Sheets
SIF	=	Safety Instrumented Function
SIL	=	Safety Integrity Level
SIS	=	Safety Instrumented System
SME	=	Subject Matter Expert
SOPs	=	Standard Operating Procedures
SP	=	Set-point
SS	=	Stainless Steel
TC	=	Temperature controller
TIC	=	Temperature Indicator Controller
TNO-MEM	=	TNO Multi Energy Method
TNT	=	Trinitro Toluene
UCD	=	User- Centered Design
UEF	=	Unmitigated event frequency
UEL	=	Upper Explosive Limit
UFL	=	Upper Flammable Limit

References Chapter 6

[1] CCPS (Center for Chemical Process Safety), Guidelines for hazard evaluation procedures, 3rd ed., John Wiley & Sons, Inc., 2008.

[2] AIChE, Chemical Reactivity Worksheet, (n.d.). https://www.aiche.org/ccps/resources/chemical-reactivity-worksheet (accessed May 24, 2023).

[3] F. Crawley, B. Tyler, HAZOP: Guide to Best Practice, 3rd ed., Elsevier, 2015. https://doi.org/https://doi.org/10.1016/C2014-0-04859-9.

[4] The British Standards Institution, BS EN 61882:2016, "Hazard and operability studies (HAZOP studies) - Application guide," 2016. https://bsol.bsigroup.com/.

[5] CCPS (Center for Chemical Process Safety), Handbook for Process Safety in Laboratories and Pilot Plants: A Risk-based Approach, John Wiley & Sons, Inc., 2023.

[6] P. Clarke, Functional Safety from Scratch, Elsevier, 2023. https://doi.org/10.1016/C2022-0-01455-0.

[7] The British Standards Institution, BS EN 61511-1:2017+A1:2017, "Functional Safety-Safety instrumented systems for the process industry sector- Part 1: Framework, definitions, system, hardware and application programming requirements," 2017. https://bsol.bsigroup.com/.

[8] The British Standards Institution, BS EN 61511-2:2017, "Functional safety - Safety instrumented systems for the process industry sector- Part 2: Guidelines for the application of IEC 61511-1 (IEC 61511-2:2016)," 2017. https://bsol.bsigroup.com/.

[9] The British Standards Institution, BS EN 61511-3:2017, "Functional safety - Safety instrumented systems for the process industry sector- Part 3: Guidance for the determination of the required safety integrity levels," 2017. https://bsol.bsigroup.com/.

[10] CCPS (Center for Chemical Process Safety), Guidelines for initiating events and independent protection layers in layer of protection analysis, John Wiley & Sons, Inc., Hoboken, New Jersey, 2015.

[11] W.M. Goble, H. Cheddie, Safety Instrumented Systems Verification: Practical Probabilistic Calculations, ISA - The Instrumentation, Systems and Automation Society, 2005.

[12] Exida, SILSafeData, (2023). https://silsafedata.com/ (accessed October 13, 2023).

[13] N. Langerman, Management of Change for Laboratories and Pilot Plants, Org. Process Res. Dev. 12 (2008) 1305-1306. https://doi.org/10.1021/op8001855.

[14] American Petroleum Institute, API Standard 520, "Sizing, Selection, and Installation of Pressure- relieving Devices. Part I: Sizing and Selection," 2014. https://www.api.org/.

[15] American Petroleum Institute, API STD 520 Part 1: Sizing, Selection, and Installation of Pressure-Relieving Devices in Refineries, (2023). https://www.apiwebstore.org/standards/520 Part_1 (accessed October 30, 2023).

[16] R.H.J. Hill, Recognizing and understanding hazards - The key first step to safety, J. Chem. Heal. Saf. 26 (2019) 5-10. https://doi.org/10.1016/j.jchas.2018.11.005.

[17] The British Standards Institution, BS EN ISO 11114-1:2020, "Gas cylinders. Compatibility of cylinder and valve materials with gas contents - Part 1: Metallic materials," 2020. https://bsol.bsigroup.com/.

[18] The British Standards Institution, BS EN ISO 11114-2:2021,"Transportable gas cylinders-Compatibility of cylinder and valve materials with gas contents - Part 2: Non-metallic materials", 2021. https://bsol.bsigroup.com/.

[19] R.K. Sinnott, G.P. Towler, Chemical engineering design, 6th ed., Butterworth-Heinemann, Oxford, 2020.

[20] R.K. Sinnott, G.P. Towler, Corrosion Chart, Chem. Eng. Des. (2020) e1-e19. https://doi.org/10.1016/b978-0-08-102599-4.09991-4.

[21] Work Metal S.p.A., Compatibility table, (n.d.). https://www.metalwork.it/media/Stumenti_manuali/Tab_compatibilita_19_02_2019.pdf (accessed April 26, 2023).

[22] The British Standards Institution, BS EN IEC 60079-10-1:2021, "Explosive atmospheres Part 10-1: Classification of areas - Explosive gas atmospheres," 2021. https://bsol.bsigroup.com/.

[23] The British Standards Institution, PD IEC/TS 60079-46:2017, "Explosive atmospheres Part 46: Equipment assemblies," 2017. https://bsol.bsigroup.com/.

[24] D.A. Crowl, J.F. Louvar, Chemical process safety: Fundamentals with applications, 2. ed, Prentice Hall PTR, Upper Saddle River, 2002.

[25] M. Sharifian, F. Galli, B. Timbers, N. Hudon, G.S. Patience, Safety analysis and risk assessment of a Micro-GtL Plant, J. Loss Prev. Process Ind. 83 (2023) 105071. https://doi.org/10.1016/j.jlp.2023.105071.

[26] The British Standards Institution, BS EN 764-7:2002, "Pressure equipment Part 7: Safety systems for unfired pressure vessels," 2002. https://bsol.bsigroup.com/.

[27] ABB, Manuale tecnico di riferimento Parametri di sistema, 20th Sept. 2023. (2023). https://search.abb.com/library/Download.aspx?DocumentID=3HAC050948-007&LanguageCode=it&DocumentPartId=&Action=Launch (accessed October 13, 2023).

[28] S.-W. Jeen, S. Lazar, L. Gui, R.W. Gillham, Degradation of chlorofluorocarbons using granular iron and bimetallic irons., J. Contam. Hydrol. 158 (2014) 55-64. https://doi.org/10.1016/j.jconhyd.2014.01.002.

[29] M.D. Greenhalgh, A.S. Jones, S.P. Thomas, Iron-catalysed hydrofunctionalisation of alkenes and alkynes, 2015. https://doi.org/10.1002/cctc.201402693.

[30] Q. sheng ZHOU, C. LI, X. bin LI, Z. hong PENG, G. hua LIU, T. gui QI, Reaction behavior of ferric oxide in system Fe_2O_3-SiO_2-Al_2O_3 during reductive sintering process, Trans. Nonferrous Met. Soc. China (English Ed. 26 (2016) 842-848. https://doi.org/10.1016/S1003-6326(16)64175-4.

[31] M. Zhou, L. Zhang, H. Lu, L. Shao, M. Chen, Reaction of silicon dioxide with water: A matrix isolation infrared and density functional theoretical study, J. Mol. Struct. 605 (2002) 249-254. https://doi.org/10.1016/S0022-2860(01)00767-0.

[32] T. Mori, W. Ueda, Y. Morikawa, Hydrodechlorinative dimerization of 1,1,1-trifluorohaloethanes over Ru/SiO_2 catalyst, Catal. Letters. 38 (1996) 73-76. https://doi.org/10.1007/BF00806902.

[33] X. Yong, J.S. Tse, J. Chen, Mechanism of Chemical Reactions between SiO_2 and CO_2 under Mantle Conditions, ACS Earth Sp. Chem. 2 (2018) 548-555. https://doi.org/10.1021/acsearthspacechem.7b00144.

[34] M.J. Mitchell, O.E. Jensen, K.A. Cliffe, M.M. Maroto-Valer, A model of carbon dioxide dissolution and mineral carbonation kinetics, Proc. R. Soc. A Math. Phys. Eng. Sci. 466 (2010) 1265-1290. https://doi.org/10.1098/rspa.2009.0349.

[35] H. Idriss, M. Scott, V. Subramani, 1 - Introduction to hydrogen and its properties, in: V. Subramani, A. Basile, T.N.B.T.-C. of H.E. Veziroğlu (Eds.), Woodhead Publ. Ser. Energy,

Woodhead Publishing, Oxford, 2015: pp. 3-19. https://doi.org/https://doi.org/10.1016/B978-1-78242-361-4.00001-7.

[36] NOAA, CAMEO Chemicals, (n.d.). https://cameochemicals.noaa.gov/ (accessed April 26, 2023).

[37] H.H.B.T.-S. in S.S. and C. Kung, ed., Chapter 13 Cataltyic Reaction Between Hydrogen and Carbon Oxides, in: Transit. Met. Oxides, Elsevier, 1989: pp. 227-251. https://doi.org/https://doi.org/10.1016/S0167-2991(08)60936-2.

[38] V. Pattabathula, J. Richardson, Introduction to ammonia production, Chem. Eng. Prog. 112 (2016)69-75. https://www.aiche.org/resources/publications/cep/2016/september/introduction-ammonia-production.

[39] R.A. Gardner, The kinetics of silica reduction in hydrogen, J. Solid State Chem. 9 (1974) 336- 344. https://doi.org/https://doi.org/10.1016/0022-4596(74)90092-9.

[40] S. Pillot, L. Coudreuse, 2 - Hydrogen-induced disbonding and embrittlement of steels used in petrochemical refining, in: R.P. Gangloff, B.P.B.T.-G.H.E. of M. in E.T. Somerday (Eds.), Woodhead Publ. Ser. Met. Surf. Eng., Woodhead Publishing, 2012: pp. 51-93. https://doi.org/https://doi.org/10.1533/9780857093899.1.51.

[41] R. Sivaramakrishnan, M.-C. Su, J. V Michael, S.J. Klippenstein, L.B. Harding, B. Ruscic, Rate Constants for the Thermal Decomposition of Ethanol and Its Bimolecular Reactions with OH and D: Reflected Shock Tube and Theoretical Studies, J. Phys. Chem. A. 114 (2010) 9425-9439. https://doi.org/10.1021/jp104759d.

[42] P.W. Musch, B. Engels, The Importance of the Ene Reaction for the C2−C6 Cyclization of Enyne−Allenes, J. Am. Chem. Soc. 123 (2001) 5557-5562. https://doi.org/10.1021/ja010346p.

[43] W.M.T.M. Reimerink, The use of activated carbon as catalyst and catalyst carrier in industrial applications, in: A.B.T.-S. in S.S. and C. Dąbrowski (Ed.), Adsorpt. Its Appl. Ind. Environ. Prot., Elsevier, 1999: pp. 751-769. https://doi.org/https://doi.org/10.1016/S0167-2991(99)80571-0.

[44] M.A. Uddin, E.M. Kennedy, B.Z. Dlugogorski, Gas-phase reaction of CCl_2F_2 (CFC-12) with methane, Chemosphere. 53 (2003) 1189-1191. https://doi.org/10.1016/S0045-6535(03)00658-1.

[45] H. Takahashi, S. Hisaoka, T. Nitta, Ethanol oxidation reactions catalyzed by water molecules, Chem. Phys. Lett. 363 (2002) 80-86. http://linkinghub.elsevier.com/retrieve/pii/S0009261402011429.

[46] R.J. Lewis, Sax's dangerous properties of industrial materials, Choice Rev. Online. 30 (1993) 30-2435-30-2435. https://doi.org/10.5860/choice.30-2435.

7. LIFE CYCLE ASSESSMENT (LCA)

Recent advancements in FT catalysts have focused on enhancing performance metrics such as activity, selectivity, and stability without adequately considering the environmental impacts of these catalysts throughout their entire lifecycle.

This gap is particularly significant given the increasing emphasis on sustainability in chemical processes. Comprehensive Life Cycle Assessment (LCA) studies that evaluate the environmental impact of FT catalysts from production to disposal are notably lacking especially considering CO_2 as feedstock for the process [1]. This lack of in-depth and specific studies for LCA limits our understanding of the true sustainability of these catalysts, potentially leading to the adoption of technologies that are not fully environmentally viable in the long term.

Life cycle assessment is an essential tool for evaluating the sustainability of chemical processes and products or materials. It provides a holistic view by assessing the environmental impacts associated with all stages of a product's life, from raw material extraction and catalyst manufacturing to operational use and end-of-life disposal. Without LCA, the overall sustainability of advanced FT catalysts cannot be fully understood [1]. LCA has been increasingly applied to assess the environmental impacts of various experimental setups and processes in different scales, from laboratory to industrial processes. By evaluating the entire lifecycle of chemical processes, researchers can identify key areas where environmental impacts can be minimized. Clearly, at the basis of the LCA analysis assessments there are all the data that characterize the processes and the plants, such as energy consumption, materials, utilities, raw materials, disposal procedure etc. The LCA analysis is strongly dependent on the performance of the studied process, that is, on the capacity of the technology to transform the raw materials into the final products. In the specific context of technologies based on heterogeneous catalysis, this means that the use of different catalysts entails different performances that must be taken into account in the environmental impact assessments. The development of a new catalyst therefore requires evaluating its impact on the process yields and therefore in the LCA calculations. For instance, LCA can help determine the most sustainable synthesis routes, the impact of different operational conditions, and the benefits of recycling or reusing materials in a lab setting [2,3]. Furthermore, each process plant, at any scale, requires the use of energy to operate and this means that for each hour of operation of the plant a certain amount of CO_2 is produced. Therefore, the conversion of a given amount of CO_2 entering the FT plant requires the generation of additional CO_2 emissions to supply the energy necessary for its operation. Therefore, to convert a certain amount of CO_2 entering the FT plant, it is necessary to produce another amount of CO_2 to produce the energy necessary for its operation. It therefore, necessary to calculate a balance between this input and output of CO_2 and verify that the balance is positive, that is, that the CO_2 converted by the technology is greater than the CO_2 produced by the conversion process itself.

Consequently, the scope of this study is to conduct a detailed LCA of three different iron-based hydrotalcite catalysts tested at various temperatures in order to quantify the different environmental impact of the FT using different catalysts and different operating conditions and, then, to evaluate the CO_2 balance previously introduced. By integrating LCA with catalyst performance evaluations, this research aims to provide a comprehensive assessment of the

environmental impacts and benefits associated with these catalysts. The goal is to identify not only the most efficient catalysts in terms of performance but also those that offer the lowest environmental footprint. Evaluating the LCA of these catalysts under different operational conditions will help determine the optimal balance between catalytic efficiency and environmental sustainability. This approach ensures that advancements in catalyst technology are aligned with broader environmental goals, promoting the development of truly sustainable chemical processes.

7.1. LCA methodology

In order to evaluate the environmental impact and the balance on the converted and produced CO_2 from the FT reaction, the preparation methodologies and the conversion results obtained using three types of iron-based hydrotalcite catalysts will be analyzed. These catalysts were tested in a laboratory-scale plant with a continuous fixed bed reactor and the conversion and selectivity data to products were collected with different operating conditions of temperature and pressure.

7.1.1. System Boundaries

This LCA study is divided into two main phases, each with its own specific system boundaries.

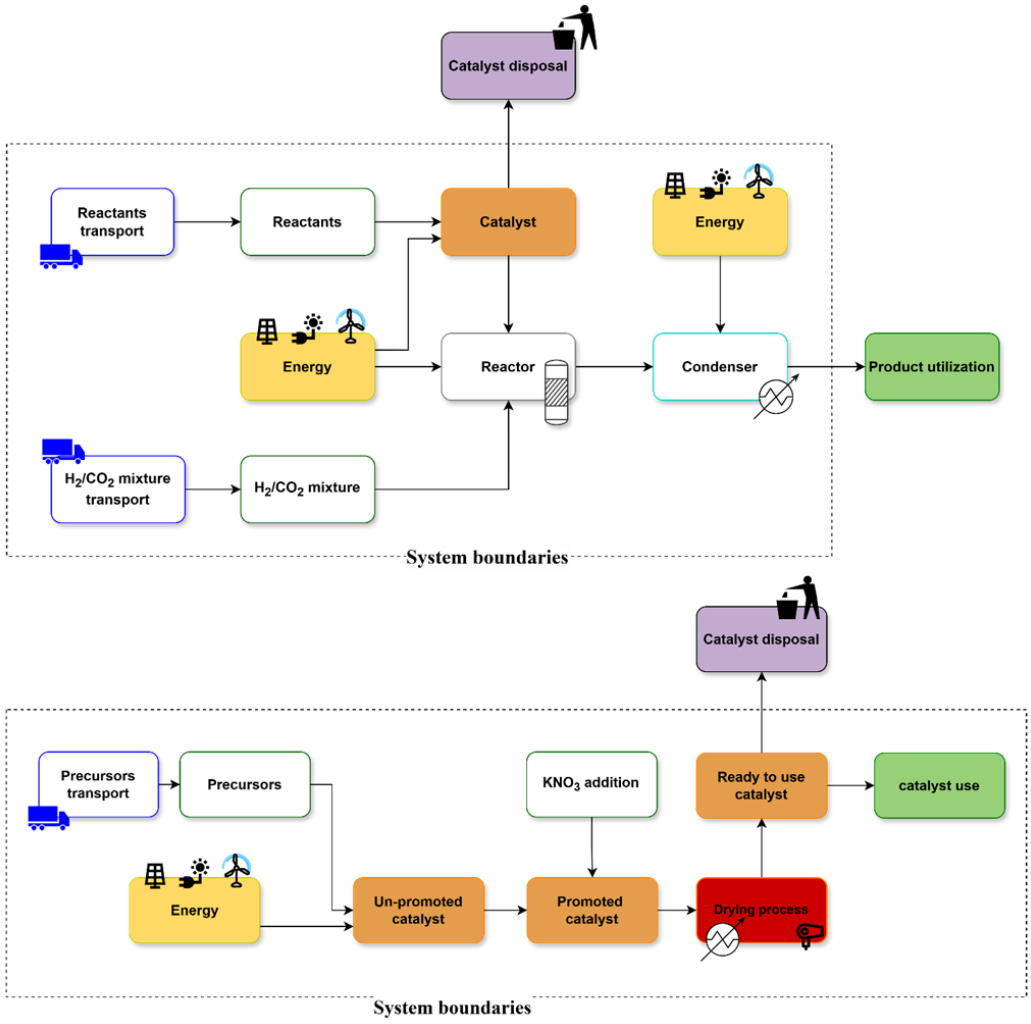

*Figure 7.1. Schematic representation of the system boundaries for the Fischer-Tropsch process and catalyst production. **(a)** Process flow diagram for the Fischer-Tropsch synthesis, including reactant transport, reaction, product separation, and utilization. **(b)** Process flow diagram for catalyst preparation, highlighting precursor transport, promotion, drying, and final catalyst use.*

The first phase focuses on the production of three different catalysts (Fe30, Fe40, Co45) for use in the Fischer-Tropsch process. The system boundaries encompass raw material extraction, including the gathering of necessary metals and chemical precursors, the transportation of these raw materials to the production site (integrated through SimaPro's "market for" data, which accounts for average market processes including transportation), the chemical reactions and processes required to synthesize the catalysts, and finally, the usage without considering the disposal of the catalysts.

The second phase of the analysis shifts to the operational process of synthesizing C2+ hydrocarbons (i. e. all the hydrocarbons molecules with more than 1 carbon atom) using the Fischer-Tropsch method with the previously produced catalysts. This phase's boundaries include catalyst use, energy consumption related to both reactor temperature maintenance and cold trap condenser unit, direct emissions from the chemical reaction, and the transportation of both raw materials and catalysts as accounted for by SimaPro's "market for" processes.

Both systems are depicted in Figure 7.1.

7.1.2. Functional Units

To adequately assess the outputs of the different phases, two distinct functional units were chosen. For the catalyst production phase, the functional unit is 1 kg of catalyst produced. For the Fischer-Tropsch operational phase, the functional unit is 1 kg of C_{2+} hydrocarbons produced. These units allow for a precise evaluation of the environmental impacts associated with each stage of the process.

7.1.3. Inventory Data

The inventory data for both phases were sourced using SimaPro software 9.4, relying on its comprehensive database of industrial processes and market scenarios. The "market for" processes were specifically selected to represent a realistic and accurate depiction of environmental impacts. This includes data on the extraction, production, and transportation of raw materials required for catalyst synthesis and the Fischer-Tropsch process. Additionally, detailed information was incorporated regarding the production processes, energy consumption, associated emissions, and waste management, ensuring a holistic view of the life cycle impacts.

To assess the environmental impacts, several standardized methods were employed:

- IPCC 2021 GWP100: this method was used to calculate the Global Warming Potential (GWP) in terms of CO_2 equivalents, providing insight into the greenhouse gas emissions associated with both the Fischer-Tropsch process and the production of the catalysts.
- CML-IA Baseline V3.08: a comprehensive method that evaluates a wide range of environmental impact categories, including abiotic depletion, ozone layer depletion, and various forms of ecotoxicity. It is particularly effective in identifying and quantifying the impacts associated with natural resource use and pollutant emissions.
- Cumulative Energy Demand (CED) V1.11: this method was utilized to quantify the total energy demand of the system, distinguishing between renewable and non-renewable energy sources. It plays a crucial role in assessing the energy efficiency of the catalyst

production process and the Fischer-Tropsch operational phase, especially when comparing the sustainability of different energy sources.

7.2. Results and discussion

7.2.1. Environmental impact for catalysts production

The detailed analysis of the environmental impacts associated with the production of the three catalysts (Fe30, Fe40, Co45) provides significant insights into the sustainability of their respective productions. However, it is important to acknowledge that the environmental impact values presented in this study are based on the extrapolation of laboratory-scale data (5g of catalyst) to an industrially relevant functional unit of 1 kg. While this approach allows for a direct calculation in the absence of industrial data, it does not fully capture the efficiency gains inherent to large-scale production.

Laboratory-scale processes typically exhibit lower material utilization efficiency, higher relative energy consumption, and increased waste generation per unit of product. In contrast, industrial-scale catalyst manufacturing benefits from economies of scale, continuous process operation, optimized heat integration, and improved reactant utilization, all of which contribute to a lower per-unit environmental burden. Studies on scaling methodologies for chemical processes suggest that direct linear extrapolation from small-scale experiments often leads to an overestimation of environmental impacts at larger scales due to these process inefficiencies [4].

To refine the accuracy of environmental impact assessments, methodologies such as those implemented in tools like CatCost, developed by the National Renewable Energy Laboratory (NREL), provide standardized approaches for estimating catalyst manufacturing costs and environmental footprints while incorporating scale-up [5]. Furthermore, ISO 14040/14044 standards emphasize the importance of defining functional units that reflect real-world industrial scenarios [6]. Consequently, the environmental impact values reported here should be interpreted as a worst-case scenario, likely overestimating the real industrial burden. Future refinements to this analysis could involve integrating industrial LCA datasets, incorporating correlation factors, or using exergy-based assessments to better approximate the true environmental impact of large-scale catalyst production.

7.2.1.1. IPCC 2021 GWP100 Analysis

The Global Warming Potential (GWP) was measured using the IPCC 2021 GWP100 V1.01 method. This method evaluates the impact of greenhouse gases in terms of CO_2 equivalents over a 100-year time horizon. The data collected indicate that the Co45 catalyst has a significantly higher impact on global warming compared to the Fe30 and Fe40 catalysts. Specifically, the CO_2 equivalent emissions for all the three catalysts are reported in Table 7.1. The higher impact of Co45 sample is primarily attributable to the increased consumption of fossil energy during its production. The extraction and processing of cobalt, a key component of the Co45 catalyst, are energy-intensive processes that contribute significantly to its overall CO_2 emissions [7]. To better understand the sources of emissions contributing to GWP, Table 7.1 further breaks down the GWP100 into its fossil, biogenic, and land transformation components. The majority of emissions originate from fossil sources, with Co45 exhibiting the highest fossil GWP100 (60.53 kg CO_2-

eq). In particular, the Co45 catalyst shows higher emissions from biogenic sources (0.450 kg CO_2-eq) and land transformation (0.13 kg CO_2-eq) compared to the Fe30 and Fe40 catalysts. The biogenic CO_2 emissions are associated with the use of biomass in the production process, while land transformation emissions are related to changes in land use for resource extraction and processing facilities. Although these contributions are smaller than those from fossil fuels, they still add to the overall GWP of the Co45 catalyst.

The Fe30 and Fe40 catalysts exhibit lower GWP values, suggesting a more sustainable production process in terms of greenhouse gas emissions. This is largely due to less energy-intensive raw material extraction and processing, as well as more efficient energy use. Consequently, the selection of the catalyst has a significant impact on the overall carbon footprint of the Fischer-Tropsch process.

Impact category	Unit	catalyst Co45	catalyst Fe30	catalyst Fe40
GWP100 - fossil	kg CO_2-eq	60,53	44,90	44,95
GWP100 - biogenic	kg CO_2-eq	0,450	0,365	0,36
GWP100 - land transformation	kg CO_2-eq	0,13	0,028	0,03

Table 7.1. Breakdown of Global Warming Potential (GWP100) for the three catalysts (Co45, Fe30, Fe40), expressed in kg CO_2-equivalent (kg CO_2-eq). The values are categorized into fossil, biogenic, and land transformation emissions.

7.2.1.2. Cumulative Energy Demand (CED) Analysis

The Cumulative Energy Demand (CED) analysis, shown in Fig 7.2, provides a comprehensive view of the total energy required during the life cycle of the catalysts, including both renewable and non-renewable energy sources. This analysis is crucial for understanding the overall energy efficiency and sustainability of the production processes for Co45, Fe30, and Fe40 catalysts.

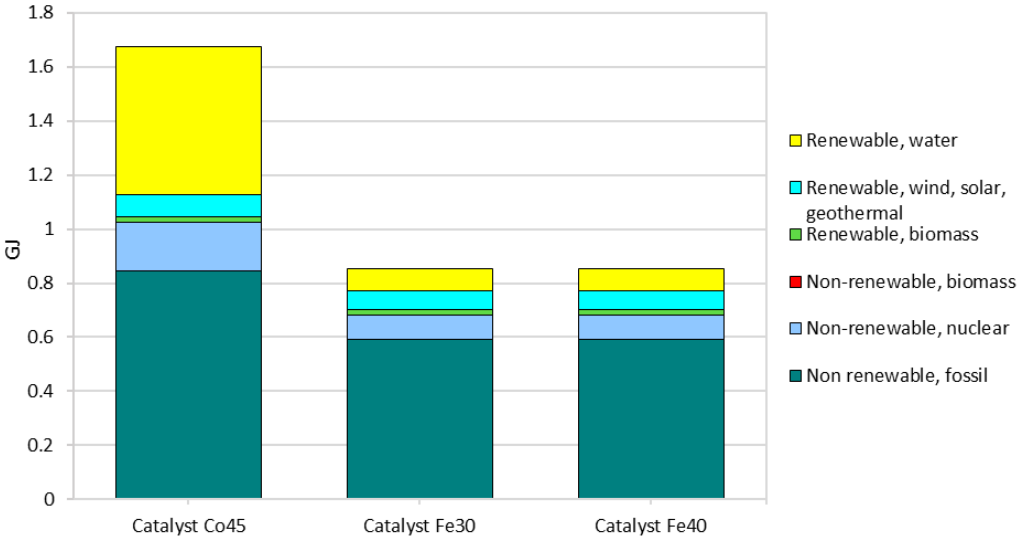

Figure 7.2. Energy consumption for the production of catalysts Co45, Fe30, and Fe40, categorized by energy source (renewable and non-renewable).

The total energy demand for producing 1 kg of each catalyst reveals significant differences. The Co45 catalyst requires nearly double the total energy compared to Fe30 and Fe40, with Co45 consuming 1.676 GJ of energy versus 0.853 GJ for both Fe30 and Fe40. This substantial difference highlights the significantly higher energy input needed for Co45 production.

The Co45 catalyst exhibits a notably higher demand for non-renewable energy, particularly from fossil fuels and nuclear energy. The consumption of fossil fuels for Co45 is significantly higher, underscoring its reliance on non-renewable energy sources. This is a critical factor contributing to its higher Global Warming Potential (GWP) and overall environmental impact. The extraction and processing of cobalt are highly energy-intensive, requiring significant amounts of fossil fuels, which in turn increases the CO_2 emissions associated with its production.

Nuclear energy consumption for Co45 production is also notably higher. While nuclear energy has a lower carbon footprint compared to fossil fuels, it poses other environmental challenges, including the management of radioactive waste. The higher use of nuclear energy in Co45 production reflects the complex energy requirements of processing cobalt.

In terms of renewable energy, Co45 also demands more from sources such as biomass, wind, solar and hydroelectric power. The use of hydroelectric power is particularly high, suggesting that while there is an effort to incorporate cleaner energy sources, the overall energy demand remains high. The renewable energy inputs, although higher for Co45, do not sufficiently offset the overall greater energy requirements compared to the iron-based catalysts.

The iron-based catalysts, Fe30 and Fe40, show a more balanced energy profile, with lower total energy consumption and a more efficient use of both non-renewable and renewable energy sources. Their production processes are less energy-intensive, leading to lower overall environmental impacts. This balance is reflected in their nearly identical CED profiles, indicating minimal differences in their composition and production processes.

7.2.1.3. CML-IA Baseline Analysis

The environmental impacts associated with the production of the three catalysts were assessed using the CML-IA baseline V3.08 method, shown in Fig 7.3 and 7.4. This method provides a comprehensive evaluation across various impact categories, including abiotic depletion, global warming potential, ozone layer depletion, human toxicity, ecotoxicity (freshwater, marine, and terrestrial), photochemical oxidation, acidification, and eutrophication.

Abiotic depletion measures the consumption of non-living resources. Co45 exhibited a significantly higher impact in this category compared to Fe30 and Fe40, primarily due to the extensive use of cobalt, which requires energy-intensive extraction. This catalyst's production demands a substantial amount of mineral resources, reflecting a notable environmental burden.

The Global Warming Potential (GWP) of Co45 was also the highest among the catalysts, largely driven by the high energy consumption and associated greenhouse gas emissions during its production, primarily from fossil fuels. This underscores Co45's greater contribution to global warming compared to the iron-based catalysts.

Ozone layer depletion impacts were higher for Co45, linked to the emissions of ozone-depleting substances during cobalt extraction and processing. Human toxicity was notably higher for Co45 as well, attributed to the release of hazardous substances during its production, which poses significant health risks [8].

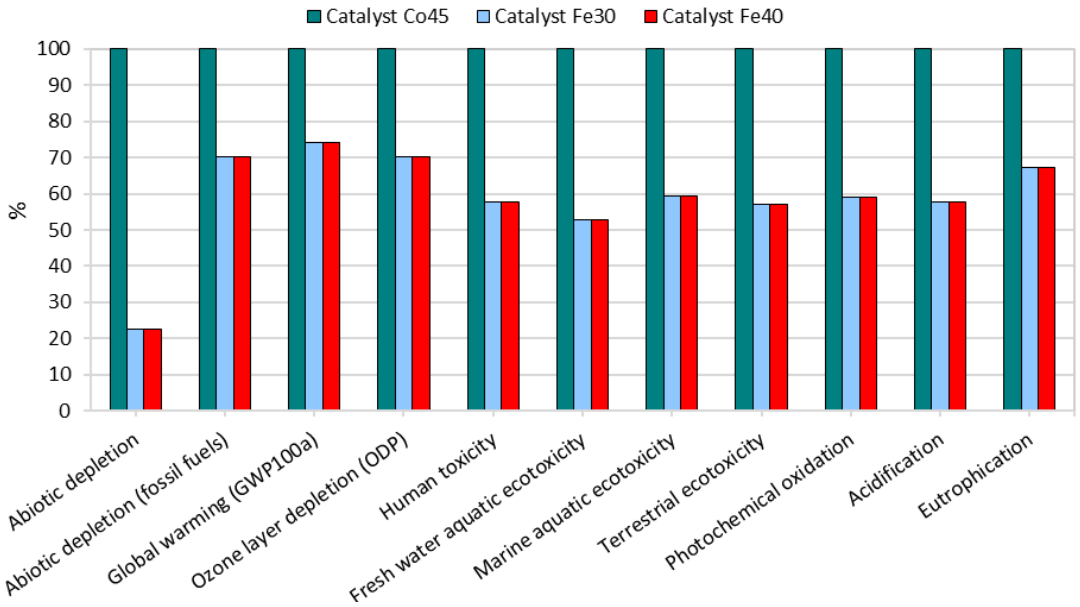

Figure 7.3. Comparative environmental impact assessment across multiple impact categories, expressed as a percentage of the highest value in each category (Characterization).

In terms of ecotoxicity too, Co45 demonstrated the highest impacts across freshwater, marine, and terrestrial categories. The production of this catalyst involves significant releases of pollutants, particularly cobalt sulphate, which contribute to its elevated ecotoxicity scores. The marine aquatic ecotoxicity, in particular, was markedly higher due to waste disposal issues associated with cobalt processing.

Photochemical oxidation, associated with smog formation, was also highest for Co45. This was primarily due to the emission of volatile organic compounds (VOCs) during cobalt processing. Acidification potential, which can lead to acid rain, was another category where Co45 had a significantly higher impact, mainly due to sulphur dioxide and nitrogen oxide emissions.

Lastly, eutrophication, indicating nutrient enrichment of water bodies, was higher for Co45, reflecting the environmental challenges posed by nutrient runoff from cobalt mining activities.

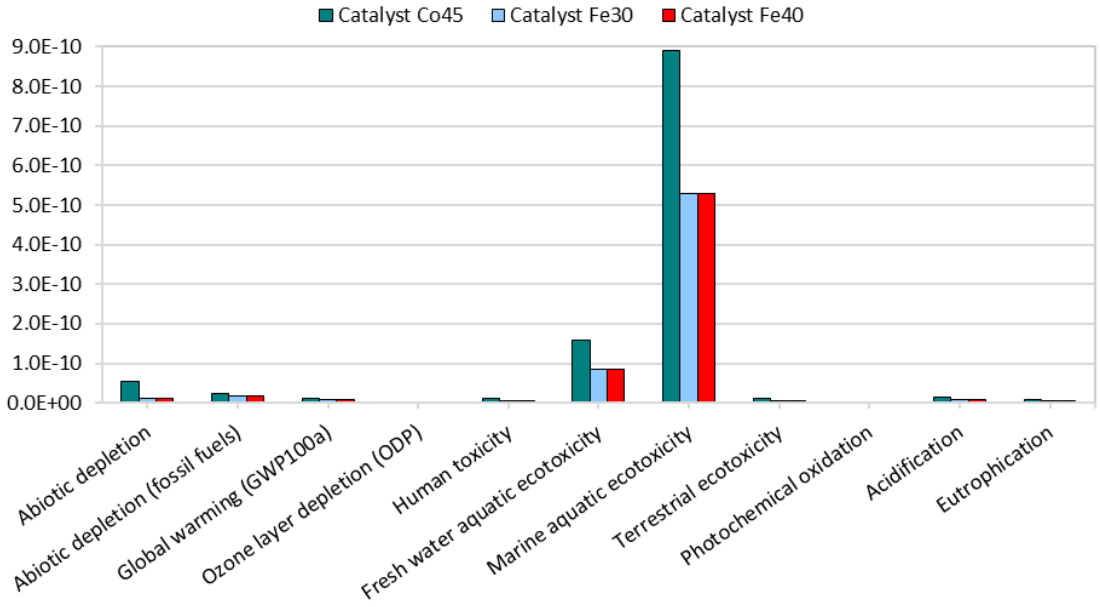

Figure 7.4. Environmental impact assessment across multiple categories, expressed in absolute values (Normalization).

Normalization, shown in Fig 7.4, is essential for contextualizing results, enabling a comparison of impact categories based on their relative significance rather than their absolute values. In the analysis of the catalysts Co45, Fe30, and Fe40, marine aquatic ecotoxicity is identified as the most significant impact category, indicating a considerable risk to marine ecosystems. This is followed by freshwater aquatic ecotoxicity, which also demonstrate substantial, though comparatively lower, impacts. These findings underscore the primary environmental concerns associated with these catalysts, particularly their potential contribution to ecological toxicity in aquatic environments. Conversely, categories such as ozone layer depletion and photochemical oxidation exhibit minimal impacts, suggesting they are of lesser concern for these specific catalysts. Consequently, normalization plays a critical role in prioritizing environmental impacts, directing attention to the most severe risks.

7.2.2. Environmental impact for FT products synthesis

7.2.2.1. Catalytic results

Although thoroughly discussed in Chapter 5, the specific catalytic performance is discussed in detail as comprehensive for the LCA study understanding. The catalytic performance in FT synthesis of the three catalysts (Fe30, Fe40, and Co45) was evaluated in terms of CO_2 conversion and product selectivity across a range of temperatures (250°C to 350°C). The results provide valuable insights into the reaction mechanisms and the influence of catalyst composition on the distribution of products.

The CO_2 conversion rates increase with temperature (Fig. 7.5) for all three catalysts, as expected, due to the enhanced kinetic energy that facilitates reaction rates. However, Co45 exhibits a notably higher conversion efficiency compared to the Fe-based catalysts across the entire temperature range. At 345°C, Co45 reaches a CO_2 conversion rate of approximately 50%, significantly outperforming Fe30 and Fe40, which plateau at around 35% and 30%, respectively. The superior performance of Co45 can be attributed to the inherent properties of cobalt, which is known to have a higher intrinsic activity for CO_2 hydrogenation, particularly in the Fischer-Tropsch synthesis [9,10]. Cobalt's ability to effectively dissociate hydrogen and its strong adsorption capacity for CO_2 likely contribute to the higher conversion rates [11,12]. The Fe-based catalysts, while still effective, show a more gradual increase in conversion, reflecting the slower reaction kinetics associated with iron.

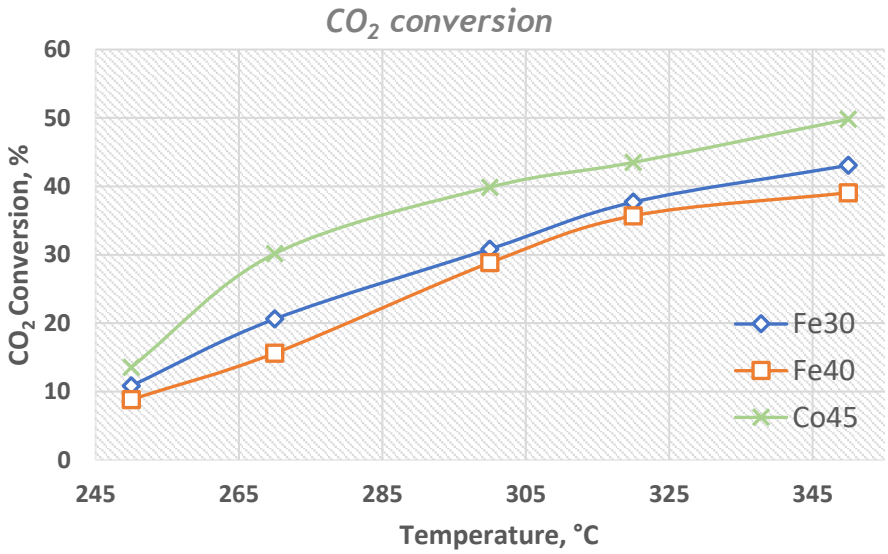

Figure 7.5. CO_2 conversion as a function of temperature for catalysts Fe30, Fe40, and Co45.

The selectivity of products CH_4, CO, light hydrocarbons (C_{2-6}), and heavier hydrocarbons (C_{7+}) reveals critical differences in the catalytic behaviour of the three catalysts, It is important to note that C_2+ selectivity refers to the sum of light hydrocarbons (C_{2-6}) and heavier hydrocarbons (C_{7+}).

Regarding methane selectivity, it increases with temperature for all catalysts, but the Fe40 catalyst consistently shows the highest selectivity for CH_4, reaching nearly 22% at 350°C. This could be due to Fe40's higher iron content, which favors the production of lighter hydrocarbons like methane [13]. Cobalt-based Co45, while less selective for CH_4, shows a moderate increase, indicating a balance between methane production and the formation of longer-chain hydrocarbons. On the contrary, CO selectivity decreases as temperature rises, which aligns with the expected behaviour of Fischer-Tropsch reactions where higher temperatures drive further hydrogenation of CO to hydrocarbons. Fe40 exhibits the highest CO selectivity at lower temperatures, suggesting that it is less effective at progressing the reaction towards complete hydrocarbon formation. Co45, in contrast, shows the lowest CO selectivity, reinforcing its superior catalytic efficiency in converting CO_2 to hydrocarbons rather than intermediate products like CO.

Shifting attention to the hydrocarbon's phases: the selectivity for light hydrocarbons (C_{2-6}) increases with temperature for all catalysts. Fe40 again shows the highest selectivity in this category, particularly at temperatures above 325°C. This trend suggests that Fe40 favors the formation of shorter-chain hydrocarbons, likely due to its iron composition, which promotes chain termination reactions leading to lighter hydrocarbon fractions whereas heavy hydrocarbon selectivity (C_{7+}) decreases with temperature for Fe40, but interestingly, Co45 exhibits a peak in heavy hydrocarbon selectivity at around 305°C, after which it slightly declines. This peak suggests that Co45 is particularly effective at producing longer-chain hydrocarbons under moderate temperature conditions, making it an attractive catalyst for applications where the production of heavier hydrocarbons is desired.

The differing behaviours of Fe30, Fe40, and Co45 can be explained by the distinct catalytic properties of iron and cobalt. Iron catalysts, particularly Fe40 with higher iron content, tend to produce lighter hydrocarbons and demonstrate higher CO and CH_4 selectivity. This could be due

to the fact that iron catalysts facilitate the Boudouard reaction ($2CO \rightarrow CO_2 + C$) and water-gas shift ($CO + H_2O \rightarrow CO_2 + H_2$) reactions, which can compete with the Fischer-Tropsch process, leading to higher methane and CO production [12]. Cobalt catalysts like Co45, on the other hand, are more efficient in hydrogenating CO_2 to longer-chain hydrocarbons, as evidenced by their lower CO selectivity and higher C_{7+} selectivity. Cobalt's ability to maintain a higher hydrogenation activity, even at elevated temperatures, allows for the production of heavier hydrocarbons, which are desirable in many industrial applications.

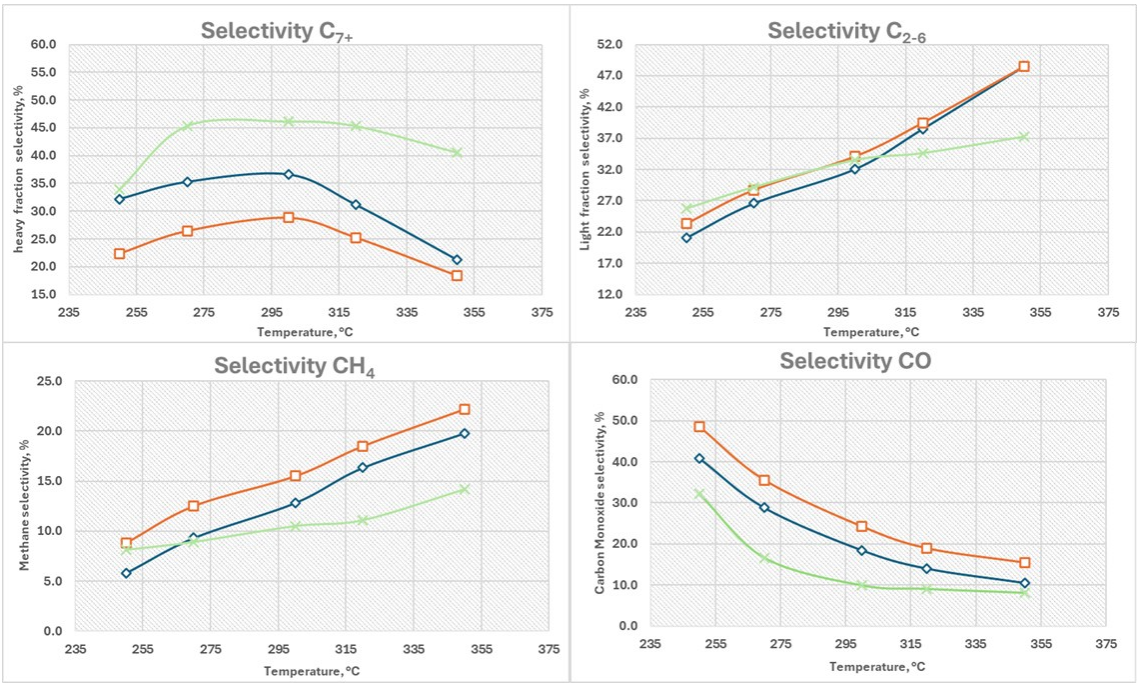

Figure 7.6. Selectivity trends of different products as a function of temperature. The top-left plot shows C_{7+} (heavy fraction) selectivity, the top-right plot presents C_{2-6} (light fraction) selectivity, the bottom-left plot displays CH_4 selectivity, and the bottom-right plot illustrates CO selectivity. The blue curve corresponds to the Fe30 catalyst, the orange curve to Fe40, and the green curve to Co45.

LCA results

On the basis of the experimental results presented in the previous section, we evaluated the environmental impacts associated with three catalysts: Co45, Fe30, and Fe40, each operating at their optimal temperature of 350°C. The functional unit in this study is defined as 1 kg of product obtained. Here, the product refers to C_{2+} hydrocarbons, ensuring a consistent and comparable assessment of environmental impacts across different impact categories. The evaluation is conducted using the methodologies described in Chapter 7.1.3 Inventory Data.

7.2.2.2. CML-IA Baseline Analysis

The CML-IA baseline method evaluates a broad spectrum of environmental impact categories. From the data, it is evident that the Fe40 catalyst exhibits the highest impact across nearly all categories, a trend that is strongly correlated with its lower catalytic performance compared to the other two catalysts. This phenomenon is consistent with previous discussions where the catalytic efficiency directly influences the environmental burden; higher efficiency typically translates to lower environmental impact per unit of product. Specifically, in the abiotic depletion category, the Fe40 catalyst shows the highest impact, which is approximately 67% higher than that of Co45 and 41% higher than Fe30, Fig 7.7-8.

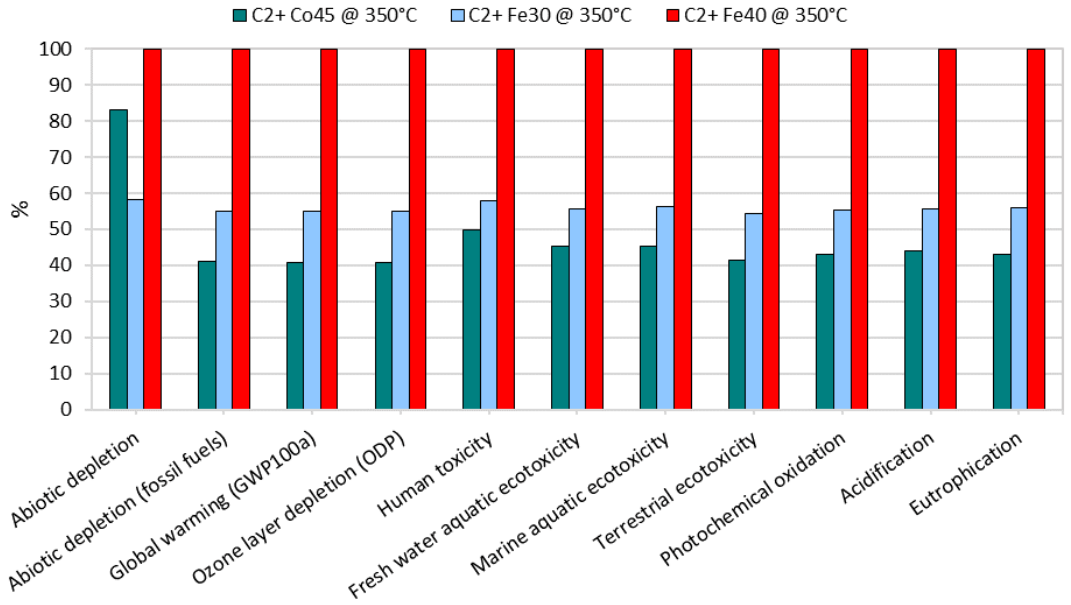

Figure 7.7. Comparative environmental impact assessment of C_2+ hydrocarbon production at 350°C for catalysts Co45, Fe30, and Fe40 across multiple impact categories.

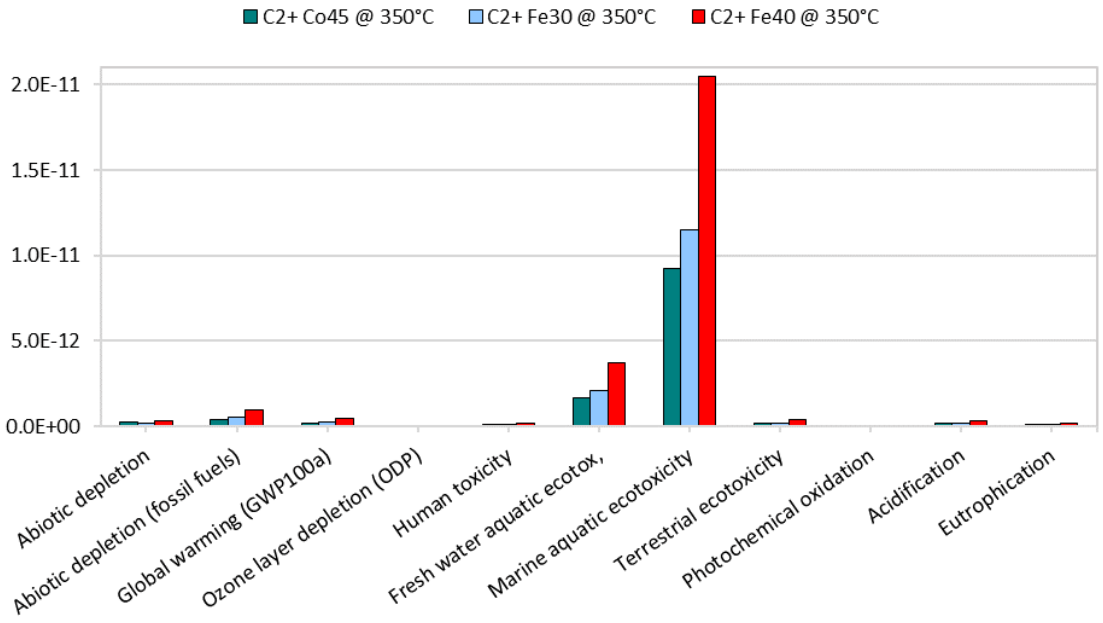

Figure 7.8. Absolute environmental impact values for C_2+ hydrocarbon production at 350°C.

This significant difference can be attributed to the greater energy consumption required for Fe40's operation and its lower efficiency in converting CO_2 into desired products. The Co45 catalyst, despite its higher initial environmental impact during production, shows a markedly lower impact in the operational phase due to its superior catalytic performance. Notably, in categories such as photochemical oxidation, terrestrial ecotoxicity, and eutrophication, the Fe40 catalyst again shows higher impacts, underscoring its inefficiency. The increased impact in terrestrial ecotoxicity and eutrophication for Fe40 is likely related to the byproducts and emissions generated during its operation, including the treatment of wood ash mixture and power sawing for wood chips, which are used in the energy mix.

7.2.2.3. IPCC 2021 GWP100 Analysis

The Global Warming Potential (GWP) analysis using the IPCC 2021 GWP100 method reveals that Fe40 also has the highest impact in terms of CO_2-eq emissions, registering 2.39 kg CO_2-eq per kg of product. This is significantly higher than Fe30 (1.31 kg CO_2-eq) and Co45 (0.976 kg CO_2-eq), Figure 7.9.

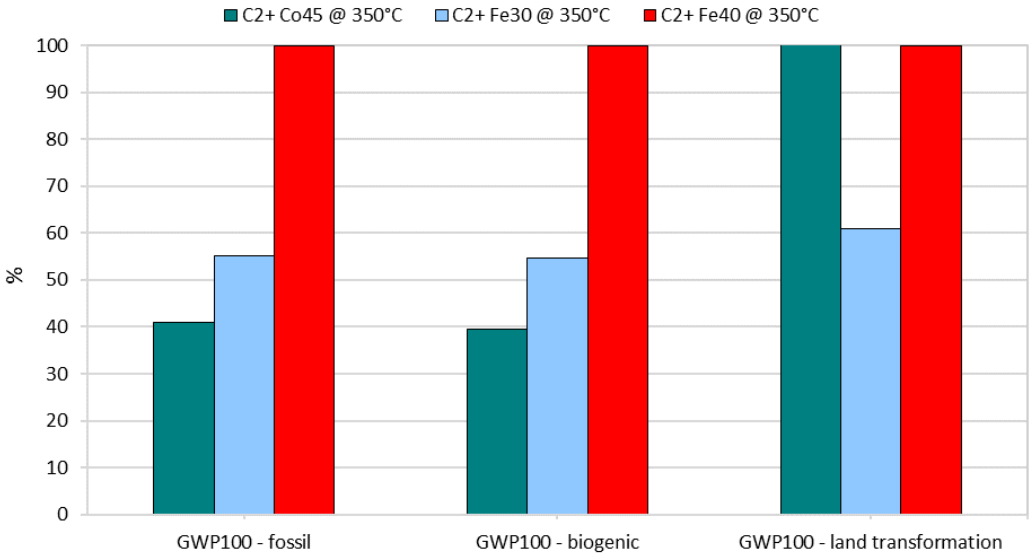

Figure 7.9. Breakdown of Global Warming Potential (GWP100) contributions for C_{2+} hydrocarbon production at 350°C using catalysts Co45, Fe30, and Fe40.

The GWP100 analysis is segmented into fossil, biogenic, and land transformation categories. Fe40 exhibits the highest impact in the fossil and biogenic categories, indicating its reliance on non-renewable energy sources and the higher carbon footprint associated with its operation. Interestingly, in the land transformation category, the Co45 catalyst shows a slightly higher impact than Fe40, which is primarily due to the specific characteristics of cobalt sulphate used in the catalyst, particularly the electricity consumption linked to the cobalt industry.

7.2.2.4. Cumulative Energy Demand (CED) Analysis

The CED analysis further supports the findings of the CML and GWP analyses, highlighting critical differences in the energy demands of the three catalysts for the Fischer-Tropsch synthesis of C_{2+} hydrocarbons.

Co45 shows the lowest total energy consumption at 22.227 MJ/kg of product, primarily due to its lower reliance on non-renewable fossil energy (13.761 MJ).

In comparison, Fe30 and Fe40 require 28.121 MJ and 51.382 MJ, respectively, underscoring Co45's superior efficiency. The reduced energy demand of Co45 is particularly significant, with a 40.94% lower fossil energy use compared to Fe40. Furthermore, Co45 also performs better in the utilization of renewable energy sources, especially in renewable water energy (3.576 MJ), suggesting a more balanced and resilient energy profile. This balanced use of renewable and non-renewable resources further supports the sustainability of Co45, making it less vulnerable to energy supply fluctuations. The nuclear energy demand for Co45 is lower than for Fe30 and Fe40, at 2.448 MJ, enhancing its versatility and sustainability.

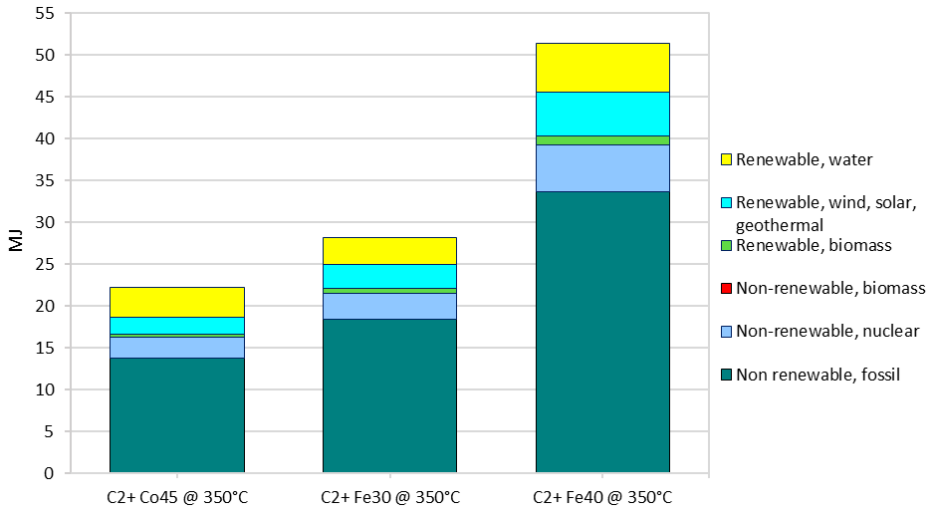

Figure 7.10. Energy consumption breakdown for C_{2+} hydrocarbon production at 350°C.

7.2.3. Carbon Neutrality evaluations

Carbon neutrality aims to balance emitted and converted CO_2, making it a key target for sustainable industrial processes. In chemical and fuel production, reducing carbon footprints is particularly challenging, but CO_2 hydrogenation offers a promising path [14]. However, achieving true carbon neutrality depends on conversion efficiency, energy source selection, and the environmental impact of catalyst production [15-17]. This study evaluates the carbon neutrality potential of FT by comparing Co45, Fe30, and Fe40 catalysts under different energy scenarios. The assessment of carbon neutrality across the three catalysts Co45, Fe30, and Fe40 requires an analysis of their CO_2 Utilization Factor (CUF), a metric representing the proportion of CO_2 converted relative to the CO_2 produced in the Fischer-Tropsch synthesis process.

$$CO_2\ Utilization\ Factor, \% = \frac{kg\ of\ CO_2\ Converted}{kg\ of\ CO_2\ Produced} \cdot 100 \quad (1)$$

where CO_2 converted refers to the amount of CO_2 transformed from raw material to products, while CO_2 produced represents the amount of CO_2 emitted in order to generate the energy needed for the process. This indicator is critical in evaluating the net carbon balance, where values above 100 indicate a net CO_2-consuming process, then potentially contributing to carbon-negative fuels. For example, a CUF of 200% means that for 1 mole of CO_2 produced, 2 moles of CO_2 are simultaneously converted into products. This implies that the process is offsetting its own emissions and also actively removing additional CO_2 from the system. In contrast, a CUF of 50% signifies that for every mole of CO_2 produced, only 0.5 moles of CO_2 are converted, meaning that more CO_2 is being generated than utilized. This results in a net CO_2-emitting process. The CUF values at different reaction temperatures are summarized in Table 7.2. At 250°C, all catalysts exhibit low conversion, with Fe40 achieving the lowest CUF, indicating only 13% of the CO_2 produced is effectively converted, while Co45 achieves 16% utilization. However, it is important to note that these CUF values are derived from laboratory-scale experiments, where gas flow rates, reaction residence times, and thermal management are not optimized to the extent possible in an industrial-scale system. In an industrial plant, process parameters are fine-tuned to maximize CO_2 conversion efficiency, leading to higher CUF values than those reported in this study. Thus, the numbers presented here should be interpreted as a conservative estimate rather than absolute

values representative of large-scale operations. As the temperature increases to 300°C, the CUF improves significantly, particularly for Co45 and Fe30, reaching 74% and 90%, respectively, suggesting enhanced CO_2 utilization at elevated temperatures. The highest CUF values are observed at 350°C, where Co45 achieves 167%, indicating that it converts 167% of the CO_2 that it produces, making it net carbon negative. Similarly, Fe30 reaches 130 CUF, reinforcing its high catalytic efficiency. The increase in CUF with temperature can be attributed to the enhanced kinetics of CO_2 hydrogenation, where higher temperatures improve reaction rates and increase the selectivity towards longer-chain hydrocarbons, effectively capturing more CO_2 into liquid fuel intermediates [18]. However, this improved CO_2 utilization comes with trade-offs, particularly in energy demand and environmental burden. While Co45 and Fe30 demonstrate high CUF at optimal temperatures, their production phase indicates substantial impacts in abiotic depletion and fossil fuel consumption, requiring a broader perspective when evaluating sustainability [19]. An essential consideration is the interaction between energy source and CUF. While a higher CUF generally correlates with improved sustainability, the energy mix used to drive the synthesis can offset or enhance these benefits. For instance, using hydroelectric power significantly reduces GWP, reinforcing the benefits of catalysts with high CUF. In contrast, fossil fuel-based energy sources may counteract the net CO_2 capture benefits, diminishing the catalysts' ability to achieve carbon neutrality.

		CO_2 Utilization Factor (CUF), %		
		250 °C	300 °C	350 °C
Low Voltage Mix (ITA)	*Fe30*	16	74	130
	Fe40	13	34	50
	Co45	18	90	167
Co-generation method	*Fe30*	70	172	207
	Fe40	61	118	145
	Co45	72	175	210
Hydroelectric	*Fe30*	132	210	225
	Fe40	120	176	195
	Co45	124	201	217

Table 7.2. Comparison between the catalysts regarding CO_2 utilization factor considering different energy sources for the system and temperatures The color gradient represents the magnitude of the CO_2 Utilization Factor (CUF), with red indicating lower values, yellow representing intermediate values, and green corresponding to the highest CUF values.

The findings indicate that catalysts alone, tested in a laboratory scale plant, cannot achieve full carbon neutrality without integrating low-carbon energy sources. While Fe30 achieves the highest CUF at 350°C, the Co45 catalyst presents a more balanced profile by maintaining a high CUF with lower energy demand compared to Fe30. However, it is important to note that at the laboratory scale, energy consumption per unit of product is significantly higher than at the industrial scale, which may influence the relative impact of different catalyst-energy combinations. The selection of the optimal catalyst-energy combination is, therefore, essential for minimizing the net environmental impact of the Fischer-Tropsch process [20]. The choice of energy source in Fischer-Tropsch synthesis is a fundamental determinant of whether the process can achieve net CO_2 reduction or even become carbon-negative [21]. While catalyst selection

plays a key role in CO_2 conversion efficiency, the environmental impact is significantly shaped by the carbon intensity of the energy input. The transition from fossil-based grid electricity to renewable sources such as hydroelectric power or biomass co-generation introduces substantial improvements in CO_2 Utilization Factor (CUF) and overall sustainability. Among the alternative energy sources, biomass-based electricity through wood chip co-generation presents a notable improvement in CO_2 utilization. Co45 at 350°C reaches a CUF of 210%, capturing more than twice the CO_2 emitted during the process. Even Fe40, which under conventional grid electricity exhibited limited carbon utilization, improves significantly to 145% CUF, demonstrating the potential of biomass energy to enhance carbon sequestration. However, despite these improvements, the sustainability of biomass co-generation remains a subject of debate. While it offers a renewable energy alternative, it also introduces critical environmental trade-offs. The combustion of wood chips produces wood ash, which contributes to terrestrial ecotoxicity and eutrophication, while large-scale biomass harvesting risks deforestation, biodiversity loss, and soil degradation. These factors highlight the importance of responsible biomass sourcing and sustainable forest management to mitigate negative externalities. Hydroelectric power stands out as the most sustainable energy option, delivering the highest CUF values across all catalysts. At 350°C, Co45 reaches 217%, Fe40 achieves 195%, and Fe30 peaks at 225%, indicating a strong carbon-negative potential. The near-zero emissions associated with hydropower eliminate fossil-derived CO_2 emissions from the energy supply chain, making it the most effective solution for reducing Global Warming Potential (GWP). Unlike biomass, hydroelectricity does not introduce uncertainties related to biogenic carbon accounting or land transformation impacts, further solidifying its position as the optimal energy source for sustainable Fischer-Tropsch synthesis. The role of biogenic carbon accounting is critical when evaluating the sustainability of biomass energy. Unlike fossil fuels, CO_2 emissions from biomass combustion are theoretically offset by carbon uptake during plant growth. However, the actual neutrality of biomass depends on the rate of forest regrowth, land-use efficiency, and indirect emissions. If biomass is harvested faster than it is replenished, the net CO_2 balance shifts toward a positive emission scenario, undermining its sustainability benefits. Additionally, land transformation effects, including soil degradation and reductions in long-term carbon stock, can significantly alter the expected carbon sequestration benefits. This is reflected in impact assessment results, where co-generation exhibits higher terrestrial ecotoxicity and eutrophication levels compared to hydroelectric power. Overall, energy source selection is as critical as catalyst optimization in determining the viability of carbon-neutral Fischer-Tropsch synthesis. Hydroelectric power offers the most effective pathway to achieving net negative CO_2 emissions while maintaining minimal environmental trade-offs. Biomass co-generation provides a compelling alternative, significantly improving CO_2 utilization, but its associated land use and ecosystem impacts necessitate careful sustainability considerations. The findings underscore that even the most efficient catalysts require a complementary low-carbon energy source to maximize their potential for CO_2 reduction. Integrating high-performance catalysts with renewable energy sources is essential to ensuring that Fischer-Tropsch synthesis serves as a viable long-term solution for carbon-neutral synthetic fuel production while addressing global CO_2 mitigation goals.

7.3. Conclusion

This study highlights the critical role of catalyst selection, energy sourcing, and process optimization in achieving sustainable Fischer-Tropsch (FT) synthesis via CO_2 hydrogenation. A key finding is the trade-off between iron-based (Fe30, Fe40) and cobalt-based (Co45) catalysts in terms of both catalytic performance and environmental impact. Cobalt-based catalysts (Co45) demonstrate superior CO_2 conversion efficiencies, achieving a CUF of 167% at 350°C, making the process net carbon-negative. This is largely due to cobalt's high intrinsic activity for CO_2 hydrogenation, which enables more efficient conversion at lower H_2/CO_2 ratios and improves selectivity towards hydrocarbons. However, Co45 presents higher environmental burdens during its production phase, particularly due to the energy-intensive extraction and processing of cobalt as well as its reliance on critical raw materials with geopolitical and supply risks [22]. Conversely, iron-based catalysts (Fe30, Fe40) are less resource-intensive and more sustainable in terms of material availability, but they exhibit lower overall CO_2 conversion efficiencies. Fe30, for instance, achieves a CUF of 130%, still making it a promising candidate, though less effective than Co45 in CO_2 utilization. However, iron-based catalysts benefit from lower production-related emissions and their ability to facilitate the water-gas shift (WGS) reaction, which improves flexibility in syngas composition. Fe40, despite being the least efficient in CO_2 conversion, exhibits the highest environmental impact, reinforcing the importance of optimizing catalyst formulation.

Beyond catalyst selection, energy sourcing plays a decisive role in determining overall sustainability. The results confirm that switching from a fossil-based grid to hydroelectric power significantly enhances environmental performance, making the process net CO_2-negative under optimal conditions. Biomass energy offers another alternative but comes with trade-offs related to land use and ecotoxicity, requiring careful sustainability oversight.

While these findings provide a strong basis for catalyst selection and process optimization, scaling laboratory data to industrial processes remains a challenge. Laboratory-scale setups typically suffer from higher relative energy consumption and inefficiencies, suggesting that CUF values in an optimized industrial setting could be significantly higher. Future studies should integrate industrial-scale LCA data, incorporate exergy-based assessments, and address material circularity to ensure real-world applicability. Ultimately, achieving sustainability in FT synthesis requires a systemic approach, combining high-performance catalysts, low-carbon energy sources, and industrial process optimization, rather than relying solely on catalyst improvements.

Reference Chapter 7

[1] Dufour, J.; Iribarren, D. Life Cycle Assessment of Biodiesel Production from Free Fatty Acid-Rich Wastes. Renew Energy 2012, 38 (1), 155-162. https://doi.org/10.1016/j.renene.2011.07.016.

[2] Erakca, M.; Pinto Bautista, S.; Moghaddas, S.; Baumann, M.; Bauer, W.; Leuthner, L.; Weil, M. Closing Gaps in LCA of Lithium-Ion Batteries: LCA of Lab-Scale Cell Production with New Primary Data. J Clean Prod 2023, 384. https://doi.org/10.1016/j.jclepro.2022.135510.

[3] Dadashi Firouzjaei, M.; Nemani, S. K.; Sadrzadeh, M.; Wujcik, E. K.; Elliott, M.; Anasori, B. Life-Cycle Assessment of $Ti_3C_2T_x$ MXene Synthesis. Advanced Materials 2023, 35 (31). https://doi.org/10.1002/adma.202300422.

[4] Finnveden, G.; Hauschild, M. Z.; Ekvall, T.; Guinée, J.; Heijungs, R.; Hellweg, S.; Koehler, A.; Pennington, D.; Suh, S. Recent Developments in Life Cycle Assessment. Journal of Environmental Management. Academic Press 2009, pp 1-21. https://doi.org/10.1016/j.jenvman.2009.06.018.

[5] Van Allsburg, K. M.; Tan, E. C. D.; Super, J. D.; Schaidle, J. A.; Baddour, F. G. Early-Stage Evaluation of Catalyst Manufacturing Cost and Environmental Impact Using CatCost. Nat Catal 2022, 5 (4), 342-353. https://doi.org/10.1038/s41929-022-00759-6.

[6] Environmental Management-Life Cycle Assessment-Requirements and Guidelines AMENDMENT 2 Management Environnemental-Analyse Du Cycle de Vie-Exigences et Lignes Directrices AMENDEMENT 2; 2020. www.iso.org.

[7] Aromaa-Stubb, R.; Rinne, M.; Lundström, M. Life Cycle Assessment of Cobalt Catalyst Production and Recycling. Journal of Sustainable Metallurgy 2024, 10 (3), 1795-1806. https://doi.org/10.1007/s40831-024-00897-0.

[8] Leyssens, L.; Vinck, B.; Van Der Straeten, C.; Wuyts, F.; Maes, L. Cobalt Toxicity in Humans A Review of the Potential Sources and Systemic Health Effects. Toxicology. Elsevier Ireland Ltd July 15, 2017, pp 43-56. https://doi.org/10.1016/j.tox.2017.05.015.

[9] Melaet, G.; Ralston, W. T.; Li, C. S.; Alayoglu, S.; An, K.; Musselwhite, N.; Kalkan, B.; Somorjai, G. A. Evidence of Highly Active Cobalt Oxide Catalyst for the Fischer-Tropsch Synthesis and CO_2 Hydrogenation. J Am Chem Soc 2014, 136 (6), 2260-2263. https://doi.org/10.1021/ja412447q.

[10] He, X.; Wang, X.; Xu, H. Advancements in Cobalt-Based Catalysts for Enhanced CO_2 Hydrogenation: Mechanisms, Applications, and Future Directions: A Short Review. Catalysts 2024, 14 (9), 560. https://doi.org/10.3390/catal14090560.

[11] Scarfiello, C.; Pham Minh, D.; Soulantica, K.; Serp, P. Oxide Supported Cobalt Catalysts for CO_2 Hydrogenation to Hydrocarbons: Recent Progress. Advanced Materials Interfaces. John Wiley and Sons Inc May 25, 2023. https://doi.org/10.1002/admi.202202516.

[12] Have, I. C. ten; Kromwijk, J. J. G.; Monai, M.; Ferri, D.; Sterk, E. B.; Meirer, F.; Weckhuysen, B. M. Uncovering the Reaction Mechanism behind CoO as Active Phase for CO_2 Hydrogenation. Nat Commun 2022, 13 (1). https://doi.org/10.1038/s41467-022-27981-x.

[13] Ma, W.; Jacobs, G.; Sparks, D. E.; Todic, B.; Bukur, D. B.; Davis, B. H. Quantitative Comparison of Iron and Cobalt Based Catalysts for the Fischer-Tropsch Synthesis under Clean and Poisoning Conditions. Catalysis Today. Elsevier B.V. March 1, 2020, pp 125-136. https://doi.org/10.1016/j.cattod.2019.04.011.

[14] Roy, S.; Cherevotan, A.; Peter, S. C. Thermochemical CO_2 Hydrogenation to Single Carbon Products: Scientific and Technological Challenges. ACS Energy Lett 2018, 3 (8), 1938-1966. https://doi.org/10.1021/acsenergylett.8b00740.

[15] Wang, L.; Wang, D.; Li, Y. Single-Atom Catalysis for Carbon Neutrality. Carbon Energy. John Wiley and Sons Inc November 1, 2022, pp 1021-1079. https://doi.org/10.1002/cey2.194.

[16] Srivastava, R. K.; Shetti, N. P.; Reddy, K. R.; Kwon, E. E.; Nadagouda, M. N.; Aminabhavi, T. M. Biomass Utilization and Production of Biofuels from Carbon Neutral Materials. Environmental Pollution 2021, 276. https://doi.org/10.1016/j.envpol.2021.116731.

[17] He, M.; Sun, Y.; Han, B. Green Carbon Science: Efficient Carbon Resource Processing, Utilization, and Recycling towards Carbon Neutrality. Angewandte Chemie - International Edition. John Wiley and Sons Inc April 4, 2022. https://doi.org/10.1002/anie.202112835.

[18] Amin, M.; Shah, H. H.; Naveed, A. B.; Iqbal, A.; Gamil, Y.; Najeh, T. Life Cycle Assessment of Iron-Biomass Supported Catalyst for Fischer Tropsch Synthesis. Front Chem 2024, 12. https://doi.org/10.3389/fchem.2024.1374739.

[19] Ye, R. P.; Ding, J.; Gong, W.; Argyle, M. D.; Zhong, Q.; Wang, Y.; Russell, C. K.; Xu, Z.; Russell, A. G.; Li, Q.; Fan, M.; Yao, Y. G. CO_2 Hydrogenation to High-Value Products via Heterogeneous Catalysis. Nature Communications. Nature Research December 1, 2019. https://doi.org/10.1038/s41467-019-13638-9.

[20] Piccinno, F.; Hischier, R.; Seeger, S.; Som, C. From Laboratory to Industrial Scale: A Scale-up Framework for Chemical Processes in Life Cycle Assessment Studies. J Clean Prod 2016, 135, 1085-1097. https://doi.org/10.1016/j.jclepro.2016.06.164.

[21] Medrano-García, J. D.; Charalambous, M. A.; Guillén-Gosálbez, G. Economic and Environmental Barriers of CO_2-Based Fischer-Tropsch Electro-Diesel. ACS Sustain Chem Eng 2022, 10 (36), 11751-11759. https://doi.org/10.1021/acssuschemeng.2c01983.

[22] Sun, X.; Hao, H.; Liu, Z.; Zhao, F.; Song, J. Tracing Global Cobalt Flow: 1995-2015. Resour Conserv Recycl 2019, 149, 45-55. https://doi.org/10.1016/j.resconrec.2019.05.009.

8. NEURAL NETWORK MODELLING

Addressing climate change, reducing CO_2 emissions from fossil fuels is crucial. The shift towards sustainable initiatives like 'energy transition' presents both environmental and economic opportunities for businesses. Strategies like Carbon Capture and Storage (CCS) and Carbon Capture Utilization (CCU) are pivotal, with CCU gaining attention for converting CO_2 into valuable chemicals and fuels [1]. Power-to-Liquid (PTL) approaches in CCU are significant for producing high-energy-density fuels like methanol, gasoline, and diesel, which are easier to store and transport. Fischer-Tropsch Synthesis (FTS), since 1925, has been effective in generating hydrocarbons like alpha-olefins and linear paraffins from various feedstocks, crucially without sulfur, nitrogen, and aromatic compounds [2]. The adaptation of CO_2-based FTS for fuel production is a notable advancement under stringent environmental regulations [3].

Artificial Neural Networks (ANN) play a vital role in the process industry, enhancing equipment failure prediction, maintenance [4], and system optimization. Their application in conventional FT synthesis for process optimization and kinetic modeling has been successful [5,6,7]. This study applies ANN (Section 8.1) to FT synthesis with CO_2 feedstock, aiming to predict the selectivity of key species like CO, CH_4, C_{2-4}, and C_{5+}, using Fe-based catalysts promoted with K. To enhance predictions, five networks were developed for each output, based on parameters like catalyst composition, surface area (BET), temperature, and pressure, identified through Kendall correlation coefficient analysis. The ANN's architecture was optimized using a mixed-integer genetic algorithm methodology.

In section 8.2, the Random Forest (RF) model is developed and evaluated for predicting catalyst performance (CO_2 conversion and product selectivities), and its results are compared to the prior ANN model. Key aspects analyzed include the prediction quality (regression metrics, parity plots, residuals) and the insights gained from feature importance, highlighting how RF can guide catalyst optimization.

8.1. Neural Network Architecture

The architecture of the ANN is based on the relations between the biases and weight of each node, the neuron activation function, and the training function. Firstly, cascade forward network has been considered, since it relates the output layer weights with an additional weight evaluated from the values of the input variables. It has been seen that it helps to better identify and exploit all the dependences between the input and output variables, given the nature of the system [8]. The other network characteristics have been chosen by optimizing the performance of the network. This was done through a genetic algorithm, which selected through a random generation of points (i.e., generation), the best one that minimize the mean square error (MSE) or the network. Both activation functions (AF) and training functions (TF) have been labeled with integers numbers, to be successfully read from the optimizer. Thus, a mixed-integer approach has been used; and the hidden layer have been constrained between 1 and 10 layers. In fact, the variability and quantity of data in the dataset considered is not enough to achieve good performances with high hidden layers number [9]. Table 8.1 shows the list of the activation and training functions. The

modeling and optimization have been performed through MATLAB©, from which it has also been chosen the type of activation and training function.

Label	Activation function	Training function	Abbreviation
1	Pure linear	Levenberg-Marquardt	LM
2	Log-sigmoidal	Bayesian regularization	BR
3	Tan-sigmoidal	Quasi-Newton BFGS	QN-BFGS
4	-	Resilient Back Propagation	RBP
5	-	Scaled conjugate gradient	SCG
6	-	Conjugate gradient with Powell/Beale restarts	P/B-CG
7	-	Fletcher-Powell conjugate gradient	F/P-CG
8	-	Polak-Ribiére conjugate gradient	P/R-CG
9	-	One-pass secant	OPS
10	-	Gradient drop-down variable learning rate	GDVLR
11	-	Gradient disc with momentum	GDM
12	-	Gradient Discess	GD

Table 8.1. Labeling of activation and training functions selected for the mixed-integer optimization.

8.1.1. Input variable definition

The input variables (visible in Table 8.5 at the end of the chapter) to the model have been chosen accordingly to the nature of the catalyst and of the process. Since the aim of the model is to predict the kinetic results and performances of the process, the catalyst composition has been addressed, in terms of density and (ρ_cat) and specific surface (BET). Since the active phase and promotor have been fixed a priori, the density gathers the information of the catalyst intrinsic composition. Finally, the Kendall correlation coefficients evaluation (Figure 8.1) confirms the goodness of the dependences between catalyst features and products, which shows that at higher catalyst density, higher chain products are preferred, but at higher BET, lighter hydrocarbons are favored, since increase the selectivity of the catalyst itself in terms of pore dimension and tortuosity. Moreover, two more input variables have been selected: temperature (T) and pressure (P). By defining the state of the system, these are important information since highlights both the sensitivity to the process to produce a certain group of species and the catalyst operational window. At higher temperature, lower chain hydrocarbons are expected, and at higher pressure higher chain hydrocarbons are favored [10].

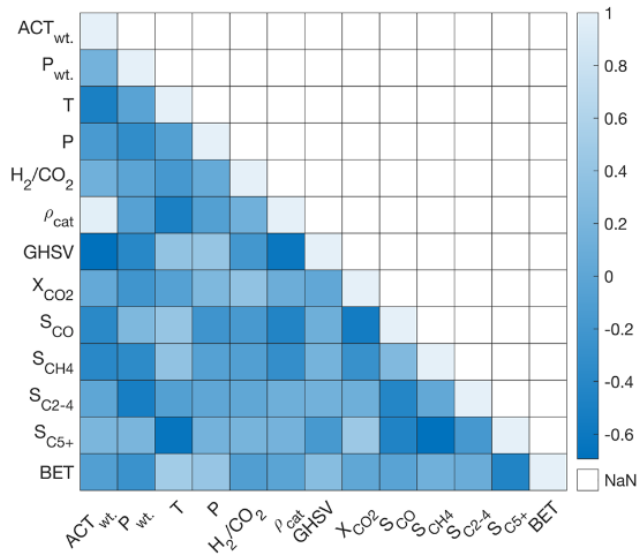

Figure 8.1. Heatmap of the correlation coefficients of the dataset features.

8.1.2. Dataset Compilation for Artificial Neural Network Training

To facilitate the modeling process through an artificial neural network (ANN), a comprehensive dataset was necessary. This dataset was compiled from a combination of 12 articles [11] and experimental results. From these articles, a variety of data points were extracted, encompassing reaction conditions such as temperature, pressure, gas hourly space velocity (GHSV) and ratios of reactants. Additionally, reaction outputs were included, such as: CO_2 conversion and selectivities towards products. The nature of the catalysts used in these studies was also a critical component of the dataset, represented by their densities, which were calculated (Eq. 1) based on the amounts of active metals, promoters and the porosity (φ). The latter was calculated as the average between the experimental values of the catalysts used and literature values taken as standard case [12].

$$\rho_{cat} = \varphi \cdot \left(\frac{\%\,K}{100} \cdot \rho_K + \frac{\%\,Fe}{100} \cdot \rho_{Fe} + \frac{100 - \%\,K - \%\,Fe}{100} \cdot \rho_{Ti_2O}\right) \quad (1)$$

In total, literature review yielded data for 70 different reaction conditions, providing a robust foundation for the ANN. To complement this, experimental data reflecting similar parameters were incorporated into the dataset. This experimental contribution added 25 unique data sets, ensuring a diverse and comprehensive pool of information for training the neural network. This amalgamation of literature-derived and experimental data forms the backbone of the ANN model, ensuring its relevance and applicability in the context of Fischer-Tropsch synthesis.

8.1.3. Results and Discussion

The best architecture for the five networks is found from the optimization (Table 8.2). Two activation functions, one for the hidden layers (HL) and one for the output layer (OL) are selected. It must be said that the learning rate and normalization of input/output variables are done automatically by the MATLAB© algorithm used for the modeling. The performances of these networks are assessed with the value of the MSE (Table 8.3). These values are in line with the

ones obtained in literature [13]. As it is possible to notice, the highest performances are reached for XCO_2 and SC_{2-4} predictions, while the worst one came from the modeling of the SC_{5+}.

Output	Symbol	N° HL	AF HL	AF OL	TF
CO_2 conversion	X_{CO_2}	9	Log-sigmoidal	Pure linear	P/B-CG
CO selectivity	S_{CO}	2	Pure linear	Tan-sigmoidal	F/P-CG
CH_4 selectivity	S_{CH_4}	9	Log-sigmoidal	Pure linear	OPS
C_{2-4} selectivity	S_{C2-4}	4	Log-sigmoidal	Tan-sigmoidal	OPS
C_{5+} selectivity	S_{C5+}	8	Tan-sigmoidal	Tan-sigmoidal	BR

Table 8.2. Optimization architecture from the genetic algorithm solution.

However, despite the MSE gives to this the highest value, the mean prediction error (MPE), evaluated as the relative error between the experimental data and the network calculations, has its highest value on the prediction of the CO selectivity. This is principally due to the intrinsic nature of the ANN when applied on chemical processes.

Network	Total epochs	Epoch at minimum MSE	MSE	MPE
CO_2 conversion	16	10	92.87	0.30
CO selectivity	28	22	118.4	0.82
CH_4 selectivity	12	6	112.3	0.58
C_{2-4} selectivity	20	14	81.62	0.19
C_{5+} selectivity	45	44	167.3	0.37

Table 8.3. Performance indicators of the networks.

On the other hand, other algorithms have been used for comparison; with particular focus on SCO evaluation. To make the comparisons, MSE has been used as performance indicator. Firstly, Multiple Linear Regression (MLR) and Decision Tree Regression (DTR) are tested, using as independent variable the same used in ANN. Results are shown in Table 8.4.

Algorithm	Average MSE	STD.DEV	S_{CO} MSE
ANN	114.5	33.00	118.4
MLR	157.3	36.75	193.1
DTR	138.6	44.30	172.5

Table 8.4. Performance indicators and comparison with other algorithm.

As it is possible to notice, ANN outperformance the other algorithm tested; MLR, the simplest one, has the lowest score, and this is reasonable since the behavior of the species, including CO, is strongly nonlinear, depending on the thermodynamic of the process. On the other hand, DTR has a better score with respect to MLR, but still is not performing enough well. This is because the decision tree can be overwhelmed from the variability of the data, which led to a drastically change in the tree structure during the regression. In conclusion, it is recommended to still use ANN as primary algorithm for the prediction of these parameters and, if possible, evaluate the CO selectivity as a complementary to the other parameters.

8.1.4. Conclusions

The application of artificial neural networks (ANN) in this Fischer-Tropsch synthesis study demonstrates a balance of success and challenges. The ANN's ability in predicting CO_2 conversion and C_{2-4} hydrocarbon selectivity, in line with existing literature [13], underscores its effectiveness in modeling specific aspects of the synthesis process. However, the model's struggles with accurately predicting longer chain hydrocarbons (SC_{5+}), as reflected by a higher Mean Square Error (MSE), reveal limitations in its capacity to handle the complexities of these reaction pathways. This could stem from data variability, limitations in the network architecture, or insufficient training data. The most significant Mean Prediction Error (MPE) in predicting CO selectivity highlights a critical area of improvement. It suggests the model's limited sensitivity to subtle variations in reaction conditions, a crucial aspect for precise chemical process modeling. This finding calls for a deeper exploration into refining the ANN architecture, possibly integrating more diverse and complex datasets or adopting more sophisticated machine learning techniques. Overall, the study presents a promising yet incomplete picture of ANN's capability in chemical process optimization. Future research should focus on enhancing the model's accuracy across a broader range of outputs and delving into more complex reaction dynamics. Such advancements are essential for realizing the full potential of ANN in this field.

8.2. Random Forest Modeling

The performance of CO_2 hydrogenation catalysts were modeled using a Random Forest regression approach on the same dataset of catalyst formulations and reaction conditions (Table 8.5). While artificial neural networks (ANNs) are powerful, their performance can suffer with limited data, which is often the case in catalyst studies. Random Forest (RF) models offer a robust alternative for modeling catalyst behavior on small experimental datasets [14].

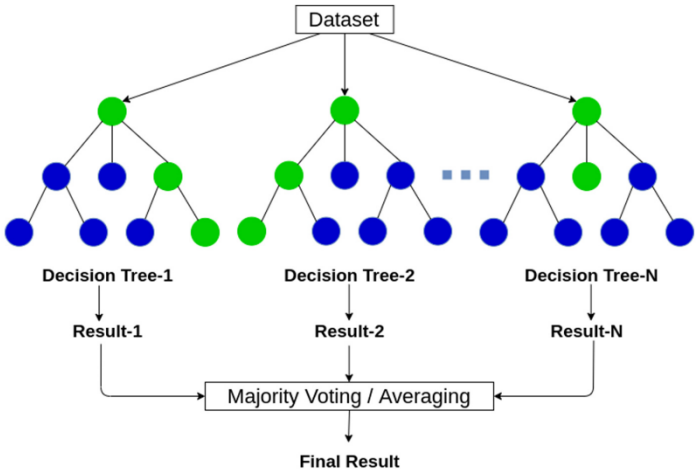

Figure 8.2. Schematic illustration of a Random Forest model consisting of multiple decision trees that collectively make a prediction. The training data is used to generate many decision trees (Tree 1, Tree 2, … Tree n) via random sampling of data and variables. Each tree produces a prediction (indicated by colored terminal nodes), and the final output is obtained by averaging all tree predictions (for regression) or taking a majority vote (for classification).

An RF is an ensemble learning method: instead of a single complex model, it builds a “forest” of many decision tree models and combines their outputs. Each decision tree in the ensemble is trained on a random subset of the data (both samples and descriptors) and thus learns a slightly different “view” of the problem. For a new input, each tree makes a prediction, and the final RF

output is the average of all tree predictions (for a regression task) or the majority vote (for classification) [15]. This approach is analogous to consulting multiple experts and aggregating their opinions, often yielding more reliable results than any individual model alone. By averaging over an ensemble of de-correlated trees, Random Forests tend to produce accurate and stable predictions [16] and are less prone to overfitting than single predictive models, an example is shown in Fig. 8.2.

A lone decision tree can perfectly fit (and thus overfit) the training data, including noise, but in a Random Forest the collective "wisdom" of many trees filters out random errors. In effect, the model's complexity (variance) is tamed by this averaging effect, improving generalization to new data. RF models inherently capture nonlinear relationships and interactions between variables, since each tree splits data based on threshold rules that can carve out complex decision boundaries. This means RF can model complicated catalyst performance trends (e.g. composition vs. activity relationships) without requiring a predefined mathematical form. Another practical advantage is that RF algorithms typically require minimal parameter tuning and are relatively robust to issues like outliers or irrelevant input features, properties that make them well-suited to experimental datasets that can be noisy or limited in size. Importantly, Random Forests also provide a degree of interpretability that is attractive for scientists. Because each decision tree is built from simple if-then rules, the ensemble can be analyzed to estimate the importance of each input feature in determining the output. In catalysis modeling, this means an RF model can help identify which catalyst descriptors (composition, structure, reaction conditions, etc.) have the strongest influence on activity or selectivity. Such insight is difficult to extract from an ANN, reinforcing why RF is a good choice to complement the earlier ANN approach. Furthermore, experience in catalysis and materials science has shown that RF models can perform exceptionally well even with relatively small datasets. For example, Mu et al. achieved a high predictive accuracy ($R^2 \approx 0.87$) using a Random Forest to model electrocatalyst performance from a modest number of training samples [17]. This robust performance on limited data, combined with RF's resistance to overfitting and its ability to handle nonlinear trends, makes it a natural fit for modeling catalyst systems in this work.

8.2.1. Results and Discussion

The RF model achieved strong predictive performance for all target variables, as evidenced by high coefficients of determination (R^2) and low error metrics on test data [18]. For instance, the R^2 values for CO_2 conversion and the major product selectivities were all close to unity (≥ 0.90), indicating that the model captures the majority of variance in the experimental data. The mean absolute error (MAE) for each target was on the order of only a few percentage points. Such accuracy is visualized in the parity plots (Figure 8.3), where predicted values of CO_2 conversion and selectivities closely track the experimental values along the ideal 45°.

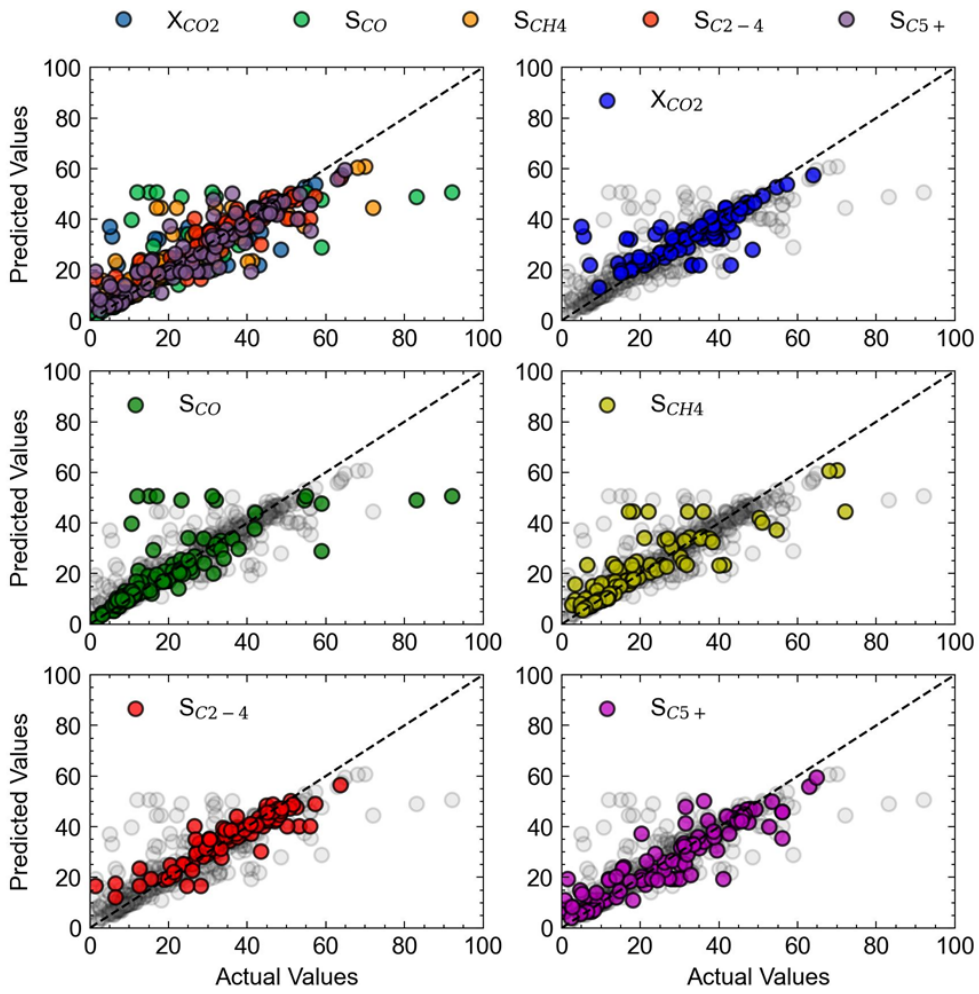

Figure 8.3. Parity plots comparing Random Forest-predicted vs. experimental values for all five target variables (CO_2 conversion and selectivities to CO, CH_4, C_2-C_4, and C_{7+}). The data points lie near the diagonal parity line, indicating high predictive accuracy across the full range of catalyst performance metrics.

The tight clustering of points around the parity line confirms the RF's excellent fit to the data without significant systematic deviation [19].

To quantitatively evaluate model errors, residuals (prediction minus actual) were examined. The RF's residuals exhibited a narrow distribution centered at zero for each output, with no obvious bias across the range of predictions. Figure 8.4 shows histograms of the residuals for each target variable; these roughly follow a normal distribution and are symmetric about zero. Such patterns suggest the model errors are largely random noise rather than structured error, implying that the RF has not missed any dominant nonlinear trend. Notably, even at the extremities of conversion or selectivity values, the residuals remain small, underscoring that the RF model generalizes well across the domain. This robust performance aligns with reports in catalysis literature where RF models often outperform other algorithms in predicting reaction outcomes. For example, in a recent study of propane dehydrogenation with CO_2, a RF regressor yielded the lowest RMSE and highest R^2 compared to support vector and k-nearest neighbor models, making it the preferred predictive tool. The strong agreement between RF predictions and experiments in our case gives confidence that the model can be used to screen catalyst formulations and conditions with reasonable accuracy.

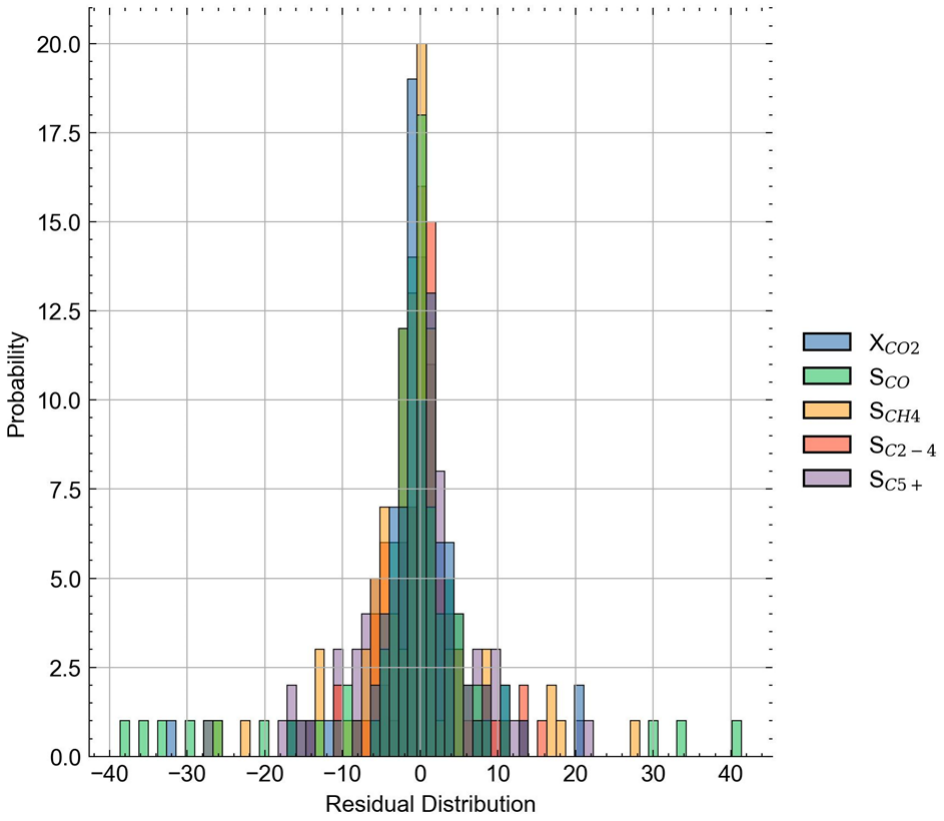

Figure 8.4. Histograms of the residuals for the Random Forest predictions of each target variable. All residual distributions are approximately normal and centered around zero, indicating unbiased predictions with no significant systematic error across the range of catalyst performance data.

A major advantage of RF modeling is the ability to extract the importance of each input feature in determining the output. Using the trained RF, we analyzed feature importance scores to identify which catalyst descriptors and process conditions most strongly influence CO_2 conversion and product distributions. The RF's intrinsic feature ranking (based on mean decrease in impurity) revealed a clear hierarchy of influential variables. The top five features were:

- Promoter loading (e.g. K content in wt%): the amount of alkali promoter had the single highest influence on performance. Higher promoter levels strongly affected product selectivities, consistent with alkali promoters (K, Cs, etc.) enhancing CO_2 dissociation and chain growth in Fischer-Tropsch pathways.
- Reaction temperature (T): temperature was equally critical, strongly governing CO_2 conversion and shifting selectivity (higher temperatures generally increase conversion but favor CH_4 over heavier products).
- Catalyst surface area (BET): a larger BET surface area correlated with improved catalytic activity (higher conversion), underscoring the role of dispersion and available active sites.
- Gas hourly space velocity (GHSV): the contact time influenced conversion (lower GHSV/higher residence time gives higher conversion) and indirectly the product slate.
- Active metal loading: the Fe-based active phase fraction in the catalyst (sometimes partially substituted with Co/Ru) also impacted performance, though to a lesser extent than the above process conditions and promoter effects.

These top variables had significantly higher importance scores than other inputs like pressure or feed H_2/CO_2 ratio, which appeared relatively less sensitive in the studied range. The feature importance bar chart (Figure 8.5) illustrates this ranking. Notably, qualitative agreement is found with domain expectations: for example, temperature and space velocity are well-known to affect conversion in CO_2 hydrogenation, and alkali promoters are known to enhance heavier hydrocarbon synthesis. Such alignment between the data-driven importance and chemical intuition adds credence to the model's relevancy. It also reflects observations from other catalysis ML studies, where key reaction conditions often emerge as top features for predicting performance. In one report on CO_2-assisted dehydrogenation, for instance, the RF model's interpretability analysis (via SHAP values) highlighted that reaction temperature and WHSV were among the most impactful factors on conversion and selectivity [20], in agreement with our findings. This ability to pinpoint critical parameters is invaluable for catalyst development - by knowing which levers (e.g. increase promoter level or optimize temperature) yield the greatest changes in performance, researchers can prioritize those in experimental optimization.

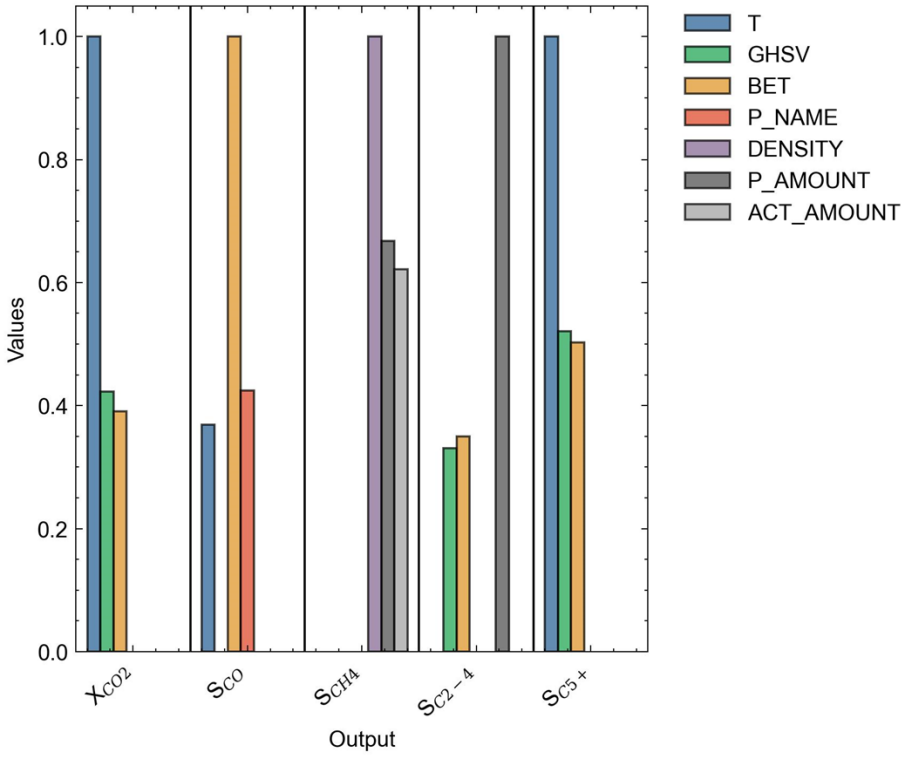

Figure 8.5. Feature importance ranking. Each bar represents the relative importance of an input feature (catalyst composition or operating condition) in the RF predictions. Reaction temperature, alkali promoter content, catalyst BET surface area, and GHSV emerge as the most influential factors governing CO_2 conversion and product selectivities.

Beyond identifying important features, the RF model's interpretability provides guidance on how these features affect outcomes. Partial dependence analysis (not shown) can further illuminate trends, for example, RF predictions indicated that increasing reaction temperature boosts CO_2 conversion but can reduce C_{7+} selectivity (shifting towards lighter products), whereas higher K promoter loadings tend to suppress methane formation in favor of heavier hydrocarbons. These insights align with known kinetics (higher temperatures favor methanation and reverse water-gas shift, while potassium promotes chain growth and CO formation). Thus, the RF not only predicts performance but also helps rationalize the catalyst behavior via data-driven evidence. This

interpretable aspect addresses a common challenge in catalyst modeling: understanding why a certain composition or condition is optimal. Recent literature emphasizes that such explainable ML, using tools like feature importance or SHAP, can accelerate catalyst innovation by revealing which factors to tune and how they drive performance [21]. In the context of CO_2 hydrogenation, our RF model provides a quantitative basis for focusing future efforts (e.g. optimizing promoter levels or operating temperature) to achieve desired outcomes.

8.2.2. Comparison with ANN Results

Compared to the previous chapter's ANN model (Section 8.2), the Random Forest approach demonstrated superior generalization on this dataset. While the ANN was powerful in fitting complex nonlinear relationships, it required careful regularization to avoid overfitting given the limited 92 data points. In contrast, the RF model, through its ensemble averaging of decision trees, inherently mitigated overfitting by reducing model variance. This is evidenced by the RF's small train-test performance gap: the model's R^2 on the test set was nearly as high as on the training set, unlike a baseline neural network which initially showed signs of memorizing the training data. Such behavior is consistent with broader findings that tree-based ensemble methods tend to excel in small-data regimes where deep neural networks struggle to achieve comparable accuracy. The literature on data-driven catalyst modeling also supports this trend - for example, SVM or RF models have been found to outperform ANNs on modest-sized catalyst datasets by avoiding the high complexity that can lead to ANN overfitting [14, 22].

Another noteworthy distinction is model interpretability. The ANN model, being a densely connected black box, offered limited direct insight into which inputs were driving the predictions (aside from ad-hoc sensitivity analyses). The RF model, on the other hand, provides clear importance metrics and allows extraction of rules (from individual trees) that can be interpreted in chemical terms. This transparency is a practical advantage: researchers can validate that the model's behavior aligns with known catalysis principles or use it to discover unexpected feature interactions [6]. Ultimately, the RF's better generalization and interpretability make it a more reliable choice for extrapolating catalyst trends from limited data. Indeed, an interpretable machine learning framework was recently shown to improve prediction accuracy (to R^2 ~0.96) while broadening the range of catalyst compositions considered, precisely because researchers could trust and understand the model's guidance. In summary, for the CO_2 hydrogenation dataset the RF proved to be a robust predictor that complements the ANN approach: it sacrifices a bit of the universal function approximation capacity of ANNs in exchange for stability and clarity, which is often a worthwhile trade-off in catalyst informatics when data are scarce.

8.2.3. Implications for Catalyst Design Workflows

The successful application of RF modeling to CO_2 hydrogenation performance has several practical implications for catalyst design. First, the strong prediction capability means that such models can be used as surrogate simulators for catalyst screening. Instead of trial-and-error experiments on every candidate, researchers can use the RF to rapidly predict which new catalyst compositions or operating condition combinations are likely to yield high CO_2 conversion or selectivity. This can guide the selection of experiments, focusing resources on the most promising areas of the catalyst formulation space. Notably, our RF model could be integrated with an

experimental design strategy: by identifying the top influencers (e.g. promoter content, temperature), one can design targeted experiments varying those factors to further improve performance. This approach aligns with emerging closed-loop catalyst development processes, where machine learning models propose candidates or conditions, experiments are performed, and the data feedback updates the model. Studies have demonstrated that even with moderate datasets, machine learning can capture complex performance trends and suggest optimal conditions for improved catalytic output [23]. For instance, in oxidative coupling of methane, an ensemble tree model captured yield trends with high fidelity (R^2 ~0.86) and could still make reliable recommendations with as few as 45 data points. This exemplifies how data-driven models help determine the next experimental steps and accelerate finding the best catalyst conditions.

Second, the interpretability of the RF offers a form of knowledge extraction that can directly inform catalyst design rules. By highlighting which features are most important and how they influence outcomes, the model outputs can suggest mechanisms or emphasize catalyst properties that deserve attention. In our case, the RF results underscored the importance of alkali promotion and sufficient residence time for boosting heavy product synthesis - information that could inspire modified catalyst recipes (e.g. adding a certain promoter level) or process adjustments (e.g. lower GHSV for higher hydrocarbon yield) [24]. Such insights, supported by the model, provide a data-backed rationale to make design decisions, thereby reducing reliance on purely empirical intuition. As noted in recent literature, combining efficient ML models with interpretability tools "gives insight into what factors are important for catalysts, and what needs to be improved in the catalyst design," ultimately accelerating research and making the development process more reliable [21]. This means future catalyst optimization can proceed in a more informed way: instead of blindly varying all parameters, scientists can focus on the key levers identified by the RF (for example, optimizing the Fe/K ratio or exploring support modifications that increase surface area) [21].

8.2.4. Conclusion

In conclusion, the Random Forest modeling of CO_2 hydrogenation catalysts not only provides accurate performance predictions but also integrates seamlessly into a catalyst design workflow. The model's strong generalization with limited data, combined with its ability to guide experiment planning and elucidate structure-property relationships, demonstrates the value of data-driven approaches in heterogeneous catalysis. Going forward, such models can be expanded with more data (or enhanced via transfer learning and active learning) to further improve their predictive power. Even in the present form, the RF model serves as a powerful decision-support tool for researchers aiming to rationally design and optimize catalysts for CO_2 conversion, thereby contributing to more efficient development of catalysts for sustainable fuel synthesis

ACT_ NAME	ACT_ REF	ACT_ AMOUNT	P_NAME	P_REF	P_AMOUNT	DENSITY	T	P	H_2_CO_2	GHSV	X$_{$CO_2$}$	S$_{CO}$	S$_{$CH_4$}$	S$_{$C_{2-4}$}$	S$_{$C_{5+}$}$	BET
Fe	1	92.6	K	1	7.4	3.03	300.00	25.00	3.00	560.00	41.70	6.00	10.30	27.80	56.00	19.20
Fe	1	92.6	K	1	7.4	3.03	300.00	25.00	4.50	560.00	51.10	4.70	13.90	33.60	47.70	19.20
Fe	1	92.6	K	1	7.4	3.03	300.00	25.00	6.00	560.00	63.90	3.10	16.40	35.40	45.00	19.20
Fe	1	100	K	1	7.4	3.15	300.00	25.00	3.00	560.00	30.80	15.70	30.10	38.40	15.80	19.20
Fe	1	92.6	K	1	7.4	3.03	300.00	25.00	3.00	560.00	41.70	6.00	10.30	27.80	56.00	19.20
Fe	1	80.7	K	1	19.3	2.69	300.00	25.00	3.00	560.00	37.80	7.30	8.30	21.40	62.90	19.20
Fe	1	67.5	K	1	32.5	2.31	300.00	25.00	3.00	560.00	35.20	9.00	7.40	18.80	64.80	19.20
95Fe-5Co	2	92.91	K	1	7.06	3.04	300.00	25.00	3.00	560.00	54.60	2.00	18.90	32.10	47.00	19.20
90Fe-10Co	3	93.47	K	1	6.72	3.06	300.00	25.00	3.00	560.00	57.20	1.60	22.40	32.20	43.80	19.20
95Fe-5Ru	4	92.91	K	1	7.06	3.04	300.00	25.00	3.00	560.00	47.10	3.10	16.40	27.10	53.40	19.20
75Fe	5	75	K	1	25	2.52	300.00	25.00	3.00	560.00	17.40	58.80	3.30	6.50	31.40	10.70
65Fe-35Co	6	82.15	K	1	17.85	2.73	300.00	25.00	3.00	560.00	30.30	12.30	30.80	19.80	37.10	10.50
79Fe-21Co	7	79.17	K	1	20.83	2.65	300.00	25.00	3.00	560.00	23.80	31.40	17.00	15.50	36.10	10.50
Fe	1	75	K	1	25	2.52	400.00	10.00	3.00	1120.00	16.50	83.10	6.40	1.40	9.00	5.70
Fe	1	75	K	1	25	2.52	400.00	10.00	3.00	1120.00	40.70	23.20	41.20	28.10	7.40	5.70
Fe	1	75	K	1	25	2.52	400.00	10.00	3.00	1120.00	39.50	31.90	25.40	24.60	18.10	5.70
Fe	1	75	K	1	25	2.52	400.00	10.00	3.00	1120.00	35.90	54.50	22.40	12.60	10.60	5.70
Fe	1	75	K	1	25	2.52	300.00	25.00	3.00	562.00	17.40	58.80	3.30	6.50	31.40	5.70
Fe	1	97.2	K	1	2.8	3.17	300.00	10.00	3.00	2700.00	48.50	10.60	15.00	35.00	39.40	5.70
Fe	1	9.9	K	1	0	1.79	340.00	20.00	3.00	2700.00	32.00	25.00	70.00	29.10	0.90	5.70
Fe	1	9.9	Na	2	1	1.78	340.00	20.00	3.00	2700.00	39.00	21.00	21.00	57.20	21.20	5.70
Fe	1	9.9	Lo	3	1	1.78	340.00	20.00	3.00	2700.00	26.00	42.00	68.00	31.40	0.60	5.70
Fe	1	9.9	K	1	1	1.78	340.00	20.00	3.00	2700.00	43.00	15.00	18.00	53.20	28.80	5.70
Fe	1	9.9	Rb	4	1	1.78	340.00	20.00	3.00	2700.00	31.00	15.00	19.00	51.00	30.00	5.70
Fe	1	9.9	Cs	5	1	1.78	340.00	20.00	3.00	2700.00	39.00	16.00	26.00	52.40	21.40	5.70
Fe	1	9.9	K	1	1	1.78	340.00	20.00	3.00	2700.00	7.10	92.00	72.00	26.60	1.40	5.70
Fe	1	9.9	K	1	1	1.78	340.00	20.00	3.00	2700.00	33.00	17.00	17.00	42.00	41.00	5.70
Fe	1	9.9	K	1	1	1.78	340.00	20.00	3.00	2700.00	21.00	55.00	22.00	50.20	27.80	5.70
Fe	1	9.9	K	1	1	1.78	340.00	20.00	3.00	2700.00	33.00	31.00	32.00	56.00	12.00	5.70
Fe	1	9.9	K	1	1	1.78	340.00	20.00	3.00	2700.00	35.00	12.00	36.00	44.00	30.00	5.70
Fe	1	10	K	1	1	1.78	400.00	30.00	3.00	3600.00	34.60	41.80	32.50	20.50	5.40	139.00
Fe	1	10	3Mn-K	6	4	1.74	400.00	30.00	3.00	3600.00	42.00	23.00	36.10	29.80	11.10	139.00
Fe	1	10	3Mo-K	7	4	1.74	400.00	30.00	3.00	3600.00	39.20	31.30	31.10	28.70	8.90	139.00

Fe	1	10	3Zn-K	8	4	1.74	400.00	30.00	3.00	3600.00	38.60	33.30	35.80	24.10	6.80	139.00
Fe	1	10	3Cu-K	9	4	1.74	400.00	30.00	3.00	3600.00	41.70	26.50	27.80	31.90	13.80	137.00
Fe	1	10	3Zr-K	10	4	1.74	400.00	30.00	3.00	3600.00	39.60	28.90	37.50	26.00	7.60	137.00
Fe	1	10	3Zn-K	11	4	1.74	400.00	30.00	3.00	3600.00	36.10	36.10	35.20	23.70	5.00	137.00
Fe	1	46.73	Cu	12	53.27	1.71	300.00	10.00	3.00	1800.00	18.10	31.90	2.70	21.30	44.10	10.98
Fe	1	100	Cu	12	0	3.25	300.00	10.00	3.00	1800.00	14.30	33.20	27.00	37.50	2.30	12.45
Fe	1	100	K	1	0	3.25	340.00	20.00	3.00	1200.00	5.60	12.00	54.56	33.44	0.79	54.00
Fe	1	99	K	1	1	3.22	340.00	20.00	3.00	1200.00	5.00	10.00	40.05	44.59	4.72	67.00
Fe	1	98	K	1	2	3.19	340.00	20.00	3.00	1200.00	37.00	5.80	24.08	50.74	8.77	67.00
Fe	1	95	K	1	5	3.10	340.00	20.00	3.00	1200.00	38.00	7.30	16.38	37.44	23.40	63.00
Fe	1	90	K	1	10	2.96	340.00	20.00	3.00	1200.00	27.00	7.20	19.58	46.28	22.43	54.00
Fe	1	84	K	1	16	2.79	340.00	20.00	3.00	1200.00	25.00	8.30	18.17	43.45	21.88	21.00
Fe	1	68	K	1	32	2.32	340.00	20.00	3.00	1200.00	25.00	20.00	17.04	33.37	20.24	21.00
Fe	1	95	K	1	5	3.10	340.00	20.00	3.00	1200.00	38.00	7.30	16.38	37.44	23.40	54.00
Fe	1	94.5	5K-05B	13	5.5	3.09	340.00	20.00	3.00	1200.00	43.00	6.40	17.82	42.12	20.25	60.00
Fe	1	94	5K-B	14	6	3.07	340.00	20.00	3.00	1200.00	38.00	7.60	18.17	45.82	14.69	95.00
Fe	1	92	5K-3B	15	8	3.02	340.00	20.00	3.00	1200.00	25.00	26.00	12.92	46.92	8.16	122.00
Fe	1	90	5K-5B	16	10	2.96	340.00	20.00	3.00	1200.00	23.00	29.00	12.35	46.80	6.44	117.00
Fe	1	89	5K-6B	17	11	2.93	340.00	20.00	3.00	1200.00	22.00	19.00	26.64	42.92	4.74	118.00
Fe	1	87	5K-8B	18	13	2.87	340.00	20.00	3.00	1200.00	21.00	21.00	38.25	34.50	2.33	120.00
Fe	1	100	Na	2	0	3.25	320.00	30.00	3.00	2000.00	29.30	16.60	50.30	30.40	2.60	57.80
Fe	1	99.92	Na	2	0.08	3.25	320.00	30.00	3.00	2000.00	35.70	15.10	17.70	44.30	22.90	60.10
Fe	1	99.84	Na	2	0.16	3.24	320.00	30.00	3.00	2000.00	38.40	13.60	13.70	45.40	27.30	62.30
Fe	1	99.57	Na	2	0.43	3.24	320.00	30.00	3.00	2000.00	39.60	14.00	13.60	46.50	26.00	68.00
Fe	1	98.82	Na	2	1.18	3.21	320.00	30.00	3.00	2000.00	40.50	13.50	13.70	46.80	26.00	52.90
Fe	1	92.97	Na	2	7.03	3.04	320.00	30.00	3.00	2000.00	40.00	14.20	14.80	47.40	23.70	39.00
Fe	1	20	K	1	0.91	1.94	340.00	20.00	3.00	1200.00	30.30	19.90	51.00	12.60	17.40	32.00
Fe	1	65.34	Na	2	2.44	2.66	320.00	30.00	3.00	4000.00	34.50	12.40	7.30	28.30	47.50	59.00
Fe	1	52.65	Na	2	0.5	2.48	320.00	30.00	3.00	4000.00	28.60	10.90	31.80	40.90	15.50	65.00
Fe	1	51.07	Na	2	2.68	2.42	320.00	30.00	3.00	4000.00	38.60	11.10	11.10	31.10	43.60	54.00
Fe	1	49.78	Na	2	4.25	2.38	320.00	30.00	3.00	4000.00	38.40	11.20	9.30	33.20	42.00	43.00
Fe	1	48.66	Na	2	5.79	2.34	320.00	30.00	3.00	4000.00	33.80	10.50	8.40	27.00	49.20	19.00
Fe	1	38.47	Na	2	20	2.00	320.00	30.00	3.00	4000.00	29.30	14.80	7.80	25.90	46.50	1.00
Fe	1	49.78	Na	2	4.25	2.38	320.00	30.00	3.00	4000.00	38.40	11.20	9.30	29.40	45.80	43.00
Fe	1	98.7	K	1	1.3	3.21	300.00	15.00	3.00	1160.00	43.50	6.80	10.10	26.80	56.10	25.00

Fe	1	98.7	04Mn-09K	19	1.3	3.21	300.00	15.00	3.00	1160.00	42.30	8.00	8.90	30.40	52.70	38.00
Fe	1	0.4	K	1	0.05	1.64	300.0	20.0	3.00	1769.29	21.3	25.4	11.1	51.6	11.9	75.0
Fe	1	0.4	K	1	0.05	1.64	320.0	20.0	3.00	1769.29	28.5	16.4	9.1	46.4	28.1	75.0
Fe	1	0.4	K	1	0.05	1.64	250.0	20.0	3.00	1769.29	9.5	13.1	10.7	44.9	31.3	75.0
Fe	1	0.4	K	1	0.05	1.64	300.0	20.0	3.00	1769.29	19.7	23.2	5.9	46.5	24.3	75.0
Fe	1	0.4	K	1	0.05	1.64	350.0	20.0	3.00	1769.29	28.0	23.6	7.0	47.9	21.6	75.0
Fe	1	0.3	K	1	0.05	1.63	275.0	20.0	4.00	3892.43	29.8	11.7	13.4	40.9	35.0	112.0
Fe	1	0.3	K	1	0.05	1.63	310.0	20.0	4.00	3892.43	31.5	22.6	10.3	37.2	30.3	112.0
Fe	1	0.3	K	1	0.05	1.63	350.0	20.0	4.00	3892.43	37.9	33.9	4.8	30.5	31.0	112.0
Fe	1	0.3	K	1	0.05	1.63	275.0	20.0	4.00	3892.43	15.0	37.8	12.2	45.2	5.1	87.0
Fe	1	0.3	K	1	0.05	1.63	310.0	20.0	4.00	3892.43	33.3	25.0	8.8	34.4	31.9	87.0
Fe	1	0.3	K	1	0.05	1.63	350.0	20.0	4.00	3892.43	47.2	16.9	7.6	39.2	36.2	87.0
Fe	1	0.3	K	1	0.05	1.63	275.0	20.0	3.00	3184.71	27.6	18.8	4.8	33.9	42.5	112.0
Fe	1	0.3	K	1	0.05	1.63	310.0	20.0	3.00	3184.71	31.6	12.5	10.3	42.4	34.7	112.0
Fe	1	0.3	K	1	0.05	1.63	350.0	20.0	3.00	3184.71	41.6	10.3	7.9	48.2	33.4	112.0
Fe	1	0.3	K	1	0.05	1.63	275.0	20.0	3.00	3184.71	17.6	22.7	11.8	37.3	32.8	87.0
Fe	1	0.3	K	1	0.05	1.63	310.0	20.0	3.00	3184.71	34.0	18.6	9.3	34.5	33.5	87.0
Fe	1	0.3	K	1	0.05	1.63	350.0	20.0	3.00	3184.71	43.1	10.6	9.3	48.6	31.2	87.0
Fe	1	0.3	K	1	0.05	1.63	275.0	20.0	3.20	1663.13	15.0	11.1	11.5	63.7	13.8	87.0
Fe	1	0.3	K	1	0.05	1.63	310.0	20.0	3.20	1663.13	44.8	7.1	7.3	46.5	38.8	87.0
Fe	1	0.3	K	1	0.05	1.63	350.0	20.0	3.20	1663.13	48.9	9.5	6.8	45.1	38.6	87.0
Fe	1	0.3	K	1	0.05	1.63	275.0	20.0	3.20	1663.13	19.6	22.5	8.5	48.6	20.3	112.0
Fe	1	0.3	K	1	0.05	1.63	310.0	20.0	3.20	1663.13	35.5	15.2	5.9	35.8	44.5	112.0
Fe	1	0.3	K	1	0.05	1.63	350.0	20.0	3.20	1663.13	45.5	8.2	5.2	40.7	45.7	112.0

Table 8.5. Summary of the CO_2 hydrogenation catalyst performance dataset used for Random Forest modeling. The dataset (92 entries) compiles various iron-based catalyst formulations (often Fe with small Co/Ru additions) with different promoters (K, Na, Cs, etc.) and textural properties. Key input variables include catalyst composition (active metal and promoter loadings), BET surface area, bulk density, reaction temperature (°C), pressure (bar), H_2/CO_2 feed ratio, and gas hourly space velocity (GHSV). Performance outputs comprise CO_2 conversion (X${CO₂}$) and product selectivities to CO (S${CO}$), CH_4 (S${CH₄}$), light hydrocarbons C_2-C_4 (S${C₂-₄}$), and gasoline-range C_{7+} (S$_{C₅+}$). The data spans a range of conditions (e.g. 250-350 °C, 1-30 bar, H_2/CO_2 ratios 2-6, GHSV 500-5000 h^{-1}).

Reference Chapter 8

[1] Chou Wonsuk Chung, Sunwoo Kim, Ali S. Al-Hunaidy, Hasan Imran, Aqil Jamal, Jay H. Lee, Identification of sustainable carbon capture and utilization (CCU) pathways using state-task network representation, Computers & Chemical Engineering, Volume 178, 2023.

[2] Mohajerani, S., Kumar, A., & Oni, A. O. (2018). A techno-economic assessment of gas-to-liquid and coal-to-liquid plants through the development of scale factors. Energy, 150, 681–693.

[3] Martín, N., & Cirujano, F. G. (2022). Multifunctional heterogeneous catalysts for the tandem CO_2 hydrogenation-Fischer Tropsch synthesis of gasoline. Journal of CO_2 Utilization, 65(August), 102176.

[4] Nadai, N., Melani, A., Souza, G., Nabeta, S., 2017. Equipment failure prediction based on neural network analysis incorporating maintainers inspection findings. https://doi.org/10.1109/RAM.2017.7889684.

[5] Adib, H., Haghbakhsh, R., Saidi, M., Takassi, M.A., Sharifi, F., Koolivand, M., Rahimpour, M.R., Keshtkari, S., 2013. Modeling and optimization of Fischer–Tropsch synthesis in the presence of Co (III)/Al_2O_3 catalyst using artificial neural networks and genetic algorithm. J. Nat. Gas Sci. Eng. 10, 14–24. https://doi.org/10.1016/j.jngse.2012.09.001.

[6] Chakkingal, A., Janssens, P., Poissonnier, J., Virginie, M., Khodakov, A.Y., Thybaut, J.W., 2022. Multi-output machine learning models for kinetic data evaluation : A Fischer–Tropsch synthesis case study. Chem. Eng. J. 446, 137186. https://doi.org/10.1016/j.cej.2022.137186.

[7] Sharma, B.K., Sharma, M.P., Kumar Roy, S., Kumar, S., Tendulkar, S.B., S. Tambe, S., Kulkarni, B.D., 1998. Fischer–Tropsch synthesis with Co/SiO_2–Al_2O_3 catalyst and steady-state modeling using artificial neural networks. Fuel 77, 1763–1768. https://doi.org/10.1016/S0016-2361(98)00110-0.

[8] Zimmermann, A.S., Mattedi, S., 2022. Feedforward and cascade forward networks for viscosity prediction for binary mixtures of ammonium-based ionic liquids and water. Fluid Phase Equilibria 556, 113416. https://doi.org/10.1016/j.fluid.2022.113416.

[9] Ogunbo, J.N., Alagbe, O.A., Oladapo, M.I., Shin, C., 2020. N-hidden layer artificial neural network architecture computer code: geophysical application example. Heliyon 6, e04108. https://doi.org/10.1016/j.heliyon.2020.e04108.

[10] Chen, J., Yang, C., 2019. Thermodynamic Equilibrium Analysis of Product Distribution in the Fischer–Tropsch Process Under Different Operating Conditions. ACS Omega 4, 22237–22244. https://doi.org/10.1021/acsomega.9b03707.

[11] Qingxin Yang, Andrey Skrypnik, Alexander Matvienko, Henrik Lund, Martin Holena, Evgenii V. Kondratenko,Revealing property-performance relationships for efficient CO_2 hydrogenation to higher hydrocarbons over Fe-based catalysts: Statistical analysis of literature data and its experimental validation,Applied Catalysis B: Environmental,Volume 282,2021,119554.

[12] Yulan Zhang, Longlong Ma, Junling Tu, Tiejun Wang, Xinjun Li, One-pot synthesis of promoted porous iron-based microspheres and its Fischer–Tropsch performance,Applied Catalysis A: General, Volume 499, 2015, Pages 139-145.

[13] Fernandes, F.A.N., 2006. Optimization of Fischer-Tropsch Synthesis Using Neural Networks. Chem. Eng. Technol. 29, 449–453. https://doi.org/10.1002/ceat.200500310.

[14] McCullough K, Williams T, Mingle K, Jamshidi P, Lauterbach J. High-throughput experimentation meets artificial intelligence: a new pathway to catalyst discovery. Phys Chem Chem Phys 2020;22:11174–96. https://doi.org/10.1039/D0CP00972E.

[15] Takahashi K, Ohyama J, Nishimura S, Fujima J, Takahashi L, Uno T, et al. Catalysts informatics: paradigm shift towards data-driven catalyst design. Chemical Communications. 2023 Jan 1;59(16):2222–38. Available from: https://doi.org/10.1039/d2cc05938j.

[16] Yang W, Fidelis TT, Sun WH. Machine learning in catalysis, from proposal to practicing. ACS Omega. 2019 Dec 24;5(1):83–8. Available from: https://doi.org/10.1021/acsomega.9b03673.

[17] Wang C, Wang B, Wang C, Li A, Chang Z, Wang R. A machine learning model with minimize feature parameters for multi-type hydrogen evolution catalyst prediction. Npj Computational Materials. 2025 Apr 24;11(1). Available from: https://doi.org/10.1038/s41524-025-01607-4.

[18] Yılmaz B, Oral B, Yıldırım R. Machine learning analysis of catalytic CO_2 methanation. International Journal of Hydrogen Energy 2023;48:24904–14. https://doi.org/10.1016/j.ijhydene.2022.12.197.

[19] Yılmaz B, Ceylan HB, Yaz G, Yıldırım R. Performance Assessment of Catalyst Materials for CO2 Hydrogenation to Methanol Using Explainable Machine Learning. Energy Fuels 2025:acs.energyfuels.5c00792. https://doi.org/10.1021/acs.energyfuels.5c00792.

[20] Liu H, Liu K, Zhu H, Guo W, Li Y. Explainable machine-learning predictions for catalysts in CO2 -assisted propane oxidative dehydrogenation. RSC Adv 2024;14:7276–82. https://doi.org/10.1039/D4RA00406J.

[21] Roh J, Park H, Kwon H, Joo C, Moon I, Cho H, et al. Interpretable machine learning framework for catalyst performance prediction and validation with dry reforming of methane. Applied Catalysis B: Environmental 2024;343:123454. https://doi.org/10.1016/j.apcatb.2023.123454.

[22] Lachaud, A., Adam, M., & Mišković, I. (2023). Comparative Study of Random Forest and Support Vector Machine Algorithms in Mineral Prospectivity Mapping with Limited Training Data. Minerals, 13(8), 1073. https://doi.org/10.3390/min13081073

[23] Takahashi K, Ohyama J, Nishimura S, Fujima J, Takahashi L, Uno T, et al. Catalysts informatics: paradigm shift towards data-driven catalyst design. Chem Commun 2023;59:2222–38. https://doi.org/10.1039/D2CC05938J.

[24] Fedorov A, Linke D. Data analysis of CO_2 hydrogenation catalysts for hydrocarbon production. Journal of CO_2 Utilization 2022;61:102034. https://doi.org/10.1016/j.jcou.2022.102034.